

Electrochemical Impedance Spectroscopy to Monitor the Hydration of
Cementitious Materials

HUSSAMELDIN MOHAMED TAHA ABDALGADIR

Submitted for the degree of Doctor of Philosophy

Heriot-Watt University

School of Energy Geoscience, Infrastructure and Society

May 2018

The copyright in this thesis is owned by the author. Any quotation from the thesis or use of any of the information contained in it must acknowledge this thesis as the source of the quotation or information.

ABSTRACT

The electrical properties of Portland cement, and cements containing supplementary cementitious materials (SCM), were obtained over the frequency range 1Hz-10MHz during both the initial 24-hours after gauging with water and up to 1 year. During the initial 24-hours period, the response was measured in terms of conductivity and permittivity with both parameters exhibiting significant temporal changes. It was also evident that whilst the conductivity increased only marginally with increasing frequency of applied electrical field, the permittivity decreased by several orders of magnitude over this range. Moreover, certain features of the permittivity response – which are related to bulk polarization processes – only revealed themselves in the higher frequency range (100kHz-1MHz), and went undetected at lower frequencies. The detailed frequency- and time- domain measurements allowed identification of several stages in the early hydration of cement-based materials and the response can be interpreted in terms of hydration kinetics, physico-chemical processes and microstructural development. It is shown that the methodology can be equally applied to cement-pastes and concretes.

In the hardening stage, the conductivity response showed a clear influence of the SCM type, the age of the samples and the used water binder ratio (w/b) in the mixes. The pore solution conductivity has been shown to have a significant effect on the conductivity values particularly at the high replaced mixes. The electrical permittivity showed two different polarization signals depending on the frequency range used, as at frequencies in the range of 100kHz-1MHz, the permittivity response is more related to the samples electrical conductivity, however at higher frequencies (1MHz-10MHz) the permittivity is influenced more by the SCM type and the replacement level in the mixes when w/b is constant.

The durability ranking which was obtained from the non-steady-state migration coefficient and the electrical conductivity, showed a strong linear relationship which is in contrast to the relationship between the ranking obtained from the formation factor. This would suggest that both the non-steady-state migration coefficient and the conductivity are affected by the pore solution conductivity of the mixes which, consequently, would give a false indication with regard to the real ranking of the mixes.

DEDICATION

For my mother's soul and my father who raised me on the values of honesty and hard work.

Acknowledgments

The author would like to gratefully acknowledge the research funding provided by Heriot-Watt University through the James Watt Scholarship from October 2013 to October 2016.

The author would also like to express his deep gratitude to all Heriot-Watt University staff for putting their experience and effort to facilitate whatever necessary to make the research journey as interesting and as fruitful as possible.

The author is very grateful for Professor William John McCarter for his supervision, guidance and patience through the research and for the detailed revision of the thesis.

The author would also like to deeply thank Dr Gerard Starrs for the helpful discussion and for putting his valuable expertise in terms of the measuring devices and data acquisition systems at the disposal of the research. Deep thanks are expressed to the School of Energy, Geoscience, Infrastructure and Society workshop staff represented in Mr Alastair M MacFarlane for helping in conducting the Isothermal calorimetry experiment, Mr Graham Sorley for helping in casting concrete samples as well as coring the concrete slabs for the rapid chloride migration test, Tom Stenhouse and David Murray for helping in preparing the electrodes arrays for conducting the electrical measurements.

Deep thanks are expressed for Dr Jim Buckman for his help with regards to the Environmental scanning electron microscopy facility at the Institute of Petroleum Engineering at Heriot-Watt University. Also, many thanks for Vicki Goodfellow from the School of Life Sciences for helping in the freeze-drying process.

Finally, I would like to thank my father Mohamed, my sister Samah, my brother Tarig and my nephew Eyad for their unconditional support throughout the research journey.

DECLARATION STATEMENT

ACADEMIC REGISTRY Research Thesis Submission

Name:	HUSSAMELDIN MOHAMED TAHA ABDALGADIR		
School:	EGIS		
Version: <i>(i.e. First, Resubmission, Final)</i>	Final	Degree Sought:	PhD

Declaration

In accordance with the appropriate regulations I hereby submit my thesis and I declare that:

- 1) the thesis embodies the results of my own work and has been composed by myself
- 2) where appropriate, I have made acknowledgement of the work of others and have made reference to work carried out in collaboration with other persons
- 3) the thesis is the correct version of the thesis for submission and is the same version as any electronic versions submitted*.
- 4) my thesis for the award referred to, deposited in the Heriot-Watt University Library, should be made available for loan or photocopying and be available via the Institutional Repository, subject to such conditions as the Librarian may require
- 5) I understand that as a student of the University I am required to abide by the Regulations of the University and to conform to its discipline.
- 6) I confirm that the thesis has been verified against plagiarism via an approved plagiarism detection application e.g. Turnitin.

* Please note that it is the responsibility of the candidate to ensure that the correct version of the thesis is submitted.

Signature of Candidate:		Date:	
-------------------------	--	-------	--

Submission

Submitted By <i>(name in capitals)</i> :	HUSSAMELDIN MOHAMED TAHA ABDALGADIR
Signature of Individual Submitting:	
Date Submitted:	

For Completion in the Student Service Centre (SSC)

Received in the SSC by <i>(name in capitals)</i> :			
<i>Method of Submission</i> <i>(Handed in to SSC; posted through internal/external mail):</i>			
<i>E-thesis Submitted (mandatory for final theses)</i>			
Signature:		Date:	

TABLE OF CONTENTS

ABSTRACT.....	i
DEDICATION.....	ii
Acknowledgments.....	iii
DECLARATION STATEMENT.....	iv
TABLE OF CONTENTS.....	v
LISTS OF TABLES.....	ix
LISTS OF FIGURES.....	xi
List of Mathematical Symbols.....	xxii
List of Abbreviations.....	xxiv
PUBLICATIONS.....	xxvi
Chapter 1 – Introduction.....	1
1.1 Background.....	1
1.2 Cement and concrete characterization testing techniques.....	2
1.3 Electrical measurements.....	3
1.4 Research significance.....	5
1.5 Research aim.....	5
1.6 Research objectives:.....	6
Chapter 2 – Cement Manufacture and the Hydration Process.....	7
2.1 Cement manufacturing process.....	7
2.1.1 Raw materials.....	7
2.1.2 Mixing and grinding.....	8
2.1.3 Burning process.....	9
2.1.4 Cooling process.....	9
2.1.5 Cement milling.....	9
2.2 Cement chemical composition.....	9
2.2.1 The Alite phase (C_3S).....	10
2.2.2 The Belite phase (C_2S).....	10
2.2.3 The Aluminate phase (C_3A).....	11
2.2.4 The Ferrite phase (C_4AF).....	11
2.3 Hydration reaction of cement phases.....	11
2.3.1 Hydration of Tricalcium silicate (C_3S).....	12

2.3.2	Hydration of Dicalcium silicate (C_2S)	17
2.3.3	Hydration of Tricalcium aluminate (C_3A)	17
2.3.4	Hydration of the Ferrite phase.....	19
2.4	Hydration reaction of Portland cement	19
2.4.1	Cement setting process.....	21
2.4.2	Pore structure development.....	21
2.5	Supplementary cementitious materials.....	23
2.5.1	Ground granulated blast furnace slag (GGBS)	23
2.5.2	Fly-ash.....	26
2.6	Summary	27
	Figures.....	29
	Tables	32
Chapter 3	– Electrical Property Measurements on Cementitious Materials	34
3.1	Introduction	34
3.2	Preliminaries.....	34
3.2.1	Impedance level.....	34
3.2.2	Permittivity Level.....	35
3.3	Review of electrical property measurements on cementitious materials	41
3.3.1	Early hydration (0-24hrs)	41
3.3.2	Hardening stage (>24hrs).....	49
3.4	Summary	56
	Figures.....	58
	Tables	75
Chapter 4	– Experimental Design and Data Acquisition	77
4.1	The early hydration stage	77
4.1.1	Materials and mixes	77
4.1.2	Mixing procedures.....	78
4.1.3	Samples sizes and dimensions	78
4.1.4	Tests and devices.....	79
4.1.5	Initial 24 hours bulk conductivity experimental estimation.....	83
4.2	The hardening stage	89

4.2.1	Materials and mixing procedure.....	90
4.2.2	Samples sizes and dimensions	90
4.2.3	Electrode configuration	91
4.2.4	Concrete mixes electrical measurements	98
4.2.5	Durability ranking	98
4.3	Summary	99
	Figures.....	101
	Tables	122
Chapter 5 – The electrical Properties of Cementitious Materials during Early Hydration		
	127
5.1	Introduction	127
5.2	Results	127
5.2.1	Early hydration electrical conductivity	127
5.2.2	Early hydration permittivity	131
5.3	Discussion	134
5.3.1	Conductivity of cement pastes	135
5.3.2	Permittivity of Cement pastes	143
5.3.3	Conductivity of GGBS pastes	151
5.3.4	Permittivity of GGBS pastes	152
5.3.5	Electrical response of Fly-ash pastes	153
5.3.6	Equivalent electrical circuit for cementitious pastes.....	154
5.3.7	Concrete mixes early hydration electrical response	160
5.3.8	Superplasticizers (SP) effect on the electrical response of concrete at the early hydration stage	162
5.4	Summary:	163
	Figures.....	165
	Tables	207
Chapter 6 – Electrical Properties of Cementitious Materials during Long-term Hardening		
	212
6.1	Bulk electrical conductivity	212
6.1.1	Formation Factor and Pore Solution Conductivity	214
6.2	Dispersion in permittivity and conductivity	216

6.2.1 Dispersion and temporal effects on relative permittivity	216
6.2.2 Hydration effect.....	217
6.2.3 Water/binder (w/b) ratio.....	218
6.3 Nyquist Plots and Equivalent Circuit Model.....	218
6.3.1 Bulk arc Characteristic Frequency (f_c)	219
6.3.2 Bulk arc CPE exponent (p).....	219
6.1.1 Concrete hardening stage EEC.....	220
6.4 Relation between the electrical response and mixes durability.....	225
6.1.2 Electrical measurements results and NT Build results comparison	226
6.5 Summary	227
Figures.....	229
Tables	249
Chapter 7 – Conclusions and Recommendations.....	251
7.1 Conclusions	251
7.2 Recommendations	254
Published Papers	257
References	290

LISTS OF TABLES

Table 2.1:	LSF, SR, AR of clinker produced in Germany adapted from (Bensted and Barnes, 2002).	32
Table 2.2:	Chemical composition for blast furnace slag in the UK (Bensted and Barnes, 2002).	32
Table 2.3:	Chemical composition of low calcium fly-ash (Taylor, 1997).	33
Table 3.1:	Formation factor results obtained by electrical conductivity method and by the two chamber diffusion method for 0.8w/b cement paste at the age of 7 days (Taffinder and Batchelor, 1993).	75
Table 3.2:	Permittivity values for one-year old saturated cement paste samples with different w/b.	75
Table 3.3:	Changes in Characteristic frequency, f_c , bulk frequency, f_{bulk} , electrode bulk frequency, f_{elec} as a function of sample age.	75
Table 3.4:	Bulk frequency ranges attained in different studies.	76
Table 3.5:	Bulk Frequency values at 68 hours for cement paste samples with 20% silica fume replacement (Christensen et al., 1994).	76
Table 4.1:	XRF for CEM I, GGBS and FA as obtained from suppliers.	122
Table 4.2:	Cement pastes mixes used through the early hydration.	122
Table 4.3:	Concrete mixes used for early hydration experiments.	123
Table 4.4:	Concrete mixes used for the hardening stage experiments.	124
Table 4.5:	Mean compressive strength for Set 1.	124
Table 4.6:	Mean compressive strength for Set 2.	125
Table 4.7:	Suggested ranges for concrete durability classification	125
Table 4.8:	Empirical concrete resistivity thresholds for protection of embedded steel reinforcement (adapted from (Langford and Broomfield, 1987; Broomfield, 2006)).	125
Table 4.9:	Circuit simulation parameters for PC and GGBS concrete mixes.	126
Table 5.1:	Product of the equivalent ionic conductivity (λ_i) and valance (z) for different ions.	207
Table 5.2:	Degree of hydration for the different w/b cement pastes mixes (0.30,0.35,0.45) at the age of the P point and at the acceleration stage peak.	207

Table 5.3:	Effect of different CaSO ₄ additions on the 0.35w/b cement paste with regard to the early conductivity peak values and age, and the conductivity rate peak age.	207
Table 5.4:	Relative permittivity values for the PC 0.3w/b, PC 0.35w/b and PC 0.45w/b at different frequencies (15mins).	207
Table 5.5:	Relative permittivity values for the PC 0.3w/b, PC 0.35w/b and PC 0.45w/b at different frequencies (10hrs).	208
Table 5.6:	Relative permittivity values for the PC 0.3w/b, PC 0.35w/b and PC 0.45w/b at different frequencies (20hrs).	208
Table 5.7:	Best fit parameter for the electric circuit in Figure 5.20 for the PC 0.3w/b, PC0.35w/b and PC0.45w/b at different ages.	208
Table 5.8:	Possible origins for different generated capacitance values adapted from (Irvine et al., 1990; Ford et al., 1998)	208
Table 5.9:	Best fitting parameters for the EEC in Figure 5.23 for the PC0.35w/b cement paste at of 15mins, 10hrs and 20hrs	209
Table 5.10:	Best fit parameters for the EEC at Figure 5.36 at 9 hrs for the pure paste mixes and GGBS replaced mixes.....	210
Table 5.11:	Best fit parameters for the 35%FA cement paste of 2hrs, 5hrs and 9hrs	211
Table 5.12:	Best fit parameters for the 65%FA cement paste at the ages of 2hrs, 5hrs and 9hrs.....	211
Table 6.1:	Best fit parameters for the experimental degree of hydration in Figure 6.3	249
Table 6.2:	Best fit parameters for the 0.35w/b PCC mixes.....	249
Table 6.3:	Best fit parameters for the 0.35w/b 35%GGBS mixes.	249
Table 6.4:	Best fit parameters for the 0.35w/b 65%GGBS mixes.	249
Table 6.5:	Best fit parameters for the 0.35w/b 35%FA mixes.	250
Table 6.6:	Results of pore solution conductivity, bulk conductivity and the non-steady state migration coefficient for the different concrete mixes at the age of 400 days.	250

LISTS OF FIGURES

Figure 2.1:	C ₃ S phase Rate of heat evolution through the hydration time.....	29
Figure 2.2:	CaO and SiO ₂ concentrations on the C-S-H phase solution (Taylor, 1997).	29
Figure 2.3:	Hydration kinetics for different cement phases (Hewlett, 2003).....	30
Figure 2.4:	Hydrates formations on the surface of a cement grain during hydration. (a) unhydrated cement grain with different composing phases; (b) at 10mins hydration, AFt short rods and aluminium gel start to appear on the surface of the grain due to C ₃ A reaction with gypsum; (c) at 10hrs age outer C-S-H hydration product forms on the ettringite short rods leaving 1µm gap from the surface of the cement grain; (e) at 18hrs gradual formation of AFm inside the hydration shell as well as the C-S-H inner product, (f) at 1-3days C-S-H inner product fills the gap between the outer product and the unhydrated cement grain (Taylor, 1997).	30
Figure 2.5:	Normalised heat evolution for Portland cement paste denoted S0A0, and 20%Fly-ash replaced paste denoted S0A20 at (a):0.35w/b, (b):0.4w/b and (c):0.5w/b (Langan et al., 2002).	31
Figure 3.1:	(a) Influence of the constant phase element (CPE) on the Nyquist plot—the solid line is the Nyquist plot for a pure capacitor (C = 10 ⁻¹⁰ F) in parallel with a resistor (R = 1.0 kΩ and the dashed line is a CPE (C ^o = 10 ⁻¹⁰ F s ⁻² and p = 0.8) in parallel with a resistor (R = 1.0 kΩ) (b) schematic diagram of Nyquist plot for a saturated porous material showing arc depression angle, α, phase angle, θ, and impedance, Z*(ω).....	58
Figure 3.2:	Polarization processes within homogenous materials: (a) Orientation polarization, (b) electronic and atomic polarization mechanisms, (c) Ionic polarization mechanism (Nyame and Illston, 1981; Feldman et al., 2015)...	59
Figure 3.3:	Polarization mechanisms occurrence through frequency ranges (adapted from Beek (2000)).	59
Figure 3.4:	Schematic diagram showing (a) Interfacial (or space-charge) polarization, and (b) Double-layer polarization.....	60
Figure 3.5:	Different models for electrodes double layer (a) Helmholtz model (b) Gouy-Chapman model and (c) Stern model (Martinsen and Grimnes, 2011).	61

Figure 3.6: Equivalent electrical circuit for electrode/sample polarization effect. (Schwan, 1963).	61
Figure 3.7: Specific electrical conductivity through time for 0.27w/b Portland cement pastes (Shimizu, 1928).	62
Figure 3.8: Electrical resistivity response during the early hydration period for (a) cement pastes with different alkali content, and (b) pure cement components (Monfore, 1968).	62
Figure 3.9: Change on the permittivity, resistivity and temperature over the initial 24 hrs since hydration initiation (McCarter and Afshar, 1985).	63
Figure 3.10: Effect of the measuring electrical frequency on the electrical resistivity of cement pastes (McCarter, 1987).	63
Figure 3.11: Relation between gel-space ration and the percentage frequency effect PFE for different w/b cement paste at the age of 24hrs (McCarter, 1987).	64
Figure 3.12: Conductivity and its derivative diagram for a 0.3 w/b OPC paste illustrating the early hydration stages (Sanish et al., 2013).	64
Figure 3.13: Electrical resistivity of pore fluid for different Portland cement samples with: 20% FA replacement (L-P0.4FA20), 10% FA replacement (L-P0.4FA10) and Pure Portland cement (L-P0.4)(Xiao and Li, 2008). ..	65
Figure 3.14: Resistivity of concrete mixes with different aggregate volumetric fraction ranging from 0%-70% (Wei and Xiao, 2011).	65
Figure 3.15: Normalised conductivity plot with time for concrete samples with different aggregate contents (Princigallo et al., 2003).	66
Figure 3.16: Permittivity/Conductivity dispersion diagrams for 0.35w/b cement paste at the ages of 23, 35, 52hrs. (Taylor and Arulanandan, 1974).	66
Figure 3.17: Relative permittivity at 10GHz during the early hydration period and the heat of hydration for 0.4w/b cement paste (Moukwa et al., 1991).	67
Figure 3.18: Permittivity variation through time for cement pastes at different	67
Figure 3.19: Capacitance and temperature variations through time for aluminate cement at 20°C ambient temperature (Nyame and Illston, 1981; Smith et al., 2002).	68
Figure 3.20: Enhancement of permittivity values due to addition of fly-ash to the Portland cement paste where, P1: pure Portland cement paste, P2: 10 % replacement fly-ash, P3: 25% replacement fly-ash, P4: 40% replacement fly-ash, P5: paste with micro silica addition. Measurements were taken at the age of 60mins (McCarter et al., 1999).	68

Figure 3.21: Permittivity response (at 9.5GHz) through time due to different slag percentages replacements to cement pastes (Zhang et al., 1995).	69
Figure 3.22: Nyquist plot for cement paste of 0.3w/b ratio during the early hydration period (Manchiryal and Neithalath, 2009).....	69
Figure 3.23: Plateau region which formed in the impedance complex plot due to the inclusion of fly-ash in the Portland cement, mortars and concrete mixes at the age of 60 minutes (McCarter et al., 1999).	70
Figure 3.24: Capacitance, C_p , and conductance, G_p , frequency sweep through time for 0.5 w/b cement paste samples (Adapted from Camp and Bilotta (1989)).	70
Figure 3.25: Conductivity measurement for a Portland cement concrete through time at different depths from the surface under cyclic wetting and drying (McCarter et al., 2003).	71
Figure 3.26: Comparison between the predicted permeability results through Katz-Thompson equation, and the experimental data from Nyame and Illston (1981) and Illston (1980).	71
Figure 3.27: Influence of w/b on the permittivity of hardened cement-paste (Christensen, 1993). Values are presented at 11-months hydration.	72
Figure 3.28: Effect of silica fume addition on the relative permittivity of Portland cement pastes (a) at different frequencies and (b) through time (Gu and Beaudoin, 1997) (Christensen, 1993).....	72
Figure 3.29: Electrodes / Bulk Impedance representation in the complex plane	73
Figure 3.30: Different equivalent electrical circuits used to model the response of cementitious materials after (a) Kim et al. (1995) (b) Andrade et al. (1999) (c) (Cabeza et al., 2002; Cabeza et al., 2003; Cabeza et al., 2006) (d). Cruz et al. (2013) (e) Macphee et al. (1997) (f) Tang et al. (2014).....	74
Figure 4.1: Diagrammatic representation of the experimental programme.	101
Figure 4.2: (a) Plexiglass cuboidal cell, (b) early hydration cell with sample and electrodes, and (c) X-X` cross-section showing positioning of electrodes and thermistor.	102
Figure 4.3: Early hydration cell for concrete.	103
Figure 4.4: Calorimeter can for paste sample.....	103
Figure 4.5: Schematic diagram of the connection between the PC, impedance analyser and the sample.	104
Figure 4.6: Temperature logger and multiplexer.....	104

Figure 4.7: Calorimeter parts (a) acrylic calorimeter, and (b) cross-section for the polypropylene container with the sample and the calorimeter inside.....	105
Figure 4.8: Variation in frequency at which bulk conductance can be obtained over the initial 24-hours for PC pastes: 0.35w/b, 0.45w/b and 0.45w/b.....	106
Figure 4.9: Variation in frequency at which bulk conductance can be obtained over the initial 24-hours for GGBS pastes: 35%, 50% and 65% (0.35w/b).	106
Figure 4.10: Variation (%) from the DC conductance of the samples as a function of time and frequency for, (a) PC 0.3w/b, (b) PC 0.35w/b and (c) PC 0.45w/b.	107
Figure 4.11: +5% upper frequency limit window conductance difference through frequencies and time, and -5% lower frequency limit window electrical conductance difference through frequency and time for the 0.3 w/b, 0.35w/b and 0.45w/b cement pastes.	108
Figure 4.12: Percentage difference in the electrical conductance from the DC conductance through time recorded at the frequencies (a) 100kHz and (b) 1MHz for the 0.3, 0.35, 0.45w/b cement pastes.	108
Figure 4.13: The variation (%) from the DC conductance of the samples as a function of time and frequency for (a) 35% GGBS 0.35w/b (b) 50% GGBS 0.35w/b, and (c) 65% GGBS 0.35w/b.	109
Figure 4.14: +5% upper frequency limit window conductance difference through frequencies and time and (-5% Lower) electrical conductance difference through frequency and time for the 0.35w/b 35%, 50% and 65% GGBS replaced cement pastes.....	110
Figure 4.15: Percentage difference of the electrical conductance from the DC conductance through time recorded at the frequencies (a) 10kHz (b) 100kHz (c) 1MHz for the 35% GGBS, 50% GGBS and 65% GGBS (0.35w/b)....	111
Figure 4.16: (a) Schematic of testing arrangement for two-point AC end-to-end measurements and (b) laboratory setup.	112
Figure 4.17: (a) Schematic of testing arrangement for four-point measurements and (b) laboratory setup.....	112
Figure 4.18: Nyquist plot for synthetic sponges placed between the electrodes with saturating liquids indicated.	113
Figure 4.19: (a) Nyquist, and (b) Bode plots for PC concrete mixes (error bars are presented on Bode plot and represent \pm one standard deviation). (Note:	

where error bars to be missing the data marker is larger than the error bar).	113
Figure 4.20: (a) Nyquist and (b) Bode plots for GGBS concrete mixes (error bars are presented on Bode plot and represent \pm one standard deviation).	114
Figure 4.21: (a) Nyquist, and (b) Bode plots for FA concrete mixes (error bars are presented on Bode plot and represent \pm one standard deviation).	115
Figure 4.22: Proposed circuit model for electrode–sponge–specimen.	115
Figure 4.23: Measured and simulated responses for (a) PC concrete (w/b = 0.65) and (b) GGBS concrete (w/b = 0.35). The simulated response is based on the model presented in Figure 4.22, and circuit parameters in Table 4.9.	116
Figure 4.24: Influence of sponge saturation liquid on (a) Nyquist and (b) Bode plots for PC concrete (w/b = 0.65).	117
Figure 4.25: Influence of sponge saturation liquid on (a) Nyquist, and (b) Bode plots for GGBS concrete (w/b = 0.65).	118
Figure 4.26: Influence of sponge saturation liquid on (a) Nyquist, and (b) Bode plots for FA concrete (w/b = 0.65).	119
Figure 4.27: Bode plots obtained using the four-point testing arrangement presented in figure 2 for (a) PC concrete (w/b = 0.65) and (b) GGBS concrete (w/b = 0.35).	120
Figure 4.28: Arrangement of the migration set-up.	121
Figure 5.1: (a) and (b) conductivity recorded at 100kHz, (c) conductivity derivative, $d\sigma/dt$, and (d) temperature rise for different w/b cement pastes through the first 24h from gauging.	165
Figure 5.2: Conductivity and Temperature rise through the first 24hrs for PC 0.35w/b.	166
Figure 5.3: (a) and (b) conductivity recorded at 100kHz (c) conductivity derivative, $d\sigma/dt$, and (d) temperature rise for 35% ,50%,65% GGBS replaced pastes at 0.35w/b through the initial 24h after gauging.	167
Figure 5.4: PC Relative permittivity at selected frequencies during the initial 24hrs for cement pastes(a) 0.3w/b (b) 0.35w/b and (c) 0.45w/b. (legend in (a))....	168
Figure 5.5: Normalised permittivity for PC 0.3w/b paste response through time and frequency (1Hz-1MHz) for the first 24hrs (a) 1-10Hz, (b) 10-100Hz, (c) 100Hz-1kHz, (d) 1kHz-10kHz, (e) 10kHz-100kHz and (f) 100kHz-1MHz.	169

Figure 5.6: Normalised permittivity for PC 0.35w/b paste response through time and frequency (1Hz-1MHz) for the first 24hrs (a) 1-10Hz, (b) 10-100Hz, (c) 100Hz-1kHz, (d) 1kHz-10kHz, (e) 10kHz-100kHz and (f) 100kHz-1MHz.	170
Figure 5.7: Normalised permittivity for PC 0.45w/b paste response through time and frequency (1Hz-1MHz) for the first 24hrs (a) 1-10Hz, (b) 10-100Hz, (c) 100Hz-1kHz, (d) 1kHz-10kHz, (e) 10kHz-100kHz and (f) 100kHz-1MHz.	171
Figure 5.8: Selected frequencies relative permittivity response during the early 24hrs of the samples ages for the (a) 35%GGBS 0.35w/b (b) 50%GGBS 0.35w/b (c) 65%GGBS 0.35w/b [legend in (a)].....	172
Figure 5.9: Normalised permittivity for 35%GGBS 0.35w/b paste response through time and frequency (1Hz-1MHz) for the first 24hrs (a) 1-10Hz, (b) 10-100Hz, (c) 100Hz-1kHz, (d) 1kHz-10kHz, (e) 10kHz-100kHz and (f) 100kHz-1MHz.	173
Figure 5.10: Normalised permittivity for 50%GGBS 0.35w/b paste response through time and frequency (1Hz-1MHz) for the first 24hrs (a) 1-10Hz, (b) 10-100Hz, (c) 100Hz-1kHz, (d) 1kHz-10kHz, (e) 10kHz-100kHz and (f) 100kHz-1MHz.	174
Figure 5.11: Normalised permittivity for 65%GGBS 0.35w/b paste response through time and frequency (1Hz-1MHz) for the first 24hrs (a) 1-10Hz, (b) 10-100Hz, (c) 100Hz-1kHz, (d) 1kHz-10kHz, (e) 10kHz-100kHz and (f) 100kHz-1MHz.	175
Figure 5.12: Concentration through time for (a) C ₃ S paste and (b) for Portland cement paste (Double et al., 1983).....	176
Figure 5.13: Aqueous phase Calcium and silicon concentration during the early hydration period for: (a) 0.4w/b cement paste, (b)0.7w/b cement paste (Kelzenberg et al., 1998).....	176
Figure 5.14: Relation between Gibbs free energy of dissolution and dissolution rates of minerals (Lasaga and Lutge, 2001; Nicoleau et al., 2013)	176
Figure 5.15: Conductivity rate, $d\sigma/dt$, and heat emission rate, dQ/dt , for (a) PC 0.30w/b, (b) PC 0.35w/b, and (c) PC 0.45w/b.....	177
Figure 5.16: Nucleation and growth of hydration product on the surface of the cement particles through the hydration reaction	178

Figure 5.17: (a) Conductivity (σ), (b) conductivity rate ($d\sigma/dt$) and (c) Heat emission rate (dQ/dt) for 0.35w/b cement paste and PC0.35 w/b with two different percentages calcium sulphate additions, 0.5% and 2%.	179
Figure 5.18: Dispersion plots for permittivity and conductivity for PC 0.30w/b, PC0.35w/b and PC 0.45 w/b at the ages of 15mins ,10hrs and 20hrs. The characteristic frequency for conductivity dispersion is indicated.....	180
Figure 5.19: Dielectric loss ϵ'' for (a) PC 0.3w/b; (b) PC 0.35w/b and(c) PC 0.45w/b at the ages of 15mins, 10hrs and 20hrs. The characteristic frequency, f_c , is indicated.....	181
Figure 5.20: Electrical circuit used to model the low-frequency relaxation processes in the measured system	181
Figure 5.21: (a)Typical Nyquist plot for PC0.30w/b at 9hrs age, (b) simulated electrode processes response by EEC in Figure 5.20. Bulk frequency and the characteristic frequency are indicated in the figures.	182
Figure 5.22: PC0.30w/b experimental and fitted response according to the EEC in Figure 5.20 for the relative permittivity and imaginary dielectric constant at the ages of (a) 15mins (b) 10hrs and (c) 20hrs.	182
Figure 5.23: Equivalent Electrical circuit used to correct for the EP effect on the obtained electrical response for the different w/b cement pastes samples.	183
Figure 5.24: Electrical impedance real-part and the phase angle fitted with the EEC in Figure 5.23 for the PC0.30w/b cement paste at the ages of (a) 15mins, (b) 10hrs and (c) 20hrs.	183
Figure 5.25: Normalised Permittivity response through time for PC 0.30w/b (a) Before EP correction (b) After EP correction (c) Normalised Permittivity response through time for PC 0.35w/b after EP correction (d) Normalised Permittivity response through time for PC 0.45w/b after EP correction.	184
Figure 5.26: Illustration of the different features appearing on the normalised permittivity response ϵ_N during the early hydration period for PC0.35w/b, together with the derivative of the electrical conductivity $d\sigma/dt$, and the calorimeter heat emission rate dQ/dt	185
Figure 5.27: ESEM images at for PC0.35w/b at the ages of (a) and (b): 11mins, (c) and (d): 2hrs, (e) and (f): 5.5hrs.....	186
Figure 5.28: Normalised permittivity through the first 25hrs for the PC0.w/b +0.5% gypsum at different frequencies for (a): electrode uncorrected response and (b): corrected response.....	187

Figure 5.29: Normalised permittivity through the first 25hrs for the PC0.35w/b +2% gypsum at different frequencies for (a) EP uncorrected (b) corrected. ...	187
Figure 5.30: ESEM images for PC0.35w/b at point E at the age of 8hrs.....	188
Figure 5.31: Conductivity rate, $d\sigma/dt$, and heat emission rate, dQ/dt , for (a) 35%GGBS 0.35w/b, (b) 50%GGBS 0.35w/b, and (c) 65%GGBS 0.35w/b.....	189
Figure 5.32: Electrode polarization corrected normalised permittivity through the first 25hrs for the (a) 35%GGBS 0.35w/b (b) 50%GGBS 0.35w/b and (c) 65%GGBS 0.35w/b pastes at different frequencies.....	190
Figure 5.33: Normalised permittivity through time for the (a) PC0.35w/b (b) 35%GGBS0.35w/b, (c) 50%GGBS0.35w/b, and (d) 65% GGBS 0.35w/b... ..	191
Figure 5.34: Conductivity and heat emission rate for the first 100hrs for pastes (a) PC0.35w/b, and (b) 65%GGBS 0.35w/b.	191
Figure 5.35: (a) Electric conductivity and heat emission (a) Normalised permittivity at 100kHz, 200kHz, 500kHz and 1MHz response for 35% FA 0.35W/b paste.	192
Figure 5.36: Equivalent electrical circuit proposed for the early hydration period of cement pastes.	192
Figure 5.37: Typical Nyquist plots for pastes, 9hrs after mixing, (a) PC pastes, (b) GGBS pastes.....	193
Figure 5.38: Connected liquid phase EEC related electrical parameters (a) G_e (b) C_{oe} which is the CPE_e coefficient, and (c) p_e ; particle related electrical parameters (d) G_p , and (e) C_p for the PC0.30w/b, PC0.35w/b and PC0.45w/b cement pastes.	194
Figure 5.39: Connected liquid phase EEC related electrical parameters (a) G_e (b) C_{oe} which is the CPE_e coefficient, and (c) p_e ; particle related electrical parameters (d) G_p , and (e) C_p for the 35%GGBS, 50%GGBS and the 65%GGBS replaced cement pastes.....	195
Figure 5.40: Salient points on the PC0.35w/b EEC electrical parameters response for (a) G_p and C_p and dQ/dt responses through time, and (b) p_e , C_{oe} responses through time.....	196
Figure 5.41: Nyquist plot for cement pastes, PC0.35w/b, 35%FA0.35w/b and 65%FA0.35w/b at the age of 2hrs.	197

Figure 5.42: (a) Permittivity through frequency for the PC0.35w/b, 35%FA0.35w/b and 65%FA0.35w/b at the age of 2hrs (b) an enlargement for the permittivity in the frequency range between 10kHz- 10MHz.	198
Figure 5.43: (a)Proposed EEC for the early hydration period of fly-ash replaced pastes, (b) experimental data at different ages for the 65%Fa paste and their related best fitting simulations.	199
Figure 5.44: 35%FA 0.35w/b early hydration EEC parameters response through time the first 25 hours of the samples age.	200
Figure 5.45: ESEM images (a): 11 mins (b): 5.5 hours, and (c) 5.5 hours for PC0.35w/b includes dispersed fly-ash particles.	201
Figure 5.46: Conductivity of concrete mixes at 100kHz and temperature through the first 24hrs after mixing for (a) Portland cement, (b) 35%GGBS, (c) 65%GGBS and (d) 35%FA concrete mixes at 0.45w/b.....	202
Figure 5.47: Normalised permittivity at 100kHz, 200kHz, 500kHz and 1MHz for, (a) Portland cement (b) 35%GGBS, (c) 65%GGBS and (d) 35%FA concrete mixes at 0.45w/b.	203
Figure 5.48: (a) Conductivity, (b) temperature (c) conductivity derivative, $d\sigma/dt$, through time, and (d) normalised permittivity, ϵ_N , for 0.45w/b Portland cement concrete mix with 1% SP addition and without SP addition.	204
Figure 5.49: (a) Conductivity, (b) temperature (c) conductivity derivative, $d\sigma/dt$, through time, and (d) normalised permittivity, ϵ_N , for 0.45w/b 35%GGBS replaced concrete mix with 1% SP addition and without SP addition.	205
Figure 5.50: (a) Conductivity (b) Temperature (c) conductivity derivative $d\sigma/dt$ through time and (d) normalised permittivity ϵ_N for 0.45w/b 65%GGBS replaced concrete mix with 1% SP addition and without SP addition.	206
Figure 6.1: Conductivity during hardening stage for (a) 0.35w/b, (b) 0.45w/b and (c) 0.65w/b concrete mixes.	229
Figure 6.2: Pore size distribution in hydrated cement pastes for (a) 0.7w/b at different ages, and (b) for different w/b at 28 days age after (Mehta and Monteiro, 2013).	230
Figure 6.3: Degree of hydration experimental data from isothermal calorimetric test and their pertinent fitting results through the first 160 hrs for the different pastes samples.....	230
Figure 6.4: Pore solution conductivity for (a):0.35w/b (b):0.45w/b and (c):0.65w/b. concrete mixes.	231

Figure 6.5:	1/F response through time for (a):0.35w/b mixes, (b):0.45w/b mixes and (c):0.65w/b mixes.	232
Figure 6.6:	Electrical permittivity/conductivity for 0.35w/b (a) PCC, (b) 35% GGBS, (c) 65% GGBS and (d) 35%FA at 28,180 and 360 days. [legend given in (a)]... ..	233
Figure 6.7:	Relative permittivity at (a) 100kHz, (b) 500kHz, (c) 1MHz and (d) 5MHz for different concrete mixes at 0.35w/b.	234
Figure 6.8:	Relative permittivity at (a) 100kHz, (b) 500kHz, (c) 1MHz and (d) 5MHz for different concrete mixes at 0.45w/b.	235
Figure 6.9:	Relative permittivity at (a) 100kHz, (b) 500kHz, (c) 1MHz and (d) 5MHz for different concrete mixes at 0.65w/b.	236
Figure 6.10:	Nyquist plot using a two-point embedded electrode configuration Nyquist plots for (a) 0.35w/b Portland cement concrete mix, (b) 35% GGBS concrete mix (c) 65% GGBS concrete mix and (d) 35%FA concrete mix.	237
Figure 6.11:	Nyquist plots using a two-point end-to-end electrode configuration for 0.35w/b concretes (a) Portland cement concrete mix, (b) 35% GGBS concrete mix (c) 65% GGBS concrete mix and (d) 35%FA concrete mix..... ..	238
Figure 6.12:	Nyquist plot using the two-point end-to-end configuration for 0.35, 0.45, 0.65 w/b mixes at 28-days (a) PCC concrete, (b) 35% GGBS concrete (c) 65% GGBS concrete and (d) 35%FA concrete.	239
Figure 6.13:	Bulk arc Characteristic Frequency response through time for (a): 0.35w/b (b) 0.45w/b and (c) 0.65w/b concrete mixes.	240
Figure 6.14:	Bulk arc CPE exponent p response through time for (a) 0.35w/b (b) 0.45w/b and (c) 0.65w/b concrete mixes	240
Figure 6.15:	Equivalent electrical circuit used to model the electrical response of concrete mixes.	241
Figure 6.16:	Experimental data fitting by the EEC in figure 6.15 for (a) PCC0.35w/b, (b) 35% GGBS0.35w/b, (c) 65% GGBS0.35w/b and (d) 35%FA0.35w/concrete mixes at different ages	242
Figure 6.17:	Effect of different SCM types on the EEC electrical parameters through time for the 0.35w/b concrete mixes.....	243
Figure 6.18:	Effect of different SCM types on the EEC electrical parameters through time for the 0.45w/b concrete mixes.....	244

Figure 6.19: Effect of different SCM types on the EEC electrical parameters through time for the 0.65w/b concrete mixes.....	245
Figure 6.20: (a) non-steady state diffusion coefficient, (b) bulk conductivity, and (c) 1/F for all the mixes at the age of 415 days.	246
Figure 6.21: Relation between non-steady state diffusion coefficient and (a) bulk conductivity (b) The inverse of the formation factor.....	247
Figure 6.22: Relation between w/b and (a) non-steady state diffusion coefficient (b) The inverse of the formation factor.....	248

List of Mathematical Symbols

- α : Degree of hydration (%).
- α_{ult} : Ultimate degree of hydration (%).
- β : Pore tortuosity parameter (dimensionless)
- C_o : Coefficient of constant phase element ($F s^{p-1}$).
- C : Capacitance (F).
- C_c : Cementitious material content (unit weight).
- c_i : Concentration of the charges (mol/l).
- χ : Dielectric susceptibility of the material (dimensionless)
- D : Total charge density at the electrodes (Electric displacement) (C/m^2).
- D_o : The diffusivity of ion at infinite dilution (equals $2.03 \times 10^{-9} m^2/sec$ at $25^\circ C$ for the chloride ion).
- D_{eff} : Effective chloride diffusion coefficient (m^2/s).
- D_{nssm} : Non-steady state migration coefficient (m^2/s).
- E_o : Electric field amplitude (V/m).
- ϵ_o : Vacuum permittivity ($8.854 \times 10^{-12} F/m$)
- $\epsilon''(\omega)$: Electrical permittivity imaginary part (loss) (F/m).
- $\epsilon'(\omega)$: Electrical permittivity real part (F/m).
- $\epsilon^*(\omega)$: Complex permittivity (F/m).
- ϵ_N : Normalised relative permittivity (dimensionless).
- ϵ_r : Relative permittivity (dimensionless).
- F : Formation factor (dimensionless).
- G : Electrical conductance (S).
- H_{cem} : Heat emitted per unit mass cement (J/gm).
- H_T : Total heat emitted at 100% hydration degree for the cementitious material (J).
- H_u : Heat emitted per unit weight cementitious material (J/gm).
- k' : Permeability (m^2).
- K_1 : First calorimeter constant (watts/mV).
- K_2 : Second calorimeter constant (J/mV).
- k_B : Boltzmann constant (J/K).
- L_c : Energy loss rate due to electrical conduction ($J/s.m^3$).
- L_D : Energy loss rate due to polarization process ($J/s.m^3$).
- λ_D : The characteristic length of the diffused double layer (nm).
- λ_i : Equivalent ionic conductivity ($cm^2 S/mol$).

- ω : Angular frequency (radians).
 P : Polarization density in the dielectric material (C/m^2);
 p : Constant phase element exponent ($0 < p < 1$).
 ϕ_c : Volume fraction of the capillary porosity (%).
 R : Electrical resistance (Ohm).
 ρ : Electrical resistivity (Ohm.m).
 σ_o : Pore solution conductivity (S/m).
 σ : Bulk conductivity (S/m).
 $\sigma(\omega)$: Electrical conductivity at angular frequency ω (S/m).
 T : Temperature ($^{\circ}C$).
 θ : Phase angle (degree).
 U : Absolute value of the applied voltage (V).
 V : Volume fraction of the suspended resistive particles.
 V_{ps} : Volume of pore solution (l/kg).
 W : Rate of heat production (Watts).
 x_d : Average value of chloride penetration depth (mm).
 $Z^*(\omega)$: Complex electrical impedance (ohm).
 $Z'(\omega)$: Electrical impedance real component (Ohm).
 $Z''(\omega)$: Electrical impedance imaginary or reactive component (Ohm).
 z_i : charge valance.

List of Abbreviations

AC	: Alternating current.
AFm	: Monosulfoaluminate.
AFt	: Ettringite.
A _R	: Alumina ratio in the raw cement meal.
BSE	: Back scatter scanning electron microscopy.
C ₂ S	: Dicalcium silicate.
C ₃ A	: Tricalcium aluminate.
C ₃ S	: Tricalcium silicate.
C ₄ AF	: Tetracalcium aluminoferrite .
CH	: Calcium hydroxide.
C-S-H	: Calcium silicate hydrate.
d _c	: Critical pore diameter.
DC	: Direct current.
EEC	: Equivalent electrical circuit.
EP	: Electrode polarization.
ESCA	: Electron spectroscopy for chemical analysis technique.
ESEM	: Environmental scanning electron microscopy.
FA	: Fly-Ash.
FRA	: Frequency analyser.
GGBS	: Ground granulated blast furnace slag.
ICC	: Isothermal conduction calorimeter.
ITZ	: Interface transition zone.
LSF	: Lime saturation factor.
MIP	: Mercury intrusion porosimetry.
NAD	: Nitrogen adsorption/desorption.
OPC	: Ordinary Portland cement.
PRC	: Pore-reduced cement paste.
RCMT	: Rapid chloride migration test.
RCPT	: Rapid chloride penetration test.
SCM	: Supplementary cementitious material.
SEM	: Scanning electron microscopy.
SP	: Superplasticizers.
S _R	: Silica ratio.

STEM : Scanning transition electron microscopy.

TDR : Time domain reflectometry.

TGA : Thermogravimetric analysis techniques.

w/b : Water binder ratio.

XRD : X-Ray Diffraction.

PUBLICATIONS

- 1. TAHA, H., MCCARTER, WJ, SURYANTO, B & STARRS, G 2017. Frequency- and Time- Domain Dependency of Electrical Properties of Cement-Based Materials During Early Hydration. *Advances in Civil Engineering Materials*, 6 (2), 65-83.**
- 2. MCCARTER, W., TAHA, H., SURYANTO, B. & STARRS, G. 2015. Two-point concrete resistivity measurements: interfacial phenomena at the electrode–concrete contact zone. *Measurement Science and Technology*, 26, 085007, 13pp.**

Chapter 1 – Introduction

1.1 Background

Throughout history, different adhesive materials have been used by ancient civilizations to provide bonding strength between fragments of construction materials. The ancient Egyptians (3000 BC) used Nile mud with and without chopped straw to build brick walls; they also used burnt gypsum as an alternative adhesive material in the great pyramids. The Babylonians and Assyrians used bituminous materials to construct stones and bricks walls. Both the Greeks and Romans discovered (800 BC) the cementitious properties of burnt lime when it is slaked and mixed with sand to form mortars. This was before the discovery of volcanic deposits (300 BC-476 AD) which displayed hydraulic properties and high adhesive strength when mixed with lime. The volcanic deposits (volcanic tuff) were acquired from Pozzouli in Italy from which the term pozzolana derives its name. Also, the Romans used blood, animal fat and milk as admixtures in their mixes to increase the cementitious properties of their pozzolanic material.

In 1756 John Smeaton developed the hydraulic properties of lime to arrive at the conclusion that the hydraulicity of this material depended on the amount of clay incorporated. His hydraulic lime was used to rebuild the Eddystone lighthouse in 1759. In 1824, Joseph Aspdin introduced a type of hydraulic cement which he named as Portland cement due to its colour which was similar to the Portland stone. Portland cement was prepared from limestone which was crushed and calcined before it was mixed with clay. The mix was then ground together and calcined. The temperature which was used in the calcination process of this early product was low, which affected its quality due to insufficient formation of the calcium silicate phases. Later, in the mid-1800s, it was discovered that the over-burning increases the quality of the Portland cement properties by the formation of the calcium silicate phases despite the heterogeneity which these phases showed due to the slow cooling process followed at that time. Modern Portland cement, which is burned at high temperature ($\sim 1450^{\circ}\text{C}$), which, together with relatively rapid burning time and rapid cooling time, is used to decrease the amount of the free lime in the final product as well as increasing the calcium silicate phases.

An increasing demand for Portland cement had taken place through time due to the increase in urbanization. In 2006, Portland cement production was 2.55 billion tonnes and expected to rise to 4.4 billion tonnes by 2050 (Kavitha, 2017). This has triggered concerns

about the impact of cement production on the environment as both the burned fuel, as well as the decomposition of lime, contributes to almost 8% of the total anthropogenic CO_2 emitted into the atmosphere (Ortega et al., 2015; Tang et al., 2016). Therefore, other industrial by – products such as fly-ash (FA) and ground granulated blast furnace slag (GGBS) have been extensively used to replace normal Portland cement in concrete mixes. These by-products have shown to have positive effects on the long-term durability of concrete mixes due to their influence on the material pore structure.

1.2 Cement and concrete characterization testing techniques

One of the major advantages which normal Portland cement, hence concrete, possess in addition to strength development through time, is the transformation of the mixes from a liquid phase during the early hydration period, to a solid porous material at later stages. This gives the ability to cast complex shapes and facilitates the transportation of the fresh mix from the production site to the construction site. The hydration process which is initiated by mixing cement with water allows this transformation process. The hydration process is a complex reaction which involves several physical and chemical processes which take place simultaneously. The phases which compose the Portland cement all contribute to the hydration reaction; however, the influence of the silicate phases on early hydration kinetics is more pronounced, which led many researchers to focus on the hydration reaction of these particular phases to reduce the complexity exerted by the chemical contribution of other cement phases (Alizadeh et al., 2009b; Bellmann et al., 2010; Bellmann et al., 2012). Despite this simplification, the early hydration of Portland cement is still not fully explained and many theories have been proposed to understand this chemical process.

By utilizing the exothermic nature of cement hydration, isothermal conduction calorimeter (ICC) tests are widely used to monitor the hydration kinetics of the early stages for cement pastes. In addition, auxiliary tests such as scanning electron microscopy (SEM), back scatter electron microscopy (BSE) and X-rays diffraction (XRD) are also used to characterise the phases formed and to support the features which are observed from the ICC results. After setting, and through the hardening stage, the heat emitted from the hydrated samples decreases, hence the ability of the continuous monitoring which is provided by the ICC. The hydration phases are characterized at the latter stages by the SEM, XRD or thermogravimetric analysis techniques (TGA), in which the latter shows

efficiency in monitoring the calcium hydroxide profile through time, particularly when the pozzolanic reaction initiated.

As the material changes from the liquid state to a porous solid, other testing techniques such as mercury intrusion porosimetry (MIP), nitrogen adsorption/desorption (NAD) and SEM are used to study the pore structure. The characterization of the pore structure is important in terms of assessing the long-term durability and performance by assessing the critical pore diameter (d_c) as well as the pore size distribution. On the other hand, assessing the penetrability of concrete by aggressive ions (e.g. chloride) is an important factor in terms of maintaining the functionality of concrete structures (Atkinson and Nickerson, 1984; Buenfeld and Newman, 1984; Martys, 1996; Elahi et al., 2010). Therefore, durability oriented tests, which directly characterize the long-term performance of concrete mixes under chloride exposure, had been used for this purpose. These tests include the rapid chloride penetration test (RCPT), natural chloride ponding test and non-steady-state chloride migration test.

1.3 Electrical measurements

Due to the destructive nature of many tests, as well as the sample scale which is normally used, limitations in the accuracy as well as in the ability for continuous monitoring are encountered. These shortcomings have triggered the necessity to explore other types of test which could provide a continuous, non-destructive testing ability at both the early hydration stages as well as during the hardening stage.

The intrinsic electrical properties of any non-magnetic material can be fully specified by its frequency dependent parameters relative permittivity, $\epsilon_r(\omega)$, and conductivity, $\sigma(\omega)$, which are dependent upon the polarization and conduction of bound and free charges within the material. If the material is heterogeneous, $\epsilon_r(\omega)$ and $\sigma(\omega)$ will be strongly correlated to the properties of the individual components and the way in which these components interact. It is, therefore, possible to identify and characterize porous cementitious materials by their electrical properties provided that these are observed over a wide enough frequency range. The conductivity of hydrating cement-paste is related to both the conductivity of the pore-fluid (hence ionic concentration within the pore fluid) and the continuity and tortuosity of the pore network. The relative permittivity, on the other hand, is associated with polarization processes operative within the paste, which are

themselves related to the mobility of charges adsorbed on the grain and crystal surfaces and at crystal/pore-water interfaces.

Electrical measurements have a number of advantages in comparison to the previously mentioned tests such as:

(a) The samples do not need special preparation prior to testing at least in the frequency range from Hz – MHz as at much higher frequency ranges in the GHz the tests need more attention with regard to the sample cell design.

(b) Some stages during the early hydration period do not emit heat such as the induction period, hence heat emission dependent tests will not be able to give a precise interpretation to the ongoing reaction. However, electrical measurements depend on the ionic situation in the mixes, therefore another perspective on these non-active heat emission stages could be obtained by the use of electrical measurements. In addition, calorimetric testing techniques are not suitable to assess the hydration process after the first few days as the noise from the test instrument has a significant influence on the accuracy of the test due to the low heat emission, therefore the sensitivity of the electrical measurements at these stages could be more reliable over conventional tests (Zhang et al., 1995; Ridi et al., 2011).

(c) As they are non-destructive, the tests can be performed on the same samples continuously throughout the hydration process, or throughout any other physical or chemical process applied on the material continuously through time (for example, wetting and drying cycles). This offers the ability to monitor the development and changes which occur on the same sample continuously without any disruption (Manchiryal and Neithalath, 2009; Pasquale, 2009; Cruz et al., 2013). This is of particular interest during the hardening stage.

(d) The analogy between the movement of ions under an electrical potential and the movement of ions under a chemical potential suggests electrical measurements could be developed as a durability indicator (Christensen et al., 1994; Shi et al., 1999; McCarter et al., 2000). Furthermore, the use of impedance spectroscopy methods gives both the ability to assess the macro-response of the material through its bulk conductivity / permittivity (McCarter and Afshar, 1985; McCarter et al., 2005; McCarter et al., 2013) and the

material micro-response through the use of representative electrical circuit models (Barsoukov and Macdonald, 2005; Sánchez et al., 2013; Ortega et al., 2015).

1.4 Research significance

A considerable amount of work has been presented on the electrical properties of cementitious materials to study the hardening process (i.e. periods > 24-hours). In a similar fashion, the electrical conductivity (and its reciprocal, resistivity) of cement pastes has been used to study the initial 24-hours of the hydration process (see, for example, (Torrents et al., 1998; Morsy, 1999; Levita et al., 2000; Salem, 2002; Princigallo et al., 2003), although studies on the relative permittivity over the same periods are more limited (see, for example, (Gorur et al., 1982; Moukwa et al., 1991; Zhang et al., 1996)). An important limitation of the studies up to date are:

(a) Most studies have obtained the electrical response at a fixed frequency of electrical field, or the frequency range used was limited. Regarding the latter, conductivity measurements tend to be taken in the low kilohertz range (100Hz-10kHz) whereas relative permittivity measurements are generally measured in the gigahertz (GHz) region.

(b) Lack in the long-term measurements during the hardening stage, as most of the studies limited their measurements to the first 28-days of hydration.

(c) Limitation in the type of mixes characterized by the electrical measurements techniques. As most of the available studies have focused on the electrical response for pure cement pastes, there is a paucity of studies which address supplementary cementitious materials (SCM) at both the early hydration and the hardening stages. In addition, there is a lack of work which addresses the response of concrete mixes.

1.5 Research aim

With regard to the application of electrical measurements on cement based materials, the overall aim of this research is to obtain the AC Immittance response in the frequency range of (1Hz-10MHz) for different cement pastes and concrete mixes with different additions of supplementary cementitious materials, through the setting stage and the hardening stages. In addition, to relate this response to changes which take place in the liquid phase chemistry, the nucleation and growth of hydration products, pore structure formation, as well as to durability.

1.6 Research objectives:

To fulfil this aim, the following specific objectives need to be met:

- (a) Assessing the effect of electrode configuration on the electrical response, to account for the possibility of measurement artefacts which could affect the accuracy of the measurements.
- (b) Obtaining a detailed AC immittance response for cement pastes and concrete mixes which contain different SCMs in the frequency range 1Hz-10MHz, through the first 24 hours.
- (c) Undertaking parallel calorimetry and ESEM measurements for the cement paste samples to assist in understanding the immittance spectroscopy response during the initial 24 hrs period.
- (d) Obtaining detailed long-term AC immittance measurements for concrete mixes which contain different SCM in the frequency range 1Hz-10MHz.
- (e) Developing a durability ranking for the concrete mixes through the use of electrical measurements, and comparison with the durability ranking obtained from rapid chloride migration test (RCM).

Chapter 2 – Cement Manufacture and the Hydration Process

This review is divided to two main sections, the first section presents the necessary information on the manufacturing process, cement phases, composition and hydration reactions. The second section presents a brief explanation of the principals of the AC immittance spectroscopy techniques as well as reviewing key work in terms of their application in monitoring cementitious materials through the initial 24hrs and the hardening process.

2.1 Cement manufacturing process

2.1.1 Raw materials

In the manufacture of cement, clay or shale, is normally used as a source of silicate, alumina and ferrite. The thermal decomposition of the clay occurs at $\sim 600^{\circ}\text{C}$ as in equation (2.1):



Limestone (or chalk) is the lime source and it decomposes at $700\text{-}900^{\circ}\text{C}$ (calcination temperatures) as in equation (2.2):



The main phases of cement, which are C_2S (belite) and C_3S (alite), form at higher temperatures than the decomposition temperature of the clay and the limestone, as they form at 1200°C and 1400°C respectively (i.e. clinkering temperature). There are some minor components whose presence adds specific advantages to the cement, such as gypsum, which is normally added at the end stage in the cement manufacturing process (milling stage). Gypsum assists in hindering the flash-setting effect which is caused by the rapid hydration of the C_3A phase, and normally it is added between 4-5% by weight. In this range, the gypsum possesses the ability to react with the aluminate phase in cement producing ettringite. If the amount added is $<4\text{-}5\%$, monosulfoaluminate phase will form either accompanying the ettringite or individually.

In order to realise the targeted clinker chemical composition, the raw meal is normally subjected to quality control tests to obtain an indication of its chemical composition. According to the chemical composition of the raw meal, the following ratio thresholds have been proposed to be used as quality control factors:

$$A_R = \frac{Al_2O_3}{Fe_2O_3} \quad (2.3)$$

$$LSF = \frac{CaO}{2.8SiO_2 + 1.2Al_2O_3 + 0.65Fe_2O_3} \quad (2.4)$$

$$S_R = \frac{SiO_2}{Al_2O_3 + Fe_2O_3} \quad (2.5)$$

In which: A_R : Alumina ratio; LSF: The lime saturation factor; S_R : Silica ratio. The mean values and the thresholds for the above ratios are shown in Table 2.1

Bogue's equations are normally used to estimate the potential phases for the clinker based on the oxide analysis of the cement (Neville and Brooks, 1987):

$$C_4AF = 3.04(Fe_2O_3) \quad (2.6)$$

$$C_3S = 4.07(CaO) - 7.60(SiO_2) - 6.72(Al_2O_3) - 1.43(Fe_2O_3) - 2.85(SiO_3) \quad (2.7)$$

$$C_2S = 2.87(SiO_2) - 0.754(3CaO.SiO_2) \quad (2.8)$$

$$C_3A = 2.65(Al_2O_3) - 1.69(Fe_2O_3) \quad (2.9)$$

The term in the brackets is the weight percentage of the oxide.

With regard to the manufacturing processes, these can be summarised as follows (Neville and Brooks, 1987):

2.1.2 Mixing and grinding

The raw materials are ground and mixed with water to form a slurry. In the wet process, the materials fed into the kiln at 30% moisture content; in the case of the dry process the material has a moisture content of 0.5% and fed to the preheated cyclones before introduced to the kiln. Despite the fact that the wet process is more controllable in terms of the produced material, this method consumes much energy due to the drying process (Hewlett, 2003).

Another two additional cement manufacturing processes have been introduced to the industry to reduce the energy consumption of the manufacturing process which are the semi-wet process and the semi-dry process (P.Barnes, 1983). These two processes differ in the moisture content of the fed material, as in the former the wet slurry is dewatered in a filter-pressed process which reduces the amount of water in the material to 20%, and in the semi dry-process the moisture content of the fed material is approximately 12%.

2.1.3 Burning process

After the grinding and mixing processes, the material is fed into a rotary kiln which is heated to 1500°C. As the raw material moves through the kiln, a progressive increase in the temperature occurs which is responsible of the gradual water evaporation from the meal as well as the formation of the different cement phases. The movement of the material in the kiln is either due to the slippage of the material or the rolling of the material. The kiln assists this movement through its inclined position. Normally the wet-process kiln is much longer than the dry-process one due to the longer heat exposure duration which is needed to reduce the excess water.

Once the meal is exposed to the heat, water is removed followed by CO_2 emission due to the thermal decomposition of limestone/chalk. At this stage 20-30% of the mix will fuse and the combination between lime, silica and alumina will take place. The material at this stage is called 'clinker' which is basically small spheres with 3-25mm diameter.

2.1.4 Cooling process

The clinker is then cooled down to make sure a thorough crystallization of the material takes place. Different cooling rates have shown to have different effects on the produced clinker; for example, rapid cooling has been recommended as it produces smaller alite crystals which assist in the later grinding process. In addition, rapid cooling produces small amount of MgO crystals which form separately, as the majority of the MgO will be incorporated within the clinker. In slow cooling, the MgO can form large separated crystals; rapid cooling forms an amorphous glassy material which subsequently represents a problem in the grinding process. Therefore, choosing a suitable cooling rate is an important factor in the cooling process.

2.1.5 Cement milling

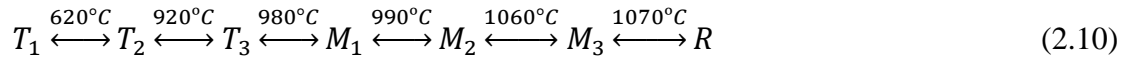
Finally, the clinker is ground with gypsum added to modify the flash-setting nature of the C_3A phase. The grinding process takes place in a rotating ball-mill and, as has been mentioned earlier the grindability at this stage depends on the cooling history of the clinker (P.Barnes, 1983).

2.2 Cement chemical composition

Cement as a material is composed of different phases which show different hydration reactions when they are assessed separately. Four phases dominate the chemical composition of cement which are as follows (Taylor, 1997):

2.2.1 The Alite phase (C_3S)

Alite is an impure version of tricalcium silicate (Ca_3SiO_2) and denoted C_3S in cement chemistry nomenclature (Bellmann et al., 2010). The alite phase constitutes ~50-70% of normal Portland cement and it is the main phase which is responsible for strength development during the first 28-days. The pure C_3S is a result of the combination of calcium oxide and silicate and exists in different polymorphic modifications (crystal structures) which depend on the formation temperature as shown in equation (2.10):



Where: T: Triclinic; M: Monoclinic; R: Rhombohedral

As it is shown in equation (2.10), the pure C_3S occurs in the T_1 polymorphism at room temperature; however, in the cement manufacturing process, and due to the presence of other ions in the clinker (e.g. Na^+ , K^+ , Mg^{2+} , Fe^{3+}), alite normally occurs in the form of M_1 or M_3 . The probability of crystallizing a specific type of C_3S polymorphism in the clinker, depends on the MgO/SO_3 ratio in the clinker. When this ratio is high it gives rise to M_3 polymorphism and when it is low M_1 is more likely to be present (Maki and Kato, 1982; Taylor, 1997). Also, the burning duration in the kiln has an effect as longer heating duration gives rise to the M_1 polymorphism.

2.2.2 The Belite phase (C_2S)

Belite is the impure version of dicalcium silicate (Ca_2SiO_2), denoted C_2S . This phase constitutes ~15-30% of normal Portland cement and it contributes little to the early strength development; however, by the age of one year, its strength is comparable with the alite phase strength at the same age and curing conditions. Similar to the case of the alite phase, the pure C_2S phase is also affected by temperature changes as well as different ion substitutions as it transforms to different polymorphs such as β , γ , α'_L , α''_H , α . The most common in Portland cement clinker are β and γ polymorphs. The βC_2S modification polymorph is normally unstable at normal temperature unless it is incorporated with other impurities. The only modification of the C_2S which is stable at ambient temperatures is the γC_2S . It should be noted that the rate of hydration for the different polymorph modifications of the C_2S phase is different, as the $\alpha' C_2S$ is more hydraulic than βC_2S ; γC_2S has been reported to be non-hydraulic and the αC_2S has been reported to record reactivity between the $\alpha' C_2S$ and βC_2S polymorphisms. However, it should be considered that the reactivity is dependent on the impurity ions which stabilize the polymorph and,

in the case of using the same stabilizer, the thermal history of the stabilized C_2S phase will also be the factor which determines its reactivity. The stabilization process of the C_2S phase polymorphs is usually done by the incorporation of barium oxide in its crystal lattice (Bensted and Barnes, 2002; Hewlett, 2003).

2.2.3 The Aluminate phase (C_3A)

Tricalcium aluminate ($Ca_3Al_2O_3$) is a combination of calcium oxide and aluminate, which is expressed in cement chemistry as C_3A . This phase constitutes ~5-10% of normal Portland cement. An excess of this phase causes the rapid setting of cement pastes and gypsum is normally added to inhibit this undesirable effect. The crystal structure of the pure C_3A is cubic; however, in the case of Portland cement, it can exist in cubic or orthorhombic and sometimes monoclinic forms. A combination between the cubic and orthorhombic or the cubic and the monoclinic forms can also take place (P.Barnes, 1983). These different crystal structures also depend on the amount of the alkalis in the clinker.

2.2.4 The Ferrite phase (C_4AF)

Tetracalcium aluminoferrite ($Ca_4.AL_2O_3.Fe_2O_3$) and is expressed in cement chemistry as $C_4(AF)$ and constitutes ~5-15% of normal Portland cement. The chemical composition of this phase is between the two solid phases of C_4AF and C_6A_2F and the actual composition depends on the thermal history of the clinker as well as on the chemical composition of the clinker. If the clinker is cooled rapidly the ferrite phase is close to C_6A_2F ; however, if the clinker is cooled slowly the composition is closer to C_4AF (P.Barnes, 1983).

2.3 Hydration reaction of cement phases

The hydration of cement is an exothermic process which is initiated by mixing the cement with water. This process is responsible for the physical and chemical changes which occur in the cement paste as it changes from a liquid state to the solid state. The cement paste passes through the setting stage in which the material is stiffening without developing significant compressive strength and it is during the hardening stage in which the material develops strength.

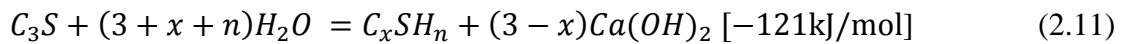
Cement comprises different phases and constituents which possess different chemical compositions; therefore, when explaining cement hydration, the reaction of these phases is considered separately as the reaction of cement with water is a complex process. However, the general features of cement hydration are much related to the C_3S phase due to the high percentage of this phase in cement (Bullard et al., 2011).

2.3.1 Hydration of Tricalcium silicate (C_3S)

Two primary products are produced in the hydration reaction of both the C_3S and the C_2S phases which are:

- (a) Calcium hydroxide (CH). However, the C_3S produces more CH and has a greater reactivity than the C_2S phase; and
- (b) an amorphous calcium silicate hydrate which has no definite composition and referred to as C-S-H gel (Taylor, 1997).

The hydration reaction of the C_3S phase takes place according (Bensted and Barnes, 2002):



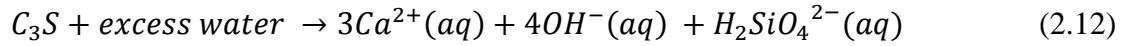
x and n can reach 1.7 and 4, respectively, when the concentration of the $Ca(OH)_2$ reaches saturation level. Due to the uncertain chemical composition for the C-S-H, attempts have been made to approximate its crystalline structure to already known calcium silicate hydrate crystalline structures which are (Chen et al., 2004):

- (a) 1.4 Tobermorite [$Ca_4(Si_3O_9H)_2 Ca.8H_2O$], has a Ca/Si molar ratio of ~0.83; the prefix 1.4 indicates the compositional layer thickness.
- (b) Jennite [$(Ca_8(Si_3O_9H)_2 (OH)_8) Ca.6H_2O$] which has a Ca/Si molar ratio of ~1.5.
- (c) C-S-H I with Ca/Si molar ratio of 0.67-1.5.
- (d) C-S-H II the Ca/Si molar ratio is ~2.

Due to the similarity between the C-S-H gel studied by XRD and the C-S-H crystalline structures noted above, the Ca/Si molar ratio has been used in characterizing the C-S-H gel. The Ca/Si ratio of the C-S-H gel is in the range of 1.7-1.8, despite the fact that it has been shown that at the initiation of hydration the Ca/Si ratio decreases sharply during the first 30 seconds, then increases before decreasing in a gradual manner to 1.7-1.8 after few minutes (Taylor et al., 1984). By plotting the rate of heat evolution with time for the C_3S hydration reaction, six stages are observed as shown in Figure 2.1.

Pre-Induction period (Stage 0-I)

Once the C_3S phase contacts water a rapid dissolution takes place with ions moving into solution. The ions which pass to the solution are Ca^{2+} , OH^- and $H_2SiO_4^{2-}$ according to the following:



Equation (2.12) has been considered as congruent dissolution which means both the Ca^{2+} ions and the silicate ions move to the solution together in a certain dissolution ratio which is 3:1. This is despite the fact that some theories as discussed later propose an incongruent dissolution to explain the slow dissolution rate which has been detected for the C_3S phase in the early reaction stage.

The end of Stage 0 and the beginning of Stage I, as shown in Figure 2.1, is distinguished by the first peak in the heat rate graph. It is also worth mentioning that Stage 0 is very rapid as it lasts for only few minutes and is very often unobservable by calorimetric methods. A decrease in the reactivity is noticed in the heat evolution rate after this first peak due to several proposed theories which signify the beginning of Stage I and the end of Stage 0.

Induction period (Stage I-Stage II)

Bensted and Barnes (2002) have shown that C_3S has a high solubility in water; however, that is not the case when compared to its actual dissolution rate after the initial fast reaction stage, as lower dissolution rates are observed. The possible causes of this slower dissolution rate and its accompanied decrease in the hydration reaction rate which occurs after Stage 0 and through Stage I leading to Stage II, have been summarized as follows (Hewlett, 2003):

(a) Impermeable barrier layer theory

In this theory, it is proposed that at a certain concentration of Ca^{2+} and silicate ions in the solution, and due to the initial congruent dissolution of the C_3S phase, a metastable C-S-H layer is formed on the surface of the C_3S particles. This hinders water from reaching the C_3S as well as Ca^{2+} and silicate ions from reaching the solution (Greenberg and Chang, 1965; Barret et al., 1983; Ings et al., 1983; Grutzeck and Ramachandran, 1987; Bensted and Barnes, 2002; Cordes and Odler, 2002; Bellmann et al., 2010;

Bellmann et al., 2012). This theory has been based on the finding that the equilibrium state for the concentration of the SiO_2 and CaO tends to fall on either one of two curves which have been denoted as curve A and curve B (Taylor, 1997) in the solubility curve of the C-S-H product (see Figure 2.2). Curve B has been attributed to the early metastable C-S-H layer which covers the C_3S phase and, consequently, stops the first accelerated reaction. Regarding Curve A, it has been attributed to the stable C-S-H product which is produced in later stages (the main acceleration stage) and it is worth noting that curve B displays much higher concentrations than curve A as potential evidence that the origin of product A is product B (Ings et al., 1983).

Other researchers considered this impermeable layer as a charge separation layer produced by the superficial hydroxylation on the C_3S surface (Barret et al., 1983). This postulation assisted in explaining the gradual decrease in the C_3S dissolution rate through the initial fast reaction and the first deceleration period. If the newly formed early hydration C-S-H layer is considered responsible for the first deceleration period, the dissolution rate of the C_3S phase will be rapid until the formation of the early C-S-H; however, this is not the case as the dissolution rate undergoes a gradual decrease from the beginning of the hydration process (Bullard et al., 2011).

It has been argued (Bensted and Barnes, 2002) that due to the considerable thickness of the impermeable layer which has been measured by electron spectroscopy for chemical analysis technique (ESCA), the concept of a new phase layer formation is more reasonable than the superficial hydroxylation layer. This is despite the lack of evidence on the coverage of the newly formed phase on the surfaces of the C_3S that has been recorded (Taylor et al., 1984; Bullard et al., 2011). Bellmann et al. (2010) have arrived at the same conclusion, attributing the formed layer to a separate phase rather to a superficial hydroxylation layer. Justification was based on assessing the volume fraction of the silicate ions on the layer as it showed that this layer contained a larger silicate volume fraction (79%) than the expected percentage for a superficial hydroxylation layer (1%) therefore a new phase must be formed to accommodate this high percentage of silicate.

(b) The electrical double-layer theory

In this theory, an incongruent dissolution at the early stages has been proposed rather than a congruent one. The Ca^{2+} ions, as well as the OH^- ions, move into solution without the silicate ions which, in turn, form a rich silicate layer on the surface of the C_3S phase. Re-

adsorption of the Ca^{2+} ions is assumed to take place on the silicate rich surface forming an electric double-layer, therefore decreasing the rate of the initial accelerated reaction. The end of the induction period, which is followed by the acceleration period, is assumed to take place after the electrical double-layer gradually breaks down (Tadros et al., 1976). This theory has been given support by ESCA results which show an initial decrease in the Ca/Si ratio during the first minutes, when assessing the chemical composition of the C_3S phase giving an indication of a silicate layer that is formed on the surface.

(c) $Ca(OH_2)$ nucleation theory

It has been observed that the saturation level for the portlandite ($Ca(OH_2)$), which is referred to as CH in cement nomenclature, in the solution due to the hydration of the C_3S phase can be very high, exceeding a value of 2 without a significant precipitation of Portlandite. The non-precipitation of CH has been attributed to the poisoning effect of the silica ions due to their adsorption on the surface of the CH. Eventually, the concentration of the CH becomes high enough to overcome this poisoning effect and the CH starts to precipitate again (Young et al., 1977). An argument against this has been presented due to the lack of influence on the reaction rate when CH particles are added separately to the solution (P.Barnes, 1983; Taylor, 1997).

(d) Nucleation of C-S-H theory

In this theory, the end of the induction period has been related to the nucleation and growth of stable C-S-H in the main reaction. It has been proposed that the isolation effect of the meta-stable C-S-H has no influence and the CH concentration level plays a secondary role. However, the beginning of the formation of the main C-S-H phase which is product A in Figure 2.2 is the main cause of the acceleration stage (Taylor, 1997; Hewlett, 2003). Regarding the nucleation theory of the C-S-H, it has been supported by the fact that the addition of supplementary cementitious materials such as silica fume or the addition of C-S-H seeds accelerates the hydration reaction. These provide more C-S-H nucleation sites therefore increasing the conversion of the early stage metastable C-S-H to the stable one, this reaction takes more time if natural nucleation alone proceeds (Stein and Stevels, 1964; Alizadeh et al., 2009a).

A period of slow reactivity takes place as shown in Figure 2.1 and is called the induction period and referred to as Stage II. The induction period ends with 'renewed' chemical activity within the paste. The cause of this activity depends on which theory of the above is used:

(a) Impermeable barrier theory: it has been proposed that the end of the induction period is due to either a change in the morphology of the metastable C-S-H layer due to aging process, or due to the effect of the osmotic pressure due to the ions confined between the unreacted C_3S and the metastable C-S-H layer which leads to ‘bursting’ of this layer (Double et al., 1978).

(b) Electrical double-layer theory: the aging process has been suggested as a main cause for its degradation.

(c) Nucleation of CH theory: the increase in the concentration of the CH thereby overcoming the silicate poisoning effect on the surfaces of the CH.

(d) C-S-H nucleation theory: at the end of the induction period the metastable C-S-H which has been formed undergoes a change in its structure due to the formation of dimer silicates on its surface (Bullard et al., 2011). However, no direct relation has been mentioned to correlate the change in the structure of the metastable C-S-H and the self-triggering growth of the stable C-S-H which ends the induction period as has been postulated in the nucleation of C-S-H theory. Ings et al. (1983) have stated that the stable C-S-H gel which forms during the main acceleration period i.e. after the induction period, forms at expense of the pre-formed metastable C-S-H and the crystallised CH. Hence, the change in the chemical structure which has been mentioned by Bullard et al. (2011) and the work of Ings et al. (1983) theory could explain the end of the induction period.

The main acceleration period (Stage III)

During Stage III, a rapid dissolution of the C_3S phase again takes place resulting in a precipitation and crystallisation of the hydration products. The C-S-H product in this Stage is more stable in comparison to the early C-S-H product and it has been referred to as product A in the solubility curves in Figure 2.2. This Stage is shown in the calorimeter as an increase in the heat rate till reaching a second global peak which is shown in Figure 2.1. The acceleration of the reaction continues and the hydration products, particularly the C-S-H, fill the spaces between the hydrated grains until the process begins to change from a growth controlled process to a diffusion controlled process.

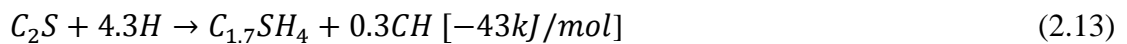
The second deceleration and the late hydration period (Stage IV-Stage V)

The second deceleration period begins when the stable C-S-H hydration product starts to precipitate and increase in thickness around the C_3S phase thereby hindering further

reaction with water. The process therefore becomes a diffusion control process, however it is not well defined what is the diffusing element which causes the deceleration period whether it is the ions diffusing from the C_3S or water to the C_3S (Bensted and Barnes, 2002). However, it is worth noting that the hydration process continues as long as there is enough space and water for the hydration reaction to proceed, albeit at a reduced rate.

2.3.2 Hydration of Dicalcium silicate (C_2S)

The hydration kinetics of the βC_2S has been described as similar to the C_3S phase; however, slowness in the reactivity has been observed in comparison to the C_3S . Also, the CH produced from the reaction is less when compared to the C_3S with the same degree of hydration (Hong and Young, 1999). The main acceleration period is barely detected by calorimetric methods due to the low heat evolution in comparison to the C_3S phase. The first acceleration stage has been shown to be similar in its intensity to the C_3S phase (P.Barnes, 1983). Due to the general agreement in heat rate evolution through time between the C_3S and the C_2S , it could be divided to the same hydration stages as the C_3S phase (Bensted and Barnes, 2002). The main chemical equation for the hydration reaction for the C_2S phase is:



In terms of the C-S-H, the C_2S phase forms the same C-S-H hydration products in terms of the composition as the C_3S phase. This includes both the metastable C-S-H and the stable C-S-H at the main acceleration period.

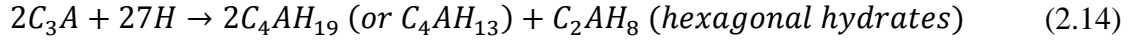
2.3.3 Hydration of Tricalcium aluminate (C_3A)

The tricalcium aluminate phase (C_3A) is the most reactive phase in the Portland cement clinker and has a considerable influence during the first 24hrs hydration. Due to its reactivity, gypsum is added to the clinker to inhibit flash setting (Black et al., 2006; Pourchet et al., 2009). Figure 2.3 shows the hydration degree through time for the different cement phases and it is evident that, during the early stages, the degree of hydration of C_3A exceeds all the other phases; also, the C_3S reactivity only exceeds the C_3A after ~20hrs from the start of the hydration process.

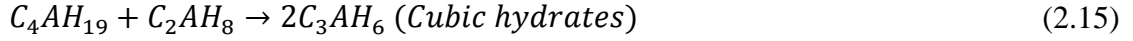
From Figure 2.3, the addition of gypsum to the C_3A phase lowers its reactivity; therefore, it is more appropriate to review the hydration kinetics of the C_3A phase in both the presence and absence of SO_4^{2-} ions.

(a) Hydration of C_3A in the absence of Sulphate:

The main chemical equation which represents the C_3A phase reaction with water in the absence of sulphate is as follows (Bensted and Barnes, 2002):



Followed by:



Equations (2.14) and (2.15), show the first formed components are hexagonal hydrates C_2AH_8 and $2C_4AH_{19}$. These are metastable and, subsequently, converted to cubic hydrate, C_3AH_6 , which is the only stable calcium hydrate formed at ambient temperature. The conversion of C_3A to the C_3AH_6 directly, without passing through the hexagonal hydrate stage, could be achieved at higher temperatures ($>80^\circ\text{C}$) to form a stronger mix than a mix which forms from passing over the hexagonal hydrate stage (Bensted and Barnes, 2002).

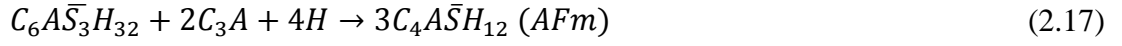
(b) Hydration of C_3A in the presence of Sulphate

Normally sulphate is added to the C_3A phase in the form of calcium sulphate $\text{CaSO}_4 \cdot 2\text{H}_2\text{O}$ ($C\bar{S}H_2$), as this reduces the reaction rate. The main initial product is the ettringite $C_6A\bar{S}_3H_{32}$ (AFt), according to the following equation:



After the initial hydration reaction of the aluminate phase with sulphate, a number of theories have been proposed to account for the dormant period which takes place, whose duration has been found to be in proportion to the amount of gypsum added to the mix (Minard et al., 2007). The most accepted theory regarding this dormant period is the barrier layer in which ettringite forms around the calcium aluminate phase and prevents the diffusion of ions (SO_4^{2-} , OH^- , Ca^{2+}), therefore reducing the reaction rate.

After the dormant period, a second rapid reaction takes place after the calcium sulphate is consumed in the initial reaction. In this second reaction, ettringite reacts with the C_3A phase to produce monosulphoaluminate (AFm) and this is due to the instability which occurs to the ettringite resulting from a lack of SO_4^{2-} ions:

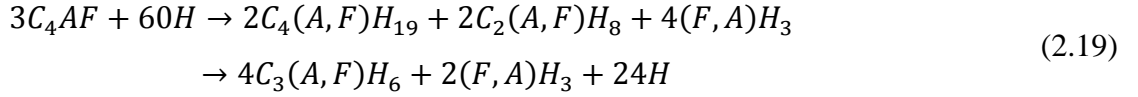


And straight formation of AFm in limited amounts of gypsum:



2.3.4 Hydration of the Ferrite phase

The hydration reaction of the ferrite phase is similar to the hydration reaction for the C_3A phase despite the difference in the reaction rate. In the absence of gypsum, it forms hexagonal hydrates in the form of $C_4(A,F)H_{19}$ and $C_2(A,F)H_8$ which, subsequently, convert to $C_3(A,F)H_6$ according to equations (2.19)



The $(F,A)H_3$ hydroxide which forms, is a consequence of the high A/F ratio of the phases formed, therefore it is created to maintain the stoichiometry balance. In the presence of gypsum, the ferrite phase forms the AFt phase ($C_6(A,F)\bar{S}H_{32}$) on its surface which leads to a decrease in the reaction rate, later, when gypsum is consumed, the AFm phase ($C_4(A,F)\bar{S}H_{12}$) forms.

2.4 Hydration reaction of Portland cement

When assessing the hydration of Portland cement or cements in general, interactions and synergistic effects occur between the clinker phases during the hydration process. As a result, cement hydration is a complex reaction (Bensted and Barnes, 2002); however, as the alite phase forms a high percentage of the clinker (~55%) the hydration of the cement is modelled on hydration of the alite phase:

(a) Pre-Induction stage

This stage lasts for few minutes during which rapid dissolution of ions from the different cement phases takes place; however, not all the reactions in this period are exothermic, as in the case of the alkali sulphates, they undergo a complete dissolution. Alkali ions and SO_4^{2-} ions pass into the solution through an endothermic process; on the other hand, the dissolution of calcium sulphate is exothermic (Bensted and Barnes, 2002). During the pre-induction stage, a congruent dissolution of the alite phase takes place and a metastable C-S-H phase forms on the cement particle surfaces. This dissolution provides the aqueous

phase with both calcium and silicate ions. During this stage, the percentage of the reacted alite normally does not exceed 10-20%.

The calcium aluminate and ferrite phases react with calcium sulphate to produce AFt (ettringite). This forms on the cement particle surfaces and is highly exothermic. In this stage, a high concentration of aluminate ions forms in solution which, subsequently, decreases due to the formation of the AFt phase (Bensted and Barnes, 2002). The iron ions do not show the same trend as the aluminate ions, as they are not observed in the solution in such high concentrations, and is due to the formation of hydrated oxides which coat the surface of the ferrite phase.

(b) The Induction stage

The causes of the induction period, which lasts for the first few hours of the hydration reaction, have been discussed in Section 2.3.1. During this Stage, the hydration reaction progresses at a slow rate as in the case of the pure alite phase.

(c) The Acceleration Stage

During this Stage the hydration rate increases with rapid precipitation of hydration products such as stable C-S-H and Portlandite. A noticeable difference between the hydration products of the pure phases and Portland cement could appear in the C-S-H hydration product as sulphate ions have been observed to be adsorbed onto the C-S-H phase (Gallucci et al., 2010). A complete consumption of calcium sulphate takes place due to the formation to the AFt, as well as the adsorption of the sulphate ions on the C-S-H (Taylor, 1997).

From the main differences between the C-S-H in cement and those formed in the pure C_3S phase, a shell of C-S-H forms immediately on the surface of the C_3S . However, in cement a 'gap' has been detected between the C-S-H shell and the cement grain which is in the range of $0.5\mu\text{m}$ (Taylor, 1997). The C-S-H, which is adjacent to the aqueous phase, is called the outer product and the C-S-H which is adjacent to the anhydrous grain is called the inner product which, in turn, gradually increases in its volume until bridging occurs between the outer product and the anhydrous grain by the inner product (see Figure 2.4). The acceleration period reaction slows down after the inner product fills the gap between the cement grain and the outer product.

(d) Post acceleration stage

The main feature of this stage is the decreasing rate of the hydration reaction due to the diffusion-controlled process which takes place due to the thickening of the precipitated hydration products. After the consumption of the calcium sulphate, the available C_3A phase starts to react with the AFt already formed to produce monosulphaaluminate (AFm).

2.4.1 Cement setting process

The setting process can be described as the process whereby the cement paste turns from a plastic, workable material, to a rigid brittle material and this due to the interlocking between the hydration products. The setting process depends on the water/binder (w/b) ratio as, the larger this ratio, the more hydration products are needed to bridge the spaces between them (Nonat et al., 1997; Bentz, 2008). However, in the case of constant w/b ratio, it has been noticed that the smaller the particle size of the cement, the shorter time needed to achieve setting (Bentz et al., 1999). The setting process for cement passes through the following stages (Hewlett, 2003):

(a) Once cement is mixed with water a dispersion of the cement particles in the solution takes place.

(b) Flocculation (coagulation) of cement particles, which has been attributed to electrostatic forces (Hewlett, 2003). The electrostatic forces are related to the concentration of CH in the mix (Nonat et al., 1997). The flocculation process leads to increase in the viscosity of the mix and it should be noted that these fluctuations are reversible as they can be dispersed by mixing (Jiang et al., 1995).

(c) At the acceleration Stage, the volume of hydration products increases and, consequently, that of the aqueous phase decreases. Furthermore, chemical bonds between the hydration products is strengthened in a 'rigidification process'.

2.4.2 Pore structure development

As has been discussed above, during the main acceleration stage, a rapid precipitation of hydration products takes place. These are normally C-S-H and CH as products from the two silicate phases, and AFt and AFm as hydration products of the aluminate and ferrite phases. Efforts have been made at the atomic level (<2nm) to correlate the chemical structure of the C-S-H gel to one of the known chemical compounds such as the 1.4 tobermorite, Jennite, C-S-H I and C-S-H II. When assessing hardened cement paste

pore structure, larger scales are normally used which are in the range 1nm-100nm (Jennings, 2000). In hardened cement pastes, water-filled spaces, unhydrated cement particles and hydration products co-exist.

Two pore types exist in hardened cement paste which are gel pores within the C-S-H product, and capillary pores between the hydration products in the residual water-filled spaces (Garboczi and Bentz, 1996; Taylor, 1997).

Gel pores

The C-S-H itself is a porous material which has a porosity of ~28%. The gel pores within the C-S-H have an average diameter of about 0.5nm, which is an order of magnitude greater than the water molecule (2.75Å). This size for the gel pores has been suggested due to the fact that the hydration products do not form in pores which are less than 2nm. This makes the C-S-H gel porosity fixed and does not change to any great extent unlike the capillary pores (Aligizaki, 2006).

Capillary pores

The capillary pores within hardened cement paste exist as an interconnected network of continuous and discontinuous channels. This type of pore is the main factor which affects the durability properties in the hardened cement paste and concrete (Richardson, 2000), unlike the gel pores which do not contribute to transport processes. As it has been stated, in comparison to the gel pores the capillary pores are much larger and their diameters can vary within a wide range from 2nm-10µm. Pores, in terms of their diameters, are classified into 3 groups:

- (a) Micro pores: which have a diameter less than 2nm;
- (b) Mesopores: includes pores sizes in the range between 2nm to 50nm; and,
- (c) Macropores: contains pores which are >50nm.

The pore sizes have a significant influence on the ease of ionic transport through the pore network. In the case of the mesopores, electrostatic interaction between the pore-walls and the pore-liquid could have an extended effect through a significant fraction of the pore diameter, which affects transport processes. Pore tortuosity, pore connectivity and pore size distribution are much more important than the total porosity in terms of concrete durability, as aggressive agents (such as chloride) will normally travel through the connected pore network (Diamond, 2004; Ye, 2005).

2.5 Supplementary cementitious materials

Supplementary cementitious materials (SCMs) are inorganic materials which are added to Portland cement. These materials have been shown to enhance the long-term properties of concretes in terms of both the durability performance and increasing concrete strength. An additional advantage of using SCMs is the utilization of industrial by-products thereby lowering the production cost in the cement industry (Wu et al., 1983).

There are two types of SCMs based on their reactivity to produce hydration products:

(a) Pozzolanic materials: These are materials which are rich in SiO_2 and Al_2O_3 with a deficiency in CaO. These materials need a source of CaO to react with water at normal temperature, which is normally provided by the CH produced from the hydration reaction of Portland cement when mixed together. An example of this type of material is fly-ash (Taylor, 1997; EN197-1:2011, 2011).

(b) Latent hydraulic binder: This type of material acts as hydraulic cement as it reacts when it is mixed with water but at a slow rate. Reaction rate is increased by materials such as CH. An example of a latent hydraulic cement is ground granulated blast-furnace slag (GGBS) (Chen, 2006).

These inorganic materials are added to cement by two ways: either by grinding the SCM material with cement during the cement manufacturing process, or by mixing them together in the concrete production process. The later procedure is preferred due to the control of each component separately (Taylor, 1997).

2.5.1 Ground granulated blast furnace slag (GGBS)

Manufacturing process and chemical composition

GGBS is a product from the production of pig iron. In the manufacturing process, limestone reacts with materials which are rich in silicate and aluminate and are present in the iron ore and coke. At high temperature (1350°C - 1550°C) the slag forms a layer above the liquid iron due to its low density in comparison to the molten iron (Taylor, 1997; Hewlett, 2003; Chen, 2006). The cooling process is an important factor which consequently defines the slags cementitious properties and hydraulicity. Rapid cooling to below 800°C forms a glassy material which is desirable if it is to be used as a cement replacement material (Taylor, 1997). The cooling process can be performed by three different procedures:

(a) The use of high pressure water (2-3.5 bar) which is sprayed onto the molten liquid slag, with the slag: water ratio in the range from 1:6-1:10. This produces a wet, sandy glassy, material which is subsequently dried and ground to give a 95% glassy material of ground granulated blast-furnace slag (Bensted and Barnes, 2002).

(b) Another method is called the 'Pelletization method'. In this method, the cooling process depends partially on water and throwing the partially cooled molten material in to the air by a rotating drum to produce pellets. These pellets vary in size with a glassy content of about 50%. The resultant product in this process is called pelletized slag (Taylor, 1997) .

(c) The third method is performed by cooling the slag slowly through the use of air and then accelerate the cooling process by the use of water. The material produced in this process is called air-cooled slag which is a dense solid material and normally used as concrete aggregate, paving aggregate and road-bases (Hewlett, 2003; Chen, 2006).

All three cooling procedures are used in the manufacturing process in the iron industry; however, in terms of the quality of GGBS produced, the first cooling process is preferable due to the glassy content of the final product which, ultimately has a great effect on the activity of the GGBS (Fu et al., 2000). On the other hand, the second cooling process is preferable in terms of the iron manufacturing industry as it provides low-cost for the industry as well as reducing the emission of gases, but in terms of the GGBS produced it contains less glassy material in comparison to the first method (Taylor, 1997).

The major chemical composition of GGBS: MgO (0-21%), Al_2O_3 (5-33%), SiO_2 (27-42%), CaO (30-50%) (Taylor, 1997) together with other minor components as shown in Table 2.2 for UK slag.

Hydration reaction of slag cements

When GGBS is mixed with water, a small heat evolution peak is observed due to the initial dissolution of ions (Shi and Day, 1995). However, this immediate initial reaction halts due to the formation of a protective glassy layer on the surface of the GGBS which prevents the diffusion of water to the particles. Normally activators such as $Ca(OH)_2$ are added to accelerate the dissolution of the glassy network of the slag which leads, eventually, to the precipitation of calcium silicate, calcium aluminate and magnesium aluminate. In the presence of sulphate ions, ettringite is also formed due to the reaction

between the aluminate phase and the sulphate ions. Portland cement can be used as one of the activation agents for the GGBS due to the release of alkalis and CH during the hydration process.

The hydration of the slag cements is slower than pure Portland cement as is reflected in the total heat evolution as well as in the rate of the heat evolution (Kolani et al., 2012). This low heat emission of slag cements has been used as an advantage in mass concrete structures to minimizing thermal cracking.

Wu et al. (1983) and other researcher (Wu et al., 1990; De Schutter and Taerwe, 1995) have noted three peaks in the slag-cement heat evolution rate plot in the early hydration period. In pure Portland cement pastes only two peaks are detected during the same period. The authors have attributed the first two peaks to the rapid dissolution of ions and the accelerated period which both are normally observed in pure Portland cement. On the other hand, the third peak in the heat evolution rate has been attributed to the reaction of the GGBS in the mix which is activated by the release of the CH and alkalis from the Portland cement hydration (De Schutter and Taerwe, 1995). Wu et al. (1983) have noticed that the third peak, which has been attributed for the GGBS reaction, always occurs at the same time regardless of the slag content, however, its intensity is proportional to the amount of the slag replaced in the mix.

In terms of strength development, the short-term strength has shown to be lower in slag cements in comparison to pure Portland cement, as the Portland cement is responsible for the early strength development. In the long term, it has shown that the strength of slag cement is higher than Portland cement mixes (Wu et al., 1990; Osborne, 1999; Hewlett, 2003; Chen, 2006).

The amount of the CH produced from the hydration of the slag cement is less than pure Portland cement hydration (Fu et al., 2000; Kolani et al., 2012) as well as the Ca/Si ratio of the produced C-S-H. For example, in a 50% slag replacement the Ca/Si ratio is 1.55 in comparison to 1.8 for the pure Portland cement (Taylor, 1997).

2.5.2 Fly-ash

Manufacturing process and chemical composition

Fly-ash (FA) is a by-product from thermal power stations. The FA is produced from the burning and the pulverizing process which the coal passes through before being utilized in power plants. The coal is pulverized before it is supplied to the boilers where the coal is burned to generate steam which is required in the power generation process. During the burning process, which is performed at a temperature in the range of (1000-1500°C), fine particles in the flue gases are precipitated by electrostatic or mechanical processes to form the FA. Coarser particles accumulate at the bottom of the furnace to form what is called bottom ash (Bensted and Barnes, 2002). Fly-ash quality depends on the type of coal, hence its mineral composition as well as the burning process. In terms of the coal, bituminous coals are high in their glassy content ($Fe_2O_3 + Al_2O_3 + SiO_2$) but lower in their lime content CaO (<10%). Whereas fly-ash formed from sub-bituminous coal has a CaO content >20% (Papadakis, 1999). The chemical composition of typical low CaO fly-ash (ASTM class F) is presented in Table 2.3.

Fly-ash particles have a glassy, spherical shape with a diameter between 10µm-40µm; however, the thermal history plays a role in the topology of the fly-ash, as irregular particles could appear if insufficient burning temperature or burning duration was implemented (Taylor, 1997; Bensted and Barnes, 2002). Carbon can also be present in fly-ash in spherical or irregular porous particles which leads to lowering the specific gravity of the fly-ash. The specific gravity for fly-ash is in the range 1.6-2.8 and the low limit associated with the presence of carbon or the presence of hollow spheres.

Hydration reaction of fly-ash

The main features which can distinguish the hydration reaction of fly-ash cement are low heat emission and delay in the setting time (Jun-yuan et al., 1984; Langan et al., 2002; Sakai et al., 2005; Dittrich et al., 2014). In terms of the hydration products, FA mixes produce less CH in comparison to the pure cement mixes due to the reaction between FA and CH to form C-S-H hydration products. The amount of the CH in the mix has been used in some studies as an indication to the pozzolanic reaction rate (Mehta and Gjrv, 1982; Jun-yuan et al., 1984). The retardation in the induction period has been investigated by the addition of FA to pure tricalcium silicate (C_3S) and is due to the adsorption of the Ca^{2+} on the FA particles which delays the nucleation of the CH in the solution (Langan et al., 2002).

In terms of the effect of the FA on the acceleration stage of cement, it has been observed that the FA acts as a nucleation site for the C-S-H and CH, as at relatively early ages (~1hr) a C-S-H film forms on the FA particles. It has been argued that this C-S-H is not a part of the hydration products of the FA as the FA hydration products do not form on the surface of the FA but precipitate elsewhere. The nucleation effect of the FA has been detected through comparing the rate of heat generation in the mixes. The rate of heat shows an increase for the FA mixes in comparison to the pure Portland cement mixes (see Figure 2.5) (Langan et al., 2002). It should be mentioned that, in the latter study the heat rate was normalised by the cement weight to separate the effect of the FA as it is well known that FA reduces the absolute heat evolution in the mixes.

FA hydration reaction can be explained by a model which illustrates the process (Bensted and Barnes, 2002). In the proposed model, the dissolution of alkalis from cement, produces a rich Al-Si layer on the FA particles; calcium ions from the aqueous phase are adsorbed to this layer forming C-S-H hydration product. The model proposes that the dissolution of the alkalis accelerates the generation of AlO^{-2} from the FA surface which reacts with the calcium ions increasing the surface layer. Eventually, an osmotic pressure between the interior and the exterior of the surface layer ruptures the layer which leads to the precipitation of more hydration products away from the FA surfaces.

Papadakis (1999) has shown that FA particles during the early hydration period (<3days) are used as nucleation sites for cement hydration products which are, for example, ettringite and CH. No traces of the FA particle reaction could be detected within the first 21 days after mixing with water. During the first 21days, the hydration products surrounding the FA particles have been attributed to the reaction of the cement clinker, as the hydration of the FA has been shown to commence after 6 months.

In terms of strength development, the replacement of cement by FA decreases the early strength development due to its low reactivity in comparison with the pure cement. However, at the late stages (>3months) the FA mixes show a higher strength than the pure cement mixes (Mehta and Gjörv, 1982; Jun-yuan et al., 1984; Papadakis, 1999), but the increase depends on the replacement level.

2.6 Summary

In this chapter, the steps of cement manufacturing process have been illustrated, and the quality control measures which are normally conducted to ensure the compliance of the

raw meal and the clinker to the chemical composition have been shown. The polymorphs of the four phases which constitute cement are dependent on the thermal history as well as the impurities which are used to stabilise these phases.

Six periods in the calorimeter response are normally identified through the first 24hrs after mixing Portland cement with water. These periods have shown to be similar for the hydration reaction of the alite phase and the belite phase despite the delay and the low thermal activity for the hydration process of the latter. The main hydration products for the silicate phases (alite/belite) are C-S-H and the CH. The belite gives less CH when compared with the alite phase.

Both the hydration reactions of the aluminate phase and the ferrite phase are shown to be affected by the addition of calcium sulphate. Calcium sulphate reduces the reactivity of the mentioned phases by forming a diffusion barrier layer of ettringite. In the absence of sulphate ions, hexagonal hydrates form rapidly leading to the flash setting phenomena

Different theories were presented to explain the induction period in the hydration of cement, and the triggering causes of the acceleration period according to each theory has been discussed. The different processes which contribute, together on the setting process, have been illustrated and the different types of pores which form consequently have been categorized according to their sizes and their influence on the transport processes of ions through the cement matrix.

The difference between the two main types of SCMs (pozzolanic and latent) has been discussed and the manufacturing process, as well as the hydration process for both the GGBS and the fly-ash, has been illustrated.

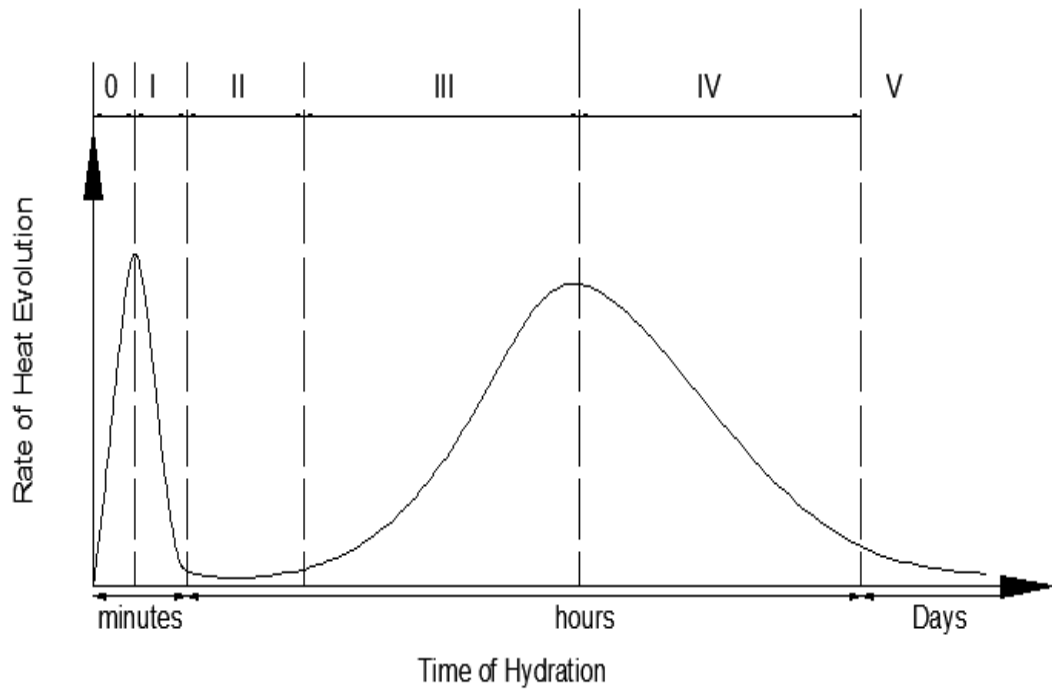


Figure 2.1: C_3S phase rate of heat evolution through the hydration time.

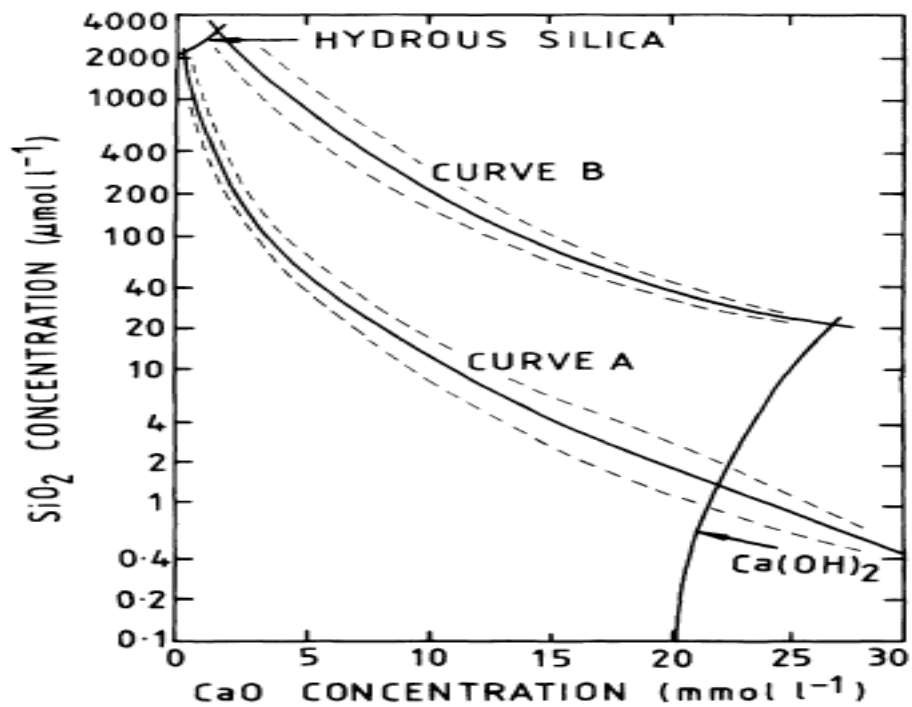


Figure 2.2: CaO and SiO_2 concentrations on the C-S-H phase solution (Taylor, 1997).

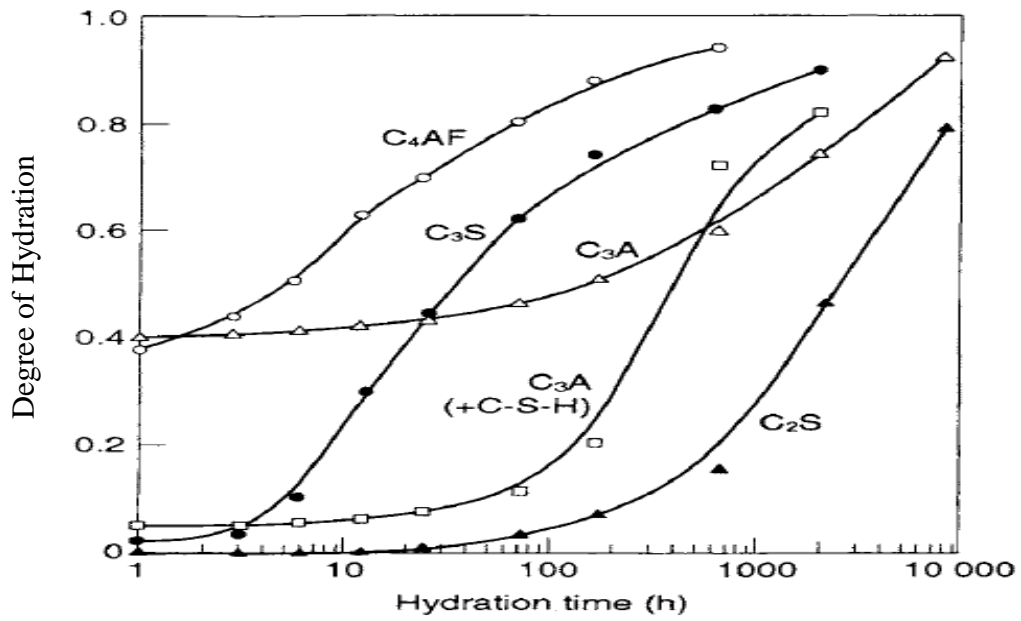


Figure 2.3: Hydration kinetics for different cement phases (Hewlett, 2003).

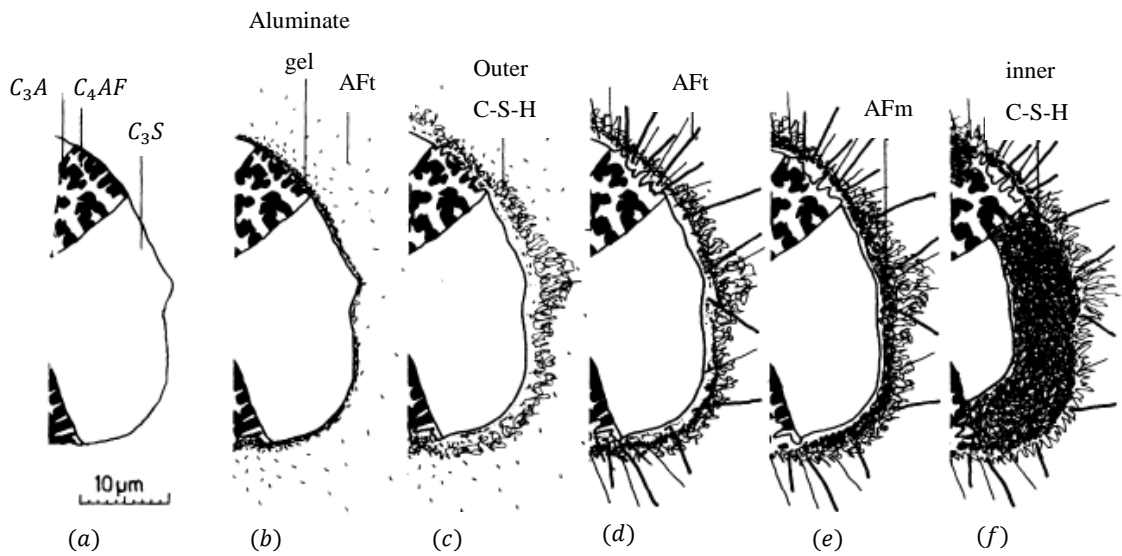


Figure 2.4: Hydrate formations on the surface of a cement grain during hydration. (a) unhydrated cement grain with different composing phases; (b) at 10mins hydration, AFt short rods and aluminium gel start to appear on the surface of the grain due to C₃A reaction with gypsum; (c) at 10hrs age outer C-S-H hydration product forms on the ettringite short rods leaving 1 μm gap from the surface of the cement grain; (e) at 18hrs gradual formation of AFm inside the hydration shell as well as the C-S-H inner product, (f) at 1-3days C-S-H inner product fills the gap between the outer product and the unhydrated cement grain (Taylor, 1997).

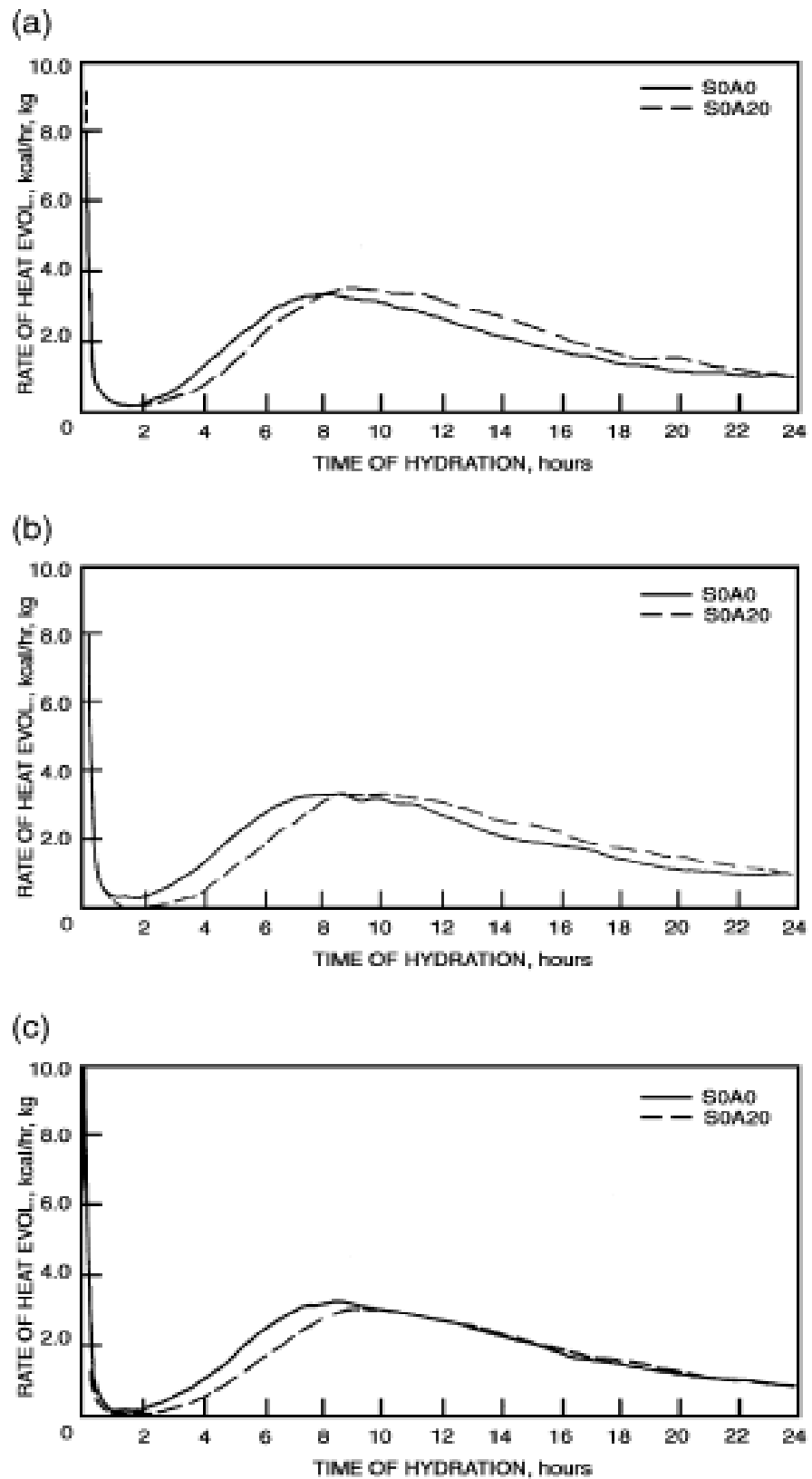


Figure 2.5: Normalised heat evolution for Portland cement paste denoted S0A0, and 20% Fly-ash replaced paste denoted S0A20 at (a):0.35w/b, (b):0.4w/b and (c):0.5w/b (Langan et al., 2002).

Controlling ratio	Highest Value	Mean Value	Lowest Value
LSF	101	96	90
SR	4.2	2.5	1.4
AR	4.2	2.3	0.6

Table 2.1: LSF, SR, AR of clinker produced in Germany adapted from (Bensted and Barnes, 2002).

Oxide type	Weight percentage% in UK
CaO	39.9-40.5
MgO	8.3-8.8
Al_2O_3	11.0-13.1
SiO_2	35.2-37.0
S	0.9-1.1
Na_2O+K_2O	0.5-0.7
Mn	0.28-0.35
$CaO+MgO+Al_2O_3/SiO_2$	16.5-1.74

Table 2.2: Chemical composition for blast furnace slag in the UK (Bensted and Barnes, 2002).

Oxide type	Composition percentage %
Na_2O	1.5
MgO	1.6
Al_2O_3	27.9
SiO_2	48.7
P_2O_5	0.2
SO_3	1.2
K_2O	4.2
CaO	2.4
TiO_2	0.9
Fe_2O_3	9.5
C	1.5
H_2O	0.3

Table 2.3: Chemical composition of low calcium fly-ash (Taylor, 1997).

Chapter 3 – Electrical Property Measurements on Cementitious Materials

3.1 Introduction

Monitoring the electrical properties of cementitious materials can provide valuable information in terms of characterizing the effect of different physical and chemical processes which take place. Environmental exposure, wetting and drying cycles, hydration process and mechanical loading effects (Cabeza et al., 2003), can be monitored non-destructively by the use of AC immittance spectroscopy which is sensitive to the changes in the pore structure as well as the ongoing chemical reactions in the cementitious materials (McCarter and Brousseau, 1990; Gu et al., 1992; Gu et al., 1993; Gu and Beaudoin, 1997; Cabeza et al., 2006; Sanish et al., 2013). In order to explain the background to AC immittance techniques, there are a total of four levels: impedance $Z(\omega)$; admittance $Y(\omega)$ ($=1/Z(\omega)$); relative permittivity, $\epsilon_r(\omega)$ and the electric modulus, $M(\omega)$ ($=1/\epsilon_r(\omega)$). The impedance and the permittivity levels will be considered in the following discussion as a general case for the other levels. It is also shown that the different formalisms are all related mathematically to each other.

3.2 Preliminaries

Acquiring the AC immittance response from a material requires the application of an electrical stimulus over a range of frequencies. The electrical stimulus which is normally used is either a constant voltage or a constant current and is applied to the material through electrodes. General examples of the electrical parameters obtained from AC immittance tests are the bulk conductivity (or its reciprocal resistivity) and permittivity.

3.2.1 Impedance level

It has been shown that the impedance of a cementitious material, $Z^*(\omega)$ (in ohms, Ω), can be represented in complex format through the relationship (McCarter and Brousseau, 1990; Christensen, 1993):

$$Z^*(\omega) = Z'(\omega) - iZ''(\omega) \quad (3.1)$$

where ω is the angular frequency ($= 2\pi f$ where f is the frequency of the applied field in Hertz), $Z'(\omega)$ is the real or resistive component, $Z''(\omega)$ is the imaginary or reactive component and $i = \sqrt{-1}$. Plotting equation (3.1) in rectangular coordinates is known as the Nyquist format i.e. $-iZ''(\omega)$ versus $Z'(\omega)$. Regarding the Nyquist formalism, if the

system can be electrically modelled as a resistor in parallel with a pure capacitor whose capacitance (in Farads) is constant with increasing frequency, the polar plot will take the form of a semicircle. Figure 3.1(a) displays the plot for a pure resistor/capacitor combination with $R = 1.0 \text{ k}\Omega$ and $C = 10^{-10} \text{ F}$, which produces a semicircle whose centre is located on the real axis. Frequency increases from right to left across the plot. However, for saturated porous media, such as cementitious materials (see, for example, (McCarter and Brousseau, 1990; Christensen et al., 1994; Keddam et al., 1997; Cabeza et al., 2002; Ball et al., 2011)), the plot takes the form of a circular arc whose centre is depressed below the real ($Z'(\omega)$) axis. This is due to relaxation of polarization processes within the system and results in dielectric dispersion, i.e. the decrease in the capacitance with increasing frequency. To account for this phenomenon, the ideal capacitor is replaced by a pseudo-capacitance or constant-phase element (CPE) to account for the dispersive behaviour of the medium. The CPE is a complex, frequency-dependent parameter defined by the relationship:

$$Z''_{CPE}(\omega) = \frac{1}{C_0(i\omega)^p} \quad (3.2)$$

C_0 is a coefficient and the exponent, p , has a value such that $0 < p < 1$; if p equals 1, then the equation is identical to the reactive component of a pure capacitor of value C_0 with units in farads (F). When a CPE with value of $p < 1$ is placed in parallel with a resistor, a circular arc is produced with its centre depressed below the real axis with C_0 having units F s^{p-1} . Figure 3.1(a) also presents the Nyquist plot for a CPE ($C_0 = 10^{-10} \text{ F s}^{-0.2}$ and $p = 0.8$) in parallel with a resistor $R = 1.0 \text{ k}\Omega$ which now results a circular arc with its centre below the real axis. With reference to the schematic diagram in Figure 3.1(b), the depression angle, α (in degrees) of the circle centre (O) is related to the exponent, p , in equation (3.3) through the relationship:

$$\alpha = (1 - p)90^\circ \quad (3.3)$$

3.2.2 Permittivity Level

When inserting a dielectric material between two electrodes, the surface charge density drops by an amount which is equal to the polarization density, hence the total charge density at the electrodes will be equal to the free charge density induced by the electrical field plus the bound charge density which is represented by the polarization density as in equations (3.4) and (3.5),

$$P = \varepsilon_o \chi E \quad (3.4)$$

$$D = P + \varepsilon_o E \quad (3.5)$$

Where: D = the total charge density at the electrodes (Electric displacement) (C/m^2); P = the polarization density in the dielectric material (C/m^2); ε_o = vacuum permittivity (8.854×10^{-12} F/m); χ = dielectric susceptibility of the material (dimensionless); E = electrical field (V/m);

From equations (3.4) and (3.5), equation (3.6) below can be deduced which, in turn, relates the total charge density to the permittivity of the material between the electrodes, as well as with the generated electrical fields:

$$D = \varepsilon_o \varepsilon_s E \quad (3.6)$$

Where ε_s is the static permittivity and equals $(\chi + 1)$ (F/m). When an alternating electrical field is used in characterizing the cementitious material instead of a static field, both the electric field and the electric displacement in this case are time-variant and can be expressed as (Feldman et al., 2015):

$$E(t) = E_o e^{i\omega t} \quad (3.7)$$

and,

$$D(t) = D_o e^{i(\omega t - \delta(\omega))} \quad (3.8)$$

Where: $E(t)$ = time variant electric field (V/m); E_o = Electric field amplitude (V/m); ω = angular frequency (rad/sec); $D(t)$ = Time variant total charge density (C/m^2); D_o = total charge density amplitude (C/m^2); and $\delta(\omega)$ = Phase lag of the electric field (rad).

By substituting equation (3.7) and (3.8) in equation (3.6) to get the time variation effect on the material electric permittivity, the complex permittivity (instead of the static permittivity) is defined according to equations (3.9) and (3.10):

$$\varepsilon^*(\omega) = \varepsilon'(\omega) - i\varepsilon''(\omega) \quad (3.9)$$

$$\varepsilon^*(\omega) = \left(\frac{D_o}{\varepsilon_o E_o} \right) \times e^{i\delta\omega} \quad (3.10)$$

where $\varepsilon^*(\omega)$ the complex permittivity (F/m); $\varepsilon'(\omega)$ the real part of the permittivity (F/m); $\varepsilon''(\omega)$ the permittivity imaginary part (loss) (F/m). The relative permittivity, ε_r which is a dimensionless parameter, is normally used in material characterization, which is the ratio of the real part of the permittivity and permittivity of a vacuum ε_0 (i.e. $\varepsilon_r = \frac{\varepsilon'(\omega)}{\varepsilon_0}$).

From both equations (3.9) and (3.10) it can be deduced that the permittivity of materials is frequency dependent, and it has been shown that as the AC frequency increases, the permittivity decreases. This is physically attributed to the inability of the material charges to follow the alternation of the electrical field at high frequencies. This process is known as relaxation. Therefore, at low frequencies the permittivity records high values due to the contribution of different polarization mechanisms, in contrast to its values at higher frequencies as polarization processes relax. Through the frequency spectrum, different polarization processes have been shown to appear and relax at different frequency ranges. The type of the dominant polarization process is material dependent as well as frequency dependant.

Bulk polarization processes

Six types of polarization processes are present depending on the AC frequency range as well as on the type of material (Hasted, 1973; Scaife, 1998; Beek, 2000). Four polarization processes take place in homogeneous materials (see Figure 3.2), and the remainder take place in heterogeneous materials. In homogeneous materials, polarization processes are as follows:

(i) Orientation dipole polarization:

This occurs in dielectrics with a permanent dipole structure such as water. In this molecular structure the dipole rotates when an electrical field is applied (see Figure 3.2 (a)). Other types of molecules do not possess this permanent dipole property because of their symmetrical molecular structure, such as in the case of CO_2 molecule. At sufficiently high frequency values, normally more than the microwave frequency range for the water molecule, the rotational dipole polarization relaxes, and in consequence it will not contribute any more to the polarization process hence permittivity (Hasted, 1973).

(ii) Atomic polarization:

This type of polarization occurs at infra-red frequencies and is due to the rearrangement of the natural distribution of atoms or atom groups in molecules in sympathy to the applied electrical field (see Figure 3.2(b)) (Van Beek and Hilhorst, 1999).

(iii) *Electronic polarization:*

In which the electron cloud in atoms is shifted from the nuclei to one side due to the imposed electrical field and is similar to atomic polarization (see Figure 3.2(b)).

(iv) *Ionic polarization:*

This type of polarization occurs at visible light frequencies in ionic crystals by rearranging the distribution of the negative and the positive ions in the lattice according to the direction of the applied electric field (see Figure 3.2(c)).

It could be noticed that the electronic, atomic and ionic polarization processes induce charge rearrangement in the dielectric material; however, the scale of charge localization differs for each polarization processes, i.e. atomic scale, nuclei/electron scale and crystal scale, respectively. Figure 3.3 shows the frequency ranges at which the different polarisation mechanisms in a homogeneous material take place, and the effect of AC frequency increase on the real and imaginary permittivity.

Two additional polarization mechanisms take place in heterogeneous materials at relatively low frequencies ranges (normally in the kHz-MHz region) which are (Coelho, 1979; Beek, 2000):

(v) *The interfacial polarization (Space charge polarization):*

In which ions drift in the applied electrical field and are blocked by discontinuities in the electric paths. Ions, therefore accumulate at the interfacial zones on both sides of the discontinuous paths, forming what is known as interfacial polarization (see Figure 3.4(a)).

(vi) *The double-layer polarization:*

In which the surface of the solid /liquid interface form an electrical double layer of oppositely charged ions which can be polarized in the electrical field thereby inducing a large dipole moments (Harrop, 1972; Beek, 2000) (see Figure 3.4 (b)).

From the dependency of the polarization processes on the AC frequency, material characterization by AC immittance techniques should consider the type of the polarization mechanisms which takes place in the material due to the applied electrical field.

Electrode polarization process

This type of polarization process takes place at the sample/electrode interface particularly in ionic electrolytes. The application of electric field encourages ions to accumulate on the surface of the metallic electrodes producing a double-layer of oppositely charged ions. This polarization process contributes in reducing the electrical field in the bulk material due to the adsorption of the charges on the electrodes surface. This is significantly pronounced when using direct field or low-frequency alternating field (Schwan, 1968). Several models had been introduced to describe the double-layer at the sample/electrode interface, such as:

- (a) The Helmholtz model suggested a simple, two-plate molecular capacitor, as one of the plates represents the metallic electrode and the other represents the strongly adsorbed counterion layer originating from the solution on the surface of the metallic electrode. The distance between the two plates has been assumed to be in the order of 0.5nm therefore producing a high capacitance value. The potential drops over the thickness of the Helmholtz double-layer until it attains the bulk material potential value (Martinsen and Grimnes, 2011) (see Figure 3.5(a)).
- (b) Due to the extended thickness of the electrical-double layer in diluted electrolytes, in contrast to the concentrated ones, the Gouy-Chapman model has suggested a diffused double-layer in which the transition of the latter to the bulk solution is more gradual. In this model, an exponential decay for the electrical potential through the diffused double layer is assumed to take place (see Figure 3.5(b)). The thickness of the diffused double-layer is estimated by the Debye length according to (Lvovich, 2012):

$$\lambda_D = \sqrt{\epsilon_r \epsilon_0 k_B T / 2e^2 \sum n_j} \quad (3.11)$$

λ_D is the characteristic length of the diffused double layer; ϵ_r = relative permittivity of the medium; ϵ_0 = permittivity of free space F/m; k_B is the Boltzman constant; T: temperature (K); e = unit of charge and n = concentration of free ions.

- (c) the Stern model has considered both the adsorbed and the diffused nature of the electric-double layer on the surface of the electrodes. In this model, the double-layer is divided into outer and inner double-layers, which represent the diffuse (Gouy layer) and the adsorbed layer (Stern layer) respectively. The Gouy layer starts at a distance which is equal to the radius of the adsorbed ion (see Figure 3.5(c)).

Methods of reducing electrode polarization (EP):

The electrode polarization impedance, $Z_p(\omega)$, is represented by equation (3.12) according to Schwan (1963) in which the polarization resistance, R_p , is connected in series with the polarization capacitance C_p ; both electrical parameters are connected in series with the sample bulk circuit which is composed of a resistance R_s connected in parallel with a bulk capacitance C_s (see Figure 3.6).

$$Z_p(\omega) = R_p + \frac{1}{i\omega C_p} \quad (3.12)$$

Electrode polarization impedance can mask the bulk material response unless using a sufficiently high measuring frequency. Different electrode polarization correction techniques have been suggested in the literature. These correction techniques can be divided into two main types, which are:

Apparatus compensation methods (Emmert et al., 2011; Paul Ben et al., 2013):

(a) Changing the electrode spacing as, in this case, the electrode polarization impedance does not depend on the sample size but the spacing between the electrodes, therefore the contribution can be detected and separated from the bulk response.

(b) Using a 4-point electrode configuration, in which the potential of the sample is measured by different electrodes, therefore avoiding the current injecting electrodes and their associated double layer.

(c) Using non-polarizable electrodes such as platinum electrodes (Hoffmann et al., 2006), which have the advantage of increasing the surface area, such as by the use of a platinum black powder, therefore decreasing the EP impedance.

Analytical methods (Davey et al., 1990; Bordi et al., 2001):

(a) Modelling the measured response by the use of an equivalent electric circuit and then extracting the material response from the measured response; or,

(b) using empirical functions to fit the experimental data in order to separate the bulk response from the electrode polarization response

By taking into consideration the polarization correction techniques noted above, apparatus compensation techniques are relatively difficult to apply to cementitious materials as their conductivity and, consequently, the electrode polarization effect is continuously changing through the hydration process. This necessitates the continuous adjustment of apparatus compensation techniques to accommodate the continuously changing electrode polarization effect. Therefore, analytical methods could be more favored in this case.

3.3 Review of electrical property measurements on cementitious materials

3.3.1 Early hydration (0-24hrs)

Conductivity/Resistivity response

Electrical measurements on cement-based materials can be traced back to the 1920's. Shimizu (1928) studied the setting process in Portland cement pastes at different temperatures in the range 18°C - 50°C with the time of the break point denoted (P) in Figure 3.7 in the conductivity curve related to the time of final set. It was also shown that as the temperature increases, the final setting time decreases. Boast (1936) studied the period from gauging over the initial ~3hrs for cement pastes with different w/b ratios and at different temperatures. It was shown that the early conductivity peak, which also appeared on Shimizu (1928) data (see Figure 3.7), is affected by temperature as well as the w/b ratio. The early peak was related to the increase of ions in the mixing water due to the dissolution of the cement grains; thereafter, the decrease in the conductivity was related to the increase in the viscosity of the mix.

Monfore (1968) highlighted the effect of cement alkali content on the resistivity during early hydration. In this study two types of cement were used and the cement with higher alkali content (paste B) showed lower resistivity values when compared with the low alkali cement (paste A) (see Figure 3.8(a)). It was also shown that the early hydration resistivity response for cement pastes is similar to the resistivity response through time for the pure C_3S component (see Figure 3.8(b)). It is interesting to observe that the sudden change in the slope in Figure 3.8(a) in which Monfore (1968) had considered repeatable has also been observed by McCarter and Curran (1984). No particular hydration activity was assigned to this feature by Monfore (1968); however, McCarter and Curran (1984) have attributed this feature either to the increase in the ions in the mix due to the acceleration period of the hydration reaction, or due to the increase in the temperature of

the mix which had been monitored during their study. Whittington et al. (1981) extended their research to include both the early hydration resistivity response for concrete mixes and cement pastes. In this study, the authors noticed a systematic decrease for the electrical resistivity of both cement pastes and concrete mixes as the w/b ratio increases. Also, a noticeable decrease in the resistivity of the pastes was observed during the first 5hrs after mixing, in which the decrease was not observable in the case of the concrete mixes. The decrease in the resistivity during this period was attributed to either the increase in the temperature of the mixes due to the exothermic hydration reaction, or the increase in the number of ions in the solution due to the dissolution process.

A more detailed study had been conducted by McCarter and Afshar (1985) on a Portland cement paste with 0.27w/b ratio over selected frequencies, viz. 100Hz, 1kHz and 10kHz. Considering Figure 3.9, the early hydration resistivity response was divided into four stages which were related to the known stages of hydration as follows:

1) *Stage I 'pre-induction stage':*

This stage occurs when the resistivity records low values due to the rapid dissolution of ions from the cement particles at the start of the measurements.

2) *Stage II 'induction or the dormant stage':*

The resistivity at this stage has shown to record a slight increase. This has been attributed to the formation of an unstable weak C-S-H membrane layer on the cement grains which hinders dissolution. Also, the slight increase in Stage II regarding the resistivity value has been attributed to the formation of the contacts between the C-S-H gel surfaces which block the pathways in the cement paste hindering the free charge movement (Garvin, 1991).

3) *Stage III 'acceleration period':*

This stage has been related to setting, causing an increase in the electrical resistivity due to the formation of stable C-S-H and a capillary pore network. Also, the continuous deposition of the hydration products inside the capillary pores (C-S-H and $\text{Ca}(\text{OH})_2$) replaces the evaporable water, thereby increasing the constriction and tortuosity of the electrical conduction pathways which contributes to the increase in resistivity.

4) *Stage IV 'Steady acceleration period':*

During Stage IV the resistivity displays a steady increase although a decrease occurs at the age of 600 min which has been related to renewed activity for the C_3A phase. After Stage IV the resistivity continues its increasing trend at a steady rate as in this period the paste hardens and the pore structure continuously develops through time.

McCarter (1987) has highlighted the effect of the measuring frequency on the obtained resistivity values. It has been shown that as the measuring frequency increases the resistivity decreases (see Figure 3.10). Therefore, by using this feature two types of electrical conduction in cement pastes have been identified, the ionic electrical conduction through the connected capillary pores, and a surface conduction effect via the adsorbed gel water. The author in this study has introduced a parameter which is the percentage frequency effect factor (PFE) which is the percentage difference between the low frequency resistivity of the mix, at 100Hz, and the high frequency resistivity of the mix 300kHz. This factor has been explained in terms of the gel-space ratio in the mix, and it has been shown that it is affected by the used w/b in the mixes (see Figure 3.11).

Many studies have utilised impedance spectroscopy during early hydration in order to obtain reliable bulk electrical resistivity or conductivity rather than using selected frequencies (Christensen et al., 1994; Wei and Li, 2005; Xiao et al., 2007; Xiao and Li, 2008; Manchiryal and Neithalath, 2009; Sanish et al., 2013). By extracting the pore-water solution for different cement pastes, as well as measuring the bulk electrical conductivity, Christensen et al. (1994) were able to estimate the capillary pore fraction of the cement pastes at different ages. Also, as an example of impedance spectroscopy to extract the bulk resistivity/conductivity of cementitious materials through time, is the study which has been conducted by Manchiryal and Neithalath (2009) to evaluate the effect of different w/b ratios, aggregate /cement ratios and SCM additions on concrete and cement pastes electrical response. In this study, it has been shown that the setting time, which is obtained from the minima of the conductivity derivative diagram in the early hydration period, is related to the setting time results which were obtained from the Vicat needle test

Sanish et al. (2013) compared the stages which appear in the isothermal calorimetric studies diagrams during the early hydration period with the conductivity for the cement pastes, as well as the conductivity derivative diagram through time. Four stages were identified between the electrical conductivity and the calorimeter tests for a 0.3w/b ratio normal Portland cement, which are presented below (see Figure 3.12):

- I. An increase in the conductivity, reaching a maximum between 0-1.2hrs due to ion dissolution. The end of this zone is marked in the conductivity diagram as point (a);
- II. The zone extending from point (a) to point (b) witnesses a gradual decrease in conductivity. This zone could be related to the induction period which extends, according to this study, of 1.2hrs to 3hrs;
- III. In this zone (from point (b)-(c)) a rapid decrease in conductivity occurs revealing an accelerated reaction and the formation of the hydration products (3-12hrs); and,
- IV. A gradual decrease in the conductivity through time as the hardening stage proceeds and more constricted electrical paths are produced (>12hrs) which corresponds to the zone after point (c).

With regard to the effect of SCM's on the conductivity/resistivity of the material, Wei and Li (2005) have shown that the resistivity of pastes with fly-ash additions has higher values during the early hydration stage and a lower electrical resistivity after the setting stage. These findings have been obtained through the use of a single frequency electrical resistivity measurement for 0.4 w/b ratio pastes. The same findings regarding the electrical resistivity in the first hours during the early hydration stage, have been reported in other studies (Xiao and Li, 2008; Manchiryal and Neithalath, 2009; Sanish et al., 2013). This increase in the resistivity was attributed to the more conductive pore solution which the Portland cement possesses in comparison to the fly-ash replaced samples (see Figure 3.13).

Regarding the GGBS resistivity/conductivity response, there are two types of studies found in the literature: the response of the activated GGBS, and the response of GGBS as a replacement material for Portland cement with a specific addition percentage. By activating the GGBS with sodium silicate (NS) and calcium hydroxide (CH), it has been shown that the electrical conductivity for all the mixes with time shows the same early hydration stages (McCarter and Ezirim, 1998b). However, the early hydration stages of the GGBS mixes are significantly delayed and extended through time than the normal Portland cement mixes. Also, it has been shown that the GGBS with CH as activator is more delayed in its reaction in comparison to plain Portland cement mixes and the GGBS activated with NS.

The delaying effect of the GGBS when added to Portland cement paste mixes has been noticed by Zhang et al. (1995), as it has been shown that the lower the slag replacement level the conductivity curve is much closer to the conductivity curve for the pure Portland

cement, despite the lengthening in the induction period in the slag mixes. It had been shown by McCarter et al. (2013) that the initial values for the electrical conductivity for the GGBS replaced materials for concrete samples, are inversely related with the increasing addition percentage of GGBS. This has been attributed to the dependency of the conductivity during early hydration on the ionic concentration within the aqueous phase which is provided by the cement particles rather than by the GGBS particles.

With regard to the effect of aggregate addition to cement pastes on electrical response during early hydration, it has been shown that the general trend and stages observed from the resistivity is similar to the plain cement pastes (Wei and Xiao, 2011) although the absolute values of the resistivity increases as the volume fraction of the aggregate increases in the mixes (Afshar, 1986 ; Wei and Xiao, 2011) (see Figure 3.14). The increase in resistivity is not just limited to the reason of including resistive particles (aggregate) in a conductive phase (cement paste), but it has been attributed to the formation of the interfacial transitional zone (ITZ), as this zone imposes a wall effect which leads to higher water-content in these zones leading to a reduction in the actual w/b in the cement matrix hence, the resistivity value. The influence of the aggregate addition on the ITZ has been observed by assessing the normalized conductivity response through time. The high volume of aggregate in the mix (60-70%) showed higher normalized conductivity values due to the percolation of the interfacial transition zones (Figure 3.15). Furthermore, the inclusion of aggregate extends the induction period during early hydration, as the decrease in conductivity after the induction period, was progressively delayed in comparison to cement pastes with increasing aggregate content (Princigallo et al., 2003).

Permittivity response

Despite the paucity of work on the permittivity response during early hydration, studies can be traced back to the 1970's. One of the first studies which evaluated the permittivity of cement-pastes was Taylor and Arulanandan (1974). In this study, the dispersion diagrams for both the conductivity and the permittivity for 0.35 w/b cement-paste were presented. The dispersion plots were obtained at times >23hrs over the frequency range of 10MHz-50MHz (see Figure 3.16). The permittivity displayed a decrease as the frequency increases highlighting the relaxation of low-frequency polarization processes.

A more detailed study had been conducted by McCarter and Afshar (1985) with regard to the temporal variation in the permittivity of cement paste. In this study, permittivity displayed four stages as in the case of the resistivity, and these stages have been explained as follows (see Figure 3.9):

1) Stage 1: Once the samples are mixed with water, the permittivity displays an anomalously large value (in the range of 10^4), this has been explained in terms of the polarization process associated with the cement grain surfaces, as mainly the Ca^{++} , OH^- ions form a double layer polarization mechanism around the weak thin C-S-H gel which, in turn, surrounds the cement grain. The electrical double layer induces a large dipole moment, therefore a large value for the permittivity is recorded in this early stage (Afshar, 1986 ; Garvin, 1991).

2) Stage 2: In this stage, the permittivity displays a slow decrease value reflecting a period of low reactivity.

3) Stage 3: This stage extends from 180-600mins. The permittivity displays a peak at 200 mins followed by a rapid decrease. This feature has been attributed to the rupture of the C-S-H membrane around the cement grains, allowing ions to be released into the double-layer region surrounding the cement grain and therefore increasing the polarizability of the paste which results in an increase in the permittivity. The decrease in the permittivity after the peak is taken to indicate that the charges released from the cement grain form a stable C-S-H outer hydration product (Garvin, 1991).

4) Stage 4: During this stage, the value of the permittivity increases which coincides with the decrease in resistivity at the same time and attributed to the renewed activity of the aluminate phase. This Stage could be considered in agreement with the results of the TDR (time domain reflectometry) performed on the early hydration period of cement pastes by Hager and Domszy (2004). In this work, an increase in the permittivity values has been observed from the age of 9.6 hrs to 19.3hrs, before the permittivity decreases.

After Stage 4, there follows a period of low reactivity, as the permittivity decreases gradually with time and attributed to an irrotational binding of charges resulting from an increase in rigidity of the paste.

It is noteworthy that at higher frequencies (10GHz) a different behaviour for the permittivity has been observed through the first 24hrs for cement pastes (Moukwa et al., 1991). In this case, the permittivity at this high frequency displayed a 'conductivity-like'

curve (see Figure 3.17), which indicates other polarization processes take place within the material during this early hydration stage; however, their detection depends on the measuring frequency. It is interesting to note that Van Beek and Hilhorst (1999) have shown that at low measuring frequency ranges (lower MHz values), the permittivity displays the same peak which has been shown in McCarter and Afshar (1985), whereas at high frequencies, this peak cannot be detected. This is possibly due to relaxation processes as when the frequency increases, charges lose their ability to follow the alternation of the applied electrical field, therefore their contribution to the permittivity reduces (see Figure 3.18). In another study performed on an aluminous cement in the frequency range of 1MHz-1.8GHz (Smith et al., 2002), the capacitance response through time was explained in terms of three stages (see Figure 3.19):

- (i) Zone I: A slight increase in the capacitance which is more discernible at low frequencies, and attributed to the dissolution of calcium and aluminium ions into solution;
- (ii) Zone IIa: The capacitance value starts to rapidly increase, and is attributed to the precipitation of hydration products;
- (iii) Zone IIb: The capacitance value decreases due to coalescence of the hydration products;
- (iv) Zone III: This has been related to the period after the setting process, as in this period the capacitance displays a low variation through time.

Therefore, from the permittivity response through the early hydration period, it can be concluded that the measuring frequency range has a significant influence in detecting the polarization process(es) which take place in the material.

In terms of mixes with fly-ash addition, permittivity values display an increase as the replacement addition increases. This is observed in the frequency region $>1\text{kHz}$ (see Figure 3.20). With regard to GGBS addition, Zhang et al. (1995) investigated the permittivity during early hydration at 9.5GHz for different percentages of slag (0%, 30% , 60%, 90%). It was shown that the initial values for the permittivity after mixing display a clear relation with the percentage of the slag, despite the retarding effect which the addition of the slag caused during the induction period. In general, the permittivity behaviour with time for the lowest slag percentage (30%) was similar to the pure Portland cement mix. The permittivity with higher slag addition, showed larger

values after the induction period which was particularly evident for the 90% slag cement mixes (see Figure 3.21).

Nyquist plot

Manchiryal and Neithalath (2009) have shown that during the early hydration of cement pastes, the Nyquist plot displays one arc which represents the electrode arc. The fresh material at this early stage acts primarily as a conductive fluid; however, as the material hydrates, another arc appears which represents the bulk material response (McCarter, 1994; Kim et al., 1995; Cormack et al., 1998) (see Figure 3.22). It is evident that with increasing hydration time the bulk arc develops progressively, and becomes noticeable at 9hrs after mixing the samples with water.

Nyquist plots have shown to be sensitive to the addition of the fly-ash during early hydration, as three distinctive zones are discernible which are (see Figure 3.23) (McCarter et al., 1999; McCarter et al., 2003):

- (i) A low-frequency arc in the range $< 1\text{kHz}$ which has been attributed to the electrode /sample interface polarization process;
- (ii) A high frequency arc which is attributed to the bulk sample polarization processes which appears in the frequency range $>150\text{kHz}$; and,
- (iii) A plateau region in the frequency range $1\text{kHz}-150\text{kHz}$ which separates the electrode arc from the bulk arc and is attributed to the effect of the fly-ash.

It is worth mentioning that the prominence of this intermediate plateau region is affected by the amount of the fly-ash replacement in the Portland cement paste and related to carbon content, as the plateau region increases as the replacement amount increases from 10% to 40% (McCarter et al., 1999).

McCarter (1994) has also reported an early appearance of the bulk impedance arc in mortar samples. The early appearance of the high frequency arc has been attributed to the increase in the bulk resistance caused by the addition of aggregate which, in consequence, reduces the characteristic frequency of the bulk arc to an observable range according to equation (3.13):

$$1=2\pi f_c R_b C_b \tag{3.13}$$

Where: f_c : Bulk characteristic frequency (Hz); R_b : Bulk resistance (Ohm); C_b : Bulk capacitance (Farad)

3.3.2 Hardening stage (>24hrs)

Conductivity/Resistivity response

Camp and Bilotta (1989) have shown in experiments extending over 225 days on sealed mortars and cement paste samples, that conductance values decrease through time which is in agreement with other studies (Afshar, 1986 ; Garvin, 1991; Hager and Domszy, 2004). The authors in this study divided the conductance dispersion diagram in the frequency range from 100Hz-7MHz (see Figure 3.24), into three frequency regions which were: a low-frequency dispersion region in which the conductance values increase with frequency due to the relaxation of the electrode polarization effect (Starrs and Mc Carter, 1998), an intermediate plateau region which starts at approximately 1kHz, and a high frequency dispersion region at 100kHz which has been related to the weakly adsorbed water relaxation process. In the same study, it has been shown that the amount of sand in the mix plays a dilution effect which reduces the conductance of the samples.

With regard to the influence of w/b ratio on the electrical properties during the hardening stage, Scuderi et al. (1991) and Christensen et al. (1994) used three cement pastes with different w/b ratios. By obtaining the bulk resistance from impedance spectroscopy, it was clear that the lower the w/b ratio of the cement paste, the higher the bulk resistance, which became more prominent as hydration time increases. This has been attributed to a more connected pore network at the high w/b mixes which facilitates ionic conduction, whereas the low w/b cement pastes have a more constricted and tortuous capillary pore network which hinders the conduction process. This is despite the fact that the low w/b ratio mixes acquire a higher pore solution conductivity which increases with time in comparison to the high w/b ratios mixes (Christensen et al., 1992; Christensen et al., 1994). From this it could be deduced that the conduction process during the hardening stage is more affected by the pore structure rather than the pore solution conductivity.

The latter conclusion has encouraged other researchers to utilize the conductivity/resistivity of cementitious materials during the hardening stage to study the effect of external environmental variables on the pore structure (e.g dry/wetting), or evaluation of material properties such as permeability, tortuosity and diffusivity. McCarter and Ezirim (1998a) and McCarter et al. (2013) used electrodes embedded at different depths within the cover zone of concrete samples which were subsequently

exposed to cyclic wetting and drying cycles - 24hrs absorption followed by 12 weeks drying. It has been found that the conductivity in the cover-zone before wetting increases with depth. This has been related to the more moist 'heartcrete' than the surface of concrete. In terms of the absorption cycles, it has been shown that the conductivity values after the absorption cycles generally increase in comparison to their values after the drying cycle, however this effect decreases with increasing depth from the surface. In addition, at depths >40 mm it has been shown that the conductivity is least affected by the wetting and drying cycles. The constant value of the conductivity at the 'heartcrete' has shown to decrease as a result of the ongoing pore structure development due to the hydration process, and this reduction in the conductivity due to the hydration process is very clear in the case of fly-ash mixes (see Figure 3.25).

Christensen et al. (1996) were in favour of using electrical measurements to evaluate the permeability of cement pastes, due to the time, accuracy and cost which are associated with conventional methods. The permeability of the cement pastes was estimated by Katz and Thompson equation:

$$k' = \frac{1}{226} \frac{\sigma}{\sigma_o} l_c^2 \quad (3.14)$$

k' = Permeability (m^2); σ = bulk conductivity (S/m); σ_o = pore solution conductivity (S/m); l_c = critical pore diameter of porous material. The critical diameter obtained from the mercury intrusion porosimetry (MIP) is used to substitute this parameter. The pore solution in this study was extracted from the samples to obtain its conductivity. The comparative permeability data was obtained from Nyame and Illston (1981) and Illston (1980). It was concluded that despite the high permeability results which the application of Katz and Thompson gives, the trend with time was constant especially in the high w/b mixes (see Figure 3.26). McCarter et al. (2000) have shown the application of equation (3.14) on mortar mixes with different SCM's at the age of 450days, and that ternary blended mortars gave a lower permeability than the 50% GGBS mortar mixes. On the other hand, 20% micro-silica mortars gave a lower permeability than both the 20% metakaolin and the 20% GGBS mortars. In the same study, the effective chloride diffusion coefficient, D_{eff} , has shown to follow the same ranking order as their permeability. The D_{eff} has been obtained by applying Nernst-Einstein equation:

$$\frac{\sigma}{\sigma_0} = \frac{D_{eff}}{D_0} \quad (3.15)$$

In which, D_0 is the diffusivity of the ion at infinite dilution, in this case the chloride ion which is $2.03 \times 10^{-9} \text{ m}^2/\text{sec}$ at 25°C (Spragg et al., 2016). Other studies have used the same equation to assess the diffusivity of pollutants through cement pastes. Taffinder and Batchelor (1993) obtained the effective diffusion coefficient for bromide and lithium ions in Portland cement pastes by two methods: an electrical conductivity method according to equation (3.15), and a two-chamber conventional method. It has been shown that for 0.8w/b cement paste mixes at the age of 7days, the inverse of equation (3.15), which is known as the MacMullin number, or in some studies the formation factor (Weiss et al., 2017), showed similar results (see Table 3.1).

Therefore, both D_{eff} which has been estimated from conductivity measurements and the conventional divided compartment test are also equivalent. During this study, no tests were undertaken on concrete mixes or mixes with SCM's.

Permittivity response

With regard to the permittivity through the hardening stage, in the frequency range of 10kHz - 8GHz, Hager and Domszy (2004) observed a continuous decreasing trend through time for Portland cement pastes. This was attributed to the increase in the adsorption of charges on the pore surfaces and the formation of hydration products. Al-Qadi et al. (1995) studied the permittivity of concrete in the frequency range 0.1MHz-40MHz for different w/b mixes from 1day up to 28days, and the same decreasing trend with time and frequency was found.

With regard to the effect of w/b ratio on the permittivity during the hardening stage, Christensen (1993) had shown that the permittivity of cement pastes increased with increasing w/b ratio (see Figure 3.27). In the same context, Gu and Beaudoin (1997) have also shown the same relation between the permittivity and the change in the w/b for 1-year old cement paste samples in a frequency range of 1MHz-1.5GHz which was also found in another study by Al-Qadi et al. (1995) (see Table 3.2)

It is also evident that as the frequency increases the permittivity decreases and this is attributed to polarization relaxation processes. The permittivity/w/b ratio relation is independent of the frequency range, as this relation is observed in both the low to the medium frequency range (Hz-10MHz), and the high frequency zone (54MHz-1GHz).

In terms of the effect of SCM's on the permittivity during the hardening stage, Wen and Chung (2001) obtained values at 10kHz, 100kHz and 1MHz for a 0.35w/b cement paste with 15% by weight silica fume replacement. At the age of 28-days, it was shown that the permittivity of the replaced paste displayed lower values than the pure cement paste mix. This has been attributed by the authors to the lower permittivity of silica fume when compared to the cement, as moisture and ions in the cement cause the permittivity to be larger. In the same study, it was shown that the addition of latex and carbon fibres to the mixes increases the permittivity, which was attributed to the effect of the interfaces between these materials and the matrix. The effect of silica fume on permittivity results in a decrease as replacement level increases up to ~15%, thereafter, a noticeable increase was observed by Gu and Beaudoin (1997) (see Figure 3.28(a)). No explanation has been offered for this trend. Christensen (1993) has shown that for different silica fume replacement levels, the permittivity decreases through time until the age of ~100hrs, thereafter an increase in this parameter takes place (see Figure 3.28(b)), and has been attributed to the formation of the C-S-H from the silica fume.

Nyquist plot

When performing AC impedance spectroscopy in the Hz-MHz frequency range for hardened cement-based materials, normally two arcs are observed in the impedance complex plot which are (see Figure 3.29):

- (a) The low-frequency arc normally appears in the range from (mHz to kHz), and is attributed to the polarization process at the electrode / cement-based interface as discussed in Section 3.2.2 (Coverdale et al., 1995a). The high frequency intercept of this arc with the real axis gives the bulk resistance, R_{bulk} , for the cement-based material.
- (b) The second (high frequency) arc is normally present in the kHz – MHz frequency range for hardened material and represents the bulk material response as discussed in Section 3.2.1. The arc centre is normally depressed below the real axis indicating a spread in the relaxation times of the cement based material (see Figure 3.29) (McCarter et al., 1988; McCarter and Brousseau, 1990; Gu et al., 1992; Christensen et al., 1994).

The main parameters which can be extracted from the AC Impedance plot for cement based materials, according to Figure 3.29 are:

- (i) The bulk characteristic frequency (f_c) in which the imaginary value for the arc attains its highest (negative) value;

- (ii) The bulk frequency (f_{bulk}), which is the frequency at the intercept of the low frequency arc and the real axis where the bulk material resistance (R_{bulk}) is obtained;
- (iii) The electrode characteristic frequency (f_{elec}) in which the largest recorded (negative) imaginary value for the electrode arc; and,
- (iv) The offset resistance (R_0). With regard to this parameter, different interpretations have been proposed to explain its physical meaning, such as:
 1. Christensen et al. (1992) have suggested that R_0 resistance could be attributed to the formation of parallel conduction paths in the cement paste; these conductive paths have been attributed to the conduction process through ions on the surface of the hydrating cement grains or due to the formation of the C-S-H gel.
 2. It is considered as a 'graphical' requirement which has not got any real physical meaning (Christensen et al., 1994; Loche et al., 2005).
 3. Ford et al. (1995) have suggested that the offset resistance is an artefact due to the used electrode configuration, and by a proper 'nulling' process this could be eliminated.
 4. Coverdale et al. (1995a) have suggested the existence of a second-high frequency arc instead of just an offset resistance. This second high frequency arc is due to the in-series connection between the formed C-S-H phase and the pore fluid phase in the continuous capillary pores. However, the authors have not mentioned a justification for the reported relative constant value for the offset resistance through the hydration process.
 5. Song (2000) has attributed this resistance for the continuous and discontinuous pores which are filled with pore-water.

With regard to the hydration effect on the bulk arc development through time, Gu et al. (1992) have shown that by the use of a saturated Portland cement paste ($w/b=0.35$), the appearance of the bulk arc was recorded after 169hrs hydration. Further, the bulk arc diameter displays a continuous increase through time which has been observed in other studies (McCarter and Garvin, 1989; Dotelli and Mari, 2001). Also, it has shown that at the age of 380hrs, the diameter of the cement paste arc recorded its highest value throughout the testing period.

Regarding the frequencies f_c , f_{bulk} , f_{elec} (see Figure 3.29) McCarter and Brousseau (1990) have shown that these change as hydration proceeds and this has been attributed to the reduction in charge mobility (see Table 3.3). According to McCarter and Brousseau (1990), and from Table 3.3, it is evident that the bulk frequency, f_{bulk} , values throughout the study were in the kHz range, however a decreasing trend through time was observed which has also been shown by Scuderi et al. (1991). Table 3.4 shows the bulk frequency values acquired from different studies. It has been argued that the frequency range in which the bulk frequency takes place is related to the electrode geometry (Scuderi et al., 1991). This argument could be considered reasonable when comparing the bulk frequency range of Christensen et al. (1994) and Scuderi et al. (1991), as the frequency range is much closer despite the difference in the w/b. It worth mentioning that both these studies used the same electrode configuration and geometry as shown in Table 3.4.

Regarding the effect of the w/b ratio on the bulk frequency values, Christensen et al. (1994) have shown that these follow a clear increasing trend as the w/b ratio increases for the samples (see Table 3.5).

Equivalent Electrical circuit for cementitious materials:

For AC immittance spectroscopy to deliver a meaningful analysis and explanation regarding the material under test, the data can be modelled by an equivalent electrical circuit (EEC). The equivalent circuit should comprise electrical elements which represent the material micro-scale electrical response (Bauerle, 1969). After suggesting a representative equivalent electrical circuit, a curve-fitting process is performed on the experimental data to assess its accuracy. If a good agreement between the simulated EEC response and the experimental data is found, then the proposed model can be used to explain the material response under different conditions, such as temperature, hydration and different environmental exposure.

The challenge which is normally encountered in the selection of the EEC, is the non-uniqueness of the equivalent circuits which could give the same response. Therefore, the selection should be based on the pre-understanding of the material, as any selection which is proposed should have a clear physical meaning which can be related to the material micro-electrical response (Sinclair and West, 1989; Macdonald, 1990). Also, the non-ideal distributed electrical behaviour in the material could represent a serious difficulty when coming to the fitting process (Macdonald, 1990), as the use of lumped electrical elements could lead to errors in the fitting process. Therefore, the use of distributed circuit

elements such as the constant phase element (CPE) can assist in the fitting process, despite the ambiguity which surrounds their physical meaning and origin (Coverdale et al., 1995b).

Different EECs have been proposed in the literature to account for the electrical response for hardened cementitious material. Kim et al. (1995) have modelled the bulk electrical response of cement paste sample by the use of an EEC which is composed of a CPE which represents the interfacial polarization process in the blocked pores. This CPE has been proposed to be in series with a resistive element which also has been related to the conduction process in the blocked pores. This electrical path is placed in parallel with a resistive element which represents the conduction process in the continuous capillary pores (see Figure 3.30(a)). The response of the EEC proposed by Kim et al. (1995) has been monitored through the first 10 days hydration; however, the response of the EEC has not been verified against different w/b ratios or different SCM additions.

Andrade et al. (1999) have used the same electrical circuit as Kim et al. (1995), however, these authors have substituted the parallel resistance which represents the conduction process in the connected capillaries by a capacitive element which has been related to the solid phase polarization phenomena (see Figure 3.30(b)). The verification of the physical relations between the bulk material and the EEC electrical parameters in this case has been verified by monitoring the electrical parameters through time and at different w/b ratios. The model showed, however, some conflicting results, as the capacitance displays an early decrease through time, which is not explainable if this electrical parameter truly represents the continuous formation of the solid phase through time.

In other studies (Cabeza et al., 2002; Cabeza et al., 2003; Cabeza et al., 2006), the same model which has been suggested by Andrade et al. (1999) has been used in the case of a non-contacting electrode configuration. However, in the contacting electrode configuration the model presented in Figure 3.30(c) has been used and the additional resistance, R_c , has been related to the continuous conductive paths in the sample between the electrodes. In this case, the verification of the relation between the electrical parameters of the EEC and their suggested physical meaning has been performed through the use of different w/b mixes, wetting/drying processes and static load application. In the same context, Cruz et al. (2013) have used the EEC shown in Figure 3.30 (d) to simulate the electrical response of different mortar samples, and the CPE_c parameter has

been proposed to account for the polarization processes which take place on the surface of the connected pores. CPE_b has been related to the ionic diffusion process near the nanopores.

In all these studies, a depressed arc in the impedance Nyquist diagram has been observed for the hardened cementitious materials. Therefore, distributed electrical elements such as the CPE have been used to account for this phenomenon. Macphee et al. (1997) have used lumped elements such as ideal capacitors and resistances to simulate the response of a pore-reduced cement paste (PRC). In this study, the authors have proposed two main paths for the electrical conduction, the connected pores path (CP) and the gel path. The gel path has been further divided to the electrical contribution of the blocked pores (BP), the hydration product (HP) and the unreacted cement (UC). The electrical contribution of these mentioned paths to the electrical response are illustrated in the EEC in Figure 3.30(e). Tang et al. (2014) have also used lumped electrical parameters to develop a fractal equivalent electrical circuit to simulate the electrical response of cement paste (see Figure 3.30(f)). From the EEC proposed by these authors, the fractal dimension of the pore structure has been extracted by simulating the 1kHz impedance response and the 100kHz impedance response on the basis that at the larger the electrical frequency, the lower the penetration depth of the electrical field through the pore structure.

3.4 Summary

In this chapter, a review for the work which has been undertaken on characterizing the hydration process of cementitious material through the setting and the hardening process is presented. The review included studies which used both the conductivity/resistivity responses, as well as permittivity through the mentioned hydration periods. Also, a review on the utilization of the EEC in characterizing the pore-structure of the cementitious materials has been presented. From this chapter, the following points can be drawn:

- (a) There is a paucity in studies which utilise a wide frequency range to characterise the permittivity and the conductivity of the mixes at both the early stages and the hardening stages.
- (b) Few studies have addressed the relation between the electrical response and the chemical and physical reactions which take place in the material through the early hydration period, and comparing the electrical measurement during this stage to conventional tests.

- (c) There is a lack of data on the long term electrical response studies which characterise the effect of SCM additions to the mixes through the permittivity and the conductivity responses
- (d) Few studies have used equivalent electrical circuits to show the difference in the pore structure formation between the mixes which comprise SCMs and the pure cement mixes; and,
- (e) No equivalent electrical circuit has been used, or proposed, during the early hydration of cementitious materials in order to show the micro response of the different phases during the dissolution and the setting periods.

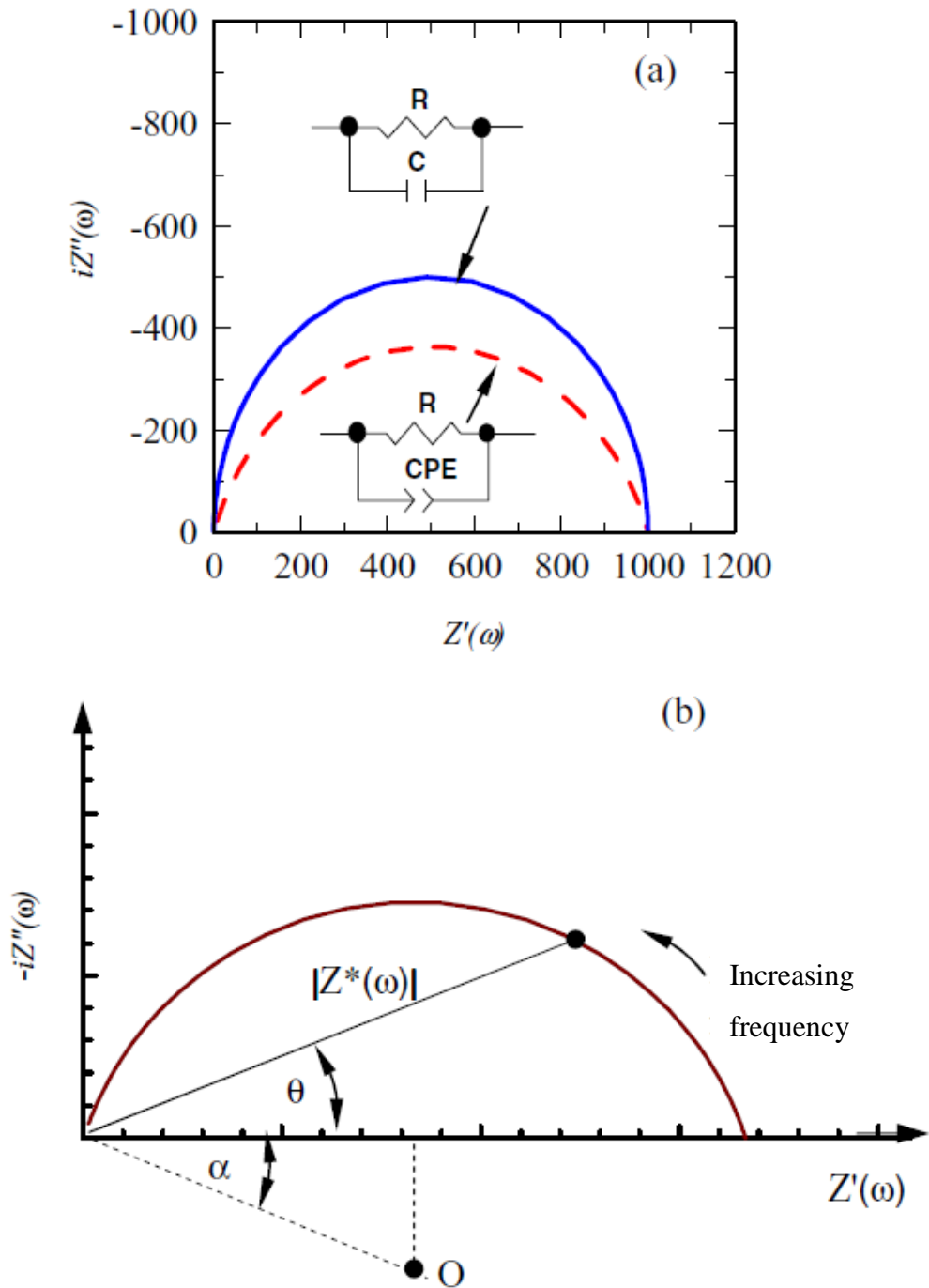


Figure 3.1:(a) Influence of the constant phase element (CPE) on the Nyquist plot—the solid line is the Nyquist plot for a pure capacitor ($C = 10^{-10}\text{F}$) in parallel with a resistor ($R = 1.0 \text{ k}\Omega$) and the dashed line is a CPE ($C_0 = 10^{-10} \text{ F s}^{-0.2}$ and $p = 0.8$) in parallel with a resistor ($R = 1.0 \text{ k}\Omega$) (b) schematic diagram of Nyquist plot for a saturated porous material showing arc depression angle, α , phase angle, θ , and impedance, $Z^*(\omega)$.

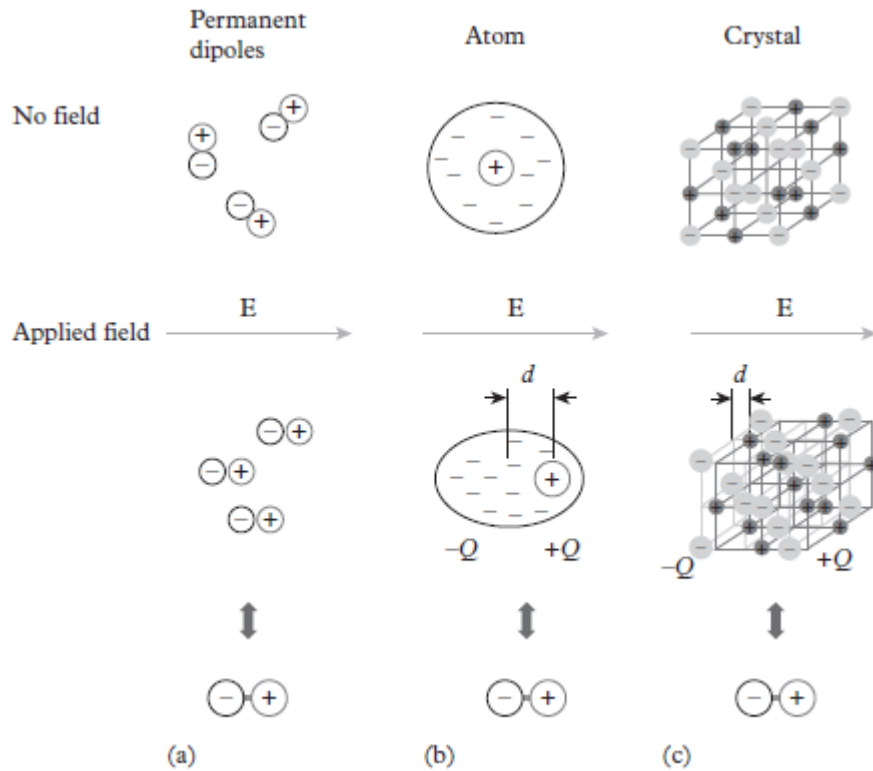


Figure 3.2: Polarization processes within homogeneous materials: (a) Orientation polarization, (b) electronic and atomic polarization mechanisms, (c) Ionic polarization mechanism (Nyame and Illston, 1981; Feldman et al., 2015).

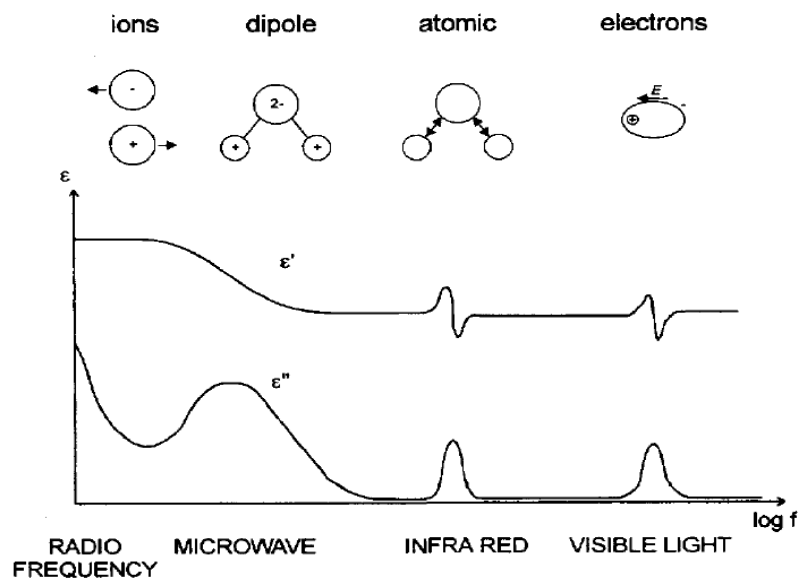
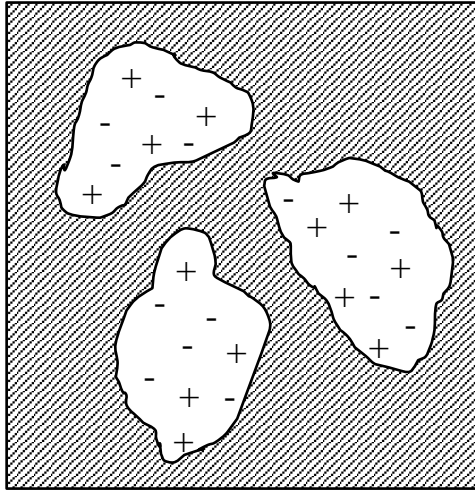
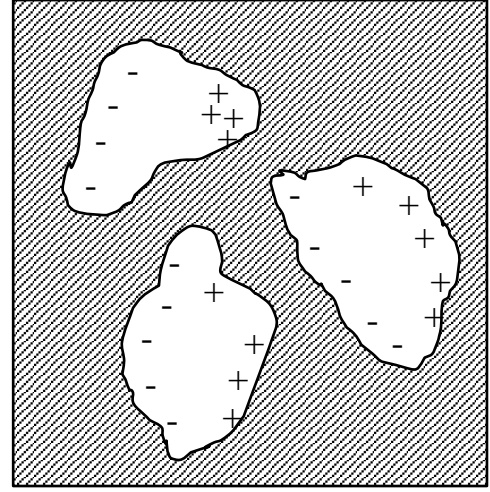


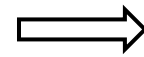
Figure 3.3: Polarization mechanisms occurrence through frequency ranges (adapted from Beek (2000)).



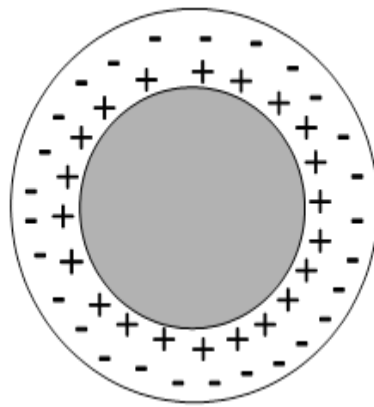
No Field ($E = 0$)



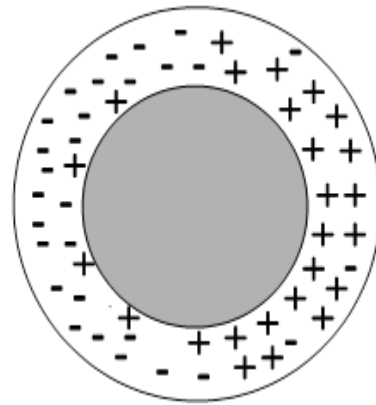
Applied Field ($E \neq 0$)



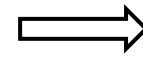
(a)



No Field ($E = 0$)



Applied Field ($E \neq 0$)



(b)

Figure 3.4: Schematic diagram showing (a) Interfacial (or space-charge) polarization, and (b) Double-layer polarization.

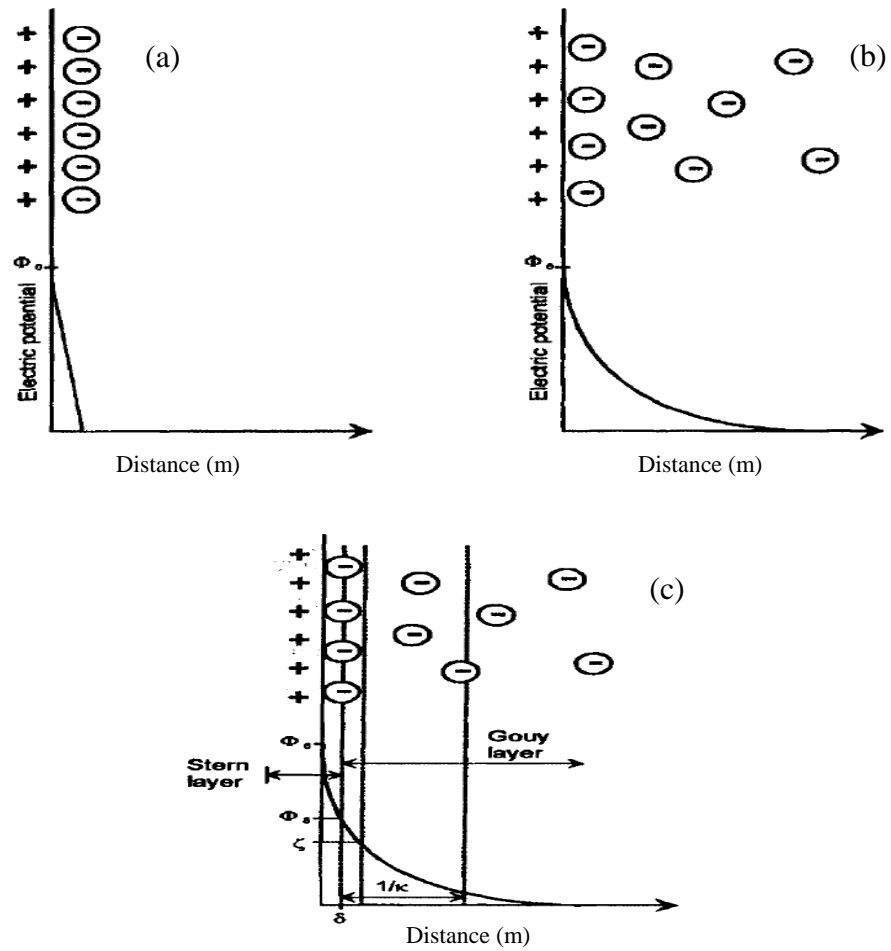


Figure 3.5: Different models for electrodes double layer (a) Helmholtz model (b) Gouy-Chapman model and (c) Stern model (Martinsen and Grimnes, 2011).

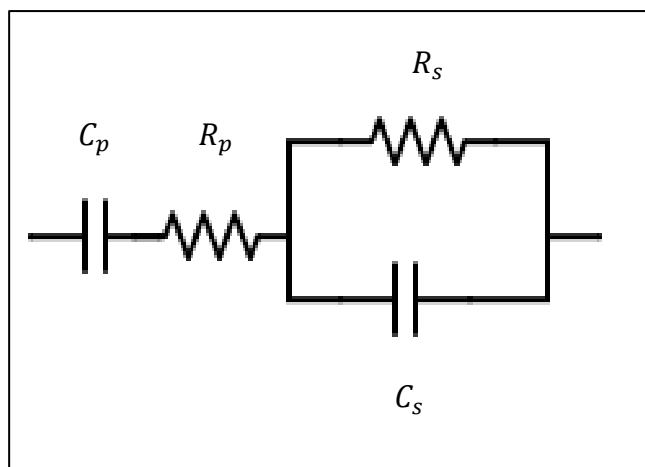


Figure 3.6: Equivalent electrical circuit for electrode/sample polarization effect. (Schwan, 1963).

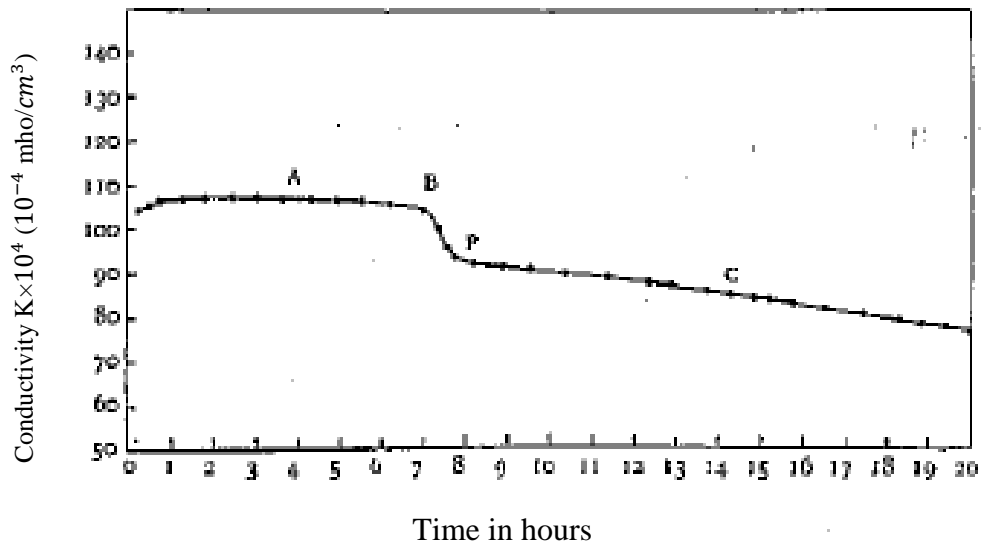


Figure 3.7: Specific electrical conductivity through time for 0.27w/b Portland cement pastes (Shimizu, 1928).

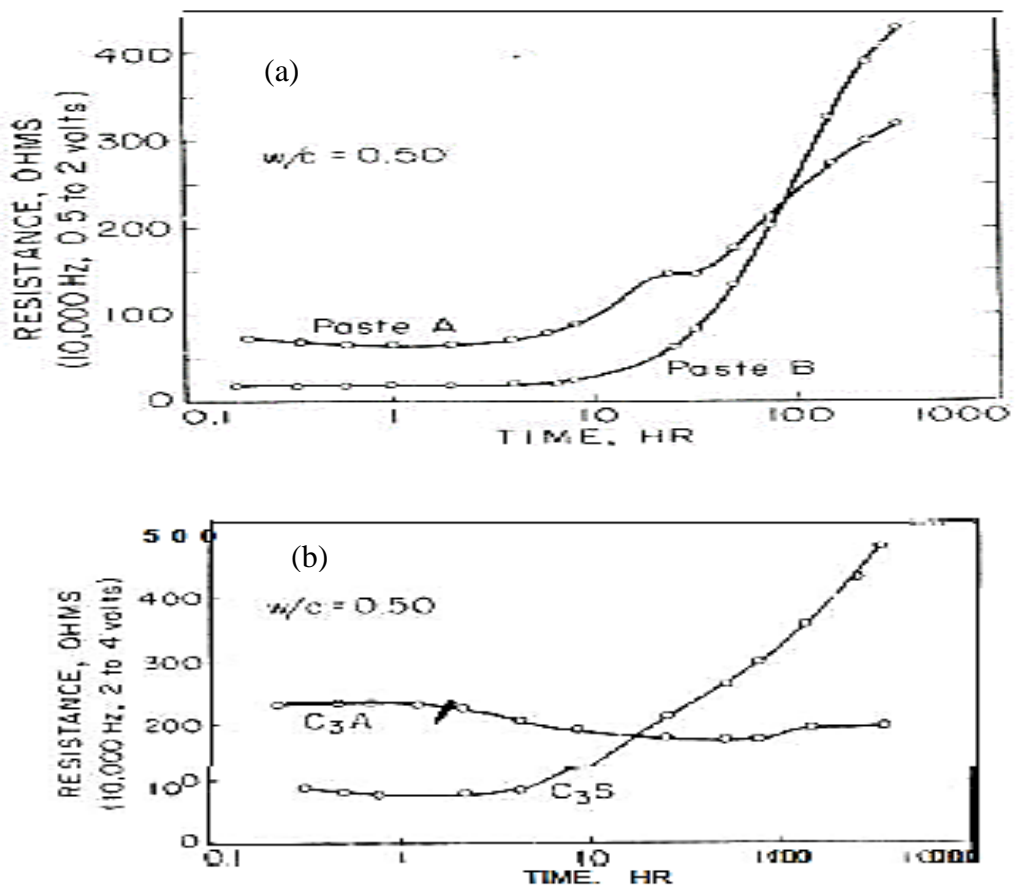


Figure 3.8: Electrical resistivity response during the early hydration period for (a) cement pastes with different alkali content, and (b) pure cement components (Monfore, 1968).

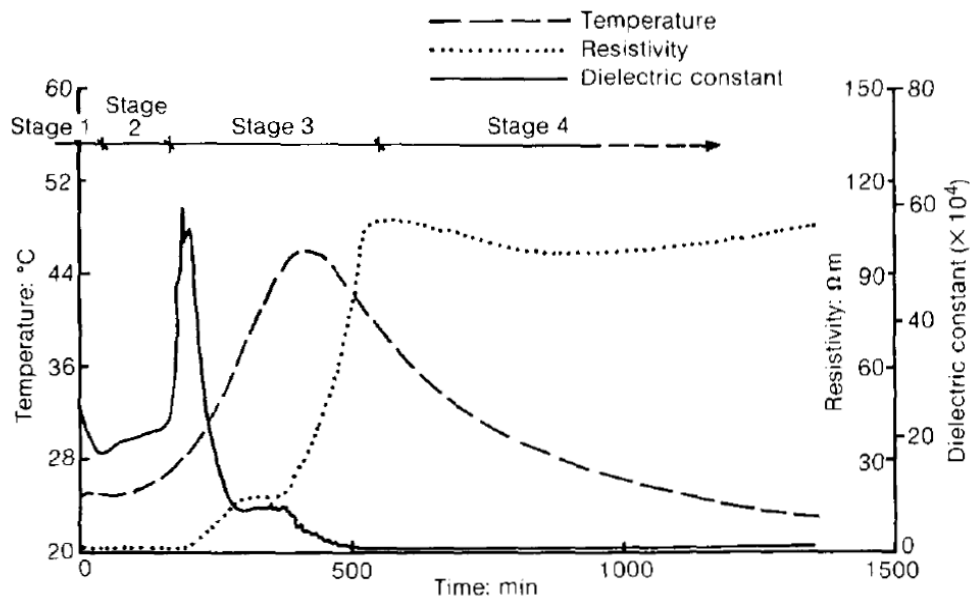


Figure 3.9: Change on the permittivity, resistivity and temperature over the initial 24 hrs since hydration initiation (McCarter and Afshar, 1985).

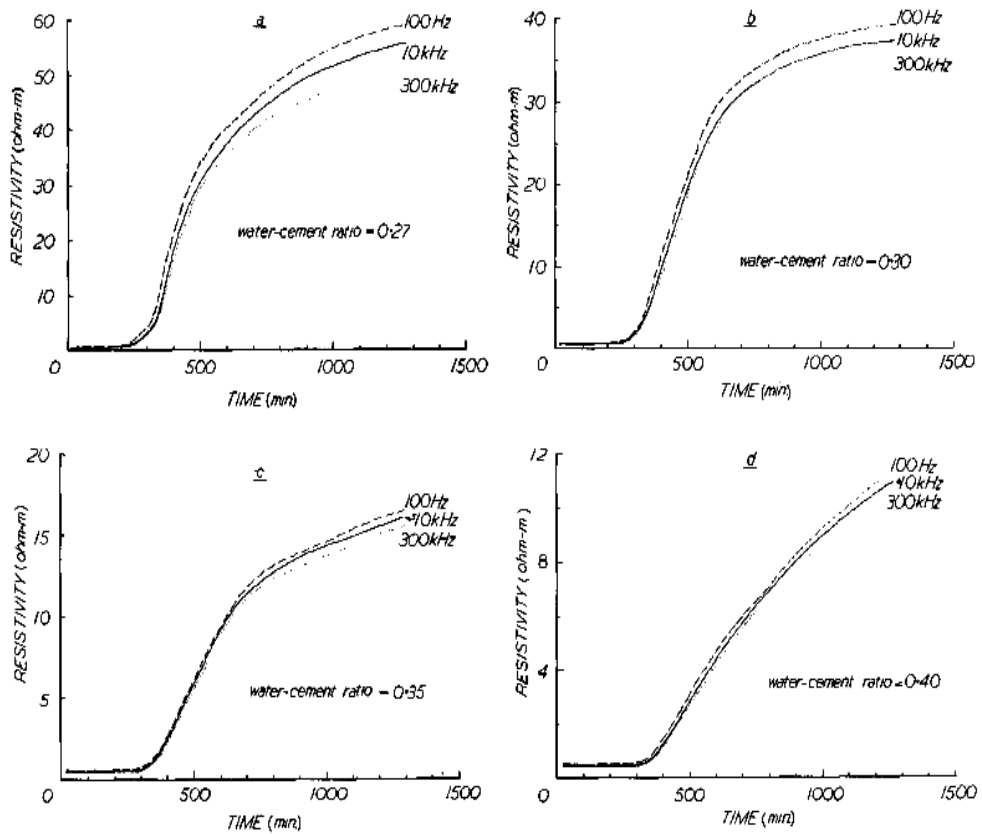


Figure 3.10: Effect of the measuring electrical frequency on the electrical resistivity of cement pastes (McCarter, 1987).

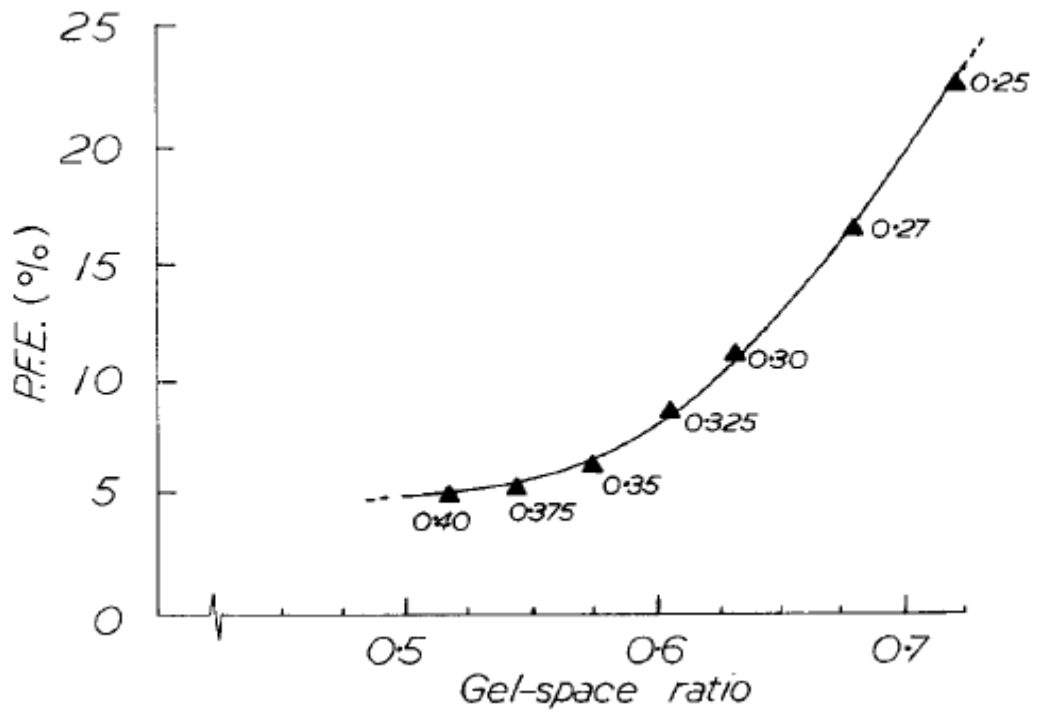


Figure 3.11: Relation between gel-space ratio and the percentage frequency effect PFE for different w/b cement paste at the age of 24hrs (McCarter, 1987).

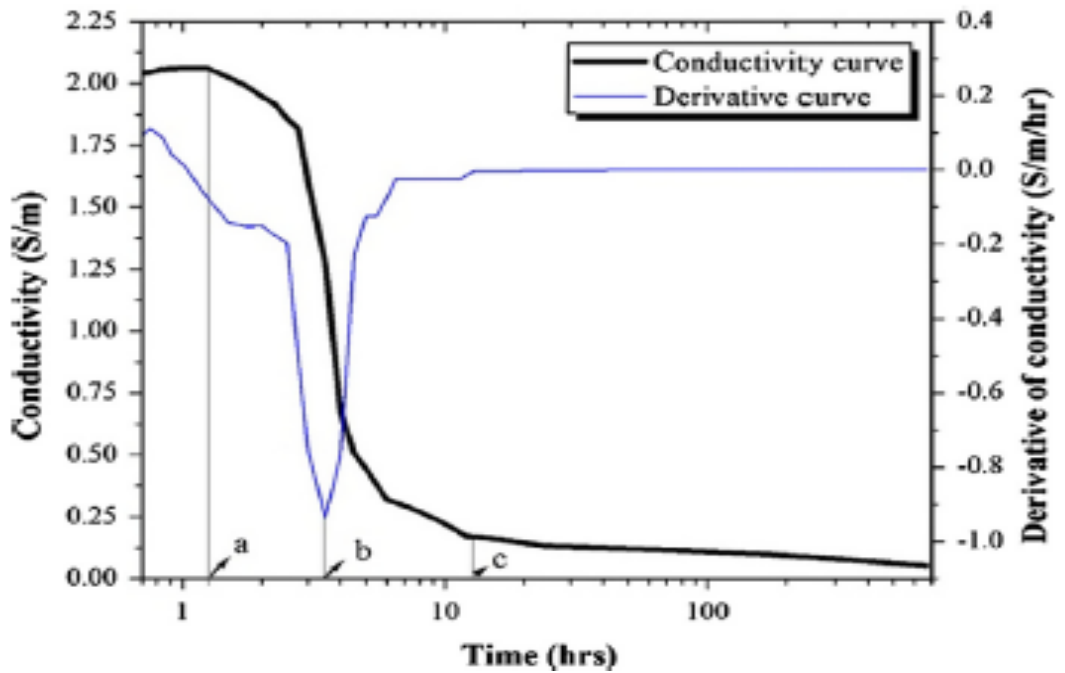


Figure 3.12: Conductivity and its derivative diagram for a 0.3 w/b OPC paste illustrating the early hydration stages (Sanish et al., 2013).

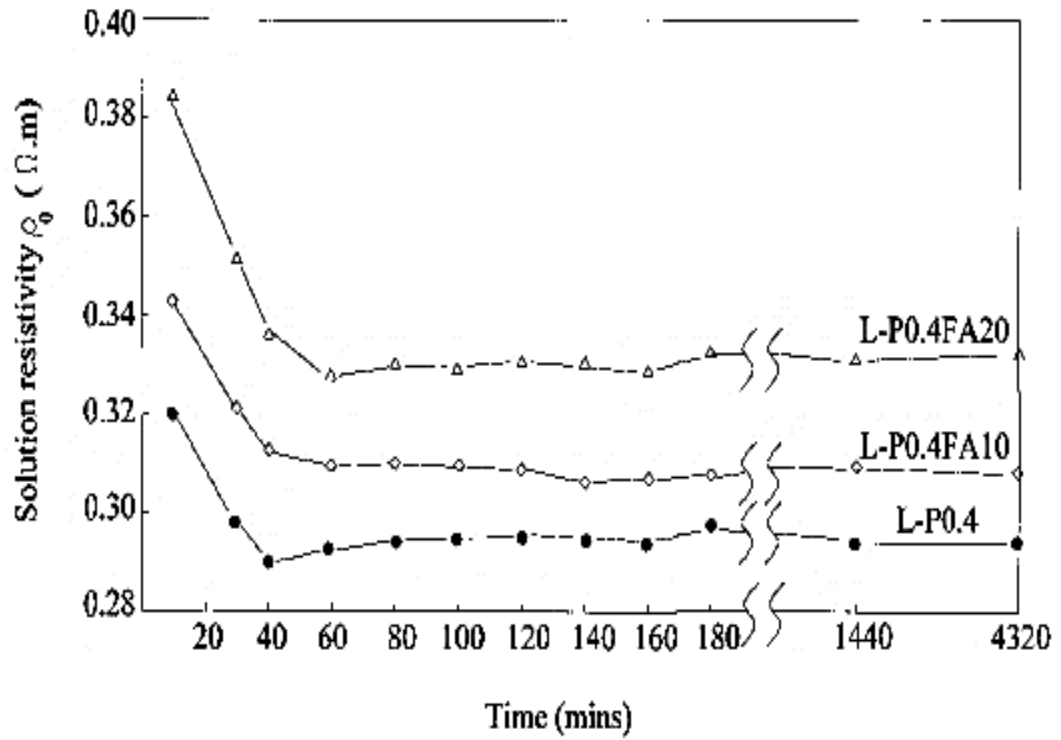


Figure 3.13: Electrical resistivity of pore fluid for different Portland cement samples with: 20% FA replacement (L-P0.4FA20), 10% FA replacement (L-P0.4FA10) and Pure Portland cement (L-P0.4)(Xiao and Li, 2008).

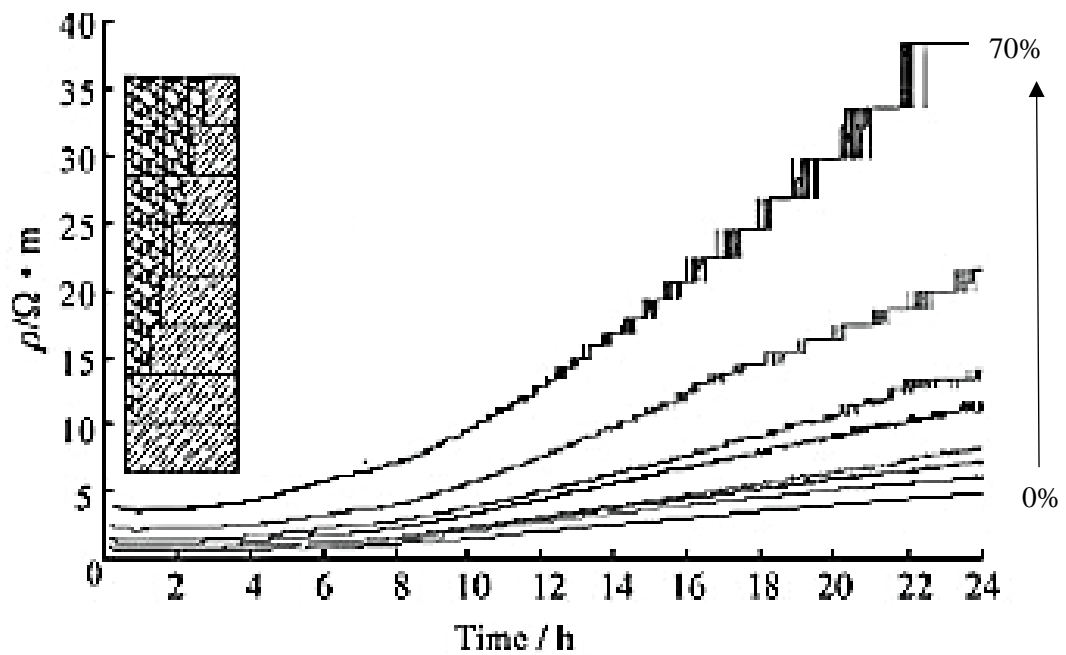


Figure 3.14: Resistivity of concrete mixes with different aggregate volumetric fraction ranging from 0%-70% (Wei and Xiao, 2011).

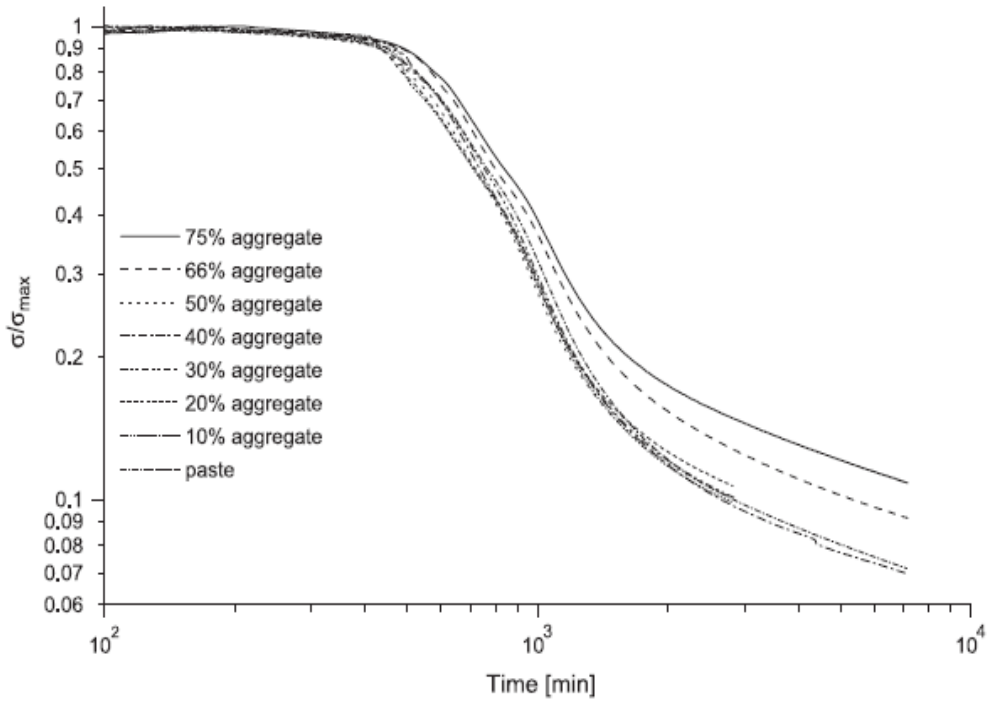


Figure 3.15: Normalised conductivity plot with time for concrete samples with different aggregate contents (Princigallo et al., 2003).

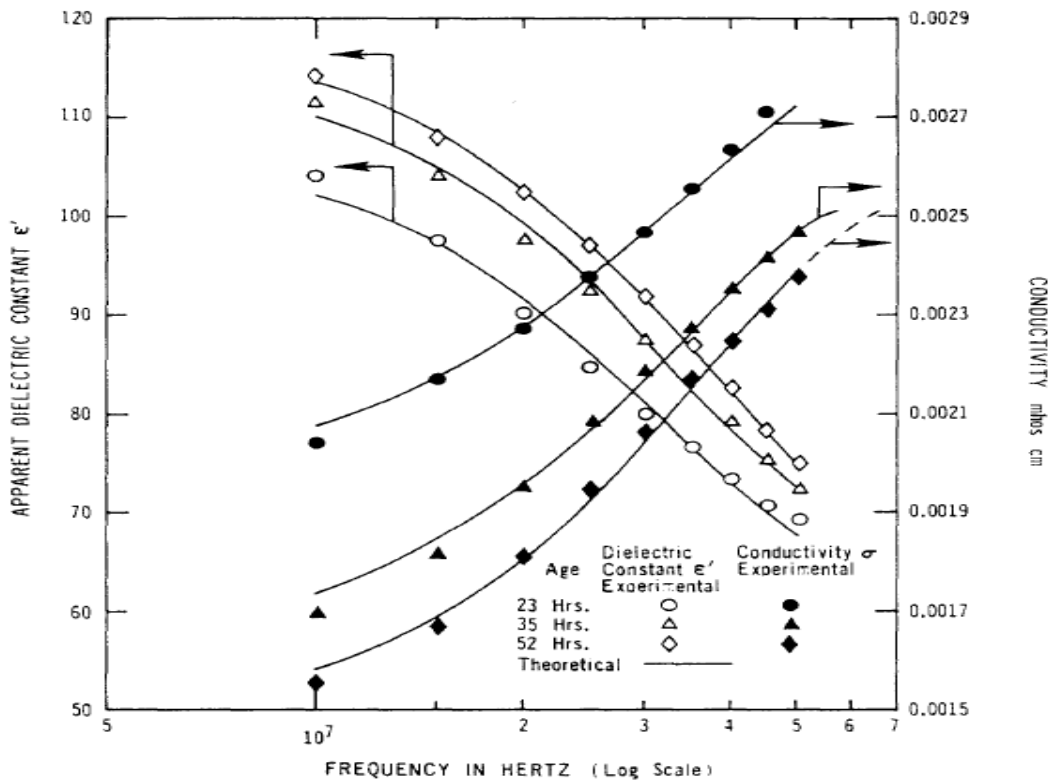


Figure 3.16: Permittivity/Conductivity dispersion diagrams for 0.35w/b cement paste at the ages of 23, 35, 52hrs. (Taylor and Arulanandan, 1974).

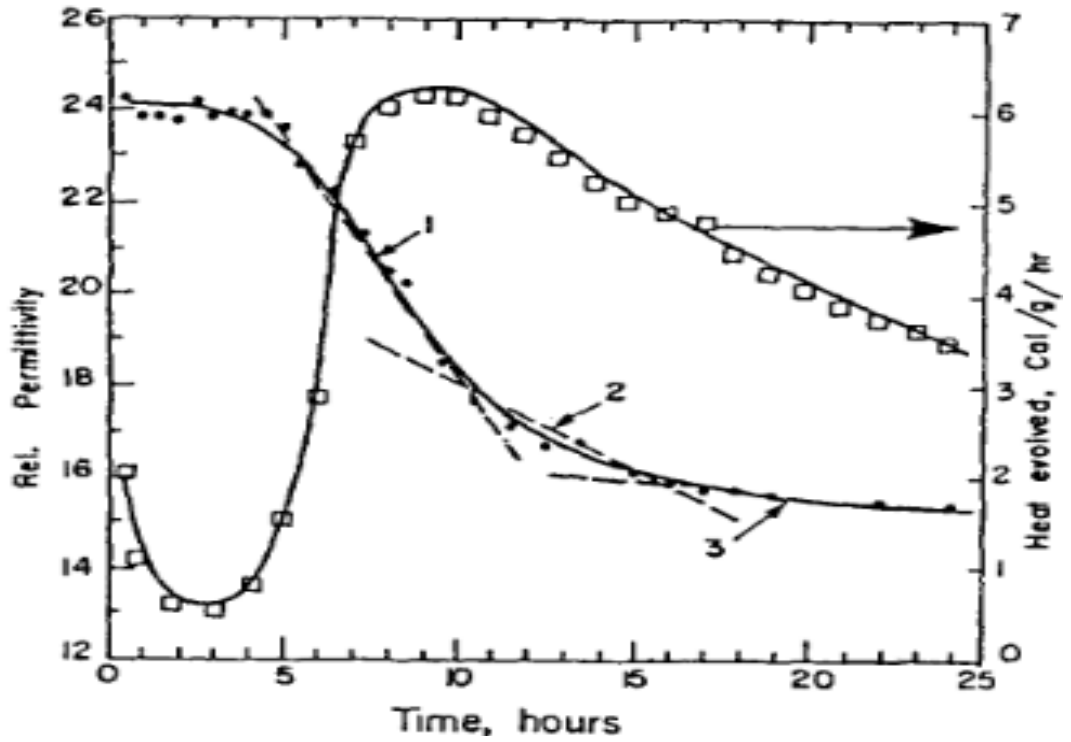


Figure 3.17: Relative permittivity at 10GHz during the early hydration period and the heat of hydration for 0.4w/b cement paste (Moukwa et al., 1991).

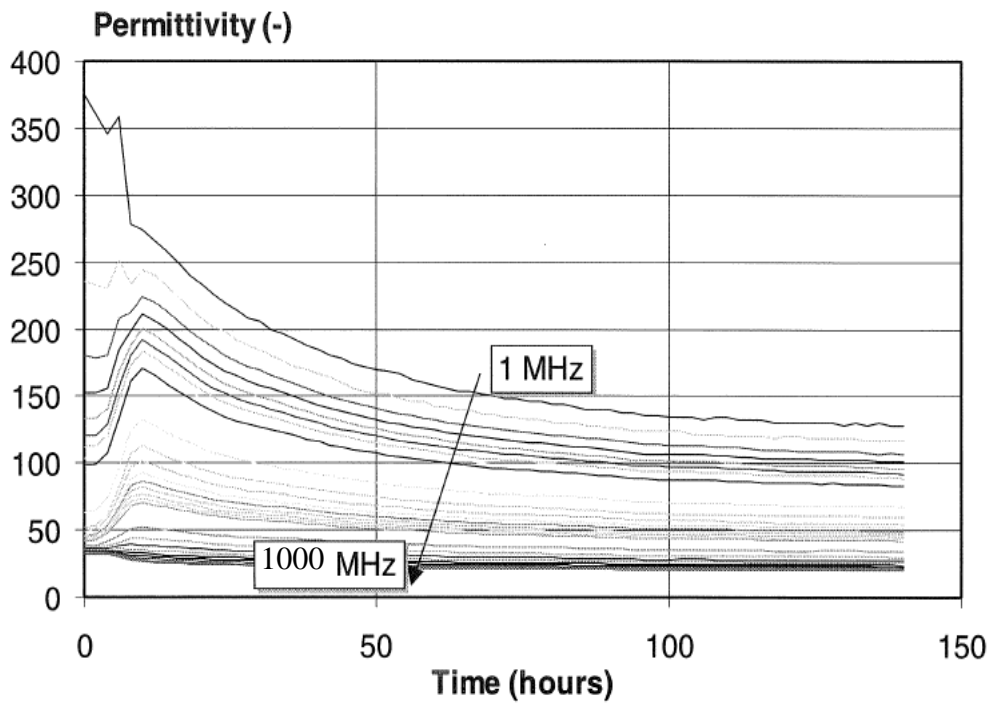


Figure 3.18: Permittivity variation through time for cement pastes at different frequencies in the MHz range (Van Beek and Hilhorst, 1999).

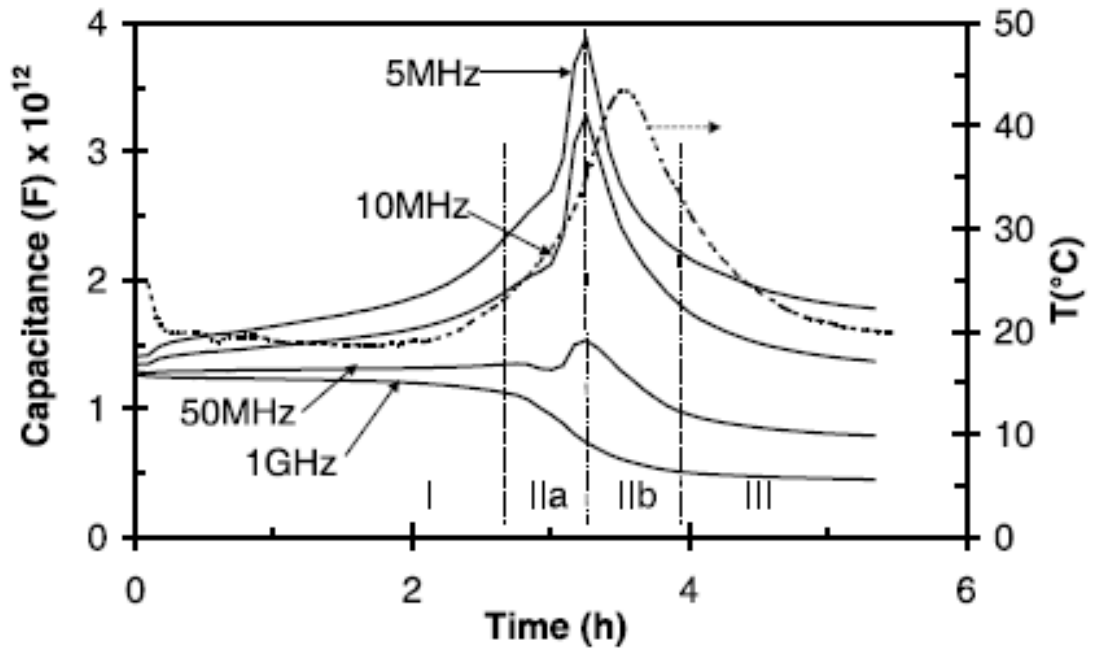


Figure 3.19: Capacitance and temperature variations through time for aluminate cement at 20°C ambient temperature (Nyame and Illston, 1981; Smith et al., 2002).

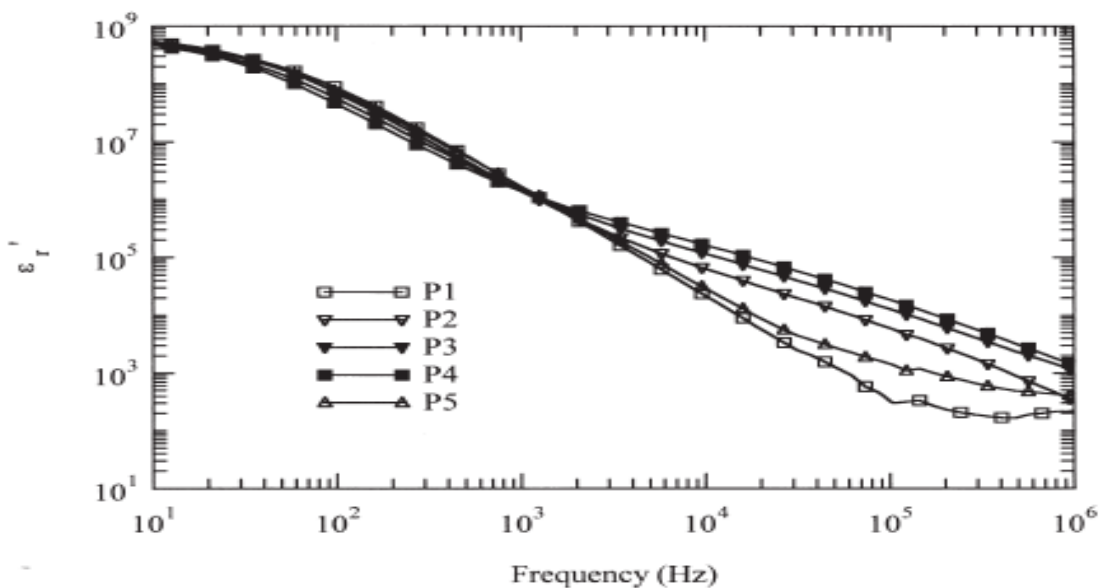


Figure 3.20: Enhancement of permittivity values due to addition of fly-ash to the Portland cement paste where, P1: pure Portland cement paste, P2: 10 % replacement fly-ash, P3: 25% replacement fly-ash, P4: 40% replacement fly-ash, P5: paste with micro silica addition. Measurements were taken at the age of 60mins (McCarter et al., 1999).

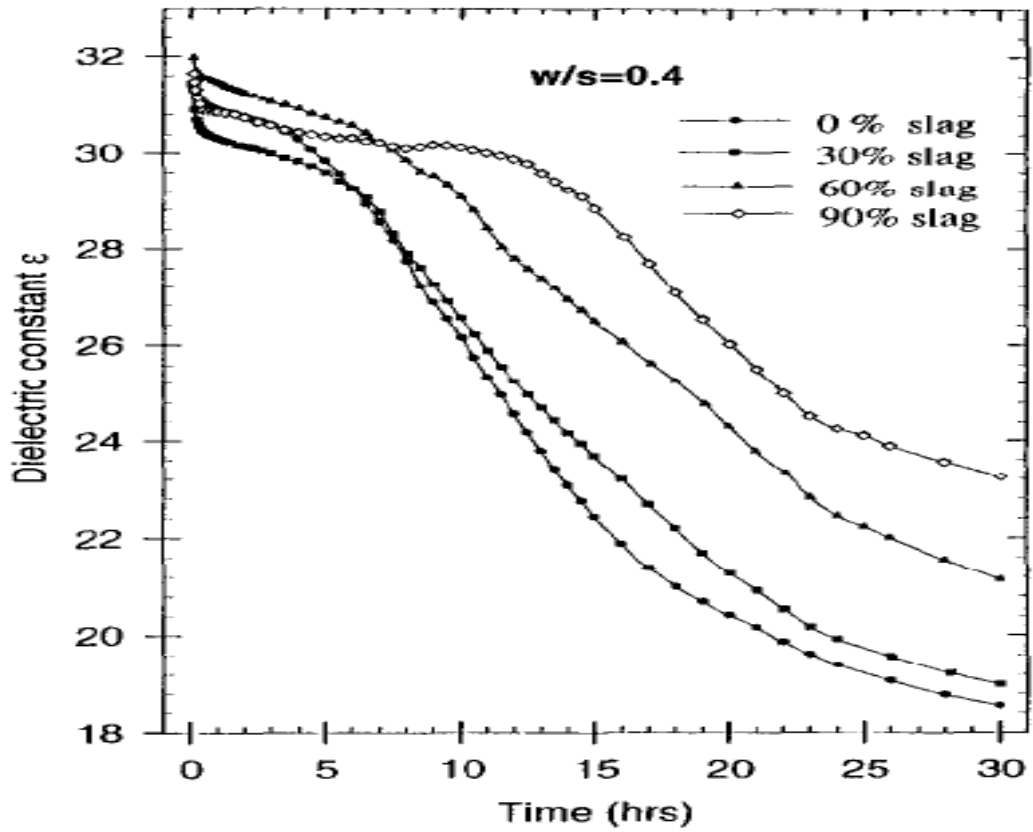


Figure 3.21: Permittivity response (at 9.5GHz) through time due to different slag percentages replacements to cement pastes (Zhang et al., 1995).

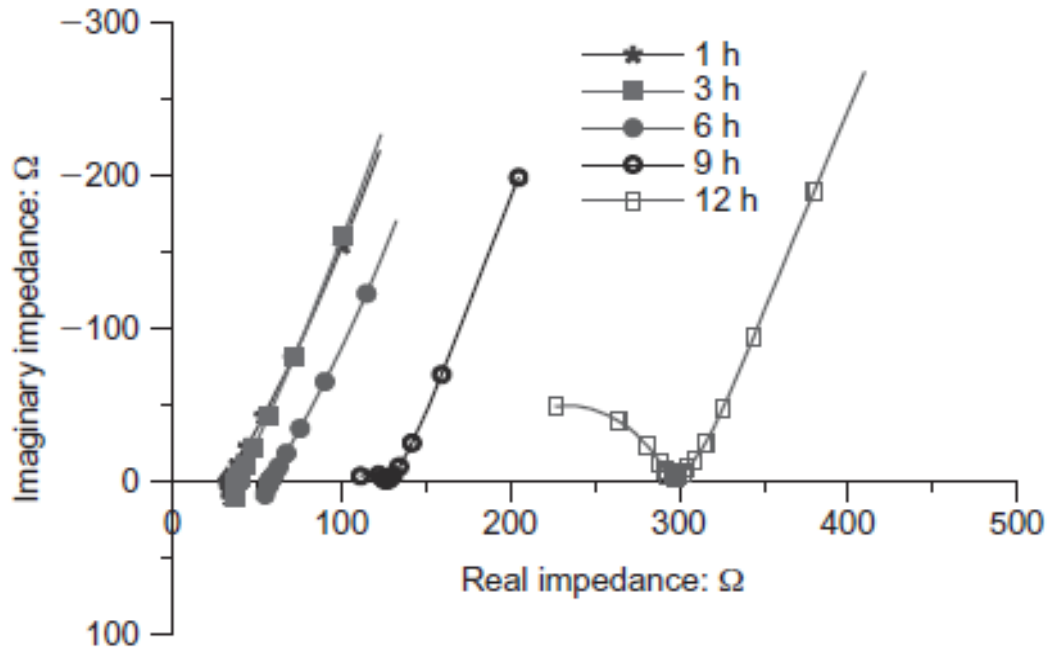


Figure 3.22: Nyquist plot for cement paste of 0.3w/b ratio during the early hydration period (Manchiryal and Neithalath, 2009).

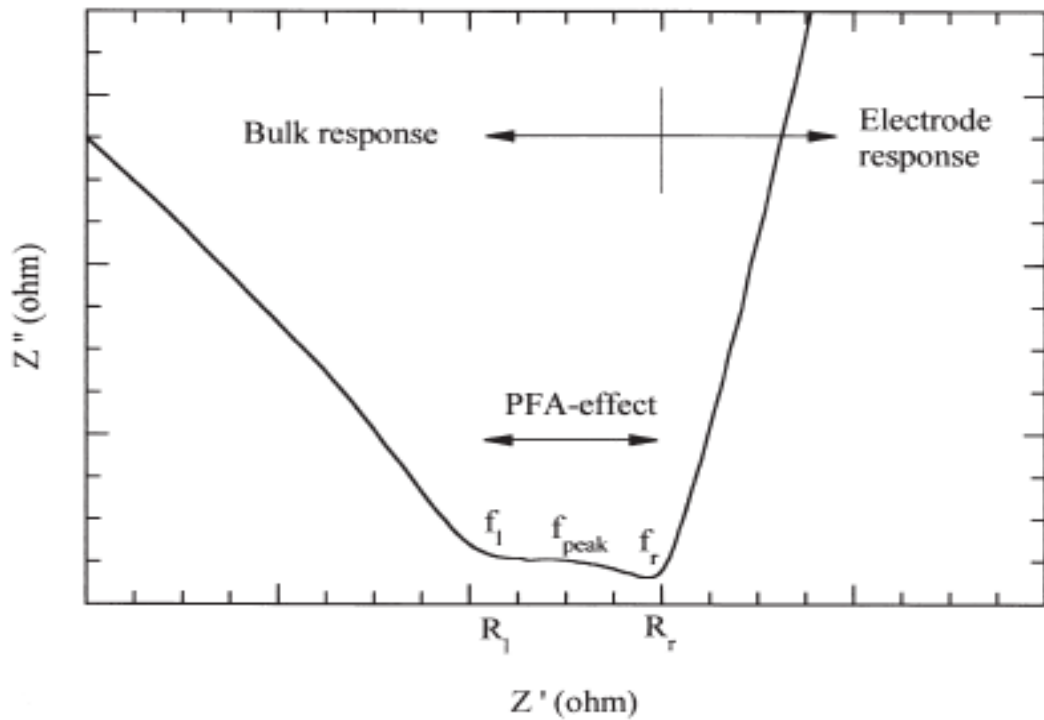


Figure 3.23: Plateau region which formed in the impedance complex plot due to the inclusion of fly-ash in the Portland cement, mortars and concrete mixes at the age of 60 minutes (McCarter et al., 1999).

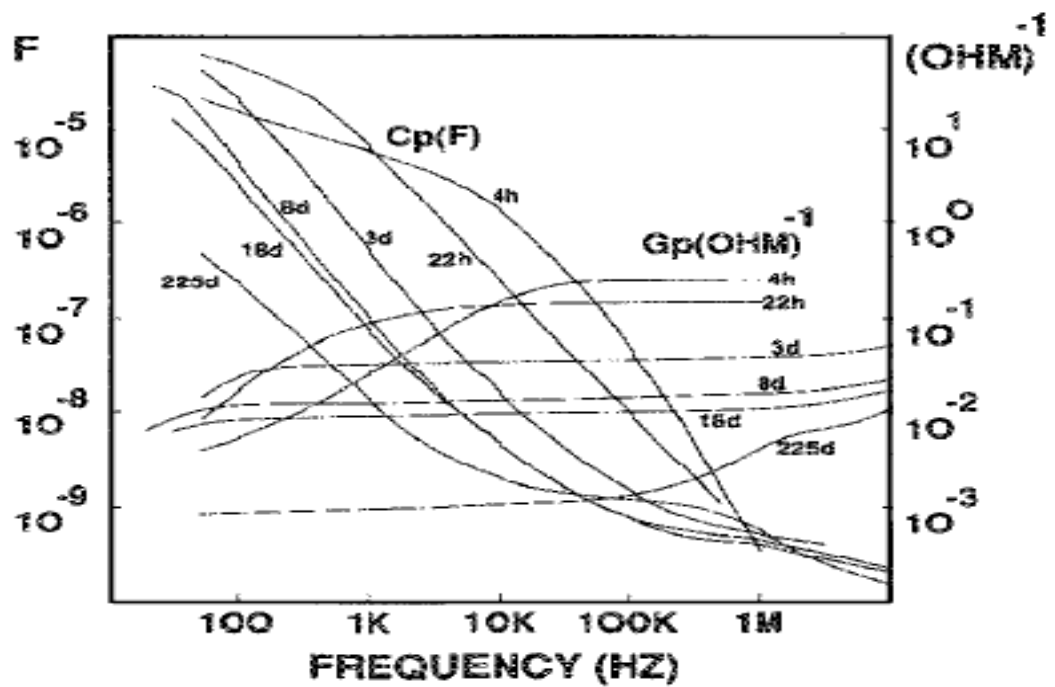


Figure 3.24: Capacitance, C_p , and conductance, G_p , frequency sweep through time for 0.5 w/b cement paste samples (Adapted from Camp and Bilotta (1989)).

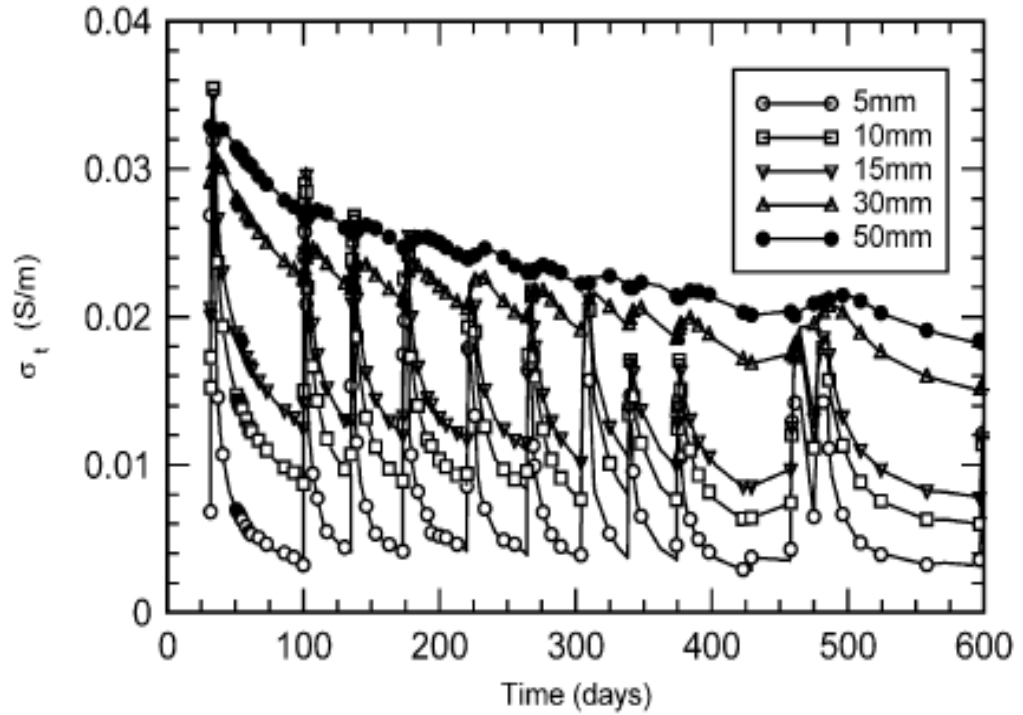


Figure 3.25: Conductivity measurement for a Portland cement concrete through time at different depths from the surface under cyclic wetting and drying (McCarter et al., 2003).

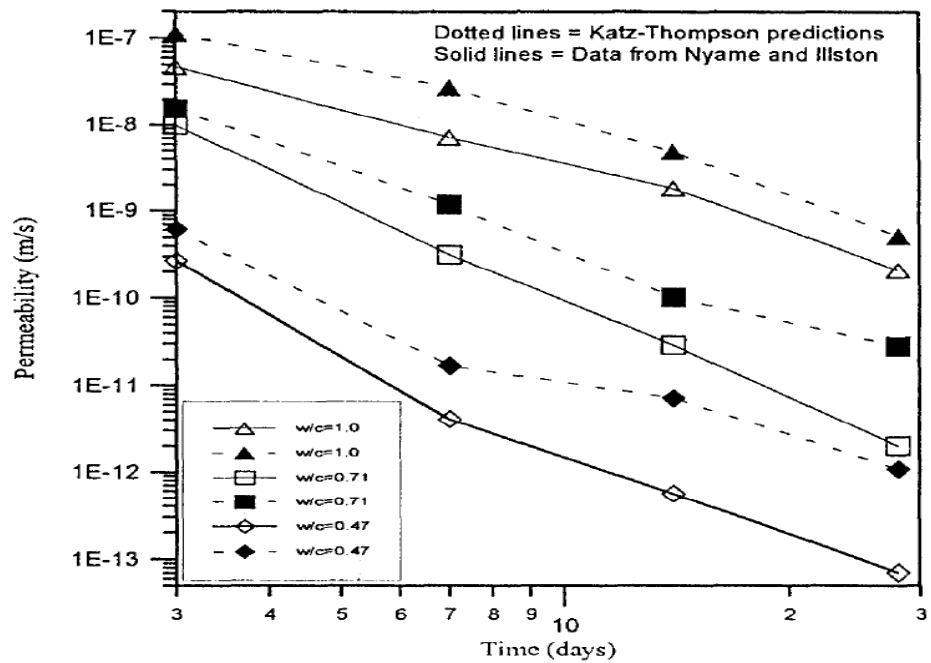


Figure 3.26: Comparison between the predicted permeability results through Katz-Thompson equation, and the experimental data from Nyame and Illston (1981) and Illston (1980).

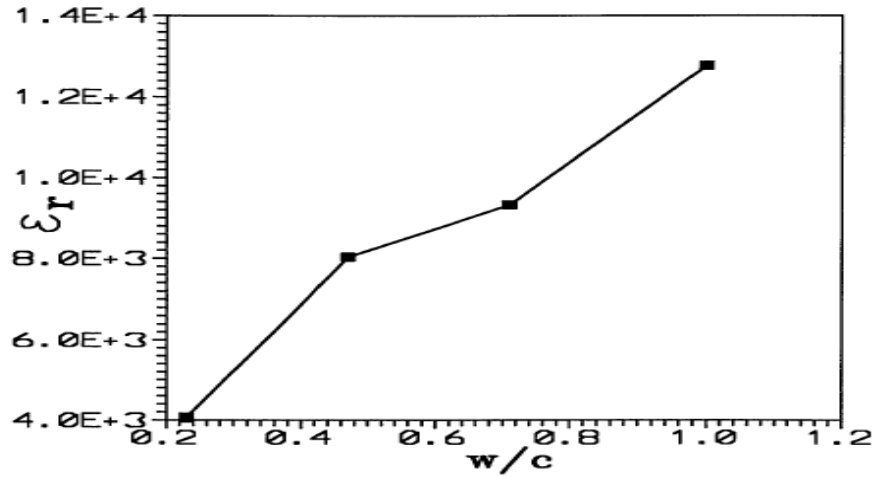


Figure 3.27: Influence of w/b on the permittivity of hardened cement-paste (Christensen, 1993). Values are presented at 11-months hydration.

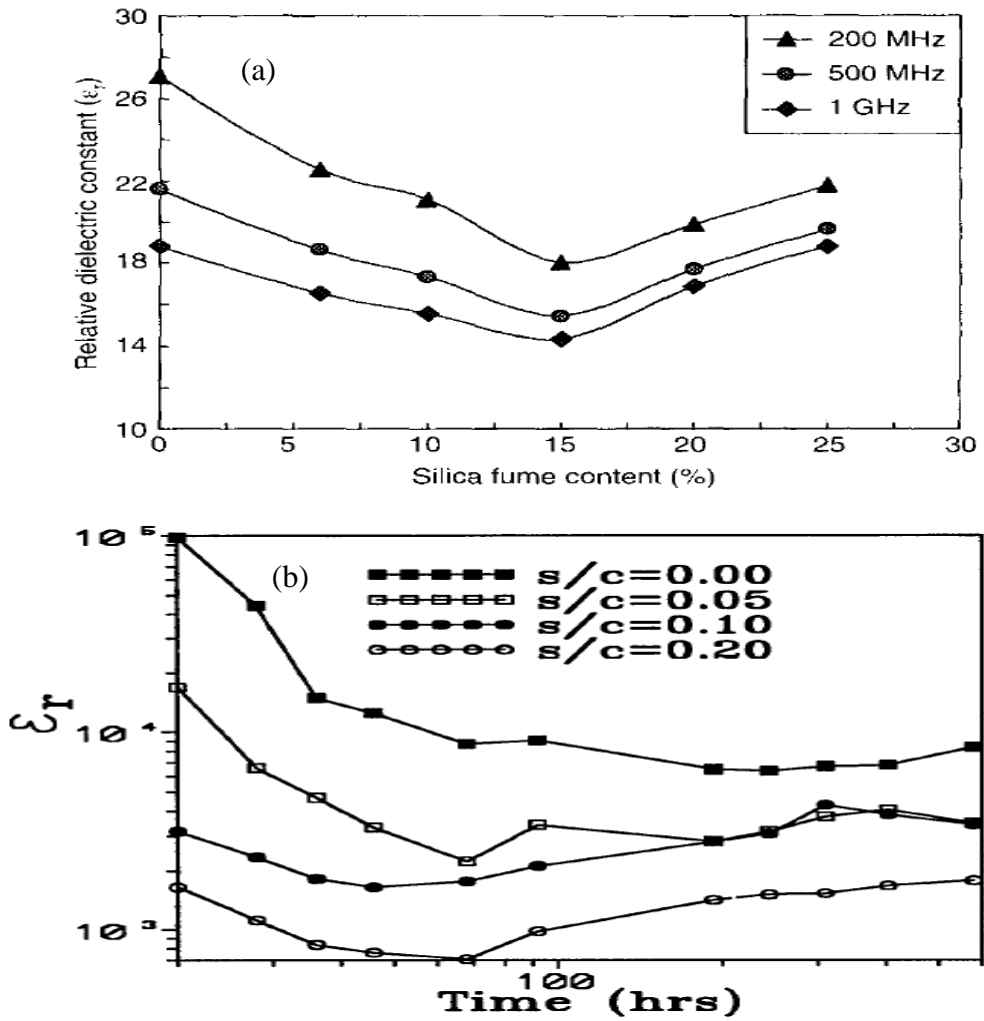


Figure 3.28: Effect of silica fume addition on the relative permittivity of Portland cement pastes (a) at different frequencies and (b) through time (Gu and Beaudoin, 1997) (Christensen, 1993).

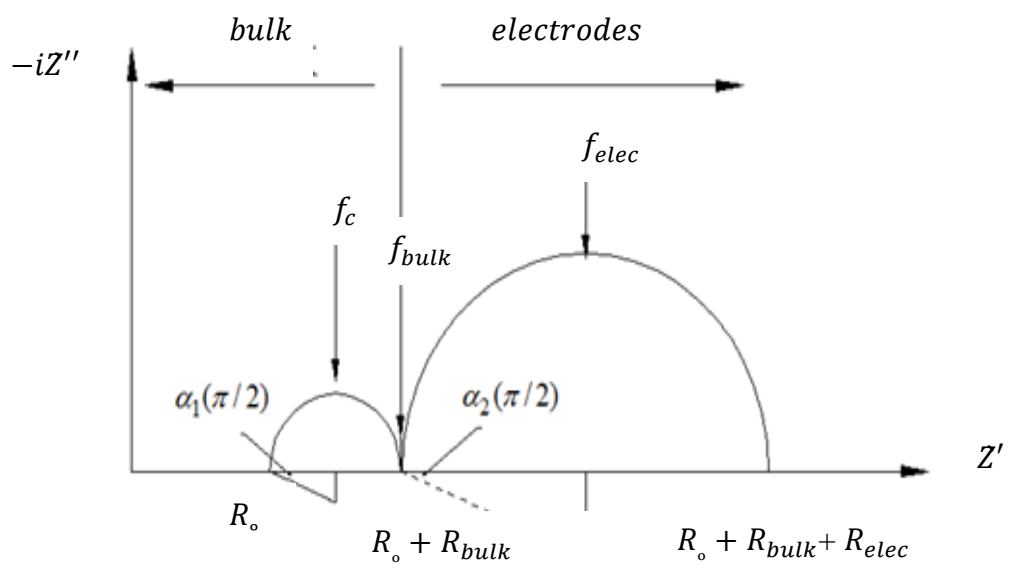


Figure 3.29: Electrodes / Bulk Impedance representation in the complex plane
Adapted from McCarter and Brousseau (1990).

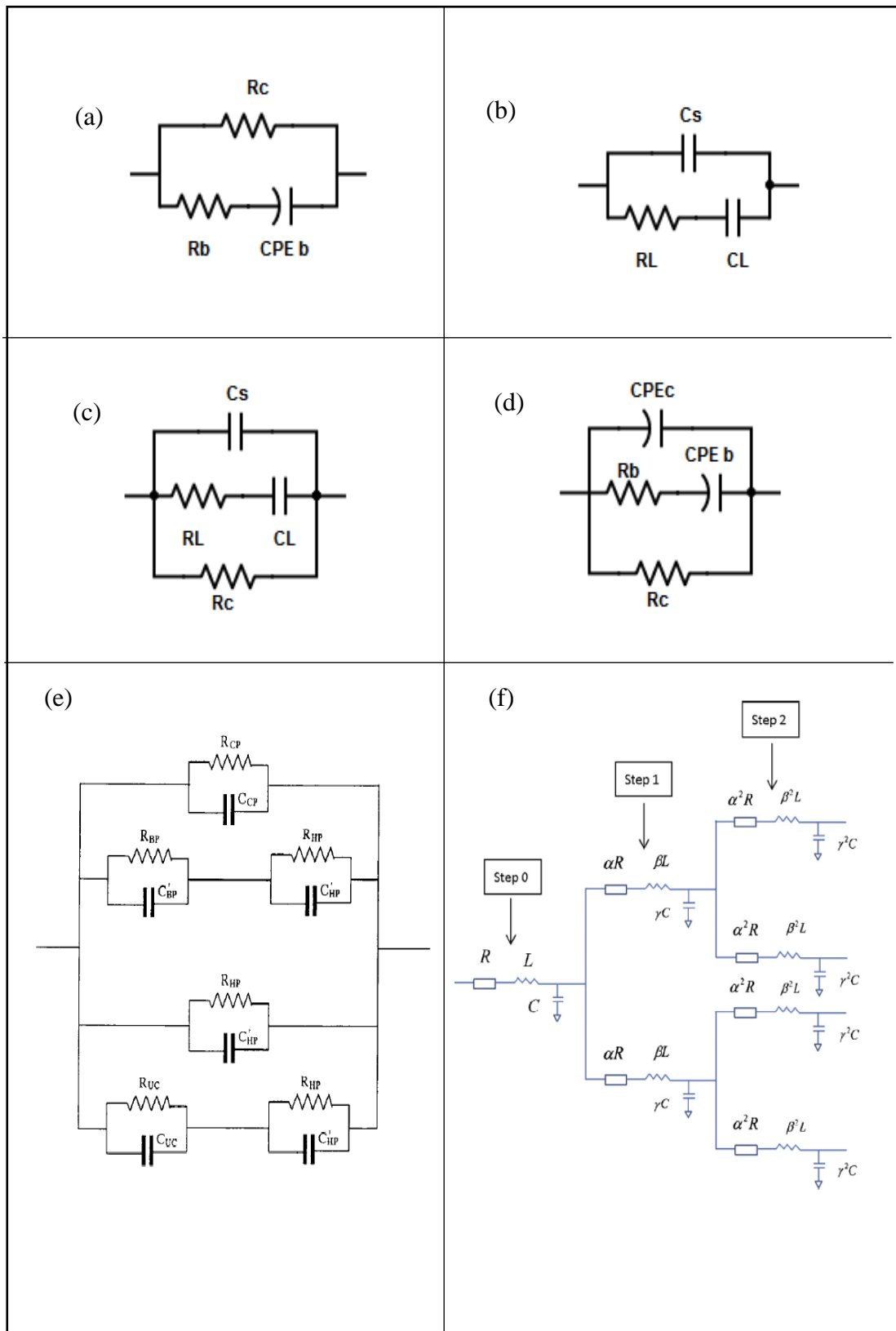


Figure 3.30: Different equivalent electrical circuits used to model the response of cementitious materials after (a) Kim et al. (1995) (b) Andrade et al. (1999) (c) (Cabeza et al., 2002; Cabeza et al., 2003; Cabeza et al., 2006) (d). Cruz et al. (2013) (e) Macphee et al. (1997) (f) Tang et al. (2014)

Testing method	Formation factor (Mean values)
Electrical conductivity	40.6
Bromide with two chamber method	31.1
Lithium with two chamber method	36.0

Table 3.1: Formation factor results obtained by electrical conductivity method and by the two chamber diffusion method for 0.8w/b cement paste at the age of 7 days (Taffinder and Batchelor, 1993).

w/b ratio	54MHz	100MHz	200MHz	300MHz	500MHz	1GHz
0.3	38.37	32.41	27.08	24.52	21.59	18.78
0.4	44.34	37.04	30.25	27.04	23.44	20.25
0.5	56.35	44.97	35.11	30.90	26.80	23.72
0.6	62.43	49.29	37.99	33.24	28.89	25.84
0.7	69.14	53.33	40.91	36.05	31.72	28.97

Table 3.2: Permittivity values for one-year old saturated cement paste samples with different w/b.

Sample age	f_c MHz	f_{bulk} kHz	f_{elec} mHz
1 Day	5.55	8.17	31.1
10 Days	4.82	2.28	20.3
100 Days	2.73	1.49	<10

Table 3.3: Changes in Characteristic frequency, f_c , bulk frequency, f_{bulk} , electrode bulk frequency, f_{elec} as a function of sample age.

Study	Electrodes geometry	Age range	w/b ratio	Bulk frequency range
McCarter and Brousseau (1990)	2-point measurement with embedded bar electrodes	1Day-100Day	0.27	8.17kHz-1.49kHz
Scuderi et al. (1991)	2-point measurement with outer cylindrical electrode and embedded bar electrode	9hrs -479hrs	0.3	500kHz-15.8kHz
Christensen et al. (1994)	2-point measurement with outer cylindrical electrode and embedded bar electrode	0hr-500hrs	0.35	128kHz-20kHz

Table 3.4: Bulk frequency ranges attained in different studies.

w/b ratio	Bulk frequency, f_{bulk} (kHz)
0.3	10
0.35	22.4
0.4	79.4

Table 3.5: Bulk Frequency values at 68 hours for cement paste samples with 20% silica fume replacement (Christensen et al., 1994).

Chapter 4 – Experimental Design and Data Acquisition

The experimental program was divided into two stages:

- a) The early hydration stage (initial 24hrs); and,
- b) The hardening stage up to 400 days hydration.

Within each of these, a range of tests were used to support the findings of the electrical measurements which formed the focus of this research. A diagrammatic representation for the experimental programme is shown in Figure 4.1.

4.1 The early hydration stage

This stage concerns itself with monitoring the electrical conductivity and permittivity of different cementitious materials through the initial 24hrs hydration. This experiment comprises three parallel experiments which are:

- a) The early electrical response with measurements taken over the frequency range 1Hz-10MHz;
- b) Heat output measurements using the isothermal conduction calorimeter; and,
- c) To study hydrate formation on the grain surfaces using the environmental scanning electron microscope.

4.1.1 Materials and mixes

Both cement pastes and concretes were used with different water/binder (w/b) ratios and supplementary cementitious materials (SCMs). Binders complied with EN197-1:2011 (2011) which were:

- Ordinary Portland cement (CEM I);
- Portland-slag cement CEM II/B-S (65% K+35%S);
- Blast furnace cement CEM III/A (35%K+65%S); and,
- Portland – fly ash cement CEM II/B-V (65%K+35%fly ash /V).

The oxide analysis of the materials provided by the suppliers is shown in Table 4.1. In addition, two different calcium sulphate additions (0.5% and 2%) were used in selected

mixes. Table 4.2 shows the cement-paste mixes which were used through the early hydration stage experiments. Concrete mixes with 0.45w/b ratio, with and without superplasticiser (sp) additions, were also studied during this period, and Table 4.3 presents the concrete mixes used in the current study. Crushed rock aggregate both coarse (20mm and 10mm) and fine (<4mm) was used throughout. The aggregate was saturated for 24hrs in water before it was placed in the laboratory environment to attain saturated surface-dry conditions.

4.1.2 Mixing procedures

With regard to the cement pastes, both the cement powder and the required amount of SCM were initially dry mixed by hand in a ceramic bowl for two minutes. Thereafter, half of the mixing water was added and the mixture was again mixed by hand for a further two minutes before the rest of the water was added and the mixture subjected again to another 2mins of hand mixing process. The time was recorded from the first contact between the dry mixture and water.

With regard to the concrete mixes, a mechanical pan mixer ($0.1m^3$) was used in the mixing process. Both the CEM I cement and the SCM were combined together in the mechanical mixer pan and the mixing process for the concretes followed ASTM (2006):

- 1) With the mechanical mixer off, the coarse aggregate; ~50% of the mixing water and soluble admixture were added;
- 2) The mixer was turned on and the cement; fine aggregates and remainder of the water were added;
- 3) The mixing time duration was as follows: 3mins after all the constituents were placed inside the mixer, followed by 3mins resting time and then another 2mins mixing.
- 4) Regarding the SCM addition, the cement and the SCM were added together at the same time.

4.1.3 Samples sizes and dimensions

Three types of samples were prepared for the early hydration study;

Electrical measurements during initial 24hrs

Pastes samples were prepared by compacting the paste into Plexiglas cuboidal cells of internal dimensions 50×50×50mm. A pair of stainless steel (s/s) electrodes, 2.4mm diameter with a centre-to-centre spacing of 25mm were embedded centrally inside each

specimen to a depth of 25mm. This was achieved by using a plastic former for each sample to facilitate the electrode positioning process (see Figure 4.2). The plastic formers were fixed to the Plexiglas cuboidal cells by threaded screws.

With regard to the concrete samples, the mixed concrete was compacted in 150×150×150mm plastic cube moulds in three layers; each layer was compacted for 1min on a vibrating table. Prior to placing the third layer, two 2.4mm diameter s/s electrodes with a centre-to-centre spacing of 75mm were embedded centrally inside the concrete specimens to a depth of 75mm. The electrodes were fixed in position by the use of a plastic former which was attached to the plastic cube by threaded screws (see Figure 4.3). Embedding the electrodes in this fashion ensured intimate contact with the sample and reduced any interference with the natural distribution of aggregate in the case of concretes. The third layer was added and concrete was vibrated again for 1min; the top surface of the cells was then smoothed with a trowel and covered by polyethylene sheeting to prevent evaporation. A thermistor was also placed through the sample holder and embedded to the same depth as the electrodes for both the concrete samples and the paste samples for temperature recording during early hydration. Three samples of each mix in Table 4.2 and Table 4.3 were batched.

Samples for the calorimeter test.

From the same batch which was used to prepare each paste sample for electrical measurements, 30gm of the paste was placed in a polyethylene bag for testing in the calorimeter. These samples were sealed before they were introduced to the calorimeter device in an aluminum can which, in turn, was filled with oil to conduct the heat generated from the samples to the can (see Figure 4.4)

Samples for the ESEM.

A set of 11 polyethylene bags were filled with 30gm paste from the PC0.35w/b sample (see Table 4.2). The cement pastes in these bags were made as thin as possible to allow stopping of the hydration process when required before imaging.

4.1.4 Tests and devices

Electrical measurements data acquisition system

In order to obtain the electrical response for both cement pastes and concretes during the initial 24hrs period, a Solartron 1260 Impedance analyser was used. The frequency range

was 1Hz-10MHz using 20 steps per decade, giving a total of 140 measurement points during each sweep. Each sweep took approximately 4.5mins to complete, giving 320 sweeps over the 24hrs test period. The voltage amplitude during the measurements was kept at 350 mV to reduce lead inductive effects thereby giving relatively noise-free data. The impedance analyser was connected to an HP computer desktop through a GPIB/USB cable and Zplot /Zview commercial software was used for the data acquisition process.

Four coaxial (RG 58 A/U) screened leads with equal length (75cm) were used to connect the electrodes in the samples with the impedance analyser. The coaxial leads at the sample end were connected to the electrodes through alligator clips and at the other end, the impedance analyser and the leads were connected through BNC connectors. All the four leads were grounded together by connecting the grounding screen mesh around each lead together to reduce the possibility of any potential stray current effect (see Figure 4.5).

A two-point embedded electrode configuration was used during the initial 24hrs. In this configuration, the sensing voltage lead (Hi) and the current lead (output) were coupled together at one stainless steel electrode, and the other voltage sensing lead (Low) and the current lead (input) were coupled together to the other electrode. Both the voltage injecting and the current sensing were performed at the same electrodes (see Figure 4.2(b)). This particular embedded electrode configuration has been used in other studies (Rajabipour et al., 2007; McCarter et al., 2013). Three replicate tests for each mix were carried out with tests undertaken in a temperature controlled laboratory ($21^{\circ}\text{C}\pm 1^{\circ}\text{C}$).

Due to the low impedance of the samples at this early stage, a nulling process was performed to account for the lead inductive effect by performing open circuit/closed circuit measurements for the four leads together by using the same voltage amplitude (350mV) and the same frequency range which were used during the experiment. The procedure adopted by Edwards et al. (1997) has been used to correct the data for the inductive effect. The impedance, $Z(\omega)$, of the sample, can be written as, in equation (3.1)

At any angular frequency, ω , the electrical response of such a system will result from the superposed phenomena of conduction and polarization processes. These are quantified, respectively, by the bulk conductivity, $\sigma(\omega)$, and relative permittivity, $\epsilon_r(\omega)$, which are obtained from the impedance through the following relationships,

$$\varepsilon_r(\omega) = \frac{1}{\varepsilon_o \omega} \left(\frac{Z''(\omega)}{Z'(\omega)^2 + Z''(\omega)^2} \right) \frac{L}{A} \quad (4.1)$$

$$\sigma(\omega) = \left(\frac{Z'(\omega)}{Z'(\omega)^2 + Z''(\omega)^2} \right) \frac{L}{A} \quad (4.2)$$

where ε_o is the permittivity of a vacuum (8.854×10^{-12} Farads/m) and L/A is a factor which is related to the electrode geometry and sample configuration. As the electrical field between the electrodes is non-uniform, the geometrical factor L/A in equations (4.1) and (4.2) cannot be readily calculated and was evaluated by calibrating the electrode array using a liquid of known electrical properties. For the electrode arrangements used in the current work, the geometrical factor L/A was evaluated as 41.67m^{-1} for the paste electrode arrangement, and 17.34m^{-1} for the concrete electrode arrangement.

Temperature data acquisition system

The internal temperature changes through the initial 24hrs for both the concrete mixes and pastes, were recorded in parallel with the electrical impedance by obtaining the electrical resistance of the embedded thermistor. A data logger was connected to the thermistor through a multiplexer and used to apply the voltage as well as registering the resistance every 2mins (see Figure 4.6). Thermistor measurements were converted to temperature using the Steinhart-Hart equation as follows,

$$T = [A + B \ln R + C(\ln R)^3]^{-1} - 273.15 \quad (4.3)$$

where R is the measured resistance of the thermistor (ohms); T is the temperature ($^{\circ}\text{C}$); A , B and C are coefficients which depend on the type of thermistor and \ln is the natural logarithm. For the thermistors used in the current work, A , B and C were obtained from manufacturer data, respectively, to be: $1.287 \times 10^{-3} \text{K}^{-1}$; $2.357 \times 10^{-4} \text{K}^{-1}$ and $9.509 \times 10^{-8} \text{K}^{-1}$.

Heat output data acquisition system

The heat output for the pastes through the initial 24hrs, was recorded by a JAF type isothermal conduction calorimeter. The device is composed of 4 main units which are,

- (a) An aluminium can, in which the sample is placed, is flooded with non-conductive oil. The sample polyethylene bag is closed and wrapped around an electric heater inside the aluminium can for later calibration process.

- (b) An acrylic cylindrical calorimeter inside which the aluminium can is placed (see Figures 4.7(a) and (b)). A set of thermopiles are fixed at the bottom of the acrylic cylinder and the sample can is positioned above them. These set of thermopiles are acting as thermal path for the heat which is generated from the hydration reaction. The thermopiles generate an electrical signal which is proportional to the generated heat. The space between the upper cover of the acrylic cylinder and the sample can is filled with a polystyrene thermal insulator to prevent heat escaping and thermal air movements (see Figure 4.7(a)).
- (c) A controlled temperature water-bath, containing polypropylene containers which were filled with water from the water-bath through two holes, one at the upper-end and the other at the lower-end. The acrylic calorimeter was immersed in the polypropylene container. The water-bath temperature is controlled through its own heating system and pumping cooling water from an adjacent water reservoir unit in which its temperature is adjusted lower than the target temperature by 3°C. The water-bath temperature in this study was controlled at 21°C to replicate the laboratory temperature in which the electrical measurements are conducted.
- (d) The signal which was generated from the thermopiles, was read through a digital voltmeter which was fitted in an interface module linking the calorimeter and the data logging PC.

After the heat output from the hydration reaction relaxes (after almost a week), a calibration process was performed to determine the calorimeter constants which allow the conversion of the voltage data to heat measurements (energy units). This process was conducted by supplying the electrical heater inside the sample can by a known electrical power which allows plotting of the linear relationship which exists between the derivative of the voltage recorded through time and the voltage values according to the Tian-Calvet equation(4.5).

$$W = K_1 E + K_2 \frac{dE}{dt} \quad (4.4)$$

In which; W is the heat production (Watts); K_1 and K_2 are the calorimeter constants; E is the thermopiles output (mV) and $\frac{dE}{dt}$ is the voltage rate change.

SEM experiment

With regard to the ESEM samples, liquid nitrogen was used to instantly freeze the bagged samples at the ages of 11mins, 2hrs and 5.5 hrs after mixing the samples with water. This was achieved by immersing the polyethylene bag which contains the sample for 5mins in the liquid nitrogen. After ceasing the hydration reaction, all the frozen bagged samples were stored in a domestic freezer at a temperature of $< -20^{\circ}\text{C}$ degrees until required for testing. The samples were taken out from the freezer on the testing day and a freeze-drying process was used for the sublimation of ice to water-vapour. Thereafter, the samples were studied using the ESEM in the secondary mode operated at 1KeV.

4.1.5 Initial 24 hours bulk conductivity experimental estimation

Preliminaries

The imaginary part of equation (3.9) is related to the dissipation of energy in the material due to friction generated by the rotational movement of the dipoles as in equation (4.5),

$$L_D = \frac{\varepsilon'' \omega \varepsilon_0 E_o^2}{2} \quad (4.5)$$

where L_D is the energy rate loss due to polarization process (J/s.m^3).

Therefore, from equation (4.5), as the imaginary part of the complex dielectric constant increases, more energy is dissipated due to the motion of the dipoles charges and its associated thermal losses. On the other hand, and in the case of conductive materials, the current conduction process also causes energy dissipation which is expressed as,

$$L_C = \frac{1}{2} \sigma_{AC} E_o^2 \quad (4.6)$$

Where L_C is the energy loss rate due to conduction (J/s.m^3).

Therefore, from equations (4.5) and (4.6), it is evident that the imaginary part of the complex dielectric constant (i.e. the loss) can also be expressed in terms of the conductivity of the material as in equation (4.7),

$$\varepsilon'' = \frac{\sigma_{AC}}{\omega \varepsilon_0} \quad (4.7)$$

However, from equation (4.7), the conductivity, is a frequency dependent parameter as it increases with increasing frequency of applied field. Ionically conductive porous materials such as cementitious systems, in addition to the contribution of the losses to AC conductivity, the material itself possesses a static DC (or low-frequency) conductivity which is a material property, temperature dependent and an ionic concentration dependent parameter. Therefore, the measured conductivity at frequency, ω , is the sum of both the DC conductivity of the material and the losses contributing to the AC conductivity, hence,

$$\sigma(\omega) = \sigma_{AC} + \sigma_{DC} \quad (4.8)$$

where $\sigma(\omega)$ is the electrical conductivity (S/m) at angular frequency ω .

Evaluating the DC conductance/resistance of the material, requires minimizing,

- (a) the AC conductance contribution of the material; and,
- (b) the contribution from electrode polarization (McCarter and Brousseau, 1990).

This can be evaluated by measuring the material electrical resistance/conductance at a specific frequency of electrical field (from now on called the ‘bulk frequency’). The bulk frequency can be obtained at the cusp point in the Nyquist plot as shown in Figure 3.29.

During the early hydration period, cementitious materials undergo physical and chemical changes and chemical processes which will influence charge mobility and their ease of oscillation in response to the applied alternating electrical field. As it has been shown in previous studies (McCarter and Brousseau, 1990; Christensen et al., 1992), the bulk frequency value for the fresh material is expected to change through time as it changes from a liquid to plastic state, and then to a solid state. Therefore, the first step in evaluating and relating the early hydration electrical properties for cementitious materials to their hydration characteristics, is to assess the response of the bulk frequency through time and the influence of mix composition, before deciding on using an arbitrary frequency to cover the entire 24-hours of the initial hydration period. Therefore, the motivation for this are as follows,

- (i) Assessing the response of the bulk frequency through time for different mix constituents; and,
- (ii) Identify the most suitable frequency range to extract the bulk material electrical properties during the early hydration stage.

Early hydration bulk frequency response

The change in bulk frequency for three different w/b ratio cement pastes (0.3, 0.35, and 0.45) through time is shown in Figure 4.8. As is evident from this Figure, and as a general trend for the bulk frequency, initial values are high and decrease with time. Regarding the PC 0.3w/b cement paste, the initial value for the bulk frequency which was obtained 6 minutes after mixing, recorded a value of 1.26MHz; values of 794kHz and 1.12MHz were recorded for the 0.35w/b paste and the 0.45w/b paste, respectively, at the same age.

At 24hrs, the recorded bulk frequency values were 17.8kHz, 22.4kHz and 70.8kHz for the PC 0.3w/b, PC 0.35w/b and the PC 0.45w/b pastes, respectively. Therefore, the bulk frequency values decrease by almost three orders of magnitude over the initial 24 hrs. It is also noticeable that as the w/b ratio increases, the bulk frequency values increase and is clearly shown in Figure 4.8.

Figure 4.9 presents the bulk frequency values for cement pastes with different GGBS replacements percentages (35%, 50% and 65%) at 0.35w/b ratio. When compared with the pure cement paste bulk frequency values (Figure 4.8) the following should be noted for the GGBS mixes,

- (a) The initial bulk frequency value recorded for the GGBS pastes is considerably lower than the pure pastes as the initial values are in the range 110kHz-125kHz.
- (b) For the replaced pastes, the decreasing rate is inversely proportion to the replacement percentage and is observed by comparing the initial values for the bulk frequencies for the mixes with values recorded at the age of 24hrs; for the 35% replaced mix the bulk frequency decreased by ~70% from its initial value in comparison to ~55% for the 65%GGBS replaced mix. This is lower than that for the pure Portland cement paste which was ~90% from the initial recorded bulk frequency value.

It is evident that the bulk frequency values of the mixes are affected by the mix constituent as during this early hydration period replacing the cement with different amounts of GGBS affects the decreasing rate as well as the final values at 24hrs.

Cement pastes optimum bulk frequency range

Figure 4.10 shows the percentage difference of the recorded electrical conductivity for the Portland cement pastes (PC 0.3w/b, PC0.35w/b and PC0.45w/b) over the frequency range 1Hz-10MHz. For this Figure, the percentage difference is evaluated from equation (4.9),

$$\%Difference = \left\{ \frac{\sigma(\omega) - \sigma_{DC}}{\sigma_{DC}} \right\} \times 100 \quad (4.9)$$

where $\sigma(\omega)$ is the conductivity value at angular frequency, ω , and σ_{DC} is the conductivity recorded at the bulk frequency (i.e. cusp point frequency). See also equation (4.8). In Figure 4.10(a) a $\pm 5\%$ accuracy window has been selected in order to study the deviation of the recorded electrical conductivity as a function of time and frequency from the DC conductivity of the samples. It could be noticed that the percentage difference from the DC conductance at low frequencies such as in the range from 1Hz-10kHz is lower than (-5%).

However, with time the 'accuracy zone' of the DC conductivity reduces to lower frequency ranges. This can be seen by observing the 1kHz frequency value through time for the 0.3w/b paste, as the electrical conductivity value recorded at 1kHz at the end of the 24hrs monitoring period displays a lower percentage difference than its initial value. This behaviour of increasing the accuracy of the 1kHz conductivity as time advances is also observed for the 0.35w/b paste; the 0.45w/b cement paste also shows an increase in accuracy of the 1kHz electrical conductivity through time however this is not as pronounced as in the case of the 0.3w/b and the 0.35w/b pastes. The following factors, which affect the accuracy of the DC conductivity estimation, can be summarised:

(a) Measuring frequency value

The conductance recorded at lower frequencies can deviate from the value of the DC conductance of the material by $< -5\%$ (see Figure 4.10) depending on the applied frequency and is attributed to the contribution of the sample/electrode interface impedance. Conversely, at a higher frequency than the bulk frequency, the recorded conductivity values also deviate from the bulk conductivity by $> +5\%$ due to the effect of the AC conductivity contribution.

(b) Water/binder ratio

As the w/b ratio increases, a higher frequency range should be used in order to obtain conductivity values in the accuracy range of $\pm 5\%$ of the DC conductivity (see Figure 4.11). This can be attributed to the increase in the DC conductivity of the samples as the w/b ratio increases.

(c) Hydration reaction effect

As hydration time increases, the $\pm 5\%$ accuracy window for the conductivity can be attained at lower frequency ranges in comparison to the early hydration stages. This can be viewed in the same context as the bulk frequency response through time for the samples as shown in Figure 4.8. Therefore, the $\pm 5\%$ conductivity accuracy range for the samples after the addition of water can be obtained in the frequency ranges of 31kHz-8.91MHz, 11kHz-8.91MHz and 79kHz-8.91MHz for, respectively, the PC0.3w/b, PC0.35w/b and PC0.45w/b. At the end of 24hrs these ranges have reduced to 398Hz-700kHz, 316Hz-891kHz and 794Hz-1.4MHz for the respective samples (see Figure 4.11).

From both Figures 4.10 and 4.11, it is evident that the conductivity which is recorded within the frequency range 100kHz-1MHz during the initial 24hrs for the different w/b samples, is within $\pm 5\%$ DC conductivity accuracy window. However, the 1MHz conductivity value through time in some mixes (see Figure 4.12(a)) deviates at later ages from the $\pm 5\%$ accuracy window, especially in the case of the lower w/b mixes. From Figure 4.12(a) the 1MHz conductivity with regard to the DC values of the mixes, has a high accuracy during the early stages in the 24hr monitoring period, as values recorded at this frequency through the initial 6hrs are in the range of $\pm 1\%$ from the DC conductance. On the other hand, and with regard to the 100kHz conductivity accuracy, at early ages (<1hr) the 100kHz conductivity records a deviation in the range of -4.5% from the DC conductivity; however, with the time, the accuracy of the 100kHz conductance increases as the deviation from the DC conductance by the age of 6hrs decreases from -1.75% to -0.5%. After the age of 6hrs, the 1MHz conductance accuracy decreases rapidly especially for the 0.3w/b mix to almost +5% at the age of 13hrs and by the end of the monitoring period the deviation is $> +7\%$ from the DC conductance of the sample. However, for the other two mixes, (0.35w/b and the 0.45w/b) the conductivity values at 1MHz after the age of 6hrs also show the same deviation from the DC value, but with a relatively low rate in comparison to the 0.3w/b mix. The 100kHz conductivity also

deviates from the DC conductivity, however, not at the same rate which was detected for the 1MHz conductivity. By the end of the monitoring period the maximum percentage difference which is recorded for the different samples is in the range 0 to +1.5% from their DC conductivity, and the maximum difference (+1.5%) was recorded for the 0.3w/b ratio paste (see Figure 4.12 (b)).

The rapid deviation from the DC conductivity values for the mixes through time, especially in the case at 1MHz, shows a progressive AC conductance contribution to the value of the DC conductivity of the material. This is an indication of the developing dielectric properties of the material which shows that the material is gradually changing from an almost purely conductive solution to a lossy dielectric material with a displacement current contribution from polarization processes.

The rapid increase in the 1MHz conductivity with respect to the DC conductance values for the low w/b pastes in comparison to the higher ones, indicates that the low w/b pastes develop their dielectric properties much faster than the high w/b pastes. This indicates a rapid consumption of the liquid phase and the development of a continuous/discontinuous liquid path due to the formation of hydration products. Such a system will possess both conductive and capacitive behaviour rather than just a conductive nature, as in the case of the fresh cement paste.

Replaced pastes optimum bulk frequency range

The same analysis regarding the accuracy of the conductivity at different frequencies, as well as through time, has been performed on the replaced mixes. From Figure 4.13, the conductivity in the frequency range 1Hz-1kHz is $\leq -5\%$ from its DC value; at the frequencies in the 6MHz-10MHz the recorded conductivity is $\geq +5\%$ from its DC value. In the frequency range 10kHz-1MHz the accuracy for the replaced mixes is in the range of $\pm 5\%$ of the DC conductivity. The same justification which has been presented in the case of the pure cement pastes regarding the deviation from the DC conductance at the lower and higher frequency ranges can also be invoked here. In the low-frequency range, the contribution from the electrodes/sample interface impedance contributes significantly in deviating the recorded sample conductivity from their DC conductivity, whereas the higher frequency range the contribution from the AC conductance deviates the value of the conductivity from its original DC value.

As it can be seen from Figure 4.14, the frequency range 10kHz-1MHz gives a conductivity accuracy in the range of $\pm 5\%$ from the DC conductance. It is also useful in this case to assess the accuracy of selected different frequencies in this range and to compare them with the pure cement pastes in order to obtain the most accurate frequency for the purpose of obtaining the bulk DC conductivity for all the mixes. Figure 4.15 displays the accuracy of the conductivity at 10kHz, 100kHz and 1MHz through time in relation to the DC conductivity of the samples for the GGBS replaced pastes (35%GGBS, 50%GGBS, 65%GGBS). Regarding Figure 4.15, the accuracy for the recorded conductivity at the three frequencies displays minimum deviation $<3.5\%$ over the 24hr test period for all the GGBS mixes. This is contrary to what has been obtained for the pure cement pastes with the same w/b ratio. Regarding the latter, as shown in Figure 4.12, the 1MHz conductivity for the PC 0.35w/b paste at the end of the 24hr monitoring period is $\sim 6\%$ greater than the DC conductivity of the sample. However, for the replaced mixes the highest deviation at 1MHz at the age of 24hrs is $\sim 3.25\%$ for the 35%GGBS which is considerably less than the pure cement pastes at the same age and frequency. From Figure 4.15 it is also evident that a frequency of 100kHz records the most acceptable accuracy for all the mixes in comparison to the other frequencies.

Therefore, regarding the replaced mixes and pure cement pastes at different w/b ratios, it is clear that 100kHz would give an acceptable level of accuracy with regard to the bulk conductivity (or resistivity) of the samples during the initial 24hrs monitoring period.

4.2 The hardening stage

This stage is divided into three main sections which are:

(a) Electrode configuration

The purpose of these experiments is to assess the factors which affect the evaluation of the bulk conductivity/resistivity of the material using a 2-point, end-to-end plate electrode configuration. This electrode configuration is relatively easy to setup and is frequently used in estimating the electrical resistivity of concretes. With regard to this study, this particular electrode configuration was used to obtain the electrical response of the material through the hardening stage.

(b) Concrete mixes electrical measurement

The purpose of these experiments is to characterise and relate the electrical response which was obtained from the different concrete mixes through the period of 365 days after casting, with the chemical and physical processes in the different concrete mixes.

(c) Durability ranking

The purpose of these experiments was to establish a ranking methodology with regard to the material durability using electrical property measurements and by comparing these measurements with a standard durability ranking test, in this instance, the NTBuild492 test.

4.2.1 Materials and mixing procedure

With regard to the materials which have been used through the hardening stage, the same binder types as in Section 4.1.1 were used. The concrete mixes are presented in Table 4.4. The same mixing procedure as for the concrete samples in section 4.1.2 was used in this stage.

4.2.2 Samples sizes and dimensions

After mixing, three types of samples were cast:

- (a) Two sets of 150×150×150mm concrete cubes were cast separately. The first set (set 1) was for the electrode configuration experiment which was undertaken on C1, C3, G1, G3, P1 and P3 concrete samples according to Table 4.4. Set 1 samples also had embedded s/s rod electrodes to facilitate 4-point measurements. The rods were embedded centrally within the cube and sleeved to expose a 10mm tip. The second set of samples (Set 2) was used for the electrical characterisation through the hardening stage and includes all the mixes in Table 4.4. With regard to electrical characterization (Set 2 samples), plastic moulds were used for casting as in Section 4.1.3. However, for the electrode configuration experiments (Set 1 samples) steel moulds were used. Three samples from each concrete mix were produced for both sets of experiments. After casting, the concrete samples were covered by polyethylene sheets to prevent water evaporation and left in the laboratory atmosphere for a period of 24hrs. After 24hrs, the samples were demoulded and stored in a curing tank ($21 \pm 1^\circ\text{C}$) until required for testing.

- (b) 100×100×100mm concrete cube samples were cast from the same batch as those used for electrical measurements (Set 2) and electrode configuration experiments (Set 1). The compressive strength of Set 2 samples was obtained at the ages of 28, 180 and 400 days, for Set 1 samples the compressive strength was obtained at the ages of 28, and 180 days. The compressive strength for the samples are shown in Table 4.5 and Table 4.6.
- (c) One 250×250×150 (thick) mm concrete slab was cast from the same batch as that used for Set 2. The slabs were stored in the laboratory atmosphere for the initial 24hrs, and then stored in a saturated condition until the age of 400 days. Each slab was then cored to produce two 100Ø mm×150mm concrete cylinders, these, in turn, were wet cut by a diamond saw to produce three 100Ø mm×50mm concrete disks from each mix.

4.2.3 Electrode configuration

As electrical resistivity/conductivity is being increasingly considered as ‘a durability index’ for assessing the long-term performance of concrete structures (see, for example Table 4.7 and Table 4.8 (Gehlen and Ludwig, 1999; Torrents et al., 2007; Alexander et al., 2008; Alexander et al., 2010; Andrade, 2010; Muigai et al., 2012; Andrade et al., 2013; Nganga et al., 2013; Andrade et al., 2014)), this parameter should be obtained as accurately as possible if it is to be utilized. Therefore, this study critically examines the electrical response acquired through the 2-point, end-to-end electrode configuration. This allows evaluation of its effect on the value obtained for the concrete, as well as the optimum frequency range which should be used when using this particular electrode configuration. This is of importance, as no particular AC frequency value is specified for this electrode configuration, although a frequency in the range 50-100Hz has been recommended (Tang et al., 2011). In the measurement of concrete resistivity using two- and four-electrode methods, a frequency in the range 50Hz-1kHz has also been suggested (Polder et al., 2000). More specifically, frequency values of 108Hz (Gehlen and Ludwig, 1999), 128 Hz (Newlands et al., 2007), 107 Hz and 120 Hz (Osterminski et al., 2012) have been used for two-electrode measurements. In the following sections, both the experimental program for this particular work and its results are presented.

Electrical measurements and data acquisition

Two-point electrical impedance measurements were obtained on each sample using a Solartron 1260 frequency response analyser (FRA). The signal amplitude used in the

experimental programme was 350 mV with the impedance measured over the frequency range 1Hz-10MHz using a logarithmic sweep with 10 frequency points per decade. After removal from the curing tank, the concrete cube was wiped with an absorbent towel and allowed to surface-dry before testing (to negate any possible surface conduction effects) with testing undertaken in a laboratory at a temperature of $21 \pm 1^\circ\text{C}$. The samples were approximately 36-months old at the time of testing. At this age, the change in resistivity/conductivity due to hydration will be negligible (Whittington et al., 1981); furthermore, it is only at such longer time-scales that the influence of the fly-ash and GGBS on pore structure becomes evident.

Figure 4.16(a) presents a schematic of the two-electrode testing arrangement. In this Figure, external stainless steel (s/s) plate-electrodes were placed against opposite faces of the concrete cube (i.e. the faces cast against the steel mould). Intimate contact between the electrodes and concrete was obtained by means of $150 \times 150 \text{mm}^2$ synthetic sponges, each 2mm thick, saturated with a contact solution. Leads from the current (I_{output}) and potential (V_{high}) connections on the FRA were coupled at one of the electrodes and the current (I_{input}) and potential (V_{low}) connections coupled at the other electrode. Open- and short-circuit residual lead impedances were automatically *nulled* from the measurements at every spot frequency using the FRA's on-board lead-correction facility. The overall testing arrangement is displayed in Figure 4.16(b) with a mass of 2kg placed on the upper electrode to ensure uniform contact and giving a contact pressure of approximately 1kPa. Regarding the contact solution noted above, three were used in the current experimental programme with separate sets of sponges were used for each saturating liquid:

- (a) mains tap-water;
- (b) a saturated solution of calcium hydroxide (Saremi and Mahallati, 2002) (as calcium hydroxide is released during the hydration of the silicate phases within the cement clinker); and,
- (c) a simulated cement pore solution comprising 0.1 molar sodium hydroxide and 0.3 molar potassium hydroxide (Ghods et al., 2013; Yang et al., 2014) (as the alkali-oxides Na_2O and K_2O within the cement clinker are highly soluble).

The impedance response of the sponges placed between the electrodes, loaded as above, was measured separately at the end of each test. In addition to two-electrode measurements, a four-electrode testing configuration was also used, as shown

schematically in Figure 4.17(a). In this setup, the external s/s plate-electrodes served as the current (output/input) electrodes and the embedded s/s rods acted as the potential (high/ low) electrodes. Figure 4.17(b) displays the testing arrangement with the plates placed on the faces perpendicular to the embedded pin-electrodes. In this Figure, the spacing $s = 75\text{mm}$. In connection with bulk resistivity measurements on concrete, it is generally accepted that electrodes should be spaced apart at least 1.5 times the maximum aggregate size (du Plooy et al., 2013) to obtain values representative of the bulk material. The maximum aggregate size used in the experimental programme was 20mm, hence electrode spacings should be $>30\text{ mm}$ which is the case for both the external plate-electrodes and the internal pin-electrodes.

Results:

In this study two presentation formalisms are used:

(a) Nyquist format i.e. $-iZ''(\omega)$ versus $Z'(\omega)$, which is the polar plot (see equation (3.1)).

(b) Bode format. This plot highlights the frequency domain behaviour of both the impedance, $|Z^*(\omega)|$, and phase angle, $\theta (= \tan^{-1}(Z''(\omega)/Z'(\omega)))$. A phase angle $\theta = -90^\circ$ would represent purely capacitive behaviour whereas a phase angle $\theta = 0^\circ$ would represent purely resistive behaviour.

Figure 4.18 presents the Nyquist plots with only the sponges placed between the electrodes, saturated with the three different liquids: water, calcium hydroxide and simulated pore solution. This figure indicates an almost linear decrease with increasing frequency and would represent part of a much larger arc associated with polarization phenomena at the electrode-sponge interface; the full extent of this arc would only become evident at frequencies considerably lower than the current work, i.e. $<1\text{Hz}$. Regarding Figure 4.18, the plots converge on the real axis as the frequency increases and, in all cases, at a frequency of approximately 40kHz touches the real axis; this point gives the bulk resistance of the sponges. Some residual lead inductive effects are evident in this Figure as the reactance turns positive at frequencies in excess of 40kHz. Regarding the sponge resistance at 40 kHz, these values are $7.9\ \Omega$, $2.8\ \Omega$ and $0.75\ \Omega$ for, respectively, the sponges saturated with tap-water, calcium hydroxide and simulated pore solution. Figures 4.19 – 4.21 display the impedance response for the concrete mixes in Table 4.4

using the testing arrangement presented in Figure 4.16(a), with the simulated pore solution used as the sponge-saturating liquid.

Generally, each response has a single dominant circular arc (denoted arc-1) however, the frequency range over which this arc dominates, the frequency at which it maximizes, the arc diameter and the depression angle (α) are all dependent on the concrete mix proportions. On closer examination, a second small, flat arc (denoted arc-2) is evident at the low-frequency end of the Nyquist plots (right-hand side) presented in Figures 4.19 – 4.21. In some instances, a small *spur* is also present on the right-hand side of the plot see, for example, Figure 4.19(a).

In terms of representing the response as an electrical circuit, this is presented in Figure 4.22 and comprises four, series-connected, parallel circuit elements (the bulk resistance of the sponges has been omitted from this model as their resistance is negligible in comparison to the impedance of the system):

- (i) a resistor R_s which represents the projected intercept of the high-frequency end of arc-1 with the real axis (see section 3.3.2 for the possible physical meanings for this electrical parameter).
- (ii) a parallel combination of resistor, R , and constant-phase element, CPE, for both arc-1 ($R1$ and CPE1) and arc-2 ($R2$ and CPE2); and,
- (iii) the small spur at the low-frequency end of the response would represent part of a much larger arc which would only become evident at frequencies $<1\text{Hz}$. For completeness, this is also represented by a parallel combination of resistor ($R3$) and constant phase element (CPE3) although it is not present in some of the concrete mixes.

Discussion

In attempting to offer a phenomenological interpretation for the circuit, consider again the testing arrangement in Figure 4.16(a). There are two interfaces present in this arrangement: the electrode-sponge interface and the sponge-concrete interface. If each interface can be electrically modelled as a parallel combination of resistor and CPE, then $R3$ -CPE3 (exponent $p3$) would account for the response from the electrode-sponge

interface; $R2$ -CPE2 (exponent $p2$) the response from the sponge-specimen interface; and $R1$ -CPE1 (exponent $p1$) and R_s the *bulk* response from the concrete specimen.

Consider, for example, the Nyquist plots for the PC mix ($w/b=0.65$) and the GGBS mix ($w/b=0.35$) presented in Figure 4.19 and Figure 4.20 respectively; using the parameter values for the circuit elements presented in Table 4.9, the simulated Nyquist responses over the frequency range 1Hz-10MHz are presented in Figure 4.23(a) and (b). The simulated circuit and the measured data show good agreement indicating that the model is a good electrical representation of the system. Regarding the GGBS concrete (Figure 4.23(b)), as this mix did not display a spur in the low-frequency region circuit element, $R3$ -CPE3 is not included in the model simulation.

The following general features are evident from Figures 4.19 – 4.21:

- (a) an increase in the w/b ratio results in a decrease in the bulk impedance of the specimen causing a decrease in the diameter of the dominant (bulk) arc (i.e. circuit element $R1$ -CPE1). $R1$, together with R_s , would represent the resistance associated with the continuous capillary porosity within the concrete i.e. the percolated porosity;
- (b) concretes containing SCMs have an increased impedance in comparison to the equivalent PC mix. Although concretes containing GGBS and FA may not necessarily be of lower total porosity than the PC concretes, it is of a much more disconnected and tortuous nature (Li and Roy, 1986; Lu et al., 2006). This feature is reflected in the increased impedance of these mixes;
- (c) the frequency at which the $R1$ -CPE1 arc maximizes falls within the range 150kHz-5MHz and is binder-specific, with the maximum frequency increasing in the sequence FA concretes, GGBS concretes, and PC concretes; and

In order to confirm whether circuit elements $R2$ -CPE2 and $R3$ -CPE3 are, indeed, artefacts of the concrete/electrode contacting medium, Figure 4.24 – Figure 4.26 present the Nyquist and Bode plots for the concrete mixes ($w/b = 0.65$ only) with the contacting sponges saturated with tap water, calcium hydroxide and simulated pore solution. These Figures clearly highlight the influence of the saturating liquid on the impedance response. As previously noted, for sponges saturated with the simulated pore solution, this manifests itself as a small, flat arc at the low-frequency side of the Nyquist plot, but as the impedance of the sponges increases (see Figure 4.18), it can be seen that this flat arc develops into a well-defined, low-frequency circular arc.

The Bode plots show more clearly the influence of the sponge-saturating liquid on the measured impedance, $|Z^*(\omega)|$, and phase angle, θ , as both the impedance curves, and phase-angle curves, tend to merge in the frequency range 5-10kHz. At frequencies in excess of approximately 5kHz, the circuit model for the system would then be represented by R_1 -CPE1 and R_s in Figure 4.22. It is also evident that as the impedance of the concrete specimen increases, the influence of the sponge-saturating liquid diminishes.

This clearly has implications in the development of standard testing procedures for concrete resistivity measurements, particularly using AC in the low-frequency range 50-100 Hz. For example, consider the PC ($w/b=0.65$) concrete in Figure 4.24; using water-saturated sponges, the measured resistance (real component), R , at 100 Hz is 804Ω , whereas at 10kHz the resistance is 593Ω . The resistance of the sponges measured separately, denoted R_{sp} , is 9.4Ω at 100Hz and 8.1Ω at 10kHz. Using the method presented by Newlands et al. (2008), these values could then be used to evaluate the bulk resistivity of the concrete cube (ρ_{cube}) using the two-point method presented in Figure 4.16(a) as,

$$\rho_{cube} = \frac{A}{L}(R - R_{sp}) \quad (4.10)$$

where A is the cross-sectional area through which the current flows ($0.15 \times 0.15\text{m}^2$) and L is the spacing between the electrode plates (0.15 m). This obtains a resistivity of $119 \Omega \text{m}$ at 100Hz and $88 \Omega \text{m}$ at 10kHz. With reference to Table 4.8, this would move the concrete from one durability classification into another based solely on the test frequency and sponge-saturating liquid. Both these parameters need to be standardized to provide a consistent measurement procedure/protocol. This leaves the question: how is the true bulk resistance (hence resistivity/conductivity) of the specimen obtained using a two-point (end-to-end) measurement technique. This is further developed below.

The model presented in Figure 4.22 would suggest that the bulk resistance of the concrete can be obtained at the intercept of the low-frequency end of arc R_1 -CPE1 with the real axis (i.e., the value $R_s + R_1$). In the two-electrode technique, the potential drop is measured between the external plate electrodes and includes the spurious effects the sponges have on the measured impedance. By separating the current electrodes and potential electrodes as presented in Figure 4.17(a), such effects are, theoretically,

eliminated. Ideally, in the four-electrode method the potential electrodes should be moved out of the current field to ensure that no current is drawn to the sensing electrodes (Schwan and Ferris, 1968; Paul Ben et al., 2013). It was decided, however, to use embedded voltage-sensing pin-electrodes as the FRA's input impedance of $1.0\text{M}\Omega$ over the frequency range 1Hz-10kHz, then decreasing to $45\text{k}\Omega$ at 10MHz (Hsieh et al., 1997) is considerably larger than the impedance being measured, which will ensure that negligible current is drawn through the sensing electrodes. By way of illustration, using the testing arrangement in Figure 4.17(a), Figure 4.27(a) presents the Bode plots for the PC concrete ($w/b=0.65$) and Figure 4.27(b) that for the GGBS concrete ($w/b=0.35$) with simulated pore solution used to saturate the contact sponges. With the electrode/sponge effect absent, the elements $R2$ -CPE2 and $R3$ -CPE3 (Figure 4.22) are, effectively, removed and the impedance and phase angle remain virtually constant over the frequency range 1Hz-10kHz. As the phase angle is $\sim 0^\circ$, this implies that the concrete is displaying purely resistive behaviour and $Z^*(\omega) \approx Z'(\omega)$.

Consider now the resistance of the concrete specimens at 1kHz (which lies near the logarithmic centre of this frequency range); from Figure 4.27, this obtains values of 272Ω for the PC mix and 2219Ω for the GGBS mix. As the current flow-lines through the sample are parallel, the resistivity of the concrete, ρ_{conc} , (in $\Omega \cdot \text{m}$), can be evaluated,

$$\rho_{cube} = \frac{A}{d} R \quad (4.11)$$

where R is the measured resistance (real component) for this testing configuration, d is the spacing of the embedded potential electrodes (0.075 m) and A is the cross-sectional area through which the current flows ($0.15 \times 0.15 \text{ m}^2$). This gives a resistivity for the concretes of $81.6\Omega \cdot \text{m}$ for the PC mix and $666\Omega \cdot \text{m}$ for the GGBS mix. These values can now be used to compute the bulk resistance of the concrete cube (R_{cube}) using the two-point method,

$$R_{cube} = \frac{L}{A} \rho_{conc} \quad (4.12)$$

where A is defined above and L is the spacing between the electrode plates (0.15 m); hence $R_{cube} = 544\Omega$ for the PC mix and 4440Ω for the GGBS. These represent the real component of the impedance, $Z'(\omega)$, which are now located on the Nyquist plots

presented in Figure 4.19 (a) and Figure 4.20 (a) and indicated by an arrow on the real axis. This procedure was repeated for all the concrete mixes in Table 4.4 and indicated accordingly on the Nyquist plot associated with each mix in Figures 4.19 – 4.21. It is apparent that the true resistance of the cube can generally be located at the cusp point between the sponge/specimen interface arc ($R2-CPE2$) and the bulk concrete arc ($R1-CPE1$) on Figure 4.22.

In terms of standardizing testing procedures using a single frequency, end-to-end (two-point) resistance measurement, the work detailed above would indicate that the test frequency should lie in the range 5-10 kHz together with a highly conductive sponge-saturating liquid.

4.2.4 Concrete mixes electrical measurements

In these experiments (Set 2), the two-point end-to-end plates electrode configuration was used. Impedance measurements were obtained from each sample in Table 4.4 by using the Solartron 1260 FRA as noted in section 4.2.3. After removal from the curing tank, the concrete cube was wiped with an absorbent towel and allowed to surface-dry before testing, with testing undertaken in a laboratory at a temperature of $21 \pm 1^\circ\text{C}$. The electrical measurements started at the age of 1day, with a seven days interval between each measurement until the age of 90 days, thereafter, the measurements reduced to every 28days until the age of 360 days.

4.2.5 Durability ranking

In this experiment, the Nordtest NT Build 492 (NTBuild492, 1999) was used to rank the concrete mixes in Table 4.4 according to their resistance for chloride penetration by estimating the non-steady-state migration diffusion coefficient D_{nssm} . For this set of tests, the three $100\text{mm} \times 50\text{mm}$ concrete disks obtained from each mix (discussed above) were vacuum saturated in a CaOH_2 solution for 24hrs before the samples were mounted in the electrical migration test cell. This comprised two compartments in which one compartment contained the anolyte solution (0.3 Molar NaOH), and the other compartment, the catholyte solution (2.0 Molar NaCl) (see Figure 4.28)

The concrete disks were placed in the catholyte compartment in a plastic holder which is surrounded by a plastic sleeve and secured by stainless steel clamps. A 30V potential difference was applied by a set of electrodes. The duration of the test is determined by

estimating the initial current which is produced due to the application of the initial voltage, the duration could be altered accordingly by adjusting the voltage, hence the current. At the end of the migration test, the final applied voltage and the temperature were recorded and the samples were removed from the apparatus and washed with tap water before being split in two. The freshly split surface was sprayed with a 0.1 Molar silver nitrate solution to identify the penetration front of the chloride solution.

The average depth of the penetration front was used to estimate the non-steady state diffusion coefficient by the use of the following equation:

$$D_{nssm} = \left(\frac{0.0239(273 + T)L}{(U - 2)t} \right) \left(x_d - 0.0238 \sqrt{\frac{(273 + T)Lx_d}{U - 2}} \right) \quad (4.13)$$

Where: D_{nssm} : Non-steady state migration coefficient, $\times 10^{-12} m^2/s$. U: Absolute value of the applied voltage (V). T: average value of the initial and final temperatures in the anolyte solution ($^{\circ}C$). L: thickness of the sample (mm). x_d : average value of the penetration depth (mm). t: test duration (in hours).

4.3 Summary

In this chapter, a detailed description for the experimental program is presented. The experimental program is divided to two main experiments, the early hydration stage experiment, and the hardening stage hydration experiment.

Through the early hydration experiment, the electrical response over the frequency range 1Hz-10MHz has been used to characterize the material during the initial 24hrs. Parallel tests such as temperature rise, heat output and environmental scanning electron microscopy were used to support the findings of the electrical measurements. For the early hydration experiments, both cement-pastes with different w/b ratios and different GGBS/fly-ash replacements were used. Concrete mixes with different GGBS and fly-ash were also used however at one w/b ratio (0.45).

The accuracy which the AC conductivity of the material could impose on the conductivity response has been highlighted. Detailed experiments were conducted during the early hydration period to obtain a fixed measuring frequency which could be used to extract an accurate DC conductivity value. It was shown that the measuring frequency zone at which

$\pm 5\%$ accuracy of the bulk conductivity could be attained, decreases through time. This frequency zone has also been shown to be affected by the w/b ratio as well as the replacement percentage in the mixes.

With regard to the hardening stage experiment, the 2-point, end-to-end electrode configuration has been studied by impedance spectroscopy. The interface region between the concrete and the contact media has been shown to have a significant electrical impedance imposed on the material response. This effect should be considered if the electrical response is utilised as a durability ranking index. The NTbuild492 test has been used as a standard durability test for concretes with different w/b and SCMs additions at the age of 400 days. The results were assessed and compared with the electrical measurement durability ranking.

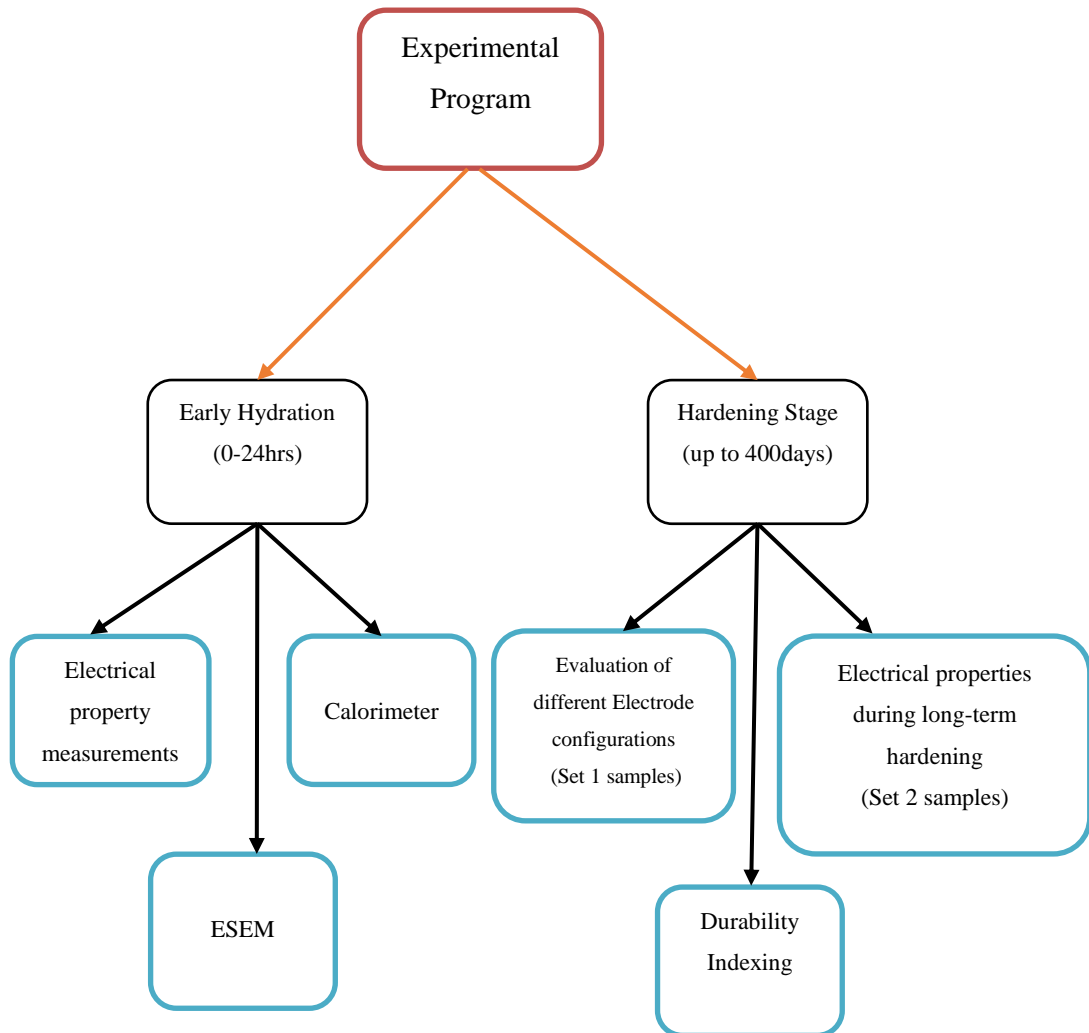


Figure 4.1: Diagrammatic representation of the experimental programme.

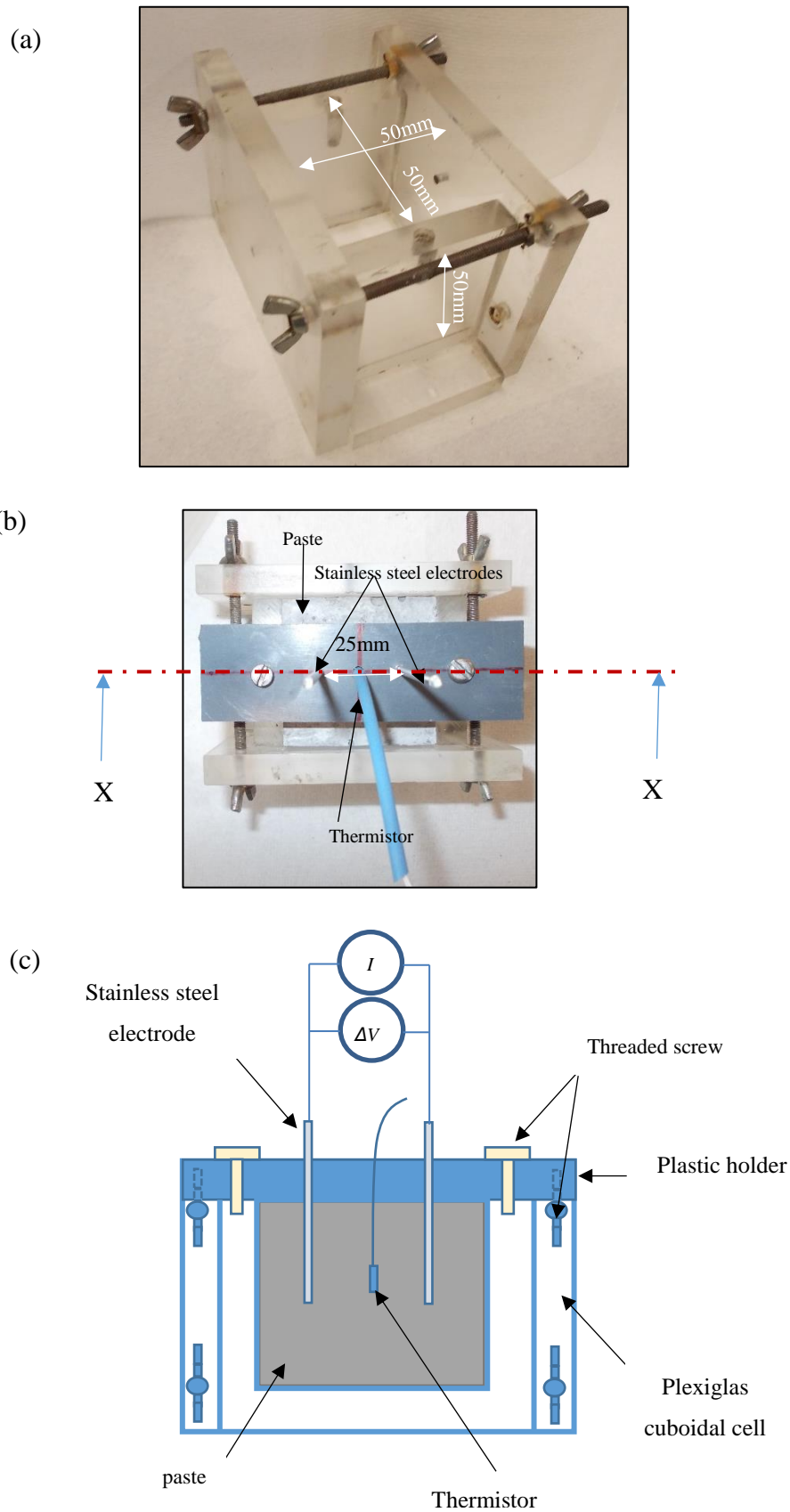


Figure 4.2: (a) Plexiglass cuboidal cell, (b) early hydration cell with sample and electrodes, and (c) X-X' cross-section showing positioning of electrodes and thermistor.

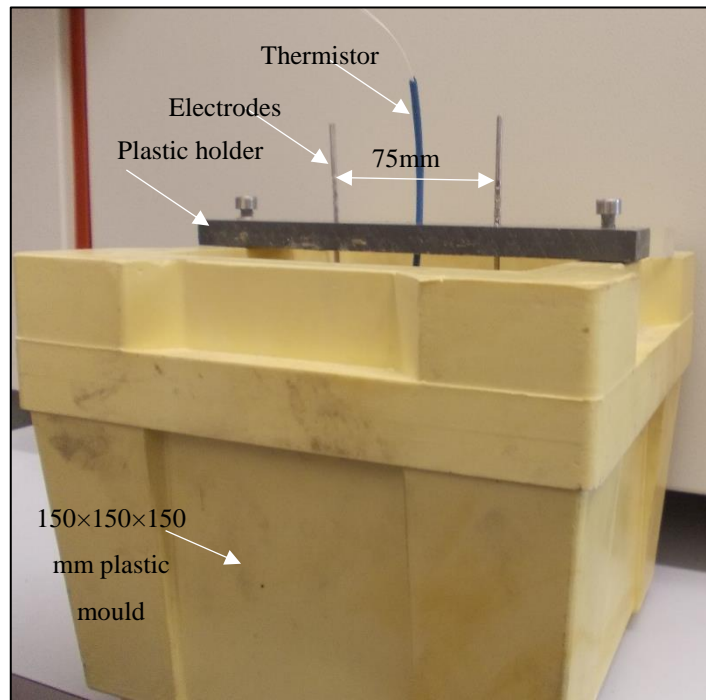


Figure 4.3: Early hydration cell for concrete.



Figure 4.4: Calorimeter can for paste sample.

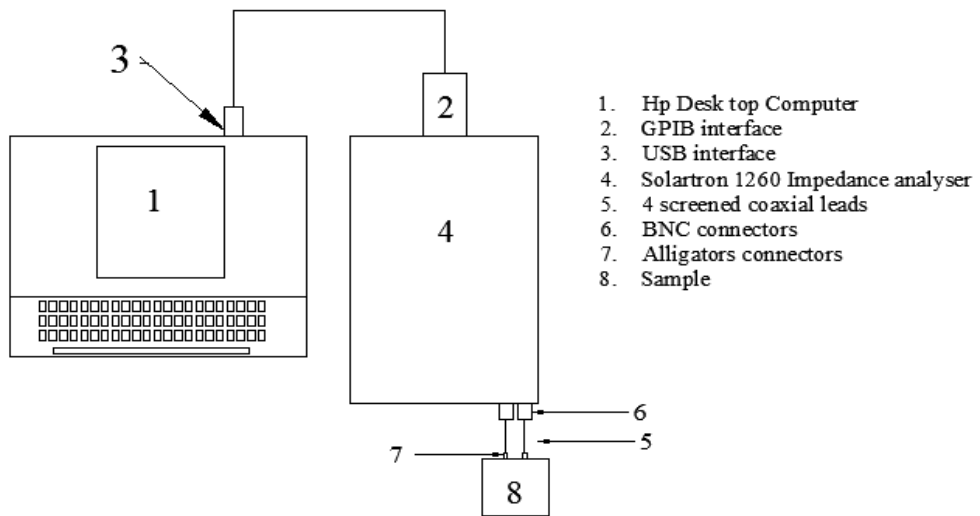


Figure 4.5: Schematic diagram of the connection between the PC, impedance analyser and the sample.

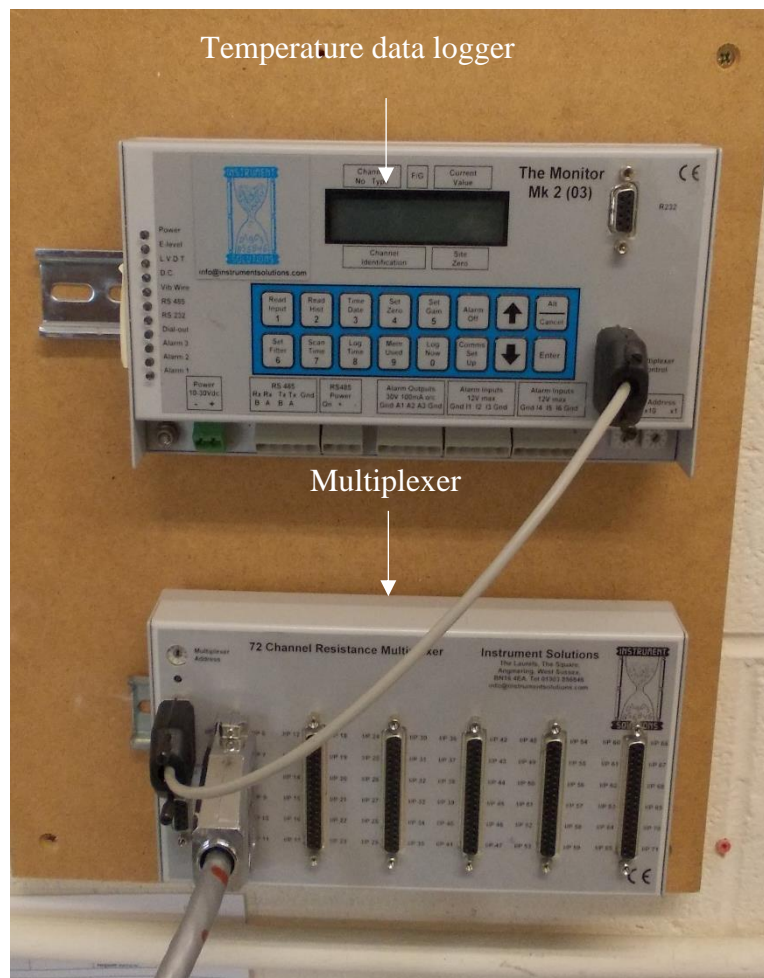


Figure 4.6: Temperature logger and multiplexer.

(a)



(b)

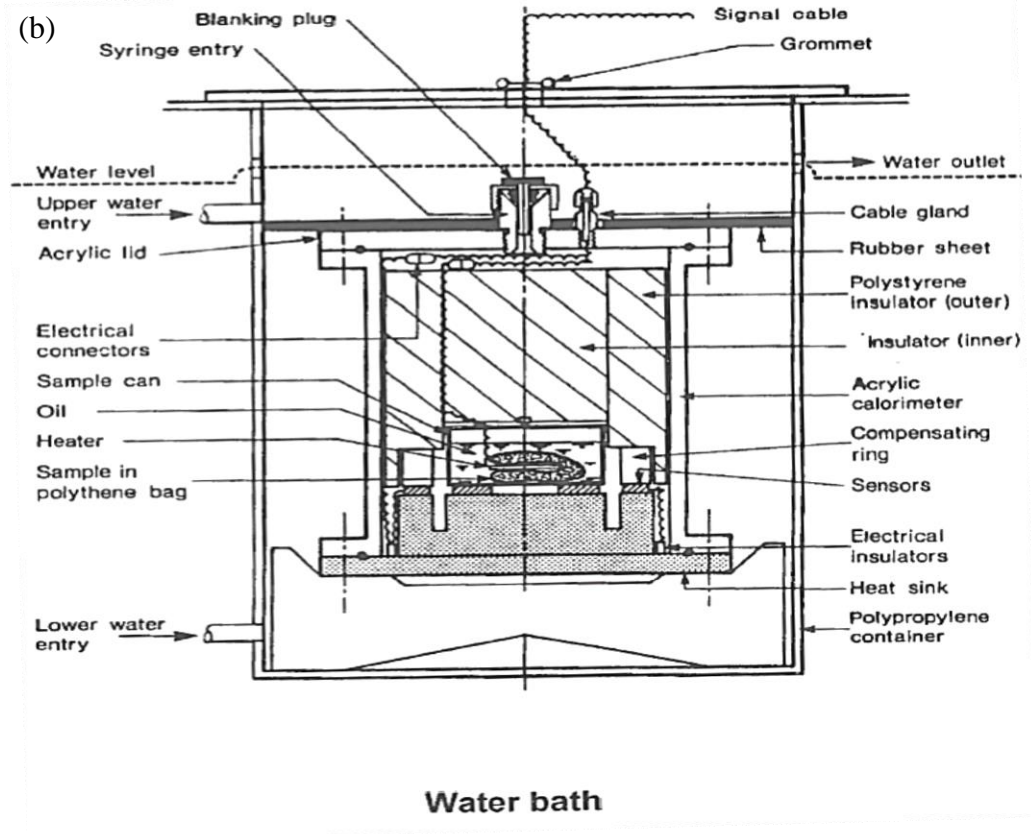


Figure 4.7: Calorimeter parts (a) acrylic calorimeter, and (b) cross-section for the polypropylene container with the sample and the calorimeter inside.

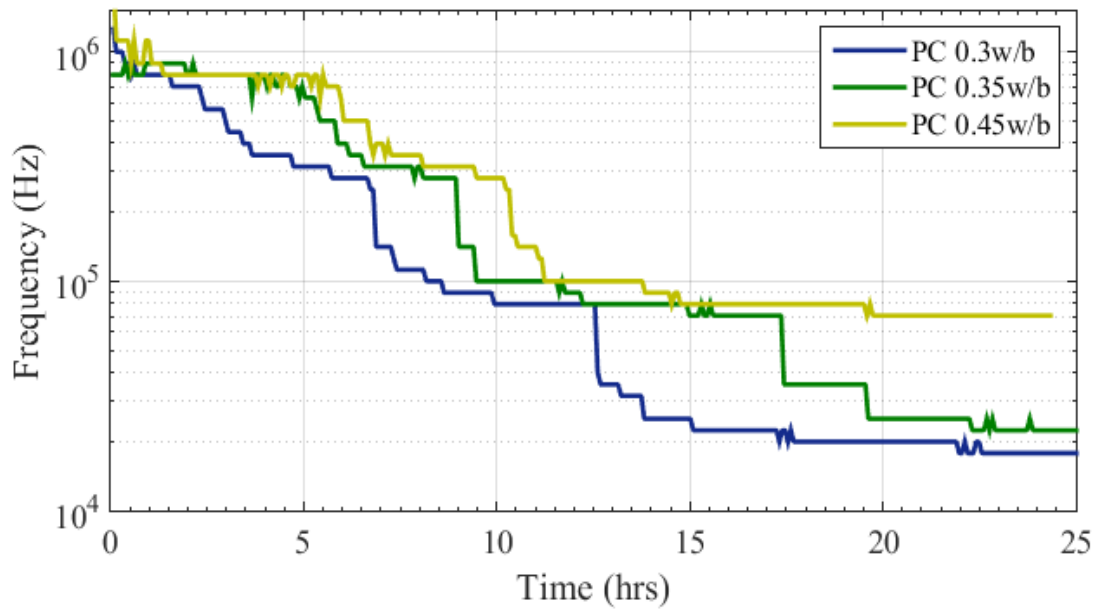


Figure 4.8: Variation in frequency at which bulk conductance can be obtained over the initial 24-hours for PC pastes: 0.30w/b, 0.35w/b and 0.45w/b.

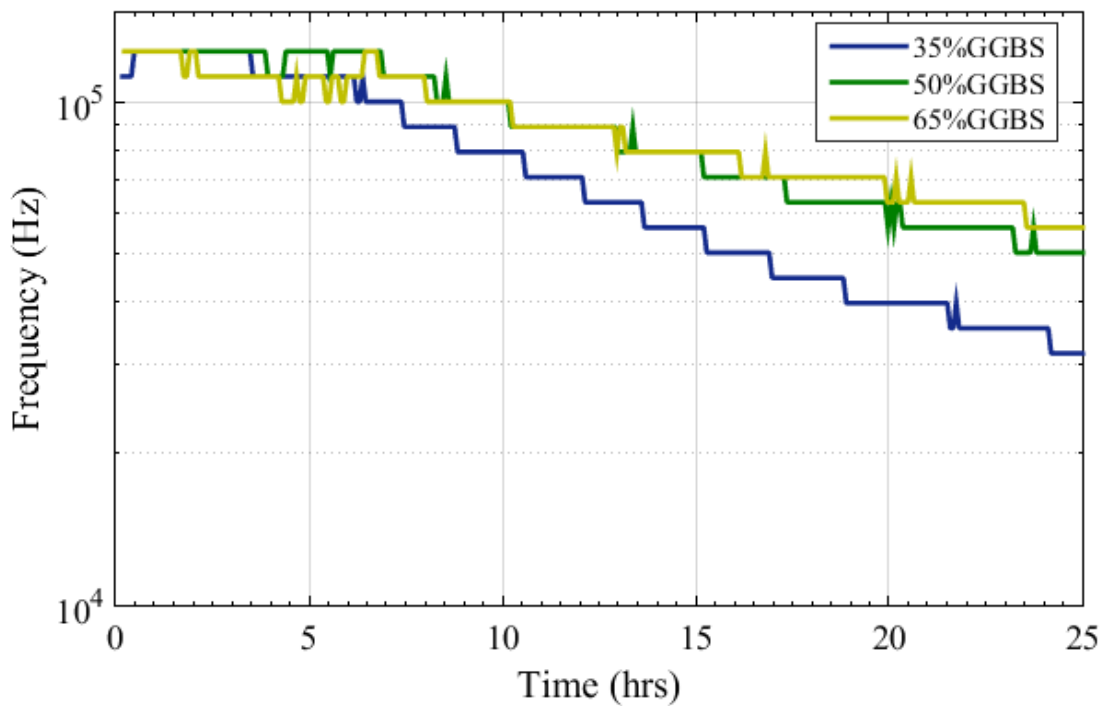


Figure 4.9: Variation in frequency at which bulk conductance can be obtained over the initial 24-hours for GGBS pastes: 35%, 50% and 65% (0.35w/b).

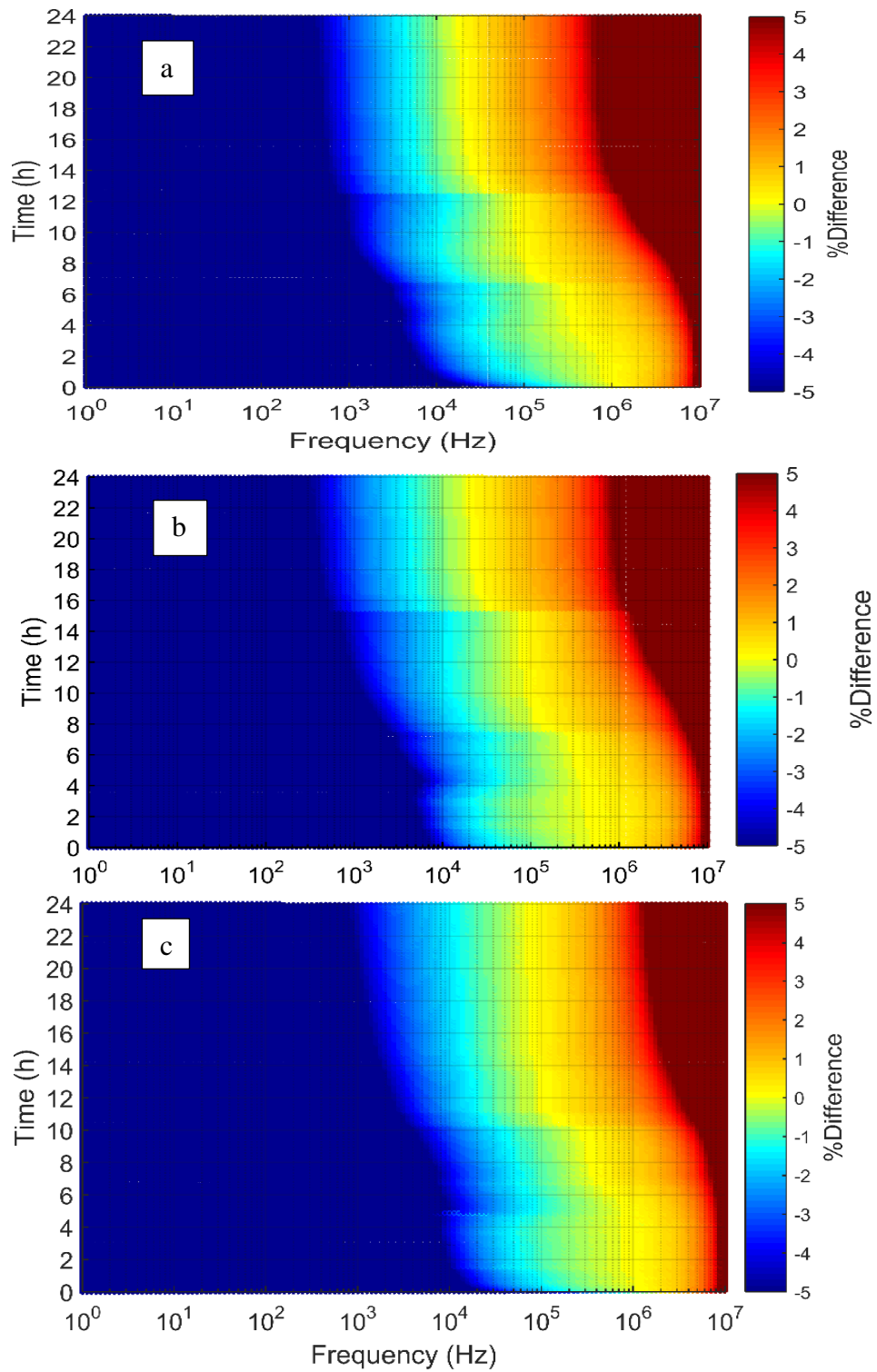


Figure 4.10: Variation (%) from the DC conductance of the samples as a function of time and frequency for, (a) PC 0.3w/b, (b) PC 0.35w/b and (c) PC 0.45w/b.

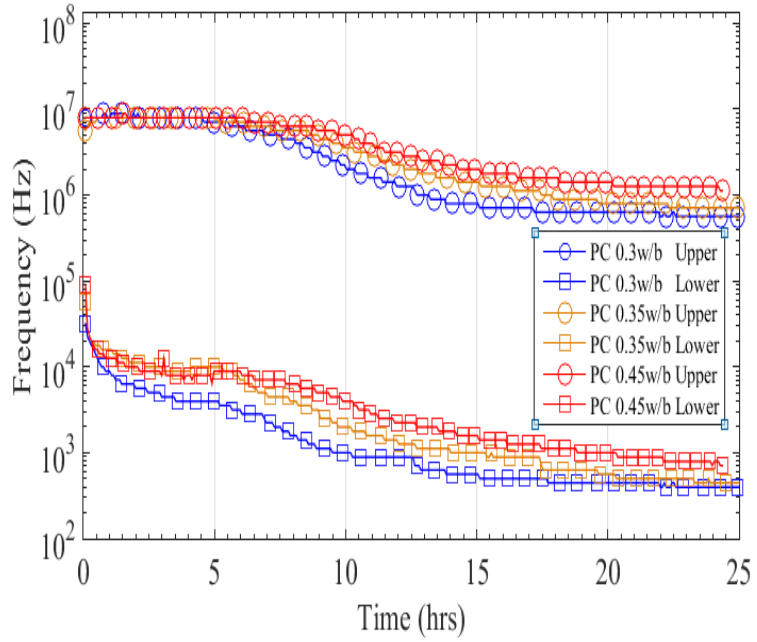


Figure 4.11: +5% upper frequency limit window conductance difference through frequencies and time, and -5% lower frequency limit window electrical conductance difference through frequency and time for the 0.3 w/b, 0.35w/b and 0.45w/b cement pastes.

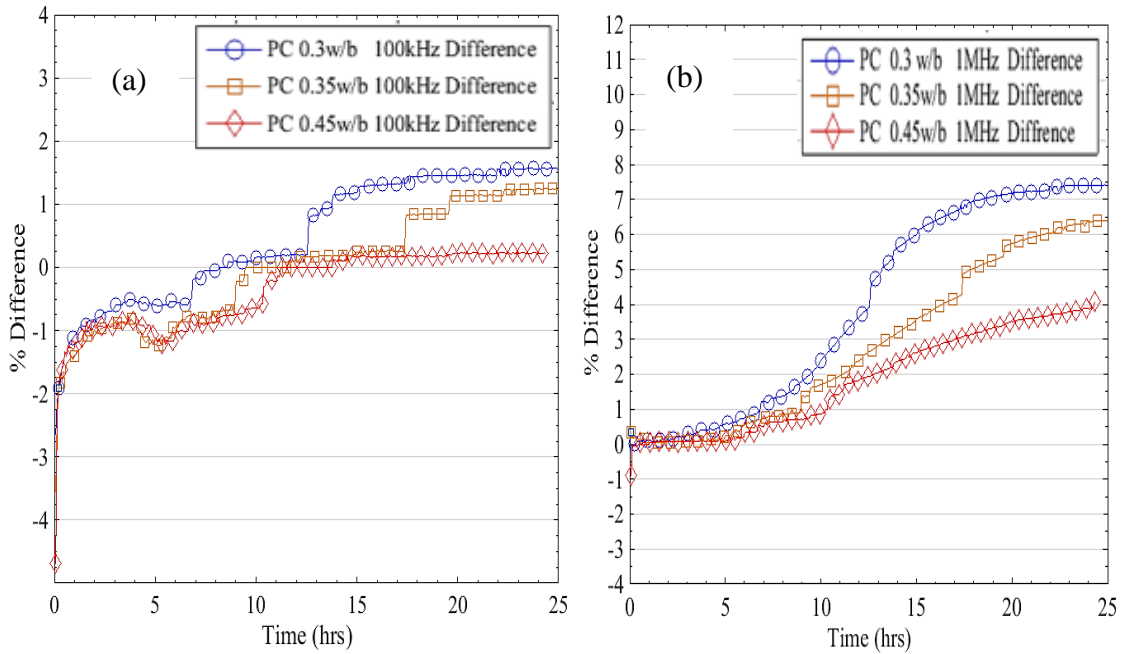


Figure 4.12: Percentage difference in the electrical conductance from the DC conductance through time recorded at the frequencies (a) 100kHz and (b) 1MHz for the 0.3, 0.35, 0.45w/b cement pastes.

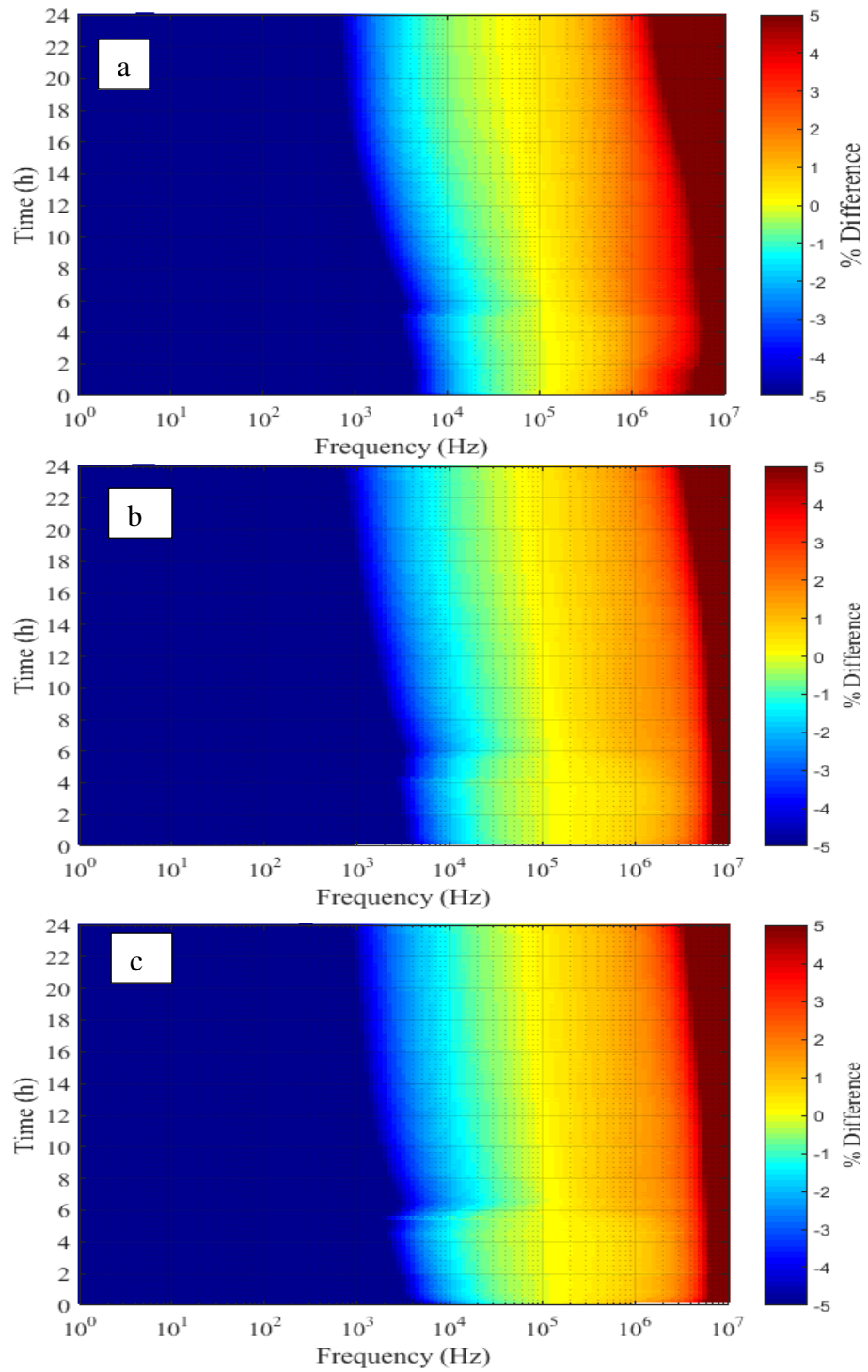


Figure 4.13: The variation (%) from the DC conductance of the samples as a function of time and frequency for (a) 35% GGBS 0.35w/b (b) 50% GGBS 0.35w/b, and (c) 65% GGBS 0.35w/b.

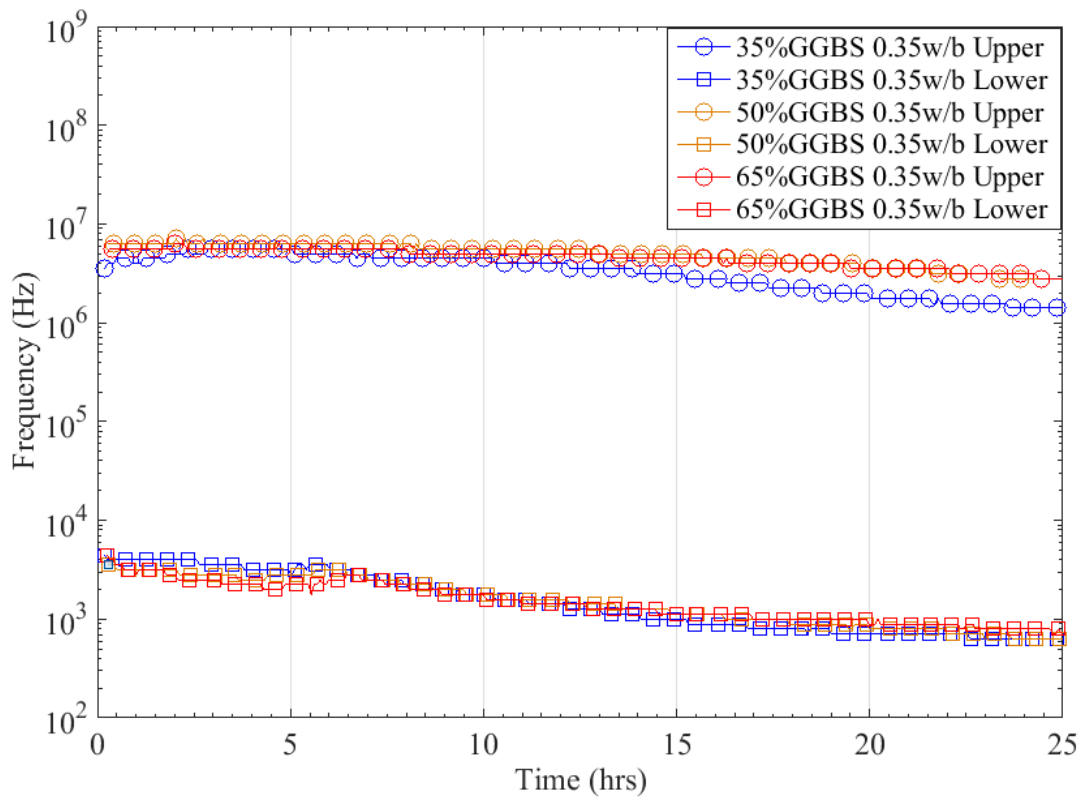


Figure 4.14: +5% upper frequency limit window conductance difference through frequencies and time and (-5% Lower) electrical conductance difference through frequency and time for the 0.35w/b 35%, 50% and 65% GGBS replaced cement pastes.

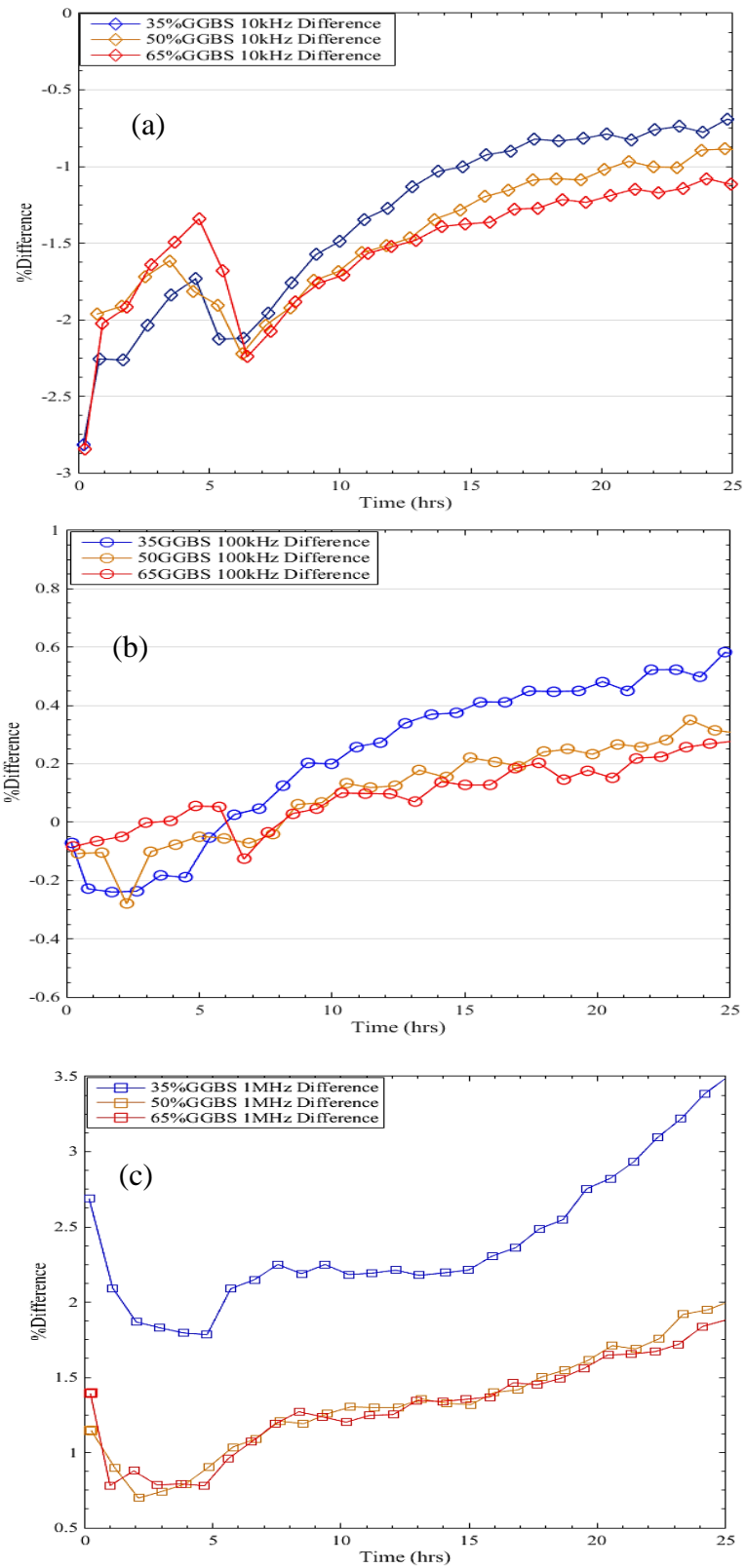


Figure 4.15: Percentage difference of the electrical conductance from the DC conductance through time recorded at the frequencies (a) 10kHz (b) 100kHz (c) 1MHz for the 35%GGBS, 50%GGBS and 65%GGBS (0.35w/b).

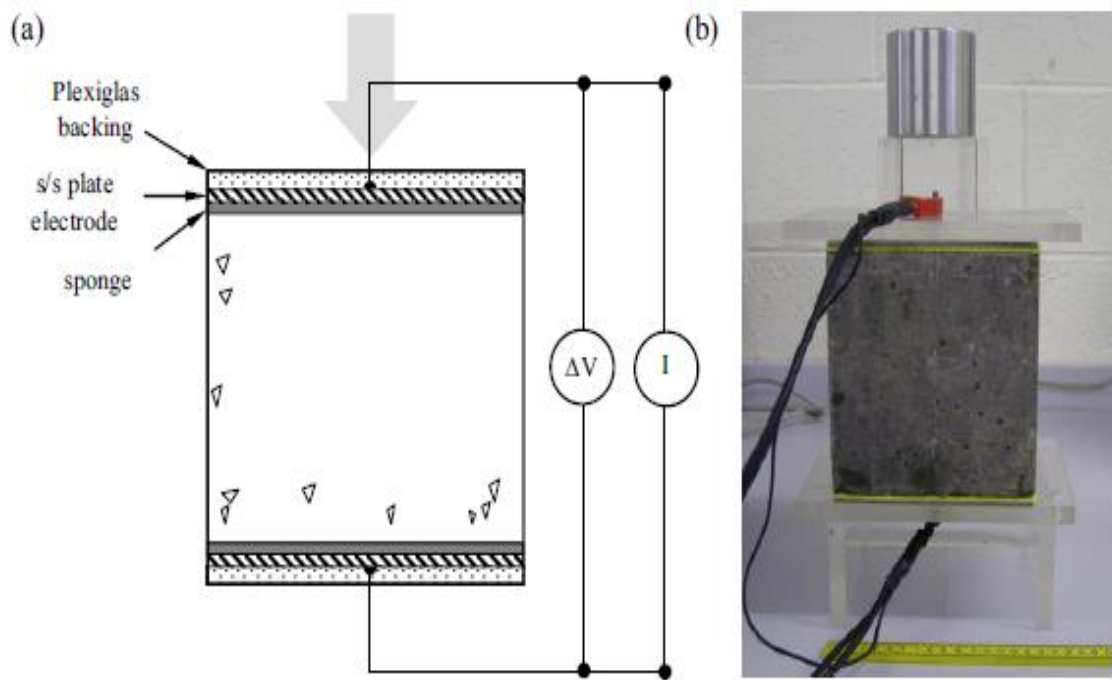


Figure 4.16: (a) Schematic of testing arrangement for two-point AC end-to-end measurements and (b) laboratory setup.

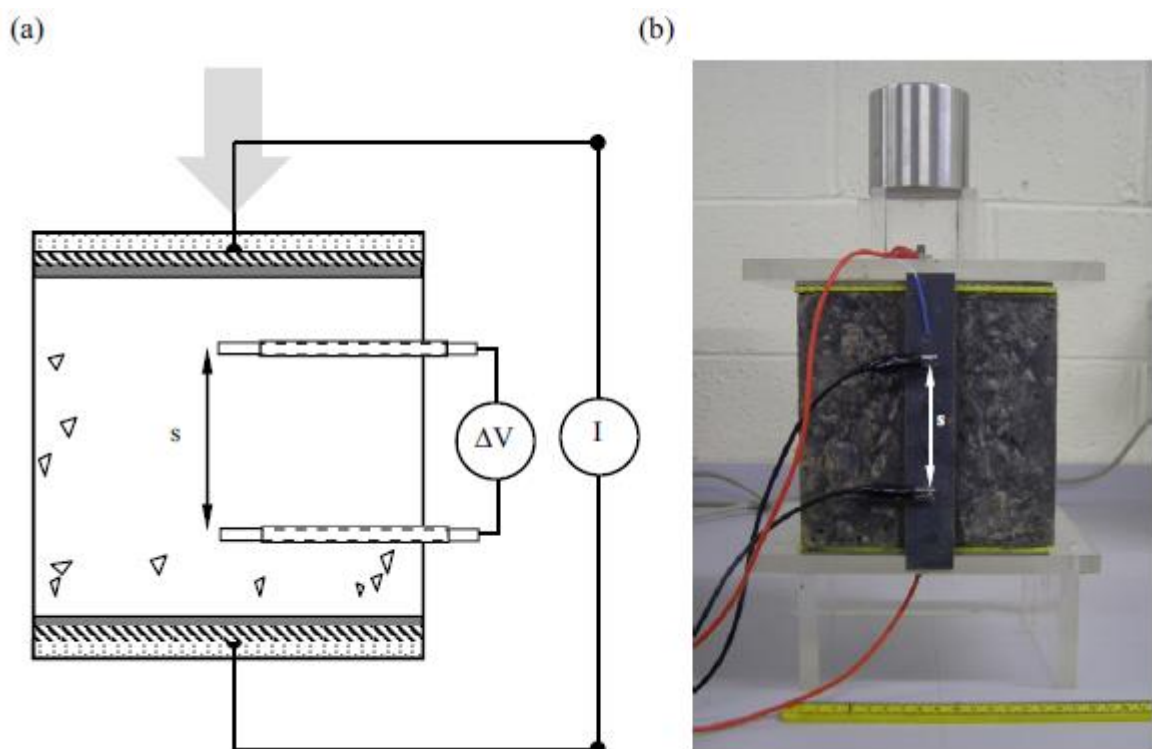


Figure 4.17: (a) Schematic of testing arrangement for four-point measurements and (b) laboratory setup.

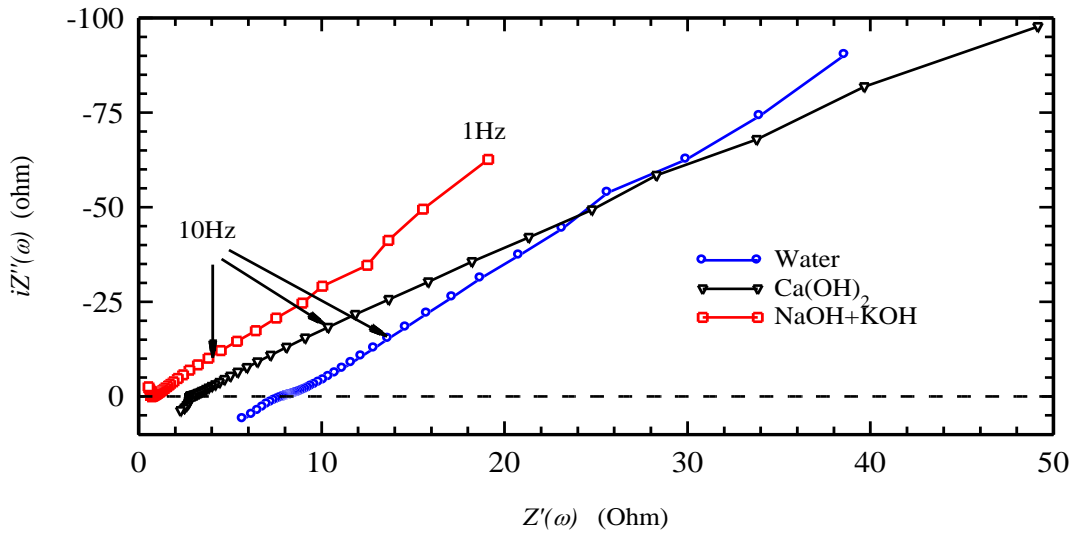


Figure 4.18: Nyquist plot for synthetic sponges placed between the electrodes with saturating liquids indicated.

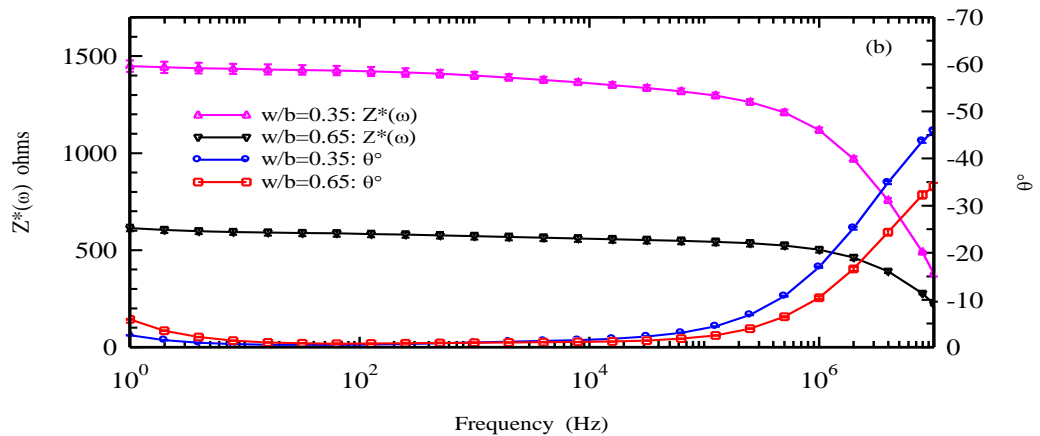
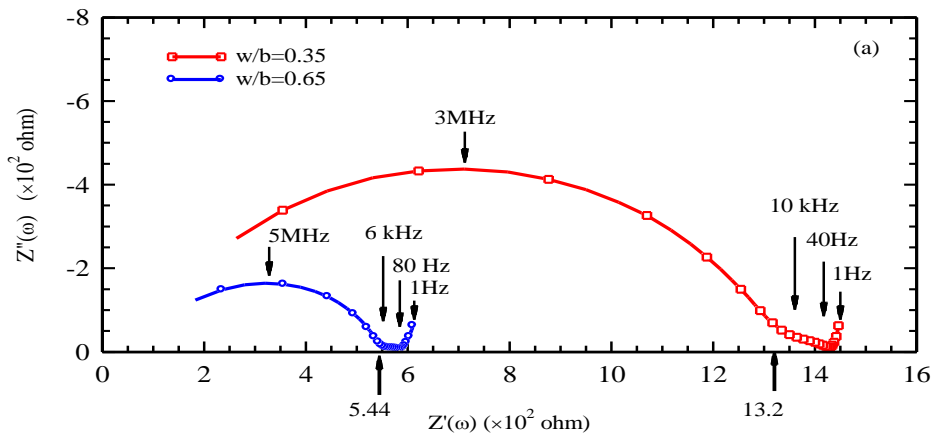


Figure 4.19: (a) Nyquist, and (b) Bode plots for PC concrete mixes (error bars are presented on Bode plot and represent \pm one standard deviation). (Note: where error bars to be missing the data marker is larger than the error bar).

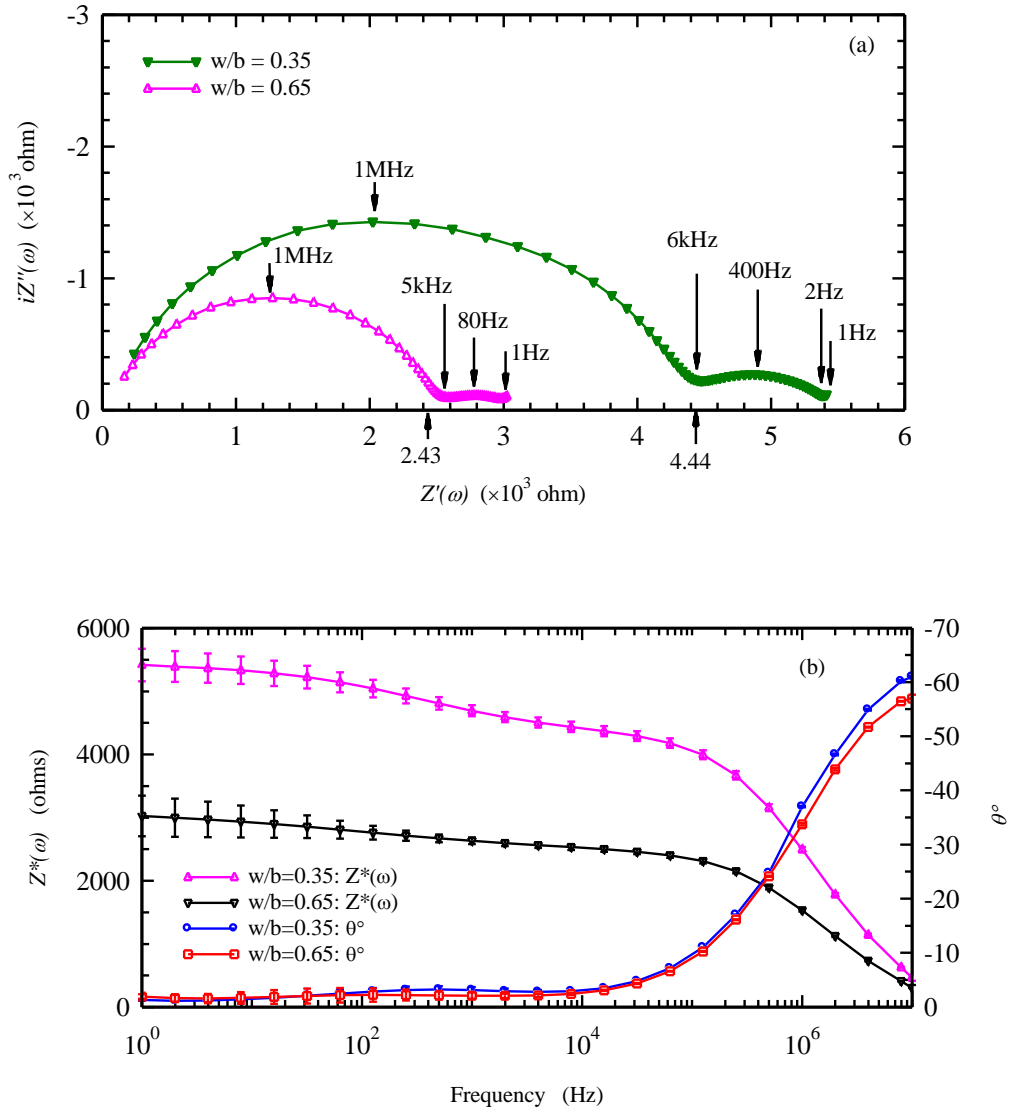


Figure 4.20: (a) Nyquist and (b) Bode plots for GGBS concrete mixes (error bars are presented on Bode plot and represent \pm one standard deviation).

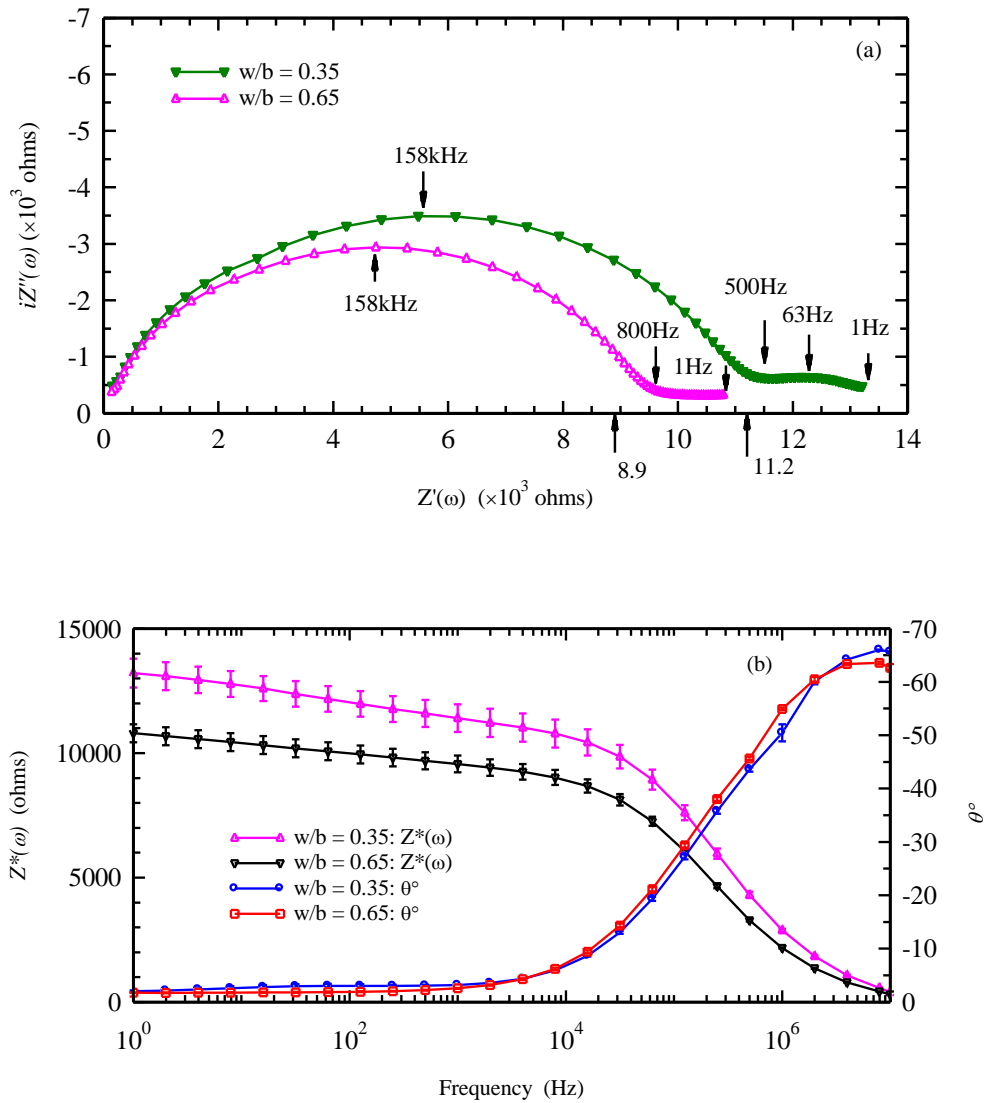


Figure 4.21: (a) Nyquist, and (b) Bode plots for FA concrete mixes (error bars are presented on Bode plot and represent \pm one standard deviation).

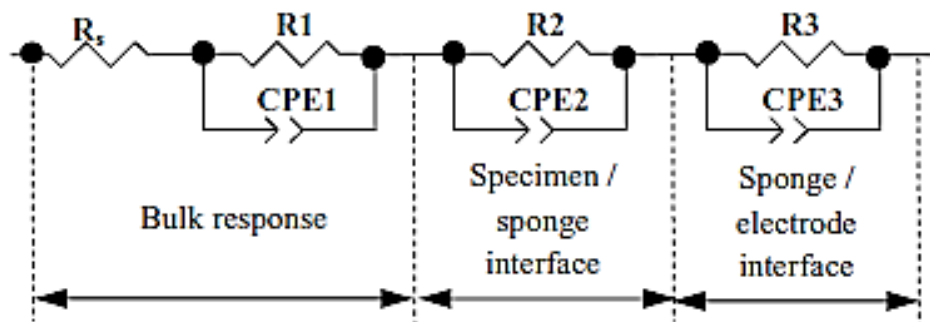


Figure 4.22: Proposed circuit model for electrode-sponge-specimen testing configuration.

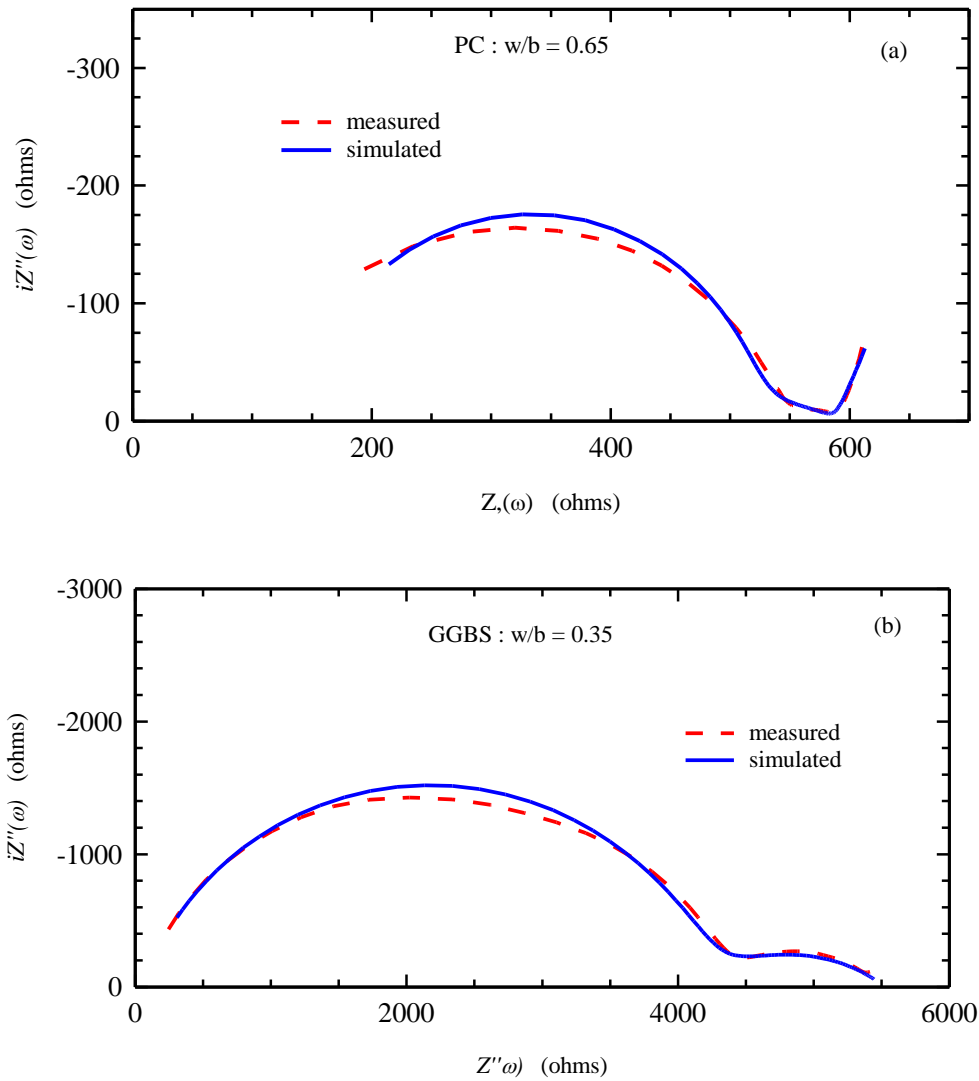


Figure 4.23: Measured and simulated responses for (a) PC concrete ($w/b = 0.65$) and (b) GGBS concrete ($w/b = 0.35$). The simulated response is based on the model presented in Figure 4.22, and circuit parameters in Table 4.9

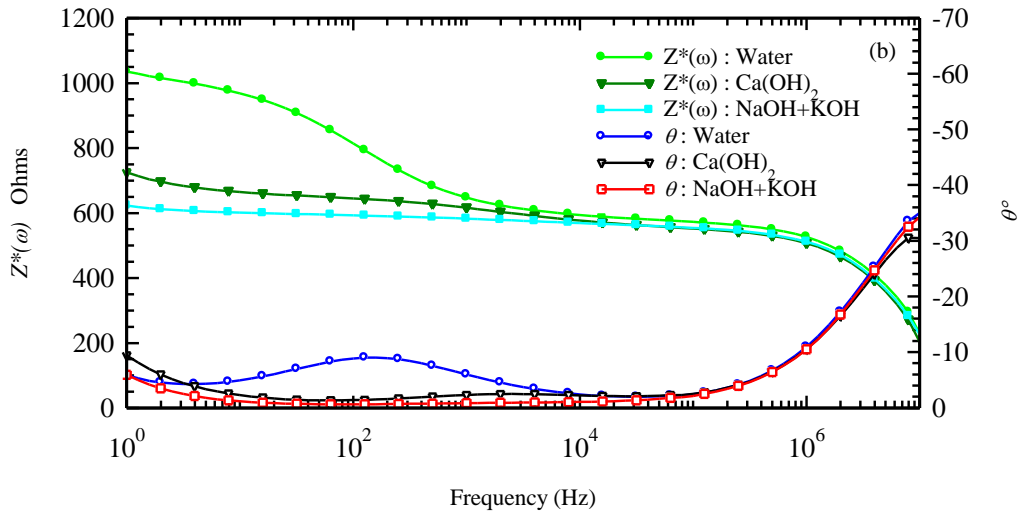
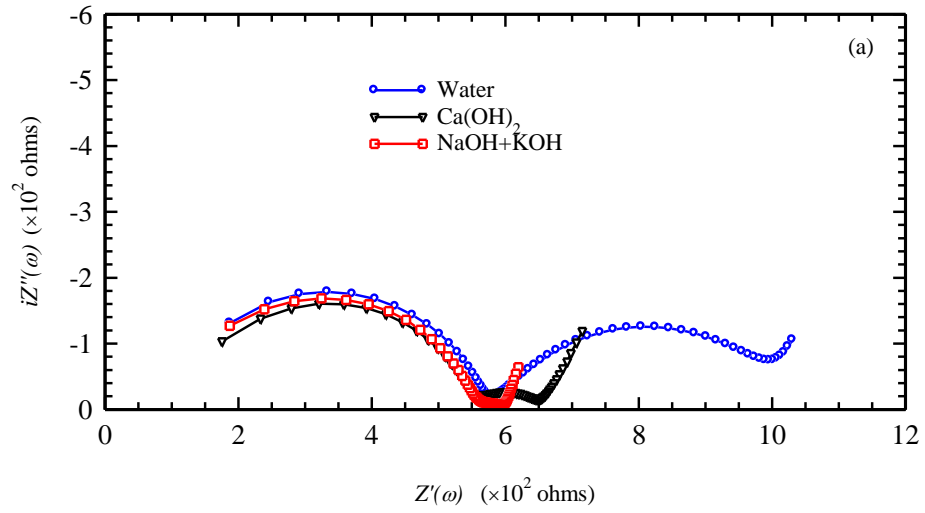


Figure 4.24: Influence of sponge saturation liquid on (a) Nyquist and (b) Bode plots for PC concrete ($w/b = 0.65$).

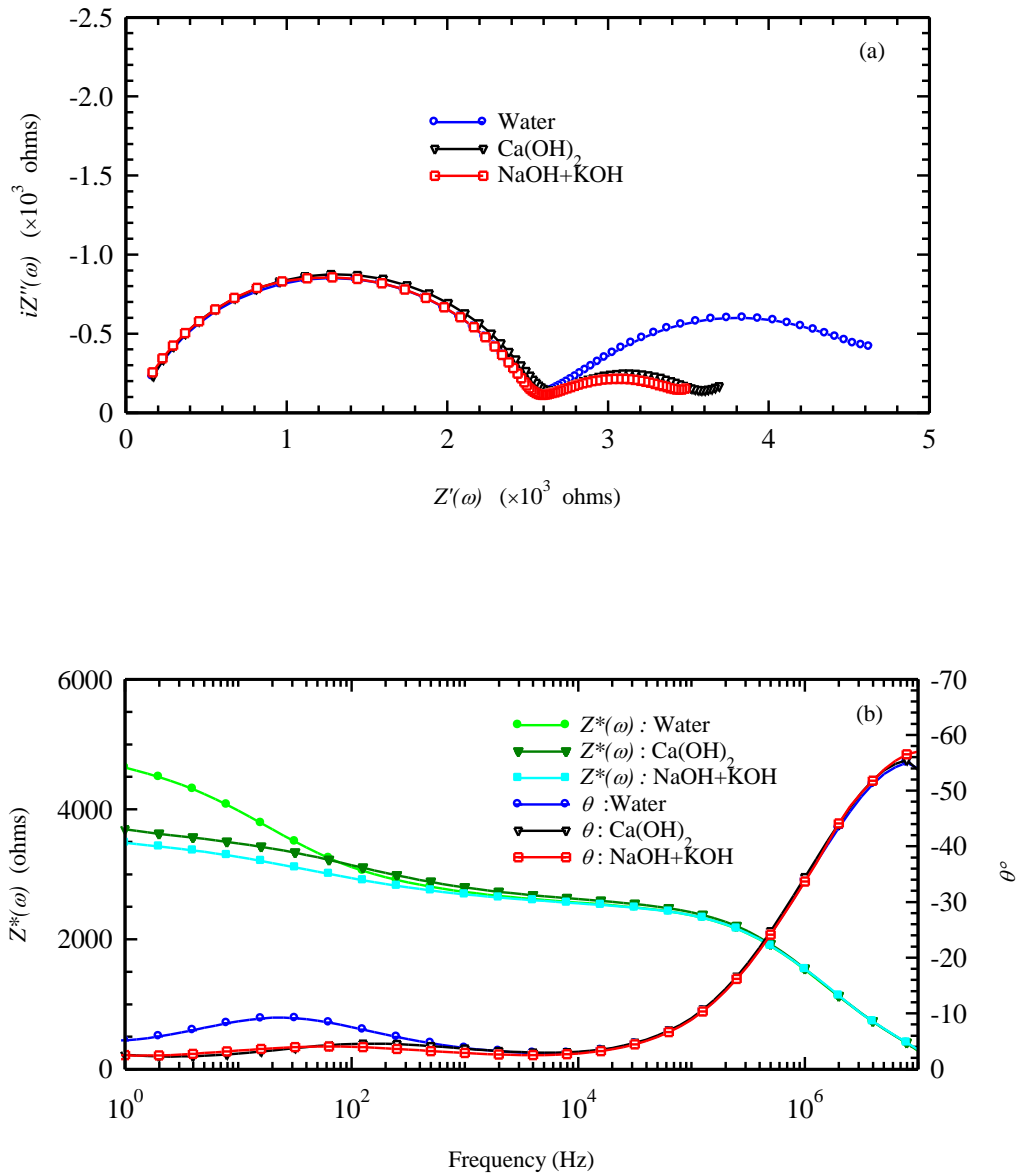


Figure 4.25: Influence of sponge saturation liquid on (a) Nyquist, and (b) Bode plots for GGBS concrete (w/b = 0.65).

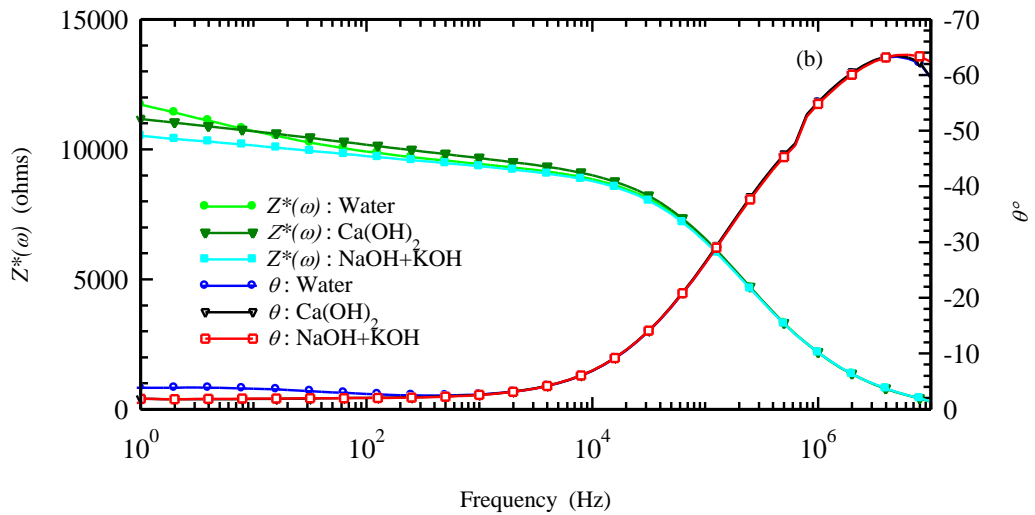
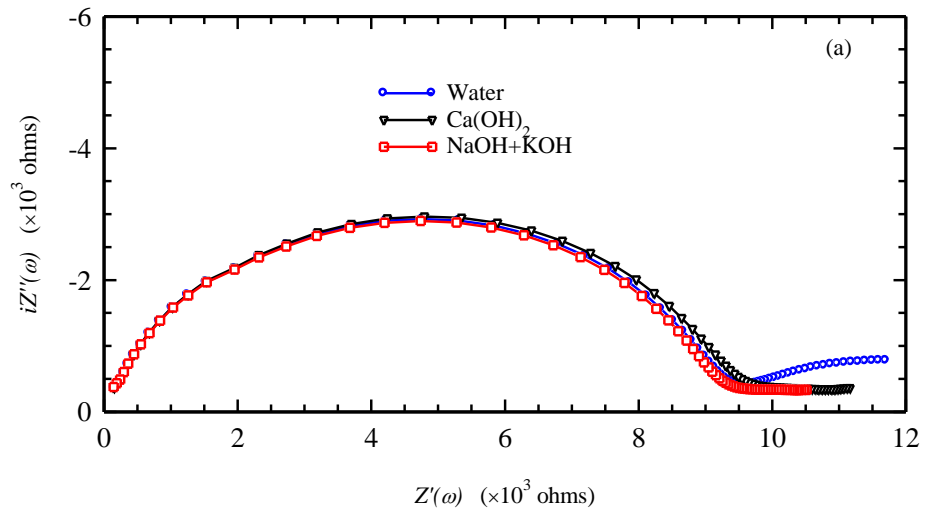


Figure 4.26: Influence of sponge saturation liquid on (a) Nyquist, and (b) Bode plots for FA concrete ($w/b = 0.65$).

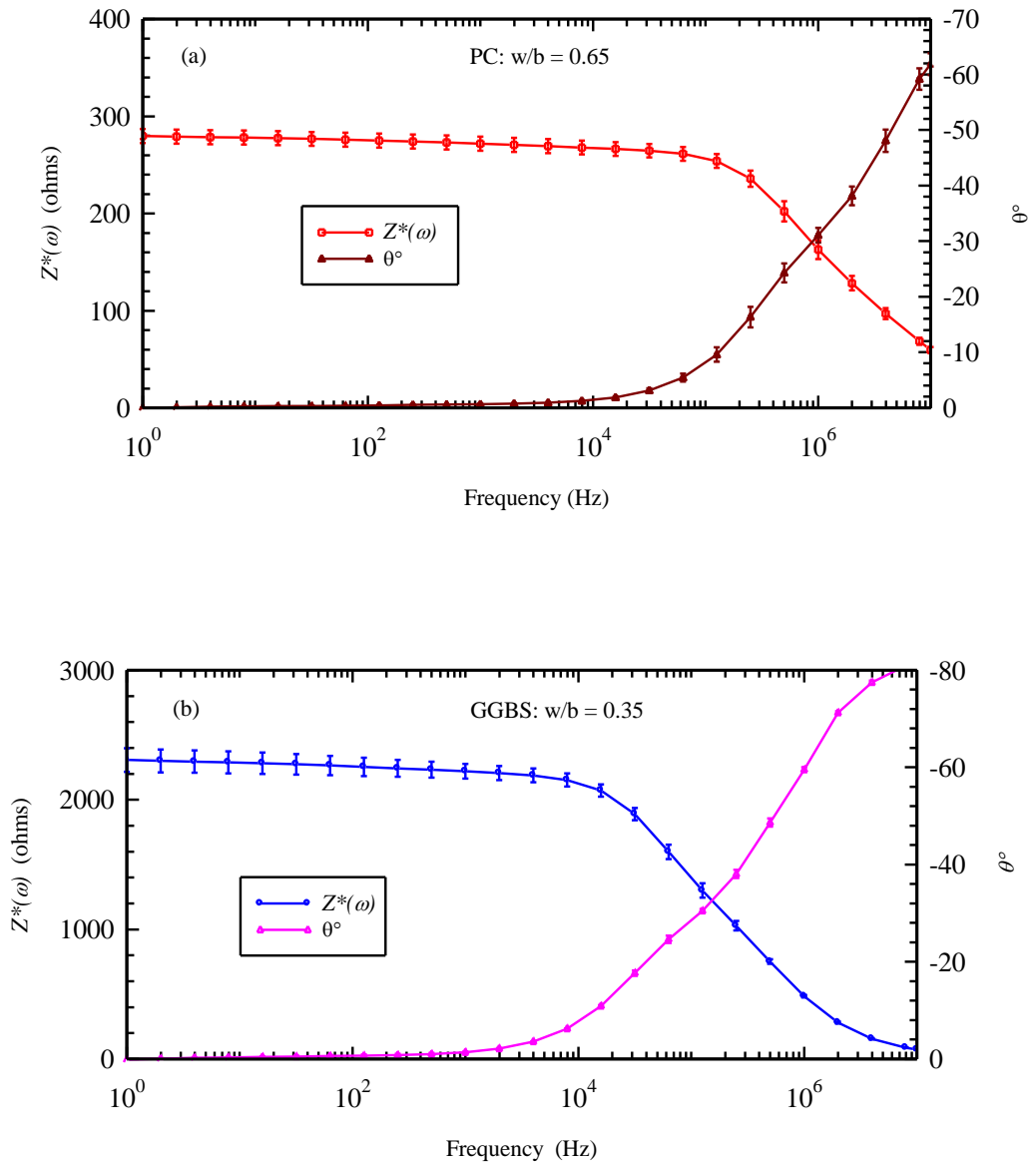


Figure 4.27: Bode plots obtained using the four-point testing arrangement presented in figure 2 for (a) PC concrete ($w/b = 0.65$) and (b) GGBS concrete ($w/b = 0.35$).

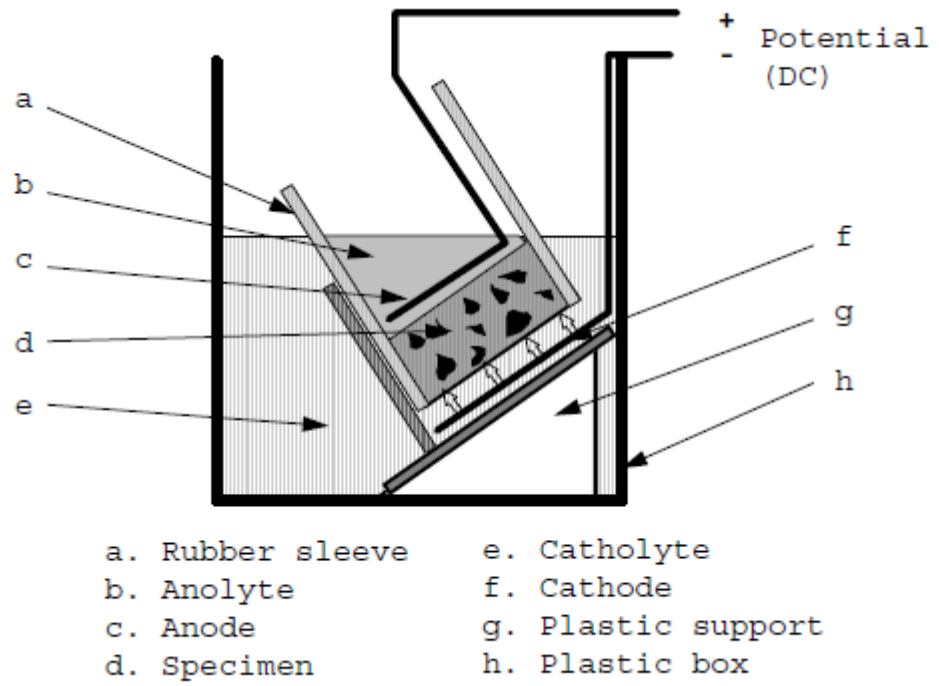


Figure 4.28: Arrangement of the migration set-up

By weight %	CEM I (%)	GGBS(%)	FA(%)
SiO ₂	20.95	33.89	45-51
Al ₂ O ₃	5.2	13.96	27-32
Fe ₂ O ₃	3.42	0.35	7-11
CaO	59.86	38.03	1-5
MgO	2.25	8.77	1-4
K ₂ O	0.56	0.67	1-5
Na ₂ O	0.21	0.24	0.8-1.7

Table 4.1: XRF for CEM I, GGBS and FA as obtained from suppliers.

Paste Mix	w/b	CEM I %	GGBS %	FA %	CaSO ₄ % addition
PC 0.30w/c	0.30	100	~	~	~
35% GGBS 0.30w/b		65	35	~	~
50% GGBS 0.30w/b		50	50	~	~
65% GGBS 0.30w/b		35	65	~	~
35% PFA 0.30w/b		65	~	35	~
PC 0.35w/c	0.35	100	~	~	~
35% GGBS 0.35w/b		65	35	~	~
50% GGBS 0.35w/b		50	50	~	~
65% GGBS 0.35w/b		35	65	~	~
35% PFA 0.30w/b		65	~	35	~
PC0.35w/c+0.5% CaSO ₄		100	~	~	0.5
PC0.35w/c+2% CaSO ₄		100	~	~	2
PC 0.45w/c	0.45	100	~	~	~
35% GGBS 0.45w/b		65	35	~	~
50% GGBS 0.45w/b		50	50	~	~
65% GGBS 0.45w/b		35	65	~	~
35% PFA 0.45w/b		65	~	35	~

Table 4.2: Cement pastes mixes used through the early hydration.

Mix	w/b	CEMI kg/m ³	GGBS kg/m ³	FA kg/m ³	20mm kg/m ³	10mm kg/m ³	Fine (<4mm) kg/m ³	Plasticiser (%)
PCC0.45w/b	0.45	339	-	-	781	390	781	~
PCC0.45w/b +1%SP	0.45	339	-	-	781	390	781	1.0
35%GGBS0.45wb	0.45	220	118	-	778	389	778	~
35%GGBS0.45wb +1%SP	0.45	220	118	-	778	389	778	1.0
65%GGBS0.45wb	0.45	118	219	-	776	388	776	~
65%GGBS0.45wb +1%SP	0.45	118	219	-	776	388	776	1.0
35%FA 0.45w/b	0.45	217	-	117	768	384	768	~
35%FA0.45w/b +1%SP	0.45	217	-	117	768	384	768	1.0

Table 4.3: Concrete mixes used for early hydration experiments.

Mix Designation	Batch	w/b	CEMI kg/m ³	GGBS kg/m ³	FA kg/m ³	20mm kg/m ³	10mm kg/m ³	Fine (m) kg/m ³	Plasticiser
CEM I (PC)	C1	0.35	380	-	-	787	395	790	1.43
	C2	0.45	340	-	-	781	390	780	1.0
	C3	0.65	265	-	-	790	395	790	-
CEM II/B- (GGBS/35)	G1	0.35	245	130	-	784	390	785	1.43
	G2	0.45	220	120	-	778	389	780	0.95
	G3	0.65	170	90	-	788	395	790	-
CEM III/A (GGBS/65)	X1	0.35	130	245	-	782	390	780	1.43
	X2	0.45	120	220	-	776	390	775	0.95
	X3	0.65	90	170	-	786	395	785	-
CEM II/B- (FA/35)	P1	0.35	240	-	130	773	385	775	1.43
	P2	0.45	220	-	120	768	385	770	0.95
	P3	0.65	170	-	90	780	390	780	-

Table 4.4: Concrete mixes used for the hardening stage experiments.

Mix	F ₂₈ (MPA)	F ₁₈₀ (MPA)
C1	79	88
C3	39	46
G1	81	89
G3	35	45
P1	65	81
P3	24	38

Table 4.5: Mean compressive strength for Set 1.

Mix	F ₂₈ (MPA)	F ₁₈₀ (MPA)	F ₄₀₀ (MPA)
C1	78	102	103
C2	68	80	83
C3	43	49	53
G1	81	97	99
G2	57	77	79
G3	28	44	46
X1	83	98	105
X2	56	76	81
X3	32	46	51
P1	71	97	105
P2	41	59	70
P3	25	38	47

Table 4.6: Mean compressive strength for Set 2.

Durability class	Chloride Resistivity Index (ohm-m)
Excellent	>13.0
Good	6.5-13.0
Poor	04.0-6.5
Very poor	<4.0

Table 4.7: Suggested ranges for concrete durability classification
(adapted from (Alexander et al., 2010)).

Resistance to corrosion	Resistivity (kohm-cm)
Low	< 5
Moderate / Low	5 - 10
High	10 - 20
Very High	> 20

Table 4.8: Empirical concrete resistivity thresholds for protection of embedded steel reinforcement (adapted from (Langford and Broomfield, 1987; Broomfield, 2006)).

Mix	R_s (Ω)	R (Ω)	$CPE1(C_o)$ (Fs^{p1-1})	P1	R2	$CPE2(C_o)$ (Fs^{p2-1})	P2	$R3(\Omega)$	$CPE3(C_o)$ (Fs^{p3-1})	P3
PC (w/b=0.65)	129	348	1.929×10^{-10}	0.96	114	1.16×10^{-4}	0.31	5×10^5	3.77×10^{-3}	0.77
GGBS (w/b=0.35)	44.9	4418	1.072×10^{-9}	0.80	1333	2.729×10^{-5}	0.43	+	+	+

Table 4.9: Circuit simulation parameters for PC and GGBS concrete mixes.

Chapter 5 – The electrical Properties of Cementitious Materials during Early Hydration

5.1 Introduction

In this chapter, the conductance/conductivity and the capacitance/permittivity through the initial 24hrs hydration are presented. These electrical parameters are used to study the physical, chemical and microstructural changes which take place during this early hydration period. The conductivity of the material is evaluated at one frequency (developed in Chapter 4) which is deemed to be a suitable measuring frequency with an acceptable accuracy in the bulk conductivity. In terms of polarization and conduction processes which take place during this early hydration stage, the 1Hz-10MHz frequency range is investigated through time. This chapter is divided as follows:

Part 1: Results are presented for the conductivity of the CEM I cement-pastes, as well as pastes replaced with SCM's. In parallel, the change in internal temperature was recorded for the samples. Electrical measurements highlight the effect of the measuring frequency as well as the effect of the hydration process.

Part 2: In this section, the results in Part I are discussed in conjunction with isothermal calorimetry and ESEM as well as comparing the observed electrical response with published studies on the early hydration of cementitious materials.

Part 3: The early hydration electrical response is explained using an equivalent electrical circuit (EEC), in which the circuit parameters are explained in terms of the physical and chemical processes occurring during hydration through the liquid phase as well as on the grain surfaces.

Part 4: This section focusses on the electrical response of concrete mixes during the early hydration period, as well as the effect of chemical admixtures on hydration.

5.2 Results

5.2.1 Early hydration electrical conductivity

As was shown in the previous chapter, the 100kHz frequency through time gives a good evaluation of the conductivity which lies within the range of $\pm 5\%$ of the actual DC

conductivity value. Therefore, the temporal change in conductivity at 100kHz was used for both the pure and partially replaced cement-pastes.

Pure cement pastes

Figure 5.1(a) presents the conductivity for the 0.3, 0.35, 0.45 w/b ratio cement-pastes. From this Figure, it is evident that the conductivity can be divided into two distinct regions which are:

- (i) A region of increasing conductivity reaching a maximum after ~2hrs (see Figure 5.1(b)); and,
- (ii) A region of decreasing conductivity, which starts at ~2hrs and continues over the remainder of the 24hr monitoring period.

Figure 5.1(c) presents the derivative of the conductivity ($d\sigma/dt$) and Figure 5.1(d) presents the variation in the internal temperature of the pastes over the initial 24hrs. By considering the derivative (Figure 5.1(c)), the two regions defined above can be further sub-divided into six identifiable stages. With reference to Figure 5.2, these are:

Stage I

This stage starts immediately after mixing with water. The main distinguishable feature in this stage is the high positive $d\sigma/dt$ values. The $d\sigma/dt$ response through this stage displays a rapid decreasing trend through time whilst maintaining its positive value. This rapid decreasing trend in the $d\sigma/dt$ graph for the three different pastes lasts for ~40mins before Stage II. During Stage I the temperature displays a small increase for all mixes, as it rises by ~3°C degrees from its initial value (see Figure 5.1(d)).

Stage II

Stage II is identified by a period of slowly increasing conductivity and reducing $d\sigma/dt$. For the PC 0.3w/b ratio cement-paste, this stage starts at ~54mins; however, for the PC 0.35w/b and 0.45w/b this stage is delayed to ~1hr and ~1.2hrs, respectively. Through this stage the conductivity rises and culminates in a global maximum signifying the end of Stage II. This peak occurs at ~1.6hrs, 1.8hrs and 1.9hrs for the PC 0.3w/b, PC 0.35w/b and PC 0.45w/b, respectively. It is evident that the maximum value of conductivity for the three different cement pastes is dependent upon the w/b ratio (see Figure 5.1(b)) as the peak conductivity value increases by 2% when the w/b increases from 0.30 to 0.45.

Regarding the internal temperature of the pastes during Stage II, this does not show a noticeable change after the initial increase which was observed at the end of Stage I. Indeed, some of the mixes display a slight decrease in their temperature as in the case of the PC 0.3w/b (see Figure 5.1(d)); however, the general trend during Stage II is relatively constant temperature values as displayed in PC 0.35w/b and PC 0.45w/b.

Stage III

This is a short-lived region of rapidly decreasing conductivity occurring over the period ~1.6-2.0 hrs, occurring immediately after the global maximum which occurs at the end of Stage II, and results in a local minimum on the $d\sigma/dt$ curve.

Stage IV

This stage displays a period of gradually decreasing slope ($d\sigma/dt$) which is related to the w/b ratio in the mixes. From Figure 5.1(c) the PC 0.45w/b paste has a decreasing slope through time with less negative values when compared with the 0.3 and 0.35 w/b pastes. The temperature values (Figure 5.1(d)) start to rise during this stage. By comparing the start of the temperature rise with the conductivity, it is evident that for all the cement pastes, the temperature rise takes place approximately at the same time with the sharp drop in the $d\sigma/dt$ curve. Regarding the latter, the $d\sigma/dt$ curve turns negative; for the PC 0.30w/b the decrease takes place at ~1.82hrs and for the PC 0.35w/b and the PC 0.45w/b at ~1.86hrs and 1.88hrs respectively, which are comparable to the beginning of the temperature rise in the mixes (see Figure 5.2 and Figure 5.1(b)). It is also noticeable that as the temperature rises during this stage the conductivity displays a progressive decreasing trend.

Stage V

Stage V starts after the gradual decreasing trend of the $d\sigma/dt$ graph at the end of Stage IV. It is interesting to note that this stage starts with an increasing rate with negative sign. This increasing rate continues until a sudden change in the slope takes place in the $d\sigma/dt$ graphs resulting in a local maximum for the mixes at the ages of ~8.31hrs, 8.40hrs and 8.85hrs for the PC 0.3w/b, PC 0.35w/b (Figure 5.1(c)) and the PC 0.45 w/b (Figure 5.1(c)) respectively, with a clear delaying effect with increasing w/b ratio. After this change in $d\sigma/dt$, the conductivity values continue their gradual decreasing trend with a slow changing rate which is evident by the $d\sigma/dt$ graph which gradually approaches zero.

Regarding the temperature during this period, this continues its increasing trend which started at Stage III until it peaks at ~9.65hrs, 9.85hrs, 10.02hrs for, respectively, the PC 0.3w/b, 0.35w/b and 0.45w/b. The effect of w/b ratio on the temperature is more pronounced when comparing the lowest w/b ratio mix with the highest one as in the case of the PC 0.3w/b, it records a value of 27.6°C which is higher than that recorded for the PC 0.45w/b which is 26.1°C. In terms of the temperature peaks, the PC 0.30w/b peak takes place ~22mins earlier in comparison to the PC 0.45w/b. After this peak, the temperature decreases gradually until the end of Stage V (see Figure 5.1(b)).

Stage VI

The main feature at this stage is the slowly decreasing trend evident on the electrical conductivity graph. which extends to the end of the 24hr monitoring period.

Early hydration conductivity for replaced pastes

By considering Figure 5.3, the general trend of the conductivity, and temperature for the replaced mixes is similar to those for the pure cement-pastes. The conductivity and the $d\sigma/dt$ for the replaced cement- pastes can also be divided to the same 6 Stages; however, some differences are evident regarding the start and duration of some stages. Also, the absolute values of conductivity and $d\sigma/dt$ are reduced in comparison with the pure cement-pastes.

The main features which are detectable for the replaced mixes during the six stages are:

- (a) From Figure 5.3, the replacement percentage has two different effects on the conductivity. At early ages (Stages I-V) the conductivity displays an inverse relation with the replacement level i.e. the conductivity decreases as the replacement level in the pastes increases. The maximum values which occur at the end of Stage II are 1.21S/m for 35%GGBS, 1.06S/m for 50%GGBS and 0.84S/m for 65%GGBS. However, as the samples hydrate, this trend reverses and a 'cross-over' takes place on the mixes: the 35%GGBS conductivity decreases to a value of 0.21S/m at 24hrs, whereas the 50%GGBS and the 65%GGBS have values of 0.29S/m and 0.30S/m, respectively, showing that the highest replaced mix has the highest conductivity at the end of the 24hr monitoring period.

- (b) It is evident by taking the maximum conductivity at the end of Stage II as a benchmark, this maximum is progressively delayed as the replacement percentage increases from 35%GGBS to 65%GGBS. The maximum is recorded at 1.73hrs, 1.83hrs and 2.00hrs for, respectively, the 35%GGBS, 50%GGBS and 65%GGBS. In comparison, this peak is recorded at 1.80hrs for the pure cement-paste.
- (c) During Stage IV, it is clear that as the replacement percentage increases, the slope of the $d\sigma/dt$ graph becomes less negative during this Stage (see Figure 5.3(c)), and this is equivalent to increasing the w/b ratio for pure cement-pastes.
- (d) During Stage V, it is interesting to note that the replaced mixes show the same local maximum on the $d\sigma/dt$ graph as was presented in the pure cement-pastes; however, the prominence of this maximum depends on the replacement level in the mixes. The peak gets wider and persists over a longer time scale as the replacement level increases (See Figure 5.3(b)). It should also be noted that as the replaced level in the mixes increases, the starting point of the local maximum in Stage V appears much earlier than pure cement-pastes or the low replaced mixes, as for the 65%GGBS 0.35w/b paste this local maximum appears at the age of ~6hrs as opposed to 7.5hrs for the 35%GGBS 0.35w/b mix (see Figure 5.3(c)).
- (e) Regarding Stage VI, as with the pure cement-pastes, the same trend for both conductivity and $d\sigma/dt$ is also observed in the replaced mixes. The reduced $d\sigma/dt$ indicates slower reactivity as previously discussed.
- (f) Figure 5.3(d) presents the internal temperature for the replaced mixes. The most noticeable feature is a well-defined temperature maximum for the 35%GGBS. Due to the low temperature of the other replaced mixes, the temperature recorded could be affected by the fluctuation in the ambient laboratory temperature.

From what has been discussed above regarding the conductivity and $d\sigma/dt$ for both the pure cement-paste mixes and for replaced mixes, it is clear that these pass through different stages and this highlights the occurrence of different reactions and reaction rates which take place during this early hydration period.

5.2.2 Early hydration permittivity

Pure Cement pastes

Figure 5.4 presents the permittivity (ϵ_r) at selected frequencies. It is evident from this Figure that this parameter can change by several orders of magnitude over the frequency range 1Hz–10MHz and in order to get a clear picture of the change in permittivity with

time and frequency the normalised permittivity, (ϵ_N), is used. The normalised permittivity is defined as:

$$\epsilon_N = \frac{\epsilon_r(t)}{\epsilon_r(t_0)} \quad (5.1)$$

where:

$\epsilon_r(t)$: permittivity value at time (t); and, $\epsilon_r(t_0)$: initial permittivity value at t=0.

Figures 5.5 – 5.7 present the ϵ_N versus time for the 0.3w/b, 0.35w/b and 0.45w/b cement-pastes for the initial 24hrs hydration over the frequency range 1Hz-1MHz. Figure 5.5(a), Figure 5.6(a) and Figure 5.7(a) present the frequency range 1Hz-10Hz for the three different w/b cement-pastes and it is evident that the response is almost constant with time which is in agreement with Figure 5.4 in the low frequency range. At 1Hz, it is clear that the ϵ_N response has an initially high value, before decreasing to reach a constant period which extends to almost 6hrs. At this time a noticeable plateau area appears which extends from 6hrs to 14hrs. After this plateau period, a constant trend takes place until the end of the testing period (see Figure 5.5(a), Figure 5.6(a) and Figure 5.7(a)).

At 100Hz and higher, from Figures 5.5 – 5.7, it is apparent the ϵ_N response is similar to the conductivity-time response with all the same stages which have been identified on the conductivity response. However, an interesting feature which is detected in the ϵ_N response in the frequency range ~10kHz–800kHz (see Figures 5.5 (e) – (f)), Figures 5.6 (e) – (f) and Figures 5.7(e) – (f)) is the emergence of a ‘peak’ at approximately 4hrs. This feature becomes evident at a frequency of ~10kHz, and continues until a frequency ~800kHz. The prominence of this ‘peak’ is affected by the w/b ratio, being more pronounced at 0.3w/b and 0.35w/b than 0.45w/b. This peak indicates an increase in the polarizability of the paste which is masked by other polarization processes (e.g. electrode polarization) at a lower frequency range. As the frequency increases to >1MHz, the peak is not evident, which is in agreement with other early hydration studies which have been conducted at higher frequency ranges (GHz) for the permittivity (Moukwa et al., 1991; Zhang et al., 1996), as in these studies the increase in polarization was not detected which indicates that it is feature which occurs in the mid-frequency range.

Replaced pastes (GGBS)

As with the pure cement pastes, Figure 5.8 presents the permittivity (ϵ_r) at selected frequencies. Figures 5.9 – 5.11 show the normalised permittivity for the 35%GGBS, 50%GGBS and 65% GGBS pastes for 0.35w/b ratio. It is clear that many of the features which have been detected in the pure cement- pastes are also present in the replaced mixes. These features can be summarised:

- (i) As in the case of the cement pastes, the low-frequency ϵ_N response (1Hz-10Hz) shows little change through both frequency and time. This is particularly noticeable in the high replacement mixes (65%GGBS).
- (ii) As the frequency range increases from 10Hz to higher frequencies, ϵ_N , as in the case of the cement pastes, starts to display a conductivity-like response through time.
- (iii) All the replaced mixes, show the same intermediate-high frequency permittivity polarization plateau process which was identified as the source of difference between the conductivity and the permittivity in the case of the pure cement pastes. However, in the case of the replaced cement mixes, it is interesting to note that as the replacement percentage increases, this polarization process, the intermediate-high frequency polarization process, starts to emerge at a lower frequency range when compared to the pure cement pastes. By considering the 65% GGBS paste, the mentioned polarization starts to take place at the frequency of 4kHz; on the other hand, for the 35% and the 50% GGBS pastes this polarization process starts to take place at a frequency of 20kHz and 6kHz, respectively (see Figure 5.9(e), Figure 5.10(d) and Figure 5.11(d)).
- (iv) The intermediate-high frequency polarization process extends over a longer time-scale in the case of the replaced mixes as the replacement percentage in the mixes increases. As can be seen from Figure 5.10(e) and (f) and Figure 5.11(e) and (f) which both represent the high replaced mixes, this polarization gives an indication that it is composed of two polarization processes and not just one as in the case of the cement pastes.
- (v) A noticeable enhancement in the ϵ_N response is evident at 1MHz at late ages (24hrs), and could be compared to the enhancement observed in the cement pastes at the same frequency and age. From Figure 5.9(f), Figure 5.10(f) and Figure 5.11(f), as the replacement percentage increases, the enhancement in ϵ_N also becomes more

pronounced, ϵ_N increases from 0.4 in the case of 35%GGBS to almost 0.75 in the case of the 65%GGBS replaced paste at the age of 24hrs (see Figure 5.9 and Figure 5.11).

5.3 Discussion

In order to be able to fully understand and discuss the electrical response during the first 24hrs, it should be explained within the context of the interstitial phase chemistry, and the physical/chemical and microstructural changes occurring over the testing period. The dependency of the conductivity of the cementitious materials on these factors is illustrated by equation (5.2) (Christensen et al., 1994). This equation combines the effect of both the capillary porosity (ϕ_c) and the tortuosity of the pore network on bulk conductivity.

$$\sigma = \sigma_o \phi_c \beta \quad (5.2)$$

Where:

σ : Material electrical conductivity(S/m)

σ_o : Pore solution conductivity(S/m)

ϕ_c : Volume fraction of the capillary porosity.

β : A parameter related to the pore tortuosity.

During the early stages the influence of the aqueous phase chemistry is expected to dominate the electrical response more than at later stages where microstructural changes will dominate by restricting ionic mobility in the solution (Vernet and Noworyta, 1992).

With regard to the permittivity and its dependency on the pore structure and pore solution chemistry, it is known that the presence of discontinuities and interfaces in the material promotes the presence and the operation of different types of polarization mechanisms such as Maxwell-Wagner polarization (interfacial polarization) at the frequency ranges <100MHz (Martinsen and Grimnes, 2011) (see section 3.22). The bulk permittivity is also affected by the concentration of the interstitial electrolyte (Chen and Or, 2006). In addition, the dispersion of particles in electrolytes also promotes double layer polarization on the surface of the dispersed particles particularly at lower frequency ranges (kHz-MHz) (Schwan et al., 1962; Schwarz, 1962)).

5.3.1 Conductivity of cement pastes

It is considered appropriate to discuss both Stage I and II in the conductivity together, as there is a continuous increase in the conductivity through both these stages, albeit at different rates.

Stage I and II

The hydration reaction of cement takes place through both dissolution and precipitation processes (Le Chatelier and Mack, 1905). During the first 24hrs from mixing with water, the dominant reactions being the silicate and aluminate phases. The silicate phase reaction eventually leads to the formation of crystalline CH, and a poorly crystalline C-S-H which is the main source of cement strength. The aluminate phase reaction leads to the formation of ettringite and monosulphoaluminate which depends on the availability of sulphate ions (Taylor, 1997; Hewlett, 2003; Ylmén et al., 2009; Hesse et al., 2011).

On contacting the cement grains with water, a rapid exothermic dissolution process from the surface of the cement grains takes place. This dissolution process leads to the release of Ca^{2+} , OH^- , SO_4^{2-} and a combination of H_4SiO_4 , $H_2SiO_4^{2-}$, $H_3SiO_4^-$ into solution. Alkali sulphates also contribute in this early stage solution chemistry by releasing K^+ , Na^+ in addition to SO_4^{2-} ions to the aqueous phase (Barret and Ménétrier, 1980; Bullard and Flatt, 2010; Bullard et al., 2011; Nicoleau and Nonat, 2016). After mixing calcium, aluminium and sulphate concentrations show a rapid increase before decreasing at the period between the ages of ~2mins to ~15mins which indicates significant ion - ion interaction as well as the early precipitation of hydration products (see Figure 5.12) (Double et al., 1983; Kelzenberg et al., 1998). The OH^- ions in cement pastes show a continuous increase in concentration until reaching a maximum, thereafter their concentration starts to decrease. The Ca^{2+} ions also follow the same trend as the OH^- ions. The increase in the Ca^{2+} ions is due to the early nucleation of C-S-H product, due to the difference in the stoichiometry between the dissolving alite phase and the early formed C-S-H hydration product (Ca/Si <2) (Taylor, 1997). The calcium ion concentration increases reaching a super-saturation level with respect to the Portlandite (Double et al., 1978; Odler and Dörr, 1979; Garrault and Nonat, 2001; Garrault, 2005; Bullard and Flatt, 2010). The behaviour of both the OH^- and the Ca^{2+} in the solution during this early Stage is in contrast to the silicate concentration which decreases through this Stage (see Figure 5.13).

By considering equation (5.3), the conductivity, σ , of the aqueous phase is dependent on the value of the product of the equivalent ionic conductivity of the ions, which differs depending on the type of the ion (see Table 5.1)

$$\sigma = \sum_i z_i c_i \lambda_i \quad (5.3)$$

Where: z_i : valence of the charges; c_i : concentration of the charges (mol/l); λ_i : equivalent ionic conductivity ($cm^2 S/mol$).

From Table 5.1 the product of the valence (z) and the equivalent ionic conductivity (λ_i) for the OH^- ion is almost 3 times that of the Ca^{2+} ion, therefore, it could be reasonably deduced that the conductivity at this stage is related to the hydroxyl ions which, in turn, is related to the calcium ion concentration through the electrical neutrality of the solution. Regarding the $d\sigma/dt$ response during Stage I and II, the rapid decrease in $d\sigma/dt$ during Stage I (see Figure 5.1(c) and Figure 5.2), and the relatively constant rate during Stage II, these are discussed below:

Precipitation of early hydration products, will affect the conductivity through the consumption of ions in the hydrate formation process, and/or by partially or completely covering the surface of the cement grains thereby hindering the dissolution process. These two processes will decrease $d\sigma/dt$ during Stages I and II. Two types of hydration products are expected to precipitate through this early period which are the aluminate phase hydration products, and the nucleation of C-S-H. With regard to the aluminate phase hydration products, their formation might not be able to fully explain the rapid decrease in $d\sigma/dt$. As the C_3S paste does not contain sulphate ions phases as in the case of the Portland cement paste, however it still displays a decreasing rate for the OH^- ions which are the main contributor to the conductivity response (see Figure 5.12(a) and Figure 5.12(b)).

Considering the early nucleation/precipitation of the C-S-H phase as a controlling process with regard to $d\sigma/dt$ during Stage I, this hydration product starts to nucleate immediately on mixing the cement with water (Jawed and Skalny, 1982; Damidot et al., 2007). Therefore the silicate ion concentration after the initial few minutes, acquires a low constant value and does not change significantly, at least before the Ca^{2+} and the OH^- peak (Figure 5.13) (Young et al., 1977; Ménétrier et al., 1979; Garrault and Nonat, 2001; Thomas, 2007; Bergold et al., 2013). Therefore, it is expected the OH^- ions and the Ca^{2+} concentration will continue in their increasing trend however with a decreasing rate

due to the consumed fraction of the latter ions in the nucleation process of the early C-S-H phase which, in turn, shows a decrease in $d\sigma/dt$ of the mixes see (Figure 5.1(c) and Figure 5.2).

By considering the silicate ion behaviour through Stage II and the data in Rothstein et al. (2002) the dissolution of silicate ions during the first 10 minutes decreases and levels out at low values which are in the range of $\mu\text{M/l}$ and depends on the w/b ratio as shown in Brown et al. (1984). This indicates that the early nucleation rate with regard to the C-S-H phase is continuously decreasing over this time. This strongly suggests a decrease in the dissolution rate which affects the nucleation rate of the C-S-H phase leading to the induction stage, hence the decrease in the $d\sigma/dt$.

Juilland et al. (2010) have incorporated the geochemical dissolution theory of crystals to explain the origin of the induction period. In this theory, three dissolution domains, as shown in Figure 5.14, whose rates depend on the difference in the free energy between the solid phase and the solution, were proposed to take place on the surface of the grains (Dove et al., 2005). The following scenario is proposed to explain the relation between the geochemical dissolution theory and the conductivity response for cement pastes through Stages I and II:

- (a) Through Stage I and II the conductivity increases which indicates a continuous dissolution of the minerals, from the cement grains to the aqueous phase.
- (b) Initial hydrates such as C-S-H start to nucleate, consuming both Ca^{2+} and SiO_2^{4+} from the solution which will contribute in decreasing the $d\sigma/dt$ through Stage I (Damidot et al., 1990).
- (c) As the Ca^{2+} and the OH^- concentration in the solution increases, the aqueous phase becomes more saturated with respect to CH. A decrease in the under-saturation index with respect to the dissolving cement minerals takes place, which forces the dissolution process to proceed through lower dissolution rates. This is reflected in the continuous decreasing $d\sigma/dt$ during Stage I due to the continuous decrease in the dissolution rate of the minerals from the grains surfaces.
- (d) This proposed scenario could be supported by comparing the three dissolution domains which are shown in Figure 5.14 with the $d\sigma/dt$ responses which are presented in Figure 5.1(b) and Figure 5.2 during Stage I and II. It is clear that $d\sigma/dt$ during Stage

I and II is similar, in its general features, to the second and third dissolution domains of minerals which are shown in Figure 5.14.

From Figure 5.2, Stage II ends with a maximum in the conductivity and is due to the increase in the Ca^{2+} and the OH^- concentration in the solution. The relation between the time of this maximum and the w/b ratio could be related to the diluting effect which the w/b ratio plays in the aqueous phase. The higher the w/b ratio, the longer the time required for the dissolving ions to reach their super saturation concentration level. It is also worth noting that as the w/b ratio increases, the conductivity peak value also increases due to the increase in the liquid phase which is the main current path through the mixes.

Stage III

Both the peak in conductivity as well as the rapid decrease in $d\sigma/dt$ take place within the minimum observed on the dQ/dt graph which is related to the induction period in the hydration reaction (see Figure 5.15) (Gartner et al., 2002). The decrease in $d\sigma/dt$ and conductivity during this stage is attributed to the rapid precipitation of CH, the process reduces both the Ca^{2+} and the OH^- ions in the aqueous phase which, in turn, causes the decreasing trend observed during Stage III.

Stage IV

Several physical and chemical processes influence the conductivity through Stage IV, and are as follows:

Silicate phase reactivity re-initiation

After the decreasing trend in the $d\sigma/dt$, it is evident that $d\sigma/dt$ increases and has less negative values during this period which results in peak 'S' in Figure 5.15. Both the duration and the prominence of this peak depends on the w/b ratio, as for the PC 0.30w/b this peak is more pronounced; however, for the PC 0.45w/b sample this peak is more flattened and could be perceived as a plateau region. The change in the conductivity rate during this stage could be explained in terms of the aqueous phase chemistry as shown in Figure 5.13 (Young et al., 1977; Kelzenberg et al., 1998; Lothenbach and Winnefeld, 2006; Lothenbach, 2010). Several points could be deduced from the silicon concentration profiles shown in Figure 5.13 and the dQ/dt curves which are shown in Figure 5.15.

After the rapid decrease in the silicate concentration due to the early nucleation process, an increasing period appears which takes place within or immediately after the peak of the calcium concentration (see Figure 5.13) (Brown et al., 1984). At the stage in which the ‘S’ point takes place in Figure 5.15, the dQ/dt graph starts to increase rapidly indicating the initiation of a second exothermic dissolution process, which is considered in agreement with the simultaneous increase in the silicate concentration in the aqueous phase in Figure 5.13 (L.Nicoleau, 2004). To this end, the origin of the peak in $d\sigma/dt$ after the CH precipitation, the ‘S’ point, could be attributed to the renewed silicate phase reactivity after the induction period as this renewed reactivity promotes the initiation of another dissolution period on the surface of the cement particles (Brown et al., 1984; Damidot et al., 2007). This dissolution process is responsible in reducing the negative values of the $d\sigma/dt$ due to the introduction of more ions into the solution (Ca^{2+} , OH^- , H_4SiO_4 , $H_2SiO_4^{2-}$, $H_3SiO_4^-$).

During the first dissolution Stage (Stage I and II), the conductivity displays a clear increasing trend which is in contrast to Stage IV in which only a lower negative value in $d\sigma/dt$ is observed within the overall general decreasing trend in this parameter. This difference in the conductivity behaviour between the two dissolution stages could be attributed to:

- (i) The difference in the diffusivity of ions from the cement grains due to the formation of early hydration products such as ettringite (Scrivener et al., 2004), and meta -stable C-S-H (Nicoleau and Nonat, 2016).
- (ii) The domination of the CH precipitation process on the conductivity which masks the effect of the acceleration stage ionic dissolution on the conductivity, and reveals itself just by lowering the negative value of the $d\sigma/dt$ curve.

Nucleation and growth of stable C-S-H

After the ‘S’ point, $d\sigma/dt$ starts to decrease. This gradually decreasing period continues until a minimum occurs on the $d\sigma/dt$ graph, which is denoted by ‘P’ in Figure 5.2 and Figure 5.15. At this point, $d\sigma/dt$ changes from a decreasing trend to a gradual increasing trend. The timing of point ‘P’ depends on the w/b ratio; for the 0.3w/b, this point takes place at the age of ~4.5hrs, however, for the 0.45w/b it is delayed to ~5.75hrs (see Table 5.2).

By considering the reinitiated dissolution process which causes the S point on $d\sigma/dt$ graph, a renewed nucleation process with respect to the C-S-H phase is expected to take

place and is reflected by a decreasing trend in $d\sigma/dt$ due to the consumption of ions in this process. Both the increase in the activity of the silicate ions as well as the calcium ions in the solution due to the second dissolution stage, increases the saturation index (SI) with respect to the C-S-H phase, leading to its precipitation due to the SI decreasing effect on the free energy barrier for the nucleation process (Dirksen and Ring, 1991). The heterogeneous nucleation is the most favourable mode to nucleate the C-S-H phase in the interfaces between the cement particles and the liquid phase rather than through the solution as in the case of the homogeneous type (Garrault-Gauffinet and Nonat, 1999; Sunagawa, 2005; Garrault et al., 2006; Nicoleau, 2013). As the nuclei size exceeds a specific critical size which depends on the SI, the growth process takes place.

From this, and due to the acceleration period which is detected from the calorimeter response, it is suggested that during this stage both a renewed nucleation process and a growth initiation process are taking place. Both these processes contribute to decreasing $d\sigma/dt$ by reducing ionic concentration in the aqueous phase as well as restricting ionic mobility due to the increase in the paste rigidity. Other studies which have used STEM (Gallucci et al., 2010) and SEM (Scrivener, 1989; Ylmén et al., 2009) have shown a carpet-like growth for the C-S-H phase on the surface of the cement grains at this stage, which is in agreement with decreasing conductivity during this stage.

Outgrowth of early hydration products:

After the decreasing period between 2hrs and 5hrs on $d\sigma/dt$, which has been attributed for the renewed nucleation and growth of the stable C-S-H, its decreasing trend changes to an increasing trend indicated at the point 'P' in Figure 5.2. The change in $d\sigma/dt$ suggests a change in the controlling process from the proposed ion removed process, due to the nucleation and growth process, to a further process. The outgrowth of C-S-H from the cement particles could be regarded as the controlling process during Stage IV due to the outgrowth of hydration products from the grain surfaces which impedes the conduction process through the connected liquid phase. This is supported by considering the value of the degree of hydration from the dQ/dt curves (Figure 5.15) for PC 0.3w/b, PC 0.35w/b and PC 0.45w/b at the point 'P', which records the values of 3%, 4% and 6% respectively. It is apparent that the timing of the 'P' point does not depend on the degree of hydration, hence the amount of the hydration products formed in the mix, rather it depends on the proximity of the cement particles to each other. In the high w/b mixes (and despite the higher recorded degree of hydration), the timing of the 'P' point is delayed in comparison

to the lower w/b pastes, and this is due to the increased distance which needs to be bridged by the hydration products. It is suggested that the 'P' point could be considered as the earliest point at which the microstructural changes start to significantly influence the conductivity.

Hydration products growth type:

It is interesting to note that the time interval between the 'P' point and the dQ/dt peak in Figure 5.15 depends on the w/b ratio. This time intervals varies between 4.8hrs, 4.5hrs and 4.3hrs for, respectively, the PC0.3w/b, PC0.35w/b and the PC 0.45w/b pastes (see Table 5.2) which indicates that as the w/b ratio increases, the time period between the calorimeter peak and the 'P' point decreases. Therefore, it is proposed that the bridging processes between the cement particles takes place simultaneously with the coverage of the cement particle surfaces by the hydration products during this stage. However, due to the early presence of the 'P' point in comparison to the dQ/dt peak, it is expected that the crystal outgrowth mechanism, which results in increasing rigidity, is more rapid than the lateral coverage process on the cement grain surfaces (Thomas et al., 2009). Therefore, during the period between the 'P' point and the main calorimeter peak, the expected growth type is an uneven crystal outgrowth process of hydration products from the cement particles. This occurs before the impinging process between the different growing nuclei on the surface of the cement particles which, consequently, initiate the decelerating stage in the hydration process (Christian, 2002; Thomas, 2007; Bishnoi and Scrivener, 2009). From this it is expected that the growth process proceeds on the C-S-H phase on the surface of the cement grains filling the pores space first until the space limiting conditions due to the coalescence between the different outgrowing particles takes place. Thereafter, new nucleation centres from the surface of the uncovered grains takes place again. These two growth processes continue until the cement grains are coated with the hydration products, hence transforming the hydration mode from acceleration to deceleration (Bazzoni, 2014) (see Figure 5.16).

Stage V

Considering Stage V which starts after the observed 'P' point (see Figure 5.2), the conductivity continues its decreasing trend through time and the $d\sigma/dt$ displays little change in its increasing trend. With regard to the dQ/dt response, it maximizes for all the mixes at this stage before it undergoes a continuous decreasing trend through the rest of this Stage. Therefore, it is expected that over this Stage, both the outgrowth as well as the

covering process, continue to operate. The $d\sigma/dt$ peak, which is evident in the mixes during this stage (see Figure 5.15) where peaks are denoted by 'A', indicates the presence of another process, in addition to those already mentioned.

It is known that the aluminate phase (C_3A) reactivity (after the initial ettringite (AFt) formation) is expected to occur during the period after the silicate phase (C_3S) reactivity. To support the relation between the peak, which is denoted by 'A', and the renewed aluminate phase reactivity, Figure 5.17 has been produced which shows the conductivity, $d\sigma/dt$ and dQ/dt for the PC0.35w/b mix with two different calcium sulphate additions (0.5% and 2%). With regard to the dQ/dt response, the main hydration peak in the case of the pure PC0.35w/b cement paste, is composed of two thermal activities, the first could be distinguished from the slope changing feature at ~8.5hrs and the second is centred around ~9.5hrs. As the $CaSO_4$ addition increases to 0.5%, a second peak in the dQ/dt is evident. By increasing the $CaSO_4$ to 2%, the second peak is not observed within the 24hr monitoring period presented in Figure 5.17(c).

With regard to the electrical response during this stage, as the $CaSO_4$ in the mix increases, the peak in the $d\sigma/dt$ response is delayed. By comparing the pure PC0.35w/b and the PC0.35w/b+0.5% $CaSO_4$ in which the difference between the peaks A1 and A2 records a value of 1hr, which is comparable to the delay observed in the dQ/dt response. With regard to the 2% $CaSO_4$ mix, the peak in the $d\sigma/dt$ is not present and the response displays a continuous increasing trend after the 'P' point until 15hrs at which time $d\sigma/dt$ attains an almost constant value. Due to the clear influence of the different $CaSO_4$ additions, this stage could be related to the renewed reactivity of the aluminate phase as a controlling process (Minard et al., 2007).

Effect of $CaSO_4$ addition on the early hydration reaction response

From Figure 5.17 it is evident increasing the $CaSO_4$ percentage influences the conductivity response. With regard to the conductivity during Stages I and II, it is clear that the values increase as the $CaSO_4$ percentage increases; with reference to Table 5.3, increasing the $CaSO_4$ content to 2% results in an increase in peak conductivity by ~5% (due to increased ionic concentration in the aqueous phase) and the earlier occurrence of this peak. Very dilute solutions of C_3S plus gypsum (Ménétrier et al., 1980) have been shown to give a similar response. It is also noticeable from Figure 5.17 that the 'P' point appears earlier in the more sulphated mixes. For example, in the PC0.35w/b+0.5%, this point occurs at ~4.6hrs compared to ~4.9hrs for the pure cement paste. With regard to the

effect of CaSO_4 additions on dQ/dt , as the CaSO_4 percentage increases, the heat emission rate during both the induction period and the acceleration period increases. The minimum dQ/dt recorded during the induction period for the PC0.35w/b was 1.14 (J/h.gm) and for the PC0.35w/b+2% CaSO_4 was 1.92 (J/h.gm). In terms of the silicate acceleration peak for the pure cement paste, this peak recorded a value of ~ 8.94 (J/h.gm), however, for 2% CaSO_4 this peak had a value of ~ 10.5 (J/h.gm).

From the discussion above, the addition of the CaSO_4 has an acceleration effect on the dissolution stage as well as the acceleration stage. This addition increases the Ca^{2+} in the solution thereby increasing the conductivity. As a consequence, this process accelerates the silicate phase reactivity process due to the early precipitation of the CH (Ménétrier et al., 1980). With regard to the effect of CaSO_4 during the acceleration stage on the dQ/dt response, this could be attributed to the interaction between the CaSO_4 and the aluminium ions produced from the alite phase dissolution which has a retarding effect on the alite hydration. Therefore, as a result the addition of CaSO_4 , the aluminium ions react to form ettringite which could also act as a possible nucleation site for the new formed C-S-H, hence accelerating the hydration process (Taylor, 1997; Quennoz and Scrivener, 2013). The acceleration effect of the CaSO_4 is also noticed and reflected in the early appearance of the P point in $d\sigma/dt$ for the higher sulphated mixes in comparison to the pure cement pastes.

Stage VI

This Stage starts at ~ 15 hrs at which time the conductivity continues its decreasing trend with $d\sigma/dt$ approaching zero; dQ/dt also continues its decreasing trend. It could be implied that the beginning of Stage VI is related to the transition step of the hydration process from the growth controlled process during Stage IV, in which $d\sigma/dt$ shows a continuous increasing trend, to a diffusion controlled process, whereby $d\sigma/dt$ attains a value approaching zero.

5.3.2 Permittivity of Cement pastes

It is considered appropriate to assess the behaviour of both the conductivity and permittivity in terms of their absolute values in the frequency domain as this is useful in detecting regions of relaxation/dispersion.

Figure 5.18 presents the conductivity and permittivity for the three w/b cement pastes. It is evident that both parameters display dispersion as the measuring frequency increases. Regarding the permittivity, its behaviour could be summarised in the following 3 regions (see Figures 5.18(a), (c) and (e)):

(i) Low frequency region (~1Hz–100Hz)

In this region, the permittivity values attain high values which depend on the sample age as well as the w/b ratio. It is evident that the frequency range over which this plateau region persists reduces as the w/b decreases and the age of the samples increases.

(ii) Medium frequency region (~100Hz-100kHz)

In this region, a major relaxation takes place; however, as hydration proceeds, the upper limit of this frequency range reduces. This feature is particularly noticeable at w/b = 0.30 and 0.35 where the upper limit is reduced to 100kHz.

(iii) High frequency region (~100kHz-10MHz)

After the region of relaxation noted above, the response attains another ‘plateau’ region in which the permittivity values do not show significant changes with increasing frequency. As the age of the samples increase, this plateau region becomes more defined; for example, at 20hrs (Figure 5.18) this plateau area extends over the range 100kHz-10MHz. The w/b for the samples also influences the frequency range at which this relatively high-frequency plateau permittivity region takes place. The high-frequency plateau region progresses to higher frequencies as the w/b in the mixes increases.

The effect of age, and w/b ratio on the permittivity over the three regions noted above (Low frequency, high permittivity region; mid-frequency, rapid relaxation region; high-frequency, plateau region) are illustrated in Tables 5.4 – 5.6. In these Tables it is apparent that for all the mixes, the permittivity shows an increase as the w/b ratio of the sample increases. Also, by considering the age effect, it is clear that the permittivity for the three regions decreases as the age of the sample increases. In terms of the frequency effect on the conductivity response at the same ages which have been used for the permittivity response (Figures 5.18(b), (d) and (f)), the following can be observed:

(i) Low frequency region (~1Hz-100Hz)

The conductivity in this region has low values and is attributed to the effect of electrode polarization process at lower frequencies.

(ii) Medium frequency region (~100Hz-100kHz)

It is interesting to note that as the permittivity shows a rapid decrease over this frequency range, the conductivity values show a progressive increase. This gives a strong indication of the existence of a region of dispersion over this intermediate frequency range, as the polarizability of the paste decreases with increasing frequency.

(iii) High frequency region (~100kHz-10MHz)

Following the rapid increasing period in the conductivity, a plateau-like conductivity region develops in this range and similar to the permittivity in this respect.

Origins of Polarization

In order to investigate the low frequency region with regard to the existence of additional relaxation processes, other immittances responses could be used for this purpose (Sinclair and West, 1989; McCarter et al., 1999). In this case, the frequency response for the dielectric loss (ϵ'') which is calculated according to (4.7), is presented in Figures 5.19(a) – (c). By considering the samples at 15mins for the three different mixes in Figure 5.19, the dielectric loss in the low-frequency range attains high values in comparison to values in the MHz frequency range which are lower by three orders of magnitude. It is interesting to note that during the decreasing trend for the dielectric loss with increasing frequency, a noticeable change in the slope takes place between 100Hz-1kHz depending on the w/b ratio. This change in the slope transforms through time to reveal a well-defined peak as is evident at the age of 10hrs and 20hrs in Figures 5.19(a) – (c). From Figure 5.19, it is also observed that as the age of the samples increases, the frequency at which this peak occurs (i.e. the characteristic frequency) reduces through time to lower values.

Considering the characteristic frequencies presented for both the dielectric loss (Figures 5.19(a) – (c)) and conductivity dispersion (Figure 5.18(b), (d) and (f)), it is evident that they are comparable. This would suggest that the electrode polarization processes are operative and contributing to the main region of dispersion in conductivity. Although only frequencies $>1\text{Hz}$ were used in the investigation, to account for the dielectric loss, electrode processes must exist at frequencies $< 1\text{Hz}$ due to the high value obtained for the dielectric loss at frequencies below the characteristic frequencies. The conductivity dispersion curves in Figures 5.18(a), (d) and (f) show that at frequencies $> \sim 10\text{kHz}$ (15 mins), $\sim 1.0\text{kHz}$ (10hrs) and $\sim 100\text{Hz}$ (20hrs) the conductivity increases

only gradually with increasing frequency and is attributed to relaxation of bulk (cement paste) polarization processes.

Proposed model for electrode (low-frequency) response

To account for electrode processes, the equivalent electrical circuit (EEC) is presented in Figure 5.20 and comprises two, series connected parallel circuit elements: R_{ox} and C_{ox} represent the response from the passive oxide layer on the electrode surface; R_{ct} and CPE_{DL} representing the contribution from electrode polarization processes at the electrode/sample interface. For illustrative purposes Figure 5.21(a) presents a typical Nyquist plot for cement paste (PC 0.3w/b). The best fit parameters for all mixes are presented in Table 5.7 for the electrode response. Figure 5.21(b) presents the simulated (electrode) response. The ϵ'' and ϵ_r simulated from these data are presented in Figures 5.22(a) – (c).

Considering the R_{ox}/C_{ox} circuit, C_{ox} values are in the range of 10^{-5} F and R_{ox} records high values which clearly depend on the age of the sample. At early ages (15 mins) it attains values in the range of 10^4 ohms and increases to of 10^5 ohms at 20hrs. With regard to R_{ct}/CPE_{DL} circuit, R_{ct} records values in the range of 10^3 ohm and CPE_{DL} records values in the range of 10^{-4} ($Fs^{\alpha-1}$). These values for the CPE_{DL} would give an average value of 1.35×10^{-4} F for the equivalent capacitance C_{eq} (Hsu and Mansfeld, 2001) as shown in Table 5.7. The capacitance values for the R_{ox}/C_{ox} and the R_{ct}/CPE_{DL} circuits are relatively large and cannot be attributed for bulk phenomena (Song et al., 2000) and, in accordance with Table 5.8, these two values are in the range of the electrode/sample interfaces and oxide layer zone (Yilmaz et al., 1992; Scrivener and Young, 1997; Ford et al., 1998; Andrade et al., 2001; Olsson and Landolt, 2003; Abreu et al., 2004; Priyantha et al., 2004).

Correction of the measured data for electrode polarization effects:

After assigning the different features which appear on the system dielectric response to their possible origins, the bulk material response can be assessed in the frequency range between 100kHz-1MHz. In this frequency range, bulk polarization processes start to emerge and dominate over electrode effects. Residual effects of electrode processes in this frequency range is also expected to influence the bulk permittivity (Umino et al., 2002); however the detection of the bulk polarization process(es) will depend on their intensity so as not to be masked by the residual electrode polarization.

For the electrode correction, the total impedance is modeled by an EEC which assumes that the apparent impedance response is composed of three, in-series contributing circuits, which are: the electrode impedance, bulk impedance and lead inductive effect as shown in equation (5.4).

$$Z_{measured} = Z_{leads} + Z_{Bulk} + Z_{Electrodes} \quad (5.4)$$

With regard to the bulk response, it was successfully fitted by an EEC comprising two, series electrical circuits which are $R_{s1}||CPE_{s1}$ and $R_{s2}||C_{s2}$. To account for the residual inductive effect imposed by the connecting leads, an inductive element has been introduced in series with the electrode impedance processes and the sample impedance for this purpose. The complete EEC proposed for the purpose of the electrode correction is shown in Figure 5.23. Figures 5.24(a) – (c) show the fitting of the proposed EEC for the PC0.30w/b cement paste at different ages. The best fitting parameters which are obtained from Figure 5.24 are presented in Table 5.9. By considering the in-series connection for both the electrodes impedance processes and the leads inductive effect, this allows these undesirable effects to be deducted from the measured impedance to eventually extract the electrical behavior of the sample.

Figures 5.5 – 5.7 have been reproduced in Figure 5.25 to show the normalized permittivity (ϵ_N) after correction through time at selected frequencies which are 100kHz, 200kHz, 500kHz and 1MHz and all located in the frequency range at which the bulk response dominates. The most striking feature from Figure 5.25 is the pronounced peak in ϵ_N which is recorded for the corrected 100kHz and 200kHz between 5hrs-10hrs in comparison to the relatively weak peak which appears at the uncorrected ϵ_N response. This indicates that by correcting the measured ϵ_N data with regard to the electrodes processes, other bulk polarization processes reveal themselves due to the decrease in the masking effect of the electrode processes.

Bulk Permittivity response through early hydration period

Considering Figure 5.25, the response of ϵ_N is frequency dependent, therefore different frequencies would highlight different polarization processes. In Figure 5.26 several salient points have been identified on the ϵ_N response denoted A, B, C, D, and F, accordingly, the ϵ_N response through time has been divided in to the following periods:

The period A to B

Over this period, and with regard to the ε_N response at 100kHz, two distinguishable trends are detected which are:

- (a) At the beginning of the measurement the corrected ε_N response displays values which are decreasing rapidly through time; and,
- (b) After this decreasing period, a plateau-like feature appears in the response.

Considering (a) above, this behaviour could be attributed to four possible causes which are:

- (i) The continuous reduction in the residual EP effect, resulting in a continuous decrease in ε_N .
- (ii) The gradual decrease in the rate of dissolution of the cement particles which has been shown to take place during this early hydration period.
- (iii) The coagulation of different cement particles due to active electrostatic forces in the mix, which reduces the polarizability of cement grains surfaces.
- (iv) The coverage of cement particles by early formed hydration product which decreases the polarizability of the cement grains.

With regard to (ii) the trend in ε_N during this period is similar to the trend in $d\sigma/dt$ during the same time, therefore the same chemical and physical processes which have been attributed to the conductivity during this period, would also be responsible for the ε_N response (Lasaga and Luttge, 2001; Gallucci et al., 2010; Nicoleau and Bertolim, 2015). However, this rapid dissolution process gradually reduces as the liquid phase concentration in the mixes increases. This affects ε_N by introducing a decrease in the dissolution of ions from the surface of the cement grains which in turn, renders the surface of the cement grains less polarizable through time, and this would contribute in the continuous decrease in ε_N through this period.

Regarding (b) above, during this plateau-like feature prior to reaching point B, this could be related to the low dissolution period which takes place on the cement particles after the rapid dissolution period. Due to the slight increase in ε_N during this period, the effect of the increase in ionic concentration is evident, as during this short period an increase in Ca^{+2} and the OH^{-1} concentration in the solution is taking place. With regard to the high

frequency ε_N response during this early time period, it is clear that the 1MHz ε_N response displays a conductivity-like behaviour, which is related to the chemistry of the liquid phase during this stage rather than the topochemical processes which take place on the surfaces of the cement particles.

The period between B to D

Regarding the 100kHz response, a short-lived decrease in ε_N is evident at point C, which is similar to the decrease in the conductivity at the same time and attributed to the precipitation of the CH from the aqueous phase which decreases the polarizability of the mix due to the accompanied decrease in the conductivity. With regard to the 1MHz response at point C, a sharp decrease is also noticed after the peak in ε_N which, in turn, represents the maximum supersaturation point for the solution with respect to CH before its rapid precipitation.

After the decrease at point C in the 100kHz response, a short-lived increase in ε_N takes place before a slow, decreasing period to point D, this decreasing period is more evident at 1MHz. The period between point C-D, nucleation of C-S-H from the aqueous phase is expected to take place, hence a decreasing ionic concentration in the liquid phase. This introduces the gradual decreasing trend in ε_N due to the decrease in the mix polarizability.

The period between D to E

During this period, there is a noticeable rapid increase in ε_N at 100kHz starting from point D and peaking at point E. This indicates an increase in the polarizability of the paste and the polarization process contributing at 100kHz ceases to contribute at 1MHz. Several observations could be noticed when comparing the time at which this increasing period takes place, with the behaviour of the conductivity and the dQ/dt during the same time period:

- (i) The increasing trend of ε_N at 100kHz during this stage is in contrast to both $d\sigma/dt$ and conductivity during the same period, as the latter shows a continuous decreasing trend.
- (ii) The increasing period in ε_N at 100kHz takes place within the acceleratory period in the dQ/dt response; however, ε_N peaks before the maximum heat emission point is reached in dQ/dt response.

(iii) A time lag is evident between the start of the acceleratory period in dQ/dt and the beginning of the increase in the ϵ_N response at period D. For the PC 0.30w/b and the PC0.35w/b this time lag is of ~ 2.5 hrs; however, for the PC0.45w/b it is ~ 4 hrs.

From these three observations, it could be concluded that the rapid increase in ϵ_N at 100kHz cannot be entirely attributed with variations in the liquid phase chemistry at this stage. On the other hand, both the increase in dQ/dt and the 100kHz ϵ_N response is an indication of a potential relation between the physical/chemical processes which influence heat output and polarization. It is postulated that the increase in ϵ_N at 100kHz is related to the increase in surface area of the cement particles due to growth of more crystalline C-S-H. The increase in the surface area would enhance the polarizability of the paste through double-layer process on the newly formed C-S-H. This polarization process is only operative up to ~ 500 kHz as at frequencies > 500 kHz the increasing trend in ϵ_N is not detected over this period.

Figure 5.27 shows ESEM images in the secondary electron detection mode for the PC0.35w/b paste at 11mins, 2hrs, and 5.5hrs after mixing which are the times at points A, C and P in Figure 5.26. It is evident that at 11mins (Figure 5.27(a) and (b)), the cement particle surface is almost clear apart from some diffused debris and small clusters of hydration products as shown by the dotted circle. At the same time, the cement particle edge displays a ‘corroding’ behaviour which reflects the rapid dissolution process at this early age. At the age of 2hrs (point C in Figure 5.26), some clusters of hydration products appear to be distributed randomly on the surface of the cement particles which were defined as the early heterogeneous nucleation of C-S-H (Bazzoni, 2014), although most of the grain surface is still clearly visible. At ~ 5.5 hrs, (P point in Figure 5.26), it is noticeable that the randomly distributed C-S-H hydration products, which were distinguished at early hydration ages, have developed to cover most of the cement grains showing a ‘carpet like’ behaviour (see Figures 5.27(c) and (d)). It is also worth noting that point P takes place later than point D by almost 1.5hrs at which time the ϵ_N response starts its rapid increasing trend (see Figure 5.26).

From these ESEM observations, it could be postulated that, due to the increase in the surface area of the cement particles by C-S-H products, the ϵ_N response displays an increasing trend at point D (see Figure 5.26).

The period between E to 24hrs

During this period, the main feature of the ε_N response is the continuous decrease through time, and is observed in both the high frequency, (1MHz), and low-frequency (100kHz). The most distinguishable feature during this continuous decreasing trend, is the change in the slope which occurs at point F. As is evident from Figure 5.26, this feature at point F coincides with the time at which the renewed reactivity of the aluminate phase influences the $d\sigma/dt$ response, and this could also be supported by Figure 5.28 and Figure 5.29. From Figure 5.28 it is clear that as the gypsum percentage in the mixes increases, point F is delayed by ~2hrs. An interesting feature which is discernible when comparing the pastes with and without additional gypsum, is that point E appears earlier in the ε_N response as the gypsum content increases; for example, the PC0.35w/b + 0.5% gypsum, point E peaks and starts to decrease appears at the age of 5.40hrs; for the PC0.35w/b +2% gypsum, this point appears at the age of ~4hrs. in the pure PC0.35w/b this occurs at ~6.30hrs for the pure PC0.35w/b. This also supports the calorimeter results in Figure 5.17(c) which shows an enhancement in the heat emission rate at the peak point of dQ/dt as well as an earlier presence for this peak when the gypsum addition in the mixes increases. During this period, the C-S-H hydration products show a dense fibrillar network which covers the cement particles and, as can be seen from Figure 5.30 the C-S-H hydration products are forming on the surface of a massive CH crystal in which the C-S-H exhibits a connected network structure.

5.3.3 Conductivity of GGBS pastes

The early electrical response for the replaced mixes is similar in many aspects to the response of the pure Portland cement pastes as shown in Figure 5.31. However, some minor differences could be noticed in the replaced mixes when compared with the pure pastes which are:

- (i) There is a delay in the appearance of most of the stages in the electrical conductivity as the amount of GGBS increases. In addition, due to the low reactivity of the GGBS, it is noticeable that the conductivity values during early hydration decrease as the replacement percentage in the mixes increases. (See Figure 5.3(a)).
- (ii) The maximum value of dQ/dt (Figure 5.31) decreases as the replacement percentage in the mixes increase: for example, the 35% GGBS 0.35w/b mix has a peak value in

the range of ~ 7.5 J/gm.h, however, for the 65% GGBS 0.35w/b this peak has a value of 4.25 J/gm.h.

- (iii) A feature which is evident on the dQ/dt response, is the ‘widening’ of the dQ/dt peak through time in the high replaced mixes (50% and 65%), when compared with the 35% GGBS mix and the pure pastes.
- (iv) The ‘widening’ feature on the dQ/dt response at this stage is also reflected on the $d\sigma/dt$ aluminate phase reactivity peak in the replaced mixes.
- (v) The induction plateau period in the $d\sigma/dt$ (Stage II in Figure 5.31(a)) which takes place before the rapid CH precipitation, is more pronounced in the case of the 50% and the 65% GGBS mixes, the same occurs for the point after the precipitation point of the CH which is denoted as S in Figure 5.31(a).

All these features from both $d\sigma/dt$ and the heat emission response, could be attributed to a ‘dilution effect’ in which the GGBS acts as an inert filler at this early stage (Mostafa and Brown, 2005). With regard to Stage II and point ‘S’ in the $d\sigma/dt$ response (Figure 5.31), as has been discussed before the duration of Stage II depends on the concentration of CH in the mixes. It is expected, thereby that as the source of the Ca^{2+} and the OH^- ions in the solution decrease, this period will extend and the solubility of the CH will be reached much later. On the other hand, the ‘S’ point, depends also on the ionic concentration in the mix, particularly the silicate ions (see Figure 5.13) in order to enable the rapid nucleation as well as the growth of stable C-S-H. As a consequence, due to the high replacement level in the mixes (50% and 65%) a lower nucleation rate takes place when compared with the pure cement-paste and the low-replaced mixes. Due to the lower ionic concentration in the pore solution, the period after the ‘S’ point is much more pronounced in the replaced mixes.

5.3.4 Permittivity of GGBS pastes

With regard to the permittivity in Figure 5.32, this could be considered similar to the pure cement pastes; however, in the GGBS mixes (100kHz and 200kHz) the plateau area, which has been denoted by the letter F in Figure 5.26 starts to merge with peak E, indicating the aluminate phase reactivity is accelerated due to the GGBS addition, as has been presented in other studies (Gutteridge and Dalziel, 1990a; Gutteridge and Dalziel, 1990b; Gallucci et al., 2010).

By considering Figure 5.33, ϵ_N for the GGBS pure cement paste during the initial 100hrs after mixing, it is evident that the replaced mixes, in particular the 1MHz response for the 50% and the 65% mixes, displays an additional gradual increase in polarization which is denoted by the letter M at ~30hrs. This increase in polarization of the paste becomes more pronounced as the replacement percentage increases.

Considering Figure 5.34, which shows the conductivity through the initial 100hrs for the 65%GGBS mix and pure cement paste, it is evident that the M polarization feature for the 65%GGBS does not appear on the conductivity. Interestingly, thermal activity on the dQ/dt response could be detected at the same age at which the M feature takes place on the 1MHz ϵ_N response for the 65%GGBS paste. For the pure cement paste in Figure 5.34, the same trend observed on the 65%GGBS paste is observed at 1MHz for the PC0.35w/b in Figure 5.33(a). The M polarization feature is more clearly observed in the permittivity response than its dQ/dt response. This polarization feature, (denoted by M) and the effect of both the addition of GGBS and gypsum on this feature as well as its late (weak) thermal response, is a result of the transformation of ettringite to monosulphoaluminate (Odler, 1998; Hesse et al., 2011; Berodier, 2015). The infilling effect plays a significant role in accentuating this late polarization feature, and the GGBS mixes show this more clearly in comparison to the pure pastes. In the case of the gypsum added mixes, and due to the availability of SO_4^{2-} ions, the rapid reaction of the C_3A after the silicate reaction is hampered; however, a gradual depletion of SO_4^{2-} ions from the mix takes place due to the infilling effect which the undissolved gypsum particles provide. This promotes the transformation of AFt to AFm, therefore the F polarization feature, which is related to the renewed reactivity of the C_3A , disappears in contrast to the M polarization feature which is related to the transformation of AFt to AFm and is still detectable (see Figure 5.29).

5.3.5 Electrical response of Fly-ash pastes

With regard to the response of the fly-ash replaced mixes Figure 5.35(a) shows both the conductivity and calorimeter response for the same mix, and Figure 5.35(b) shows ϵ_N at 100kHz, 200kHz, 500kHz and 1MHz for a 35%FA 0.35w/b cement paste. It is clear that replacing the cement by 35%FA does not affect the electrical response significantly, as all the features which have been identified on the conductivity for the pure cement pastes, as well as on ϵ_N , can be identified in the 35%FA replaced paste.

Therefore, from these observations with regard the effect of the different SCMs on the electrical response and on the early hydration of cement pastes, it could be deduced that

the SCMs act as a filler to the cement pastes which affects the reactivity of the C_3A in the mixes due to the increase in the nucleation sites provided by the filling materials. However, during this early hydration stage, there is no evidence that the reactivity on the SCMs is initiated during this period.

5.3.6 Equivalent electrical circuit for cementitious pastes

In this section, an equivalent electrical circuit (EEC) is proposed to account for the material response during the early hydration period. This electrical circuit is developed from the knowledge obtained in the previous sections regarding the hydrating system, in addition to the electrochemical processes which are expected to take place during this period. The contributions to the overall electrical response, can be divided to two main processes which are:

- (a) measuring system related electrical processes; and,
- (b) bulk material related processes.

With regard to (a), this has been discussed previously and an electrical circuit proposed to account for both the lead inductive effect and the electrode effect (see Figure 5.23). On the other hand, the bulk material could be perceived as a combination of the liquid phase response and the response from the dispersed solid particles. Through the hydration reaction, the liquid phase ionic concentration fluctuates and the effect of the pore structure on the conductivity of the liquid phase is evident after the setting process.

With regard to the dispersed cement particles at different stages, they are expected to exhibit different electrical properties which will be linked to the hydration stages. For example, an interfacial polarization process would be expected to take place on the surface of the cement particles which will be influenced by the surrounding electrolyte concentration, changes in the surface area of the particles, and increase in the rigidity of the paste.

To this end, the following electrical paths have been proposed to represent the electrical response of the bulk material during the early hydration period (see Figure 5.36):

- (i) A resistive path, R_e , in parallel with a capacitive path which represents the continuous connected liquid phase conduction and capacitive responses. A constant phase

element, CPE_e , has been used instead of an ideal capacitor to account for the distribution of the relaxation processes in the connected pores;

- (ii) A resistive element, R_p , in series with an ideal capacitive element, C_p , which represents, respectively, the dispersed particles surface resistance and capacitance.

A similar equivalent electrical circuit has been used to model, for example, the response of human red blood cells suspended in a phosphate buffered saline solution (Morgan et al., 2006; Sun et al., 2007; Sun et al., 2010), the only difference being that a pure capacitor was used to study the electrolyte capacitive response rather than a CPE.

For illustrative purposes, Figure 5.37 presents the Nyquist plots for the cement pastes 9hrs after mixing. The fitting parameters for the plots in Figure 5.37 based on the EEC shown in Figure 5.36 are presented in Table 5.10. However, the same fitting procedure was undertaken at each time interval (~4.5min) over the 24hr monitoring period. The variation in the fitting parameters is presented in Figure 5.38 and Figure 5.39 for the pure cement paste and the GGBS pastes, respectively.

Circuit parameter: (G_e)

By considering G_e ($1/R_e$), a conductivity-like trend is observed, as all the salient points which are detected in the conductivity response can also be detected in the G_e response, such as the early-age peak which was related to the super saturation limit of the CH and the late-age change in slope which was related to the renewed aluminate phase reactivity (Figure 5.38 (a)). This fact proves that G_e represents changes in the liquid phase as well as in the connected pore network. With regard to the effect of the w/b on G_e parameter, it is clear that the higher the w/b in the mix, the higher G_e (see Figure 5.38(a)).

Circuit parameter: $CPE_e / G_p / C_p$

The stages which are used to explain these parameters, are based on the salient points identified on Figure 5.40(a) and (b).

The period A-C

With regard to the G_p and the C_p for the pastes, these electrical parameters display a similar trend through time (see Figure 5.40(a)), as at early ages (the period between point A-B in Figure 5.40(a)), a rapid decreasing trend is evident on these both parameters.

Values for both the G_p and the C_p decrease at this stage are due to three different possible reasons:

- (i) The decrease in the particle dissolution process. It should be noticed that at this very early age (the period between point A–C in Figure 5.40 (a)), both the G_p and the C_p mimic the $d\sigma/dt$ response, as the latter is related to the dissolution rate of the cement particles at this stage.
- (ii) The coverage of early hydration products for the cement particles surfaces.
- (iii) The coagulation process between the different cement particles which decreases both the polarizability as well as the conductivity of the cement particles surfaces by covering the active dissolving area.

After point B, a rapid decrease in particle conductance takes place at point C due to the precipitation of the CH from the solution. This affects G_p due to the decrease in the ionic concentration in the vicinity of the cement; this also is reflected in C_p as it is also affected by the conductivity of the solution surrounding the particles.

With regard to the CPE_e parameter during this stage, C_{oe} does not show a noticeable change through time (see Figure 5.38(b), Figure 5.39(b) and Figure 5.40(b)). On the other hand, and with regard to the exponent, p_e , this parameter attains values >0.95 , which shows an overall ideal capacitive behaviour for the connected pores with little distribution for the CPE_e parameter. This would suggest that the sample at this stage is acting as a liquid electrolyte rather than a solid porous material, therefore an almost ideal capacitive behaviour is displayed.

The period between C-F

After the decrease at point C in Figure 5.40(a) in both G_p and C_p , a short-lived increase in G_p takes place. This small increase in the G_p could be explained in terms of the beginning of the acceleration period in the pastes as it appears simultaneously with the initiation of the acceleration stage on the dQ/dt response. After a nucleation period which extends from point C-D, there is a rapid growth on the surface of the particles which starts at point D. The hydration acceleration period will increase the ionic concentration in the vicinity of the particles, hence initiating the growth process on the particle surfaces and increasing their surface area. This is reflected as a rapid increase in both G_p and C_p .

At the same time at which point D occurs, and with regard to the C_{oe} parameter, this starts to increase in the case of the pure pastes, which continues until the end of the monitoring period. With regard to the ' p_e ' parameter for all the mixes, it starts a decreasing trend at point D, which indicates a distribution of polarization processes takes place at this time. Both C_{oe} and the p_e parameter through this stage indicate the formation of a well-defined pore structure, as the increase in C_{oe} indicates the increase in the connected pore surface area and the decrease in p_e indicates the transformation from the liquid state (in which p_e shows high values) to a solid matrix whereby p_e is decreasing with time.

During this acceleration period, in which both the G_p and the C_p reach a maximum, the aluminate phase reactivity also could be observed on both the C_p and the G_p responses at point F, although this is more pronounced in the G_p response. With regard to the replaced mixes in Figure 5.39, both the silicate and the aluminate phase reactivity merge and manifest themselves as one peak due to the infilling effect. The C_{oe} response during this stage continues its increasing trend, and the aluminate reactivity manifests itself as a change in the slope as is evident in Figure 5.40(b). This renewed reactivity of the aluminate phase on the C_{oe} response also diminishes as the replacement percentage in the mixes increases.

The period between F-M

For the pure cement pastes, the C_{oe} continues in its increasing trend until it peaks at point M in Figure 5.40(b) at which the continuous decreasing in the size of the connected pores due to the growth process, overcomes both the increasing effect due to the surface area of the connected pores as well as the increasing effect due to the AFt/AFm transformation. C_{oe} peaks for all the cement pastes within the monitoring period (24hrs) at point M. On the other hand, for the GGBS mixes the increasing trend extends beyond the initial (24hrs) which indicates the slow reduction in porosity in the replaced mixes due to the slow reactivity of the SCMs.

With regard to the effect of w/b for both C_{oe} and p_e , both these parameters increase with increasing w/b. Through the acceleration peak and thereafter, the higher w/b, the higher C_p values obtained, as could be noticed at the age of 24 hours for the pure cement pastes in Figure 5.38(e). The G_p electrical parameter also shows an increase in its value as the w/b increases in the mixes after the growth peak.

With regard to the replacement percentage effect on both C_p and the G_p (see Figures 5.39 (d) and (e)), a clear decreasing trend is evident for both these parameters as the replacement percentage in the mixes increases. This is particularly the case at early ages as the 35% GGBS 0.35w/b records the highest value for both parameters in comparison to the other mixes. At later ages, a cross-over takes place as at the age of 25hrs the higher the replacement level, the higher the G_p value due to the high conductivity of these mixes after setting. With regard to C_{oe} , as the replacement percentage increases, this parameter shows a decrease in its value, especially >10hrs. This could be attributed to the poorly developed pore structure for the replaced mixes at this age which produces less solid/liquid interfaces.

It should be emphasised that the electrical model accounts for the total dispersed particles in the mix, and is not selective towards the effect of the GGBS alone or the cement phase alone. However, due to our knowledge with regard to the early reactivity of the cement particles in comparison to the GGBS, the response of the G_p and the C_p could be attributed primarily for the cement particles, however this will not eliminate the fact that nucleation and growth processes are also taking place on the surface of the inert particles in the mix (GGBS), which could contribute to the observed electrical response for C_p .

Fly ash equivalent electrical circuit

Figure 5.41 shows the Nyquist plot for the 35%FA0.35w/b, and 65%FA 0.35w/b samples at the age of 2hrs after mixing with water. For comparison, the PC0.35w/b at this time is also plotted. Three main observations are evident when fly ash is introduced into the mixes, which are:

- a) By increasing the fly-ash replacement level, the impedance of the samples increases as the complex plot gets progressively displaced to the right. This is due to a dilution effect of the fly-ash and also acting as an inert filler.
- b) A very noticeable plateau region develops in the Nyquist plot between the electrode polarization spur on the right-hand side and the bulk arc on the left hand-side. The prominence of this plateau region, which is denoted by the letter 'V' in Figure 5.41, is directly related to the quantity of the fly-ash in the mix.
- c) From Figure 5.42(a), it is evident that as the fly-ash content of the mixes increases, an increase in the permittivity at the bulk frequency region is detected, particularly

over the range 100kHz-1MHz (Figure 5.42(b)). The plateau, has been related to the unburned carbon in the fly-ash material (McCarter et al., 1999; McCarter et al., 2004; McCarter et al., 2009; Suryanto et al., 2017), and is attributed to the increase in the surface area which the unburned carbon introduces in the mixes, thereby increasing the permittivity of the bulk response.

Therefore, in order to model the apparent electrical response obtained from the fly-ash mixes at this early hydration period, the dispersed unburned carbon in the mixes should be considered as an additional dispersed phase. From this, the proposed EEC (Figure 5.43(a)) to account for the fly ash addition has been constructed from 4 conduction paths in which two of them, C_p/R_p and R_e/CPE_e represent the same physical meaning which have been proposed for the pure cement pastes in Figure 5.36. Two additional parallel paths C_c/R_c and C_f/R_f on Figure 5.43(a) have been assumed to be related to the electrical processes on the surface of the unburned carbon, and the dispersed fly-ash in the mixes respectively.

Table 5.11 and Table 5.12 present the best fit parameters for both the 35%FA0.35w/b and the 65%FA 0.35w/b at different ages using the EEC shown in Figure 5.43 (a). Figure 5.43(b) shows the experimental data for the 65%FA 0.35w/b at different ages as well as the best fitting curve by the use of the EEC shown at Figure 5.43(a) and the electrical parameters values in Table 5.12.

It is interesting to note from the results shown at Table 5.11 and Table 5.12, that the capacitances C_c , C_p and C_f differ from each other by at least an order of magnitude, as the C_c is in the range of 10^{-8} F, whereas the C_f and the C_p are in the range of 10^{-9} F and 10^{-10} F, respectively. This indicates that the electrical paths which these capacitances represent, originate from different phases which are dispersed with in the material. With regard to C_p , this has values which are comparable to the value of the dispersed cement particles presented in Table 5.10. Due to the relatively high capacitance for the C_c this could be related to double layer polarization processes on the surface of the unburned carbon in the mix, therefore the C_f could be related to the spherical dispersed fly ash in the mix.

Figure 5.44 shows the temporal response for the 35%FA 0.35w/b. The 65%FA 0.35w/b paste is not discussed as this level of replacement is higher than would normally be specified in concreting operation. From this figure, several observations could be deduced, which are:

- a) As shown in Figure 5.44, despite the difference in the values between the C_c , C_p and C_f , all the mentioned capacitors display similar features through time which are comparable to the C_p response in the case of the pure cement paste. This would suggest that the surface of both the unburned carbon as well as the fly-ash represents a potential growth site for the different hydration products. This can be proved by assessing the surface of the fly-ash at different hydration ages as shown in Figure 5.45. It is clear that at the age of 5.5hours Figure 5.45(b) and (c), the surface of the fly-ash is covered by hydration product therefore acting as a growth site.
- b) With regard to the CPE_e parameter which represents the polarizability of the connected liquid phase, the C_{oe} parameter with regard to the 35%FA0.35w/b shows a continuous increasing trend with different slopes as in the case of the pure cement pastes due to the formation of the connected pores surfaces as well as due to the AFt/AFm transformation process.
- c) The CPE_e exponent, p_e , parameter for the 35%FA0.35w/b mix, shows a typical cement paste behaviour, which shows high values at early ages which decrease gradually as the rigidity of the mix increases.
- d) With regard to the G_e parameter, again, this parameter displays a conductivity-like behaviour; as in the case of the pure cement pastes.

5.3.7 Concrete mixes early hydration electrical response

With regard to the bulk material related electrical parameters for concrete mixes, Figure 5.46 and Figure 5.47 show both the conductivity and the normalised permittivity response, respectively, for different concrete mixes through the initial 24hrs after mixing. From these Figures, both the conductivity and the permittivity response for concrete mixes are, generally, similar to the response of their cement pastes counterparts.

Electrical conductivity (σ)

In terms of the conductivity, it shows a similar trend as the cement paste, however the values of the conductivity of the concrete are considerably less. This could be noticed by comparing the values at the early peak for the concrete and the cement pastes which recorded 0.23S/m and 1.7S/m, respectively. This decrease in the conductivity is due to the inclusion of the aggregate and is explained in terms of the addition of resistive particles with a conductivity of σ_i , to a highly conductive cement-paste with conductivity,

σ_a . The bulk conductivity in this case could be expressed through the following simple mixing law (Schwarz, 1962):

$$\sigma = \sigma_a \frac{(\sigma_i + 2\sigma_a) + 2V(\sigma_i - \sigma_a)}{(\sigma_i + 2\sigma_a) - 2V(\sigma_i - \sigma_a)} \quad (5.5)$$

In which V is the volume fraction of the suspended resistive particles. By assuming a low-conductivity aggregate, it is clear that as the volume fraction of the suspended particles increases, the bulk conductivity of the suspension decreases. Therefore, the volume fraction of the aggregate with respect to the total volume of the cement affects the conductivity of the bulk material.

Normalised permittivity response (ϵ_N)

With regard to the normalised permittivity response ϵ_N , when it is compared with cement-paste response, the concrete mixes demonstrate more pronounced features through time in comparison to the conductivity-like behaviour which is displayed by the cement-pastes response. This could be attributed to the relatively large electrical impedance of the concrete mixes in comparison to the cement pastes, as in this case the electrodes polarization masking effect decreases significantly in comparison to that of the cement paste, therefore the bulk features appear more pronounced. With regard to the temporal response for the ϵ_N parameter, the following points should be noted:

- (i) As in the case of the corrected EP response for the cement pastes (see Figure 5.25 (d)), the concrete mixes ϵ_N response shows an early age peak due to the increase in the CH super saturation in the mix.
- (ii) After the CH peak, a growth induction period is evident in the response of the concrete mixes, similar to the case of the cement pastes. In this induction period, and prior the acceleration period, nucleation processes are taking place.
- (iii) After the growth induction period, a noticeable increase in the ϵ_N takes place, which indicates the presence of the growth process on the surface of the dispersed particles as shown in Figure 5.27 and Figure 5.30.
- (iv) The aluminate phase reactivity also manifests itself as a peak in the 100kHz-500kHz ϵ_N responses (Figure 5.47). The polarizability due to aluminate reactivity can easily be distinguished from that due to growth polarization processes at lower replaced mixes, in contrast to the higher replaced mixes.

- (v) As the measuring frequency increases, the double-layer polarization process resulting from the C-S-H growth (5hrs) in the mixes relaxes, as the 1MHz frequency displays a continuous increasing trend through time which peaks at ~15hrs for the pure Portland cement concrete mix. However, for the high replaced mixes, it continues its increasing trend. This increase in the 1MHz polarization processes is due to the increase in the solid/liquid interfaces, as well as due to ettringite /monosulphoaluminate transformation process which both increase interfacial polarization process in the mixes.

5.3.8 Superplasticizers (SP) effect on the electrical response of concrete at the early hydration stage

In this study, a commercial Polycarboxylate based (SP) was used, and Figures 5.48 – 5.50 show the bulk electrical response for the pure Portland cement concrete, the 35% GGBS and the 65% GGBS concrete mixes with and without SP addition. It could be noticed that the addition of 1% SP to the mixes has a retarding effect on the hydration process during the first 24hrs of the samples age and this could be noticed through the following observations:

- (a) By considering the time at which the early hydration peak takes place (which represents the CH supersaturation level), the addition of 1% SP retards this conductivity peak which is more noticeable in the case of the replaced mixes than the pure cement concrete mixes.
- (b) The SP retarding effect on the mixes could be observed on the late reactivity of the aluminate phase which is represented by a change in the slope of the $d\sigma/dt$ curve. This feature is delayed to ~9hrs, in comparison to ~7.5hrs for the SP free concrete mixes.
- (c) The SP mixes have a lower conductivity value at the CH peak when compared with the SP free mixes.
- (d) Regarding the ϵ_N response for the SP mixes, a noticeable retarding effect is detected, and clearly observed by comparing the ages at which the increase in this electrical parameter takes place due to the increase in the surface area of the dispersed particles. As for the Portland cement concrete with SP, this increase takes place at the age of ~6hrs, which is delayed by almost 2hrs from the SP-free Portland cement concrete mixes (see Figure 5.47). By considering the high replaced mixes as an example, the growth period on ϵ_N is delayed to ~8hrs in comparison to ~6hrs in the SP-free mixes.

5.4 Summary:

In this chapter, both the conductivity and the permittivity responses for pure cement pastes, cement pastes with added SCM's, cement pastes with gypsum and concrete mixes, have been discussed and explained through the first 24hrs. The conductivity during this period, passes through six identifiable stages which have been explained in terms of the, early rapid dissolution period, the induction period, the precipitation of CH, the initiation of the nucleation and C-S-H growth process, the aluminate phase reactivity and the diffusion controlled stage.

The permittivity was shown to be frequency dependent as it decreases with increasing frequency. The electrode polarization process was shown to have a masking effect on bulk polarization processes; as a result, the electrical response was corrected by an equivalent electrical circuit to reveal polarization processes originating from the bulk material. The bulk permittivity at 100kHz-500kHz has been shown to pass through different distinguishable stages through the initial 24hrs which are as follows:

- (a) A rapid decrease in this parameter takes place during the first 1-2hrs, and is attributed to 4 possible reasons which are: the rapid decrease in the electrode polarization, the rapid decrease in the cement dissolution process, the formation of early hydration products on the cement grains and the coagulation process between the cement grains due to the active electrostatic forces.
- (b) A low reactivity period which extends between 2hrs-4hrs, which marks the start of the acceleration stage on the calorimeter response as well as the precipitation of the CH on the conductivity response.
- (c) A rapid increase in the permittivity at the age of ~4hrs. This has been attributed to the rapid growth process on the surface of the cement particles.
- (d) At the age of 7-9hrs the permittivity has been shown to be affected by the renewed activity of the aluminate phase by showing an increase in its value.
- (e) At ages >20hrs, the permittivity response has been shown to be affected by the gradual transformation of ettringite to monosulphoaluminate.

The permittivity at 1MHz displayed a conductivity-like behaviour through the initial 24hrs. The concrete mixes had a similar electrical response to the cement pastes, with lower values in terms of the conductivity due to the inclusion of the aggregate. The electrical response for the cement pates has been modelled by assuming an equivalent

electrical circuit in which each electrical path has been assumed to represent a physical meaning in the hydrating system.

The addition of super-plasticiser to concrete showed a delaying effect on all the stages identified from the electrical response.

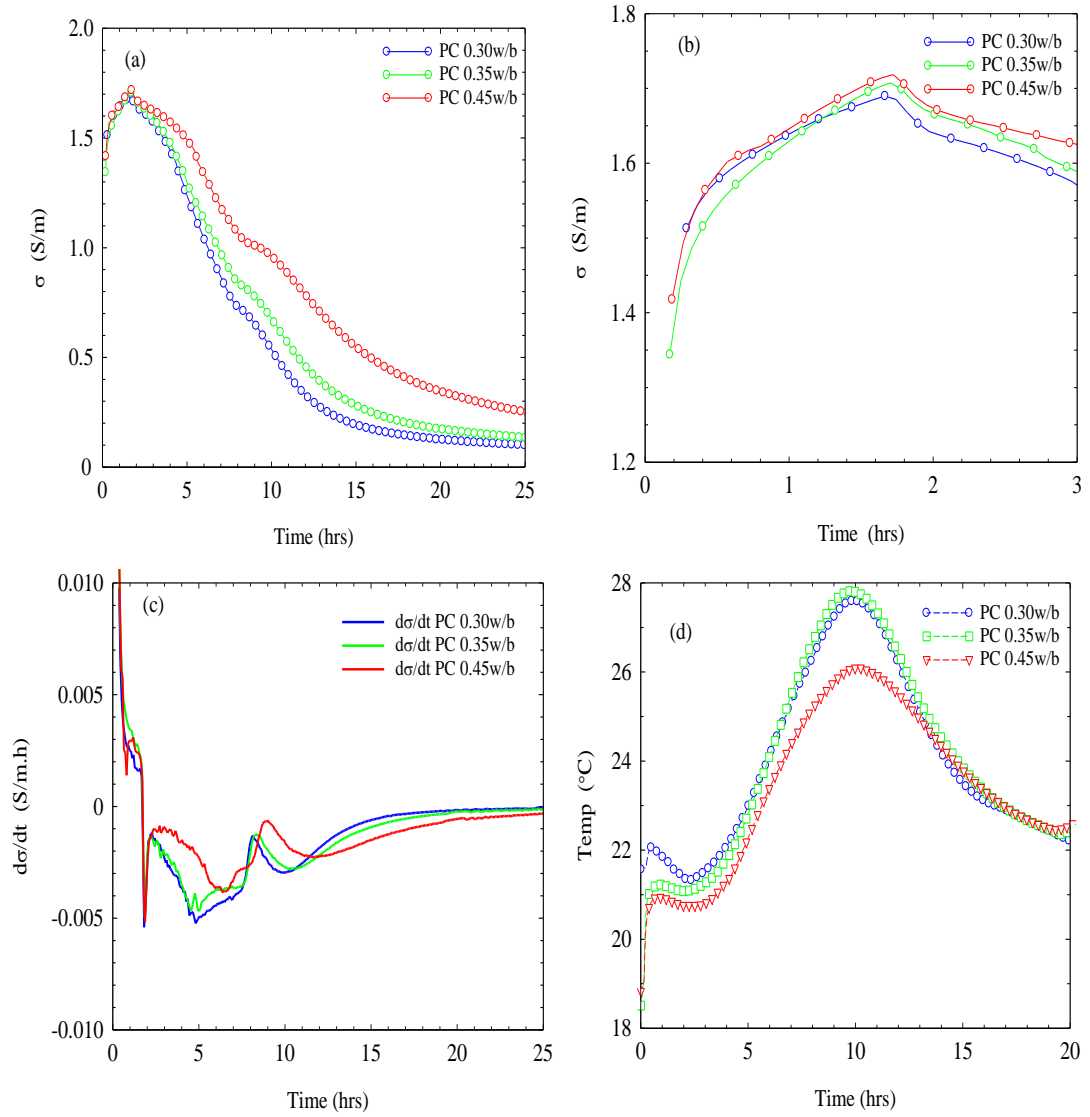


Figure 5.1:(a) and (b) conductivity recorded at 100kHz, (c) conductivity derivative, $d\sigma/dt$, and (d) temperature rise for different w/b cement pastes through the first 24h from gauging.

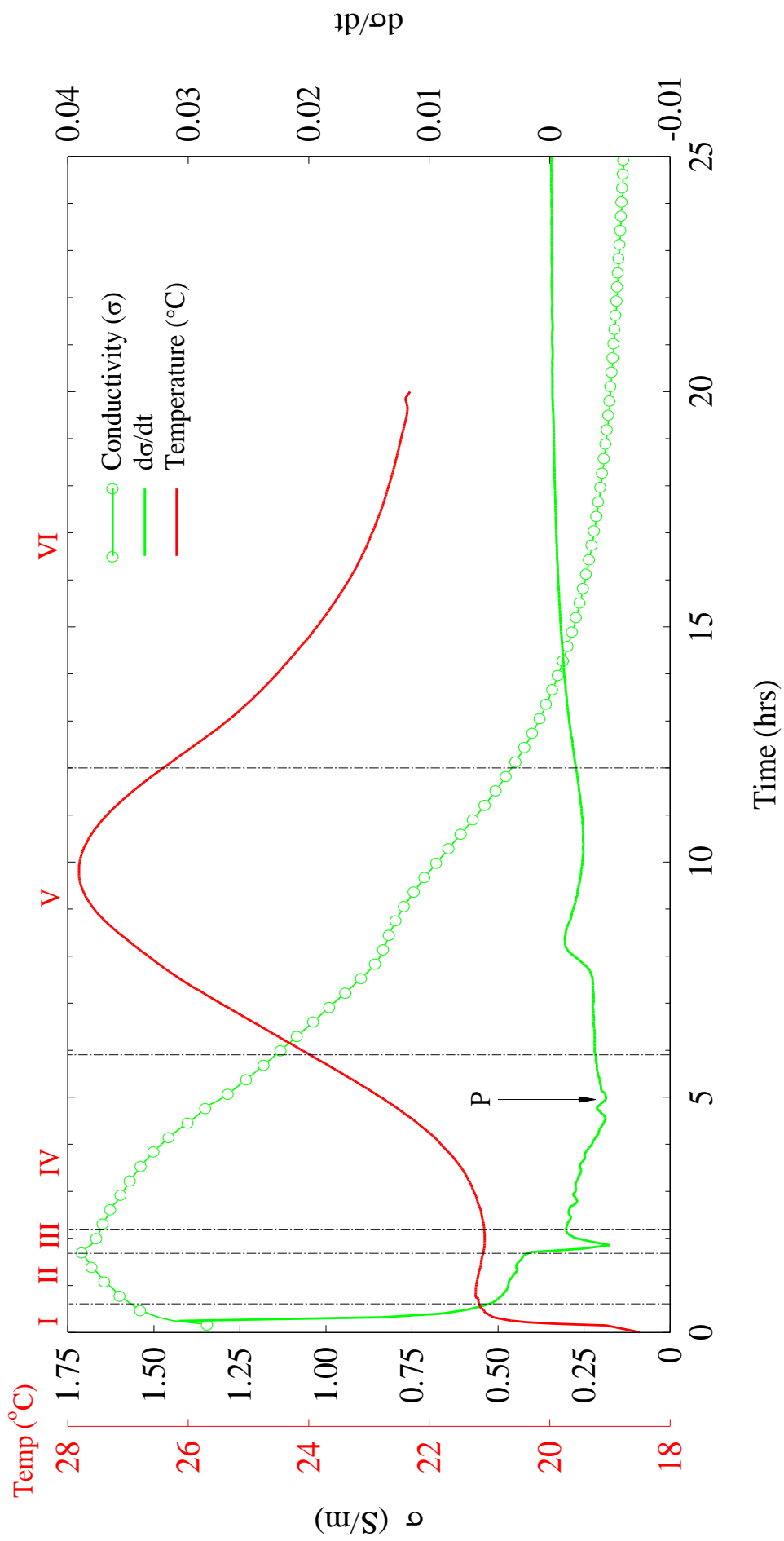


Figure 5.2: Conductivity and Temperature rise through the first 24hrs for PC 0.35w/b.

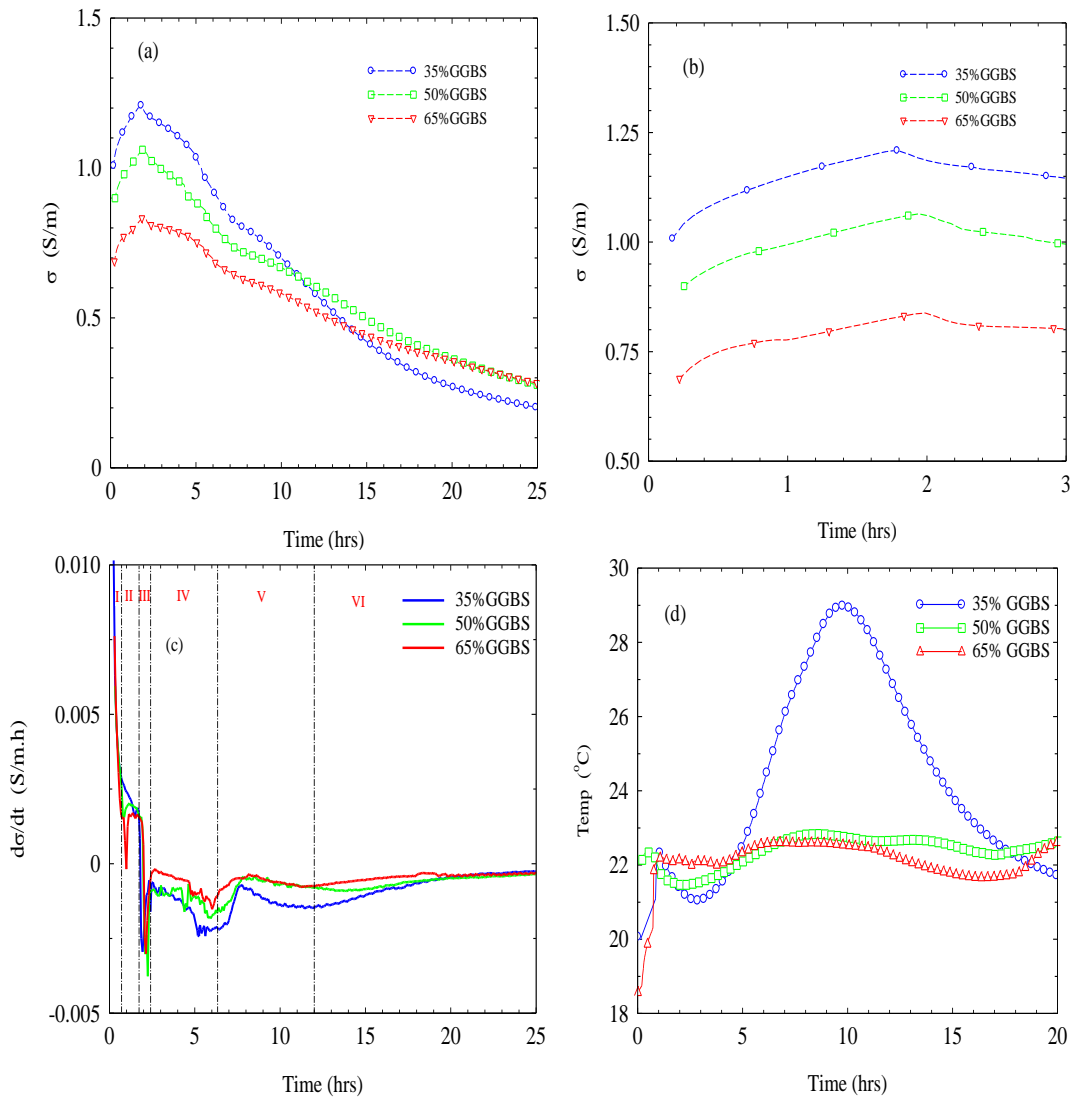


Figure 5.3: (a) and (b) conductivity recorded at 100kHz (c) conductivity derivative, $d\sigma/dt$, and (d) temperature rise for 35%, 50%, 65% GGBS replaced pastes at 0.35w/b through the initial 24h after gauging.

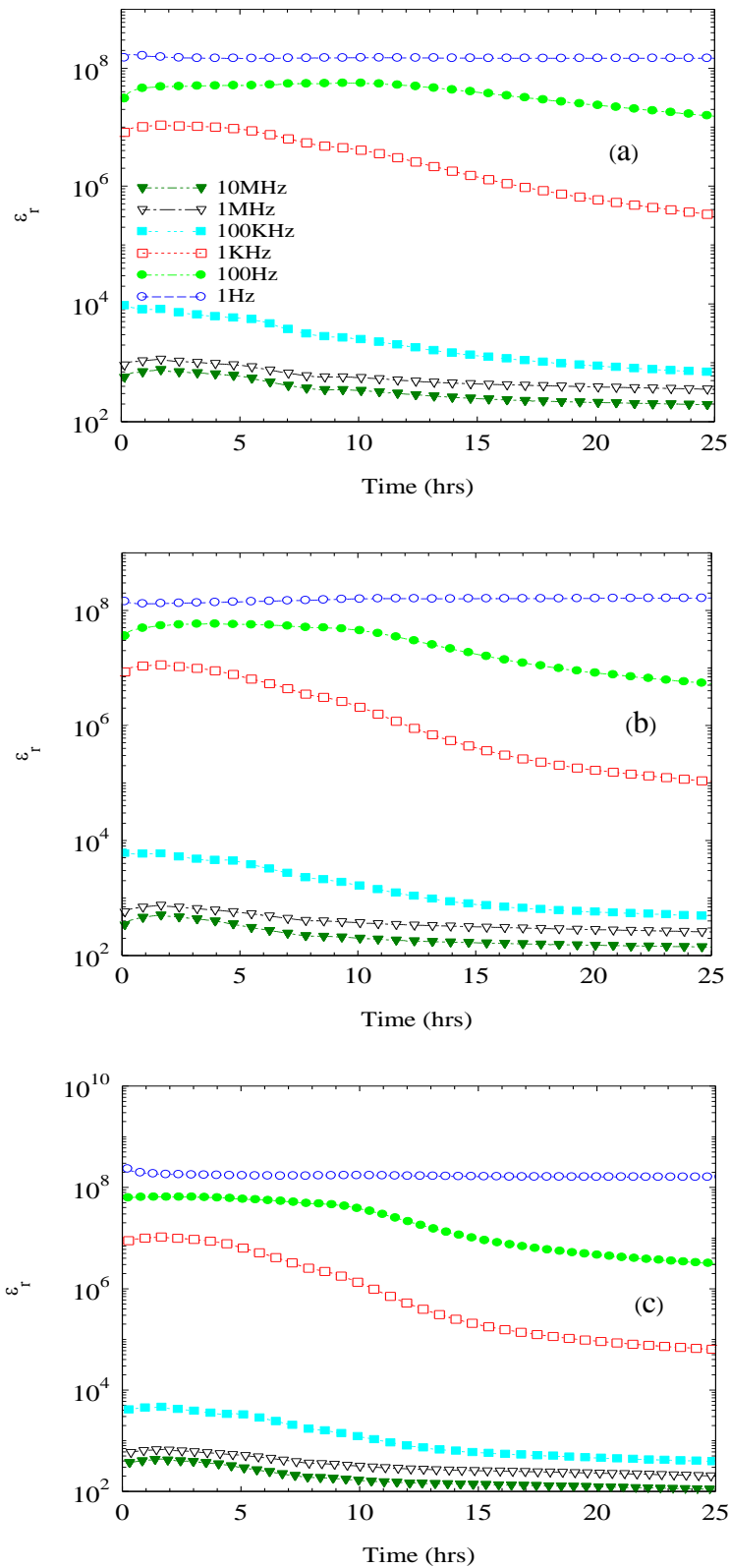


Figure 5.4: PC Relative permittivity at selected frequencies during the initial 24hrs for cement pastes(a) 0.3w/b (b) 0.35w/b and (c) 0.45w/b. (legend in (a))

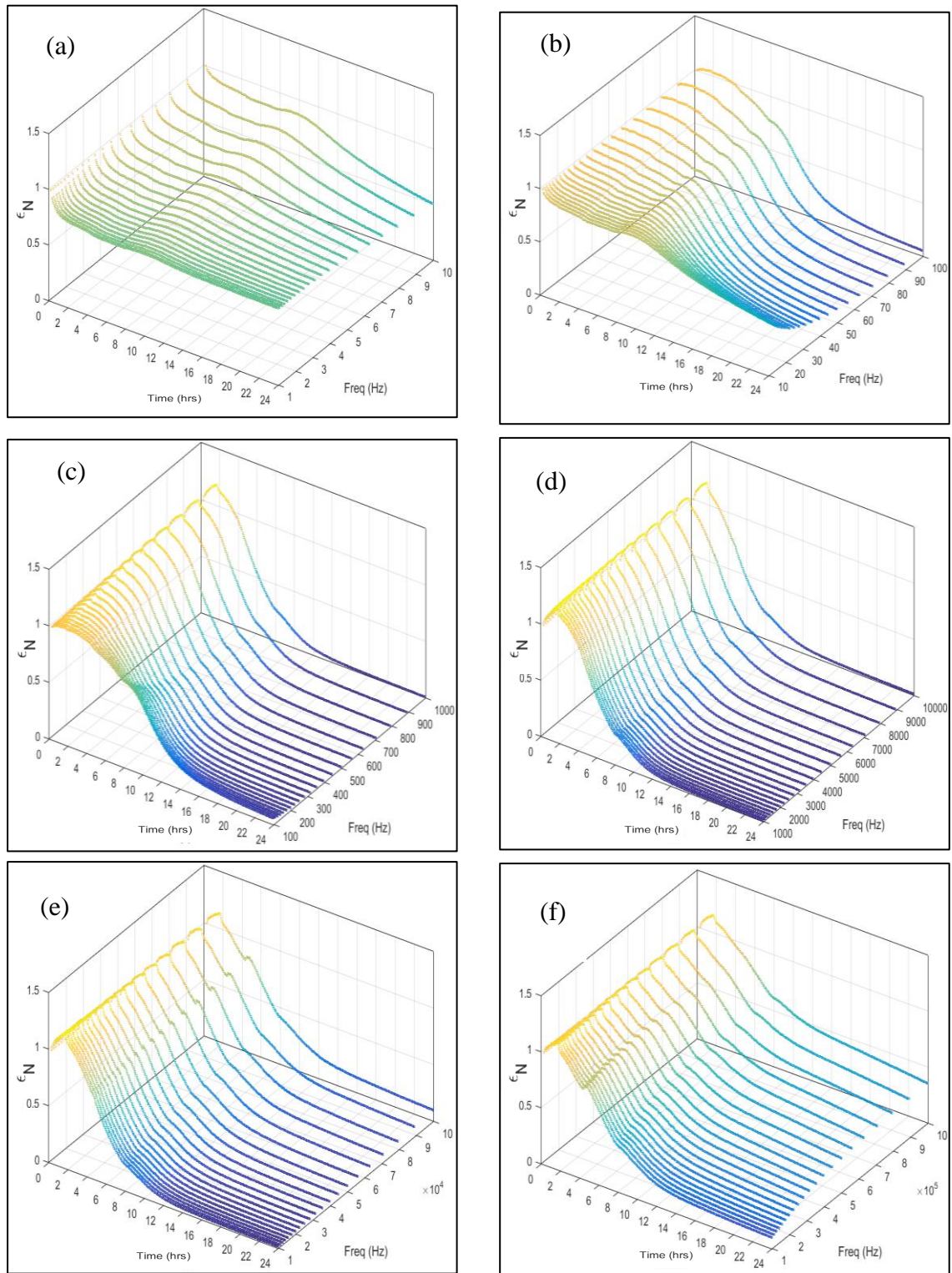


Figure 5.5: Normalised permittivity for PC 0.3w/b paste response through time and frequency (1Hz-1MHz) for the first 24hrs (a) 1-10Hz, (b) 10-100Hz, (c) 100Hz-1kHz, (d) 1kHz-10kHz, (e) 10kHz-100kHz and (f) 100kHz-1MHz.

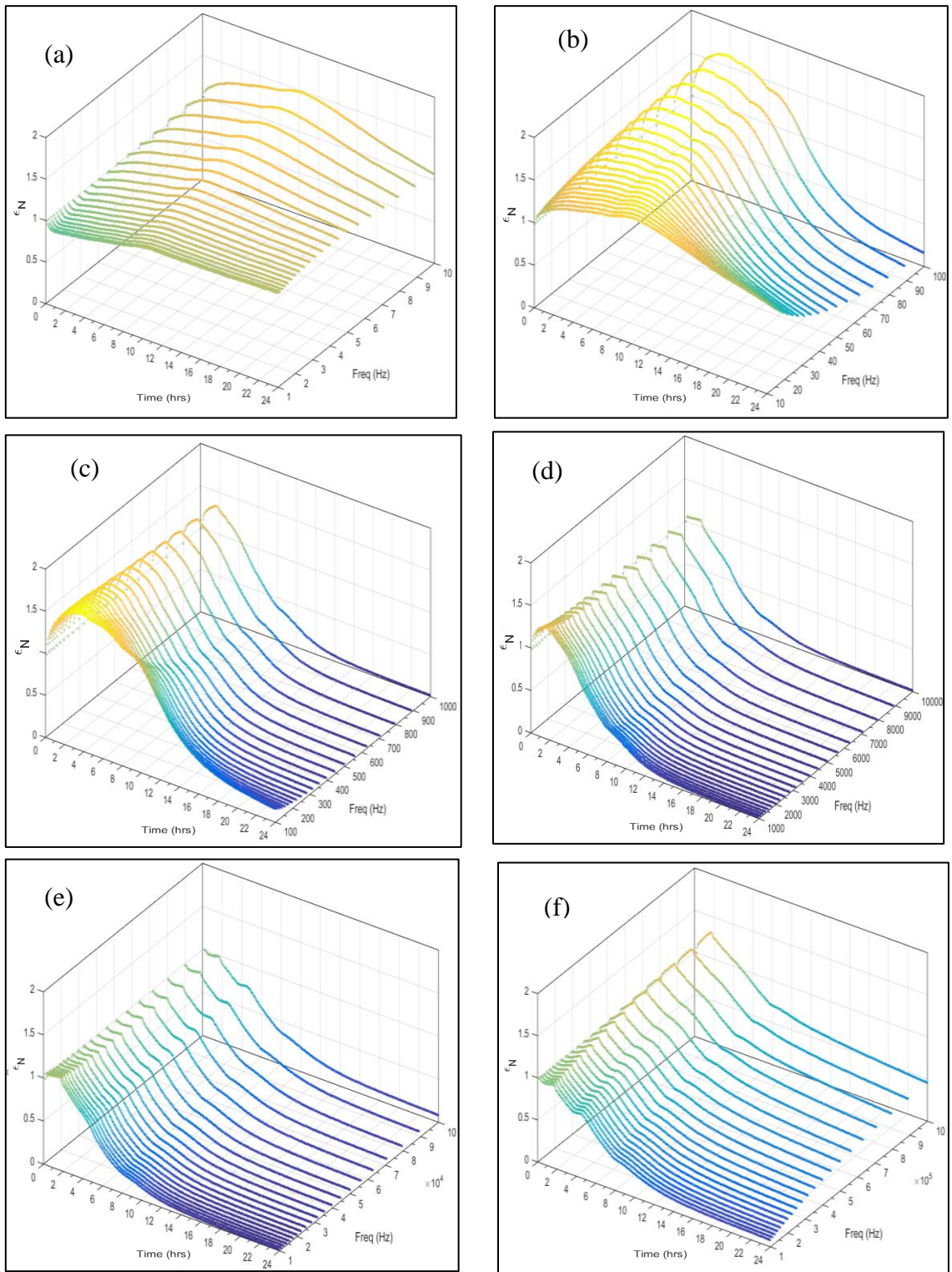


Figure 5.6: Normalised permittivity for PC 0.35w/b paste response through time and frequency (1Hz-1MHz) for the first 24hrs (a) 1-10Hz, (b) 10-100Hz, (c) 100Hz-1kHz, (d) 1kHz-10kHz, (e) 10kHz-100kHz and (f) 100kHz-1MHz.

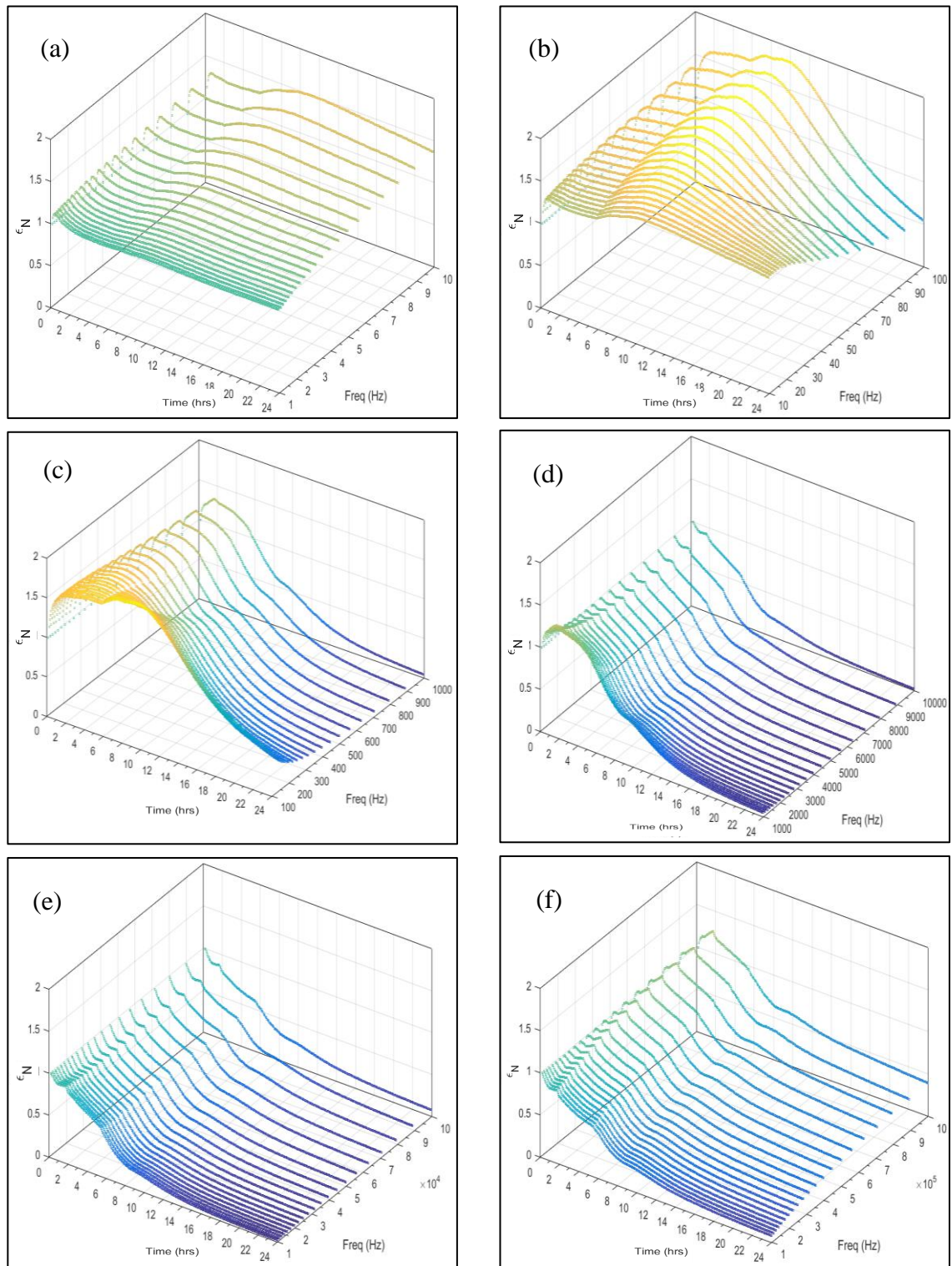


Figure 5.7: Normalised permittivity for PC 0.45w/b paste response through time and frequency (1Hz-1MHz) for the first 24hrs (a) 1-10Hz, (b) 10-100Hz, (c) 100Hz-1kHz, (d) 1kHz-10kHz, (e) 10kHz-100kHz and (f) 100kHz-1MHz.

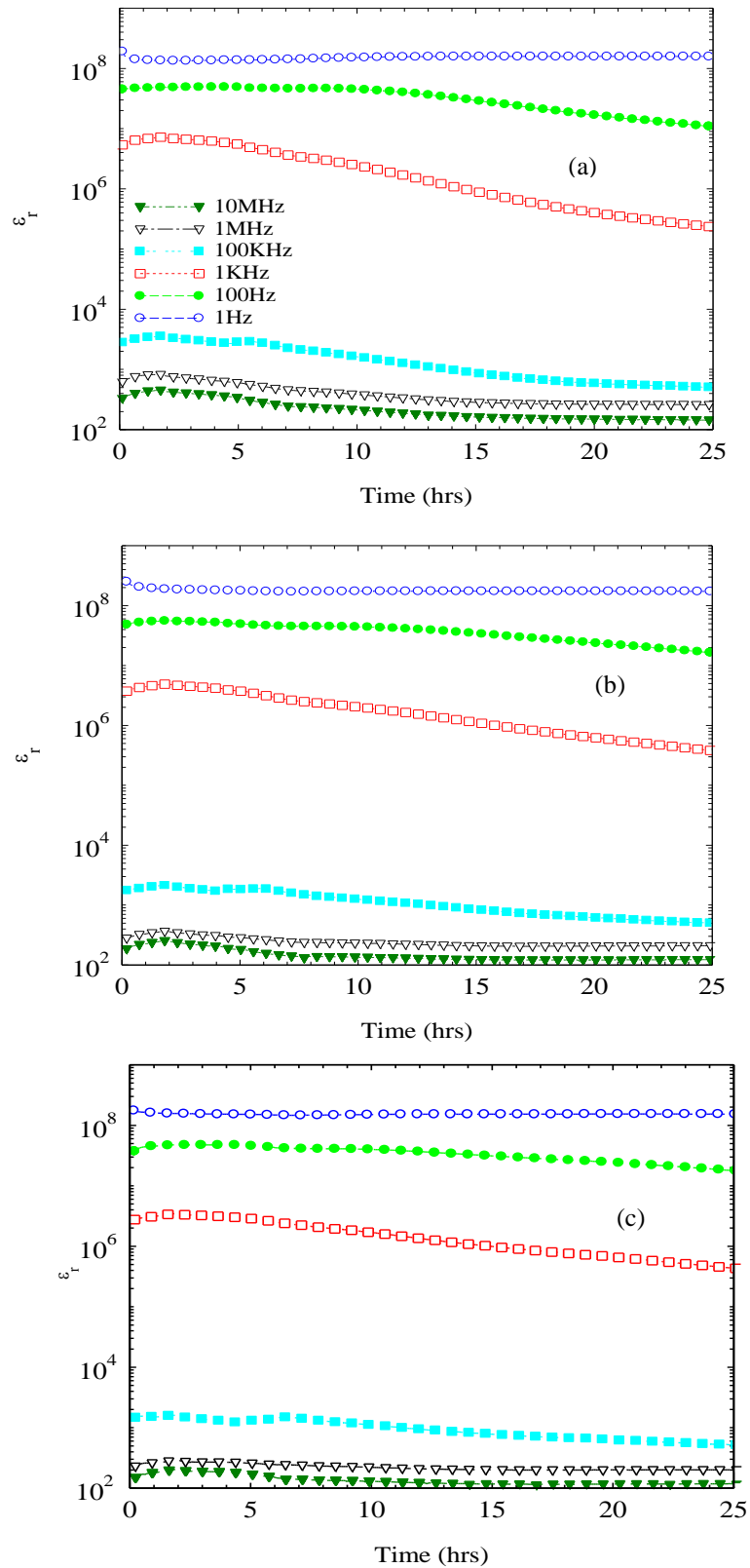


Figure 5.8: Selected frequencies relative permittivity response during the early 24hrs of the samples ages for the (a) 35% GGBS 0.35w/b (b) 50% GGBS 0.35w/b (c) 65% GGBS 0.35w/b [legend in (a)].

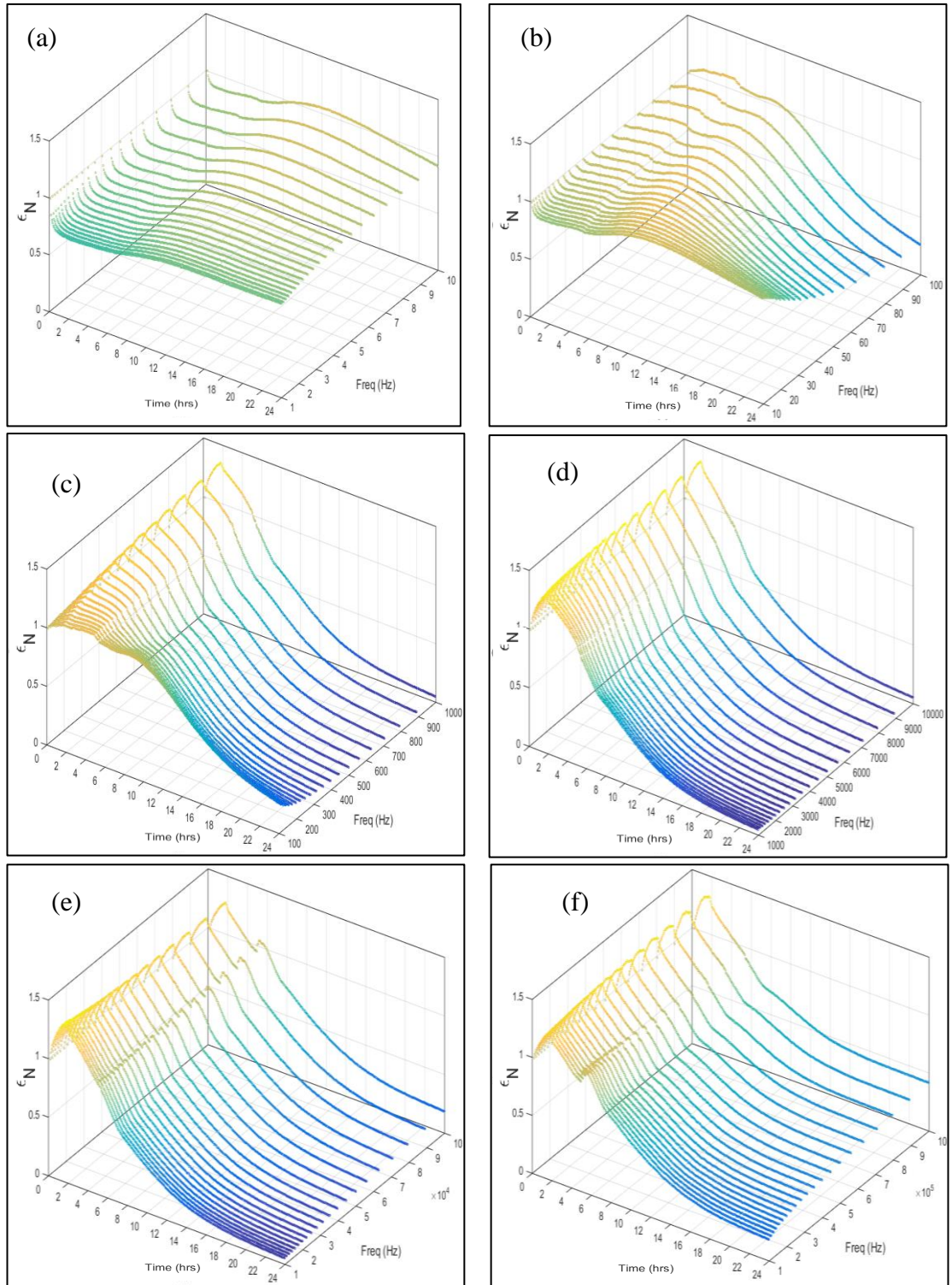


Figure 5.9: Normalised permittivity for 35% GGBS 0.35w/b paste response through time and frequency (1Hz-1MHz) for the first 24hrs (a) 1-10Hz, (b) 10-100Hz, (c) 100Hz-1kHz, (d) 1kHz-10kHz, (e) 10kHz-100kHz and (f) 100kHz-1MHz.

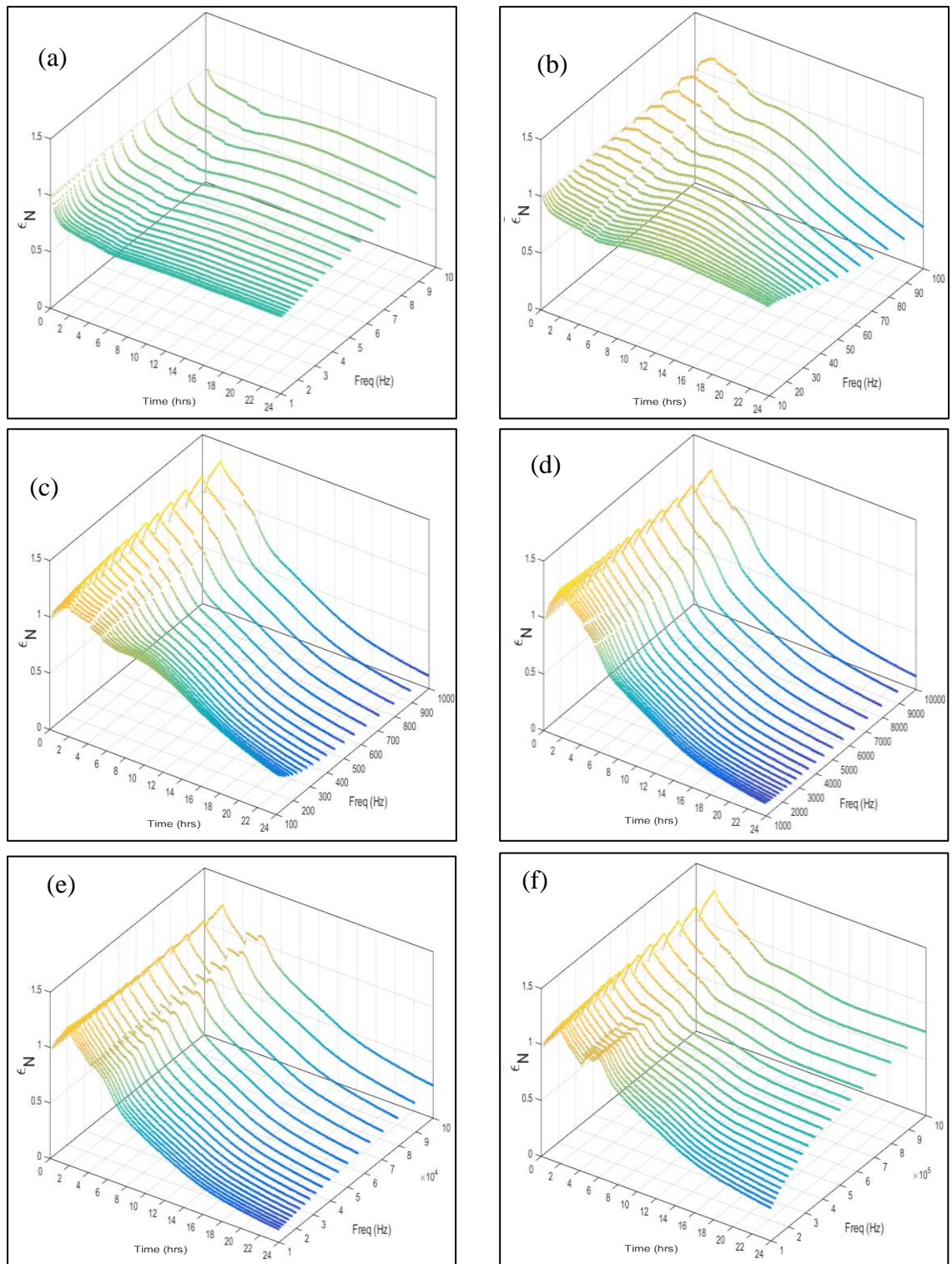


Figure 5.10: Normalised permittivity for 50%GGBS 0.35w/b paste response through time and frequency (1Hz-1MHz) for the first 24hrs (a) 1-10Hz, (b) 10-100Hz, (c) 100Hz-1kHz, (d) 1kHz-10kHz, (e) 10kHz-100kHz and (f) 100kHz-1MHz.

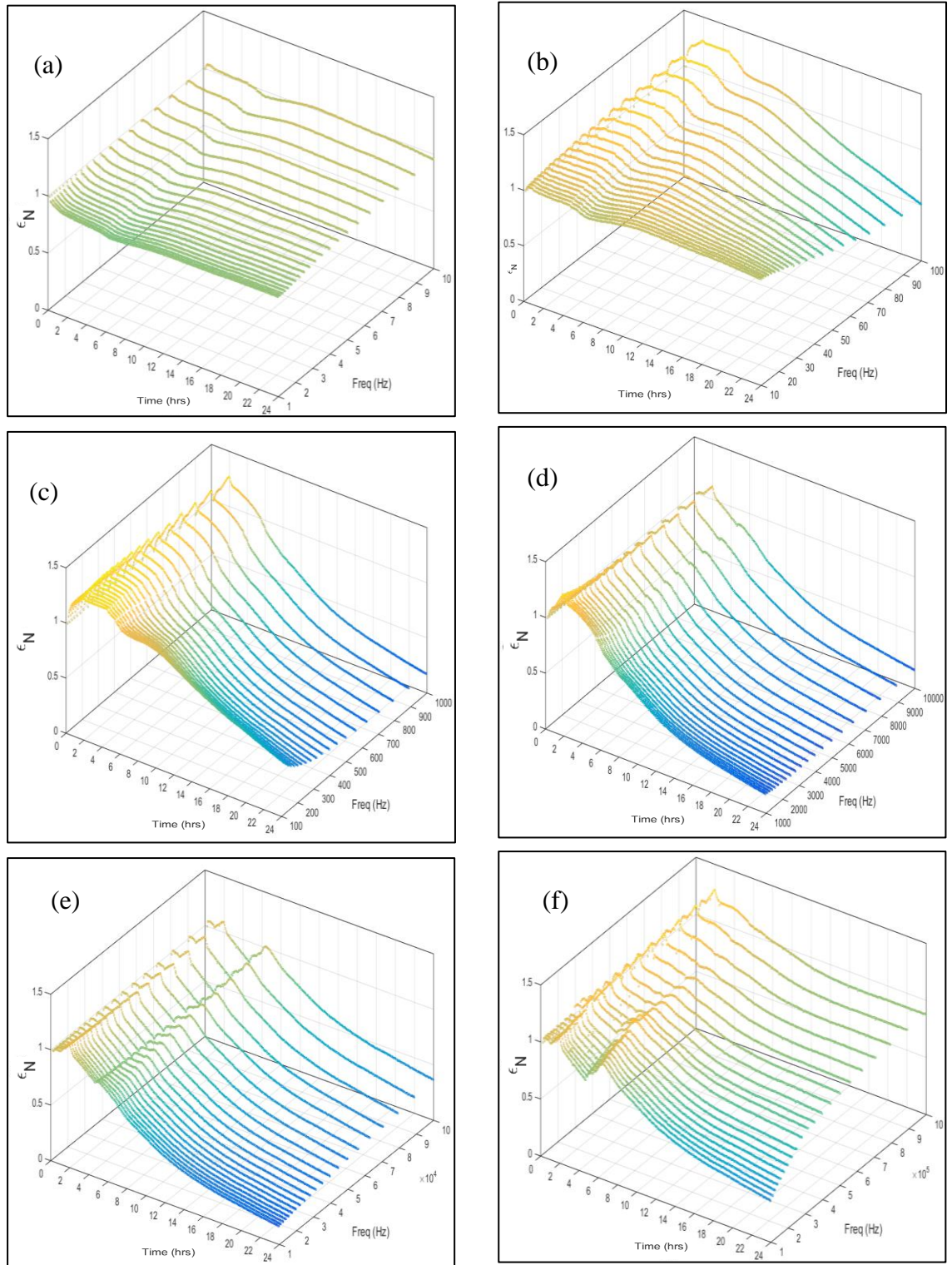


Figure 5.11: Normalised permittivity for 65%GGBS 0.35w/b paste response through time and frequency (1Hz-1MHz) for the first 24hrs (a) 1-10Hz, (b) 10-100Hz, (c) 100Hz-1kHz, (d) 1kHz-10kHz, (e) 10kHz-100kHz and (f) 100kHz-1MHz.

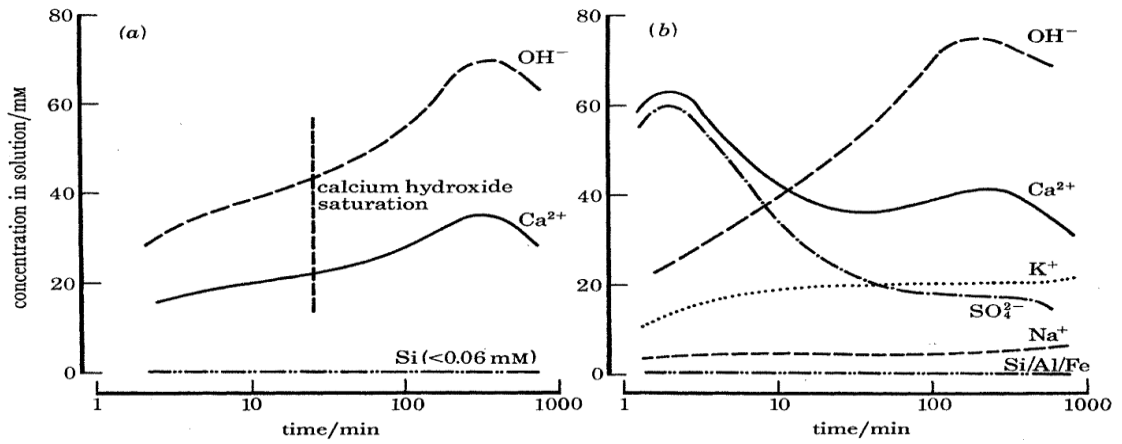


Figure 5.12: Concentration through time for (a) C_3S paste and (b) for Portland cement paste (Double et al., 1983).

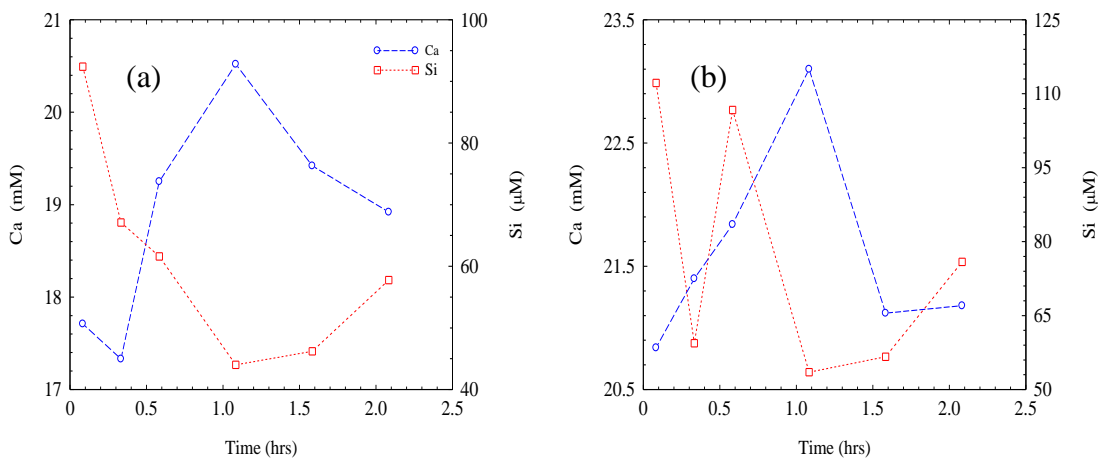


Figure 5.13: Aqueous phase Calcium and silicon concentration during the early hydration period for: (a) 0.4w/b cement paste, (b) 0.7w/b cement paste (Kelzenberg et al., 1998)

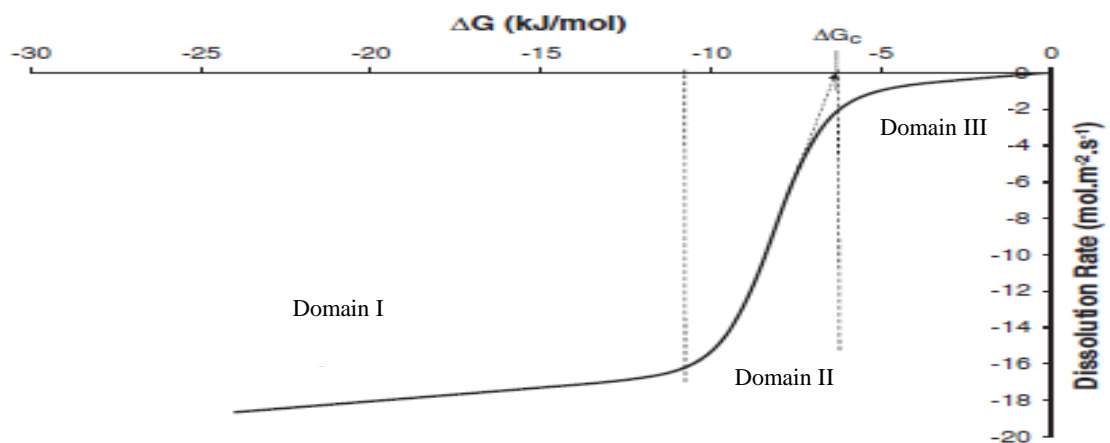


Figure 5.14: Relation between Gibbs free energy of dissolution and dissolution rates of minerals (Lasaga and Lutge, 2001; Nicoleau et al., 2013)

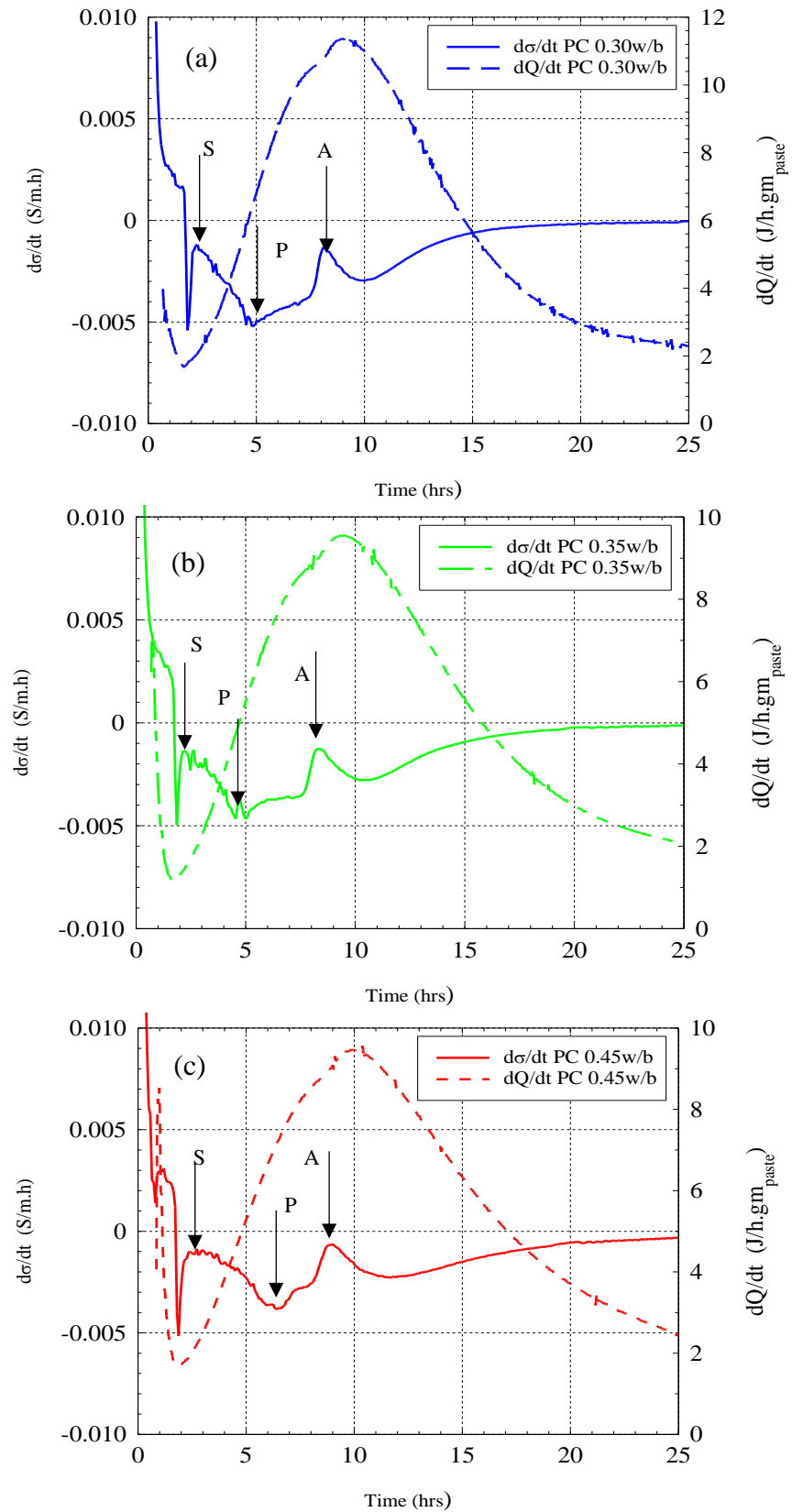


Figure 5.15: Conductivity rate, $d\sigma/dt$, and heat emission rate, dQ/dt , for (a) PC 0.30w/b, (b) PC 0.35w/b, and (c) PC 0.45w/b.

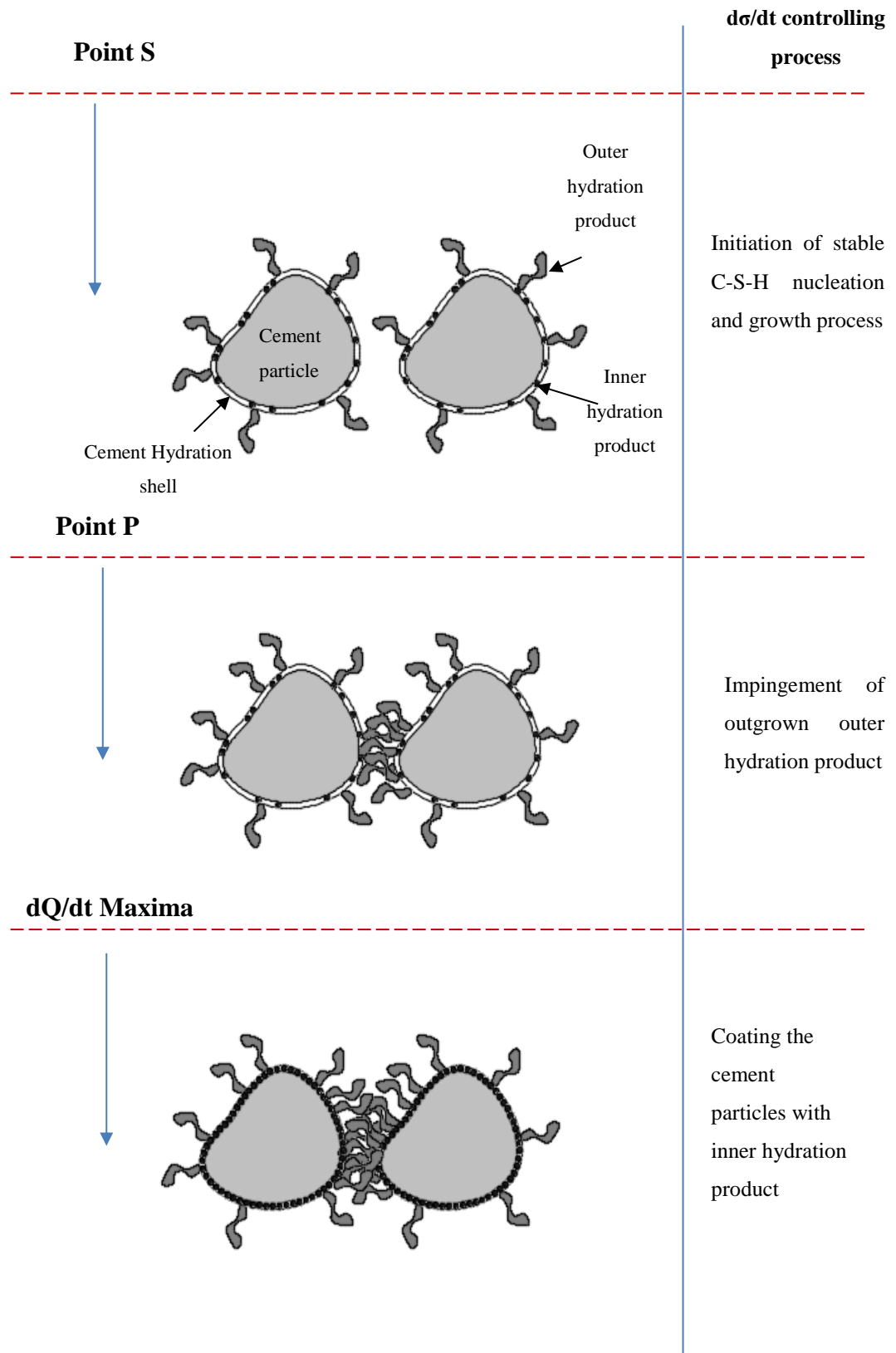


Figure 5.16: Nucleation and growth of hydration product on the surface of the cement particles through the hydration reaction

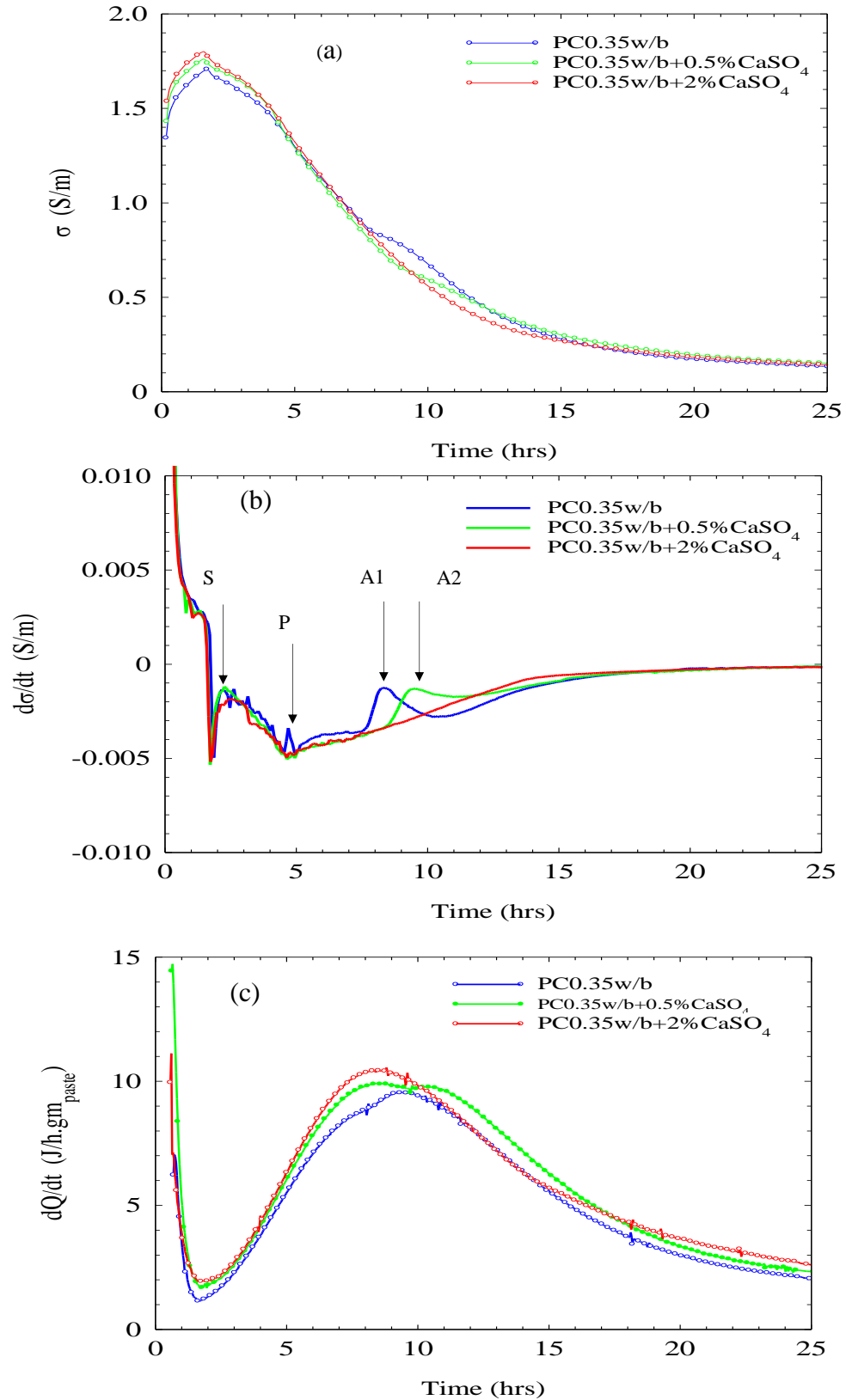


Figure 5.17: (a) Conductivity (σ), (b) conductivity rate ($d\sigma/dt$) and (c) Heat emission rate (dQ/dt) for 0.35w/b cement paste and PC0.35 w/b with two different percentages calcium sulphate additions, 0.5% and 2%.

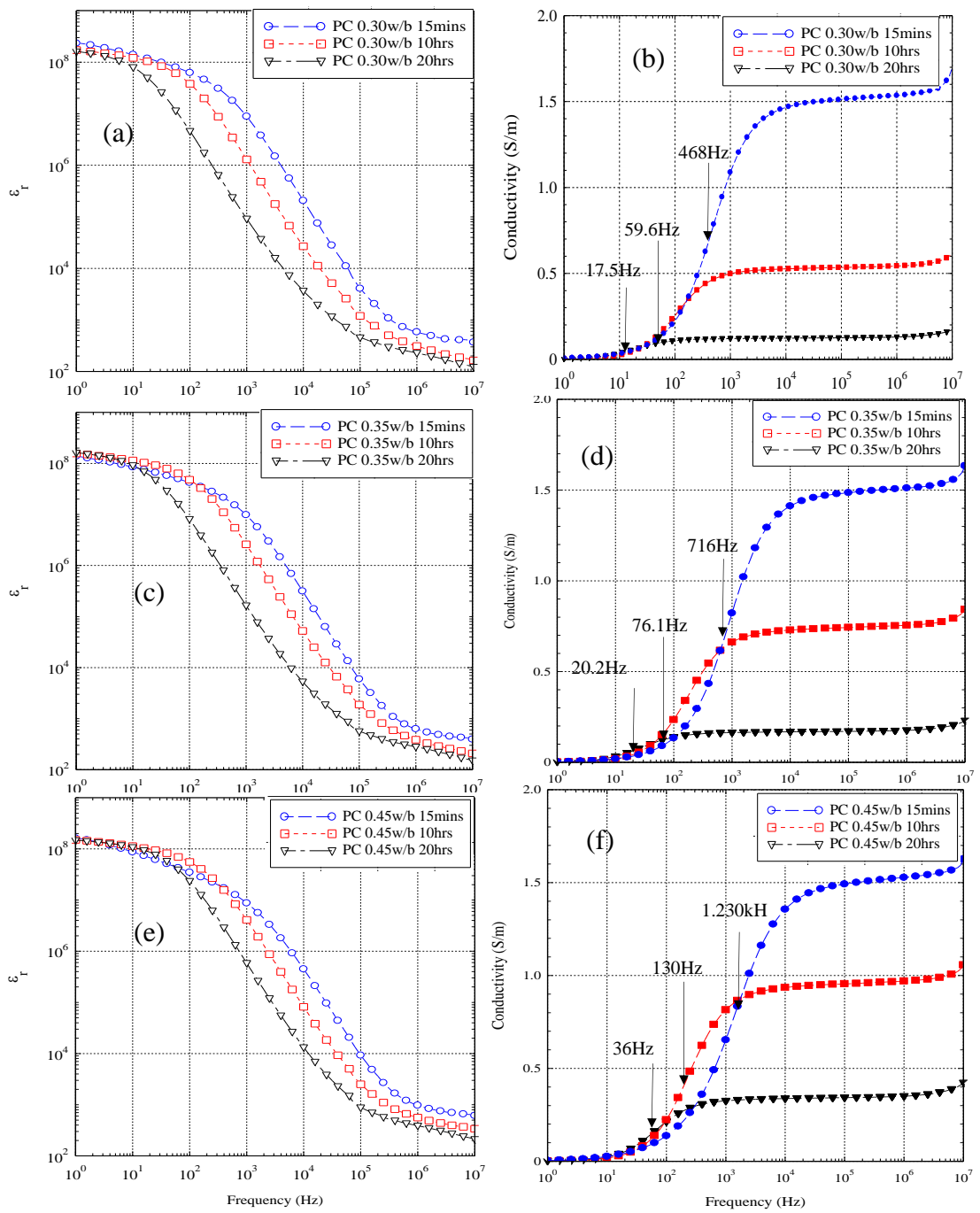


Figure 5.18: Dispersion plots for permittivity and conductivity for PC 0.30w/b, PC0.35w/b and PC 0.45 w/b at the ages of 15mins, 10hrs and 20hrs. The characteristic frequency for conductivity dispersion is indicated.

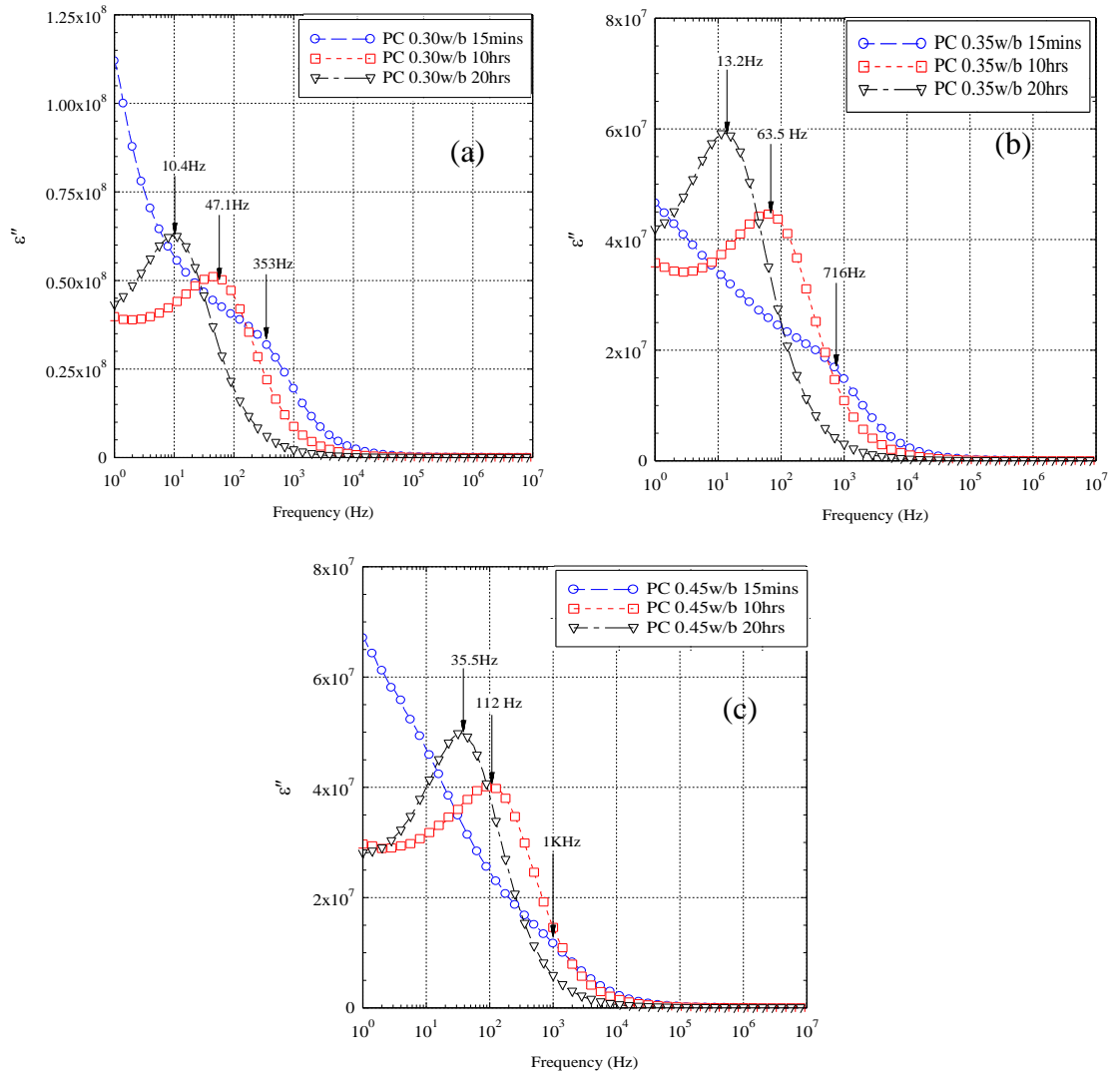


Figure 5.19: Dielectric loss ϵ'' for (a) PC 0.3w/b; (b) PC 0.35w/b and (c) PC 0.45w/b at the ages of 15mins, 10hrs and 20hrs. The characteristic frequency, f_c , is indicated.

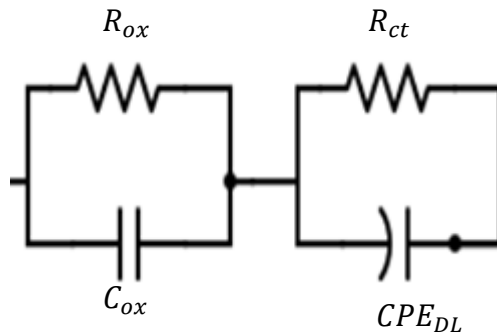


Figure 5.20: Electrical circuit used to model the low-frequency relaxation processes in the measured system

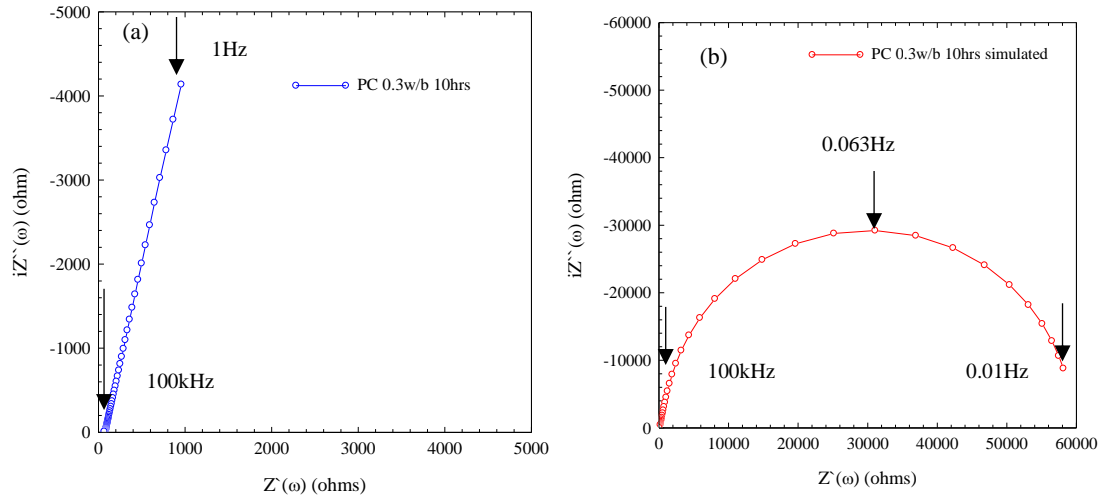


Figure 5.21: (a) Typical Nyquist plot for PC0.30w/b at 9hrs age, (b) simulated electrode processes response by EEC in Figure 5.20. Bulk frequency and the characteristic frequency are indicated in the figures.

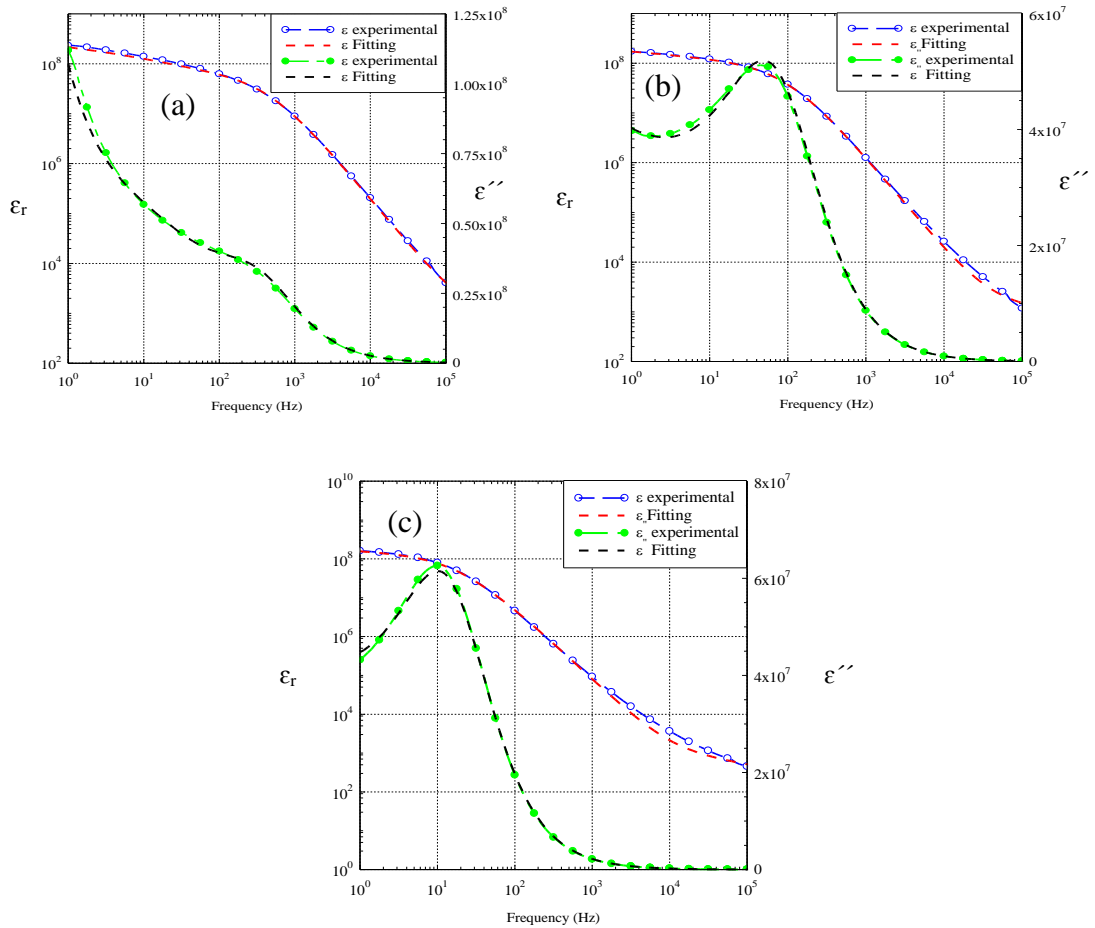


Figure 5.22: PC0.30w/b experimental and fitted response according to the EEC in Figure 5.20 for the relative permittivity and imaginary dielectric constant at the ages of (a) 15mins (b) 10hrs and (c) 20hrs.

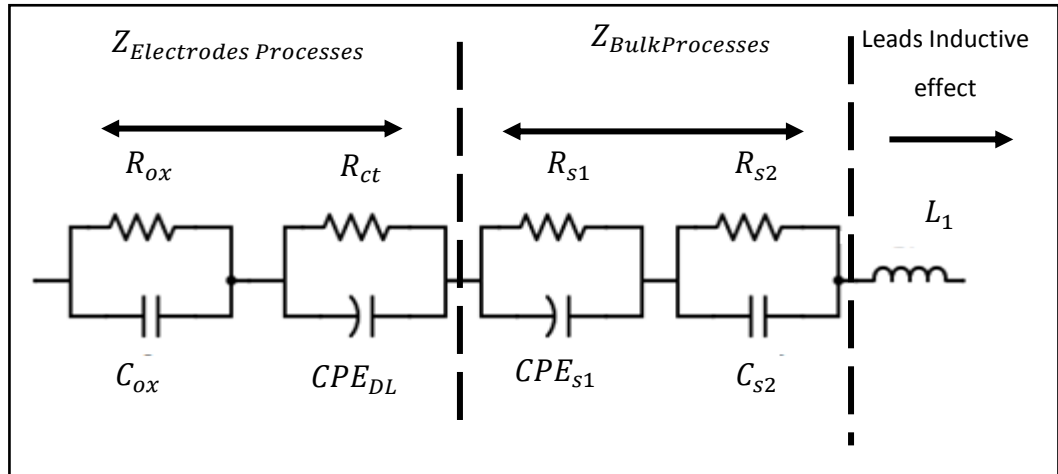


Figure 5.23: Equivalent Electrical circuit used to correct for the EP effect on the obtained electrical response for the different w/b cement pastes samples.

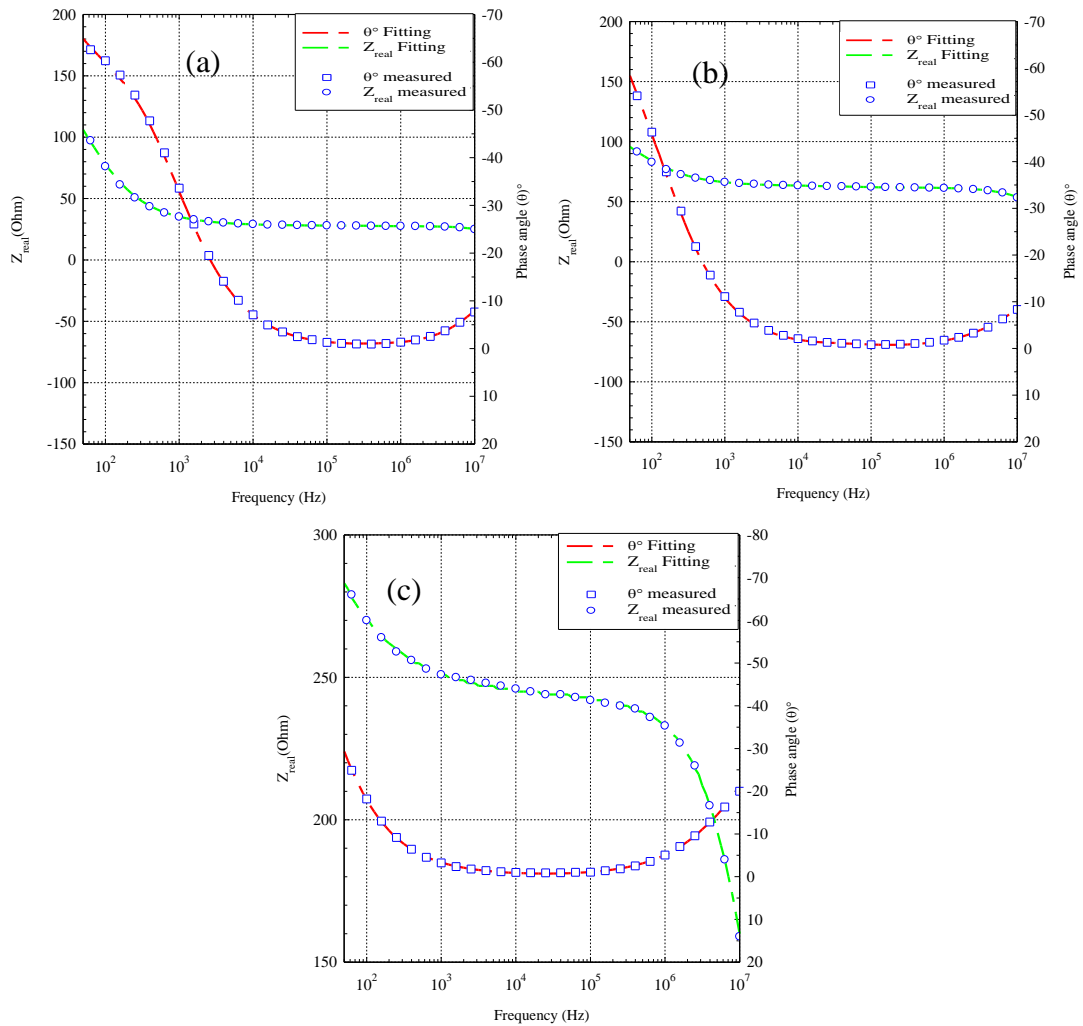


Figure 5.24: Electrical impedance real-part and the phase angle fitted with the EEC in Figure 5.23 for the PC0.30w/b cement paste at the ages of (a) 15mins, (b) 10hrs and (c) 20hrs.

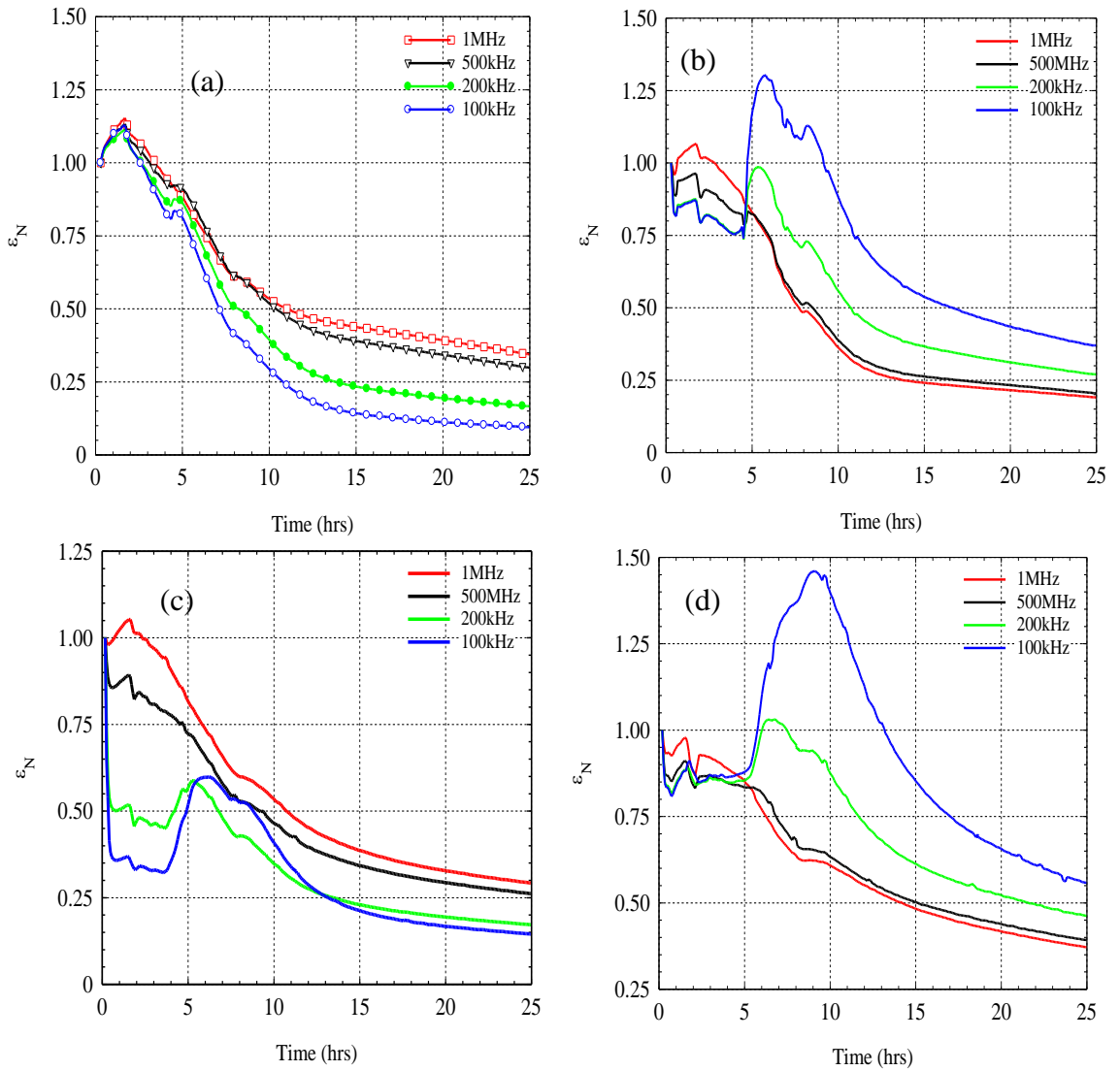


Figure 5.25: Normalised Permittivity response through time for PC 0.30w/b (a) Before EP correction (b) After EP correction (c) Normalised Permittivity response through time for PC 0.35w/b after EP correction (d) Normalised Permittivity response through time for PC 0.45w/b after EP correction.

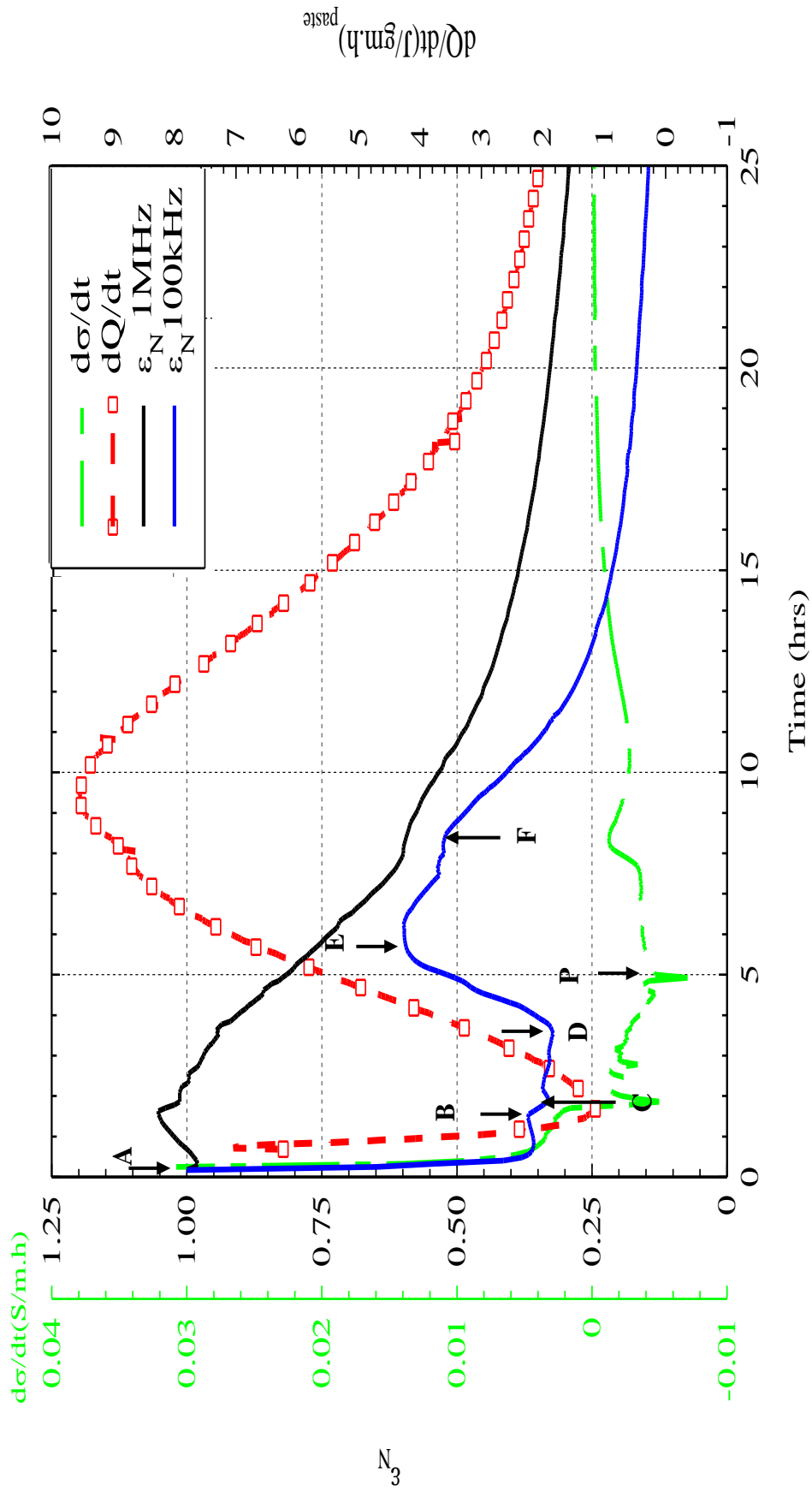


Figure 5.26: Illustration of the different features appearing on the normalised permittivity response ϵ_N during the early hydration period for PC0.35w/b, together with the derivative of the electrical conductivity $d\sigma/dt$, and the calorimeter heat emission rate dQ/dt .

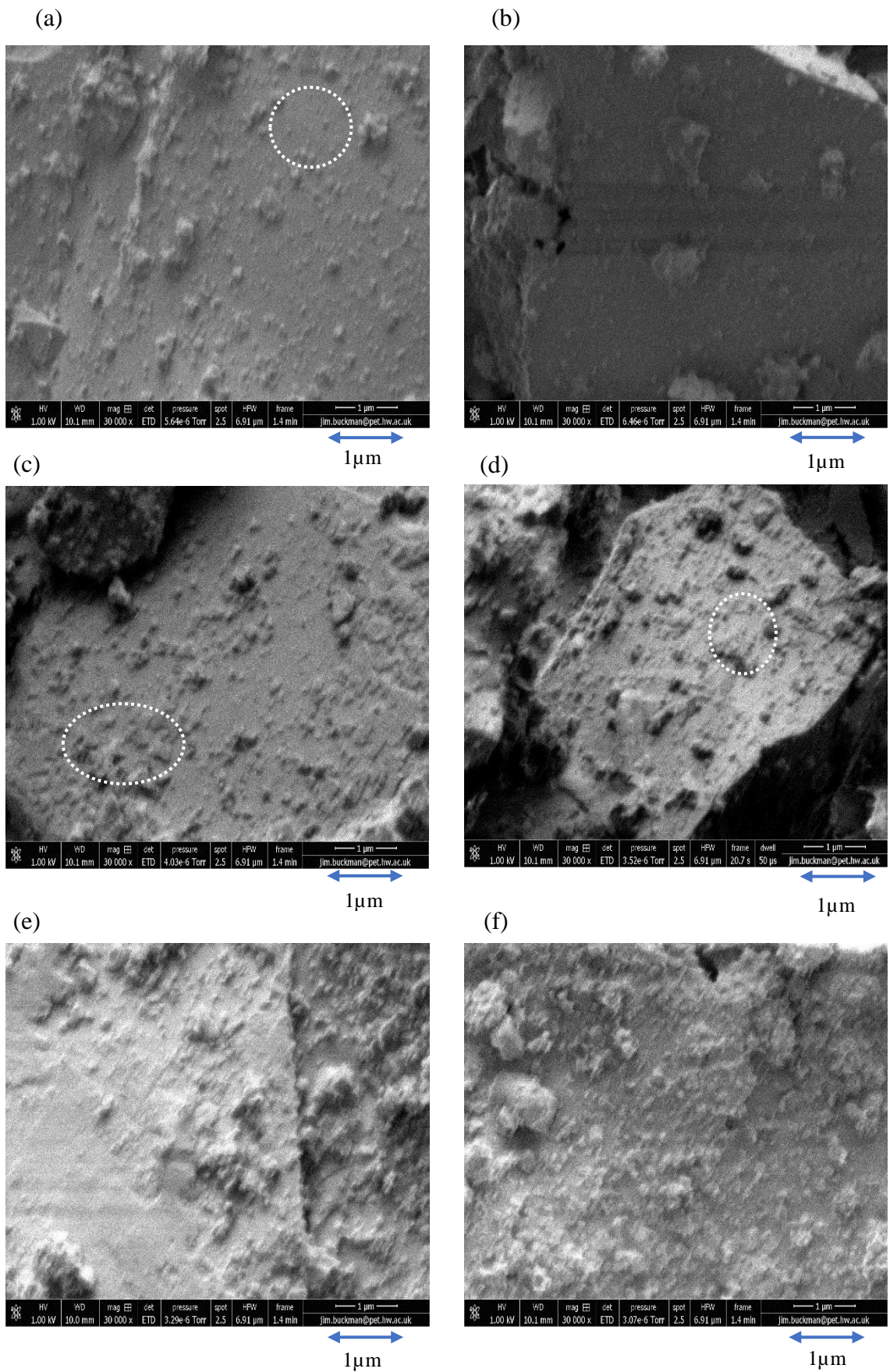


Figure 5.27: ESEM images at for PC0.35w/b at the ages of (a) and (b): 11mins, (c) and (d): 2hrs, (e) and (f): 5.5hrs.

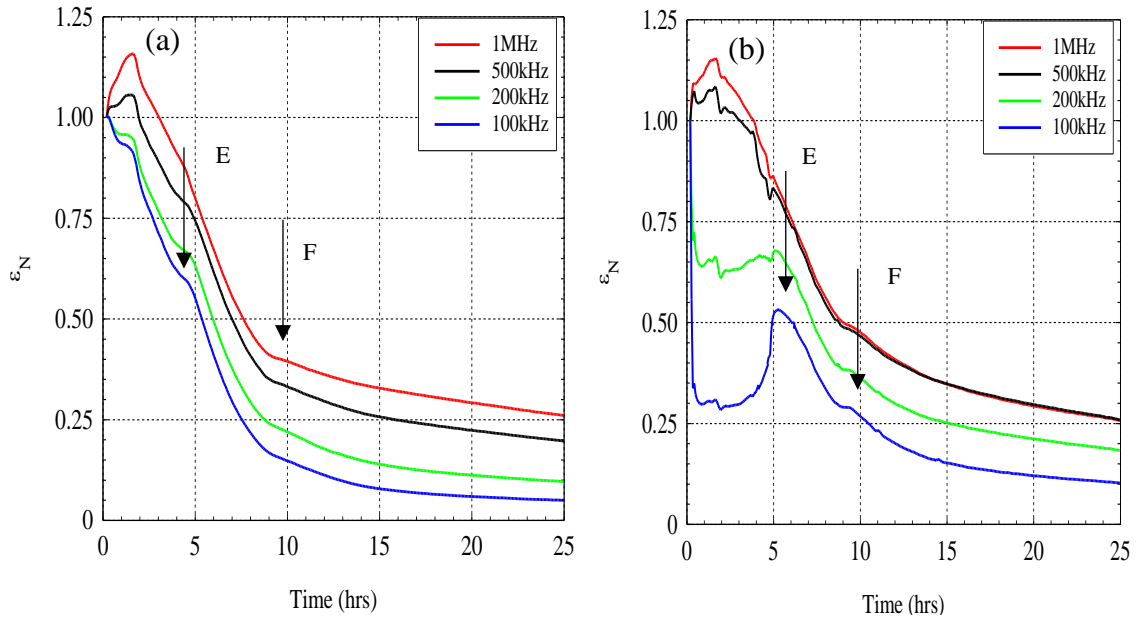


Figure 5.28: Normalised permittivity through the first 25hrs for the PC0.35w/b +0.5% gypsum at different frequencies for (a): electrode uncorrected response and (b): corrected response.

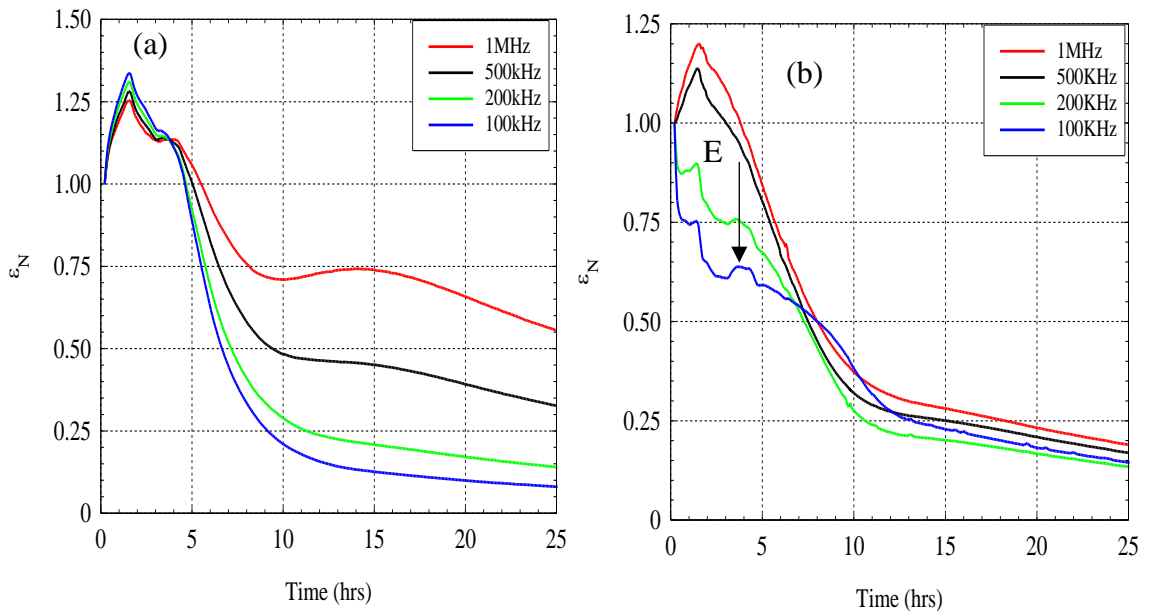


Figure 5.29: Normalised permittivity through the first 25hrs for the PC0.35w/b +2% gypsum at different frequencies for (a)EP uncorrected (b) corrected.

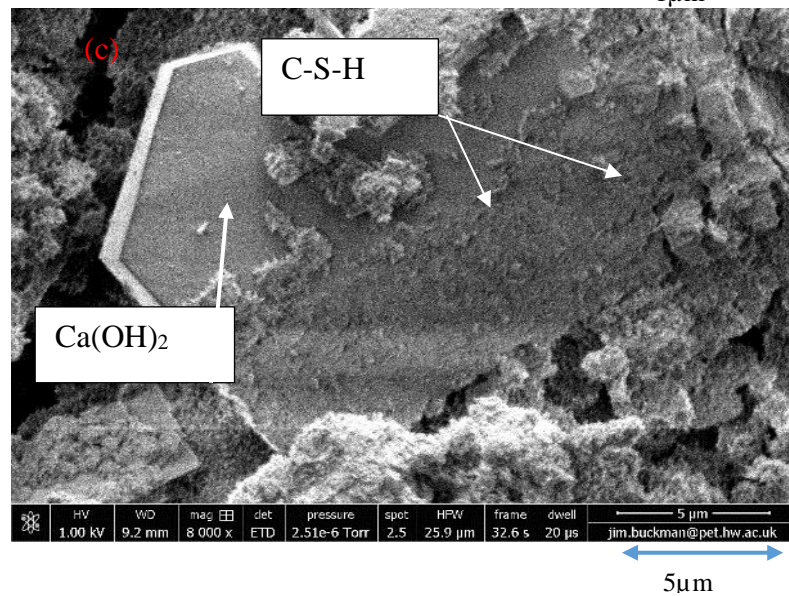
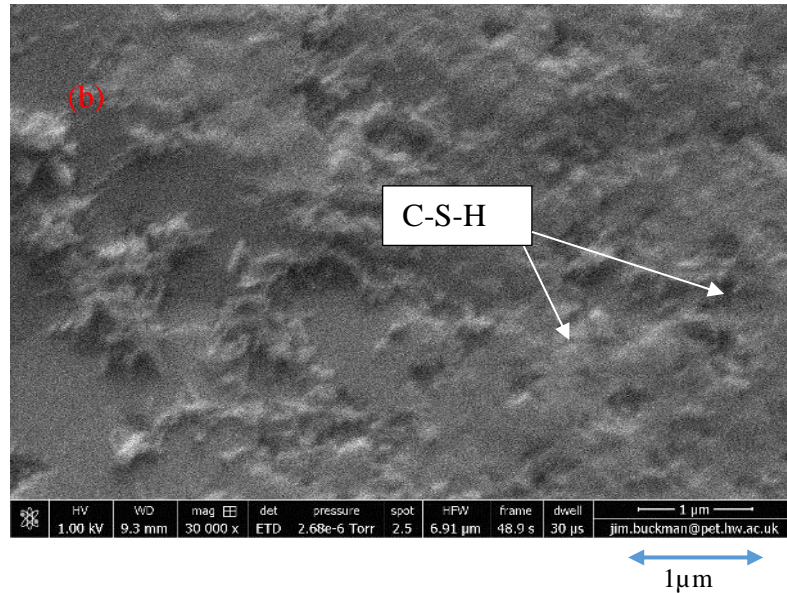


Figure 5.30: ESEM images for PC0.35w/b at point E at the age of 8hrs.

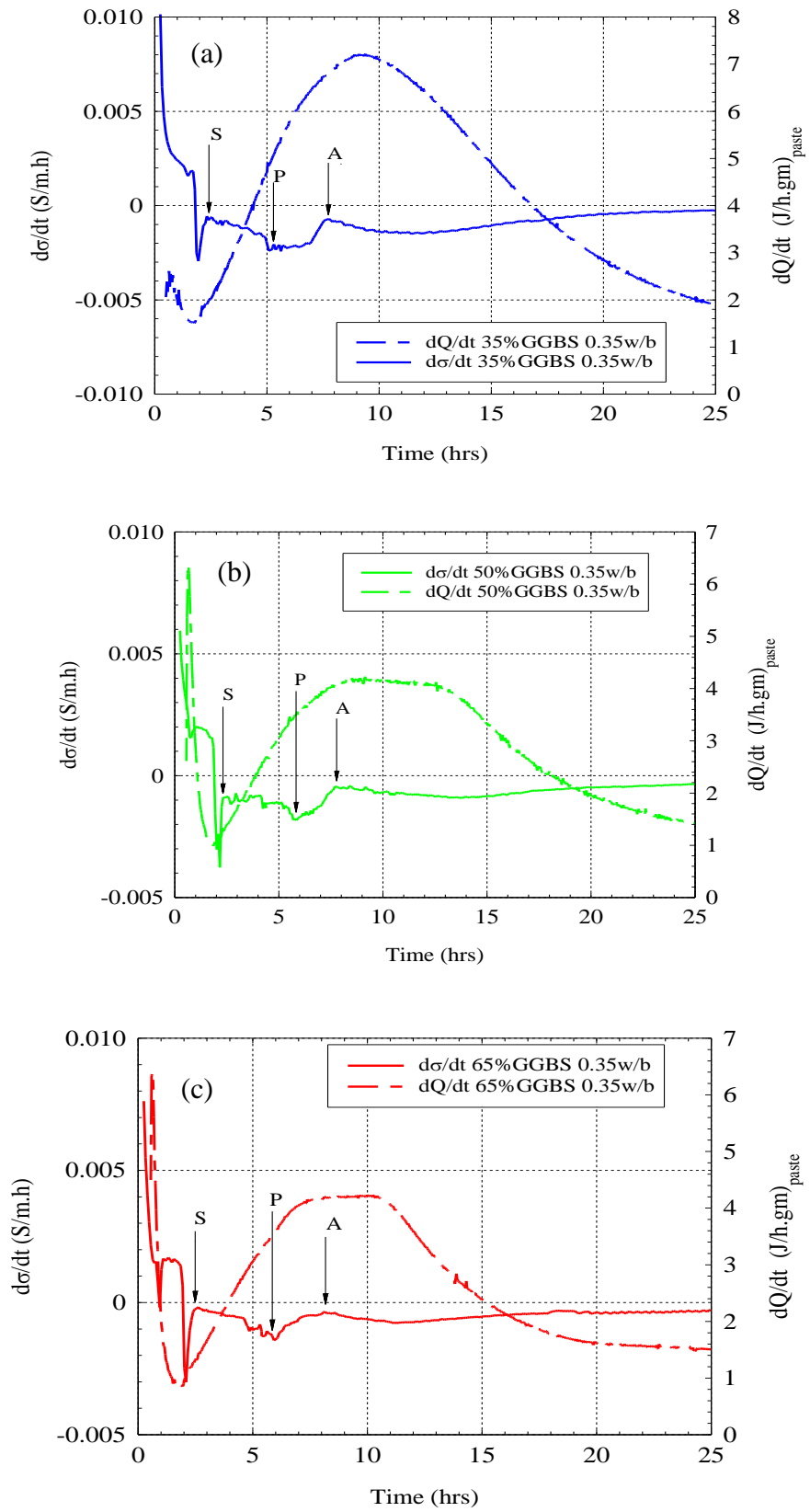


Figure 5.31: Conductivity rate, $d\sigma/dt$, and heat emission rate, dQ/dt , for (a) 35%GGBS 0.35w/b, (b) 50%GGBS 0.35w/b, and (c) 65%GGBS 0.35w/b.

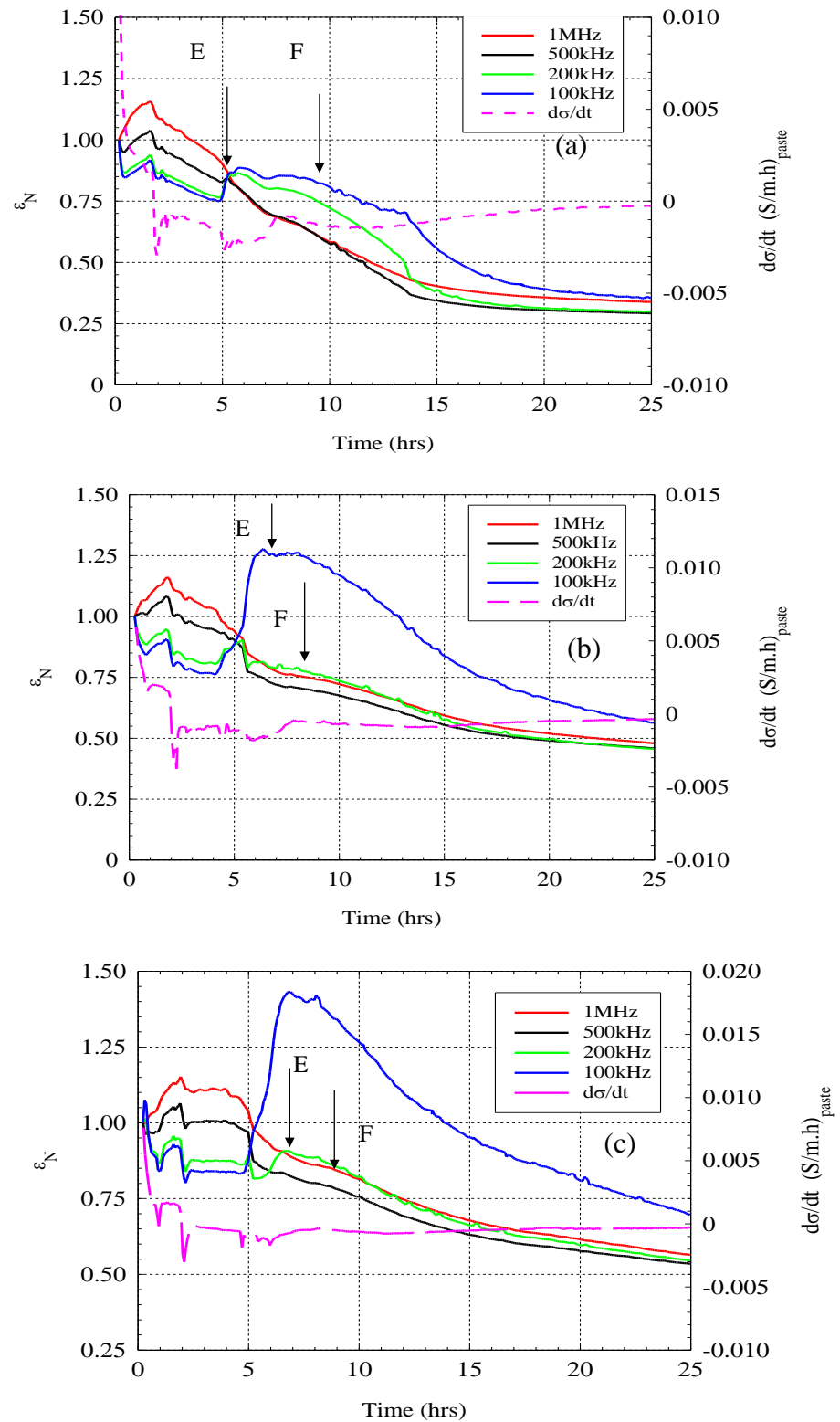


Figure 5.32: Electrode polarization corrected normalised permittivity through the first 25hrs for the (a) 35%GGBS 0.35w/b (b) 50%GGBS 0.35w/b and (c)65%GGBS 0.35w/b pastes at different frequencies.

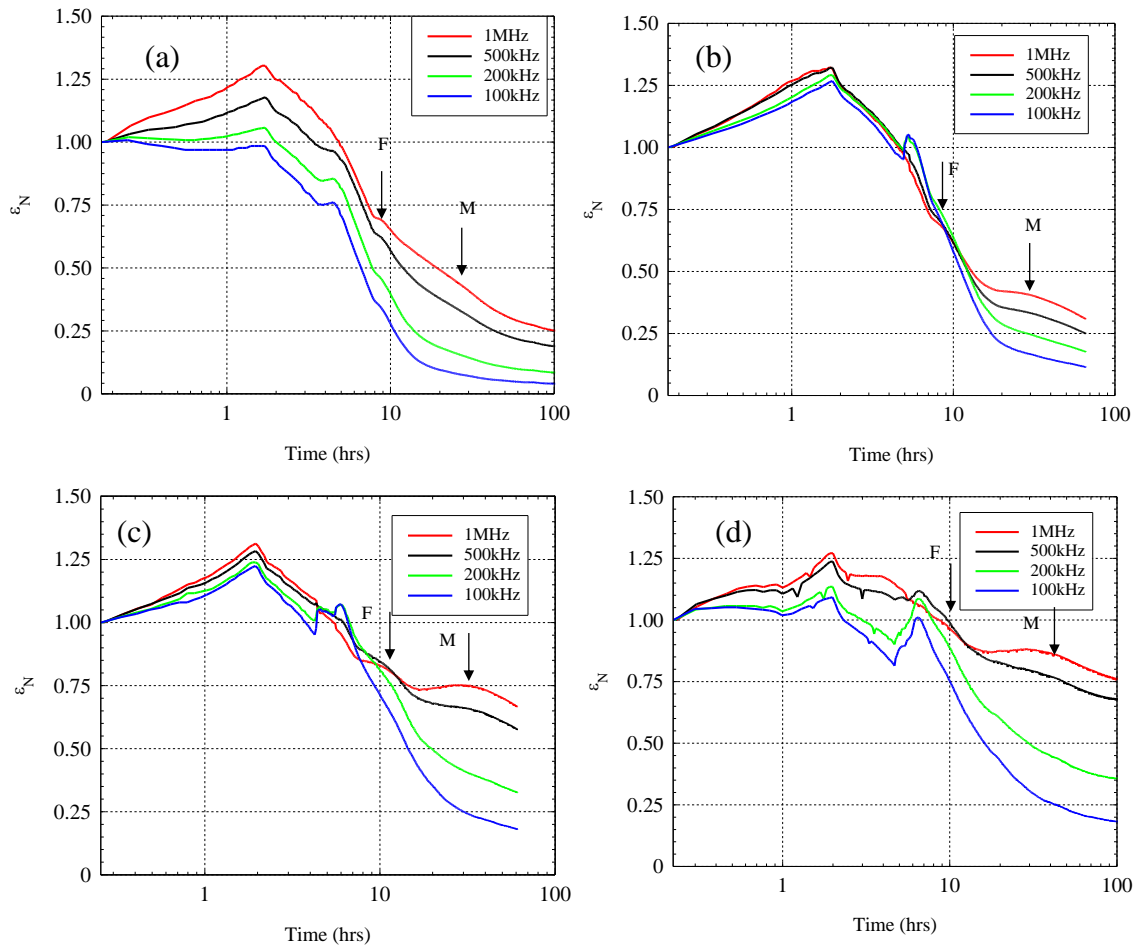


Figure 5.33: Normalised permittivity through time for the (a) PC0.35w/b (b) 35%GGBS0.35w/b, (c) 50%GGBS0.35w/b, and (d) 65% GGBS 0.35w/b.

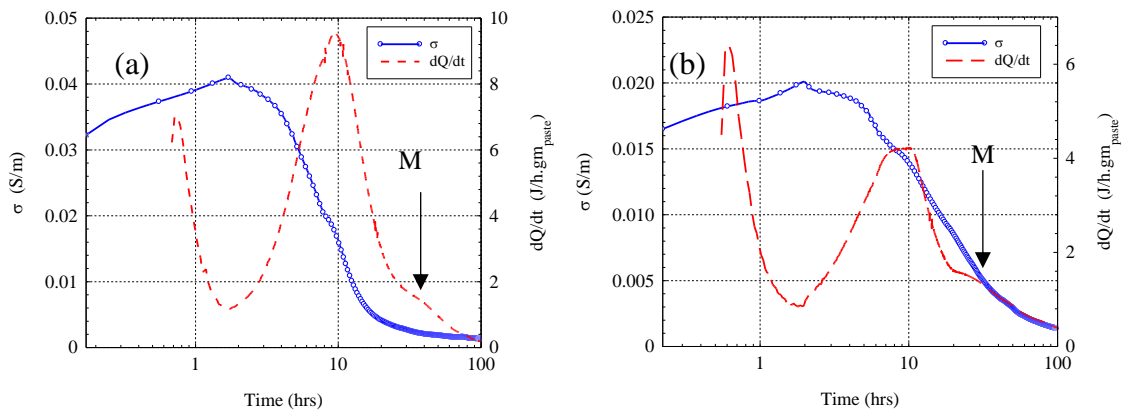


Figure 5.34: Conductivity and heat emission rate for the first 100hrs for pastes (a) PC0.35w/b, and (b) 65% GGBS 0.35w/b.

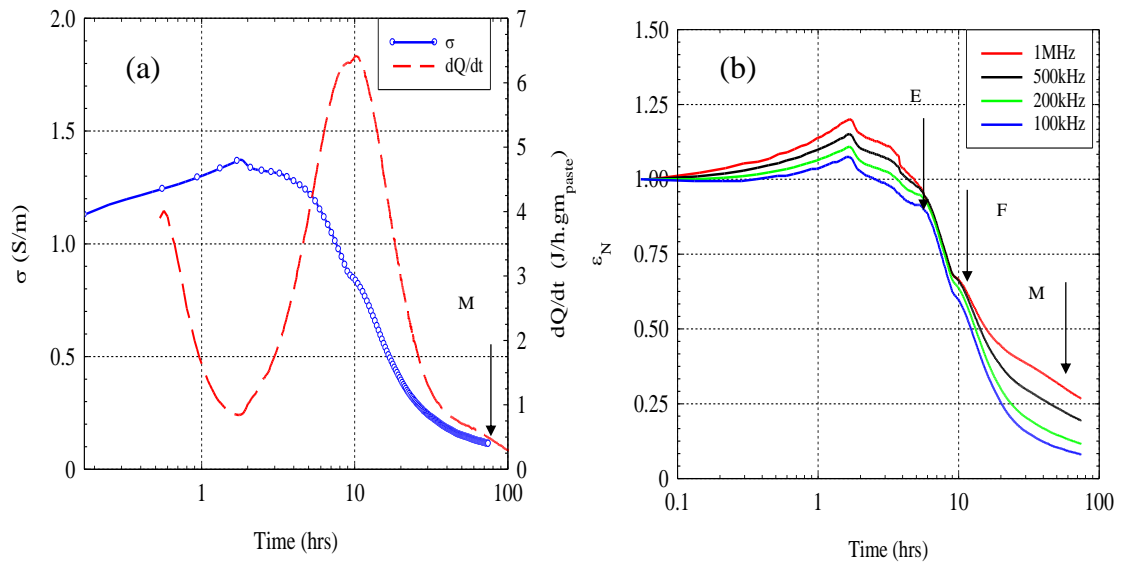


Figure 5.35: (a) Electric conductivity and heat emission (a) Normalised permittivity at 100kHz, 200kHz, 500kHz and 1MHz response for 35% FA 0.35W/b paste.

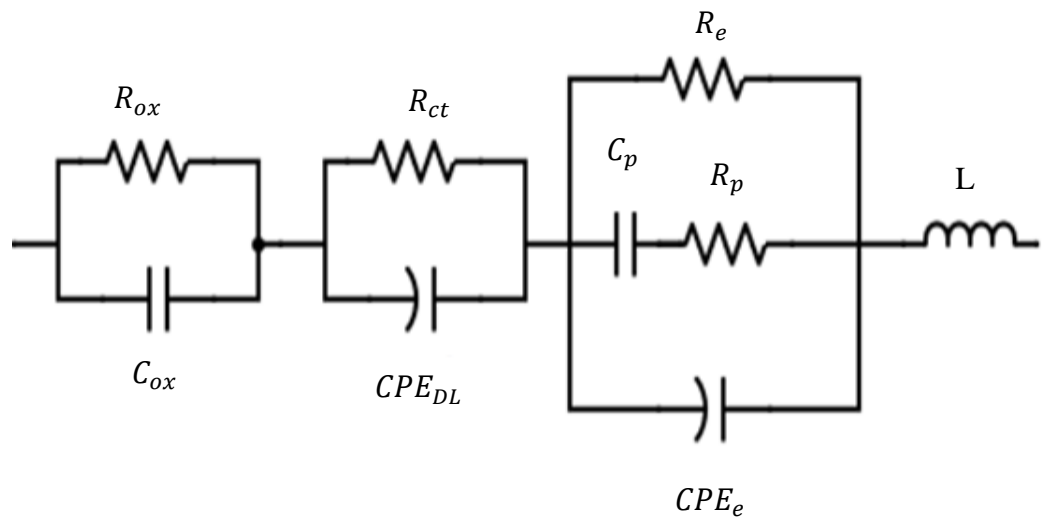


Figure 5.36: Equivalent electrical circuit proposed for the early hydration period of cement pastes.

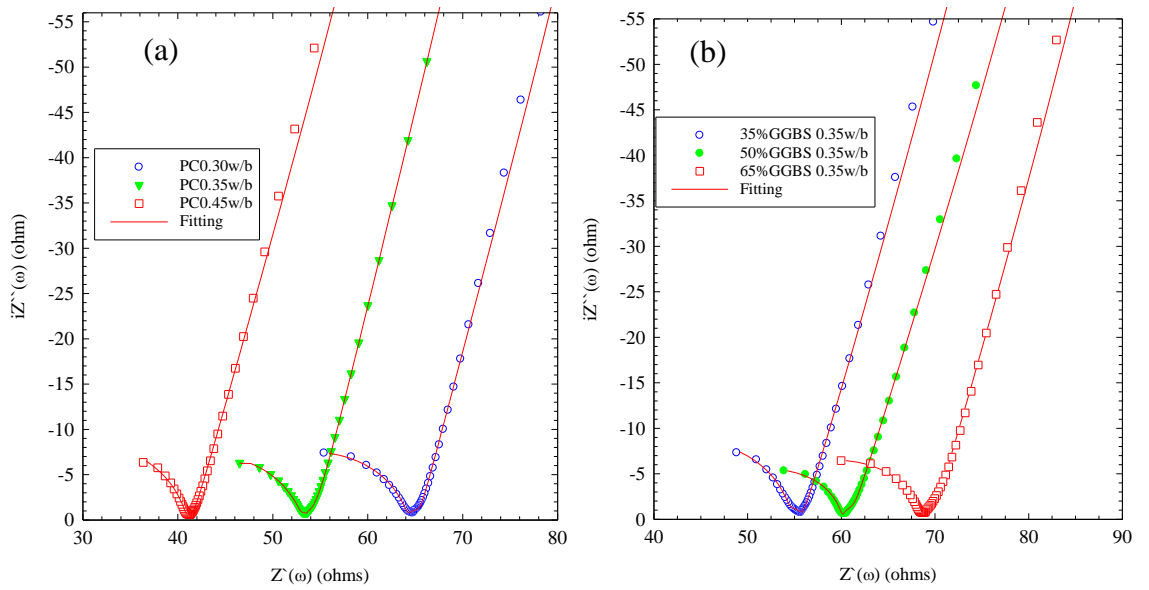


Figure 5.37: Typical Nyquist plots for pastes, 9hrs after mixing, (a) PC pastes, (b) GGBS pastes.

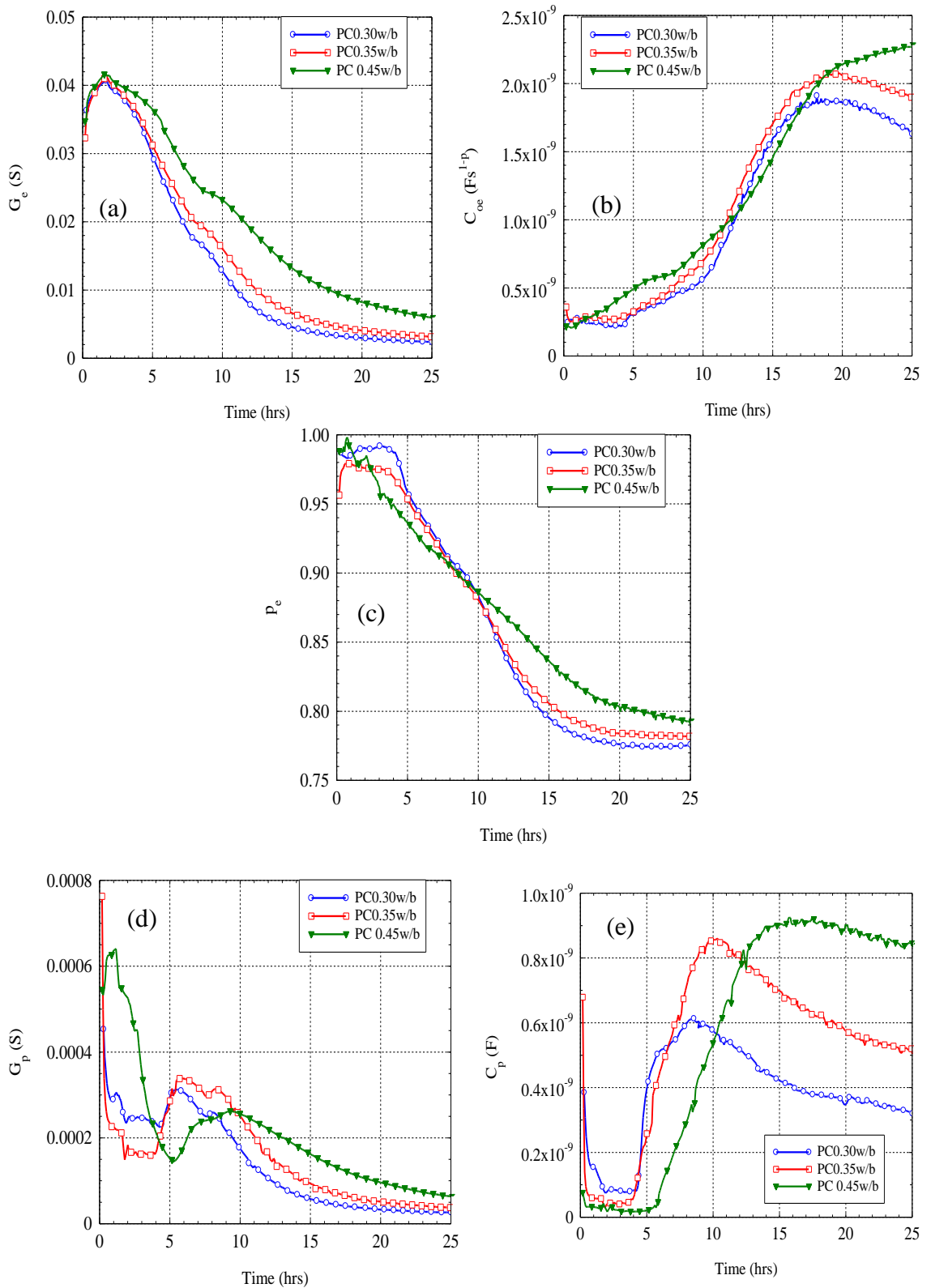


Figure 5.38: Connected liquid phase EEC related electrical parameters (a) G_e (b) C_{oe} which is the CPE_e coefficient, and (c) p_e ; particle related electrical parameters (d) G_p , and (e) C_p for the PC0.30w/b, PC0.35w/b and PC0.45w/b cement pastes.

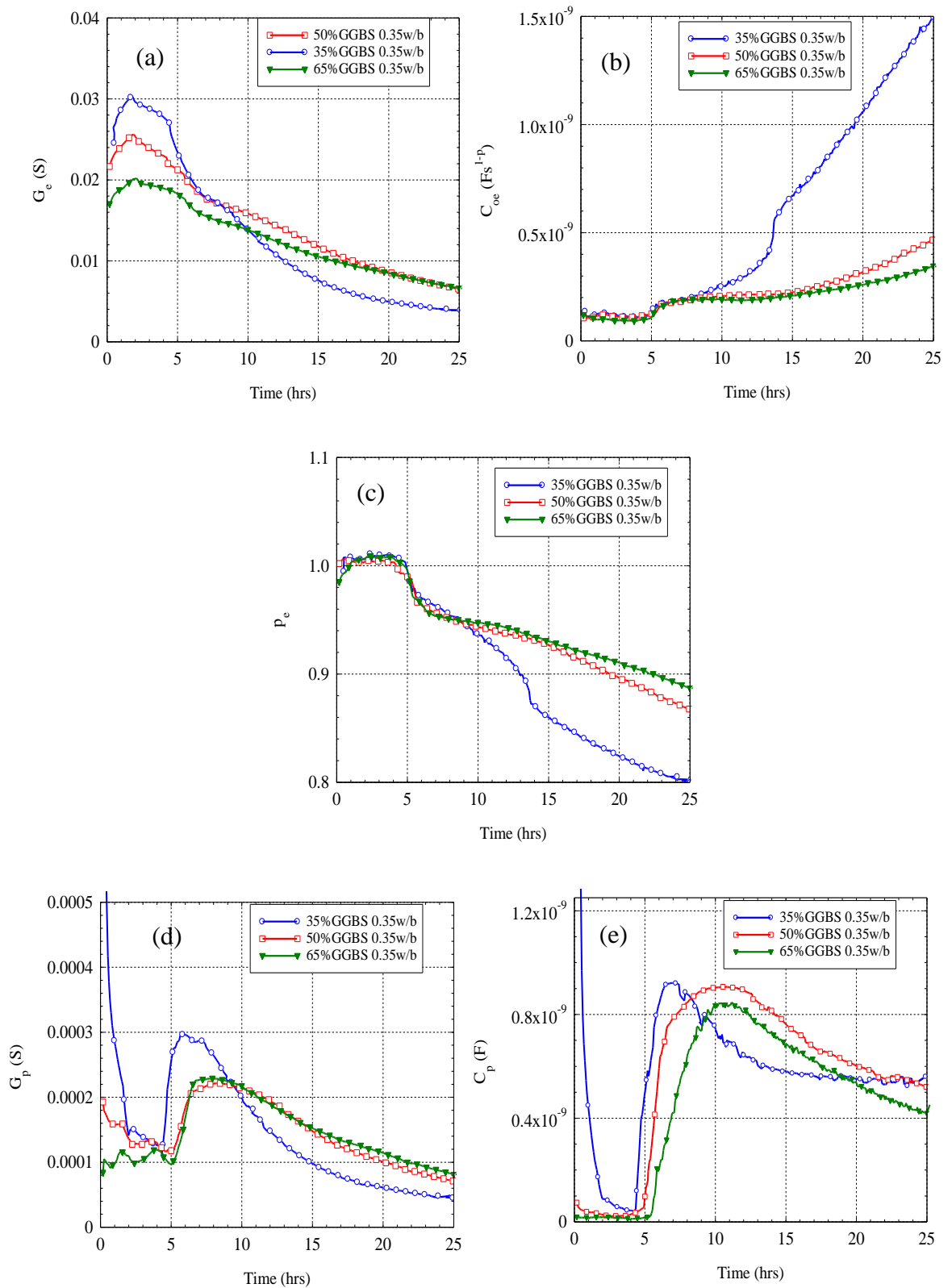


Figure 5.39: Connected liquid phase EEC related electrical parameters (a) G_e (b) C_{oe} which is the CPE_e coefficient, and (c) p_e ; particle related electrical parameters (d) G_p , and (e) C_p for the 35%GGBS, 50%GGBS and the 65%GGBS replaced cement pastes.

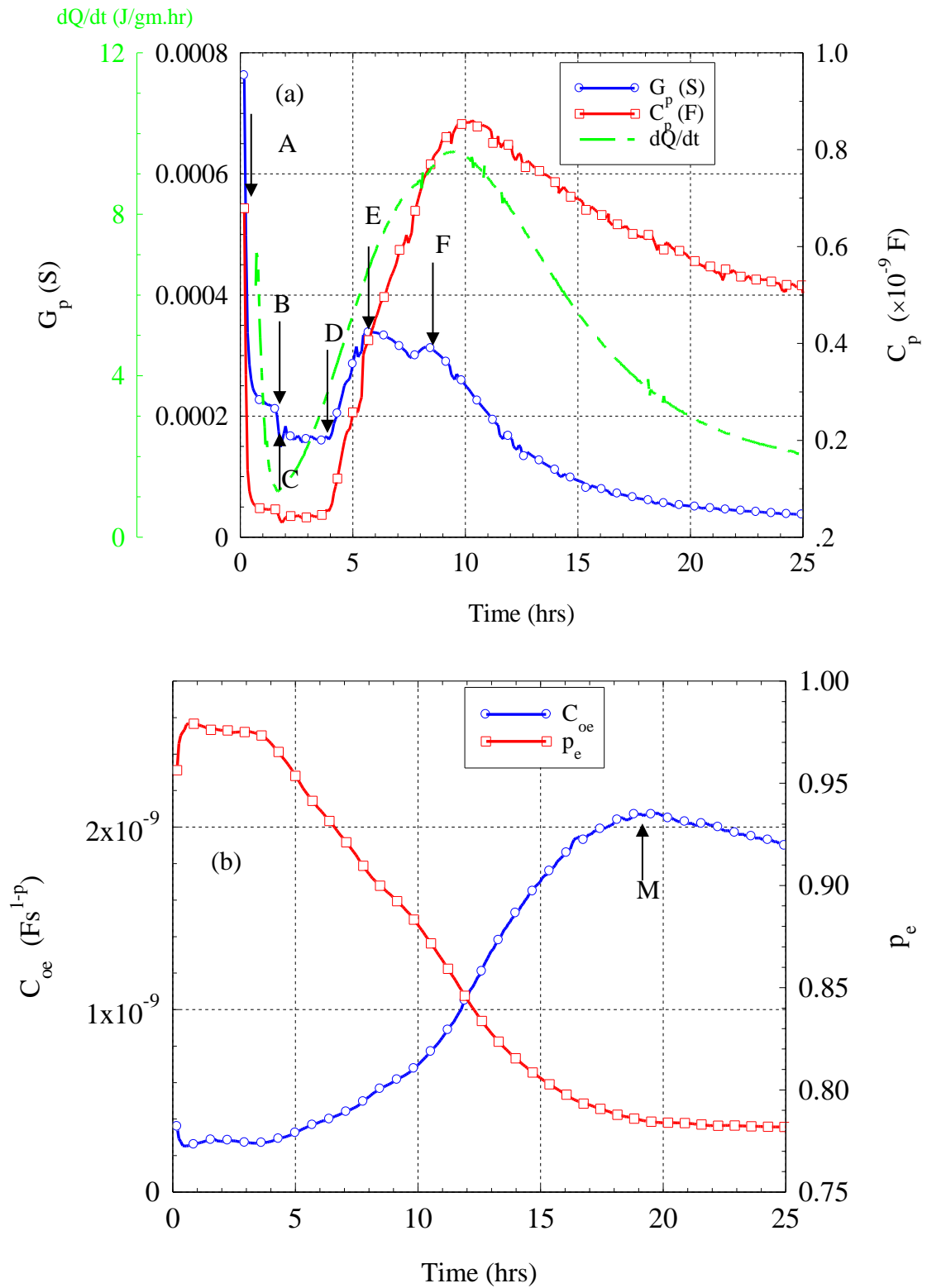


Figure 5.40: Salient points on the PC0.35w/b EEC electrical parameters response for (a) G_p and C_p and dQ/dt responses through time, and (b) p_e , C_{oe} responses through time.

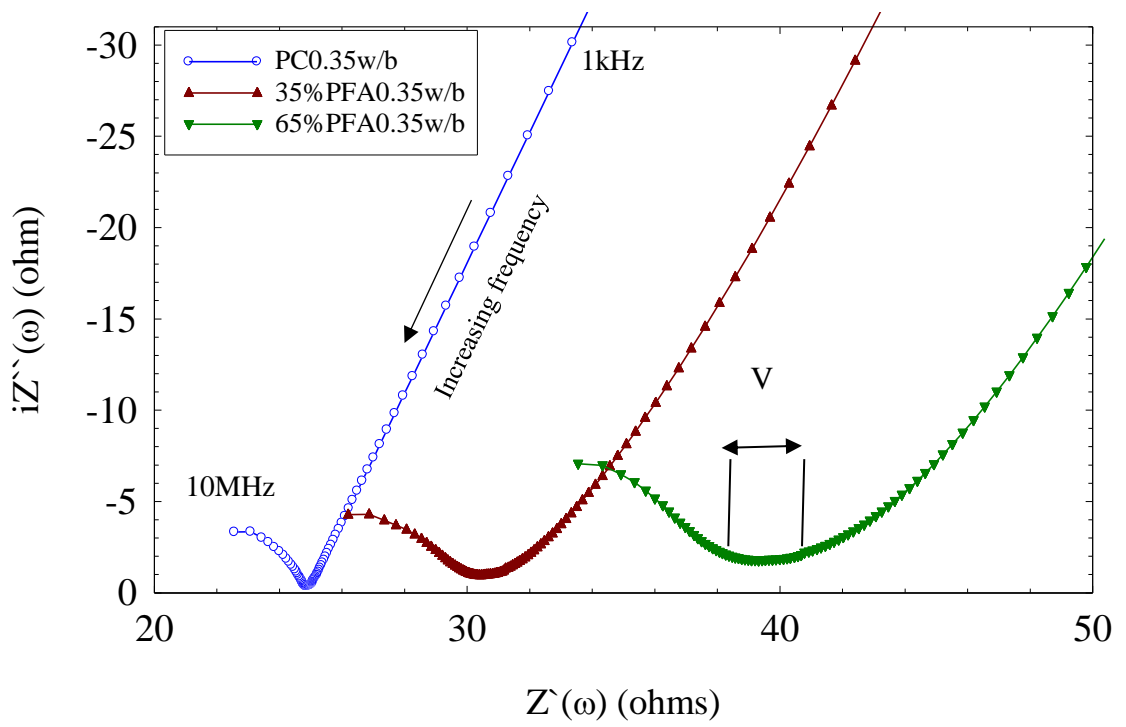


Figure 5.41: Nyquist plot for cement pastes, PC0.35w/b, 35%FA0.35w/b and 65%FA0.35w/b at the age of 2hrs.

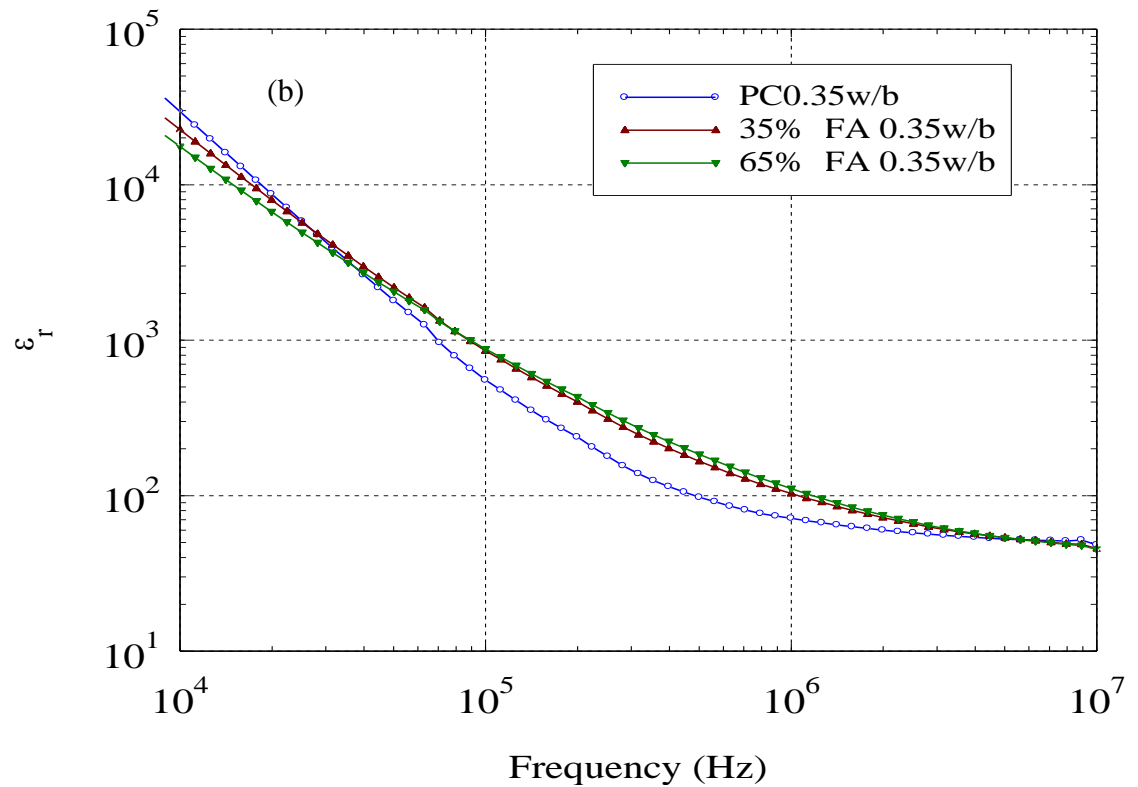
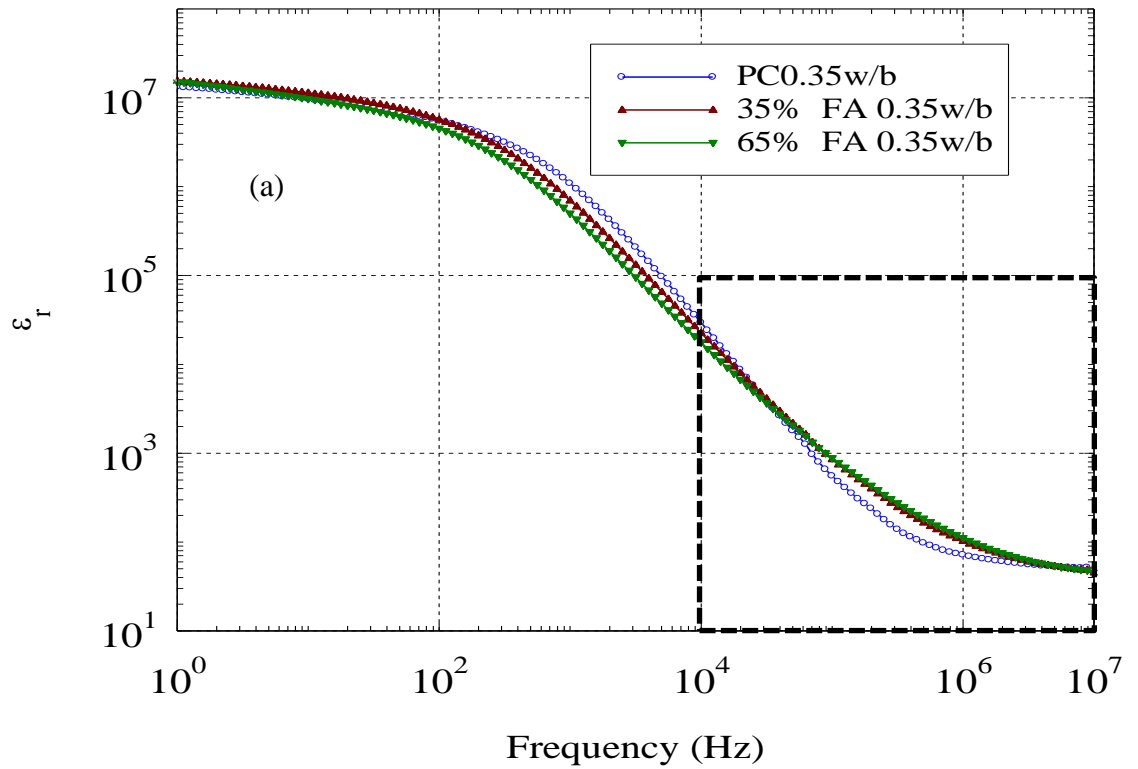


Figure 5.42: (a) Permittivity through frequency for the PC0.35w/b, 35%FA0.35w/b and 65%FA0.35w/b at the age of 2hrs (b) an enlargement for the permittivity in the frequency range between 10kHz- 10MHz.

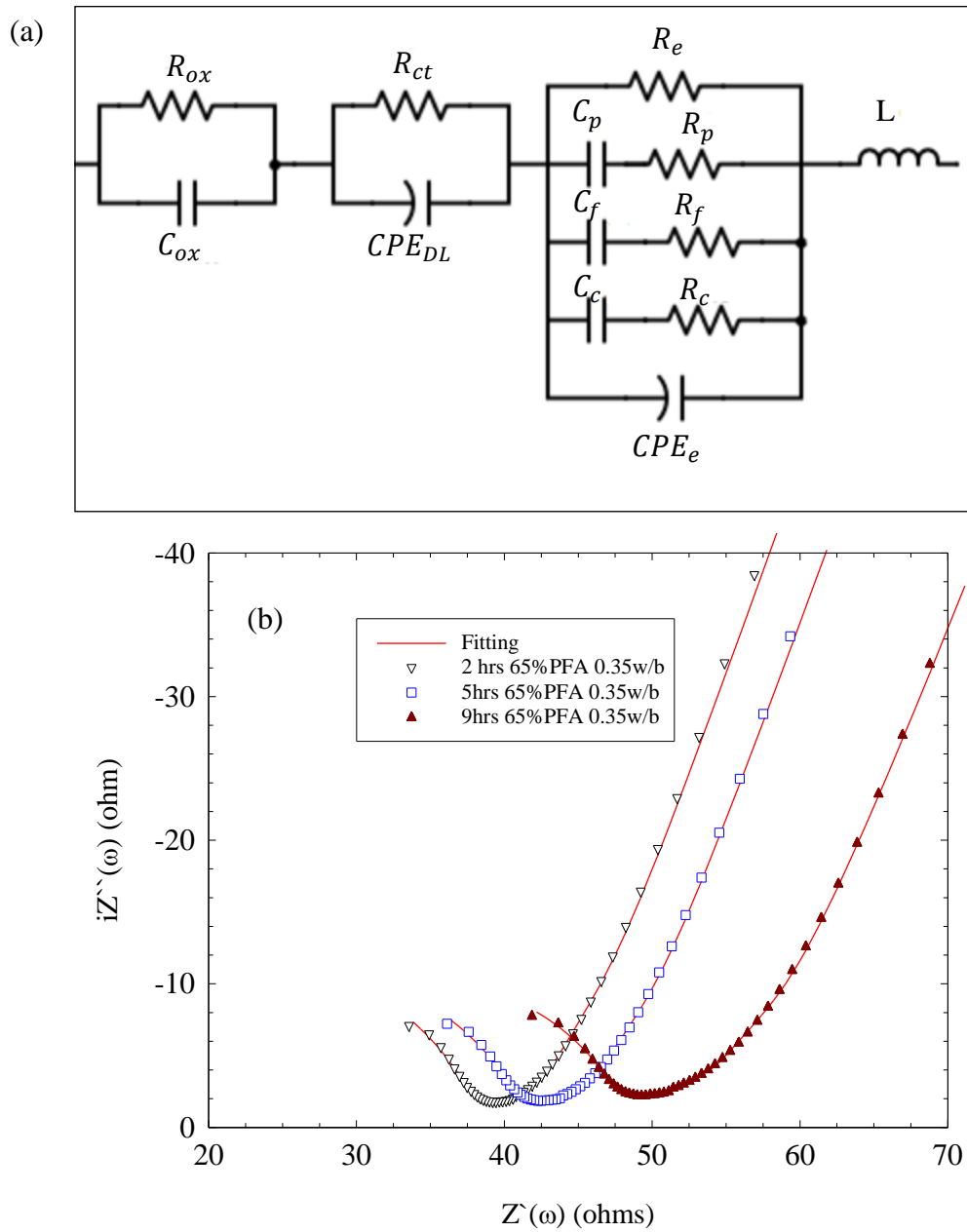


Figure 5.43: (a)Proposed EEC for the early hydration period of fly-ash replaced pastes, (b) experimental data at different ages for the 65% Fa paste and their related best fitting simulations.

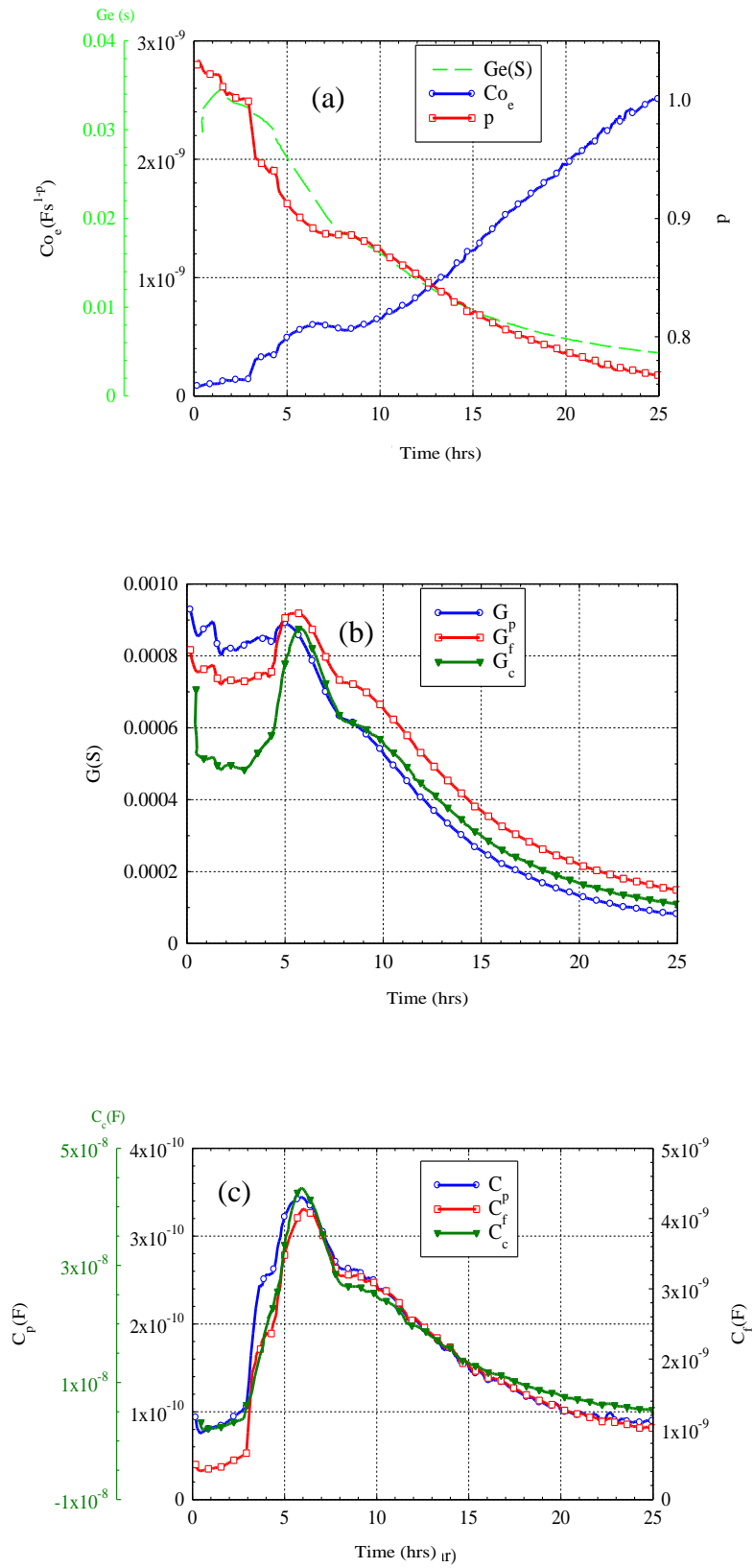


Figure 5.44: 35%FA 0.35w/b early hydration EEC parameters response through time the first 25 hours of the samples age.

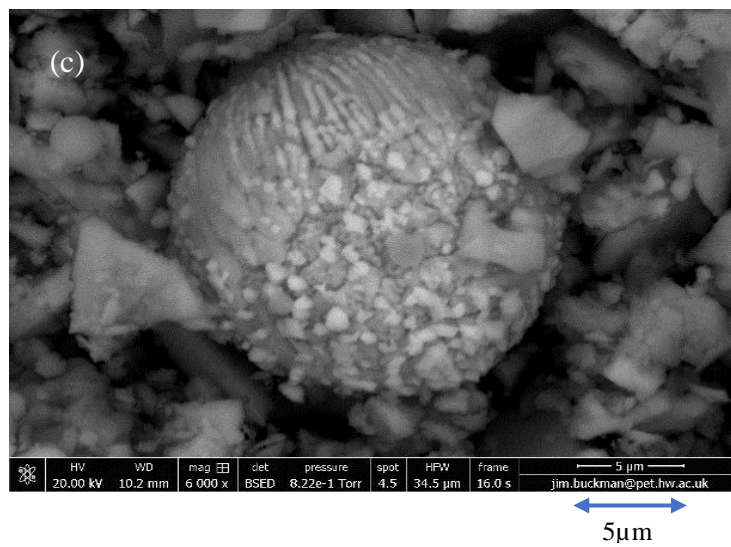
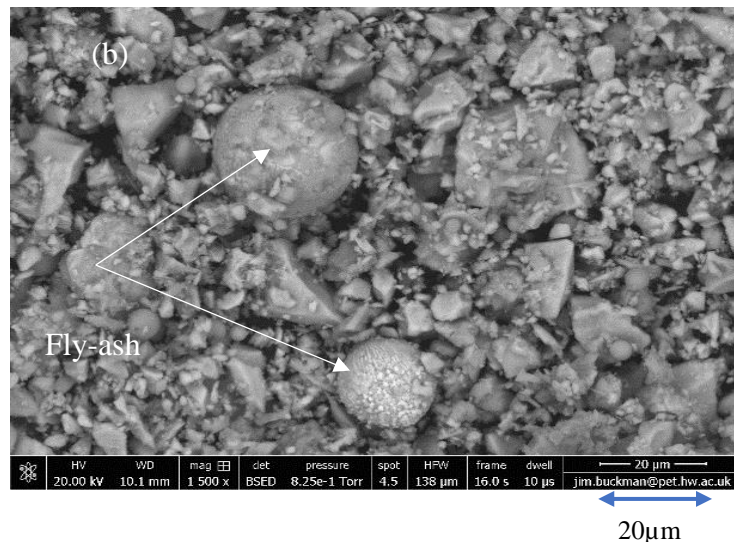
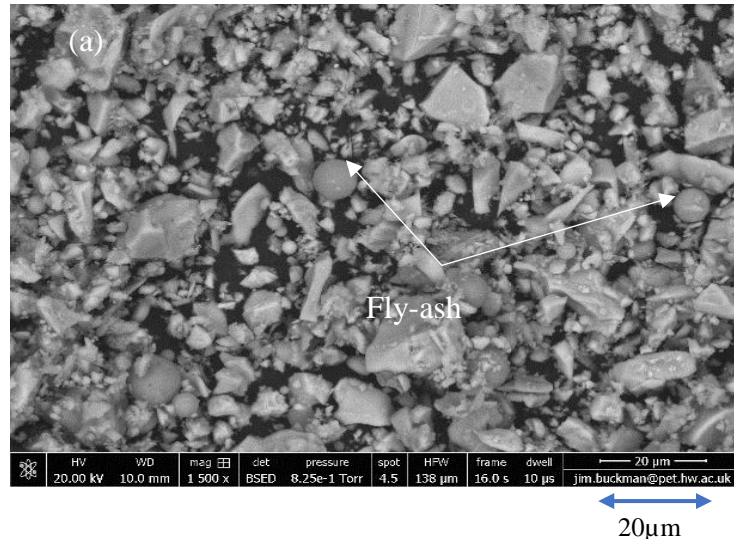


Figure 5.45: ESEM images (a): 11 mins (b): 5.5 hours, and (c) 5.5 hours for PC0.35w/b includes dispersed fly-ash particles.

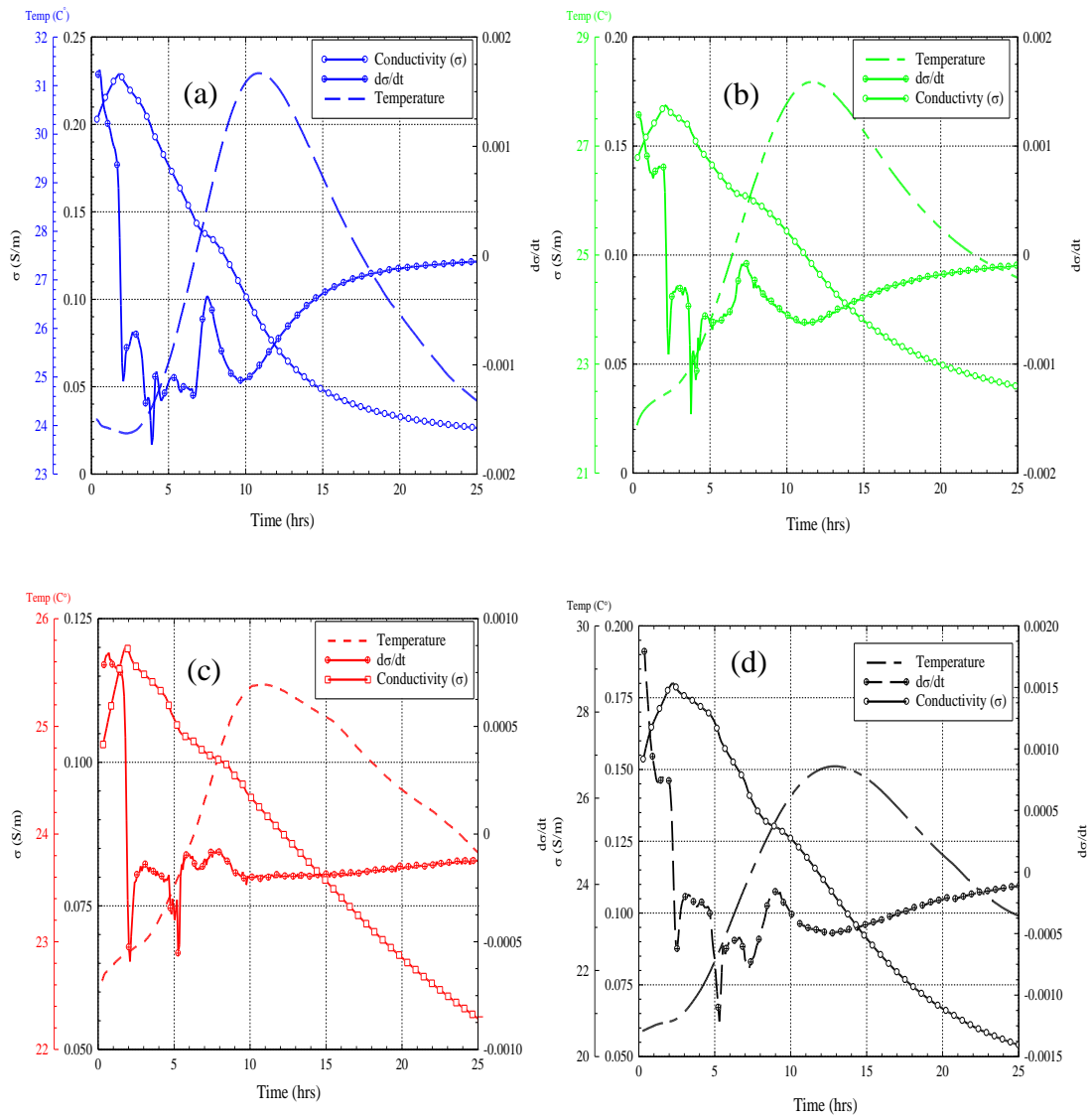


Figure 5.46: Conductivity of concrete mixes at 100kHz and temperature through the first 24hrs after mixing for (a) Portland cement, (b) 35%GGBS, (c) 65%GGBS and (d)35%FA concrete mixes at 0.45w/b.

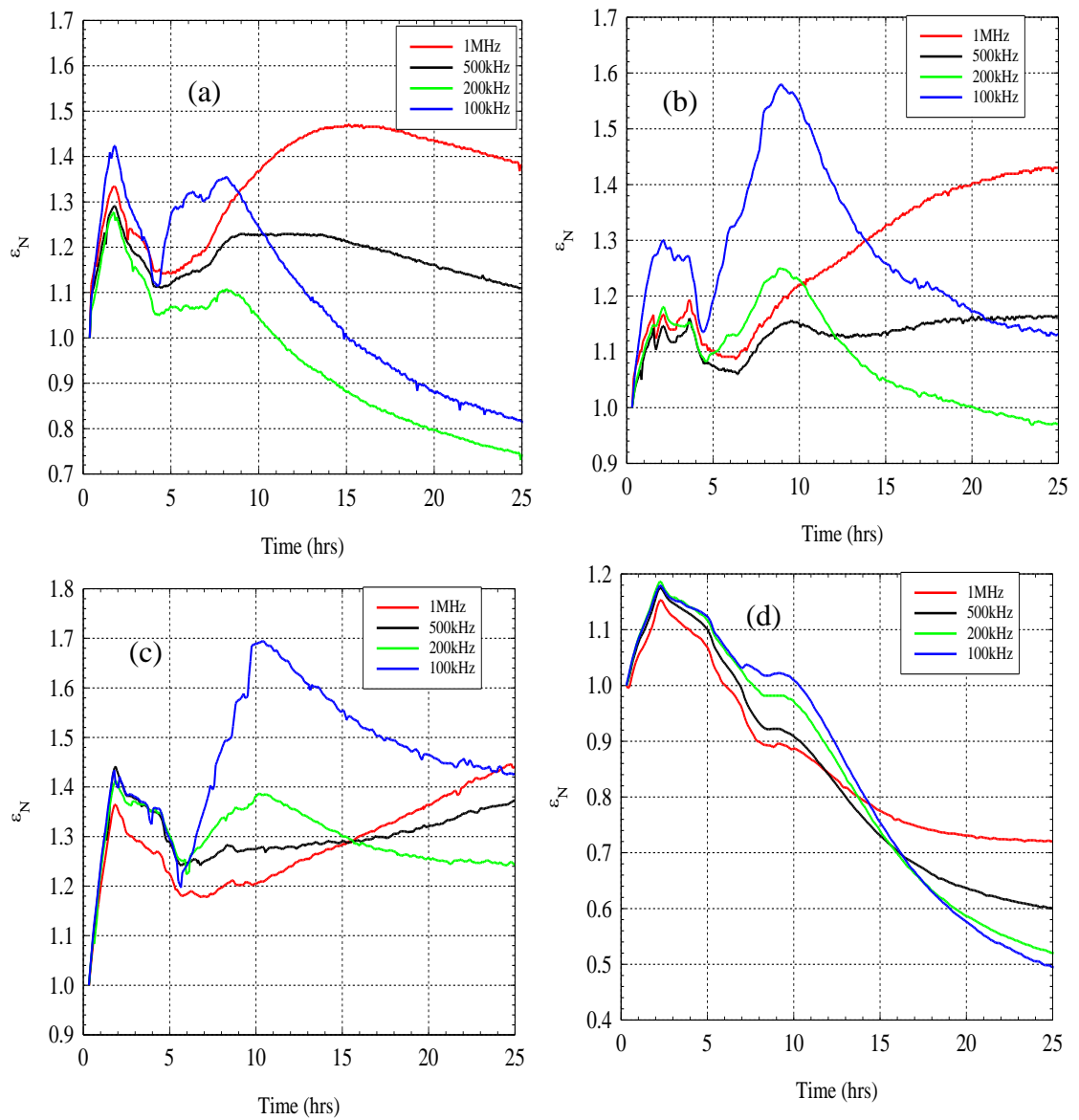


Figure 5.47: Normalised permittivity at 100kHz, 200kHz, 500kHz and 1MHz for, (a) Portland cement (b) 35%GGBS, (c)65%GGBS and (d) 35%FA concrete mixes at 0.45w/b.

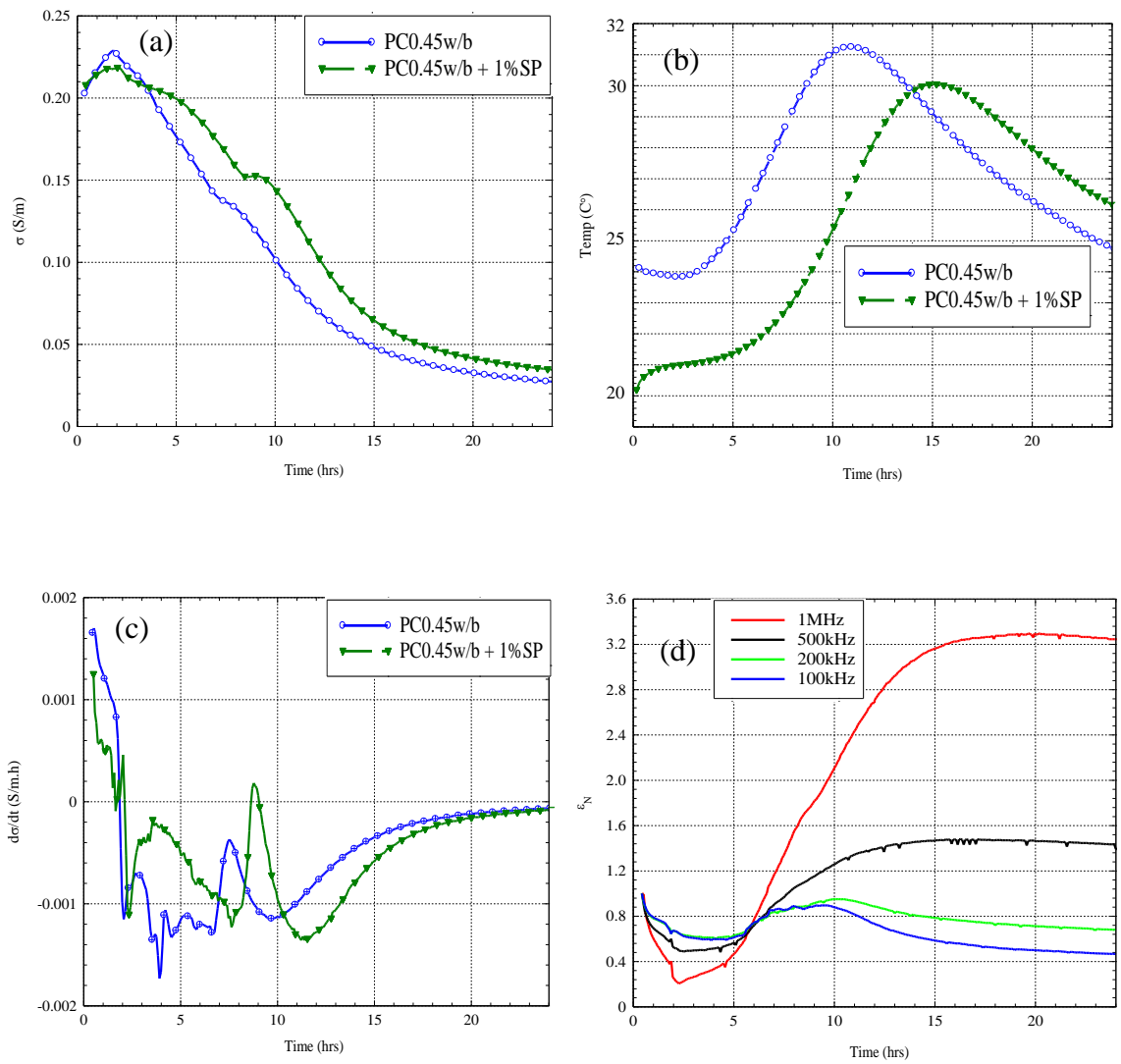


Figure 5.48: (a) Conductivity, (b) temperature (c) conductivity derivative, $d\sigma/dt$, through time, and (d) normalised permittivity, ϵ_N , for 0.45w/b Portland cement concrete mix with 1% SP addition and without SP addition.

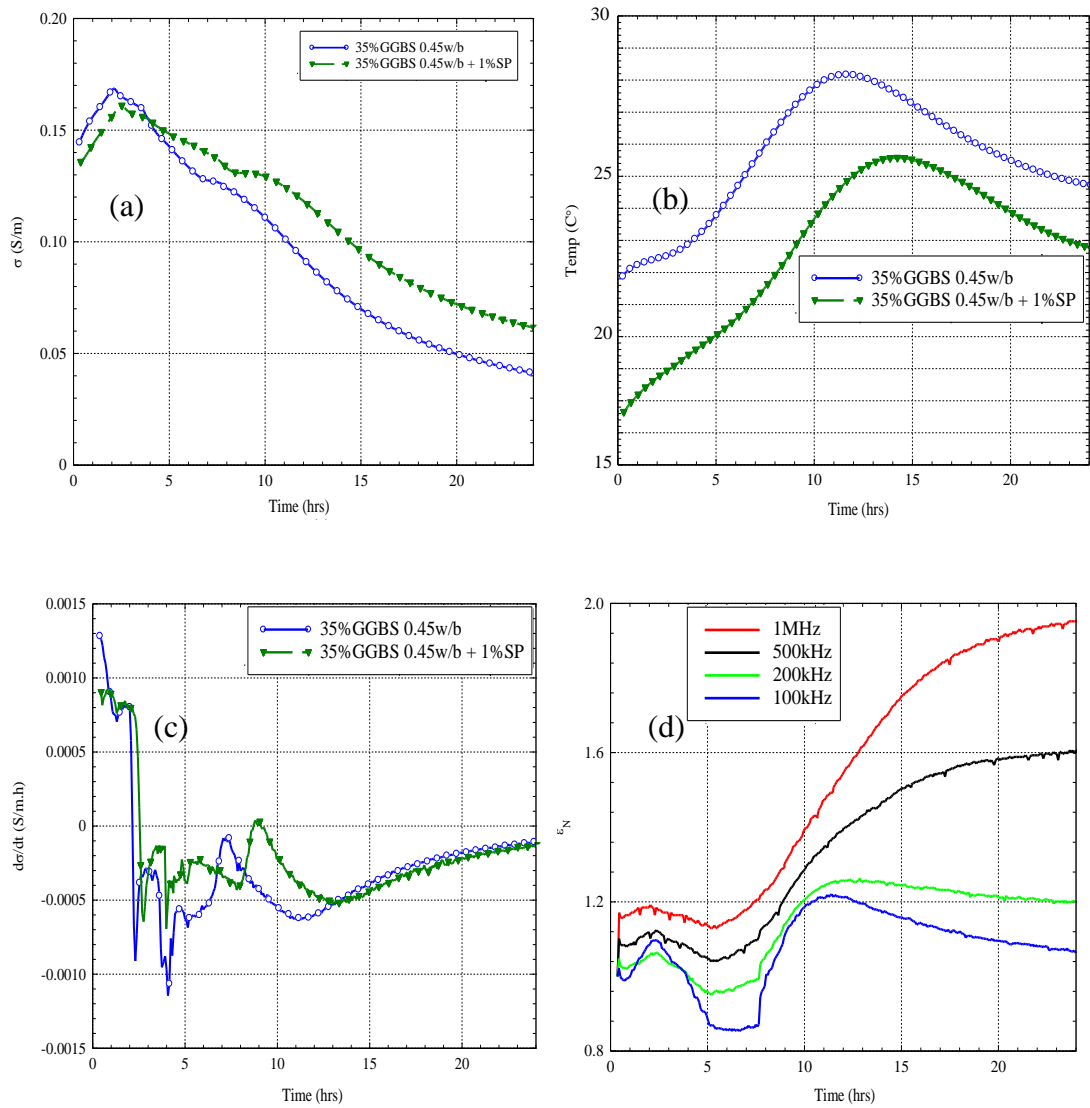


Figure 5.49: (a) Conductivity, (b) temperature (c) conductivity derivative, $d\sigma/dt$, through time, and (d) normalised permittivity, ϵ_N , for 0.45w/b 35% GGBS replaced concrete mix with 1% SP addition and without SP addition.

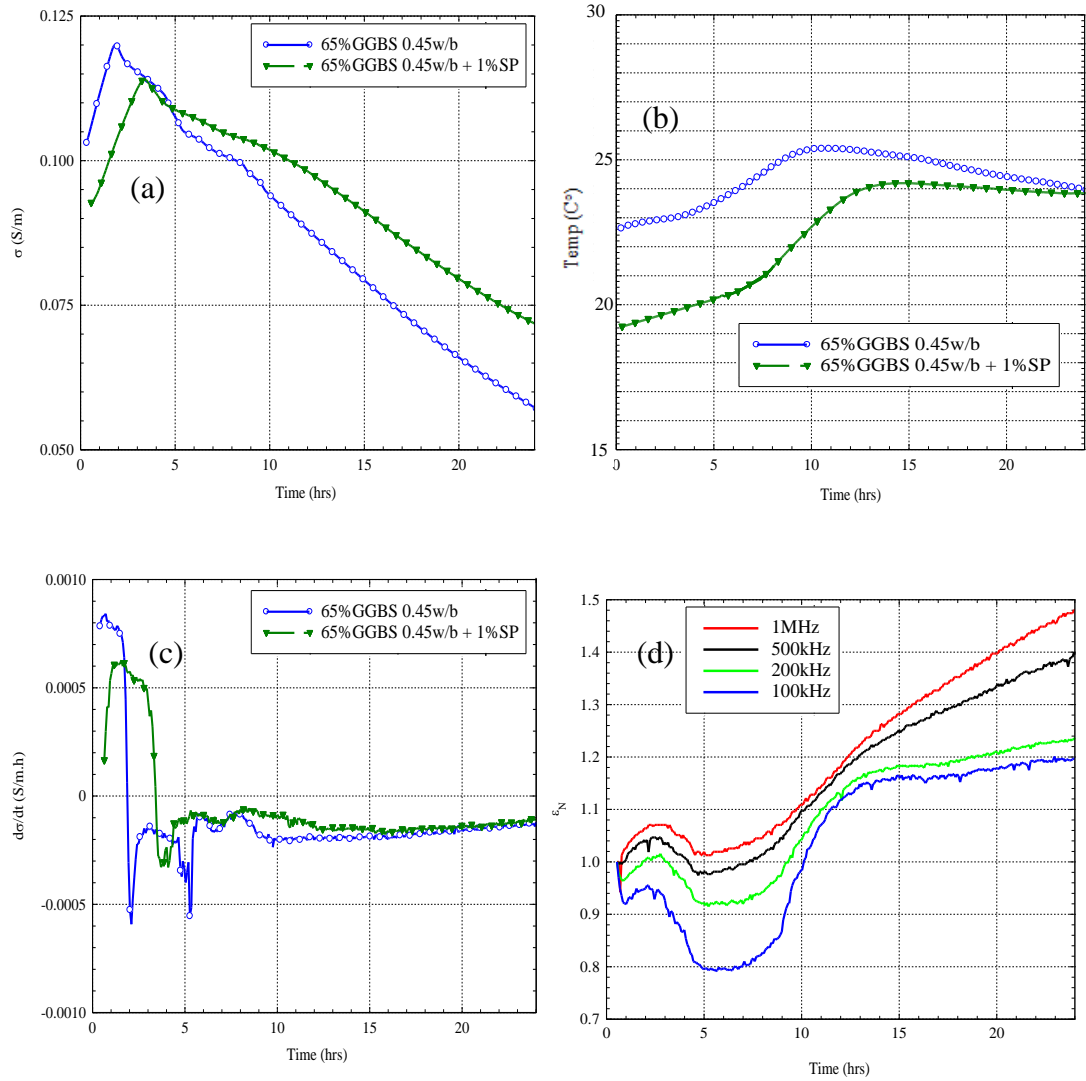


Figure 5.50: (a) Conductivity (b) Temperature (c) conductivity derivative $d\sigma/dt$ through time and (d) normalised permittivity ϵ_N for 0.45w/b 65%GGBS replaced concrete mix with 1% SP addition and without SP addition.

(Species)	$z\lambda_i$ (cm ² S/mol)
OH ⁻	198
K ⁺	73.5
Na ⁺	50.1
Ca ⁺²	59

Table 5.1: Product of the equivalent ionic conductivity (λ_i) and valance (z) for different ions.

Mix	P point age (hrs)	P point Hydration degree %	dQ/dt peak age (hrs)	dQ/dt Peak Hydration degree%
PC 0.30w/b	4.5	3%	9.30	16.78%
PC 0.35w/b	4.93	4%	9.43	15.23%
PC 0.45w/b	5.75	6%	10.05	17.69%

Table 5.2: Degree of hydration for the different w/b cement pastes mixes (0.30,0.35,0.45) at the age of the P point and at the acceleration stage peak.

Mix	First conductivity peak value (S/m)	First conductivity peak age (hrs)	$d\sigma/dt$ C_3A reactivity peak age (hrs)
PC 0.35w/b	1.71	1.66	8.32
PC0.35w/b+0.5% $CaSO_4$	1.76	1.51	9.61
PC0.35w/b+2% $CaSO_4$	1.80	1.49	--

Table 5.3: Effect of different $CaSO_4$ additions on the 0.35w/b cement paste with regard to the early conductivity peak values and age, and the conductivity rate peak age.

Mix	10Hz	100kHz	1MHz
PC0.3 w/b	1.40×10^8	4.08×10^3	583.61
PC0.35w/b	8.42×10^7	5.98×10^3	630.68
PC0.45w/b	8.70×10^7	9.27×10^3	974.26

Table 5.4: Relative permittivity values for the PC 0.3w/b, PC 0.35w/b and PC 0.45w/b at different frequencies (15mins).

Mix	10Hz	100kHz	1MHz
PC0.3 w/b	1.21×10^8	1.20×10^3	311.57
PC0.35w/b	1.14×10^8	1.88×10^3	386.41
PC0.45w/b	1.13×10^8	2.51×10^3	560.08

Table 5.5: Relative permittivity values for the PC 0.3w/b, PC 0.35w/b and PC 0.45w/b at different frequencies (10hrs).

Mix	10Hz	100kHz	1MHz
PC0.3 w/b	8.00×10^7	456.54	228.74
PC0.35w/b	9.18×10^7	564.79	281.45
PC0.45w/b	1.08×10^8	884.83	389.70

Table 5.6: Relative permittivity values for the PC 0.3w/b, PC 0.35w/b and PC 0.45w/b at different frequencies (20hrs).

Mixes	Age	R_{ox} (Ω)	C_{ox} (F)	R_{ct} (Ω)	CPE_{DL} ($F_S^{\alpha-1}$)	P_{DL}	C_{eq} (F)
PC0.30w/b	15 mins	$1.19E \times 10^4$	6.99×10^{-5}	1.64×10^3	1.40×10^{-4}	0.72	4.99×10^{-5}
	10hrs	5.82×10^4	4.21×10^{-5}	1.22×10^3	2.16×10^{-4}	0.70	1.10×10^{-4}
	20hrs	1.10×10^6	4.44×10^{-5}	3.30×10^3	2.15×10^{-4}	0.69	1.31×10^{-4}
PC0.35w/b	15 mins	2.41×10^4	3.15×10^{-5}	8.70×10^2	9.31×10^{-5}	0.72	4.08×10^{-5}
	10hrs	4.46×10^4	3.65×10^{-5}	1.00×10^3	2.12×10^{-4}	0.70	1.73×10^{-4}
	20hrs	1.28×10^5	4.37×10^{-5}	3.20×10^3	2.24×10^{-4}	0.66	2.24×10^{-4}
PC 0.45w/b	15 mins	2.03×10^4	4.37×10^{-5}	1.54×10^3	1.34×10^{-4}	0.63	6.25×10^{-5}
	10hrs	6.17×10^4	3.48×10^{-5}	1.17×10^3	2.19×10^{-4}	0.70	1.78×10^{-4}
	20hrs	1.18×10^5	3.65×10^{-5}	2.40×10^3	2.44×10^{-4}	0.68	2.44×10^{-4}

Table 5.7: Best fit parameter for the electric circuit in Figure 5.20 for the PC 0.3w/b, PC0.35w/b and PC0.45w/b at different ages.

Capacitance (F)	Responsible Phenomenon
10^{-12}	Bulk
10^{-7} - 10^{-4}	Sample /Electrodes interface/product layer
10^{-4}	Electrochemical reactions

Table 5.8: Possible origins for different generated capacitance values adapted from (Irvine et al., 1990; Ford et al., 1998)

Age	R_{ox} (Ω)	C_{ox} (F)	R_{ct} (Ω)	CPE_{DL} ($Fs^{\alpha-1}$)	p_{DL}	R_{s1} (Ω)	CPE_{s1} ($Fs^{\alpha-1}$)	p_{s1}	R_{s2} (Ω)	C_{s2} (F)	L1(H)
15mins	5.32×10^{17}	1.82×10^{-5}	154.9	8.53×10^{-5}	0.75015	27.55	2.53×10^{-10}	0.97796	0.24887	1.51×10^{-6}	6.12×10^{-8}
10hrs	$1. \times 10^{20}$	2.38×10^{-5}	849	2.19×10^{-4}	0.73938	61.94	7.05×10^{-10}	0.87968	0.97126	3.63×10^{-6}	1.27×10^{-7}
20hrs	8.21×10^{19}	2.73×10^{-5}	1015	707×10^{-4}	0.54846	240	2.41×10^{-9}	0.77565	3.546	3.90×10^{-9}	3.52×10^{-7}

Table 5.9: Best fitting parameters for the EEC in Figure 5.23 for the PC0.35w/b cement paste at of 15mins, 10hrs and 20hrs

Mix	Age hrs	R_e (Ω)	R_p (Ω)	C_p (F)	C_{oe} (Fs^{p-1})	p_e
PC0.30w/b	9	53.99	3373	8.24×10^{-10}	6.06×10^{-10}	0.89
PC0.35w/b	9	53.99	3373	8.24×10^{-10}	6.06×10^{-10}	0.89
PC0.45w/b	9	41.39	3780	4.60×10^{-10}	7.33×10^{-10}	0.89
35%GGBS0.35w/b	9	55.65	2860	1.57×10^{-10}	2.28×10^{-10}	0.94
50%GGBS0.35w/b	9	60.89	4531	8.91×10^{-10}	2.02×10^{-10}	0.94
65%GGBS0.35w/b	9	69.56	4433	1.18×10^{-9}	1.91×10^{-10}	0.94

Table 5.10: Best fit parameters for the EEC at Figure 5.36 at 9 hrs for the pure paste mixes and GGBS replaced mixes

Mix	Age (hrs)	$R_e(\Omega)$	$R_c(\Omega)$	C_c (F)	$R_f(\Omega)$	C_f (F)	$C_{oe}(Fs^{p-1})$	p_e	$R_p(\Omega)$	C_p (F)
35%PFA 0.35w/b	2	31.87	1193	1.42×10^{-8}	1040	1.09×10^{-9}	1.23×10^{-10}	0.97	841.7	1.07×10^{-10}
	5	36.8	896.3	5.59×10^{-8}	1009	4.68×10^{-9}	6.45×10^{-10}	0.96	1107	3.70×10^{-10}
	9	51.19	1371	3.16×10^{-8}	1281	3.38×10^{-9}	4.80×10^{-10}	0.92	1493	2.72×10^{-10}

Table 5.11: Best fit parameters for the 35%FA cement paste of 2hrs, 5hrs and 9hrs

Mix	Age (hrs)	$R_e(\Omega)$	$R_c(\Omega)$	C_c (F)	$R_f(\Omega)$	C_f (F)	$C_{oe}(Fs^{p-1})$	p_e	$R_p(\Omega)$	C_p (F)
65%PFA 0.35w/b	2	44.08	907.2	5.09×10^{-8}	899.9	5.37×10^{-9}	4.37×10^{-9}	0.79	970	5.00×10^{-10}
	5	47.3	1059	3.94×10^{-8}	972.7	4.54×10^{-9}	3.13×10^{-9}	0.81	1021	4.45×10^{-10}
	9	55.78	1121	3.30×10^{-8}	997.1	4.32×10^{-9}	2.04×10^{-9}	0.83	1135	4.01×10^{-10}

Table 5.12: Best fit parameters for the 65%FA cement paste at the ages of 2hrs, 5hrs and 9hrs

Chapter 6 – Electrical Properties of Cementitious Materials during Long-term Hardening

In this chapter, the change in electrical properties through the hardening stage (up to 360 days), is presented and discussed within the context of reactivity of the different binders, the development in the pore-structure and the durability of the concrete mixes. The extended monitoring period highlights the influence of the SCMs on the electrical parameters when compared to the pure PC concrete mixes. These SCMs can be related to their efficiency in modifying the pore size distribution and the porosity of the mixes. Bulk electrical measurements are compared with a conventional durability ranking test (migration test), to establish a ranking methodology using electrical monitoring.

The electrical response for the mixes in this chapter is discussed within the context of (a) the bulk conductivity response, (b) the permittivity response, (c) Nyquist plot features.

6.1 Bulk electrical conductivity

The conductivity was obtained using the 2-point end-to-end electrode configuration as detailed in Chapter 4. The frequency at the cusp point between the intermediate arc and the bulk arc was located for each mix and the corresponding resistance used in the calculation of the bulk conductivity. Figures 6.1(a) – (c) present the change in conductivity with time. A rapid decrease in conductivity for all mixes is evident over the period 1-day to 28-days; thereafter, there is more gradual decrease until the end of the monitoring period. It is interesting to note that at early ages (1-7days) the replaced mixes display a higher conductivity when compared with the Portland cement concrete mixes. For example, considering the 0.35w/b mixes, the PCC records an average value of 0.02 S/m at the age of 1-day, however the 65%GGBS, 35%GGBS, 35%FA mixes record values of, respectively, 0.037 S/m, 0.033 S/m and 0.034 S/m. The higher conductivity of the replaced mixes, in comparison to the PCC, changes with time, as a ‘cross-over’ appears as early as 7-days between the PCC mix conductivity and the 65%GGBS mix. With regard to the 0.35w/b 35%GGBS mix, the same cross-over with the PCC mix takes place; however, in this case, it takes place at the age of 14 days. For the 35%FA mixes, the cross-over point occurs at approximately 28-days. The trend for high values for the replaced mixes at early ages and the lower values at later ages in comparison to the plain concrete mixes is observed for all w/b ratios. At later ages >100 days, from Figure 6.1 all mixes continue their decreasing trend through time, and at the end of the monitoring

period the PCC mixes have a larger conductivity than the replaced mixes; for example, at the age of 365 days the 0.35w/b PCC records a conductivity of 4.16×10^{-3} S/m whereas the 35%GGBS, 65%GGBS and 35%FA have, respectively, values of 2.65×10^{-3} S/m, 1.36×10^{-3} S/m and 9.6×10^{-4} S/m.

Referring to Figure 6.1, the development in the pore structure clearly affects the conductivity of the concrete. This is observed from the continuous decreasing trend through time and indicates the progressive refinement of the interconnected capillary pores which are the main path for ionic conduction. The pore refinement process decreases with time due to the decrease in the rate of hydration. As an illustration, Figure 6.2(a) shows a rapid decreasing rate for the capillary pore sizes between the ages of 28-days and 90-days, in contrast to a relatively small change in the pore size distribution between the age of 90-days and 1 year. This agrees with the trend in the conductivity with regard to the rapid decreasing trend for the samples at the ages between 1-28 days in contrast to the more gradual decreasing rate during the period after 28 days.

With regard to the influence of the w/b ratio on the conductivity of the concrete mixes, it is evident from Figure 6.1 that as the w/b ratio of the concrete mixes increases the conductivity increases and this corroborates previously published work (see Chapter 3). This is attributed to the effect of the w/b on the pore structure as, by considering Figure 6.2(b), as the w/b in the mix increases, both the intruded mercury volume as well as the volume fraction of the large capillary pores increases (Kim et al., 2014). At 0.3w/b, the largest pores at the age of 28-days have a value of 100nm; however, by increasing the w/b to 0.9, the largest pore sizes record the value of 1 μ m. This is also reflected on the size of the interconnected capillary pores, as the critical diameter radius is expected to increase as the w/b increases. Therefore, due to the larger and more interconnected pore structure resulting from increasing the w/b, the conductivity of the samples increases.

With regard to SCM's, all the replaced mixes have a high conductivity in comparison to the PCC mixes at ages which are ≤ 7 days. The replaced mixes have a more interconnected and open pore structure than in the PCC mixes at early ages due to the slower pozzolanic reaction prior to the cross-over points shown in Figure 6.1 (Lawrence et al., 2003; Cyr et al., 2006).

6.1.1 Formation Factor and Pore Solution Conductivity

It is evident that the 65% GGBS mixes, cross-over the PCC conductivity at earlier ages when compared with the 35% GGBS mix and the 35% FA mix. In order to explain this trend for the 65% GGBS replaced samples, the Formation Factor (F) can be used. F is defined as (Archie, 1942; Kyi and Batchelor, 1994; Snyder, 2001):

$$F = \frac{\sigma_o}{\sigma_{bulk}} \quad (6.1)$$

Where σ_o is the conductivity of the pore solution (S/m) and σ_{bulk} the conductivity of the concrete. In the current work, the pore-solution conductivity was evaluated using the model developed by Snyder et al. (2003) and Bentz (2007) which is based on the following assumptions:

- (a) The main ions in the pore-water are K^+ , Na^+ and the OH^- .
- (b) 75% of the K^+ and Na^+ ions in the cementitious materials are released to the pore solution by the age of 28-days.
- (c) Alkalis in the slag material are adsorbed on the slag hydration product therefore they do not affect the pore solution concentration.
- (d) The OH^- ionic concentration is calculated based on electroneutrality, by summing the released K^+ and Na^+ concentrations.
- (e) The volume of the pore water used to calculate the concentration of the pore solution is deduced from equation (6.2):

$$V_{ps} = \frac{w}{b} - 0.23\alpha - 0.06\alpha \quad (6.2)$$

In which, V_{ps} = volume of pore solution (l/kg); 0.23α = Hydration product bound water (l/kg); 0.06α = fraction of water imbibed due to chemical shrinkage (l/kg); α = degree of hydration at time (t). In order to obtain the degree of hydration, $\alpha(t)$, a three parameter model is used (Schindler and Folliard, 2005), and summarized below. The model estimates the degree of hydration $\alpha(t)$ by fitting the equation presented in equation (6.3):

$$\alpha(t) = \alpha_{ult} \cdot e^{(-\left[\frac{\tau}{t}\right]^\beta)} \quad (6.3)$$

In which, τ = hydration time parameters (unit time); β = hydration shape parameter, and, α_{ult} = Ultimate degree of hydration. Equation (6.3) yields both τ and β from the fitting process. With regard to α_{ult} , this parameter is obtained as follows:

$$\alpha_{ult} = \frac{1.031 \cdot w/b}{0.194 + w/b} + 0.5 \cdot P_{FA} + 0.30 \cdot P_{slag} \leq 1.0 \quad (6.4)$$

In which, w/b = water to cementitious material ratio; P_{FA} = fly-ash replacement percentage in the mix, and P_{slag} = slag replacement percentage in the mix.

With regard to the experimental degree of hydration data, the heat output for representative pastes with the same mix proportions as the respective concrete mix has been obtained using an isothermal calorimetric test for a period of 168 hours. The degree of hydration of the experimental heat evolution data has been obtained according to the following equations:

$$\begin{aligned} H_{cem} (J/gm) = & 500 P_{c_3s} + 260 P_{c_2s} + 866 P_{c_3A} \\ & + 420 P_{c_4AF} + 624 P_{so_3} + 1186 P_{Free CaO} \\ & + 850 P_{MgO} \end{aligned} \quad (6.5)$$

$$\alpha(t) = H(t)/H_T \quad (6.6)$$

$$H_T(J) = C_c \cdot H_u \quad (6.7)$$

$$H_u (J/gm) = H_{cem} P_{cem} + 460 P_{slag} + 209 P_{fa} \quad (6.8)$$

In which; H(t) = the cumulative heat at time (t); H_T = the total heat emitted at 100% hydration degree for the cementitious material; C_c = cementitious material content (unit weight); H_u = heat emitted per unit weight cementitious material; H_{cem} = heat emitted per unit weight cement. This parameter is calculated according to equation (6.5) in which $P_{c_3s}, P_{c_2s}, P_{c_3A}, P_{c_4AF}, P_{so_3}, P_{Free CaO}, P_{MgO}$ are the weight percentages for the relevant cement compound calculated from the Bogue equations; P_{cem} = cement weight percentage in the mix.

Figure 6.3 presents the fitting curves for the experimental data obtained from the calorimetry studies with the best fitting parameters presented in Table 6.1. From Table 6.1 and Figure 6.3, it is evident as the w/b ratio in the mixes increases both the α_{ult} and $\alpha(t)$ record higher values at later ages (Lura et al., 2017). Also, the addition of SCM to the mixes increases the value of α_{ult} in comparison to the plain mixes.

The results of the pore solution conductivity are presented in Figure 6.4. Figure 6.5 shows the resulting 1/F – time response for the concrete mixes through the initial 60-days

hydration. It is interesting to note the time difference between the age at which the 1/F curve (Figure 6.5) and the conductivity curve (Figure 6.1) for the 65%GGBS mixes cross-over. As the 65%GGBS 1/F curve crosses the PCC curve later than the corresponding conductivity curves, this would indicate that, when comparing the 65% GGBS mix with the PCC mixes at early ages, the pore solution conductivity must be considered (Shi, 2004; Neithalath and Jain, 2010). At ages < 7 days (see Figure 6.1), the high conductivity for the 65%GGBS is due to the more porous structure in comparison to the PCC mixes. However, after the age of 7-days until the 65%GGBS 1/F curve crosses the PCC 1/F curve, the high value of the PCC conductivity is due to the high conductivity of the pore solution in the PCC mixes compared to the 65%GGBS mixes. In Figure 6.5, as it is clear that all the mixes record higher 1/F values than the PCC mixes at ages < 30 days, which implies that after this time the replaced mixes are producing a more refined pore structure in comparison to the PCC mixes.

It can be concluded that the early age low-conductivity values for the 65%GGBS in Figure 6.1, is not due to the modification in the pore structure due to the reactivity of the GGBS, but due to the low pore-solution conductivity in these mixes in comparison to the PCC mixes.

Regarding the 35%GGBS, for the 0.35w/b mix the conductivity crosses the PCC conductivity at the age of 14-days, 21-days for the 0.45w/b and 28-days for the 0.65w/b. When considering the pore-solution conductivity these cross-over times for the 35%GGBS are 35-days (0.35w/b), 40-days (0.45w/b) and 70-days (0.65w/b). With regard to the 35%FA mix, as the w/b increases the cross-over age from the 1/F curve decreases particularly the 0.65w/b mix and this is attributed to the increase in the degree of hydration as the w/b ratio increases. This indicates that at the high w/b, the FA is more efficient than the other SCMs in filling the open pores by producing ‘ink-bottle’ pores (Yu et al., 2017).

6.2 Dispersion in permittivity and conductivity

In this section, the permittivity and conductivity are presented in both the time and frequency domains for the concrete mixes.

6.2.1 Dispersion and temporal effects on relative permittivity

Figure 6.6 presents both the relative permittivity, $\epsilon_r(\omega)$, and conductivity $\sigma(\omega)$ as a function of frequency at 28-days, 180-days and 360-days for the 0.35w/b concrete mixes.

It is evident that over the frequency range 1Hz-10MHz there is an overall decrease in the $\epsilon_r(\omega)$ and increase in $\sigma(\omega)$ representing a region of dispersion and this is discussed below. From Figures 6.6 (a) – (d), the permittivity attains values in the range of $\sim 10^7$ at low frequencies ($\sim 1\text{Hz}$) and this is attributed to electrode polarization processes, before decreasing rapidly as the frequency increases, approaching values of ~ 25 in the frequency range 5MHz-10MHz. The permittivity in this frequency range displays a dependency on the mix as well as the age (Taylor and Arulanandan, 1974; Yoon et al., 1994; Al-Qadi et al., 1995; Gu and Beaudoin, 1997; Wen and Chung, 2001) however, over the period of relaxation /dispersion 3-zones can be identified:

- (i) $\sim 1\text{Hz}-100\text{Hz}$: attributed to electrode/sponge interfacial effect.
- (ii) $\sim 100\text{Hz}-10\text{kHz}$: attributed to sponge/sample interfacial effect; and,
- (iii) $\sim 10\text{kHz}-10\text{MHz}$: attributed to polarization processes within the bulk material.

The $\sigma(\omega)$ response, also displays marked changes over these frequency ranges: a low-frequency increasing region ($\sim 1\text{Hz}-100\text{Hz}$), a period of slowly increasing conductivity ($100\text{Hz}-10\text{kHz}$), and a region of rapidly increasing conductivity ($10\text{kHz}-10\text{MHz}$). At the lower end of region (ii) the DC conductivity can be located, before a rapid increase in the $\sigma(\omega)$ takes place due to the progressive contribution of relaxation of polarization processes to σ_{ac} (see equation (4.8))

6.2.2 Hydration effect

Figures 6.7 – 6.9 present $\epsilon_r(\omega)$ at four frequencies within zone (iii) represented by 100kHz, 500kHz, 1MHz and 5MHz. The permittivity is a measure of the polarizability of the material and, as discussed in Chapter 3, the main polarization processes operating with the material will be double-layer and interfacial processes (see Figure 3.4). In Figures 6.7 – 6.9, two types of responses can be observed depending on the measuring frequency range. The relative permittivity in the frequency range 100kHz-1MHz for all the mixes follows a ‘conductivity-like’ behaviour as, at early ages, the concrete has a more porous structure. This will lead to an increase in the polarizability of the concrete due to the ease of charge oscillation in sympathy with the applied electrical field. At later ages, the polarizability of the samples decreases due to pore structure refinement and reducing porosity.

In the frequency range 1MHz-5MHz, $\epsilon_r(\omega)$ becomes less sensitive to the aging process. It is evident that $\epsilon_r(\omega)$ for the replaced mixes is higher than the PC concrete mix and this becomes more discernible as the frequency increases. The conductivity for the replaced mixes, on the other hand, is lower than the PC mix particularly at later ages. This feature could be attributed to the more disconnected pore structure for the replaced mixes (but not necessarily of lower porosity) which would increase the polarizability of the material through the interfacial processes.

6.2.3 Water/binder (w/b) ratio

With regard to the effect of w/b on the permittivity, it is clear that as the w/b increases, the electrical permittivity of the mixes increases. This could be attributed to the effect of the w/b on the pore structure, as a more open pore structure is expected to exist in the samples by increasing the w/b. Therefore, this would increase the conductivity and permittivity values. It is interesting to note that both the mid-frequency (100kHz-1MHz) and high-frequency permittivity (1MHz-5MHz) are affected by the increase in the w/b ratio. This would indicate that both the mid-frequency and high-frequency permittivity, are associated with the changes in the pore structure and are both affected by increasing the w/b ratio.

6.3 Nyquist Plots and Equivalent Circuit Model

Figure 6.10 and Figure 6.11 show the Nyquist plots for different concrete mixes (w/b=0.35) at the ages of 7, 28, 56, 180 and 360 days using two different electrode configurations viz. the 2-point using end-to-end plates and 2-point using embedded pin electrodes. The difference between the Nyquist plots obtained by the 2-point embedded electrodes and the 2-point end-to-end plate could be summarised as follow:

- (a) Regarding the end-to-end configuration (Figure 6.11) an intermediate arc occupies the zone between the electrode polarization arc and the bulk material arc. This intermediate arc has been discussed by McCarter et al. (2015), and has been attributed to an interfacial phenomenon between the sponge-sample interface.
- (b) The bulk resistance which is recorded by the embedded pins is larger when compared with the resistance recorded by the 2-point end-to-end plates; however, the resistivity of the sample should be the same for both of the different electrodes configuration (McCarter et al., 2005; Rajabipour et al., 2007; McCarter et al., 2013).

Figure 6.12 shows the influence of w/b on the Nyquist plot with plots presented at 28-days. It is evident from Figures 6.10 – 6.12 that the diameter of the bulk arcs increases with time and decreases with w/b. However, the characteristic frequency f_c , and the CPE exponent, p , also change and are discussed below.

6.3.1 Bulk arc Characteristic Frequency (f_c)

From Figure 6.13, f_c shows a continual decreasing trend through time, which is similar to the conductivity response for the mixes and is attributed to the development of a more disconnected pore structure due to the hydration process. The bulk arc characteristic frequency reflects the refinement and the development in the pore structure with time. The same explanation can be adopted when considering the effect of the w/b and SCMs on f_c , as, by increasing the w/b ratio in the mixes, the pore structure becomes more open, thereby allowing charges to follow the electrical field at a higher frequency in comparison to the lower frequency which is recorded for the low w/b mixes. In a similar fashion, the addition of SCMs to the mix causes the bulk arc characteristic frequency to reduce progressively through time to a lower frequency range.

6.3.2 Bulk arc CPE exponent (p)

The CPE exponent (p) was obtained by fitting the impedance response to the EEC used by McCarter et al. (2015) for the 2-point end-to end electrodes configuration. Figure 6.14 shows the exponent, p , through time for the different mixes. For example, regarding the PCC mixes, the p value for the 0.35w/b is 0.875 at 7 days decreasing to 0.775 at 360 days; increasing the w/b ratio to 0.65 increases the p value to 0.925 at 7-days and 0.825 at 360-days. The observed CPE exponent values through time for the concrete mixes in this study, are comparable to the range which has been suggested by (Christensen et al., 1994). The p values for all other mixes display the same decreasing trend through time, hence the centre of the bulk arc becomes more depressed below the real axis. It is also evident that, at the same w/b ratio, the PCC mixes exhibit the highest p values in comparison to the other mixes and, as the GGBS replacement level in the mix increases, the p values decrease. These trends for p can be summarised as follows:

- (a) a decreasing trend for p through time for all mixes;
- (b) by including SCMs in the mix, the values of p decrease when compared with the values of the PCC mixes, particularly at late ages; and
- (c) it has been shown that as the w/b ratio increases, the p value also increases.

The trends for p can be explained in the context of the pore size distribution of the mixes and the volumetric fraction of each pore size. At very early ages at which a minimum depression angle is observed for the bulk arc (large p value), the large capillary pores are expected to dominate the porosity despite the wide pore size distribution during this early age. As the samples age, these larger capillary pores gradually decrease in diameter which increases the volumetric fraction of the smaller pores especially in the range of the gel pores, which are $<10\text{nm}$ (Zeng et al., 2012). With time, the volume fraction of small pores ($<100\text{nm}$) increases and that of the large pores ($>100\text{nm}$) decreases. The relaxation behaviour of the charges in the large capillary pores are expected to show different relaxation frequencies than the small pores due to the pore surface proximity (Gu et al., 1993). Therefore, a distribution in the relaxation time in the mixes is expected to take place on the bulk arc when a broad pore size distribution exists in the mix as well as when a significant volumetric fraction for each pore size emerges in the mixes through time (Gu et al., 1994; Andrade et al., 1999).

The addition of SCMs on the pore size distribution has been studied by Berodier and Scrivener (2015) and it has been shown that a broad distribution of pore sizes for both the FA mixes and the GGBS mixes is attained as early as 28-days when compared with the plain cement pastes. This broader distribution shows an increase in the volume of the pores in the range between 2nm - 8nm . Therefore, in this case, a larger depression angle is expected for the replaced mixes in comparison to the PCC mixes due to both the increase in the volume fraction of the small pores as well as the broad distribution of pore sizes. The effect of increasing the p values when increasing the w/b in the mixes is also attributed to the increase in the pore size; in this case, as the pore size distribution and the volume fraction of the large pores will dominate, so a small depression angle, hence large p value, is observed.

6.1.1 Concrete hardening stage EEC

In this section, the electrical response of the concrete through the hardening stage is modelled using an equivalent electrical circuit (EEC). According to the different electrical parameters in the proposed EEC, the experimental response is explained and related to the different pore structure components which exist in the hydrated material. The EEC response is verified by assessing its response through:

- (a) the hydration process;

(b) w/b ratios;

(c) the effect of different SCM's; and,

(d) comparing the modelled EEC response with the experimental data.

As was shown in Figure 6.14 and as suggested in other studies, the depressed arc for the bulk Nyquist plot is a result of the broad pore size distribution and the volumetric fraction of each pore size in the hardened cementitious material. This stems from the different physical properties of different pore sizes, especially the adsorption conditions of the pore-water (Sánchez et al., 2013). In the current study, the bulk response of the different concrete mixes has been modelled by the use of the EEC shown in Figure 6.15. In this EEC, the bulk response is represented by 3 electrical paths and 4 circuit elements. The electrical parameters are:

CPE_c = this parameter represents the polarization process on the surface of the connected pores;

R_c = represents the electrical conduction process in the connected pores;

R_{dis} = represents the conduction process in the disconnected pores;

C_{dis} = represents the polarization process in the disconnected pores and

R_s = offset resistance (Christensen et al., 1994; Kim et al., 1995; McCarter et al., 2015)

With regard to the measuring system, a parallel resistor/CPE (R_{el}/CPE_{el}) has been used to account for the electrode response at the concrete/sponge interface (McCarter et al., 2015). In some cases, an additional resistor/CPE circuit is added to account for the polarization process on the surface of the electrodes (i.e electrode/sponge interface) whenever the electrode polarization spur is detected.

Figure 6.16 shows the fitted experimental Nyquist plots for the different mixes at selected ages which are 28 days, 180 days and 360 days. In this case, only the 0.35w/b mixes are presented. Tables 6.2 - 6.5 show the best fit parameters for the Nyquist plots in Figure 6.16. Two points can be drawn from the fitting values which are:

- (i) From Tables 6.2 - 6.5, the capacitor values (C_{dis}) and the C_o , which are assumed to represent the bulk material, are in the range of 10^{-11} F and 10^{-10} Fs^{p-1} respectively; on the other hand, the CPE which is suggested to represent the electrode polarization phenomena, has a C_o coefficient in the range of $\sim 10^{-5}$ and p value is in the range

0.40-0.50 (McCarter et al., 2015). The values of these electrical parameters prove their relation to the bulk material and electrode phenomena respectively.

- (ii) It is evident that R_{dis} , which represents the disconnected pores, has larger values through the whole testing period when compared with R_c . This indicates that the R_{dis} represents more constricted/disconnected electrical paths when compared with the R_c response.

In order to assess the response of the assumed EEC through time, as well as concrete mixes, Figures 6.17 – 6.19 show the temporal response for the EEC parameters at different w/b and different SCM additions. The results for the EEC parameters are discussed in terms of the EEC capacitance/CPE responses, and the conductance of the corresponding paths (G_c , G_{dis}) instead of the resistances, in which $1/R=G$.

w/b ratio

For all the mixes, the values of the EEC bulk related electrical parameters increase as w/b increases. With regard to the conductance parameters which represent the connected pores and the disconnected pores, G_c , G_{dis} respectively, these show an increase as w/b increases. The capacitor, which is related to the polarization processes in the disconnected pores, and the CPE (represented by the C_0 and the p) which represents the connected pores, also display the same increasing trend with increasing w/b. This increasing trend is attributed to the increase in the porosity of the mix which would influence both the conductivity as well as the oscillation of charges at the solid /liquid interfaces, hence the polarizability of the mix. Therefore, the capacitive and conductive elements, in this case, reflect changes in the pore structure resulting from the change in w/b. Due to the increasing trend for EEC bulk related electrical parameters when increasing the w/b, all the EEC electrical parameters are related to the processes within the pore structure, this is contrary to what has shown in other studies which had related the CPE_c to the polarization in the solid phase (Andrade et al., 1999; Cabeza et al., 2002; Cabeza et al., 2003; Cabeza et al., 2006).

Hydration effect

As can be observed in Figures 6.17 – 6.19, all the conductance and the capacitance/ C_0 values, which are related to the bulk material, show a continuous decreasing trend through time, regardless of w/b. This can be explained in terms of the decrease in the porosity as well as the pore size for both the connected and disconnected pores. The G_c response for

the PCC mixes at the end of the monitoring period decreases by $\sim 65\%$ from its initial value, on the other hand, G_{dis} decreases by $\sim 25\%$ from its initial values. The same trend for these parameters is evident for two GGBS mixes, as G_c for the 35%GGBS and 65%GGBS decrease by 80% and 90% from their initial values, respectively. G_{dis} for the 35%GGBS decreases by $\sim 30\%$, for the 65%GGBS decreases by 40% respectively. This rapid decreasing trend which is observed for G_c for all mixes in comparison to G_{dis} could be related to the continuous conversion of the large connected pores to smaller disconnected ones.

The CPE_e exponent p shows a rapid decrease through time for all the mixes at early ages. At later ages, this parameter records relatively constant low values through time when compared with early ages as shown in the PCC, 35%GGBS and the 35%FA mixes. This would suggest at later ages the pore size distribution has stabilised due to the slow hydration reaction. With regard to the high replaced mixes (65%GGBS), a noticeable increase in this parameter takes place after the initial rapid early decrease. This is attributed to the infilling of the large pores by the GGBS hydration product at this high replacement level, and the production of more small pores with limited pore-size distribution which is reflected in the p response (Berodier and Scrivener, 2015).

SCM addition effect

Figures 6.17 – 6.19 show the response of the EEC bulk related electrical parameters through time for the different SCM's and their replacement levels. With regard to the G_c parameter, it shows a similar response for the bulk conductivity (Figure 6.1) for the different mixes. At early ages (7 days), and by taking the G_c for the PCC as a reference parameter, the G_c for the 35%GGBS mix records higher values than the G_c for the PCC. This agrees with the response which is shown by the bulk conductivity of these two mixes in Figure 6.1. On the other hand, and with regard to the 65%GGBS, this mix shows lower G_c values than the PCC mix at ages as early as 7 days. This indicates that this parameter is affected by the bulk pore solution conductivity of the mixes.

By considering the G_{dis} for the PCC, 35%GGBS and the 65%GGBS mixes, this electrical parameter displays a decreasing trend through time. Interestingly, when assessing the 'cross-over' age for the 35%GGBS and the 65%GGBS against the PCC mix, it is evident that the G_{dis} for the 35%GGBS and the 65%GGBS cross the PCC mixes at later ages when compared with the G_c . As for the 65% GGBS mixes, the G_{dis} records higher values

than the PCC mixes until the age of 28 days and, with regard to the 35% GGBS, the G_{dis} records values higher than the PCC up to the age of ~50 days. This trend would highlight two features of these mixes which are:

- (i) During the time period in which both the G_{dis} for the GGBS mixes record higher values than the PCC mix, the porosity of the disconnected pores, is higher in the GGBS mixes than the PCC mixes. This is due to the relatively slow reactivity of the replaced mixes in comparison to the PCC mixes; and,
- (ii) The lower values for both the G_{dis} for the GGBS mixes in comparison to the PCC mixes after the cross-over process, indicates the presence of more refined-disconnected electrical paths in the GGBS mixes in comparison to the PCC mixes due to shifting the pore size distribution to smaller sizes because of the GGBS effect.

It is clear from Figures 6.17 – 6.19 that C_o and C_{dis} for the GGBS mixes, show higher values than the PCC mixes over the entire monitoring period. This trend for C_o and C_{dis} can be explained in terms of pore refinement and the porosity of the mixes as follows:

- (a) At early ages, due to the slower reactivity of the GGBS mixes, larger C_o and C_{dis} values are expected at early ages in comparison to the PCC mixes due to the less developed pore structure in these mixes.
- (b) As the GGBS reaction proceeds, the pore network becomes more refined and tortuous which increases the number of the solid/liquid interfaces in the mix, as well as increasing the surface area of pores due to the increases in the tortuous length. The increase in the refinement of the pores in slag mixes has been shown to take place during the first 28 days (see, for example, Pandey and Sharma (2000); Canut (2011); Berodier and Scrivener (2015)). These studies have shown that blended cement obtains more refined pore structure than the pure cement mixes despite the larger porosity of the former mixes.
- (c) Thereafter the decrease in the sample conductivity due to the ongoing hydration process which decreases the porosity of the samples, decreases the values of C_o and C_{dis} . From this, both the GGBS replaced mixes and the PCC show decrease through time with regard to the C_o and C_{dis} .

With regard to the bulk material conductance G_c , G_{dis} in the fly-ash mixes, it is evident that these parameters follow the same trend which has been observed for the GGBS replaced mixes. Regarding G_c , this crosses over the PCC mixes at 40 days. On the other hand, and with regard to G_{dis} , this parameter crosses over its corresponding PCC at later ages when compared to the G_c cross over timing. This indicates the slow reactivity of the FA mixes in comparison to the other mixes.

With regard to the C_o and C_{dis} for the FA mixes, their response is expected to be complicated by the unburned carbon effect in the mixes, as this can increase the values of both the C_o and C_{dis} in comparison to the other mixes. However, it is interesting to note that these two parameters show a gradual increasing trend through time but with a decreasing rate. At early ages, these two parameters display higher values than the PCC mixes with an almost constant value through the first 50 days. Thereafter, they start to increase through time until ~125 days at which time they attain a constant value or decrease, as in the case of the 0.65w/b mix. The increase in C_o and C_{dis} could also be attributed to the increase in the number of the solid/liquid interfaces due to the pores refinement process through time due to the pozzolanic reaction. In this case, this effect is much more observable than in the case of the GGBS mixes due to the slow reactivity of the FA mixes in comparison to the GGBS mixes which allows the separation between the increase in the solid/liquid interface effect and the decrease in the porosity due to the pores in-filling process. This can shed a light on the FA mechanism in modifying the pore structure as it proceeds through generating more solid/liquid interface by producing more ink-bottle pores, thereafter filling the pores by hydration products. After the age of the 125 days the C_o and C_{dis} for all the FA mixes attain virtually a constant value.

6.4 Relation between the electrical response and mixes durability

In this section, the electrical response obtained at the end of the monitoring program for the concrete mixes, is compared with the results of the non-steady state chloride migration coefficient D_{nssm} obtained from NT Build 492 test (NTBuild492, 1999). Despite the many advantages which the NT Build test possesses over other existing tests such as RCPT, for example, the well-controlled temperature in this test (Tang and Nilsson, 1993), electrical measurements are considered as an easy to use, non-destructive quality control method, which can be developed for remote, in-situ monitoring of concrete structures (McCarter et al., 2000; McCarter et al., 2003; McCarter et al., 2005).

6.1.2 Electrical measurements results and NT Build results comparison

Table 6.6 and Figure 6.20 present the D_{nssm} results for the mixes at different w/b, the bulk material conductivity and the inverse of the formation factor (see equation (6.1)). From Figure 6.20, both the mixes ranking obtained from the conductivity and D_{nssm} are similar. In general, the FA mix with 0.35w/b records the lowest D_{nssm} ($8.47 \times 10^{-13} \text{ m}^2/\text{s}$), on the other hand, the PCC 0.65 w/b records the highest D_{nssm} ($12.72 \times 10^{-12} \text{ m}^2/\text{s}$). This is similar to the bulk conductivity, despite the high pore-solution conductivity (see Table 6.6) for the 35%FA 0.35w/b in comparison to the PCC 0.65w/b; the FA mix records lower bulk conductivity value when compared with the latter. The agreement between the conductivity ranking and the D_{nssm} can be illustrated more through Figure 6.21(a), as a strong linear relation between the two parameters is found with $R^2 = 0.94$.

With regard to the 1/F ranking system, here also the 35%FA 0.35w/b and the PCC0.65w/b mixes represent both the highest and the lowest limit for the mixes. However, a discernible difference in the ranking of the material based on the 1/F can be noticed when compared with the D_{nssm} and the conductivity ranking. For example, the 35%FA (0.45w/b) is ranked as more resistive in the case of the 1/F system than the 65%GGBS (0.35w/b) which is not the case on the conductivity and the D_{nssm} systems. Also, the PCC0.35w/b in the 1/F ranking system is more resistive than the 65%GGBS0.45w/b which is opposite to its ranking by the conductivity and the D_{nssm} systems. Figure 6.22 highlights clearly the discrepancy between the D_{nssm} /conductivity ranking system and the 1/F ranking system. In general, the differences between the two ranking systems can be summarized in the following points:

- (a) With regard to the 1/F ranking system, the low w/b mixes (0.35) are ranked more resistive than the higher w/b mixes which is not the case in the D_{nssm} /conductivity ranking system. The only exception for this rule in the 1/F ranking system, is the 35%FA0.45 mix, as it is ranked more resistive than the 65%, 35%GGBS 0.35w/b as well as more resistive than the PCC0.35 mix. This highlights the efficiency of the FA as a binder in producing more ink-bottle pores which offset the effect of increasing the w/b.
- (b) Within the same w/b, the 1/F ranking system ranks the fly ash mixes as the most resistive mixes, then the 65%GGBS, 35%GGBS and the PCC mixes respectively.

(c) The D_{nssm} /conductivity ranking system, and within the same w/b, the same order of the 1/F ranking system is followed for the PCC and the 35%GGBS mixes, however the 65%GGBS mixes and the fly ash mixes show a comparable ranking which is contrary to the 1/F ranking system (see Figure 6.22)

The agreement between the D_{nssm} ranking and the bulk conductivity ranking, which is not in total agreement with the 1/F ranking, could suggest that both NTbuilt492 test results and the conductivity tests depend on the pore-solution conductivity. This is very clear when assessing the durability ranking of the 65%GGBS0.65w/b by both the D_{nssm} /conductivity ranking system and the 1/F ranking system. In the former system this mix ranked as fifth, however with regard to the 1/F system this mix ranked as 9th (less durable). The high durability ranking for this mix in the D_{nssm} /conductivity ranking system is attributed to the low pore solution conductivity which this mix possess (see Table (6.6)) In the both tests (D_{nssm} /conductivity) an electrical field is applied through the samples either to obtain the bulk conductivity of the material or to accelerate the migration process of the chloride ions into the concrete (Gao et al., 2017). Therefore, both methods are expected to be influenced by the pore-solution conductivity; when the pore-solution of the mix is ‘calibrated out’ by the use of the 1/F ranking procedure, the mixes have a different order as the ranking now depends solely on the pore structure such as the connectivity and tortuosity. This difference between the both ranking systems (D_{nssm} /conductivity and the 1/F) is more highlighted in high replaced mixes due to the significant low pore solution conductivity of these mixes.

6.5 Summary

In this chapter, electrical impedance spectroscopy has been used to characterise the different concrete mixes up to the age of 400days. The effect of the pore solution on the conductivity of the mixes has been highlighted by using the Formation Factor results. The pore solution conductivity of the replaced mixes has been shown to have lower values when compared with the PCC mixes, which affects the conductivity values. The low-frequency permittivity has been shown to be influenced by the conductivity values through time; however, the high frequency permittivity is more affected by the binder type as the permittivity of the replaced mixes has been shown to be higher than the PCC mixes. An EEC model has been proposed to account for the experimental electrical response, which contained parameters related to the connected pores and disconnected pores.

A comparison between the durability ranking which obtained from the D_{nssm} /conductivity raking system and the formation factor ranking system has been conducted, and a difference between the three mentioned ranking systems was observed.

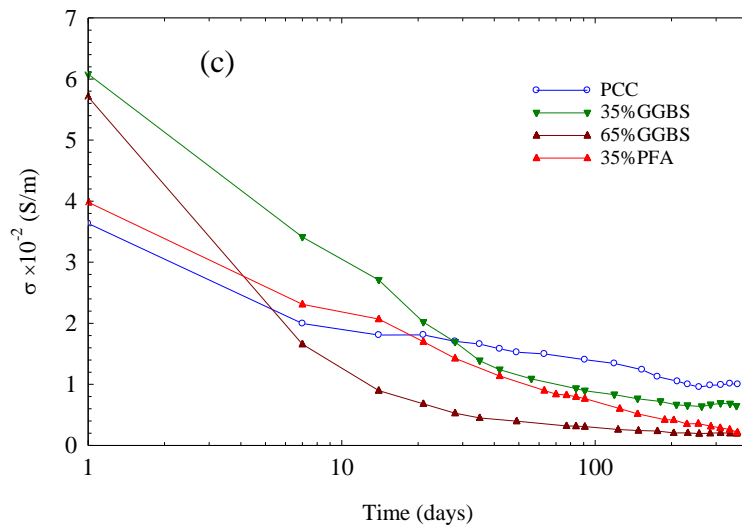
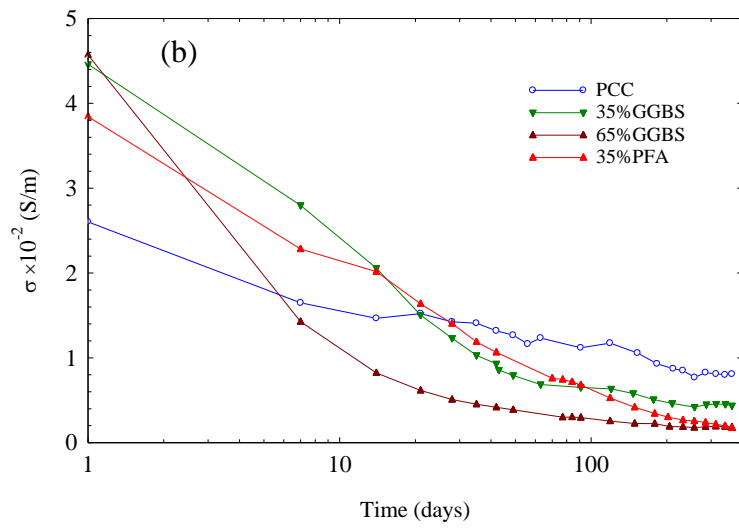
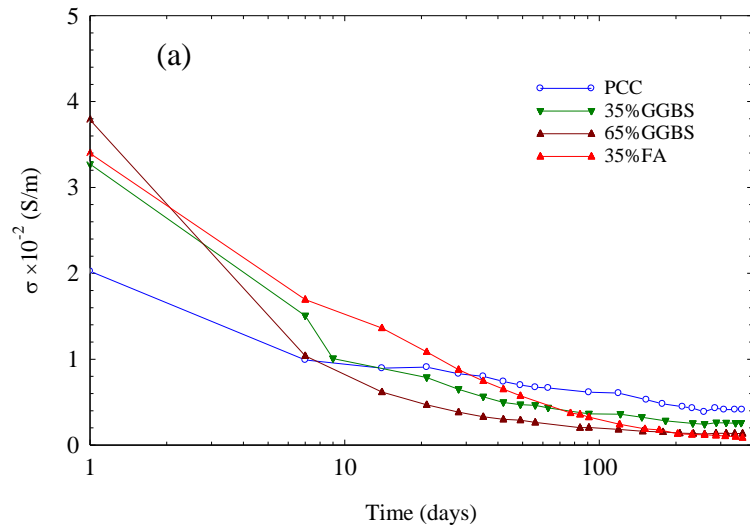


Figure 6.1: Conductivity during hardening stage for (a) 0.35w/b, (b) 0.45w/b and (c) 0.65w/b concrete mixes.

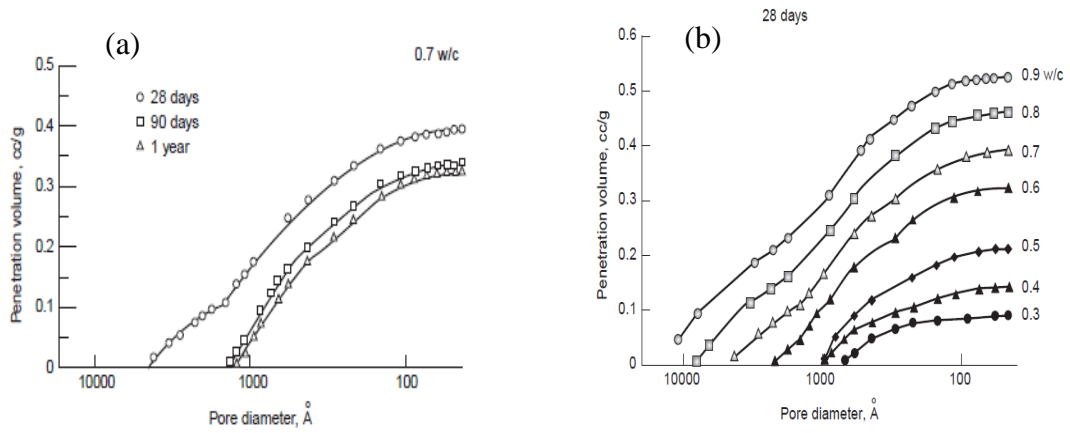


Figure 6.2: Pore size distribution in hydrated cement pastes for (a) 0.7w/b at different ages, and (b) for different w/b at 28 days age after (Mehta and Monteiro, 2013).

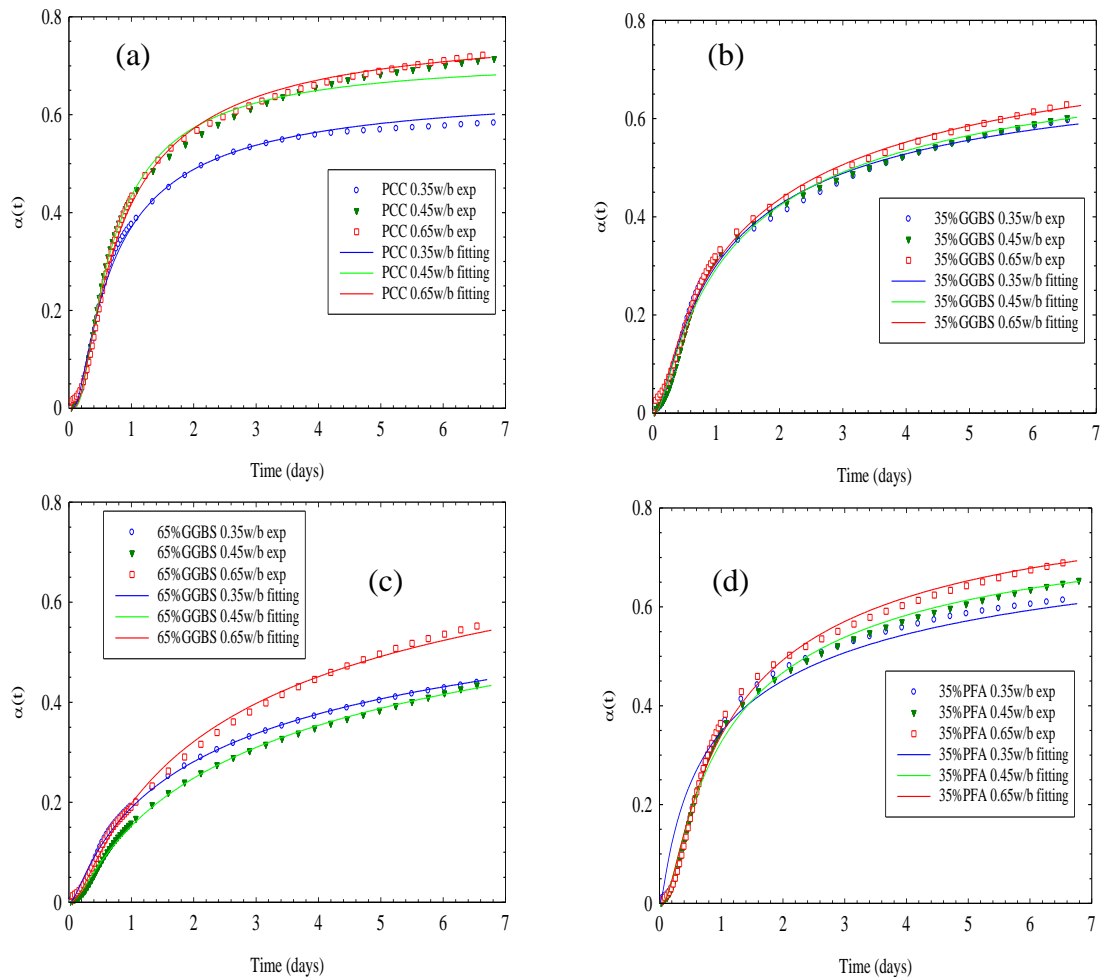


Figure 6.3: Degree of hydration experimental data from isothermal calorimetric test and their pertinent fitting results through the first 160 hrs for the different pastes samples

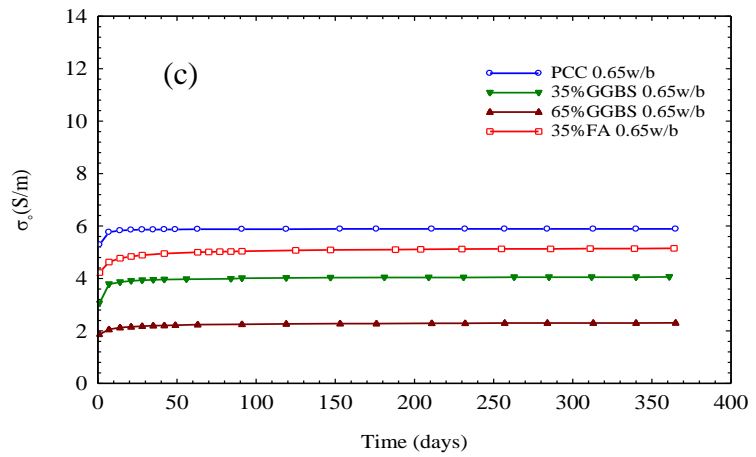
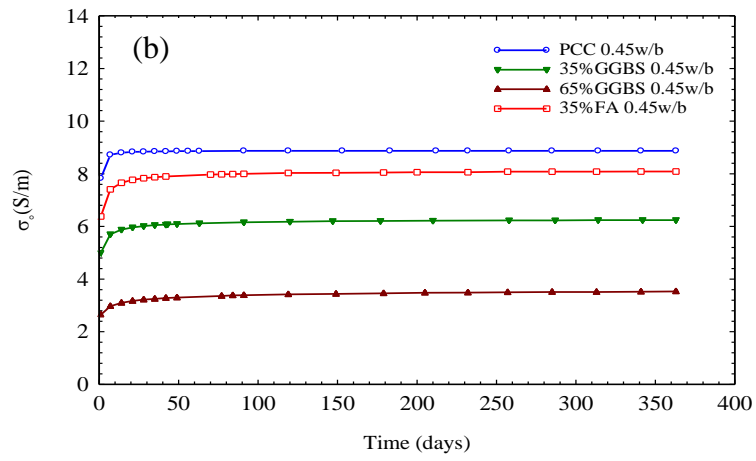
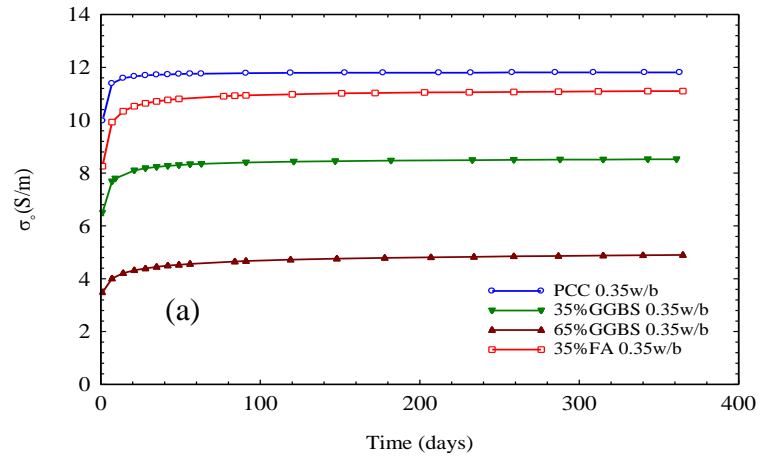


Figure 6.4: Pore solution conductivity for (a):0.35w/b (b):0.45w/b and (c):0.65w/b. concrete mixes.

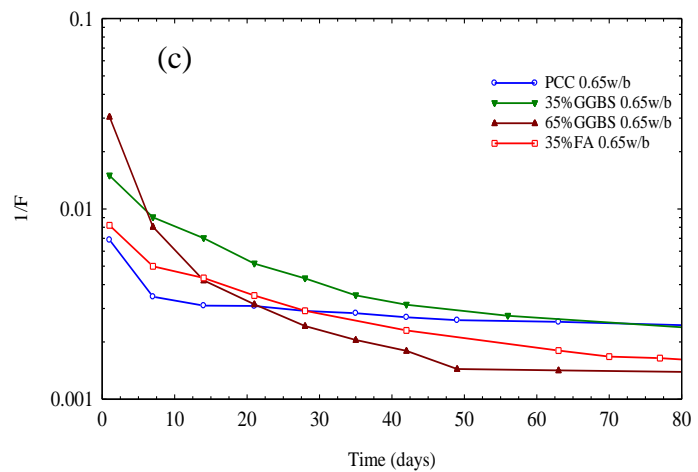
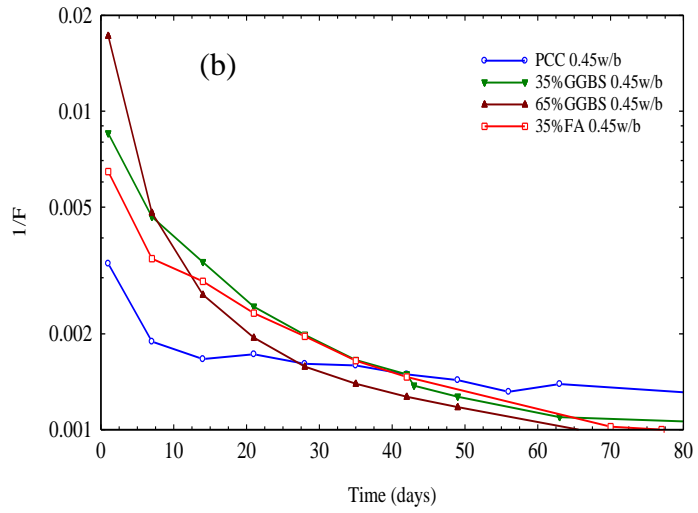
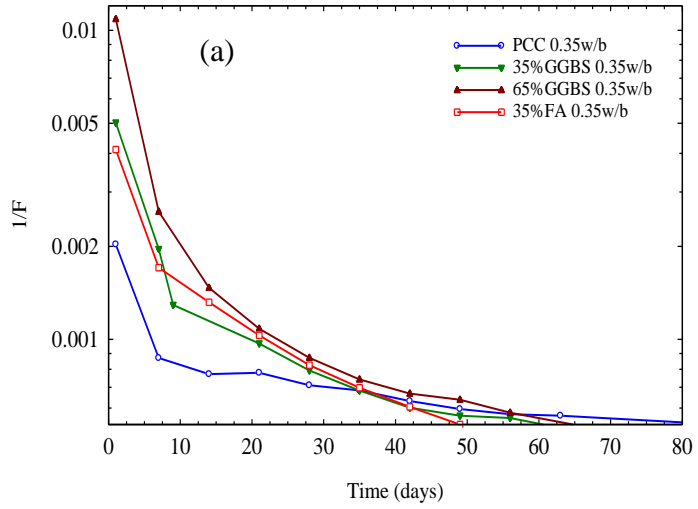


Figure 6.5: $1/F$ response through time for (a):0.35w/b mixes, (b):0.45w/b mixes and (c):0.65w/b mixes.

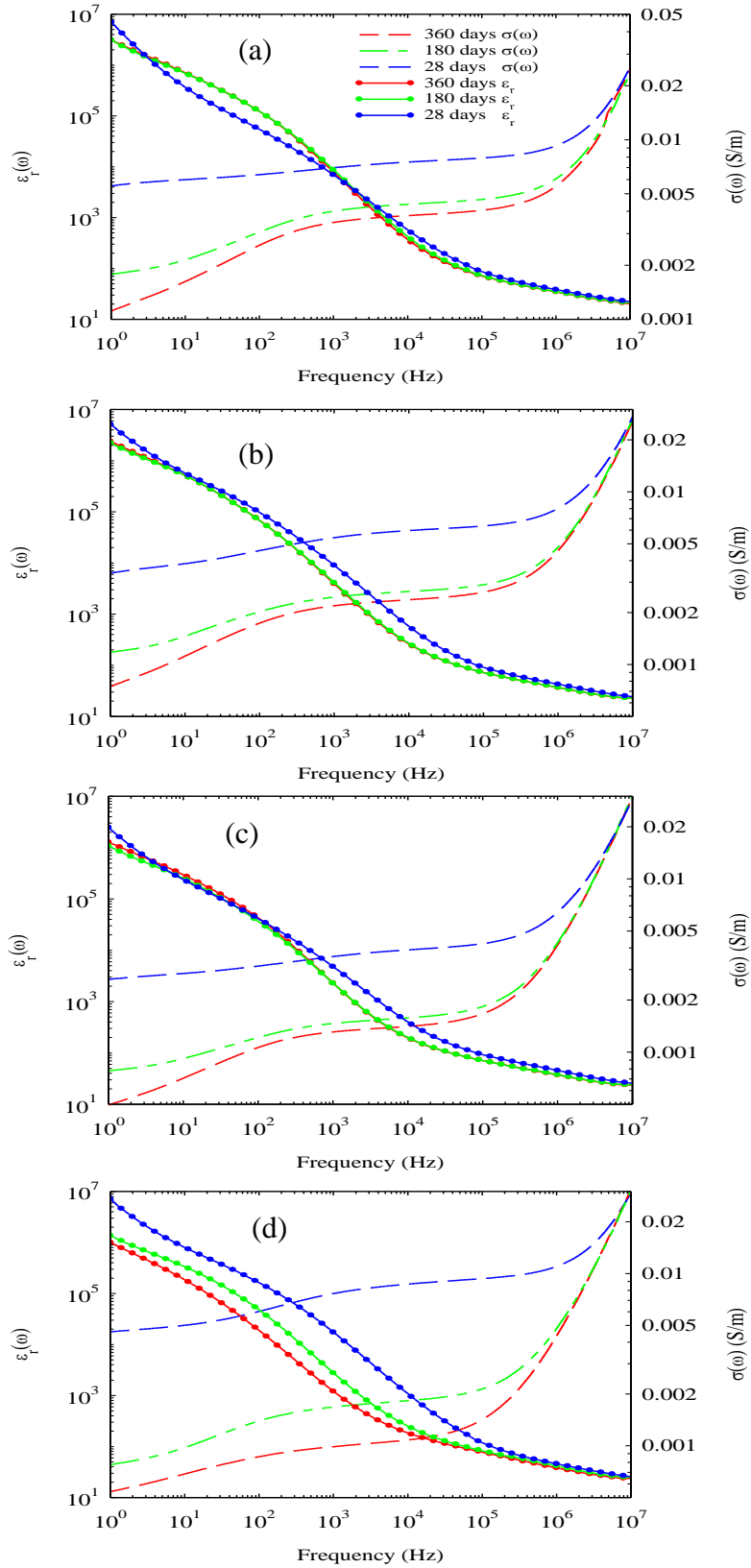


Figure 6.6: Electrical permittivity/conductivity for 0.35w/b (a) PCC, (b)35%GGBS, (c) 65%GGBS and (d) 35%FA at 28,180 and 360 days. [legend given in (a)].

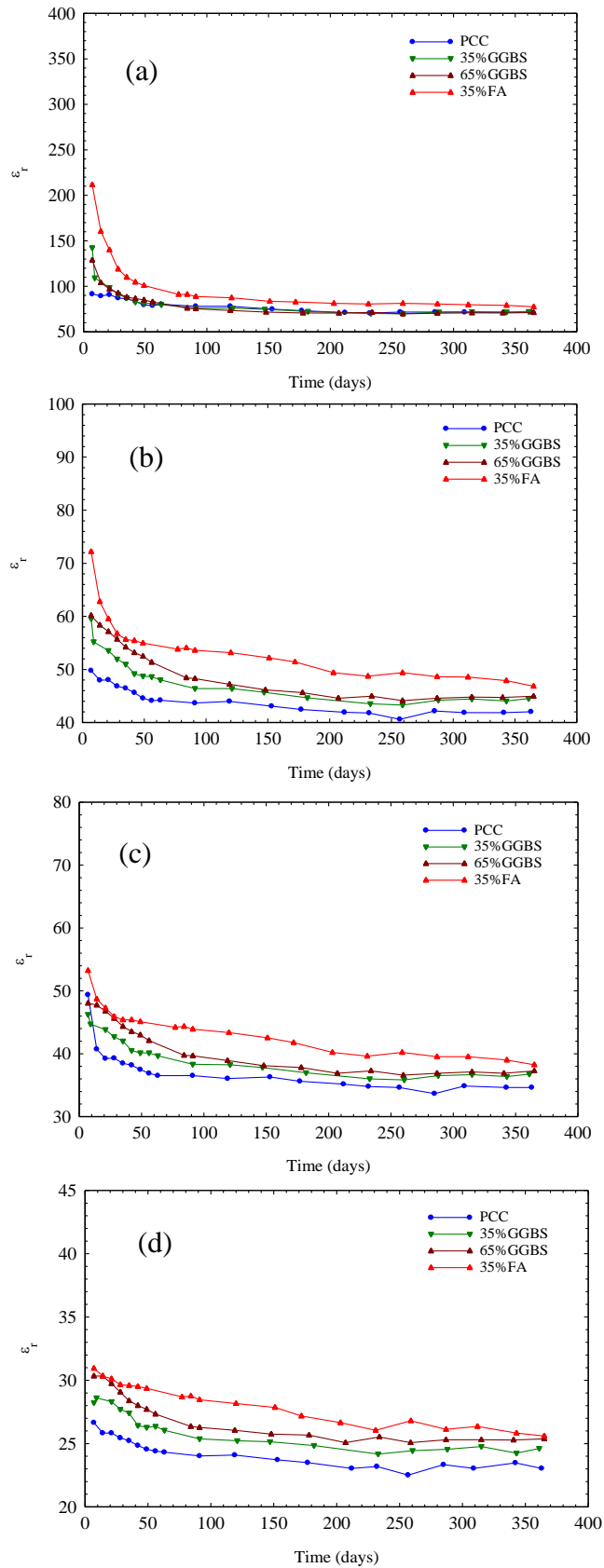


Figure 6.7: Relative permittivity at (a) 100kHz, (b) 500kHz, (c) 1MHz and (d) 5MHz for different concrete mixes at 0.35w/b.

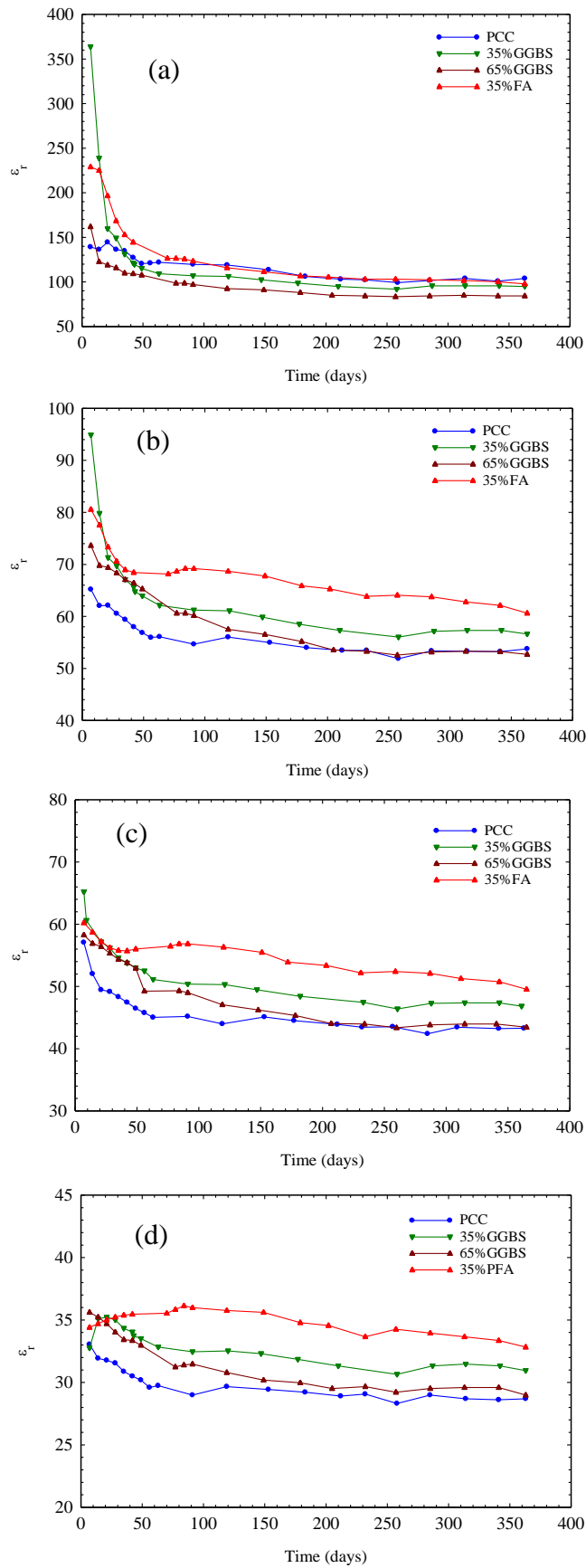


Figure 6.8: Relative permittivity at (a) 100kHz, (b) 500kHz, (c) 1MHz and (d) 5MHz for different concrete mixes at 0.45w/b.

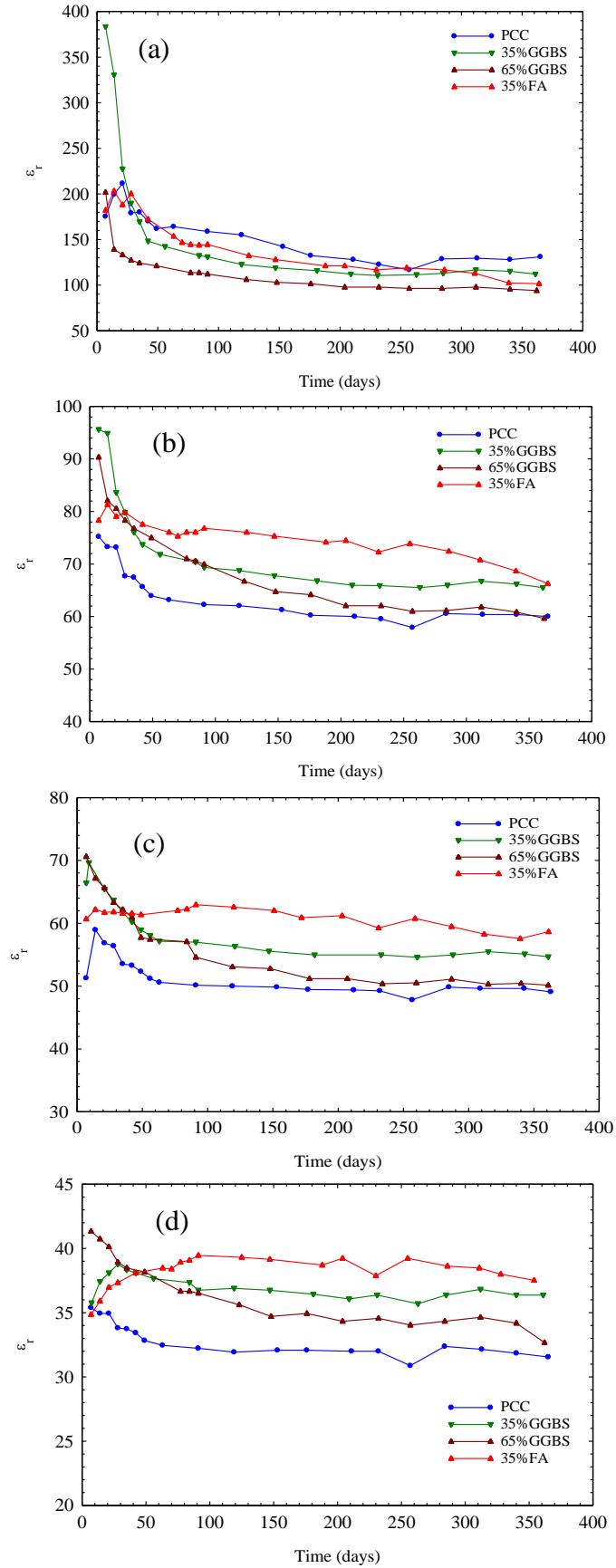


Figure 6.9: Relative permittivity at (a) 100kHz, (b) 500kHz, (c) 1MHz and (d) 5MHz for different concrete mixes at 0.65w/b.

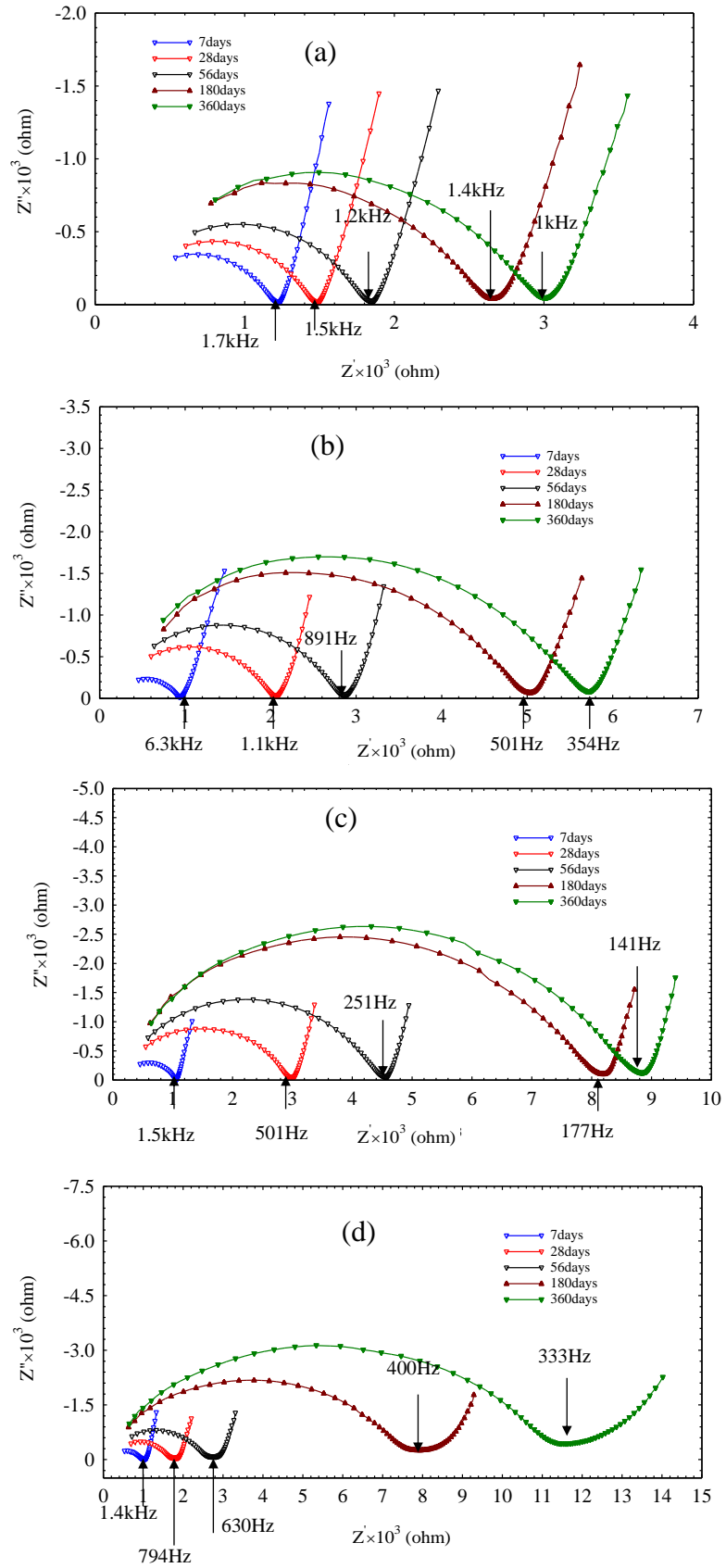


Figure 6.10: Nyquist plots using a two-point embedded electrode configuration (a) 0.35w/b Portland cement concrete mix, (b) 35% GGBS concrete mix (c) 65% GGBS concrete mix and (d) 35% FA concrete mix.

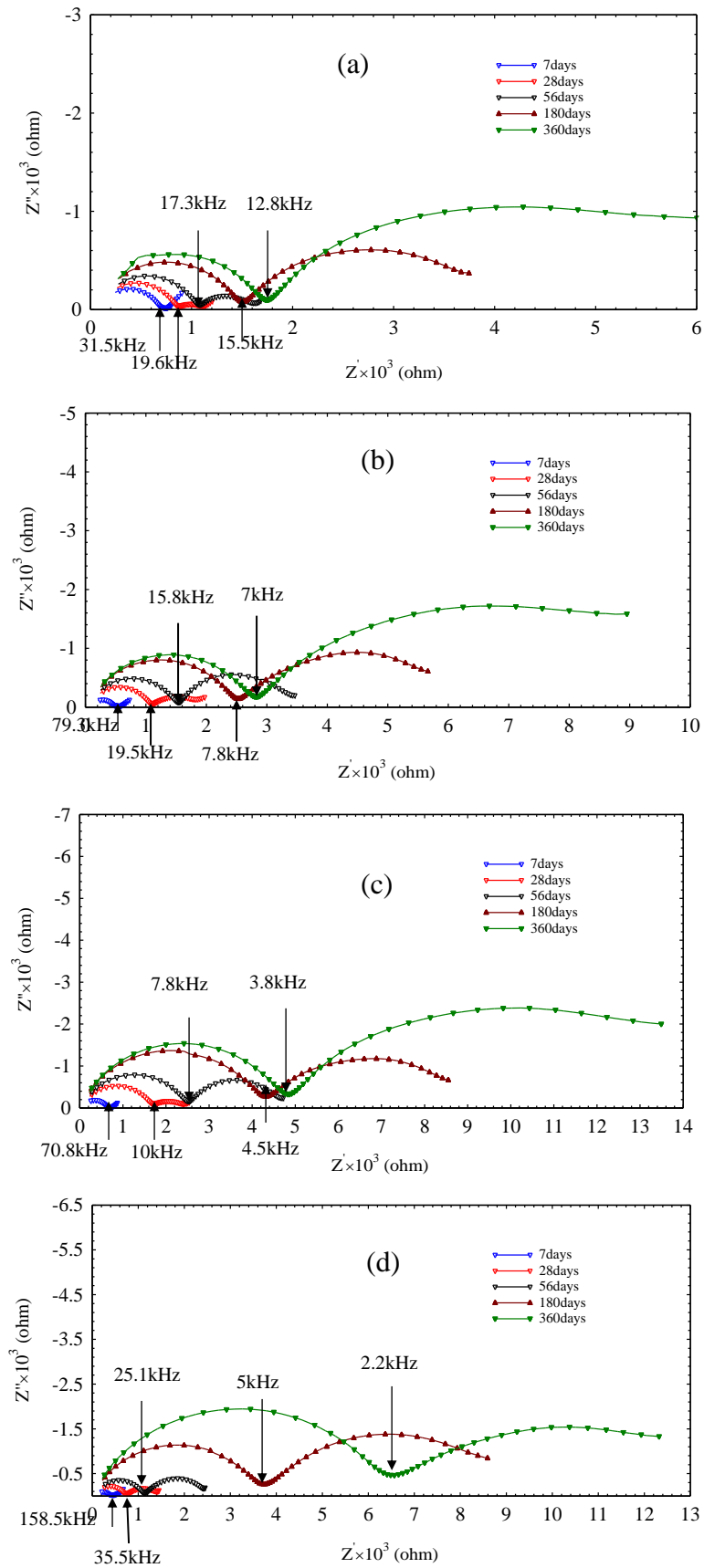


Figure 6.11: Nyquist plots using a two-point end-to-end electrode configuration for 0.35w/b concretes (a) Portland cement concrete mix, (b) 35% GGBS concrete mix (c) 65% GGBS concrete mix and (d) 35% FA concrete mix

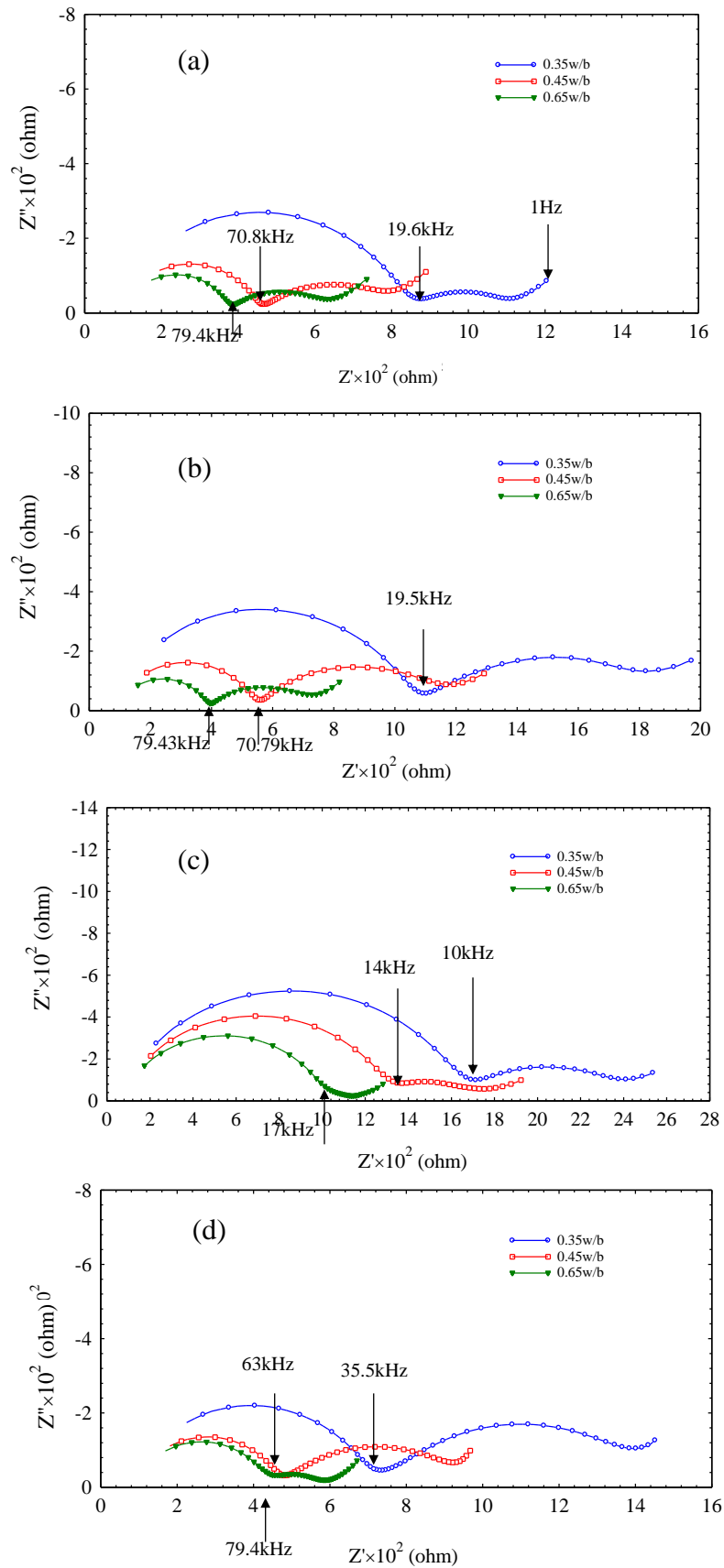


Figure 6.12: Nyquist plot using the two-point end-to-end configuration for 0.35, 0.45, 0.65 w/b mixes at 28-days (a) PCC concrete, (b) 35% GGBS concrete (c) 65% GGBS concrete and (d) 35% FA concrete.

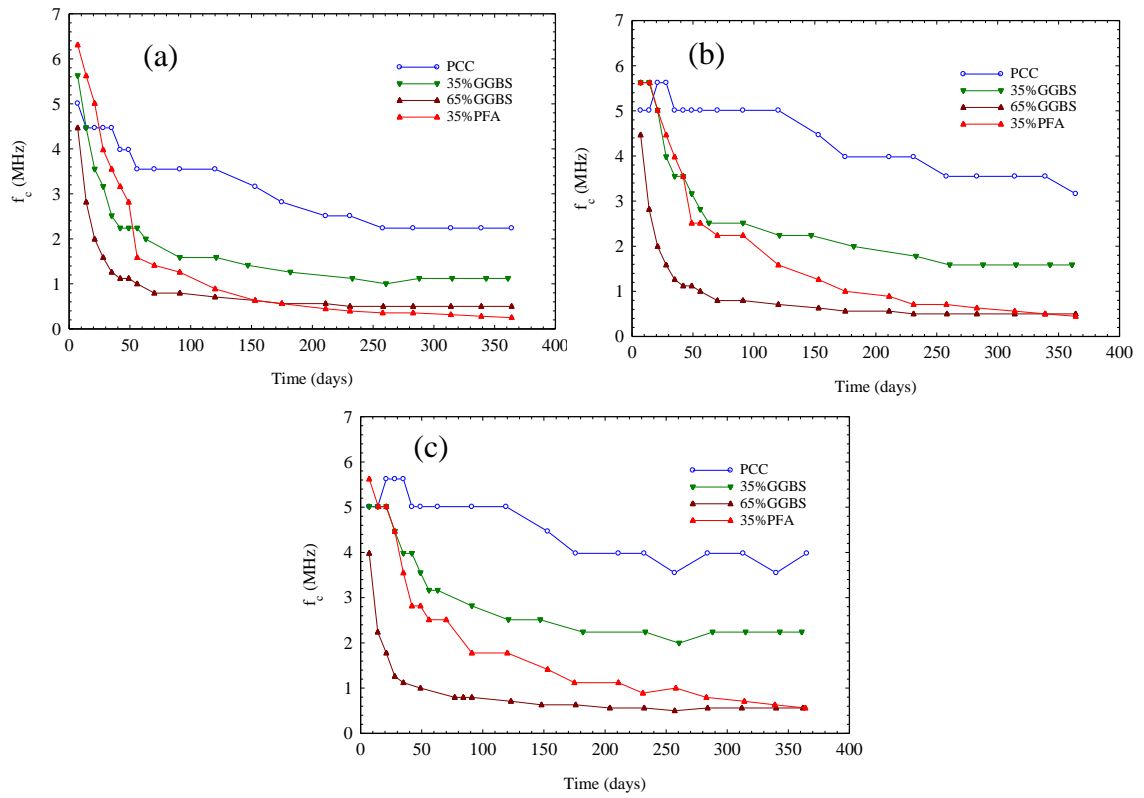


Figure 6.13: Bulk arc Characteristic Frequency response through time for (a): 0.35w/b (b) 0.45w/b and (c) 0.65w/b concrete mixes.

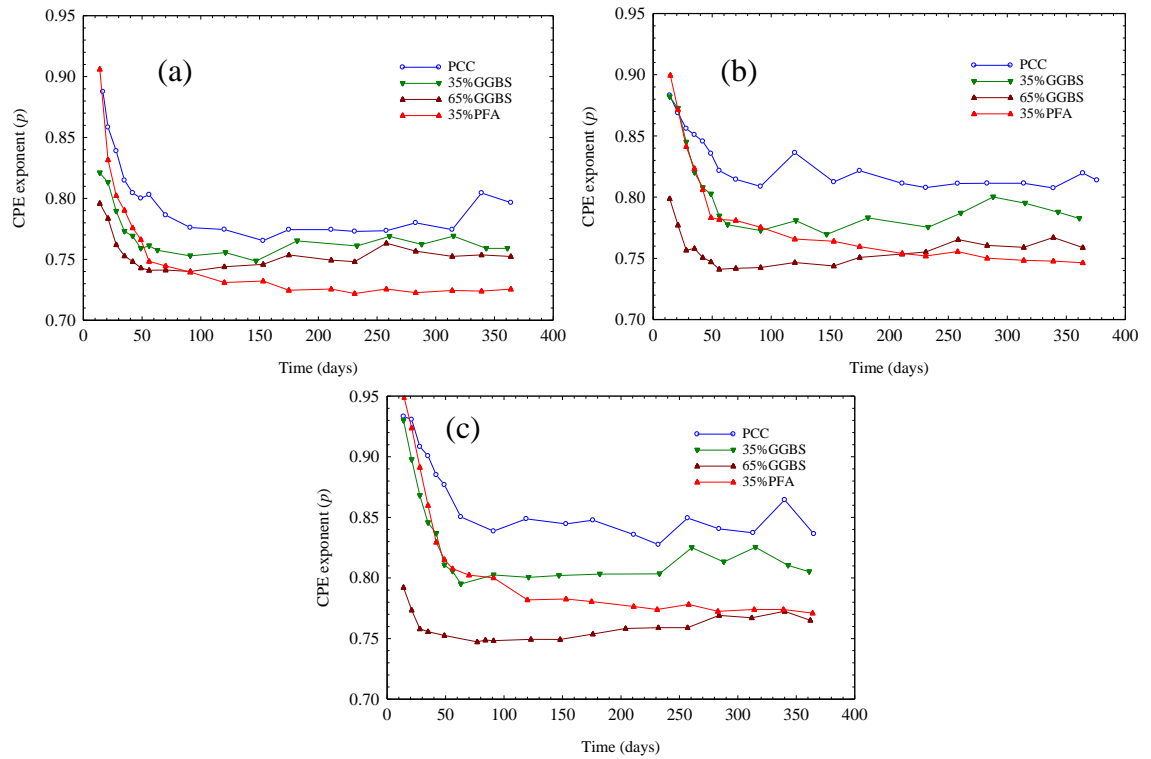


Figure 6.14: Bulk arc CPE exponent p response through time for (a) 0.35w/b (b) 0.45w/b and (c) 0.65w/b concrete mixes

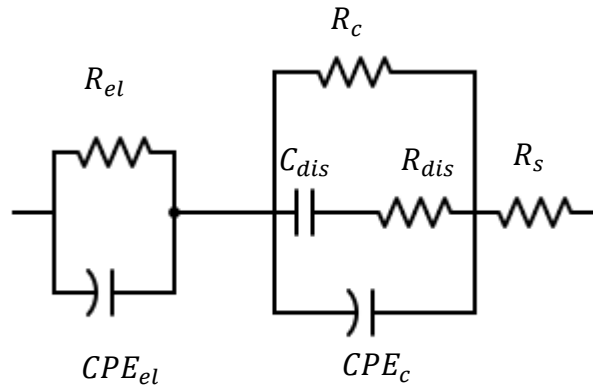


Figure 6.15:Equivalent electrical circuit used to model the electrical response of concrete mixes.

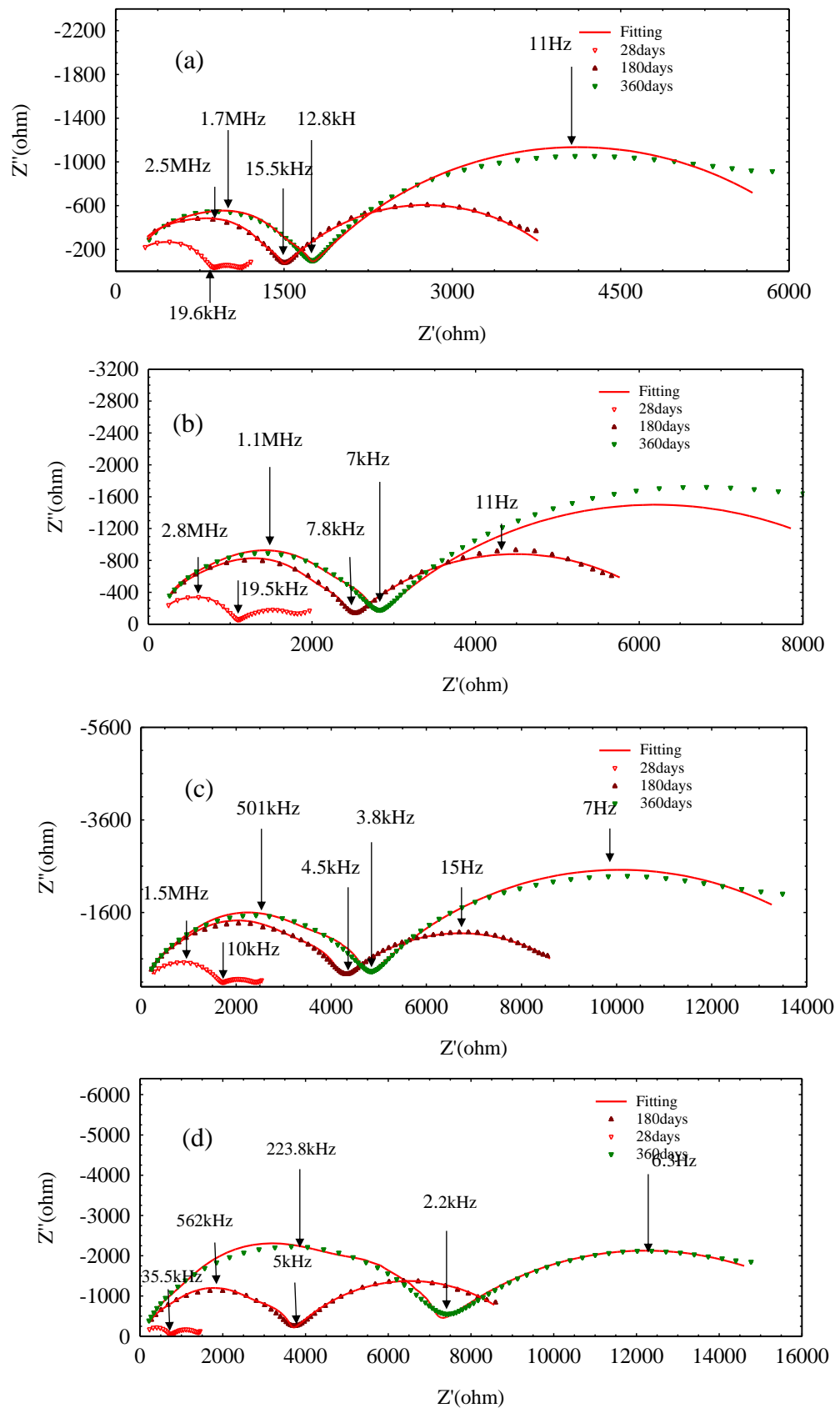


Figure 6.16: Experimental data fitting by the EEC in figure 6.15 for (a) PCC0.35w/b, (b) 35% GGBS0.35w/b, (c) 65% GGBS0.35w/b and (d) 35% PFA0.35w/concrete mixes at different ages

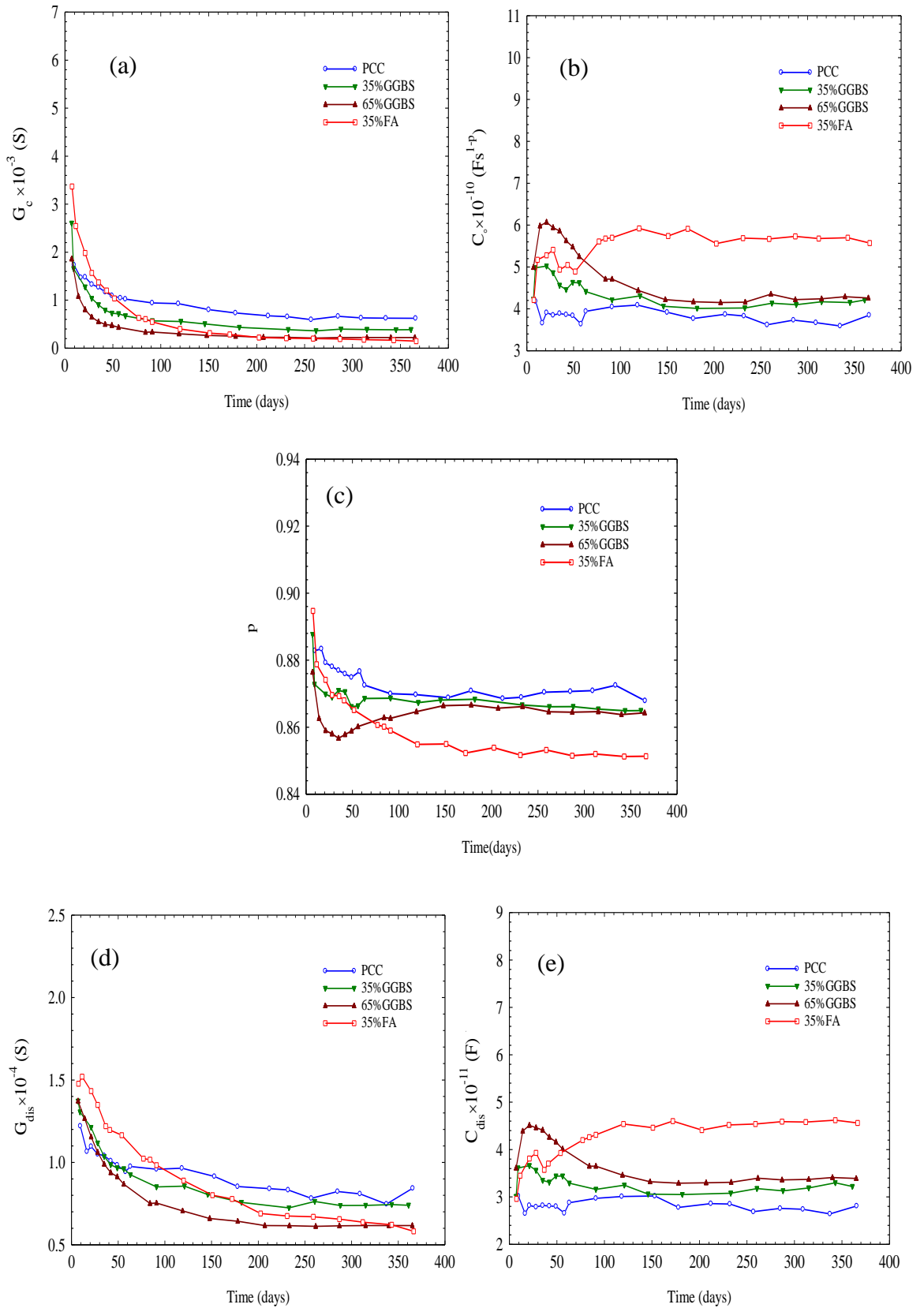


Figure 6.17: Effect of different SCM types on the EEC electrical parameters through time for the 0.35w/b concrete mixes.

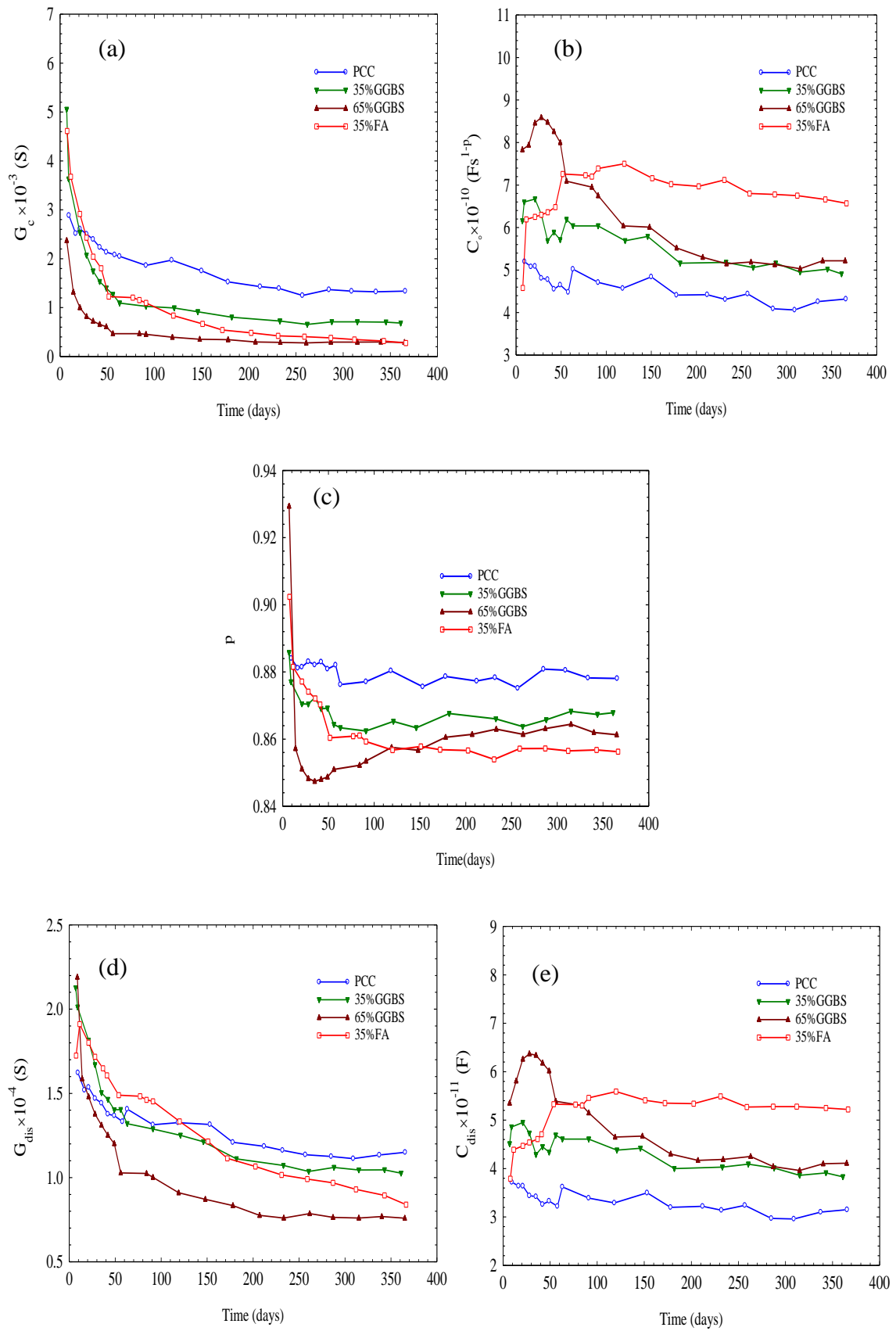


Figure 6.18: Effect of different SCM types on the EEC electrical parameters through time for the 0.45w/b concrete mixes.

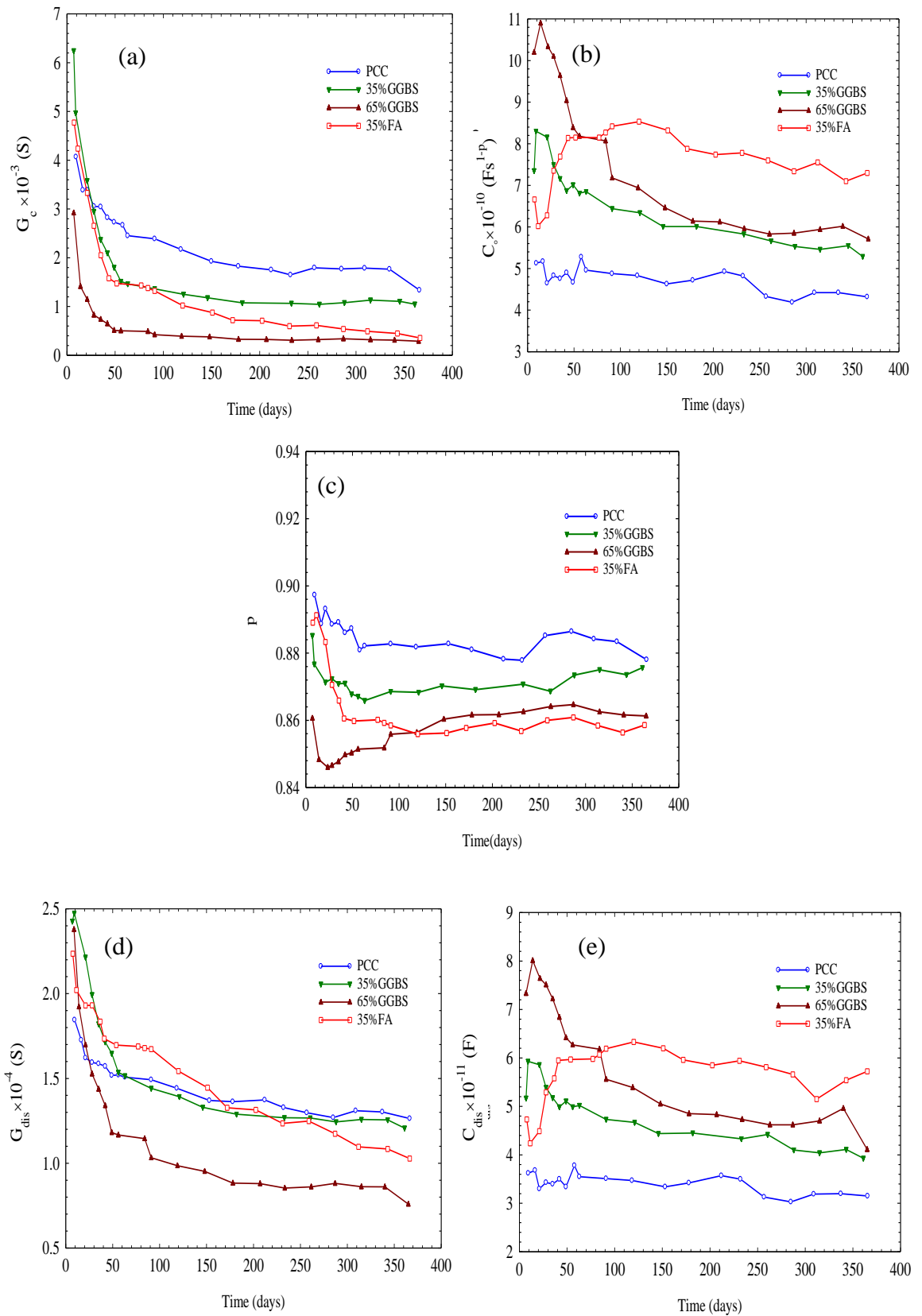


Figure 6.19: Effect of different SCM types on the EEC electrical parameters through time for the 0.65w/b concrete mixes.

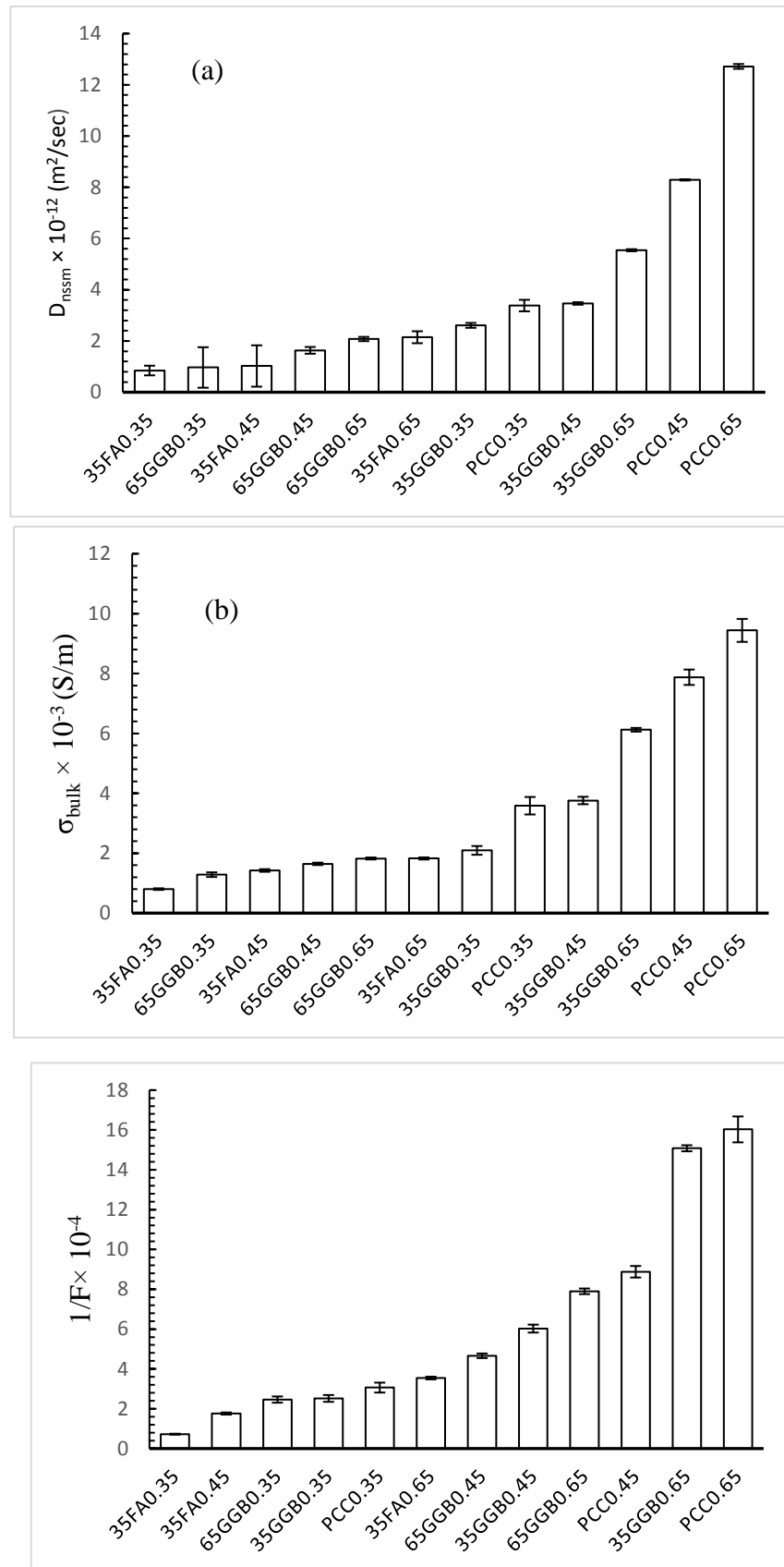


Figure 6.20: (a) non-steady state diffusion coefficient, (b) bulk conductivity, and (c) $1/F$ for all the mixes at the age of 415 days.

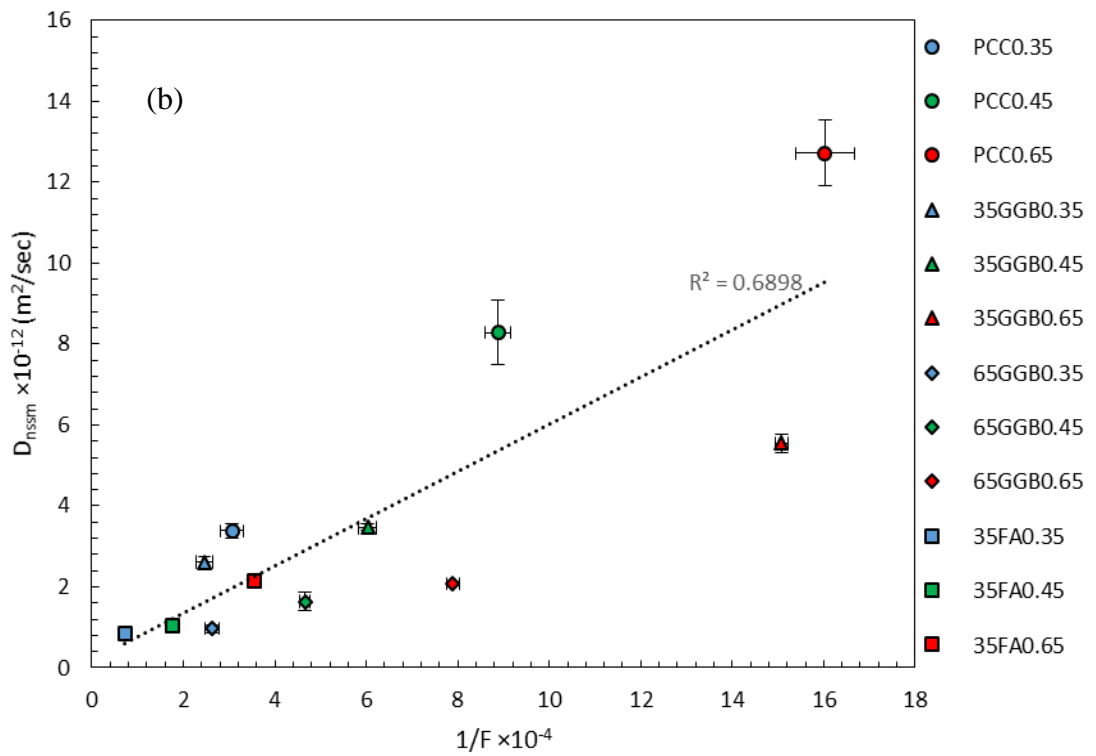
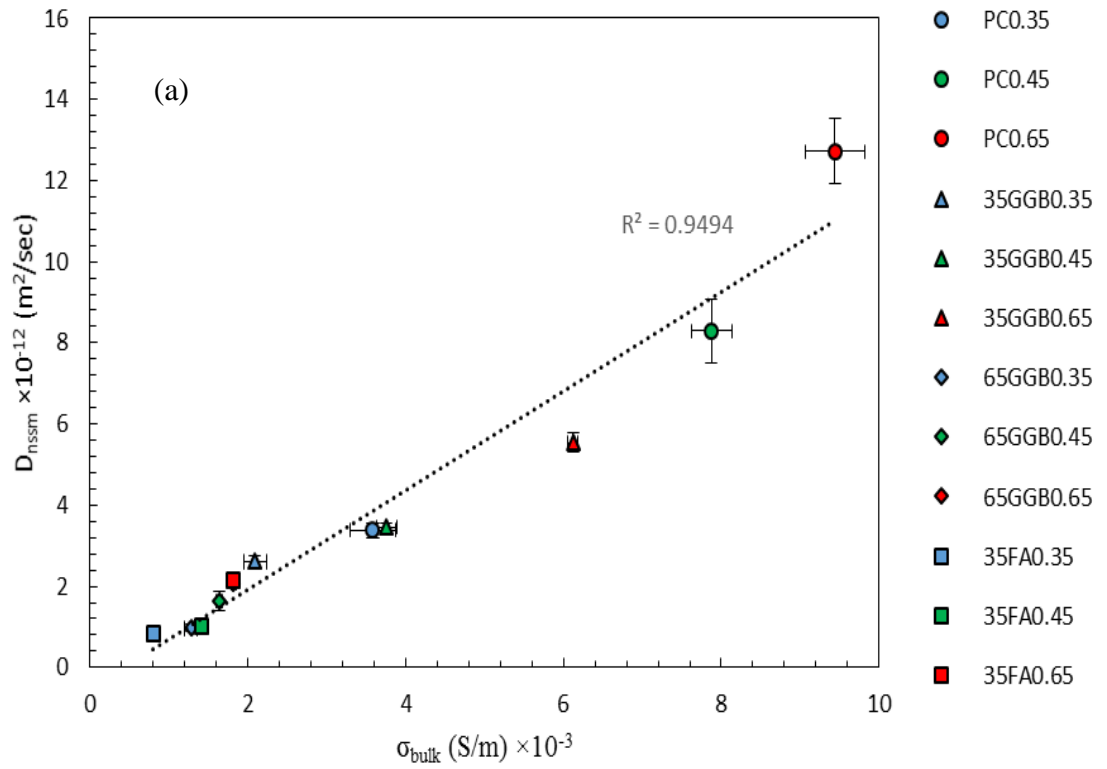


Figure 6.21: Relation between non-steady state diffusion coefficient and (a) bulk conductivity (b) The inverse of the formation factor.

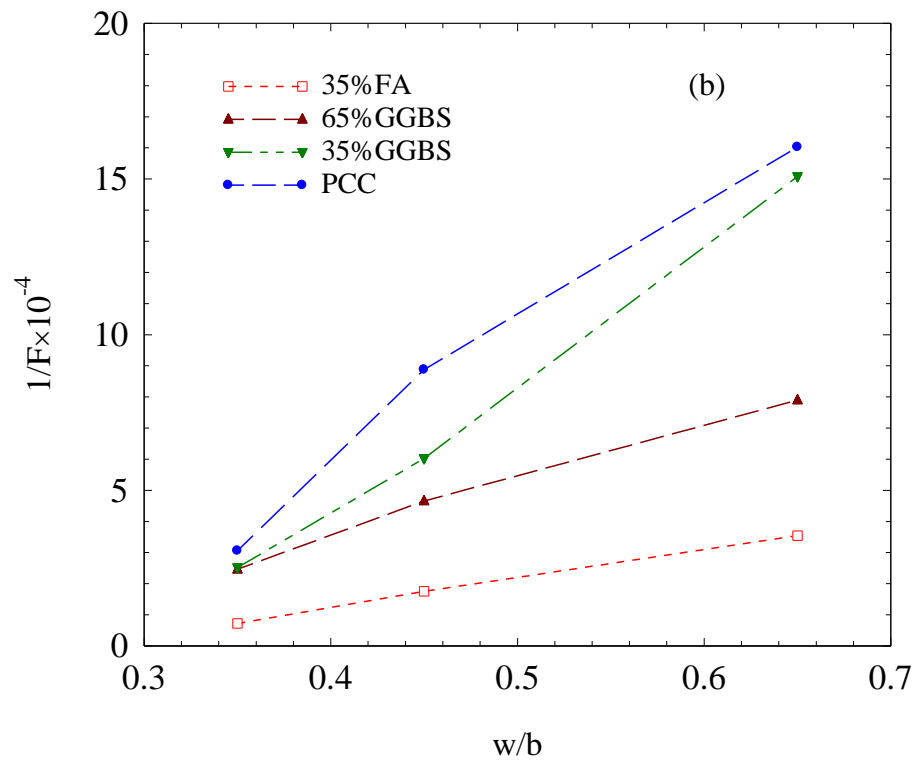
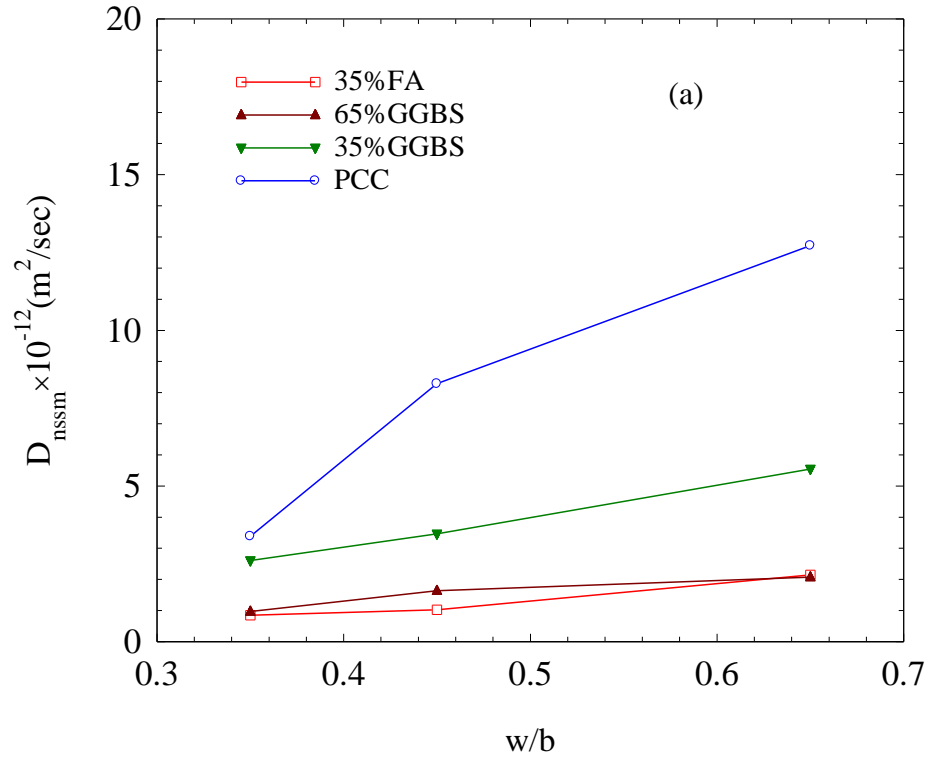


Figure 6.22: Relation between w/b and (a) non-steady state diffusion coefficient (b) The inverse of the formation factor.

Mix	w/b	$\alpha_{ult}(\%)$	τ (days)	β	R-squared
PC	0.35	66.30	0.56	0.93	0.99
	0.45	72.04	0.55	1.15	0.99
	0.65	79.40	0.64	0.97	0.99
35% GGBS	0.35	76.83	0.91	0.66	0.99
	0.45	82.54	1.06	0.63	0.99
	0.65	98.90	2.51	0.52	0.99
65% GGBS	0.35	76.83	0.91	0.66	0.99
	0.45	91.54	3.58	0.46	0.99
	0.65	98.90	2.51	0.52	0.99
35% PFA	0.35	83.83	0.92	0.69	0.99
	0.45	89.54	0.96	0.69	0.99
	0.65	96.90	2.51	0.52	0.99

Table 6.1: Best fit parameters for the experimental degree of hydration in Figure 6.3

Sample Age	R_{el} (ohm)	C_{oel} (Fs^{p-1})	p_{el}	C_o (Fs^{p-1})	p	R_c (ohm)	R_{dis} (ohm)	C_{dis} (F)
28 days	422.5	2.40×10^{-4}	0.34	3.89×10^{-10}	0.87	735.7	9607	2.82×10^{-11}
180 days	2638	2.57×10^{-5}	0.54	3.77×10^{-10}	0.87	1485	11720	2.78×10^{-11}
360 days	4943	2.19×10^{-5}	0.54	4.12×10^{-10}	0.86	1572	11855	3.06×10^{-11}

Table 6.2: Best -fit parameters for the 0.35w/b PCC mixes.

Sample Age	R_{el} (ohm)	C_{oel} (Fs^{p-1})	p_{el}	C_o (Fs^{p-1})	p	R_c (ohm)	R_{dis} (ohm)	C_{dis} (F)
28 days	1085	9.83×10^{-5}	0.41	4.86×10^{-10}	0.86	951.6	8951	3.56×10^{-11}
180 days	4194	2.83×10^{-5}	0.50	4.01×10^{-10}	0.86	2295	13202	3.05×10^{-11}
360 days	7183	2.44×10^{-5}	0.50	4.21×10^{-10}	0.86	2562	13511	3.22×10^{-11}

Table 6.3: Best -fit parameters for the 0.35w/b 35% GGBS mixes.

Sample Age	R_{el} (ohm)	C_{oel} (Fs^{p-1})	p_{el}	C_o (Fs^{p-1})	p	R_c (ohm)	R_{dis} (ohm)	C_{dis} (F)
28 days	984.2	6.16×10^{-5}	0.42	5.94×10^{-10}	0.85	1503	9416	4.46×10^{-11}
180 days	5383	1.63×10^{-5}	0.50	4.17×10^{-10}	0.86	3936	15555	3.29×10^{-11}
360 days	11201	1.23×10^{-5}	0.53	4.26×10^{-10}	0.86	4445	16217	3.39×10^{-11}

Table 6.4: Best -fit parameters for the 0.35w/b 65% GGBS mixes.

Sample Age	R_{el} (ohm)	C_{oel} (Fs^{p-1})	p_{el}	C_o (Fs^{p-1})	p	R_c (ohm)	R_{dis} (ohm)	C_{dis} (F)
28 days	834.9	6.29E-05	0.47	5.41×10^{-10}	0.86	626.4	7414	3.93×10^{-11}
180 days	6100	1.61E-05	0.53	5.91×10^{-10}	0.85	3411	12849	4.60×10^{-11}
360 days	11447	1.94E-05	0.45	5.57×10^{-10}	0.85	6656	17192	4.56×10^{-11}

Table 6.5: Best -fit parameters for the 0.35w/b 35%FA mixes.

Mix	w/b	σ_o (S/m)	$\sigma_{bulk} \times 10^{-3}$ (S/m)	$D_{nssm} \times 10^{-12}$ (m^2/s)	$1/F \times 10^{-4}$
PCC	0.35	11.71	3.58	3.38	3.06
	0.45	8.87	7.87	8.28	8.87
	0.65	5.89	9.44	12.71	16.02
35%GGBS	0.35	8.30	2.09	2.61	2.52
	0.45	6.24	3.75	3.46	6.02
	0.65	4.06	6.12	5.54	15.07
65%GGBS	0.35	5.2	1.28	0.96	2.46
	0.45	3.53	1.64	1.63	4.65
	0.65	2.31	1.82	2.07	7.89
35%PFA	0.35	11.1	0.80	0.84	0.72
	0.45	8.09	1.42	1.02	1.75
	0.65	5.15	1.82	2.14	3.54

Table 6.6: Results of pore solution conductivity, bulk conductivity and the non-steady state migration coefficient for the different concrete mixes at the age of 400 days.

Chapter 7 – Conclusions and Recommendations

7.1 Conclusions

In this study, impedance spectroscopy was used to obtain the electrical properties of cementitious materials over the frequency range 1Hz-10MHz from initial gauging with water up to 400 days hydration. Mixes comprised both cement-pastes and concretes using Portland cement as well as partially replaced with either GGBS or FA. The following conclusions can be drawn:

I. The effect of electrode configuration:

- (i) It was observed that using saturated sponges as an electrode/specimen contacting medium introduced a spurious circuit element represented by the sponge/specimen interface. Additionally, the sponge saturating liquid had a significant influence on the impedance response; as the impedance of the saturating liquid increased a well-defined, low-frequency arc developed in the Nyquist plot. However, as the frequency of the applied field increased, the influence of the electrode/sponge and sponge/specimen interfaces decreased.
- (ii) The resistance (real component) of the cube calculated from 4-point resistivity measurements was located on the Nyquist plot and occurred at the low-frequency side of the bulk material Nyquist arc.
- (iii) Regarding the testing procedure for two-point, end-to-end resistivity measurements, the work presented would suggest that using an AC frequency in the range 5kHz-10kHz with a low resistivity liquid used to saturate the sponges would result in a more accurate assessment of concrete resistivity/conductivity. This is particularly important for low resistivity concrete mixes. During the early stages of hydration, young concretes would display considerably lower impedance values and hence the sponge contacting medium would have a much greater influence on the two-point measurement with consequent greater error.

II. The Early Hydration electrical response:

- (i) Through the initial 24-hours after mixing samples with water, six regions were identified on the conductivity response which were related and explained in terms of through-solution chemical processes (i.e. dissolution, precipitation), C-S-H and AFt growth and formation, and AFt to AFm transformation.

- (ii) Electrode polarization has shown to have a masking effect on the permittivity response during this stage. This was corrected by defining and modelling the processes which take place at the steel/sample interface by an equivalent electrical circuit.
- (iii) It was observed that during this initial 24-hours period, the permittivity was frequency-dependent and related to polarization processes within the cementitious matrix.
- (iv) Permittivity measurements decreased by over four orders of magnitude as the frequency increased from 1kHz to 1MHz and features of the permittivity response, which were masked at low frequencies, only revealed themselves at higher frequencies.
- (v) Over the used frequency range, the main polarization processes operative were electrode polarization which was dominant at frequencies less than 10kHz, whereas double-layer polarization and interfacial polarization dominated in the 100kHz-1MHz frequency range.
- (vi) Three main polarization processes which were related to the bulk response were identified. The first one after the induction period, in which a polarization peak has been developed which was attributed to the increase in the surface area of hydration product. The second and the third polarization processes have been related to the formation of the AFt and the transformation of the AFt to AFm respectively.
- (vii) Both the AFt formation and the AFt to AFm transformation polarization processes, have shown to be affected by the addition of SCMs as these materials impose an acceleration effect to the AFt formation and the AFt-AFm transformation processes.
- (viii) ESEM, isothermal conduction calorimeter and temperature measurements were conducted in parallel to the electrical measurement and were used as supportive tests for the conveyed explanation of electrical response.
- (ix) The different polarization regions which appeared on the apparent dielectric response for the cement pastes have been related to their pertinent physical/chemical origins, and accordingly an equivalent electrical circuit had been proposed to account for the contributions of each composing phase. The liquid phase electrical parameters in the EEC have been shown to be affected by both the liquid phase chemistry at early ages, and by the growth of hydration products at latter ages. The dispersed particles related electrical parameters, have been shown to be more affected by the concentration in

the vicinity of the particles as well as by the increase in the particles surface area due to either the dissolution process, or due to the growth process.

- (x) The effect of SP on the early hydration period has also been studied, and a delaying effect has been observed on the mentioned bulk related electrical features. It was also shown that concrete mixes exhibit similar features to those of the respective pastes, although the absolute values are consistently much lower which can be attributed to the diluting effect of the aggregate.

III. The hardening stage electrical response for concrete mixes:

- (i) During this stage, with regard to the conductivity of the samples, it showed a continuous decreasing trend through time in agreement with the expected decrease in the sample porosity.
- (ii) The ionic concentration in the pore-water has been shown to have a significant effect on the conductivity, particularly in high replaced mixes. This effect gave a false indication about the development in the pore structure at ages < 50days when different mixes are compared. Therefore, the formation factor has been used to ‘calibrate out’ this effect.
- (iii) The permittivity of the samples showed different responses according to the used measuring frequency, as at frequencies in the range between 100kHz-1MHz, a conductivity-like behaviour is observed; however at higher frequencies, 5MHz-10MHz, the permittivity becomes less affected by the changes in the conductivity and more influenced by the binder type.
- (iv) At 5MHz-10MHz frequency range, both the GGBS and the fly-ash showed higher permittivity values than the PCC mixes which is contrary to what is expected for such low conductivity materials. This has been attributed to the more disconnected pore structure which increases the polarizability of the mixes through increasing the solid/liquid interfaces.
- (v) The electrical impedance of the cementitious materials has been modelled by a proposed EEC, which represents the connected and disconnected capillaries pores. The different decreasing rate between the connected path conductance and the disconnected path, indicates a substitution process for the connected paths by the disconnected ones through time. The high values of the permittivity for the replaced

mixes has been related to the increase in the surface area of the surfaces of the pores due to the increase in the tortuous length as well as the increase in the number of the disconnected porosity.

- (vi) A comparison between the durability ranking obtained from the NT Build 492 non-steady state diffusion coefficient, the electrical conductivity measurements and the formation factor of the mixes has been performed. It has been shown that a strong linear relation is obtained between the conductivity of the mixes and the D_{nssm} , which is in contrast to the weak relation between the formation factor and the D_{nssm} . The ranking of the mixes in the case of the formation factor is more based on the w/b ratio. The difference between the D_{nssm} /conductivity ranking and the formation factor ranking suggest the influence of the pore solution conductivity on the results of the former ranking system; therefore, when using SCMs the difference between the two ranking systems is highlighted due to the difference in the pore-solution conductivity.

7.2 Recommendations

The following recommendations for future work can be made:

- (i) A considerable amount of information can be obtained from the permittivity response during the initial 24-hrs hydration. Therefore, this parameter could be developed as a quality control test in job sites similar to the conductivity, temperature-rise, and setting time tests. From this study, the permittivity of the bulk phenomena can be obtained in the range of 100kHz-1MHz. However, this is dependent on the cut-off frequency at which the electrode polarization process relaxes. As has been shown, the effect of the electrode polarization can be corrected analytically using an equivalent electrical circuit. This correction procedure requires expensive/sophisticated impedance analyser devices which might not be suitable for job sites. Therefore, using engineering methods is more suitable in this case. This could be attained by using standardised/specific electrodes shape, and using standard mould sizes during the early hydration stage.
- (ii) The hydration of cement is a complex chemical reaction, in which all the phases are contributing in this reaction. The interaction between the different phases affects the reaction of the individual phases, as in the case of aluminate phase and gypsum, or in the case of the alite and belite phases (Odler and Schüppstuhl, 1982). Therefore, it is useful to characterise the conductivity/permittivity response for the individual cement phases as there is a paucity of information in this area.

- (iii) During the hardening stage, it has been shown in this study that the permittivity in the frequency range 100kHz-1MHz gives a conductivity-like response through hydration. On the other hand, the 5MHz-10MHz permittivity response is more dependent on the binder type, hence the modification in the pore structure which the SCMs impose. It is useful to characterise the permittivity response within the ranges at which the interfacial polarization process is expected to be operative (10MHz-100MHz). This can give useful insights on the development of the pore structure as other polarization processes could be operative at higher frequencies. Incorporating different SCMs and using parallel microstructural characterising tests such as MIP and thermogravimetric tests will be useful in establishing a clear relation between this high frequency range polarization processes and the pore sizes, pore size distribution, total porosity, the connectivity of the pores as well as the reactivity of the different binders.
- (iv) As has been shown in this research, there is a discrepancy between the ranking obtained from the formation factor ranking system and the D_{nssm} /conductivity ranking systems. This has been attributed to the effect of the pore solution conductivity on the D_{nssm} /conductivity ranking systems, particularly when using SCMs. This needs further investigation as the majority of studies which have assessed the formation factor of the mixes as a durability ranking system, have not used SCMs. Therefore, a comparison between natural diffusion tests and the formation factor is required, the pore solution contribution in both ranking systems will be eliminated as the natural diffusion test does not depend on an electrical field in accelerating chloride penetration.
- (v) In this study, the pore solution conductivity was obtained indirectly by using two models, the first was to estimate the degree of hydration and the other to estimate the pore solution conductivity. It would be useful if a direct pore-solution conductivity measurement could be obtained. Literature has shown attempts to develop imbedded sensors for measuring the pore solution conductivity (Rajabipour et al., 2007). However, no data were presented to show the effect of SCMs on the pore-solution conductivity by this sensor as the work focussed on Portland cement as a binder. Therefore, it will be useful to develop more direct methods of measuring the pore solution conductivity particularly in replaced mixes and compare the results with the available models and the degree of hydration to assess the accuracy of the results. This

is especially important in the case of SCM mixes as the pore-solution conductivity is significantly different from the pure Portland cement mixes.



H. M. Taha,¹ W. J. McCarter,² B. Suryanto,¹ and G. Starrs¹

Frequency- and Time-Domain Dependency of Electrical Properties of Cement-Based Materials during Early Hydration

Reference

Taha, H. M., McCarter, W. J., Suryanto, B., and Starrs, G., "Frequency- and Time-Domain Dependency of Electrical Properties of Cement-Based Materials during Early Hydration," *Advances in Civil Engineering Materials*, Vol. 6, No. 2, 2017, pp. 65–83, <https://doi.org/10.1520/ACEM20160057>. ISSN 2165-3984

ABSTRACT


The electrical properties of Portland cement, and cements containing supplementary cementitious materials (SCM), were obtained over the frequency range 1 kHz–10 MHz during the initial 24 h after gauging with water. The response was measured in terms of conductivity and permittivity with both parameters exhibiting significant temporal changes during this period. It was also evident that while the conductivity increased only marginally with increasing frequency of applied electrical field, the permittivity decreased by several orders of magnitude over this frequency range. Moreover, certain features of the permittivity response, which are related to bulk polarization processes, only revealed themselves in the higher frequency range (100 kHz–1 MHz), and went undetected at lower frequencies. The detailed frequency- and time-domain measurements allowed identification of several stages in the early hydration of cement-based materials and the response can be interpreted in terms of hydration kinetics, physico-chemical processes and microstructural development. It is shown that the methodology can be equally applied to cement pastes and concretes.

Keywords

cement, hydration, kinetics, electrical properties, conductivity, permittivity, supplementary cementitious materials

Manuscript received September 14, 2016; accepted for publication November 30, 2016; published online July 10, 2017.

¹ School of Energy, Geoscience, Infrastructure and Society, Inst. for Infrastructure and Environment, Heriot Watt Univ., Edinburgh, EH14 4AS, United Kingdom

² School of Energy, Geoscience, Infrastructure and Society, Inst. for Infrastructure and Environment, Heriot Watt Univ., Edinburgh, EH14 4AS, United Kingdom, (Corresponding author)
e-mail: w.j.mccarter@hw.ac.uk
 <https://orcid.org/0000-0002-1949-2856>

Introduction

Cement hydration, including hydrolysis, poly-condensation, and crystallization, is associated with heat changes and the exothermic nature of the reaction is widely used to monitor the early-age (<24 h) processes. However, the development of the microstructure is not readily identifiable from the heat-flux profiles measured by conduction calorimetry and additional tests such as scanning electron microscopy (SEM), environmental SEM, backscatter electron (BSE) imaging, and X-ray diffraction can be used to provide supporting information on microstructural development. There is a need to develop a viable, complementary testing methodology capable of continuously monitoring the setting and hardening processes under non-isothermal conditions, as is the case in normal concreting operations, and simultaneously providing information on microstructural development and physico-chemical processes.

The use of electrical property measurements to study cement hydration is a developing field and such measurements have not been fully exploited in characterizing the hydration process, although some early work was encouraging in this respect [1–3]. The intrinsic electrical properties of any non-magnetic material can be fully specified by the frequency dependent parameters relative permittivity, $\epsilon_r(\omega)$, and conductivity, $\sigma(\omega)$, which are dependent upon the polarization and conduction of bound and free charges within the material. If the material is heterogeneous, $\epsilon_r(\omega)$ and $\sigma(\omega)$ will be strongly correlated to the properties of the individual components and the way in which they are combined. It is, therefore, possible to identify and characterize porous cementitious materials by their electrical properties provided these are observed over a wide-enough frequency range. A considerable amount of work has been presented on the electrical properties of cementitious materials to study the hardening process (i.e. periods >24 h). In a similar fashion, the electrical conductivity (and its reciprocal, resistivity) of cement pastes has been used to study the initial 24 h of the hydration process (see, for example, Refs. 4–16), although studies on the relative permittivity over the same period are much more limited (see, for example, Refs. 17–21). An important aspect, and limitation, of early-age measurements to date is that these are generally obtained at a fixed frequency of applied electrical field or over a very limited frequency range. Regarding the latter, conductivity measurements tend to be taken in the low kilohertz range (100 Hz–10 kHz), whereas relative permittivity measurements are generally measured in the gigahertz (GHz) region.

The conductivity of hydrating cement-paste is related to both the conductivity of the pore fluid (hence, ionic concentration within the pore fluid) and the continuity and tortuosity of the pore network. The relative permittivity, on the other hand, is associated with polarization processes operative within the paste that are, themselves, related to the mobility of charges adsorbed on the grain and crystal surfaces and at crystal/pore-water interfaces. It is set against this background that this paper presents a detailed electrical spectroscopy study on the early hydration of cementitious materials to study hydration kinetics and physico-chemical processes. Complex impedance data, from which conductivity, $\sigma(\omega)$, and relative permittivity, $\epsilon_r(\omega)$, are subsequently derived, are acquired over the frequency range 1 kHz–10 MHz during the initial 24 h after gauging with water. It is shown that a multi-frequency approach to electrical property measurements can reveal more information than single-frequency measurements.

TABLE 1

Oxide analysis of cementitious materials.

By Weight %	CEM I	GGBS
SiO ₂	20.95	33.89
Al ₂ O ₃	5.2	13.96
Fe ₂ O ₃	3.42	0.35
CaO	59.86	38.03
MgO	2.25	8.77
K ₂ O	0.56	0.67
Na ₂ O	0.21	0.24

Experimental Program

MATERIALS AND SAMPLE PREPARATION

In the current work, the binders comprised a Portland cement (PC) clinker, CEM I 52.5N to EN197-1 [22] and CEM I (ASTM Type I) cement blended with ground granulated blast-furnace slag (GGBS) to EN15167-1 [23] at 35 %, 50 %, and 65 % replacements levels. A typical oxide composition of the materials is presented in **Table 1**. The water/binder (*w/b*) ratios for the plain CEM I paste samples were 0.30, 0.35, and 0.45; the pastes containing GGBS had a fixed *w/b* ratio of 0.35. The mix proportions for the concretes used in the experimental program are shown in **Table 2** and comprised a plain CEM I cement concrete (PCC) and two concretes with 35 % and 65 % replacement levels of GGBS. A *w/b* ratio of 0.45 was used to ensure workability without the need for the addition of plasticizer.

The paste samples were compacted into perspex cuboidal cells of internal dimensions 50 mm × 50 mm × 50 mm, whereas the cells for the concrete samples were 150 mm × 150 mm × 150 mm. A pair of stainless steel electrodes, 2.4 mm in diameter with a center-to-center spacing of 25 mm were embedded centrally inside the paste samples to a depth of 25 mm; for the concrete samples, the center-to-center spacing was 75 mm embedded to a depth of 75 mm. Embedding the electrodes in this fashion ensured intimate contact with the sample and reduced any interference with the natural distribution of aggregate in the case of concretes. In addition, the internal temperature of the samples was measured by embedding a thermistor within each sample at the time of casting. The top surface of the cell was covered to prevent evaporation with tests carried out in a temperature-controlled laboratory (22°C ± 1°C).

ELECTRICAL MEASUREMENTS AND DATA PROCESSING

A Solartron 1260 frequency response analyzer (FRA) was used to perform a logarithmic measurement sweep in the frequency range 1 kHz–10 MHz using 10 frequency points per decade. Screened BNC coaxial leads were used to connect to the FRA, whereas at the sample end, connection to the electrodes was by means of alligator clips. The impedance of the

TABLE 2

Concrete mixes used in experimental program.

Mix	<i>w/b</i>	CEM I (kg/m ³)	GGBS (kg/m ³)	20 mm (kg/m ³)	10 mm (kg/m ³)	Fine (<4 mm) (kg/m ³)
PCC	0.45	339	0	781	390	781
GGBS35	0.45	220	118	778	389	778
GGBS65	0.45	118	219	776	388	776

sample (see Eq 1 below) was taken at each test frequency. Because of the low electrical impedance of the samples during the early stages, lead inductive and stray capacitance can degrade measurements as the frequency of the electrical field increases. In this work, these effects were “nulled” from the measurements at each test frequency by utilizing a measurement conversion protocol implemented in Microsoft Excel that is based on two sets of calibration data that had been acquired prior to the start of testing, which comprised

1. An open-circuit sweep: electrical measurements with air between the electrodes in the test cell, and
2. A short-circuit sweep: electrical measurements with the electrodes connected by a small stainless steel shorting bar.

From this sequence of measurements, the true sample impedance, $Z(\omega)$, at each test frequency was obtained from the measured data. It should be noted that because of the low impedances being measured, even using this nulling protocol results in excess of approximately 5 MHz showed increased scatter and for that reason only data up to 1 MHz are presented. Measurement sweeps were initiated on a 4-min cycle throughout the initial 24 h after gauging.

The impedance, $Z(\omega)$, of the sample, obtained as above, can be written as,

$$Z(\omega) = Z'(\omega) - iZ''(\omega) \quad (1)$$

where:

$Z'(\omega)$ = the in-phase or resistive component, and

$Z''(\omega)$ = the quadrature or reactive component.

At any angular frequency, ω , the electrical response of such a system will result from the superposed phenomena of conduction and polarization (discussed below). These are quantified, respectively, by the bulk conductivity, $\sigma(\omega)$, and relative permittivity, $\epsilon_r(\omega)$, which are obtained from the impedance through the following relationships,

$$\sigma(\omega) = \left(\frac{Z'(\omega)}{Z'(\omega)^2 + Z''(\omega)^2} \right) \frac{L}{A} \quad (2)$$

$$\epsilon_r(\omega) = \frac{1}{\epsilon_0 \omega} \left(\frac{Z''(\omega)}{Z'(\omega)^2 + Z''(\omega)^2} \right) \frac{L}{A} \quad (3)$$

where:

ϵ_0 = the permittivity of a vacuum (8.854×10^{-12} Farads/m), and

L/A = a factor that is related to the electrode geometry and sample configuration.

As the electrical field between the electrodes is non-uniform, the geometrical factor L/A in Eqs 2 and 3 cannot be readily calculated and was evaluated by calibrating the electrode array using a liquid of known electrical properties. For the electrode arrangements used in the current work, the geometrical factor L/A was evaluated as 41.67 m^{-1} for the paste electrode arrangement, and 17.34 m^{-1} for the concrete electrode arrangement. Regarding the relative permittivity, it was found that this can change by more than four orders of magnitude over the frequency range 1 kHz–10 MHz. To present the responses on a single figure, the “normalized” permittivity, $\epsilon_N(\omega)$ at frequency ω , was used and is defined this as the ratio of the relative permittivity at time, t , after the start of the test, $\epsilon_{r,t}(\omega)$, to the relative permittivity at the start of the test, $\epsilon_{r,0}(\omega)$ (i.e., time, $t = 0$), hence,

$$\varepsilon_N(\omega) = \frac{\varepsilon_{r,i}(\omega)}{\varepsilon_{r,o}(\omega)} \quad (4)$$

Results and Discussion

PRELIMINARIES

The response of the cementitious system to an alternating electrical field will be directly related to both conduction and polarization processes operative within the material. The permittivity, $\varepsilon_r(\omega)$, is a measure of the polarizability of the system and, at a particular frequency of applied field, quantifies the sum total of all polarization processes operative at that frequency. Polarization can be described as the displacement of opposite charges in parallel with an applied electric field from their zero-field equilibrium position. Several mechanisms contribute to polarization and each mechanism has a characteristic relaxation frequency. As the frequency increases, the slower (i.e., low-frequency) polarization mechanisms are unable to follow the alternations of the applied electrical field and, therefore, are unable to contribute to the permittivity. This results in a decrease in permittivity with increasing frequency (i.e., relaxation). With reference to **Fig. 1**, typical polarization processes include:

1. Double-layer polarization (**Fig. 1a**), which arises from the displacement of the double-layer counterion cloud relative to the charged particle in response to the applied electric field. This can induce large dipoles, which will give rise to a high capacitance, hence, permittivity. Double-layer polarization is a low-frequency mechanism [24,25].
2. Interfacial or space charge polarization (**Fig. 1b**) occurring in heterogeneous systems when more than one material component is present and when translating charge carriers become trapped or blocked at the interfaces within the material. This results in an accumulation of charges thereby increasing the overall capacitance of the system. This is an intermediate frequency mechanism (high kHz-MHz) [26].

Conductivity can be regarded as a measure of all loss processes operative within the material and quantifies the energy dissipated by the motion of free charges in an applied electric field. Within the dynamic range under consideration, this would be dominated by the movement of ions in the continuous, water-filled capillary pore network (i.e., ionic conduction process); however, losses associated with relaxation/dispersion of the polarization process (i.e., double-layer and interfacial) will also contribute to the conductivity. The cumulative effect of these losses would result in an increase in conductivity with increasing frequency; hence, the conductivity, $\sigma(\omega)$, can be written more completely as,

$$\sigma(\omega) = \sigma_d(\omega) + \sigma(0) \quad (5)$$

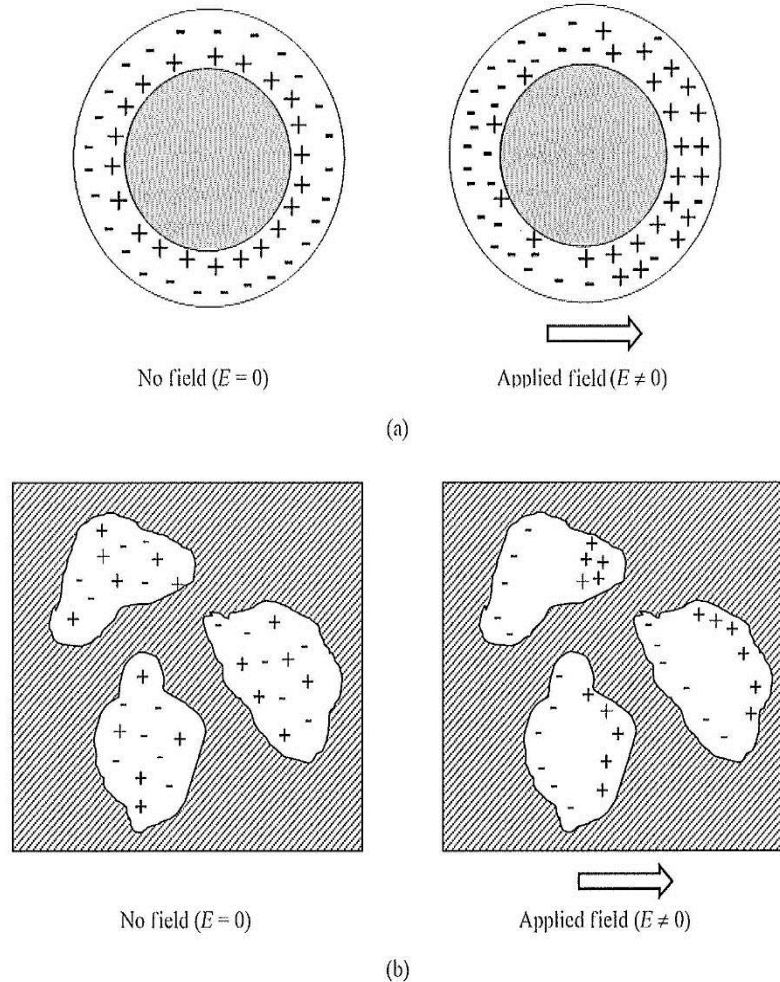
where:

$\sigma(0)$ = the low-frequency (ionic) conductivity, and

$\sigma_d(\omega)$ quantifies the losses resulting from dissipative polarization processes.

Conduction and polarization processes will thus be intimately related to pore-fluid chemistry, surface reactivity, hydration, and the continuously evolving microstructure and, as a consequence, they will not only frequency-dependent but also time-variant. It should also be noted that, in addition to the bulk polarization phenomena detailed in **Fig. 1**, electrode polarization also manifests itself in the low-frequency range. This is a well-known

FIG. 1 Schematic diagram showing (a) double-layer polarization, and (b) interfacial (or space-charge) polarization.



phenomenon that takes place at the interface between a metallic electrode and an ionically conducting material and is a result of the accumulation of a spatial charge on the surface of electrodes. Electrode polarization effects are generally avoided by using a sufficiently high frequency of applied electric field.

GENERAL OBSERVATIONS AND SALIENT FEATURES

Note that in the figures discussed below, for reasons of clarity, only every tenth measurement point is highlighted in the figures.

CEM I Mixes

Fig. 2a presents the conductivity, σ , for the Portland cement pastes at the three water/binder ratios during the initial 24 h after gauging, with measurements presented at a frequency of 100 kHz, this frequency being a priori optimized to ensure electrode polarization had a negligible effect on measurements and the bulk response was obtained.

Fig. 2b presents an enlargement of the response over the initial 2.5 h. Considering

Fig. 2a and **2b**, similar features are clearly evident on all three curves, although the time at which they occur and their prominence are related to the w/b ratio. In general terms, the curves can be divided into two distinct regions: a period of increasing conductivity reaching a maximum within 1.0–1.5 h followed by a period of decreasing conductivity over the remainder of the test period. For comparative purposes, **Fig. 2c** shows the change in temperature within the pastes, with the increase in temperature resulting from the setting process. **Fig. 2c** is not dissimilar to the rate of heat output from conduction calorimetry studies, although the work presented here was carried out under conditions that were more semi-adiabatic than isothermal (and, therefore, more representative of practice).

By considering the rate of change of the conductivity [27] over the test period, these two regions can be further subdivided. **Fig. 3a** shows the derivative, $d\sigma/dt$, of the curves presented in **Fig. 2a** over the initial 15 h. For illustrative purposes, **Fig. 3b** presents both the conductivity and its derivative ($d\sigma/dt$) versus time curves for the $w/b = 0.35$ paste. Because of the short time interval between measurements, considerably more detail can be detected than has hitherto been obtained such that within the 24-h test period, six regions in the conductivity response, and their derivatives, can now be delineated and denoted I–VI:

Region I: an initial period of rapidly increasing conductance that reduces markedly after approximately 30 min;

Region II: is characterized by a period of slowly increasing conductance and continually reducing $d\sigma/dt$, which culminates in a global maximum in conductivity at approximately 1.5 h after gauging, although its time of occurrence depends on the w/b ratio, increasing with increasing w/b ratio. The conductivity maximum signifies the start of the continual decrease in conductivity (i.e., negative $d\sigma/dt$ values);

Region III: this is a short-lived region of rapidly decreasing conductivity occurring over the period 1.5–2.0 h and results in a local minimum on the $d\sigma/dt$ curve;

FIG. 2 (a) Conductivity response during the initial 24 h for CEM I cement pastes, (b) enlargement showing initial 2.5 h after mixing (note: legend as in (a)), and (c) variation in internal temperature of CEM I cement pastes.

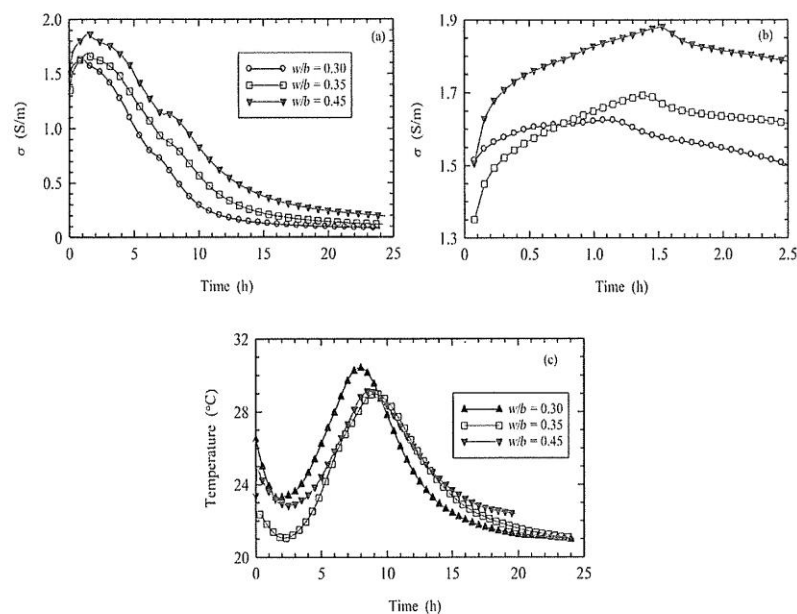
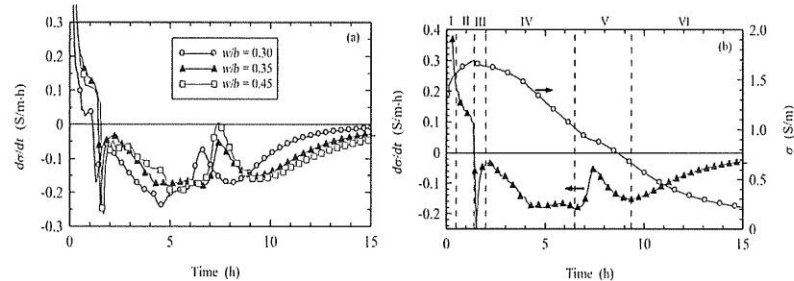


FIG. 3 (a) Derivative of curves in Fig. 2a, and (b) conductivity and derivative for $w/b = 0.35$ paste, indicating Regions I–VI.



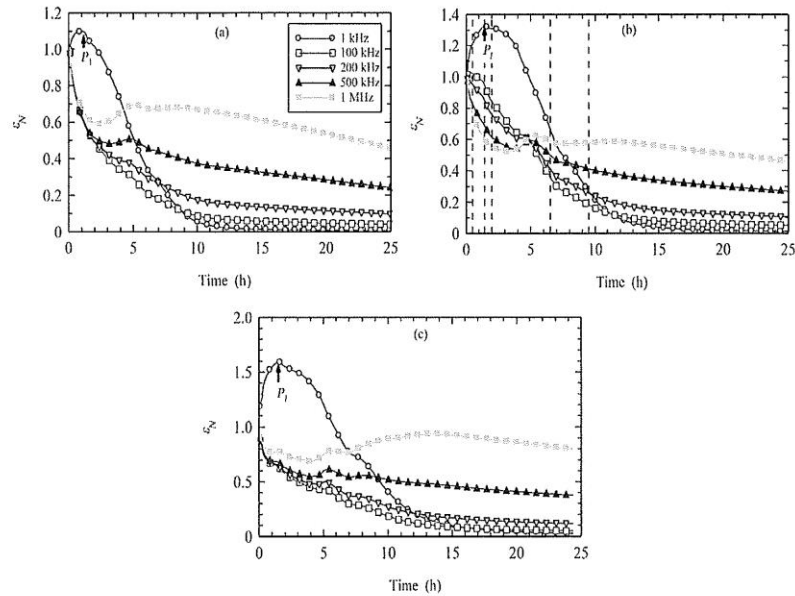
Region IV: the period 2.0–6.5 h represents a region of decreasing conductivity; $d\sigma/dt$ values reduce (i.e., become more negative) over the period 2.0–4.0, attaining an almost constant value over the remainder of this period;

Region V: this region (6.5–9.5 h) is identified as a region over which a “shoulder” or “saddle” develops in the conductivity curve, which manifests itself as a local maximum on the $d\sigma/dt$ curve; and,

Region VI: this region (>9.5 h) occurs at the point where the $d\sigma/dt$ curve starts to increase (i.e., gradient becomes less negative) with time with the conductivity gradually reducing over the remainder of the test period.

Fig. 4 shows the change in normalized permittivity, $\epsilon_N(\omega)$, over the 24-h test period for the three w/b ratios; **Fig. 4b** also indicates the times over which the six regions occur as identified from the conductivity response in **Fig. 3b** for the $w/b = 0.35$ paste. Although measurements were recorded at 40 frequencies at every time step, for clarity, ϵ_N is presented at five spot frequencies extending over three orders of magnitude: 1 kHz, 100 kHz, 200 kHz, 500 kHz, and 1 MHz. It should be noted that, although the relative change in permittivity is presented for each w/b ratio on **Fig. 4**, the absolute values of permittivity decrease by almost three orders of magnitude as the frequency increases from 1 kHz to 100 kHz and by a factor of approximately 25 as the frequency increases from 100 kHz to 1 MHz. **Table 3** presents initial permittivity values ($\epsilon_{r,o}(\omega)$) for the plain cement pastes.

Fig. 4 clearly highlights the effect of the applied frequency on the response; at low frequencies (i.e., 1 kHz), the permittivity response virtually mimics the change in conductivity presented in **Fig. 2a**. However, as the frequency increases, several features are revealed, which become more defined with increasing frequency and, to highlight these, **Fig. 5a** shows the ϵ_N value for the cement pastes at 1 MHz. From this figure, a number of peaks (or local maxima) can be detected with each peak signifying an increase in polarizability of the paste. The first peak (denoted P_1 on this figure) is only detected in the paste with $w/b = 0.45$ and coincides with the time at which the maximum value in conductivity occurs; for comparison, the time at which the conductivity maximizes for the $w/b = 0.30$ and 0.35 pastes is indicated on the respective permittivity curve. All responses display a peak (denoted P_2), which develops within the time period 2.5–6.0 h for $w/b = 0.30$, 3.5–7.0 h for $w/b = 0.35$, and 4.0–7.0 h for $w/b = 0.45$. An additional peak (denoted P_3) occurs at approximately 9.0 h for $w/b = 0.30$, 10.5 h for $w/b = 0.35$, 14.5 h for $w/b = 0.45$, although P_3 is only weakly developed for the $w/b = 0.30$ and 0.35 pastes. **Fig. 5b** presents an enlargement of the $w/b = 0.35$ paste at 1 MHz, which is further discussed below.

FIG. 4 Normalized permittivity at frequencies for CEM I pastes: (a) $w/b = 0.3$, (b) $w/b = 0.35$, and (c) $w/b = 0.45$.

GGBS Mixes

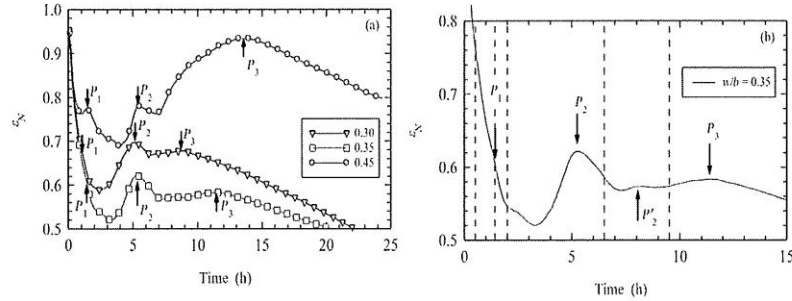
Fig. 6 shows the conductivity (**Fig. 6a**) and its derivative (**Fig. 6b**) for the pastes with slag replacement levels of 35 %, 50 %, and 65 % ($w/b = 0.35$) during the initial 24 h. This figure is similar to **Figs. 2a** and **3a** in terms of the overall profile and features, although the absolute values of the conductivity and $d\sigma/dt$ are much reduced. It is apparent that the addition of slag reduces the value of the early conductivity peak; the pure Portland cement mix recorded a maximum value of 1.70 S/m ($w/b = 0.35$), whereas replacement levels of 35 %, 50 %, and 65 % GGBS obtained maximum values of 1.16 S/m, 1.11 S/m, and 0.87 S/m, respectively, which indicates an inverse relationship between conductivity and the slag replacement level during the early stages of hydration, whereas at times in excess of ~ 13 h this relationship reverses. This indicates a reduction in ionic concentration within the interstitial aqueous phase during the early stages and an overall reduction in hydration process and reaction kinetics with increasing level of replacement at the latter stages of the 24-h test period.

Again, for illustrative purposes, **Fig. 6c** shows both the conductivity, and its derivative, for 50 % GGBS replacement over the initial 15 h with the six regions, discussed above in relation to plain cement paste, are indicated in this figure. Comparing the GGBS mix with the plain cement paste in **Fig. 3b**, it is evident that the addition of GGBS causes an

TABLE 3Initial permittivity values ($\epsilon_{r,o}(\omega)$) for cement pastes at frequencies shown in **Fig. 4**.

w/b	1 kHz	100 kHz	200 kHz	500 kHz	1 MHz
0.30	9.55×10^6	9.06×10^3	2.76×10^3	8.90×10^2	4.04×10^2
0.35	8.01×10^6	9.28×10^3	3.45×10^3	1.05×10^3	5.32×10^2
0.45	7.59×10^6	1.25×10^4	4.12×10^3	9.70×10^2	3.96×10^2

FIG. 5 Normalized permittivity (1 MHz) for CEM I pastes: (a) $w/b = 0.30, 0.35,$ and $0.45,$ and (b) $w/b = 0.35$ showing Regions I–VI and weakly developed peak, P'_2 .



increase in the duration of Region III and, from the do/dt curve, a broader maximum occurring within Region V. **Fig. 6d** presents the change in internal temperature of the GGBS samples.

Fig. 7 shows the change in the normalized permittivity over the initial 24 h for the three GGBS replacement levels at the indicated frequencies. Peak, P_1 is observed over the frequency range 1 kHz–200 kHz and peak, P_2 , is discernible in the 100 kHz–1 MHz range, although it appears as a shoulder on the curve at 1 MHz; P_3 also appears as a shoulder on the permittivity response at 35 % replacement level and is not discernible at 50 % and 65 % replacement. A further feature evident from **Fig. 7b** and **7c** (i.e., 50 % and 65 % replacement) concerns the response at 1 MHz whereby the relative permittivity increases monotonically at times in excess of ~ 3 h. This feature is observed, to some extent, at 35 % replacement (**Fig. 7a**) although after ~ 20 h, values plateau. **Fig. 7b** also indicates the

FIG. 6 (a) Conductivity response during initial 24 h for GGBS pastes, (b) derivative of curves in (a), (c) conductivity and derivative for 50 % GGBS paste indicating Regions I–VI, and (d) variation in internal temperature of GGBS pastes.

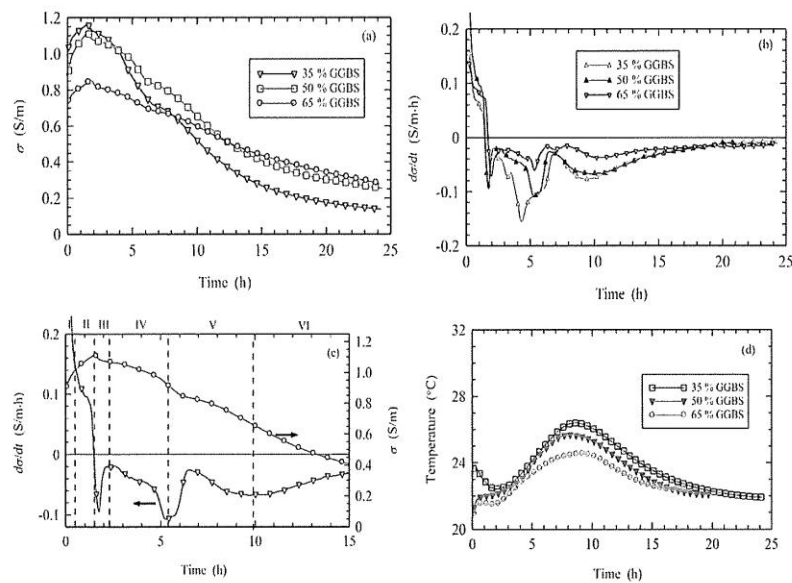
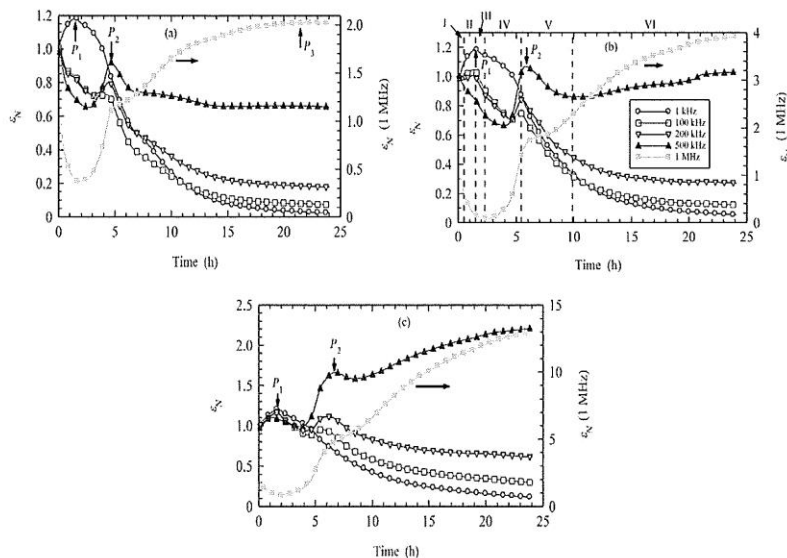


FIG. 7 Normalized permittivity for GGBS pastes: (a) 35 %, (b) 50 % with Regions I–VI indicated, and (c) 65 % (use right-hand axis for 1-MHz curve; shown in (b)).



Regions I–VI identified from the conductivity response presented in **Fig. 6c** for 50 % GGBS. **Table 4** presents the $\epsilon_{r,0}$ values for the GGBS pastes. When compared to **Table 3** (0.35 w/b paste), the values are much lower, which would be attributable to the reduced ionic concentrations.

Concrete Mixes

Fig. 8a shows the conductivity and **Fig. 8b** the $d\sigma/dt$ curve for the concrete mixes shown in **Table 2**; comparative internal temperature measurements for the concretes are shown in **Fig. 8c**. **Fig. 9** shows the normalized permittivity. When compared to the respective paste, the addition of aggregate results in a reduction in the absolute values of both conductivity and permittivity (**Table 5** shows the $\epsilon_{r,0}(\omega)$ values for the concretes). When compared to **Table 3** (0.45 w/b paste), the values are much lower, which is to be expected as the aggregate itself will have a low conductivity and permittivity in comparison to that of the paste. However, the features identified from the pastes are still evident in the respective concretes but not as prominent because of a dilution effect; Regions I–VI discussed above are also distinguishable although they are lengthened in comparison to the pastes because of the slower hydration process resulting from the reduced overall paste content. This indicates that the electrical response of concrete is controlled by the fractional volume of cementitious matrix [28].

INTERPRETATION OF ELECTRICAL RESPONSE

Both the conductivity and the relative permittivity have the potential to reveal information on pore–fluid chemistry, chemical activity on grain surfaces, the formation of hydration products, hydration kinetics, and increase in rigidity of the paste. The following sections interpret the electrical response in terms of physico-chemical and microstructure building processes and in relation to Regions I–VI identified above.

TABLE 4

Initial permittivity values ($\epsilon_{r,o}(\omega)$) for GGBS pastes at frequencies shown in Fig. 7.

w/b	1 kHz	100 kHz	200 kHz	500 kHz	1 MHz
35 % GGBS	6.50×10^6	5.46×10^3	1.72×10^3	3.47×10^2	97.5
50 % GGBS	6.03×10^6	4.59×10^3	1.45×10^3	2.84×10^3	70.7
65 % GGBS	4.76×10^6	1.96×10^3	6.12×10^2	1.04×10^2	14.2

CEM I Mixes

The discussion below relates to Figs. 3b, 4b, and 5b for $w/b = 0.35$ and are used for illustrative purposes.

Region I: 0 h–0.5 h

As the cement is gauged with water, a rapid dissolution (hydrolysis) of ions from the cement grain surfaces takes place, with the different mineralogical phases and calcium sulfate contributing to the pore-solution chemistry of the bulk electrolyte. The aqueous phase contains, primarily, Na^+ , K^+ , Ca^{2+} , SO_4^{2-} , and OH^- , which increases with time and is reflected in the rapid increase in the conductivity of the paste in Region I (Fig. 3b).

The permittivity (Fig. 4b) displays a somewhat anomalous response; at low frequencies (1 kHz), the permittivity increases, whereas at higher frequencies (>100 kHz), it is seen to decrease. On mixing with water, a colloidal suspension is formed and a diffuse electrical double layer, through adsorbed calcium ions and counterions, will be quickly established on the grain surface. Polarization of the double layer (Fig. 1a) can induce large dipole moments, hence, large permittivity values; however, superimposed upon this process will be electrode polarization effects that can also result in high permittivity values. We are of the opinion that the low-frequency (1 kHz) permittivity response is dominated by

FIG. 8 (a) Conductivity response during initial 24 h for concretes in Table 2, (b) derivative of curves in (a), and (c) variation in internal temperature of concretes.

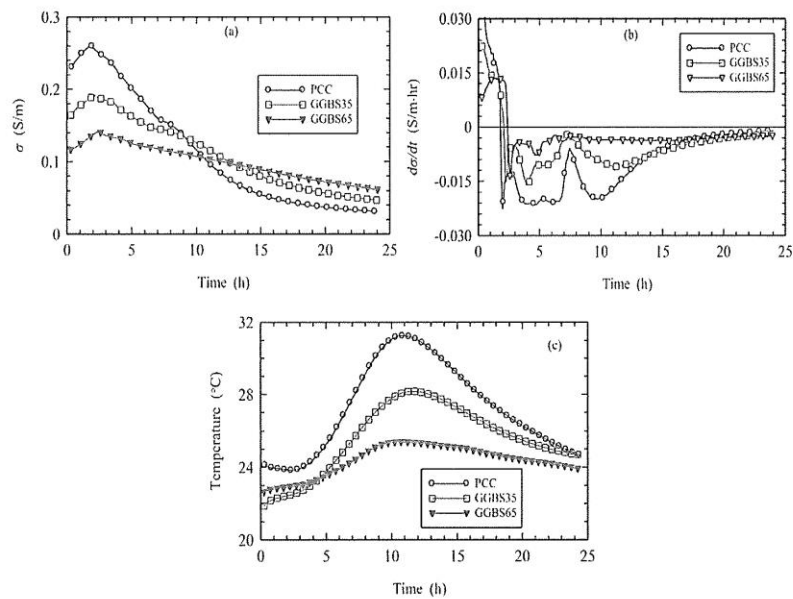
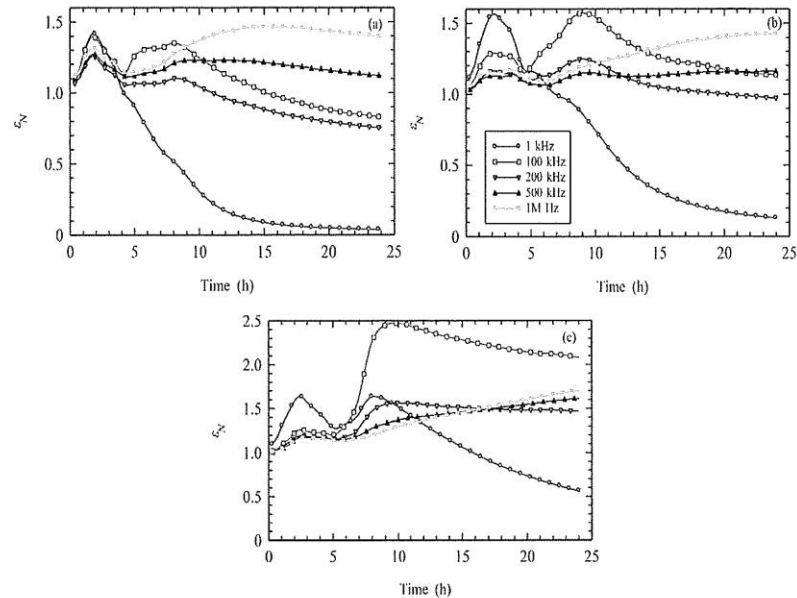


FIG. 9 Normalized permittivity for concretes in Table 2: (a) PCC, (b) GGBS35, and (c) GGBS65 (shown in (b)).

electrode effects that masks bulk polarization processes; however, the electrode polarization effect must itself be related ionic concentration in the pore water at the specimen/electrode interface [29–31]. As the frequency increases, electrode effects diminish rapidly to reveal the response from the bulk material. Evidence for the rapid reduction in electrode polarization effects comes from the fact that the permittivity decreases by almost three orders of magnitude as the frequency increases from 1 kHz to 100 kHz. However, as the frequency increases from 100 kHz to 1 MHz, ions in the diffuse double layer find it increasingly more difficult to move in sympathy with the alternations of the electrical field, which results in a continual reduction in permittivity with increasing frequency.

The temporal reduction in permittivity at frequencies in the range 100 kHz–1 MHz would be as a result of the gradual formation and build-up of a gelatinous coating on the cement grain surface reducing ionic mobility in the double layer.

Region II: 0.5 h–1.5 h

Within this region, the conductivity continues to increase (**Fig. 3b**); however, it is noticeable that there is a gradual reduction in $d\sigma/dt$ and the permittivity in the frequency range 100 kHz–1 MHz continues to decrease with time. This could be explained by invoking two opposing processes:

TABLE 5Initial permittivity values ($\epsilon_{r,o}(\omega)$) for concretes presented in **Fig. 9**.

	1 kHz	100 kHz	200 kHz	500 kHz	1 MHz
PC	2.11×10^5	1.25×10^2	81.6	33.3	19.2
GGBS35	1.27×10^5	1.02×10^2	93.3	55.1	36.4
GGBS65	6.62×10^4	54.3	55.1	31.7	23.7

1. The continual dissolution of the cement grains which serves to increase the ionic concentration within the bulk pore fluid, thereby increasing conductivity and low-frequency permittivity (1kHz); and
2. The continual build-up of hydration products on the grain surfaces hindering the dissolution process and removing ions from solution thereby causing a decrease in $d\sigma/dt$ of the paste. The build-up of gel (Aft and C-S-H) on the grain surfaces would reduce the permittivity (**Figs. 4b** and **5b**) because of reduced ionic mobility in the double layer.

Region III: 1.5 h–2.0 h

This short-lived region displays a marked decrease in conductivity that results in a transitory minimum on the $d\sigma/dt$ curve (**Fig. 3b**); over the same period, the permittivity (**Fig. 4b**) continues to decrease. We are of the opinion that the cause of this feature is as a result of the precipitation of calcium hydroxide. It is noteworthy that this feature has also been observed in dilute suspensions of C_3S with water/solids ratios in the range 5–50 [32,33] and Type I ordinary Portland cement pastes [11]. The end of the region is characterized by a reducing rate of change of conductivity (i.e., $d\sigma/dt$ becomes less negative).

Region IV: 2.0 h–6.5 h

This precipitation process occurring with within Region III appears to trigger a decrease in conductivity within Region IV and it is over this region that the paste starts to increase in rigidity and the change from an amorphous to crystalline hydrate morphology. It is also evident from **Fig. 4b** that after approximately 3 h, the permittivity of the paste increases peaking at approximately 5 h, which is at a time when the conductivity is undergoing its greatest rate of change. It is also significant that this feature becomes more prominent with increasing frequency of applied field, and to highlight this, **Fig. 5b** presents an enlargement of response at 1 MHz. We attribute the increase in polarizability (hence, permittivity) of the paste to the nucleation and outgrowth of C-S-H “needles” from C_3S surfaces; this would simultaneously result in

1. A more tortuous electrolytic conduction path, thereby decreasing the conductivity; and
2. A rapid (and short-lived) increase in the surface area of the C-S-H, which would promote both double-layer polarization processes on the C-S-H surface and, perhaps more significantly, interfacial polarization processes as hydrates grow into the aqueous phase. Hydrate accretion and infilling of the capillary pore space would then serve to reduce the polarizability of the paste.

By the end of this region, a percolated solid phase will have formed.

Region V: 6.5 h–9.5 h

This region is characterized by a shoulder in the conductivity response with a resulting peak in the $d\sigma/dt$ curve (see **Fig. 3b**). Over the same period, the permittivity curve presented in **Fig. 4b** also displays a shoulder at low frequencies; however, as the frequency of the applied field increases, this changes to a plateau region at 1 MHz. On closer examination of the response at 1 MHz, this plateau is a weakly developed peak and is indicated by P_2 on **Fig. 5b**.

The conductivity curve could be explained by considering the following:

1. As the cement paste hydrates, its porosity decreases with the pore network becoming more tortuous, constricted, and disconnected as a crystalline network is formed. As

conduction will be primarily electrolytic in nature via the continuous capillary pores, this will result in a decrease in conductivity; and

2. Increasing in ionic concentration within the pore-water, which would have the effect of increasing the bulk conductivity. This could be a result of the renewed dissolution of the C_3A phase and the formation of ettringite resulting from the reaction of the aluminate phases, which releases alkalis bound up in this phase [34,35] coupled with the desorption of sulfates from the C-S-H [36].

Considering (1) and (2), it could be inferred that microstructural changes causing a reduction in conductivity are having a greater influence than changes in pore-fluid chemistry, which would increase the conductivity. Release of ions into the pore water would also serve to increase polarizability, hence, permittivity [37]. As a pore network has been formed within the paste, in addition to double-layer polarization, interfacial polarization processes (see **Fig. 1b**) will contribute to the overall polarizability of the paste and causing a transitory increase in permittivity as continuing microstructural changes reduce ionic mobility.

Region VI: 9.5 h, end of test period

This region is characterized by a continual decrease in conductivity (**Fig. 3b**) with the rate of change decreasing with increasing hydration time. The permittivity response is, as with Region V, frequency dependent at frequencies <500 kHz; the permittivity decreases with time indicating a decrease in polarizability of the paste because of an irrotational binding of double-layer charges. The response at 1 MHz (**Fig. 5b**) reveals an increase in permittivity over this time period, peaking at approximately 11.5 h (this peak, P_3 , is more evident for the paste with $w/b = 0.45$ in **Fig. 5a**). The increase in polarizability could be attributed to increased interfacial processes at crystal boundary interfaces within the pore structure (**Fig. 1b**), resulting from an increase in ionic concentrations in the pore fluid. Interfacial polarization is a higher frequency process than double-layer effects; hence, they only become more prominent as the frequency increases. As with Region V, this could be as a result of the transformation of AFt to AFm with the release of Ca^{2+} and SO_4^{2-} (Eq 6) and reaction on the C_3A phases (Eq 7) releasing alkalis bound up in them:



There is no detectable increase in conductivity caused by release of ions into the pore network, so it could be inferred that microstructural changes in the pore network because of hydration are now having a more dominant influence on the conductivity of the paste than changes in pore-fluid chemistry.

GGBS Mixes

The electrical response of the GGBS presented in **Figs. 6** and **7** is similar in many aspects to the response for the Portland cement pastes as six regions can also be identified during the initial 24 h after gauging. However, as noted above, the duration of some of the regions identified from the conductivity response (and its derivative) is increased in comparison to the pure cement paste (in particular, Regions III and V). For illustrative purposes, **Fig. 6c** identifies the regions for the 50 % GGBS ($w/b = 0.35$) from the conductivity response and **Fig. 7b** presents the permittivity with Regions I–VI indicated. The most striking difference between the pure cement paste and the GGBS pastes concerns the permittivity response, and the following should be noted:

1. The merging of peaks P_2 (reaction on C_3S phase and CSH formation) and P_2' (renewed dissolution on the C_3A phase and AFt formation) into a single broader peak spanning across Regions IV and V; and
2. Within Regions V and VI, at 500 kHz and 1 MHz, the polarizability of the paste increases with time, and is particularly evident at 1 MHz (note: right-hand axis for 1-MHz scale). As before, at these higher frequencies we attribute this to an increase in interfacial polarization effects resulting from the AFt→AFm transformation and subsequent release of ions into the pore water. At frequencies <200 kHz, the polarizability of the paste will be dominated by double-layer polarization processes, which will decrease with time because of densification of the crystalline network and consequent reduction in charge mobility.

Concrete Mixes

Fig. 8a presents the temporal change in the conductivity over the initial 24-h hydration, with the corresponding derivative presented in **Fig. 8b**. It is immediately evident that the key features identified from the pastes earlier are still visible, albeit much less pronounced. It is also evident the absolute values of conductivity of the concrete mixes are considerably lower than those of the respective pastes, decreasing by a factor of approximately 6. This simply reflects the diluting effect of the aggregate reducing the volume fraction of cement paste. The derivative curves presented in **Fig. 8b** are also similar to those observed earlier from the pastes (see **Figs. 3a** and **6b**). The features of the normalized permittivity presented in **Fig. 9a–c** compare well with those observed from the paste samples (see **Figs. 4c** and **7a–c**) although absolute values of permittivity are much reduced (see **Table 5**).

Concluding Remarks

Conductivity and permittivity measurements have been presented over the frequency range 1 kHz–1 MHz for cement pastes and concretes, with and without GGBS replacement. Work focused on the initial 24 h after mixing with water and it was shown that the response at the permittivity level was frequency-dependent and related to polarization processes within the cementitious matrix. Permittivity measurements decreased by over four orders of magnitude as the frequency increased from 1 kHz to 1 MHz and features of the permittivity response, which were masked at low frequencies, only revealed themselves at higher frequencies. Over this frequency range, the main polarization processes operative were electrode polarization, which was dominant at frequencies less than 10 kHz, whereas double-layer polarization and interfacial polarization dominated in the 100 kHz–1 MHz frequency range. Over the frequency range 100 kHz–1 MHz, the conductivity increased by less than 15 %, the increase being a result of the relaxation of bulk polarization processes.

During the initial 24 h after mixing with water, six regions could be identified from both conductivity and permittivity measurements with measurements explained in terms of through-solution mechanisms (i.e., dissolution, precipitation), C-S-H and AFt formation and AFt to AFm transformation. It was also shown that concrete mixes exhibit similar features to those of the respective pastes, although the absolute values are consistently much lower, which can be attributed to the diluting effect of the low-conductivity and low-permittivity aggregate.

The methodology can be equally applied to concretes and there is considerable scope for development of multi-frequency impedance measurements within the range 10 kHz–1 MHz as an additional testing technique to study the early hydration of cementitious materials generally. Furthermore, the work allows optimization of the frequency at

which electrical impedance measurements are most informative with regard to hydration and microstructural development.

ACKNOWLEDGMENTS

The writers thank Hanson Cement (UK) for supplies of GGBS. H.M.T. acknowledges the financial support provided by Heriot Watt University through a James Watt Scholarship.

References

- [1] McCarter, W. J. and Curran, P., "The Electrical Response of Setting Cement Paste," *Mag. Concrete Res.*, Vol. 36, No. 126, 1984, pp. 42–49, <https://doi.org/10.1680/mac.1984.36.126.42>
- [2] McCarter, W. J. and Afshar, A. B., "Some Aspects of the Electrical Properties of Cement Paste," *J. Mater. Sci. Lett.*, Vol. 3, No. 12, 1984, pp. 1083–1086, <https://doi.org/10.1007/BF00719771>
- [3] McCarter, W. J. and Afshar, A., "A Study of the Early Hydration of Portland Cement," *Proc. Inst. Civ. Eng. (London)*, No. 79, 1985, pp. 585–604.
- [4] Torrents, J. M., Roncero, J., and Gettu, R., "Utilization of Impedance Spectroscopy for Studying the Retarding Effect of a Superplasticizer on the Setting of Cement," *Cement Concrete Res.*, Vol. 28, No. 9, 1998, pp. 1325–1333, [https://doi.org/10.1016/S0008-8846\(98\)00110-0](https://doi.org/10.1016/S0008-8846(98)00110-0)
- [5] Morsy, M. S., "Effect of Temperature on Electrical Conductivity of Blended Cement Pastes," *Cement Concrete Res.*, Vol. 29, No. 4, 1999, pp. 603–606, [https://doi.org/10.1016/S0008-8846\(98\)00198-7](https://doi.org/10.1016/S0008-8846(98)00198-7)
- [6] Levita, G., Marchetti, A., Gallone, G., Princigallo, A., and Guerrini, G. L., "Electrical Properties of Fluidified Portland Cement Mixes in the Early Stage of Hydration," *Cement Concrete Res.*, Vol. 30, No. 6, 2000, pp. 923–930, [https://doi.org/10.1016/S0008-8846\(00\)00282-9](https://doi.org/10.1016/S0008-8846(00)00282-9)
- [7] Salem, T. M., "Electrical Conductivity and Rheological Properties of Ordinary Portland Cement–Silica Fume and Calcium Hydroxide–Silica Fume Pastes," *Cement Concrete Res.*, Vol. 32, No. 9, 2002, pp. 1473–1481, [https://doi.org/10.1016/S0008-8846\(02\)00809-8](https://doi.org/10.1016/S0008-8846(02)00809-8)
- [8] Princigallo, A., van Breugel, K., and Levita, G., "Influence of the Aggregate on the Electrical Conductivity of Portland Cement Concretes," *Cement Concrete Res.*, Vol. 33, No. 11, 2003, pp. 1755–1763, [https://doi.org/10.1016/S0008-8846\(03\)00166-2](https://doi.org/10.1016/S0008-8846(03)00166-2)
- [9] Heikal, M., Morsy, M. S., and Radwan, M. M., "Electrical Conductivity and Phase Composition of Calcium Aluminate Cement containing Air-Cooled and Water-Cooled Slag at 20, 40 and 60°C," *Cement Concrete Res.*, Vol. 35, No. 7, 2005, pp. 1438–1446, <https://doi.org/10.1016/j.cemconres.2004.09.027>
- [10] Wei, X. and Li, Z., "Early Hydration Process of Portland Cement Paste by Electrical Measurement," *J. Mater. Civ. Eng.*, Vol. 18, No. 1, 2006, pp. 99–105, [https://doi.org/10.1061/\(ASCE\)0899-1561\(2006\)18:1\(99\)](https://doi.org/10.1061/(ASCE)0899-1561(2006)18:1(99))
- [11] Rajabipour, F., Sant, G., and Weiss, J., "Development of Electrical Conductivity-Based Sensors for Health Monitoring of Concrete Materials," *Transportation Research Board*, Washington, DC, 2007, <https://trid.trb.org/view.aspx?id=801858> (Last accessed 7 Nov 2016).
- [12] Xiao, L. and Li, Z., "Early-Age Hydration of Fresh Concrete Monitored by Non-Contact Electrical Resistivity Measurement," *Cement Concrete Res.*, Vol. 38, No. 3, 2008, pp. 312–319, <https://doi.org/10.1016/j.cemconres.2007.09.027>
- [13] Zhang, J., Qin, L., and Li, Z., "Hydration and Monitoring of Cement-Based Materials With Resistivity and Ultrasonic Methods," *Mater. Struct.*, Vol. 42, No. 1, 2009, pp. 15–24, <https://doi.org/10.1617/s11527-008-9363-0>

- [14] Topçu, İ. B., Uygunoğlu, T., and Hocaoğlu, İ., "Electrical Conductivity of Setting Cement Paste With Different Mineral Admixtures," *Constr. Build. Mater.*, Vol. 28, No. 1, 2012, pp. 414–420, <https://doi.org/10.1016/j.conbuildmat.2011.08.068>
- [15] Sanish, K. B., Neithalath, N., and Santhanam, M., "Monitoring the Evolution of Material Structure in Cement Pastes and Concretes Using Electrical Property Measurements," *Constr. Build. Mater.*, Vol. 49, No. 12, 2013, pp. 288–297, <https://doi.org/10.1016/j.conbuildmat.2013.08.038>
- [16] Tang, S. W., Cai, X. H., He, Z., Shao, H. Y., Li, Z. J., and Chen, E., "Hydration Process of Fly Ash Blended Cement Pastes by Impedance Measurement," *Constr. Build. Mater.*, Vol. 113, No. 15, 2016, pp. 939–950, <https://doi.org/10.1016/j.conbuildmat.2016.03.141>
- [17] Gorur, K., Smit, M. K., and Wittmann, F. H., "Microwave Study of Hydrating Cement Paste at Early Age," *Cement Concrete Res.*, Vol. 12, No. 4, 1982, pp. 447–454, [https://doi.org/10.1016/0008-8846\(82\)90059-X](https://doi.org/10.1016/0008-8846(82)90059-X)
- [18] Moukwa, M., Brodwin, M., Christo, S., Chang, J., and Shah, S. P., "The Influence of the Hydration Process Upon Microwave Properties of Cements," *Cement Concrete Res.*, Vol. 21, No. 5, 1991, pp. 863–872, [https://doi.org/10.1016/0008-8846\(91\)90181-G](https://doi.org/10.1016/0008-8846(91)90181-G)
- [19] Zhang, X., Ding, X. Z., Ong, C. K., Tan, B. T. G., and Yang, J., "Dielectric and Electrical Properties of Ordinary Portland Cement and Slag Cement in the Early Hydration Period," *J. Mater. Sci.*, Vol. 31, No. 5, 1996, pp. 1345–1352, <https://doi.org/10.1007/BF00353116>
- [20] Zhang, X., Yang, Y., and Ong, C. K., "Correlation of Microwave and Conduction Calorimeter Measurements on the Hydration of Cement," *J. Mater. Sci. Lett.*, Vol. 16, No. 23, 1997, pp. 1885–1887, <https://doi.org/10.1023/A:1018514012309>
- [21] Smith, A., Abélard, P., Thummen, F., and Allemann, A., "Electrical Characterisation as a Function of Frequency: Application to Aluminous Cement During Early Hydration," *Cement Concrete Compos.*, Vol. 24, No. 5, 2002, pp. 477–484, [https://doi.org/10.1016/S0958-9465\(01\)00079-8](https://doi.org/10.1016/S0958-9465(01)00079-8)
- [22] EN197-1, *Cement. Part 1: Composition, Specifications and Conformity Criteria for Common Cements*, British Standards Institution, London, 2000.
- [23] EN15167-1, *Ground Granulated Blast Furnace Slag for Use in Concrete, Mortar and Grout. Part 1: Definitions, Specifications and Conformity Criteria*, British Standards Institution, London, 2006.
- [24] Schwan, H. P., Schwarz, G., Maczuk, J., and Pauly, H., "On the Low-Frequency Dielectric Dispersion of Colloidal Particles in Electrolyte Solution," *J. Phys. Chem.*, Vol. 66, No. 12, 1962, pp. 2626–2635, <https://doi.org/10.1021/j100818a066>
- [25] Schwarz, G., "A Theory of the Low-Frequency Dielectric Dispersion of Colloidal Particles in Electrolyte Solution," *J. Phys. Chem.*, Vol. 66, No. 12, 1962, pp. 2636–2642, <https://doi.org/10.1021/j100818a067>
- [26] Hasted, J. B., *Aqueous Dielectrics*, Chapman and Hall, London, 1973.
- [27] McCarter, W. J. and Tran, D., "Monitoring Pozzolanic Activity by Direct Activation With Calcium Hydroxide," *Constr. Build. Mater.*, Vol. 10, No. 3, 1996, pp. 179–184, [https://doi.org/10.1016/0950-0618\(95\)00089-5](https://doi.org/10.1016/0950-0618(95)00089-5)
- [28] Whittington, H. W., McCarter, J., and Forde, M. C., "The Conduction of Electricity Through Concrete," *Mag. Concrete Res.*, Vol. 33, No. 114, 1981, pp. 48–60, <https://doi.org/10.1680/mac.1981.33.114.48>
- [29] Bordi, F., Cametti, C., and Gili, T., "Reduction of the Contribution of Electrode Polarization Effects in the Radiowave Dielectric Measurements of Highly Conductive Biological Cell Suspensions," *Bioelectrochemistry*, Vol. 54, No. 1, 2001, pp. 53–61, [https://doi.org/10.1016/S1567-5394\(01\)00110-4](https://doi.org/10.1016/S1567-5394(01)00110-4)
- [30] Ishai, P. B., Talary, M. S., Caduff, A., Levy, E., and Feldman, Y., "Electrode Polarization in Dielectric Measurements: A Review," *Meas. Sci. Technol.*, Vol. 24, No. 10, 2013, pp. 1–21.

- [31] Serghei, A., Tress, M., Sangoro, J. R., and Kremer, F., "Electrode Polarization and Charge Transport at Solid Interfaces," *Phys. Rev. B*, Vol. 80, No. 18, 2009, pp. 1–5, <https://doi.org/10.1103/PhysRevB.80.184301>
- [32] Bazzoni, A., Ma, S., Wang, Q., Shen, X., Cantoni, M., and Scrivener, K. L., "The Effect of Magnesium and Zinc Ions on the Hydration Kinetics of C3S," *J. Am. Ceram. Soc.*, Vol. 97, No. 11, 2014, pp. 3684–3693, <https://doi.org/10.1111/jace.13156>
- [33] Sowoidnich, T., "A Study of Retarding Effects on Cement and Tricalcium Silicate Hydration Induced by Superplasticizers," PhD thesis, Bauhaus University, Weimar, Germany, 2015.
- [34] Odler, I. and Wonnemann, R., "Effect of Alkalies on Portland Cement Hydration. I: Alkali Oxides Incorporated into the Crystalline Lattice of Clinker Minerals," *Cement Concrete Res.*, Vol. 13, No. 4, 1983, pp. 477–482, [https://doi.org/10.1016/0008-8846\(83\)90005-4](https://doi.org/10.1016/0008-8846(83)90005-4)
- [35] Gartner, E. M., Young, J. F., Damidot, D. A., and Jawed, I., "Hydration of Portland Cement," *Structure and Performance of Cements*, 2nd ed. Chap. 3, J. Bensted and P. Barnes, Eds., Spon, London, 2002.
- [36] Scrivener, K. L., Juilland, P., and Monteiro, P. J. M., "Advances in Understanding Hydration of Portland Cement," *Cement Concrete Res.*, Vol. 78, No. 12, 2015, pp. 38–56, <https://doi.org/10.1016/j.cemconres.2015.05.025>
- [37] Chen, Y. and Or, D., "Effects of Maxwell–Wagner Polarization on Soil Complex Dielectric Permittivity Under Variable Temperature and Electrical Conductivity," *Water Resour. Res.*, Vol. 42, No. 6, 2006, pp. 1–14, <https://doi.org/10.1029/2005WR004590>

Two-point concrete resistivity measurements: interfacial phenomena at the electrode–concrete contact zone

This content has been downloaded from IOPscience. Please scroll down to see the full text.

2015 Meas. Sci. Technol. 26 085007

(<http://iopscience.iop.org/0957-0233/26/8/085007>)

View the [table of contents for this issue](#), or go to the [journal homepage](#) for more

Download details:

IP Address: 129.89.24.43

This content was downloaded on 19/07/2015 at 21:03

Please note that [terms and conditions apply](#).

Two-point concrete resistivity measurements: interfacial phenomena at the electrode–concrete contact zone

W J McCarter, H M Taha, B Suryanto and G Starrs

Heriot-Watt University, School of Energy, Geoscience, Infrastructure and Society, Institute for Infrastructure and Environment, Edinburgh EH14 4AS, UK

E-mail: w.j.mccarter@hw.ac.uk

Received 16 March 2015, revised 6 May 2015

Accepted for publication 11 May 2015

Published 10 July 2015



CrossMark

Abstract

Ac impedance spectroscopy measurements are used to critically examine the *end-to-end* (two-point) testing technique employed in evaluating the bulk electrical resistivity of concrete. In particular, this paper focusses on the interfacial contact region between the electrode and specimen and the influence of contacting medium and measurement frequency on the impedance response. Two-point and four-point electrode configurations were compared and modelling of the impedance response was undertaken to identify and quantify the contribution of the electrode–specimen contact region on the measured impedance. Measurements are presented in both Bode and Nyquist formats to aid interpretation. Concretes mixes conforming to BSEN206-1 and BS8500-1 were investigated which included concretes containing the supplementary cementitious materials fly ash and ground granulated blast-furnace slag. A measurement protocol is presented for the end-to-end technique in terms of test frequency and electrode–specimen contacting medium in order to minimize electrode–specimen interfacial effect and ensure correct measurement of bulk resistivity.

Keywords: concrete, supplementary cementitious materials, ac impedance, two-point electrode, four-point electrode

(Some figures may appear in colour only in the online journal)

1. Introduction

The addition of water to Portland cement (PC) clinker produces a series of complex hydrolysis and hydration reactions causing a transformation of the viscous suspension of cement particles to a porous solid. The microporous nature of hardened cement has a significant influence on its permeation properties and, consequently, has implications for the durability and performance of cement-based materials such as concrete. One of the most serious problems (worldwide) associated with reinforced concrete structures is corrosion of the reinforcing steel due to the ingress of chloride ions—either from the marine environment or from de-icing salt used on roads for winter maintenance purposes. In the design of durable concrete structures, there exists a need to determine those characteristics of concrete which promote the ingress of gases and/or

liquids containing dissolved contaminants, and to define the performance of a concrete in terms of an easily measured parameter. Regarding the durability of concrete, strength *per se* is not a requirement, and properties such as absorption, diffusion and permeability are more important in this respect [1]. The permeation properties of concrete are intimately linked to the capillary pore network within the cementitious matrix which, in turn, will be influenced by the cement content, the water content and the addition of admixtures and supplementary cementitious materials (SCM) such as fly ash (FA) and ground granulated blast-furnace slag (GGBS).

As the flow of water under a pressure gradient (hence permeability) or the movement of ions under a concentration gradient (hence diffusivity) is analogous to the conduction of electrical current under a potential gradient, the electrical properties of concrete (namely resistivity or its reciprocal,

Table 1. Suggested ranges for concrete durability classification (adapted from [6]).

Durability class	Chloride resistivity index (Ωm)
Excellent	>13.0
Good	6.50–13.0
Poor	4.00–6.50
Very poor	<4.00

Note: In this test, specimens are vacuum saturated with 5.0M NaCl solution prior to the measurement.

conductivity) are being increasingly considered as a ‘durability index’ for assessing the long-term performance of concrete structures (see, for example, [2–10]). Furthermore, as capillary pore tortuosity, pore connectivity and pore constriction all influence the electrical properties of concrete, an electrical property measurement could thus quantify those microstructural characteristics which are of importance in assessing the durability of concrete structures. Tables 1 and 2 [6, 11, 12] present a concrete durability classification system based on electrical resistivity measurements.

In the development of standardized procedures for the measurement of the electrical properties of concrete—resistivity/conductivity in this instance—an *ac end-to-end* or two-electrode test method is normally used with contact between the concrete specimen and electrodes via water-saturated sponges [2, 13]. In terms of the *ac* test frequency, no particular value is specified, although a frequency in the range 50–100 Hz has been recommended [13, 14]. In the measurement of concrete resistivity using two- and four-electrode methods, a frequency in the range 50 Hz–1 kHz has also been suggested [15]. More specifically, frequency values of 108 Hz [2], 128 Hz [16] and 107 Hz and 120 Hz [17] have been used for two-electrode measurements.

As electrical property measurements—bulk resistivity in this instance—could, ultimately, be developed and exploited as an important concrete durability indicator, evaluation of this parameter is of considerable importance. This paper critically examines the end-to-end technique used for bulk resistivity measurements. Of particular interest in the current work is the influence of the electrode–specimen contact region on the measured electrical impedance and, to this end, electrical impedance spectroscopy is used with measurements taken over the frequency range 1 Hz–10 MHz.

2. Experimental programme

2.1. Materials and sample preparation

The concrete mixes used within the experimental programme are presented in table 3. The cementitious binders¹ comprised PC clinker, CEM I 52.5N to EN197-1 [18]; CEM I cement blended with GGBS to EN15167-1 [19]; and CEM I cement blended with low-lime FA to EN450-1 [20]. An oxide analysis of these materials is presented in table 4. Crushed granite aggregate, both coarse and fine, was used throughout together

¹ The binder comprises the total cementitious content of the concrete mix i.e. PC and SCM.

Table 2. Empirical concrete resistivity thresholds for protection of embedded steel reinforcement (adapted from [11, 12]).

Resistance to corrosion	Resistivity (Ωm)
Low	<50
Moderate/low	50–100
High	100–200
Very high	>200

with a mid-range water reducer/plasticizer (SikaPlast 15RM) conforming to EN934-2 [21]. The PC and SCMs were combined in the concrete pan-mixer. Regarding reinforced concrete structures, the range of mixes presented in table 3, in terms of binder content, binder composition, water–binder (*w/b*) ratio and grade strength satisfy (or exceed) the minimum requirements specified in Eurocode EN206-1:2000 [22] and British Standard BS8500-1 [23] for environmental exposure classes XC (corrosion induced by carbonation), XS (corrosion induced by chlorides from seawater) and XD (corrosion induced by chlorides other than seawater, e.g. de-icing salt) for an intended working life of 100 years, with a minimum of 0.05 m cover-to-steel.

Samples were cast as $0.15 \times 0.15 \times 0.15 \text{ m}^3$ cubic specimens in steel moulds and a total of three were cast for each mix in table 3; six $0.10 \times 0.10 \times 0.10 \text{ m}^3$ cubes were also cast for compressive strength tests at 28 d and 180 d and are presented in table 3, denoted, respectively, F_{28} and F_{180} . Specimen sizes conformed to EN12390-1 [24] and made in accordance with EN12390-2 [25] and were thus considered sufficiently large to ensure that local inhomogeneities would not have any appreciable influence on the bulk impedance response; compressive strength testing was carried out in accordance with EN12390-3 [26]. Stainless steel pin-electrodes were positioned centrally within each sample at the time of casting which ensured intimate contact between the electrodes and the surrounding concrete. Each electrode comprised a 0.0023 m diameter stainless-steel (*s/s*) rod (approximately 0.10 m in length); the rod was sleeved with heat-shrink insulation to expose a 0.01 m length of tip with the centre-to-centre spacing between the electrodes being 0.075 m. These electrodes were used for four-point electrical measurements, discussed below. A thermistor was attached to one of the electrodes to allow the cube temperature to be recorded. Samples were stored in a curing tank ($21 \pm 2^\circ\text{C}$) until required for testing which, for the current work programme, was at approximately 36 months. At this age, the change in resistivity/conductivity due to hydration will be negligible [27]; furthermore, it is only at such longer time-scales that the influence of the FA and GGBS on pore structure becomes evident.

2.2. Electrical measurements and data acquisition

Two-point electrical impedance measurements were obtained on each sample using a Solartron 1260 frequency response analyser (FRA). The signal amplitude used in the experimental programme was 350 mV with the impedance measured over the frequency range 1 Hz–10 MHz using a logarithmic sweep with 10 frequency points per decade. The

Table 3. Summary of concrete mixes.

Mix designation	w/b	CEM I (kg m ⁻³)	GGBS (kg m ⁻³)	FA (kg m ⁻³)	20mm (kg m ⁻³)	10mm (kg m ⁻³)	Fine (<4mm) (kg m ⁻³)	Pl (m ⁻³)	F ₂₈ (Mpa)	F ₁₈₀ (Mpa)
PC	0.35	378	—	—	787	393	787	5.15	79	88
	0.65	263	—	—	790	395	790	—	39	46
GGBS	0.35	245	132	—	784	392	784	5.13	81	89
	0.65	171	92	—	788	394	788	—	35	45
FA	0.35	242	—	130	773	386	773	5.06	65	81
	0.65	169	—	91	780	390	780	—	24	38

w/b = water/(cement + SCM) ratio, Pl, plasticizer.

Table 4. Oxide analysis of cementitious materials.

% by weight	PC	FA	GGBS
SiO ₂	20.68	51.0	34.33
Al ₂ O ₃	4.83	27.4	12.60
Fe ₂ O ₃	3.17	4.6	0.60
CaO	63.95	3.4	41.64
MgO	2.53	1.4	8.31
TiO ₂	+	1.6	+
P ₂ O ₅	+	0.3	+
SO ₃	2.80	0.7	+
K ₂ O	0.54	1.0	0.47
Na ₂ O	0.08	0.2	0.25

+ = not determined.

measured impedance comprised both the in-phase (resistive) component and the quadrature (reactive) component. After removal from the curing tank, the concrete cube was wiped with an absorbent towel and allowed to surface-dry before testing (to negate any possible surface conduction effects) with testing undertaken in a laboratory at a temperature of $21 \pm 1^\circ\text{C}$.

Figure 1(a) presents a schematic of the two-electrode testing arrangement. In this figure, external stainless steel (s/s) plate-electrodes were placed against opposite faces of the concrete cube (i.e. the faces cast against the steel mould). Intimate contact between the electrodes and concrete was obtained by means of $0.15 \times 0.15 \text{ m}^2$ synthetic sponges, each 0.002 m thick, saturated with a contact solution. Leads from the current (I_{output}) and potential (V_{high}) connections on the FRA were coupled at one of the electrodes and the current (I_{input}) and potential (V_{low}) connections coupled at the other electrode. Open- and short-circuit residual lead impedances were automatically nulled from the measurements at every spot frequency using the FRA's on-board lead-correction facility. The overall testing arrangement is displayed in figure 1(b) with a mass of 2 kg placed on the upper electrode to ensure uniform contact and giving a contact pressure of approximately 1 kPa. Regarding the contact solution noted above, three were used in the current experimental programme with separate sets of sponges were used for each saturating liquid:

- mains tap-water;
- a saturated solution of calcium hydroxide [28] (as calcium hydroxide is released during the hydration of the silicate phases within the cement clinker); and

- a simulated cement pore solution comprising 0.1 molar sodium hydroxide and 0.3 molar potassium hydroxide [29, 30] (as the alkali-oxides—Na₂O and K₂O—within the cement clinker are highly soluble).

The impedance response of the sponges placed between the electrodes, loaded as above, was measured separately at the end of each test. In addition to two-electrode measurements, a four-electrode testing configuration was also used, as shown schematically in figure 2(a). In this setup, the external s/s plate-electrodes served as the current (output/input) electrodes and the embedded s/s rods acted as the potential (high/low) electrodes. Figure 2(b) displays the testing arrangement with the plates placed on the faces perpendicular to the embedded pin-electrodes. In this figure, the spacing $s = 0.075 \text{ m}$.

In connection with bulk resistivity measurements on concrete, it is generally accepted that electrodes should be spaced apart at least 1.5 times the maximum aggregate size [31] to obtain values representative of the bulk material. The maximum aggregate size used in the experimental programme was 20 mm, hence electrode spacings should be $>30 \text{ mm}$ which is the case for both the external plate-electrodes and the internal pin-electrodes.

3. Test results and discussion

3.1. Two-electrode measurements

Preliminaries. It has been shown that the impedance of a cementitious material, $Z^*(\omega)$ (in ohms, Ω), can be represented in complex format through the relationship [32]

$$Z^*(\omega) = Z'(\omega) - iZ''(\omega), \quad (1)$$

where ω is the angular frequency ($= 2\pi f$ where f is the frequency of the applied field in hertz), $Z'(\omega)$ is the real or resistive component, $Z''(\omega)$ is the imaginary or reactive component and $i = \sqrt{-1}$. Two presentation formalisms are used.

- Nyquist format i.e. $-iZ''(\omega)$ versus $Z'(\omega)$, which is the polar plot.
- Bode format. This plot highlights the frequency domain behaviour of both the impedance, $|Z^*(\omega)|$, and phase angle, θ ($= \tan^{-1}(Z''(\omega)/Z'(\omega))$). A phase angle $\theta = -90^\circ$ would represent purely capacitive behaviour whereas

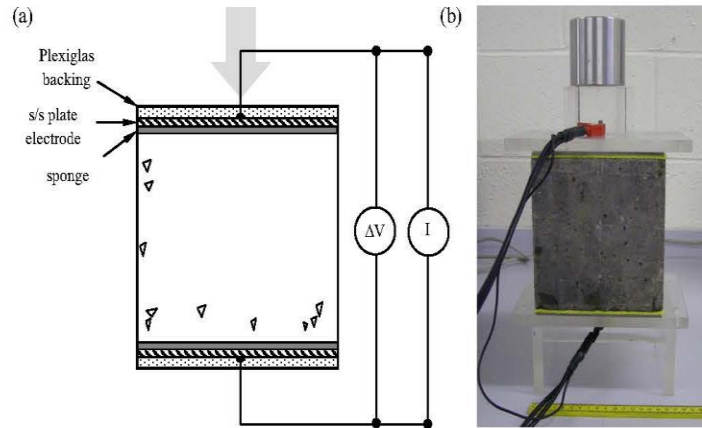


Figure 1. (a) Schematic of testing arrangement for two-point ac end-to-end measurements; and (b) laboratory setup.

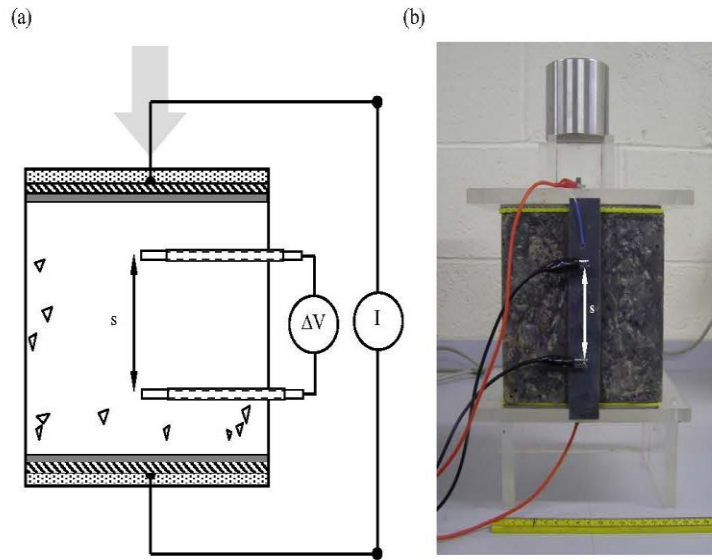


Figure 2. (a) Schematic of testing arrangement for four-point measurements; and (b) laboratory setup.

a phase angle $\theta = 0^\circ$ would represent purely resistive behaviour.

Regarding the Nyquist formalism in (i) above, if the system can be electrically modelled as a resistor in parallel with a pure capacitor whose capacitance (in Farads) is constant with increasing frequency, the polar plot will take the form of a semicircle. Figure 3(a) displays the plot for a resistor/capacitor combination with $R = 1.0\text{k}\Omega$ and $C = 10^{-10}\text{F}$, which produces a semicircle whose centre is located on the real axis. Frequency increases from right to left across the plot. However, for porous media such as cementitious materials (see, for example, [32–36]), the plot takes the form of a circular arc whose centre is depressed below the real ($Z'(\omega)$) axis. This is due to relaxation of polarization processes within the system and results in dielectric dispersion, i.e. the decrease in the capacitance with increasing frequency. To account for

this phenomenon, the capacitive reactance is replaced by a pseudo-capacitance or constant-phase element (CPE) to account for the dispersive behaviour of the medium. The CPE is a complex, frequency-dependent parameter defined by the relationship

$$Z'_{\text{CPE}}(\omega) = \frac{1}{C_0(i\omega)^p}, \quad (2)$$

where $i = \sqrt{-1}$, C_0 is a coefficient and the exponent, p , has a value such that $0 < p < 1$; if p equals 1, then the equation is identical to the reactive component of a pure capacitor of value C_0 with units in farads (F). When a CPE with value of $p < 1$ is placed in parallel with a resistor, a circular arc is produced with its centre depressed below the real axis with C_0 having units F s^{p-1} . Figure 3(a) also presents the Nyquist plot for a CPE ($C_0 = 10^{-10}\text{F s}^{-0.2}$ and $p = 0.8$) in parallel with a resistor

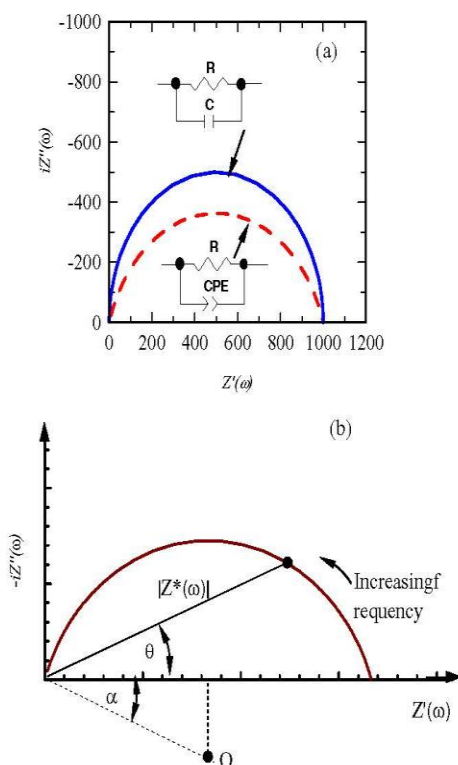


Figure 3. (a) Influence of the constant phase element (CPE) on the Nyquist plot—the solid line is the Nyquist plot for a pure capacitor ($C = 10^{-10}$ F) in parallel with a resistor ($R = 1.0$ k Ω) and the dashed line is a CPE ($C_0 = 10^{-10}$ F s $^{-0.2}$ and $p = 0.8$) in parallel with a resistor ($R = 1.0$ k Ω) (b) schematic diagram of Nyquist plot for a saturated porous material showing arc depression angle, α , phase angle, θ , and impedance, $Z^*(\omega)$.

$R = 1.0$ k Ω which now results a circular arc with its centre below the real axis. With reference to the schematic diagram in figure 3(b), the depression angle, α (in degrees) of the circle centre (O) is related to the exponent, p , in equation (2) through the relationship

$$a = (1 - p)90^\circ. \tag{3}$$

General observations and impedance modelling. Figure 4 presents the Nyquist plots with only the sponges placed between the electrodes, saturated with the three different liquids: water, calcium hydroxide and simulated pore solution. This figure indicates an almost linear decrease with increasing frequency and would represent part of a much larger arc associated with polarization phenomena at the electrode–sponge interface; the full extent of this arc would only become evident at frequencies considerably lower than the current work, i.e. <1 Hz. Regarding figure 4, the plots converge on the real axis as the frequency increases and, in all cases, at a frequency of approximately 40 kHz touches the real axis; this point gives the bulk resistance of the sponges. Some residual lead inductive effects are evident in this figure as the reactance turns

positive at frequencies in excess of 40 kHz. Regarding the sponge resistance at 40 kHz, these values are 7.9 Ω , 2.8 Ω and 0.75 Ω for, respectively, the sponges saturated with water, calcium hydroxide and simulated pore solution.

Figures 5–7 display the impedance response for the concrete mixes in table 3 using the testing arrangement presented in figure 1(a), with the simulated pore solution used as the sponge-saturating liquid. Note that for reasons of clarity, only every third data marker has been highlighted on these plots, although the curves have been drawn through all data points. The Nyquist plots in these figures represent the mean values for the three notionally identical specimens with salient frequencies indicated. On the Bode plots, error bars have been included to highlight the frequency-dependent variation in measurements between the replicate specimens, with the error bars representing \pm one standard deviation. Where error bars appear to be absent, the data markers are larger than the error bars. A feature evident from the Bode plots indicates that the scatter in the measurements from notionally identical specimens reduces with increasing frequency.

Generally, each response has a single dominant circular arc (denoted arc-1) similar to the schematic shown in figure 3(b); however, the frequency range over which this arc dominates, the frequency at which it maximizes, the arc diameter and the depression angle (α) are all dependent on the concrete mix proportions. On closer examination, a second small, flat arc (denoted arc-2) is evident at the low-frequency end of the Nyquist plots (right-hand side) presented in figures 5–7. In some instances, a small spur is also present of the right-hand side of the plot—see, for example, figure 5(a). In terms of representing the response as an electrical circuit, this is presented in figure 8 and comprises four series-connected, parallel circuit elements (the bulk resistance of the sponges has been omitted from this model as their resistance is negligible in comparison to the impedance of the system):

- (i) a resistor R_s which represents the projected intercept of the high-frequency end of arc-1 with the real axis. This would assume that there is finite resistance at infinite frequency which is clearly not tenable and would imply that a further high frequency arc exists i.e. there would be a constant-phase element (CPE) in parallel with R_s as the plot must eventually go through the origin. However, as the upper limit of the current investigation was 10 MHz and no data were recorded at frequencies >10 MHz, the circuit has simply been left as a single, shunted, resistive element;
- (ii) a parallel combination of resistor, R , and constant-phase element, CPE, for both arc-1 (R_1 and CPE $_1$) and arc-2 (R_2 and CPE $_2$);
- (iii) the small spur at the low-frequency end of the response would represent part of a much larger arc which would only become evident at frequencies <1 Hz. For completeness, this is also represented by a parallel combination of resistor (R_3) and constant phase element (CPE $_3$) although it is not present in some of the concrete mixes.

In attempting to offer a phenomenological interpretation for the circuit, consider again the testing arrangement in

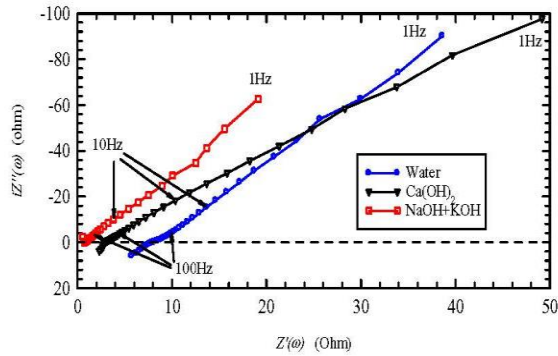


Figure 4. Nyquist plot for synthetic sponges placed between the electrodes. Saturating liquids indicated.

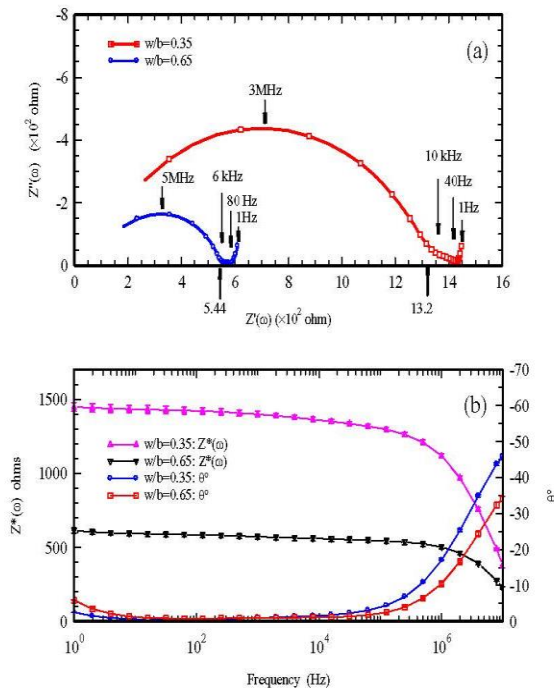


Figure 5. (a) Nyquist and (b) Bode plots for PC concrete mixes (error bars are presented on Bode plot and represent \pm one standard deviation).

figure 1(a). There are two interfaces present in this arrangement: the electrode–sponge interface and the sponge–concrete interface. If each interface can be electrically modelled as a parallel combination of resistor and CPE, then R_3 – CPE_3 (exponent p_3) would account for the response from the electrode–sponge interface; R_2 – CPE_2 (exponent p_2) the response from the sponge–specimen interface; and R_1 – CPE_1 (exponent p_1) and R_s the bulk response from the concrete specimen. Consider, for example, the Nyquist plots for the PC mix ($w/b = 0.65$) and the GGBS mix ($w/b = 0.35$) presented in figures 5 and 6 respectively; using the parameter values for the circuit elements presented in table 5, the simulated Nyquist responses (in ZView, Scribner Associates, Inc.) over the frequency range

1 Hz–10 MHz are presented in figures 9(a) and (b). For reasons of clarity, data markers have been removed from both the measured and simulated plots. The simulated circuit and the measured data show good agreement indicating that the model is a good electrical representation of the system. Regarding the GGBS concrete (figure 9(b)), as this mix did not display a spur in the low-frequency region circuit element, R_3 – CPE_3 is not included in the model simulation.

The following general features are evident from figures 5–7:

- (a) an increase in the w/b ratio results in a decrease in the bulk impedance of the specimen causing a decrease in the diameter of the dominant (bulk) arc (i.e. circuit

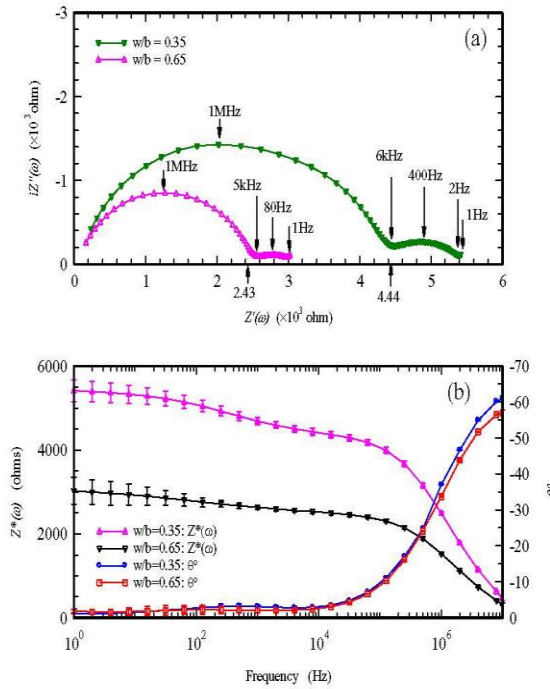


Figure 6. (a) Nyquist and (b) Bode plots for GGBS concrete mixes (error bars are presented on Bode plot and represent \pm one standard deviation).

Table 5. Circuit simulation parameters for PC and GGBS concrete mixes.

Mix	$R_s (\Omega)$	$R_1 (\Omega)$	$CPE_1 (C_0) (Fs^{p_1-1})$	p_1	$R_2 (\Omega)$	$CPE_2 (C_0) (Fs^{p_2-1})$	p_2	$R_3 (\Omega)$	$CPE_3 (C_0) (Fs^{p_3-1})$	p_3
PC ($w/b = 0.65$)	129	348	1.929×10^{-10}	0.96	114	1.160×10^{-4}	0.314	5×10^5	3.77×10^{-3}	0.768
GGBS ($w/b = 0.35$)	44.9	4148	1.072×10^{-9}	0.80	1333	2.729×10^{-5}	0.429	+	+	+

+ = not determined.

element R_1 -CPE₁). R_1 , together with R_s , would represent the resistance associated with the continuous capillary porosity within the concrete i.e. the percolated porosity; (b) concretes containing SCMs have an increased impedance in comparison to the equivalent PC mix. Although concretes containing GGBS and FA may not necessarily be of lower total porosity than the PC concretes, it is of a much more disconnected and tortuous nature [37, 38]. This feature is reflected in the increased impedance of these mixes; (c) the frequency at which the R_1 -CPE₁ arc maximizes falls within the range 150 kHz–5 MHz and is binder-specific, with the maximum frequency increasing in the sequence FA concretes, GGBS concretes, and PC concretes; and (d) the exponent, p , for the circuit element CPE₁ falls within a relatively narrow range for each concrete and is binder specific: 0.92–0.96 for the PC concretes; 0.80–0.82 for the GGBS concretes, and, 0.74–0.75 for the FA concretes. From equation (3) above, this implies that the arc depression angle, α , for the R_1 -CPE₁ circuit element increases as the impedance of the concrete increases.

Sponge-saturating liquid. In order to confirm whether circuit elements R_2 -CPE₂ and R_3 -CPE₃ are, indeed, artefacts of the concrete/electrode contacting medium, figures 10–12 present the Nyquist and Bode plots for the concrete mixes ($w/b = 0.65$ only) with the contacting sponges saturated with tap water, calcium hydroxide and simulated pore solution. These figures clearly highlight the influence of the saturating liquid on the impedance response. As previously noted, for sponges saturated with the simulated pore solution, this manifests itself as a small, flat arc at the low-frequency side of the Nyquist plot, but as the impedance of the sponges increases (see figure 4), it can be seen that this flat arc develops into a well-defined, low-frequency circular arc. The Bode plots show more clearly the influence of the sponge-saturating liquid on the measured impedance, $|Z^*(\omega)|$ and phase angle, θ , as the impedance curves, and phase-angle curves, tend to merge in the frequency range 5–10 kHz. At frequencies in excess of approximately 5 kHz, the circuit model for the system would then be represented by R_1 -CPE₁ and R_s in figure 8. It is also evident that as the impedance of the concrete specimen increases, the influence of the sponge-saturating liquid diminishes.

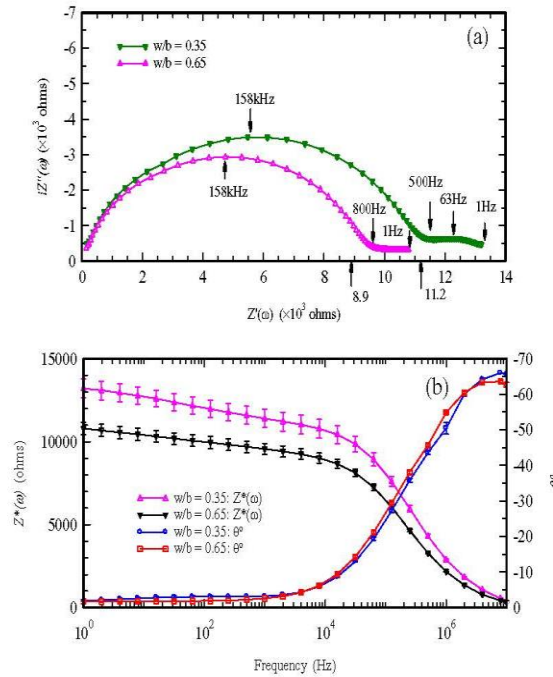


Figure 7. (a) Nyquist and (b) Bode plots for FA concrete mixes (error bars are presented on Bode plot and represent \pm one standard deviation).

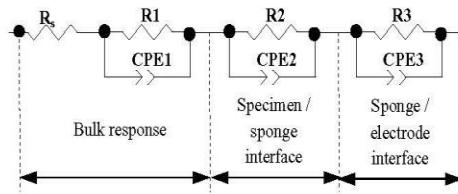


Figure 8. Proposed circuit model for electrode-sponge-specimen testing configuration.

This clearly has implications in the development of standard testing procedures for concrete resistivity measurements, particularly using ac in the low-frequency range 50–100 Hz. For example, consider the PC ($w/b = 0.65$) concrete in figure 10; using water-saturated sponges, the measured resistance (real component), R , at 100 Hz is 804 Ω , whereas at 10 kHz the resistance is 593 Ω . The resistance of the sponges measured separately, denoted R_{sp} , is 9.4 Ω at 100 Hz and 8.1 Ω at 10 kHz. Using the method presented in [13,16], these values could then be used to evaluate the bulk resistivity of the concrete cube (ρ_{cube}) using the two-point method presented in figure 1(a) as,

$$\rho_{cube} = \frac{A}{L}(R - R_{sp}), \quad (4)$$

where A is the cross-sectional area through which the current flows ($0.15 \times 0.15 \text{ m}^2$) and L is the spacing between the electrode plates (0.15 m). This obtains a resistivity of 119 Ωm at 100 Hz and 88 Ωm at 10 kHz. With reference to table 2,

this would move the concrete from one classification into another based solely on the test frequency and sponge-saturating liquid. Both these parameters need to be standardized to provide a consistent measurement procedure/protocol. This leaves the question: how is the true bulk resistance (hence resistivity/conductivity) of the specimen obtained using a two-point (end-to-end) measurement technique? This is further explored in the next section.

Four-electrode measurements. The model presented in figure 8(a) would suggest that the bulk resistance of the concrete can be obtained at the intercept of the low-frequency end of arc R_1 - CPE_1 with the real axis (i.e., the value $R_s + R_1$). In the two-electrode technique, the potential drop is measured between the external plate electrodes and includes the spurious effects the sponges have on the measured impedance. By separating the current electrodes and potential electrodes as presented in figure 2(a), such effects are, theoretically, eliminated. Ideally, in the four-electrode method the potential electrodes should be moved out of the current field to ensure that no current is drawn to the sensing electrodes [39, 40]. It was decided, however, to use embedded voltage-sensing pin-electrodes as the FRA's input impedance—1.0 M Ω over the frequency range 1 Hz–10 kHz, then decreasing to 45 k Ω at 10 MHz [41]—is considerably larger than the impedance being measured, which will ensure that negligible current is drawn through the sensing electrodes.

By way of illustration, using the testing arrangement in figure 2(a), figure 13(a) presents the Bode plots for the PC concrete ($w/b = 0.65$) and figure 13(b) that for the

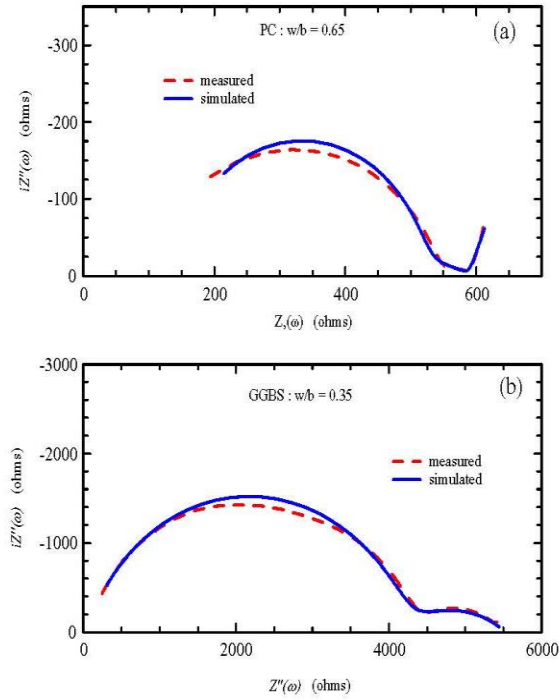


Figure 9. Measured and simulated responses for (a) PC concrete ($w/b = 0.65$) and (b) GGBS concrete ($w/b = 0.35$). The simulated response is based on the model presented in figure 8(a) and circuit parameters in table 5.

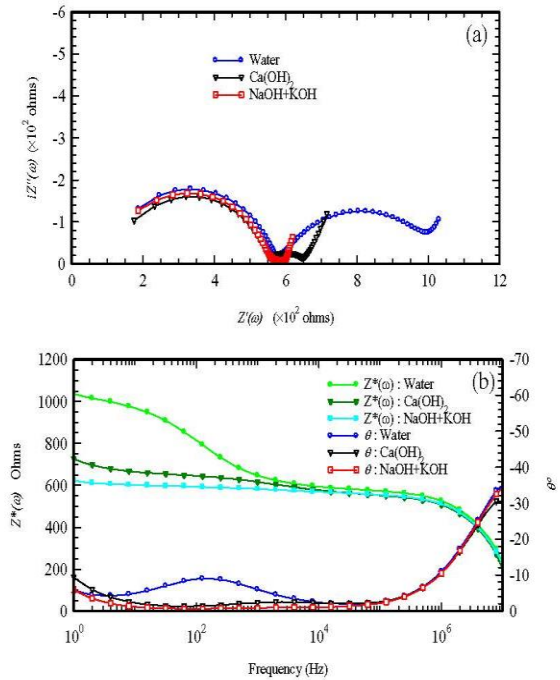


Figure 10. Influence of sponge saturation liquid on (a) Nyquist and (b) Bode plots for PC concrete ($w/b = 0.65$).

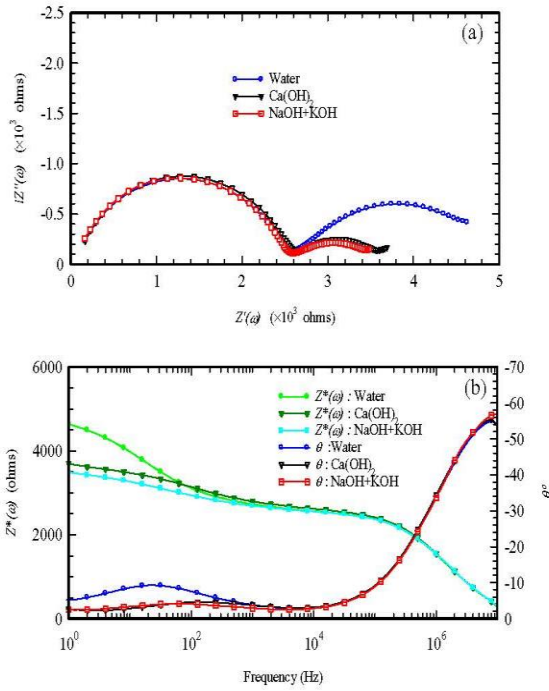


Figure 11. Influence of sponge saturation liquid on (a) Nyquist and (b) Bode plots for GGBS concrete ($w/b = 0.65$).

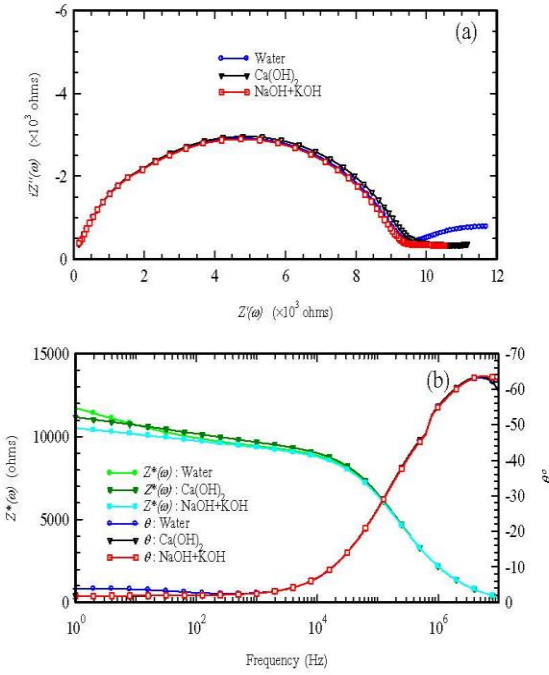


Figure 12. Influence of sponge saturation liquid on (a) Nyquist and (b) Bode plots for FA concrete ($w/b = 0.65$).

GGBS concrete ($w/b = 0.35$) with simulated pore solution electrode/sponge effect absent, the elements R_2 -CPE₂ and R_3 -CPE₃ (see figure 8(a)) are, effectively, removed and only every third data point has been highlighted). With the the impedance and phase angle remain virtually constant

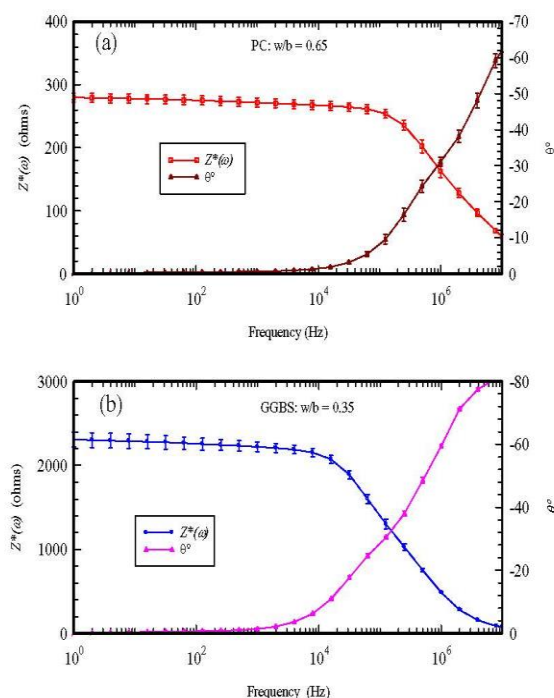


Figure 13. Bode plots obtained using the four-point testing arrangement presented in figure 2 for (a) PC concrete ($w/b = 0.65$) and (b) GGBS concrete ($w/b = 0.35$).

over the frequency range 1 Hz–10 kHz. As the phase angle is $\sim 0^\circ$, this implies that the concrete is displaying purely resistive behaviour and $Z^*(\omega) \approx Z'(\omega)$. Consider now the resistance of the concrete specimens at 1 kHz (which lies near the logarithmic centre of this frequency range); from figure 13, this obtains values of 272 Ω for the PC mix and 2219 Ω for the GGBS mix. As the current flow-lines through the sample are parallel, the resistivity of the concrete, ρ_{conc} (in Ωm), can be evaluated,

$$\rho_{\text{conc}} = \frac{A}{d}R, \tag{5}$$

where R is the measured resistance (real component) for this testing configuration, d is the spacing of the embedded potential electrodes (0.075 m) and A is the cross-sectional area through which the current flows ($0.15 \times 0.15\text{m}^2$). This gives a resistivity for the concretes of 81.6 Ωm for the PC mix and 666 Ωm for the GGBS mix. These values can now be used to compute the bulk resistance of the concrete cube (R_{cube}) using the two-point method,

$$R_{\text{cube}} = \frac{L}{A}\rho_{\text{conc}}, \tag{6}$$

where A is defined above and L is the spacing between the electrode plates (0.15 m); hence $R_{\text{cube}} = 544\ \Omega$ for the PC mix and 4440 Ω for the GGBS. These represent the real component of the impedance, $Z'(\omega)$, which are now located on the Nyquist plots presented in figures 5(a) and 6(a) and indicated by an arrow on the real axis. This procedure was repeated for

all the concrete mixes in table 3 and indicated accordingly on the Nyquist plot associated with each mix in figures 5–7. It is apparent that the true resistance of the cube can generally be located at the cusp point between the sponge/specimen interface arc ($R_2\text{--}CPE_2$ on figure 8(a)) and the bulk concrete arc ($R_1\text{--}CPE_1$ on figure 8(a)).

In terms of standardizing testing procedures using a single frequency, end-to-end (two-point) resistance measurement, the work detailed above would indicate that the test frequency should lie in the range 5–10 kHz together with a highly conductive sponge-saturating liquid.

4. Conclusions

Impedance spectroscopy was used to obtain the electrical properties of concrete over the frequency range 1 Hz–10 MHz. Concretes used in the test programme comprised PC concretes and concretes containing either GGBS or FA as a partial replacement. Measurements were presented in both Nyquist and Bode formats which gave a detailed picture of the electrical response of the electrode–concrete system with synthetic sponges used to form an electrical contacting medium between the electrode and concrete specimen. The following general conclusions can be drawn:

- (i) an equivalent electrical model for the system was presented which comprised series-connected parallel circuit elements to represent the concrete specimen, the sponge/specimen interface and the sponge/electrode interface.

The parallel circuit elements consisted of a resistor, R , and constant phase element (CPE), with the CPE being introduced to take account of the dispersion in capacitance with frequency;

- (ii) it was observed that using saturated sponges as an electrode/specimen contacting medium introduced a spurious circuit element represented by the sponge/specimen interface. Additionally, the sponge-saturating liquid had a significant influence on the impedance response of the electrode–sponge–specimen system; as the impedance of the saturating liquid increased a well-defined, low-frequency arc developed in the Nyquist plot. However, as the frequency of the applied field increased, the influence of the electrode/sponge and sponge/specimen interfaces decreased;
- (iii) the electrical impedance of the concrete mixes was strongly related to the w/b ratio and the type of cementitious binder. Increasing the w/b ratio resulted in a decrease in the overall impedance of the system whereas the addition of GGBS and FA increased the impedance of the system. Additionally, using the Nyquist formalism, several interdependent parameters of the arc associated with the bulk concrete response (circuit element R_1 –CPE $_1$) were identified—the arc depression angle, α , and the frequency at which the arc R_1 –CPE $_1$ maximized; both these parameters tended to be more influenced by binder-type and less by w/b ratio.
- (iv) Four-point impedance measurements were presented which indicated that the specimens displayed purely resistive behaviour (phase angle $\approx 0^\circ$) over the frequency range 1 Hz–10 kHz. These measurements allowed evaluation of the bulk resistivity of the concrete. The resistance (real component) of the cube calculated from four-point resistivity measurements was located on the Nyquist plot and occurred at the low-frequency side of the circuit element representing the bulk response (R_1 –CPE $_1$).

Regarding the testing procedure for two-point, end-to-end resistivity measurements, the work presented would suggest that using an ac frequency in the range 5 kHz–10 kHz with a low-resistivity liquid used to saturate the sponges would result in a more accurate assessment in concrete resistivity/conductivity. This is particularly important for low-resistivity concrete mixes, bearing in mind that the experimental programme was undertaken on mature concrete samples, as hydration and the pozzolanic reaction would be negligible and measurements would reflect the differences in the fully developed pore structure. During the early stages of hydration, young concretes would display considerably lower impedance values and hence the sponge-contacting medium would have a much greater influence on the two-point measurement with consequent greater error if a standard procedure is not developed.

Acknowledgments

One of the authors (HMT) wishes to acknowledge the financial support provided by Heriot-Watt University.

References

- [1] Basheer P A M and Barbhuiya S 2010 Pore structure and transport processes. *Concrete Durability: A Practical Guide to the Design of Durable Concrete Structures* ed M Soutsos (London: Thomas Telford Ltd) chapter 2
- [2] Gehlen C and Ludwig H-M 1999 Compliance testing for probabilistic design purposes. *DuraCrete EU-Brite EuRam III March*
- [3] Torrents J M, Juan-García P and Aguado A 2007 Electrical impedance spectroscopy as a technique for the surveillance of civil engineering structures: considerations on the galvanic insulation of samples *Meas. Sci. Technol.* **18** 1958–62
- [4] Alexander M G, Ballim Y and Stanish K A 2008 Framework for use of durability indexes in performance-based design and specifications for reinforced concrete structures *Mater. Struct.* **41** 921–36
- [5] Andrade C 2010 Types of models of service life of reinforcement—the case of the resistivity *Concr. Res. Lett.* **1** 73–80
- [6] Alexander M G, Santhanam M and Ballim Y 2010 Durability design and specification for concrete structures—the way forward *Int. J. Adv. Eng. Sci. Appl. Math.* **2** 95–105
- [7] Muigai R, Moyo P and Alexander M 2012 Durability design of reinforced concrete structures: a comparison of the use of durability indexes in the deemed-to-satisfy approach and the full-probabilistic approach *Mater. Struct.* **45** 1233–44
- [8] Andrade C, Prieto M, Tanner P, Tavares F and d'Andrea R 2013 Testing and modelling chloride penetration into concrete *Constr. Buil. Mater.* **39** 9–18
- [9] Nganga G, Alexander M and Beushausen H 2013 Practical implementation of the durability index performance-based design approach *Constr. Buil. Mater.* **45** 251–61
- [10] Andrade C, d'Andrea R and Rebolledo N 2014 Chloride ion penetration in concrete: the reaction factor in the electrical resistivity model *Cement Concr. Comput.* **47** 41–6
- [11] Langford P and Broomfield J P 1987 Monitoring the corrosion of reinforcing steel *Constr. Repair* **1** 32–6
- [12] Broomfield J P 1997 *Corrosion of Steel in Concrete* 1st edn (London: E&FN Spon)
- [13] Luping T 2005 Resistance of concrete to chloride ingress—from laboratory tests to in-field performance. EU-Project (5th FP GROWTH) G6RD-CT-2002-00855; Deliverable D22 Testing Resistance of Concrete to Chloride Ingress—A proposal to CEN for consideration as EN standard. Available at: www.civil.ist.utl.pt/~cristina/RREst/Aulas_Apresentacoes/07_Bibliografia/durabilidade%20betao%20%28durability%29/Outros/Guidline%20different%20method%20chloride%20ingress.pdf (accessed 4 May 2015)
- [14] Spanish Association for Standardization and Certification 2008 Durability of concrete: Test methods: Determination of the electrical resistivity. Part 1: Direct method (reference method) PNE 83988-1: 2008
- [15] Polder R 2000 Electrochemical techniques for measuring metallic corrosion *Mater. Struct.* **33** 603–11
- [16] Newlands M D, Jones M R, Kandasami S and Harrison T A 2008 Sensitivity of electrode contact solutions and contact pressure in assessing electrical resistivity of concrete *Mater. Struct.* **41** 621–32
- [17] Osterminski K, Polder R B and Schiessl P 2012 Long term behaviour of the resistivity of concrete *HERON* **57** 211–30
- [18] British Standards Institution 2000 *Cement-Part 1: Composition, specifications and conformity criteria for common cements* (London: BSI) EN197-1: 2000
- [19] British Standards Institution 2006 *Ground Granulated Blast Furnace Slag for Use in Concrete, Mortar and Grout—Part*

- 1: *Definitions, Specifications and Conformity Criteria* (London: BSI) EN15167-1: 2006
- [20] British Standards Institution 2005 *Fly Ash for Concrete—Part 1: Definition, Specifications and Conformity Criteria* (London: BSI) EN450-1: 2005
- [21] British Standards Institution 2009 *Admixtures for Concrete, Mortar and Grout. Part 2: Concrete Admixtures* (London: BSI) EN934-2: 2009
- [22] British Standards Institution 2000 *Concrete: Specification, Performance, Production and Conformity* (London: BSI) EN206-1: 2000
- [23] British Standards Institution 2006 *Concrete—Complementary British Standard to EN 206-1 Part 1: Method of Specifying and Guidance for the Specifier* (London: BSI) BS8500-1: 2006
- [24] British Standards Institution 2012 *Testing Hardened Concrete Part 1: Shape, Dimensions and Other Requirements for Specimens and Moulds* (London: BSI) EN12390-1: 2012
- [25] British Standards Institution 2009 *Testing Hardened Concrete Part 2: Making and Curing Specimens for Strength Tests* (London: BSI) EN12390-2: 2009
- [26] British Standards Institution 2009 *Testing Hardened Concrete Part 3: Compressive Strength of Test Specimens* (London: BSI) EN12390-3: 2009
- [27] Whittington H W, McCarter J and Forde M C 1981 The conduction of electricity through concrete *Mag. Concr. Res.* **33** 48–60
- [28] Saremi M and Mahallati E 1951 A study on chloride-induced depassivation of mild steel in simulated concrete pore solution *Cement Concr. Res.* **32** 1915–21
- [29] Ghods P, Isgor O B, Carpenter G J C, Li J, McRae GA and Gu GP 2013 Nano-scale study of passive films and chloride-induced depassivation of carbon steel rebar in simulated concrete pore solutions using FIB/TEM *Cement Concr. Res.* **47** 55–68
- [30] Yang Z, Fischer H and Polder R 2014 Synthesis and characterization of modified hydrotalcites and their ion exchange characteristics in chloride-rich simulated concrete pore solution *Cement Concr. Compos.* **47** 87–93
- [31] du Plooy R, Palma-Lopes S, Villain G and Dérobert X 2013 Development of a multi-ring resistivity cell and multi-electrode resistivity probe for investigation of cover concrete condition *NDT&E Int.* **54** 27–36
- [32] McCarter W J and Brousseau R 1990 The AC response of hardened cement paste. *Cement Concr. Res.* **20** 891–900
- [33] Christensen B J, Coverdale R T, Olsen R A, Ford S J, Garboczi E J, Jennings H M and Mason T O 1994 Impedance spectroscopy of hydrating cement-based materials: measurement, interpretation, and applications *J. Am. Ceram. Soc.* **77** 2789–804
- [34] Keddam M, Takenouti H, Novoa X R, Andrade C and Alonso C 1997 Impedance measurements on cement paste *Cement Concrete. Res.* **27** 1191–201
- [35] Cabeza M, Merino P, Miranda A, Novoa X R and Sanchez I 2002 Impedance spectroscopy study of hardened Portland cement paste *Cement Concr. Res.* **32** 881–91
- [36] Ball R J, Allen G C, Starrs G and McCarter W J 2011 Impedance spectroscopy measurements to study physico-chemical processes in lime-based composites *Appl. Phys. A* **105** 739–51
- [37] Li S and Roy D M 1986 Investigation of relations between porosity, pore structure, and Cl^- diffusion of fly ash and blended cement pastes *Cement Concr. Res.* **16** 749–59
- [38] Lu S, Landis E N and Keane D T 2006 X-ray microtomographic studies of pore structure and permeability in Portland cement concrete *Mater. Struct.* **39** 611–20
- [39] Schwan H P and Ferris C D 1968 Four-electrode null techniques for impedance measurement with high resolution *Rev. Sci. Instrum.* **39** 481–5
- [40] Ishai P B, Talary M S, Caduff A, Levy E and Feldman Y 2013 Electrode polarization in dielectric measurements: a review *Meas. Sci. Technol.* **24** 102001
- [41] Hsieh G, Ford S J, Mason T O and Pederson L R 1997 Experimental limitations in impedance spectroscopy: VI. Four-point measurements of solid materials systems *Solid State Ion.* **100** 297–311

References

- ABREU, C. M., CRISTÓBAL, M. J., LOSADA, R., NÓVOA, X. R., PENA, G. & PÉREZ, M. C. 2004. High frequency impedance spectroscopy study of passive films formed on AISI 316 stainless steel in alkaline medium. *Journal of Electroanalytical Chemistry*, 572, 335-345.
- AFSHAR, A. B. 1986 The early hydration of cement. Doctoral Thesis (Ph.D.) Heriot-Watt University.
- AL-QADI, I., HAZIM, O., SU, W. & RIAD, S. 1995. Dielectric Properties of Portland Cement Concrete at Low Radio Frequencies. *Journal of Materials in Civil Engineering*, 7, 192-198.
- ALEXANDER, M. G., BALLIM, Y. & STANISH, K. 2008. A framework for use of durability indexes in performance-based design and specifications for reinforced concrete structures. *Materials and Structures*, 41, 921-936.
- ALEXANDER, M. G., SANTHANAM, M. & BALLIM, Y. 2010. Durability design and specification for concrete structures—the way forward. *International Journal of Advances in Engineering Sciences and Applied Mathematics*, 2, 95-105.
- ALIGIZAKI, K. K. 2006. Pore structure of cement-based materials: testing, interpretation and requirements, CRC Press.
- ALIZADEH, R., RAKI, L., MAKAR, J. M., BEAUDOIN, J. J. & MOUDRAKOVSKI, I. 2009a. Hydration of tricalcium silicate in the presence of synthetic calcium-silicate-hydrate. *Journal of Materials Chemistry*, 19, 7937-7946.
- ANDRADE, C. 2010. Types of models of service life of reinforcement: The case of the resistivity. *Concrete research letters*, 1, 73-80.
- ANDRADE, C., BLANCO, V. M., COLLAZO, A., KEDDAM, M., NÓVOA, X. R. & TAKENOUTI, H. 1999. Cement paste hardening process studied by impedance spectroscopy. *Electrochimica Acta*, 44, 4313-4318.
- ANDRADE, C., D'ANDREA, R. & REBOLLEDO, N. 2014. Chloride ion penetration in concrete: The reaction factor in the electrical resistivity model. *Cement and Concrete Composites*, 47, 41-46.
- ANDRADE, C., KEDDAM, M., NÓVOA, X. R., PÉREZ, M. C., RANGEL, C. M. & TAKENOUTI, H. 2001. Electrochemical behaviour of steel rebars in concrete: influence of environmental factors and cement chemistry. *Electrochimica Acta*, 46, 3905-3912.

- ANDRADE, C., PRIETO, M., TANNER, P., TAVARES, F. & D'ANDREA, R. 2013. Testing and modelling chloride penetration into concrete. *Construction and Building Materials*, 39, 9-18.
- ARCHIE, G. E. 1942. The electrical resistivity log as an aid in determining some reservoir characteristics. *Transactions of the AIME*, 146, 54-62.
- ASTM, C. C. M. 2006. ASTM C 192/C 192M – 06. Standard Practice for Making and Curing Concrete Test Specimens in the Laboratory. West Conshohocken: ASTM International.
- ATKINSON, A. & NICKERSON, A. K. 1984. The diffusion of ions through water-saturated cement. *Journal of Materials Science*, 19, 3068-3078.
- BALL, R. J., ALLEN, G. C., STARRS, G. & MCCARTER, W. J. 2011. Impedance spectroscopy measurements to study physio-chemical processes in lime-based composites. *Applied Physics A*, 105, 739-751.
- BARNES, P. 1983. *Structure And Performance Of Cement*, Essex England, Elsevier Science Publishing Co ,INC.
- BARRET, P. & MÉNÉTRIER, D. 1980. Filter dissolution of C_3S as a function of the lime concentration in a limited amount of lime water. *Cement and Concrete Research*, 10, 521-534.
- BARRET, P., MÉNÉTRIER, D. & BERTRANDIE, D. 1983. Mechanism of C_3S dissolution and problem of the congruency in the very initial period and later on. *Cement and Concrete Research*, 13, 728-738.
- BARSOUKOV, E. & MACDONALD, J. R. 2005. *Impedance Spectroscopy: Theory, Experiment, and Applications Second Edition*. New Jersey: John Wiley & Sons.
- BAUERLE, J. E. 1969. Study of solid electrolyte polarization by a complex admittance method. *Journal of Physics and Chemistry of Solids*, 30, 2657-2670.
- BAZZONI, A. 2014. Study of early hydration mechanisms of cement by means of electron microscopy.
- BEEK, A. V. 2000. Dielectric properties of young concrete : non-destructive dielectric sensor for monitoring the strength development of young concrete.
- BELLMANN, F., DAMIDOT, D., MÖSER, B. & SKIBSTED, J. 2010. Improved evidence for the existence of an intermediate phase during hydration of tricalcium silicate. *Cement and Concrete Research*, 40, 875-884.
- BELLMANN, F., SOWOIDNICH, T., LUDWIG, H. M. & DAMIDOT, D. 2012. Analysis of the surface of tricalcium silicate during the induction period by X-ray photoelectron spectroscopy. *Cement and Concrete Research*, 42, 1189-1198.

- BENSTED, J. & BARNES, P. 2002. *Structure and Performance of Cements*, Spon Press. Taylor and Francis Group.
- BENTZ, D. P. 2007. A virtual rapid chloride permeability test. *Cement and Concrete Composites*, 29, 723-731.
- BENTZ, D. P. 2008. A review of early-age properties of cement-based materials. *Cement and Concrete Research*, 38, 196-204.
- BENTZ, D. P., GARBOCZI, E. J., HAECKER, C. J. & JENSEN, O. M. 1999. Effects of cement particle size distribution on performance properties of Portland cement-based materials. *Cement and Concrete Research*, 29, 1663-1671.
- BERGOLD, S., GOETZ-NEUNHOEFFER, F. & NEUBAUER, J. 2013. Quantitative analysis of C–S–H in hydrating alite pastes by in-situ XRD. *Cement and Concrete Research*, 53, 119-126.
- BERODIER, E. & SCRIVENER, K. 2015. Evolution of pore structure in blended systems. *Cement and Concrete Research*, 73, 25-35.
- Berodier, E.M.J., 2015. Impact of the supplementary cementitious materials on the kinetics and microstructural development of cement hydration. PhD Thesis, EPFL.
- BISHNOI, S. & SCRIVENER, K. L. 2009. Studying nucleation and growth kinetics of alite hydration using μ c. *Cement and Concrete Research*, 39, 849-860.
- BLACK, L., BREEN, C., YARWOOD, J., DENG, C. S., PHIPPS, J. & MAITLAND, G. 2006. Hydration of tricalcium aluminate (C3A) in the presence and absence of gypsum—studied by Raman spectroscopy and X-ray diffraction. *Journal of Materials Chemistry*, 16, 1263-1272.
- BOAST, W. B. 1936. *A conductometric analysis of Portland cement pastes and mortars, and some of its applications*.
- BORDI, F., CAMETTI, C. & GILI, T. 2001. Reduction of the contribution of electrode polarization effects in the radiowave dielectric measurements of highly conductive biological cell suspensions. *Bioelectrochemistry*, 54, 53-61.
- BROOMFIELD, J. P. 2006. *Corrosion of steel in concrete: understanding, investigation and repair*, CRC Press.
- BROWN, P. W., FRANZ, E., FROHNSDORFF, G. & TAYLOR, H. F. W. 1984. Analyses of the aqueous phase during early C3S hydration. *Cement and Concrete Research*, 14, 257-262.
- BUENFELD, N. R. & NEWMAN, J. B. 1984. The permeability of concrete in a marine environment. *Magazine of Concrete Research* [Online], 36. Available: <http://www.icevirtuallibrary.com/content/article/10.1680/mac.1984.36.127.67>.

- BULLARD, J. W. & FLATT, R. J. 2010. New Insights Into the Effect of Calcium Hydroxide Precipitation on the Kinetics of Tricalcium Silicate Hydration. *Journal of the American Ceramic Society*, 93, 1894-1903.
- BULLARD, J. W., JENNINGS, H. M., LIVINGSTON, R. A., NONAT, A., SCHERER, G. W., SCHWEITZER, J. S., SCRIVENER, K. L. & THOMAS, J. J. 2011. Mechanisms of cement hydration. *Cement and Concrete Research*, 41, 1208-1223.
- CABEZA, M., KEDDAM, M., NÓVOA, X. R., SÁNCHEZ, I. & TAKENOUTI, H. 2006. Impedance spectroscopy to characterize the pore structure during the hardening process of Portland cement paste. *Electrochimica Acta*, 51, 1831-1841.
- CABEZA, M., MERINO, P., MIRANDA, A., NÓVOA, X. R. & SANCHEZ, I. 2002. Impedance spectroscopy study of hardened Portland cement paste. *Cement and Concrete Research*, 32, 881-891.
- CABEZA, M., MERINO, P., NÓVOA, X. R. & SÁNCHEZ, I. 2003. Electrical effects generated by mechanical loading of hardened Portland cement paste. *Cement and Concrete Composites*, 25, 351-356.
- CAMP, P. R. & BILOTTA, S. 1989. Dielectric properties of portland cement paste as a function of time since mixing. *Journal of Applied Physics*, 66, 6007-6013.
- CANUT, M. M. C. 2011. Pore structure in blended cement pastes. DTU Civil Engineering Report R-268 (UK), Technical University of Denmark.
- CHEN, J. J., THOMAS, J. J., TAYLOR, H. F. & JENNINGS, H. M. 2004. Solubility and structure of calcium silicate hydrate. *Cement and Concrete Research*, 34, 1499-1519.
- CHEN, W. 2006. Hydration of slag cement: theory, modeling and application. PhD Thesis, University of Twente.
- CHEN, Y. & OR, D. 2006. Effects of Maxwell-Wagner polarization on soil complex dielectric permittivity under variable temperature and electrical conductivity. *Water Resources Research*, 42, W06424, doi:10.1029/2005WR004590.
- CHRISTENSEN, B. J. 1993. Microstructure studies of hydrating portland cement-based materials using impedance spectroscopy. 9415710 Ph.D., Northwestern University.
- CHRISTENSEN, B. J., COVERDALE, T., OLSON, R. A., FORD, S. J., GARBOCZI, E. J., JENNINGS, H. M. & MASON, T. O. 1994. Impedance Spectroscopy of Hydrating Cement-Based Materials: Measurement, Interpretation, and Application. *Journal of the American Ceramic Society*, 77, 2789-2804.
- CHRISTENSEN, B. J., MASON, T. O. & JENNINGS, H. M. 1992. Influence of Silica Fume on the Early Hydration of Portland Cements Using Impedance Spectroscopy. *Journal of the American Ceramic Society*, 75, 939-945.

- CHRISTENSEN, B. J., MASON, T. O. & JENNINGS, H. M. 1996. Comparison of measured and calculated permeabilities for hardened cement pastes. *Cement and Concrete Research*, 26, 1325-1334.
- CHRISTIAN, J. W. 2002. *The theory of transformations in metals and alloys*, Newnes.
- COELHO, R. 1979. *Physics of Dielectrics for the Engineer*, Elsevier Scientific Publishing Company.
- CORDES, S. & ODLER, I. 2002. Initial hydration of tricalcium silicate as studied by secondary neutrals mass spectrometry: I. Sample preparation and calibration. *Cement and concrete research*, 32, 1071-1075.
- CORMACK, S. L., MACPHEE, D. E. & SINCLAIR, D. C. 1998. An AC impedance spectroscopy study of hydrated cement pastes. *Advances in Cement Research* [Online], 10. Available: <http://www.icevirtuallibrary.com/content/article/10.1680/adcr.1998.10.4.151>.
- COVERDALE, R. T., CHRISTENSEN, B. J., JENNINGS, H. M., MASON, T. O., BENTZ, D. P. & GARBOCZI, E. J. 1995a. Interpretation of impedance spectroscopy of cement paste via computer modelling. *Journal of Materials Science*, 30, 712-719.
- COVERDALE, R. T., JENNINGS, H. M. & GARBOCZI, E. J. 1995b. An improved model for simulating impedance spectroscopy. *Computational Materials Science*, 3, 465-474.
- CRUZ, J. M., FITA, I. C., SORIANO, L., PAYÁ, J. & BORRACHERO, M. V. 2013. The use of electrical impedance spectroscopy for monitoring the hydration products of Portland cement mortars with high percentage of pozzolans. *Cement and Concrete Research*, 50, 51-61.
- CYR, M., LAWRENCE, P. & RINGOT, E. 2006. Efficiency of mineral admixtures in mortars: Quantification of the physical and chemical effects of fine admixtures in relation with compressive strength. *Cement and Concrete Research*, 36, 264-277.
- DAMIDOT, D., BELLMANN, F., MÖSER, B. & SOVOIDNICH, T. 2007. Investigation of the early dissolution behavior of C3S. *Proceedings of the 12th ICCI, Montreal, Canada*, 9-12.
- DAMIDOT, D., NONAT, A. & BARRET, P. 1990. Kinetics of Tricalcium Silicate Hydration in Diluted Suspensions by Microcalorimetric Measurements. *Journal of the American Ceramic Society*, 73, 3319-3322.
- DAVEY, C. L., MARKX, G. H. & KELL, D. B. 1990. Substitution and spreadsheet methods for analysing dielectric spectra of biological systems. *European Biophysics Journal*, 18, 255-265.

- DE SCHUTTER, G. & TAERWE, L. 1995. General hydration model for portland cement and blast furnace slag cement. *Cement and Concrete Research*, 25, 593-604.
- DIAMOND, S. 2004. The microstructure of cement paste and concrete—a visual primer. *Cement and Concrete Composites*, 26, 919-933.
- DIRKSEN, J. A. & RING, T. A. 1991. Fundamentals of crystallization: Kinetic effects on particle size distributions and morphology. *Chemical Engineering Science*, 46, 2389-2427.
- DITTRICH, S., NEUBAUER, J. & GOETZ-NEUNHOEFFER, F. 2014. The influence of fly ash on the hydration of OPC within the first 44 h—A quantitative in situ XRD and heat flow calorimetry study. *Cement and Concrete Research*, 56, 129-138.
- DOTELLI, G. & MARI, C. M. 2001. The evolution of cement paste hydration process by impedance spectroscopy. *Materials Science and Engineering: A*, 303, 54-59.
- DOUBLE, D., HEWLETT, P., SING, K. & RAFFLE, J. 1983. New developments in understanding the chemistry of cement hydration [and discussion]. *Philosophical Transactions of the Royal Society of London A: Mathematical, Physical and Engineering Sciences*, 310, 53-66.
- DOUBLE, D. D., HELLAWELL, A. & PERRY, S. J. 1978. The Hydration of Portland Cement. *Proceedings of the Royal Society of London. A. Mathematical and Physical Sciences*, 359, 435-451.
- DOVE, P. M., HAN, N. & DE YOREO, J. J. 2005. Mechanisms of classical crystal growth theory explain quartz and silicate dissolution behavior. *Proc Natl Acad Sci U S A*, 102, 15357-62.
- DU PLOOY, R., PALMA LOPES, S., VILLAIN, G. & DÉROBERT, X. 2013. Development of a multi-ring resistivity cell and multi-electrode resistivity probe for investigation of cover concrete condition. *NDT & E International*, 54, 27-36.
- EDWARDS, D. D., HWANG, J. H., FORD, S. J. & MASON, T. O. 1997. Experimental limitations in impedance spectroscopy:: Part V. Apparatus contributions and corrections. *Solid State Ionics*, 99, 85-93.
- ELAHI, A., BASHEER, P. A. M., NANUKUTTAN, S. V. & KHAN, Q. U. Z. 2010. Mechanical and durability properties of high performance concretes containing supplementary cementitious materials. *Construction and Building Materials*, 24, 292-299.
- EMMERT, S., WOLF, M., GULICH, R., KROHNS, S., KASTNER, S., LUNKENHEIMER, P. & LOIDL, A. 2011. Electrode polarization effects in broadband dielectric spectroscopy. *The European Physical Journal B*, 83, 157.

- EN197-1:2011 2011. Cement: Composition, specifications and conformity criteria for common cements. London, UK: BSI.
- FELDMAN, Y., ISHAI, P. B., PUZENKO, A. & RAICU, V. 2015. Elementary Theory of the Interaction of Electromagnetic Fields with Dielectric Materials. Dielectric Relaxation in Biological Systems. Oxford: Oxford University Press.
- FORD, S. J., MASON, T. O., CHRISTENSEN, B. J., COVERDALE, R. T., JENNINGS, H. M. & GARBOCZI, E. J. 1995. Electrode configurations and impedance spectra of cement pastes. *Journal of Materials Science*, 30, 1217-1224.
- FORD, S. J., SHANE, J. D. & MASON, T. O. 1998. Assignment of features in impedance spectra of the cement-paste/steel system. *Cement and Concrete Research*, 28, 1737-1751.
- FU, X., HOU, W., YANG, C., LI, D. & WU, X. 2000. Studies on Portland cement with large amount of slag. *Cement and Concrete Research*, 30, 645-649.
- GALLUCCI, E., MATHUR, P. & SCRIVENER, K. 2010. Microstructural development of early age hydration shells around cement grains. *Cement and Concrete Research*, 40, 4-13.
- GAO, P., WEI, J., ZHANG, T., HU, J. & YU, Q. 2017. Modification of chloride diffusion coefficient of concrete based on the electrical conductivity of pore solution. *Construction and Building Materials*, 145, 361-366.
- GARBOCZI, E. J. & BENTZ, D. P. 1996. Modelling of the microstructure and transport properties of concrete. *Construction and Building Materials*, 10, 293-300.
- GARRAULT-GAUFFINET, S. & NONAT, A. 1999. Experimental investigation of calcium silicate hydrate (CSH) nucleation. *Journal of crystal growth*, 200, 565-574.
- GARRAULT, S. 2005. Study of C-S-H growth on C3S surface during its early hydration. *Materials and Structures*, 38, 435-442.
- GARRAULT, S., BEHR, T. & NONAT, A. 2006. Formation of the CSH Layer during early hydration of tricalcium silicate grains with different sizes. *The Journal of Physical Chemistry B*, 110, 270-275.
- GARRAULT, S. & NONAT, A. 2001. Hydrated layer formation on tricalcium and dicalcium silicate surfaces: experimental study and numerical simulations. *Langmuir*, 17, 8131-8138.
- GARTNER, E., YOUNG, J., DAMIDOT, D. & JAWED, I. 2002. Hydration of Portland cement. *Structure and performance of cements*, 13, 978-0.
- GARVIN, S. 1991. Monitoring The Hydration Characteristics Of Cement-Based Materials. PhD, Heriot-Watt University.

- GEHLEN, C. & LUDWIG, H. 1999. Compliance testing for probabilistic design purposes. Brussels: European Union–Brite EuRam.
- GHODS, P., ISGOR, O. B., CARPENTER, G. J. C., LI, J., MCRAE, G. A. & GU, G. P. 2013. Nano-scale study of passive films and chloride-induced depassivation of carbon steel rebar in simulated concrete pore solutions using FIB/TEM. *Cement and Concrete Research*, 47, 55-68.
- GORUR, K., SMIT, M. K. & WITTMANN, F. H. 1982. Microwave study of hydrating cement paste at early age. *Cement and Concrete Research*, 12, 447-454.
- GREENBERG, S. A. & CHANG, T. N. 1965. The Hydration of Tricalcium Silicate. *The Journal of Physical Chemistry*, 69, 553-561.
- GRUTZECK, M. W. & RAMACHANDRAN, A. R. 1987. An integration of tricalcium silicate hydration models in light of recent data. *Cement and Concrete Research*, 17, 164-170.
- GU, P. & BEAUDOIN, J. J. 1997. Dielectric behaviour of hardened cementitious materials. *Advances in Cement Research* [Online], 9. Available: <http://www.icevirtuallibrary.com/content/article/10.1680/adcr.1997.9.33.1>.
- GU, P., XIE, P., BEAUDOIN, J. J. & BROUSSEAU, R. 1992. A.C. impedance spectroscopy (I): A new equivalent circuit model for hydrated portland cement paste. *Cement and Concrete Research*, 22, 833-840.
- GU, P., XIE, P., BEAUDOIN, J. J. & BROUSSEAU, R. 1993. A.C. impedance spectroscopy (II): Microstructural characterization of hydrating cement-silica fume systems. *Cement and Concrete Research*, 23, 157-168.
- GU, P., XIE, P., FU, Y. & BEAUDOIN, J. 1994. AC impedance phenomena in hydrating cement systems: frequency dispersion angle and pore size distribution. *Cement and concrete research*, 24, 86-88.
- GUTTERIDGE, W. A. & DALZIEL, J. A. 1990a. Filler cement: The effect of the secondary component on the hydration of Portland cement. *Cement and Concrete Research*, 20, 778-782.
- GUTTERIDGE, W. A. & DALZIEL, J. A. 1990b. Filler cement: The effect of the secondary component on the hydration of Portland cement: Part 2: Fine hydraulic binders. *Cement and Concrete Research*, 20, 853-861.
- HAGER, N. E. & DOMSZY, R. C. 2004. Monitoring of cement hydration by broadband time-domain-reflectometry dielectric spectroscopy. *Journal of Applied Physics*, 96, 5117-5128.
- HARROP, P. J. 1972. *Dielectrics*, John Wiley & Sons.

- HASTED, J. B. 1973. Aqueous dielectrics, Chapman and Hall [Distributed in the U.S.A. by Halsted Press, a division of J. Wiley & Sons, New York.
- HESSE, C., GOETZ-NEUNHOEFFER, F. & NEUBAUER, J. 2011. A new approach in quantitative in-situ XRD of cement pastes: Correlation of heat flow curves with early hydration reactions. *Cement and Concrete Research*, 41, 123-128.
- HEWLETT, P. 2003. *Lea's chemistry of cement and concrete*, Butterworth-Heinemann.
- HOFFMANN, K.-P., RUFF, R. & POPPENDIECK, W. Long-term characterization of electrode materials for surface electrodes in biopotential recording. *Engineering in Medicine and Biology Society*, 2006. EMBS'06. 28th Annual International Conference of the IEEE, 2006. IEEE, 2239-2242.
- HOLLINGSWORTH, A. D. & SAVILLE, D. A. 2003. A broad frequency range dielectric spectrometer for colloidal suspensions: cell design, calibration, and validation. *Journal of Colloid and Interface Science*, 257, 65-76.
- HONG, S.-H. & YOUNG, J. F. 1999. Hydration Kinetics and Phase Stability of Dicalcium Silicate Synthesized by the Pechini Process. *Journal of the American Ceramic Society*, 82, 1681-1686.
- HSIEH, G., FORD, S. J., MASON, T. O. & PEDERSON, L. R. 1997. Experimental limitations in impedance spectroscopy: Part VI. Four-point measurements of solid materials systems. *Solid State Ionics*, 100, 297-311.
- Hsu, C.H. and Mansfeld, F., 2001. Concerning the conversion of the constant phase element parameter Y_0 into a capacitance. *Corrosion*, 57(9), pp.747-748.
- Nyame, B.K. and Illston, J.M., 1980. Capillary pore structure and permeability of hardened cement paste. In 7th International Congress on the Chemistry of Cement, Paris.
- INGS, J. B., BROWN, P. W. & FROHNSDORFF, G. 1983. Early hydration of large single crystals of tricalcium silicate. *Cement and Concrete Research*, 13, 843-848.
- IRVINE, J. T., SINCLAIR, D. C. & WEST, A. R. 1990. Electroceramics: characterization by impedance spectroscopy. *Advanced Materials*, 2, 132-138.
- JAWED, I. & SKALNY, J. 1982. Surface phenomena during tricalcium silicate hydration. *Journal of Colloid and Interface Science*, 85, 235-243.
- JENNINGS, H. M. 2000. A model for the microstructure of calcium silicate hydrate in cement paste. *Cement and Concrete Research*, 30, 101-116.
- JIANG, S. P., MUTIN, J. C. & NONAT, A. 1995. Studies on mechanism and physico-chemical parameters at the origin of the cement setting. I. The fundamental processes involved during the cement setting. *Cement and Concrete Research*, 25, 779-789.

- JUILLAND, P., GALLUCCI, E., FLATT, R. & SCRIVENER, K. 2010. Dissolution theory applied to the induction period in alite hydration. *Cement and Concrete Research*, 40, 831-844.
- JUN-YUAN, H., SCHEETZ, B. E. & ROY, D. M. 1984. Hydration of fly ash-portland cements. *Cement and Concrete Research*, 14, 505-512.
- KAVITHA, N. A. Y. A. S. 2017. Evaluation of CO₂ emissions for green concrete with high volume slag, recycled aggregate, recycled water to build eco environment. *International Journal of Civil Engineering & Technology (IJCET)*, 8, 703-708.
- KEDDAM, M., TAKENOUTI, H., NÓVOA, X. R., ANDRADE, C. & ALONSO, C. 1997. Impedance measurements on cement paste. *Cement and Concrete Research*, 27, 1191-1201.
- KELZENBERG, A. L., TRACY, S. L., CHRISTIANSEN, B. J., THOMAS, J. J., CLARAGE, M. E., HODSON, S. & JENNINGS, H. M. 1998. Chemistry of the aqueous phase of ordinary Portland cement pastes at early reaction times. *Journal of the American Ceramic Society-Including Communications of the Amer Ceramic Soc*, 81, 2349-2359.
- KIM, H. C., KIM, S. Y. & YOON, S. S. 1995. Electrical properties of cement paste obtained from impedance spectroscopy. *Journal of Materials Science*, 30, 3768-3772.
- KIM, Y.-Y., LEE, K.-M., BANG, J.-W. & KWON, S.-J. 2014. Effect of W/C Ratio on Durability and Porosity in Cement Mortar with Constant Cement Amount. *Advances in Materials Science and Engineering*, 2014, Article ID 273460, 11, doi.org/10.1155/2014/273460.
- KOLANI, B., BUFFO-LACARRIÈRE, L., SELIER, A., ESCADEILLAS, G., BOUTILLON, L. & LINGER, L. 2012. Hydration of slag-blended cements. *Cement and Concrete Composites*, 34, 1009-1018.
- KYI, A. A. & BATCHELOR, B. 1994. An electrical conductivity method for measuring the effects of additives on effective diffusivities in portland cement pastes. *Cement and Concrete Research*, 24, 752-764.
- NICOLEAU, L.. 2004. Physico-chemical interactions between latex dispersions and cement phases. PhD Thesis, The University of Burgundy.
- LANGAN, B. W., WENG, K. & WARD, M. A. 2002. Effect of silica fume and fly ash on heat of hydration of Portland cement. *Cement and Concrete Research*, 32, 1045-1051.
- LANGFORD, P. & BROOMFIELD, J. 1987. Monitoring the corrosion of reinforcing steel. *Construction Repair*, 1, 6-32.
- LASAGA, A. C. & LUTTGE, A. 2001. Variation of crystal dissolution rate based on a dissolution stepwave model. *Science*, 291, 2400-2404.

- LAWRENCE, P., CYR, M. & RINGOT, E. 2003. Mineral admixtures in mortars: Effect of inert materials on short-term hydration. *Cement and Concrete Research*, 33, 1939-1947.
- LE CHATELIER, H. L. & MACK, J. L. 1905. Experimental researches on the constitution of hydraulic mortars. McGraw Publishing Company.
- LEVITA, G., MARCHETTI, A., GALLONE, G., PRINCIGALLO, A. & GUERRINI, G. L. 2000. Electrical properties of fluidified Portland cement mixes in the early stage of hydration. *Cement and Concrete Research*, 30, 923-930.
- LI, S. & ROY, D. M. 1986. Investigation of relations between porosity, pore structure, and C1–diffusion of fly ash and blended cement pastes. *Cement and Concrete Research*, 16, 749-759.
- LOCHE, J. M., AMMAR, A. & DUMARGUE, P. 2005. Influence of the migration of chloride ions on the electrochemical impedance spectroscopy of mortar paste. *Cement and Concrete Research*, 35, 1797-1803.
- LOTTHENBACH, B. 2010. Thermodynamic equilibrium calculations in cementitious systems. *Materials and Structures*, 43, 1413-1433.
- LOTTHENBACH, B. & WINNEFELD, F. 2006. Thermodynamic modelling of the hydration of Portland cement. *Cement and Concrete Research*, 36, 209-226.
- LU, S., LANDIS, E. & KEANE, D. 2006. X-ray microtomographic studies of pore structure and permeability in Portland cement concrete. *Materials and Structures*, 39, 611-620.
- LURA, P., WINNEFELD, F. & FANG, X. 2017. A simple method for determining the total amount of physically and chemically bound water of different cements. *Journal of Thermal Analysis and Calorimetry*, 1-8.
- LVOVICH, V. F. 2012. Impedance spectroscopy: applications to electrochemical and dielectric phenomena, John Wiley & Sons.
- MACDONALD, J. R. 1990. Impedance spectroscopy: old problems and new developments. *Electrochimica Acta*, 35, 1483-1492.
- MACPHEE, D. E., SINCLAIR, D. C. & CORMACK, S. L. 1997. Development of an Equivalent Circuit Model for Cement Pastes from Microstructural Considerations. *Journal of the American Ceramic Society*, 80, 2876-2884.
- MAKI, I. & KATO, K. 1982. Phase identification of alite in Portland cement clinker. *Cement and Concrete Research*, 12, 93-100.
- MANCHIRYAL, R. K. & NEITHALATH, N. 2009. Analysis of the influence of material parameters on electrical conductivity of cement pastes and concretes. *Magazine of*

- Concrete Research [Online], 61. Available: <http://www.icevirtuallibrary.com/content/article/10.1680/mac.2008.00064>.
- MARTINSEN, O. G. & GRIMNES, S. 2011. Bioimpedance and bioelectricity basics, Academic press.
- MARTYS, N. S. 1996. Survey of concrete transport properties and their measurement, NISTIR 5592, National Institute of Standards and Technology.
- MCCARTER, W. & AFSHAR, A. 1985. A Study Of The Early Hydration Of Portland Cement. ICE Proceedings [Online], 79. Available: <http://www.icevirtuallibrary.com/content/article/10.1680/iicep.1985.839>.
- MCCARTER, W., TAHA, H., SURYANTO, B. & STARRS, G. 2015. Two-point concrete resistivity measurements: interfacial phenomena at the electrode–concrete contact zone. Measurement Science and Technology, 26, 085007.
- MCCARTER, W. J. 1987. Gel formation during early hydration. Cement and Concrete Research, 17, 55-64.
- MCCARTER, W. J. 1994. A parametric study of the impedance characteristics of cement-aggregate systems during early hydration. Cement and Concrete Research, 24, 1097-1110.
- MCCARTER, W. J. & BROUSSEAU, R. 1990. The A.C. response of hardened cement paste. Cement and Concrete Research, 20, 891-900.
- MCCARTER, W. J., CHRISP, T. M., STARRS, G., ADAMSON, A., BASHEER, P. A. M., NANUKUTTAN, S. V., SRINIVASAN, S. & GREEN, C. 2013. Characterization of physio-chemical processes and hydration kinetics in concretes containing supplementary cementitious materials using electrical property measurements. Cement and Concrete Research, 50, 26-33.
- MCCARTER, W. J., CHRISP, T. M., STARRS, G., BASHEER, P. A. M. & BLEWETT, J. 2005. Field monitoring of electrical conductivity of cover-zone concrete. Cement and Concrete Composites, 27, 809-817.
- MCCARTER, W. J., CHRISP, T. M., STARRS, G. & BLEWETT, J. 2003. Characterization and monitoring of cement-based systems using intrinsic electrical property measurements. Cement and Concrete Research, 33, 197-206.
- MCCARTER, W. J. & CURRAN, P. N. 1984. The electrical response characteristics of setting cement paste. Magazine of Concrete Research [Online], 36. Available: <http://www.icevirtuallibrary.com/content/article/10.1680/mac.1984.36.126.42>.
- MCCARTER, W. J. & EZIRIM, H. 1998a. AC impedance profiling within cover zone concrete: influence of water and ionic ingress. Advances in Cement Research [Online],

10. Available:
<http://www.icevirtuallibrary.com/content/article/10.1680/adcr.1998.10.2.57>.
- MCCARTER, W. J. & EZIRIM, H. C. 1998b. Monitoring the early hydration of pozzolan—Ca(OH)₂. *Advances in Cement Research* [Online], 10. Available:
<http://www.icevirtuallibrary.com/content/article/10.1680/adcr.1998.10.4.161>.
- MCCARTER, W. J. & GARVIN, S. 1989. Dependence of electrical impedance of cement-based materials on their moisture condition. *Journal of Physics D: Applied Physics*, 22, 1773.
- MCCARTER, W. J., GARVIN, S. & BOUZID, N. 1988. Impedance measurements on cement paste. *Journal of Materials Science Letters*, 7, 1056-1057.
- MCCARTER, W. J., STARRS, G. & CHRISP, T. M. 1999. Immittance spectra for Portland cement/fly ash-based binders during early hydration. *Cement and Concrete Research*, 29, 377-387.
- MCCARTER, W. J., STARRS, G. & CHRISP, T. M. 2000. Electrical conductivity, diffusion, and permeability of Portland cement-based mortars. *Cement and Concrete Research*, 30, 1395-1400.
- MCCARTER, W. J., STARRS, G. & CHRISP, T. M. 2004. The complex impedance response of fly-ash cements revisited. *Cement and Concrete Research*, 34, 1837-1843.
- MCCARTER, W. J., STARRS, G. & CHRISP, T. M. 2009. Complex Impedance and Dielectric Dispersion in Carbon Fiber Reinforced Cement Matrices. *Journal of the American Ceramic Society*, 92, 1617-1620.
- MEHTA, P. K. & GJØRV, O. E. 1982. Properties of portland cement concrete containing fly ash and condensed silica-fume. *Cement and Concrete Research*, 12, 587-595.
- MEHTA, P. K. & MONTEIRO, P. J. M. 2013. *Concrete: Microstructure, Properties, and Materials*, McGraw-Hill Education.
- MÉNÉTRIER, D., JAWED, I. & SKALNY, J. 1980. Effect of gypsum on C3S hydration. *Cement and Concrete Research*, 10, 697-701.
- MÉNÉTRIER, D., JAWED, I., SUN, T. S. & SKALNY, J. 1979. ESCA and SEM studies on early C3S hydration. *Cement and Concrete Research*, 9, 473-482.
- MINARD, H., GARRAULT, S., REGNAUD, L. & NONAT, A. 2007. Mechanisms and parameters controlling the tricalcium aluminate reactivity in the presence of gypsum. *Cement and Concrete Research*, 37, 1418-1426.
- Monfore, G. E. (1968). "Electrical Resistivity of Concrete," *J. PCA (Portland Cement Association) Res. Develop. Lab.*, 10, No. 2, pp. 35-48. MORGAN, H., SUN, T.,

- HOLMES, D., GAWAD, S. & GREEN, N. G. 2006. Single cell dielectric spectroscopy. *Journal of Physics D: Applied Physics*, 40, 61.
- MORSY, M. S. 1999. Effect of temperature on electrical conductivity of blended cement pastes. *Cement and Concrete Research*, 29, 603-606.
- MOSTAFA, N. Y. & BROWN, P. W. 2005. Heat of hydration of high reactive pozzolans in blended cements: Isothermal conduction calorimetry. *Thermochimica Acta*, 435, 162-167.
- MOUKWA, M., BRODWIN, M., CHRISTO, S., CHANG, J. & SHAH, S. P. 1991. The influence of the hydration process upon microwave properties of cements. *Cement and Concrete Research*, 21, 863-872.
- MUIGAI, R., MOYO, P. & ALEXANDER, M. 2012. Durability design of reinforced concrete structures: a comparison of the use of durability indexes in the deemed-to-satisfy approach and the full-probabilistic approach. *Materials and Structures*, 45, 1233-1244.
- NEITHALATH, N. & JAIN, J. 2010. Relating rapid chloride transport parameters of concretes to microstructural features extracted from electrical impedance. *Cement and Concrete Research*, 40, 1041-1051.
- NEVILLE, A. M. & BROOKS, J. J. 1987. *Concrete technology*, Longman Scientific and technical.
- NEWLANDS, M., JONES, M. R., KANDASAMI, S. & HARRISON, T. 2008. Sensitivity of electrode contact solutions and contact pressure in assessing electrical resistivity of concrete. *Materials and Structures*, 41, 621-632.
- NEWLANDS, M. D., JONES, M. R., KANDASAMI, S. & HARRISON, T. A. 2007. Sensitivity of electrode contact solutions and contact pressure in assessing electrical resistivity of concrete. *Materials and Structures*, 41, 621.
- NGANGA, G., ALEXANDER, M. & BEUSHAUSEN, H. 2013. Practical implementation of the durability index performance-based design approach. *Construction and Building Materials*, 45, 251-261.
- NICOLEAU, L. 2013. The acceleration of cement hydration by seeding: Influence of the cement mineralogy. *ZKG international*, 1, 40-49.
- Nicoleau, L. and Bertolim, M.A., 2016. Analytical model for the alite (C3S) dissolution topography. *Journal of the American Ceramic Society*, 99(3), pp.773-786.
- NICOLEAU, L. & NONAT, A. 2016. A new view on the kinetics of tricalcium silicate hydration. *Cement and Concrete Research*, 86, 1-11.
- NICOLEAU, L., NONAT, A. & PERREY, D. 2013. The di- and tricalcium silicate dissolutions. *Cement and Concrete Research*, 47, 14-30.

- NONAT, A., MUTIN, J. C., LECOQ, X. & JIANG, S. P. 1997. Physico-chemical parameters determining hydration and particle interactions during the setting of silicate cements. *Solid State Ionics*, 101–103, Part 2, 923-930.
- NTBUILD492 1999. Concrete ,Mortar and Cement -Based Repair Materials: Chloride Migration Coefficient From NoN-Steady-State Migration Experiment. Concrete ,Mortar and Cement -Based Repair Materials: Chloride Migration Coefficient From NoN-Steady-State Migration Experiment. Finland: NORDTEST.
- NYAME, B. K. & ILLSTON, J. M. 1981. Relationships between permeability and pore structure of hardened cement paste. *Magazine of Concrete Research*, 33, 139-146.
- ODLER, I. 1998. 6 - Hydration, Setting and Hardening of Portland Cement A2 - Hewlett, Peter C. *Lea's Chemistry of Cement and Concrete (Fourth Edition)*. Oxford: Butterworth-Heinemann.
- ODLER, I. & DÖRR, H. 1979. Early hydration of tricalcium silicate II. The induction period. *Cement and Concrete Research*, 9, 277-284.
- ODLER, I. & SCHÜPPSTUHL, J. 1982. Combined hydration of tricalcium silicate and β -dicalcium silicate. *Cement and Concrete Research*, 12, 13-20.
- OLSSON, C. O. A. & LANDOLT, D. 2003. Passive films on stainless steels—chemistry, structure and growth. *Electrochimica Acta*, 48, 1093-1104.
- ORTEGA, J. M., SÁNCHEZ, I. & CLIMENT, M. A. 2015. Impedance spectroscopy study of the effect of environmental conditions in the microstructure development of OPC and slag cement mortars. *Archives of Civil and Mechanical Engineering*, 15, 569-583.
- OSBORNE, G. J. 1999. Durability of Portland blast-furnace slag cement concrete. *Cement and Concrete Composites*, 21, 11-21.
- OSTERMINSKI, K., POLDER, R. B. & SCHIEßL, P. 2012. Long term behaviour of the resistivity of concrete. *Heron*, 57 (2012) 3.
- PADMARAJ, D., MILLER, J. H., WOSIK, J. & ZAGOZDZON-WOSIK, W. 2011. Reduction of electrode polarization capacitance in low-frequency impedance spectroscopy by using mesh electrodes. *Biosensors and Bioelectronics*, 29, 13-17.
- PANDEY, S. P. & SHARMA, R. L. 2000. The influence of mineral additives on the strength and porosity of OPC mortar. *Cement and Concrete Research*, 30, 19-23.
- PAPADAKIS, V. G. 1999. Effect of fly ash on Portland cement systems: Part I. Low-calcium fly ash. *Cement and Concrete Research*, 29, 1727-1736.
- PASQUALE, A. 2009. A cultural evolutionary programming approach to automatic analytical modeling of electrochemical phenomena through impedance spectroscopy. *Measurement Science and Technology*, 20, 065601.

PAUL BEN, I., MARK, S. T., ANDREAS, C., EVGENIYA, L. & YURI, F. 2013. Electrode polarization in dielectric measurements: a review. *Measurement Science and Technology*, 24, 102001.

POLDER, R., ANDRADE, C., ELSENER, B., VENNESLAND, Ø., GULIKERS, J., WEIDERT, R. & RAUPACH, M. 2000. Test methods for on site measurement of resistivity of concrete. *Materials and Structures*, 33, 603-611.

POURCHET, S., REGNAUD, L., PEREZ, J. P. & NONAT, A. 2009. Early C3A hydration in the presence of different kinds of calcium sulfate. *Cement and Concrete Research*, 39, 989-996.

PRINCIGALLO, A., VAN BREUGEL, K. & LEVITA, G. 2003. Influence of the aggregate on the electrical conductivity of Portland cement concretes. *Cement and Concrete Research*, 33, 1755-1763.

PRIYANTHA, N., JAYAWEERA, P., MACDONALD, D. D. & SUN, A. 2004. An electrochemical impedance study of Alloy 22 in NaCl brine at elevated temperature. I. Corrosion behavior. *Journal of Electroanalytical Chemistry*, 572, 409-419.

QUENNOZ, A. & SCRIVENER, K. L. 2013. Interactions between alite and C3A-gypsum hydrations in model cements. *Cement and Concrete Research*, 44, 46-54.

RAICU, V., SAIBARA, T. & IRIMAJIRI, A. 1998. Dielectric properties of rat liver in vivo: a noninvasive approach using an open-ended coaxial probe at audio/radio frequencies. *Bioelectrochemistry and bioenergetics*, 47, 325-332.

RAJABIPOUR, F., SANT, G. & WEISS, J. Development of electrical conductivity-based sensors for health monitoring of concrete materials. *TRB Annual Conference*, 2007. 16.

RICHARDSON, I. G. 2000. The nature of the hydration products in hardened cement pastes. *Cement and Concrete Composites*, 22, 97-113.

RIDI, F., FRATINI, E., LUCIANI, P., WINNEFELD, F. & BAGLIONI, P. 2011. Hydration kinetics of tricalcium silicate by calorimetric methods. *Journal of colloid and interface science*, 364, 118-124.

ROTHSTEIN, D., THOMAS, J. J., CHRISTENSEN, B. J. & JENNINGS, H. M. 2002. Solubility behavior of Ca-, S-, Al-, and Si-bearing solid phases in Portland cement pore solutions as a function of hydration time. *Cement and Concrete Research*, 32, 1663-1671.

SAKAI, E., MIYAHARA, S., OHSAWA, S., LEE, S.-H. & DAIMON, M. 2005. Hydration of fly ash cement. *Cement and Concrete Research*, 35, 1135-1140.

SALEM, T. M. 2002. Electrical conductivity and rheological properties of ordinary Portland cement–silica fume and calcium hydroxide–silica fume pastes. *Cement and Concrete Research*, 32, 1473-1481.

- SÁNCHEZ, I., ANTÓN, C., VERA, G., ORTEGA, J. M. & CLIMENT, M. A. 2013. Moisture Distribution in Partially Saturated Concrete Studied by Impedance Spectroscopy. *Journal of Nondestructive Evaluation*, 32, 362-371.
- SANISH, K. B., NEITHALATH, N. & SANTHANAM, M. 2013. Monitoring the evolution of material structure in cement pastes and concretes using electrical property measurements. *Construction and Building Materials*, 49, 288-297.
- SAREMI, M. & MAHALLATI, E. 2002. A study on chloride-induced depassivation of mild steel in simulated concrete pore solution. *Cement and Concrete Research*, 32, 1915-1921.
- SCAIFE, B. K. P. 1998. *Principles of Dielectrics*, OUP Oxford.
- SCHINDLER, A. K. & FOLLIARD, K. J. 2005. Heat of Hydration Models for Cementitious Materials. *ACI Materials Journal*, 102, 24-33.
- SCHWAN, H. P. 1963. Determination of biological impedances. *Physical techniques in biological research*, 6, 323-407.
- SCHWAN, H. P. 1968. Electrode Polarization Impedance And Measurements In Biological Materials. *Annals of the New York Academy of Sciences*, 148, 191-209.
- SCHWAN, H. P. & FERRIS, C. D. 1968. Four Electrode Null Techniques for Impedance Measurement with High Resolution. *Review of Scientific Instruments*, 39, 481-485.
- SCHWAN, H. P., SCHWARZ, G., MACZUK, J. & PAULY, H. 1962. On The Low-Frequency Dielectric Dispersion Of Colloidal Particles In Electrolyte Solution¹. *The Journal of Physical Chemistry*, 66, 2626-2635.
- SCHWARZ, G. 1962. A Theory Of The Low-Frequency Dielectric Dispersion Of Colloidal Particles In Electrolyte Solution^{1,2}. *The Journal of Physical Chemistry*, 66, 2636-2642.
- SCRIVENER, K. & YOUNG, J. F. 1997. *Mechanisms of chemical degradation of cement-based systems*, CRC Press.
- SCRIVENER, K. L. 1989. Microstructure of concrete. *Materials Science of Concrete III*, I, 1 pp., 127.
- SCRIVENER, K. L., FÜLLMANN, T., GALLUCCI, E., WALENTA, G. & BERMEJO, E. 2004. Quantitative study of Portland cement hydration by X-ray diffraction/Rietveld analysis and independent methods. *Cement and Concrete Research*, 34, 1541-1547.
- SCUDERI, C. A., MASON, T. O. & JENNINGS, H. M. 1991. Impedance spectra of hydrating cement pastes. *Journal of Materials Science*, 26, 349-353.
- SERGHEI, A., TRESS, M., SANGORO, J. & KREMER, F. 2009. Electrode polarization and charge transport at solid interfaces. *Physical Review B*, 80, 184301.

- SHI, C. 2004. Effect of mixing proportions of concrete on its electrical conductivity and the rapid chloride permeability test (ASTM C1202 or ASSHTO T277) results. *Cement and Concrete Research*, 34, 537-545.
- SHI, C. & DAY, R. L. 1995. A calorimetric study of early hydration of alkali-slag cements. *Cement and Concrete Research*, 25, 1333-1346.
- SHI, M., CHEN, Z. & SUN, J. 1999. Determination of chloride diffusivity in concrete by AC impedance spectroscopy. *Cement and Concrete Research*, 29, 1111-1115.
- SHIMIZU, Y. 1928. An electrical method for measuring the setting time of portland cement. *Mill Section of Concrete*, 32, 111-113.
- SINCLAIR, D. C. & WEST, A. R. 1989. Impedance and modulus spectroscopy of semiconducting BaTiO₃ showing positive temperature coefficient of resistance. *Journal of Applied Physics*, 66, 3850-3856.
- SMITH, A., ABÉLARD, P., THUMMEN, F. & ALLEMAND, A. 2002. Electrical characterisation as a function of frequency: application to aluminous cement during early hydration. *Cement and Concrete Composites*, 24, 477-484.
- SNYDER, K. 2001. The relationship between the formation factor and the diffusion coefficient of porous materials saturated with concentrated electrolytes: theoretical and experimental considerations. *Concrete Science and Engineering*, 3, 216-224.
- SNYDER, K. A., FENG, X., KEEN, B. D. & MASON, T. O. 2003. Estimating the electrical conductivity of cement paste pore solutions from OH⁻, K⁺ and Na⁺ concentrations. *Cement and Concrete Research*, 33, 793-798.
- SONG, G. 2000. Equivalent circuit model for AC electrochemical impedance spectroscopy of concrete. *Cement and Concrete Research*, 30, 1723-1730.
- SONG, S., SOHN, D., JENNINGS, H. M. & MASON, T. O. 2000. Hydration of alkali-activated ground granulated blast furnace slag. *Journal of Materials Science*, 35, 249-257.
- SPRAGG, R., QIAO, C., BARRETT, T. & WEISS, J. 2016. Assessing a concrete's resistance to chloride ion ingress using the formation factor, Elsevier, London.
- STARRS, G. & MC CARTER, W. J. 1998. Impedance response of cementitious binders during early hydration. *Advanced in Cement Research*, 10, 179-186.
- STEIN, H. N. & STEVELS, J. M. 1964. Influence of silica on the hydration of 3 CaO,SiO₂. *Journal of Applied Chemistry*, 14, 338-346.
- SUN, T., BERNABINI, C. & MORGAN, H. 2010. Single-colloidal particle impedance spectroscopy: complete equivalent circuit analysis of polyelectrolyte microcapsules. *Langmuir*, 26, 3821-8.

- SUN, T., HOLMES, D., GAWAD, S., GREEN, N. G. & MORGAN, H. 2007. High speed multi-frequency impedance analysis of single particles in a microfluidic cytometer using maximum length sequences. *Lab on a Chip*, 7, 1034-1040.
- SUNAGAWA, I. 2005. *Crystals: growth, morphology, & perfection*, Cambridge University Press.
- SURYANTO, B., MCCARTER, W. J., STARRS, G. & CHRISP, T. M. 2017. Characterization of Fly-ash using Electrochemical Impedance Spectroscopy. *Procedia Engineering*, 171, 705-714.
- TADROS, M. E., SKALNY, J. A. N. & KALYONCU, R. S. 1976. Early Hydration of Tricalcium Silicate. *Journal of the American Ceramic Society*, 59, 344-347.
- TAFFINDER, G. & BATCHELOR, B. 1993. Measurement of Effective Diffusivities in Solidified Wastes. *Journal of Environmental Engineering*, 119, 17-33.
- TANG, L. & NILSSON, L.-O. 1993. Rapid determination of the chloride diffusivity in concrete by applying an electric field. *Materials Journal*, 89, 49-53.
- TANG, L., NILSSON, L.-O. & BASHEER, P. M. 2011. *Resistance of concrete to chloride ingress: Testing and modelling*, CRC Press.
- TANG, S. W., CAI, X. H., ZHOU, W., SHAO, H. Y., HE, Z., LI, Z. J., JI, W. M. & CHEN, E. 2016. In-situ and continuous monitoring of pore evolution of calcium sulfoaluminate cement at early age by electrical impedance measurement. *Construction and Building Materials*, 117, 8-19.
- TANG, S. W., LI, Z. J., CHEN, E. & SHAO, H. Y. 2014. Impedance measurement to characterize the pore structure in Portland cement paste. *Construction and Building Materials*, 51, 106-112.
- TAYLOR, H. F. 1997. *Cement chemistry*, Thomas Telford.
- TAYLOR, H. F. W., BARRET, P., BROWN, P. W., DOUBLE, D. D., FROHNSDORFF, G., JOHANSEN, V., MÉNÉTRIER-SORRENTINO, D., ODLER, I., PARROTT, L. J., POMMERSHEIM, J. M., REGOURD, M. & YOUNG, J. F. 1984. The hydration of tricalcium silicate. *Matériaux et Construction*, 17, 457-468.
- TAYLOR, M. A. & ARULANANDAN, K. 1974. Relationships between electrical and physical properties of cement pastes. *Cement and Concrete Research*, 4, 881-897.
- THOMAS, J. J. 2007. A New Approach to Modeling the Nucleation and Growth Kinetics of Tricalcium Silicate Hydration. *Journal of the American Ceramic Society*, 90, 3282-3288.

- THOMAS, J. J., JENNINGS, H. M. & CHEN, J. J. 2009. Influence of nucleation seeding on the hydration mechanisms of tricalcium silicate and cement. *The Journal of Physical Chemistry C*, 113, 4327-4334.
- TORRENTS, J. M., JUAN-GARCÍA, P. & AGUADO, A. 2007. Electrical impedance spectroscopy as a technique for the surveillance of civil engineering structures: considerations on the galvanic insulation of samples. *Measurement Science and Technology*, 18, 1958.
- TORRENTS, J. M., RONCERO, J. & GETTU, R. 1998. Utilization of impedance spectroscopy for studying the retarding effect of a superplasticizer on the setting of cement. *Cement and Concrete Research*, 28, 1325-1333.
- UMINO, M., ODA, N. & YASUHARA, Y. 2002. Experimental and theoretical studies of the effect of electrode polarisation on capacitances of blood and potassium chloride solution. *Medical and Biological Engineering and Computing*, 40, 533-541.
- VAN BEEK, A. & HILHORST, M. 1999. Dielectric measurements to characterize the microstructural changes of young concrete. *HERON-ENGLISH EDITION*-, 44, 3-3.
- VERNET, C. & NOWORYTA, G. Conductometric test for cement-admixture systems. *Proceedings of 9th International Congress on the Chemistry of Cement, New Dehli, 1992*. 627-633.
- WEI, X. & LI, Z. 2005. Study on hydration of Portland cement with fly ash using electrical measurement. *Materials and Structures*, 38, 411-417.
- WEI, X. & XIAO, L. 2011. Influence of the aggregate volume on the electrical resistivity and properties of portland cement concretes. *Journal of Wuhan University of Technology-Mater. Sci. Ed.*, 26, 965-971.
- WEISS, W. J., SPRAGG, R. P., ISGOR, O. B., LEY, M. T. & VAN DAM, T. 2017. Toward performance specifications for concrete: linking resistivity, RCPT and diffusion predictions using the formation factor for use in specifications. *Conference: fib Symposium 2017 Maastricht, The Netherlands*.
- WEN, S. & CHUNG, D. 2001. Effect of admixtures on the dielectric constant of cement paste. *Cement and Concrete Research*, 31, 673-677.
- WHITTINGTON, H. W., MCCARTER, J. & FORDE, M. C. 1981. The conduction of electricity through concrete. *Magazine of Concrete Research*, 33, 48-60.
- WU, X., JIANG, W. & ROY, D. M. 1990. Early activation and properties of slag cement. *Cement and Concrete Research*, 20, 961-974.
- WU, X., ROY, D. M. & LANGTON, C. A. 1983. Early stage hydration of slag-cement. *Cement and Concrete Research*, 13, 277-286.

- XIAO, L.-Z., LI, Z.-J. & WEI, X.-S. 2007. Selection of superplasticizer in concrete mix design by measuring the early electrical resistivities of pastes. *Cement and Concrete Composites*, 29, 350-356.
- XIAO, L. & LI, Z. 2008. Early-age hydration of fresh concrete monitored by non-contact electrical resistivity measurement. *Cement and Concrete Research*, 38, 312-319.
- YANG, Z., FISCHER, H. & POLDER, R. 2014. Synthesis and characterization of modified hydrotalcites and their ion exchange characteristics in chloride-rich simulated concrete pore solution. *Cement and Concrete Composites*, 47, 87-93.
- YE, G. 2005. Percolation of capillary pores in hardening cement pastes. *Cement and Concrete Research*, 35, 167-176.
- YILMAZ, V. T., SAGOE-CRENTSIL, K. K. & GLASSER, F. P. 1992. Properties of inorganic corrosion inhibition admixtures in steel-containing OPC mortars Part 2: Electrochemical properties. *Advances in Cement Research*, 4, 97-102.
- YLMÉN, R., JÄGLID, U., STEENARI, B.-M. & PANAS, I. 2009. Early hydration and setting of Portland cement monitored by IR, SEM and Vicat techniques. *Cement and Concrete Research*, 39, 433-439.
- YOON, S. S., KIM, S. Y. & KIM, H. C. 1994. Dielectric spectra of fresh cement paste below freezing point using an insulated electrode. *Journal of Materials Science*, 29, 1910-1914.
- YOUNG, J. F., TONG, H. S. & BERGER, R. L. 1977. Compositions of Solutions in Contact with Hydrating Tricalcium Silicate Pastes. *Journal of the American Ceramic Society*, 60, 193-198.
- YU, Z., MA, J., YE, G., VAN BREUGEL, K. & SHEN, X. 2017. Effect of fly ash on the pore structure of cement paste under a curing period of 3 years. *Construction and Building Materials*, 144, 493-501.
- ZENG, Q., LI, K., FEN-CHONG, T. & DANGLA, P. 2012. Pore structure characterization of cement pastes blended with high-volume fly-ash. *Cement and Concrete Research*, 42, 194-204.
- ZHANG, X., DING, X. Z., LIM, T. H., ONG, C. K., TAN, B. T. G. & YANG, J. 1995. Microwave study of hydration of slag cement blends in early period. *Cement and Concrete Research*, 25, 1086-1094.
- ZHANG, X., DING, X. Z., ONG, C. K., TAN, B. T. G. & YANG, J. 1996. Dielectric and electrical properties of ordinary Portland cement and slag cement in the early hydration period. *Journal of Materials Science*, 31, 1345-1352.

